Academic Press is an imprint of Elsevier
The Boulevard, Langford Lane, Kidlington, Oxford, OX51GB, UK
32 Jamestown Road, London NW1 7BY, UK
Radarweg 29, PO Box 211, 1000 AE Amsterdam, The Netherlands
225 Wyman Street, Waltham, MA 02451, USA
525 B Street, Suite 1900, San Diego, CA 92101-4495, USA

First edition 2012

British Library Cataloguing in Publication Data
A catalogue record for this book is available from the British Library

Library of Congress Cataloging-in-Publication Data
A catalog record for this book is available from the Library of Congress

ISBN: 978-0-12-397020-6
ISSN: 0066-4103

Printed and bound in Great Britain
12 13 14 11 10 9 8 7 6 5 4 3 2 1

CONTRIBUTORS

Ruud L.E.G. Aspers
Radboud University, Institute for Molecules and Materials, Biophysical Chemistry, Heyendaalseweg, Nijmegen, The Netherlands

Bruce J. Balcom
MRI Research Centre, Department of Physics, and Department of Chemistry, University of New Brunswick, P.O. Box 4400, Fredericton, New Brunswick, Canada

Teresa Blasco
Instituto de Tecnología Química (UPV-CSIC), Universidad Politécnica de Valencia-Consejo Superior de Investigaciones Científicas, Avda. de los Naranjos, s/n, Valencia, Spain

Angel C. de Dios
Department of Chemistry, Georgetown University, Washington, DC, USA

Martin Jaeger
DSM Nutritional Products Ltd., Analytical Research Center, Wurmisweg, Kaiseraugst, Switzerland

Cynthia J. Jameson
Department of Chemistry, University of Illinois at Chicago, Chicago, Illinois, USA

Luís Mafra
Department of Chemistry, CICECO, University of Aveiro, Aveiro, Portugal, and Departamentos de Química Física y Analítica y Química Orgánica e Inorgánica, Universidad de Oviedo, Oviedo, Spain

Colleen E. Muir
MRI Research Centre, Department of Physics, and Department of Chemistry, University of New Brunswick, P.O. Box 4400, Fredericton, New Brunswick, Canada

José Alejandro Vidal-Moya
Instituto de Tecnología Química (UPV-CSIC), Universidad Politécnica de Valencia-Consejo Superior de Investigaciones Científicas, Avda. de los Naranjos, s/n, Valencia, Spain

PREFACE

As is usual in this series of reports, Volume 77 of *Annual Reports on NMR Spectroscopy* consists of accounts of recent progress in several areas of molecular science. The volume commences with a discussion of 'Recent Advances in Nuclear Shielding Calculations' by A. C. de Dios and C. J. Jameson; this is followed by a review of 'Pure Phase Encode Magnetic Resonance Imaging of Fluids in Porous Media' by C. E. Muir and B. J. Balcom; M. Jaeger and R. L. E. G. Aspers report on 'Steroids and NMR'; the final chapter, by L. Mafra, J. A. Vidal-Moya and T. Blasco, covers 'Structural Characterization of Zeolites by Advanced Methods of Solid State NMR Spectroscopy'. It is a great pleasure for me to thank all of the contributors for their timely and significant contributions.

G. A. Webb
Royal Society of Chemistry
Burlington House
Piccadilly
London
UK

CHAPTER ONE

Recent Advances in Nuclear Shielding Calculations

Angel C. de Dios*, Cynthia J. Jameson†
*Department of Chemistry, Georgetown University, Washington, DC, USA
†Department of Chemistry, University of Illinois at Chicago, Chicago, Illinois, USA

Contents

Annual Reports on NMR Spectroscopy, Volume 77
ISSN 0066-4103
http://dx.doi.org/10.1016/B978-0-12-397020-6.00001-5

Abstract

Nuclear magnetic shielding calculations have reached a great deal of sophistication, as these now incorporate both relativistic and correlation effects. Approaches now include molecular dynamics as well as effects of the medium in condensed phases. With these computational tools, calculated shielding values are now obtained under conditions as close as possible to those of a sample inside a nuclear magnetic resonance spectrometer. Indeed, computations are approaching the limits of experimental uncertainty. A brief description of new methodologies of shielding calculations is presented followed by a review of the various factors that may influence shielding. The usefulness of being able to reproduce experimental data is highlighted by citing how shielding calculations in many instances have enabled avenues for extracting information on various systems.

Key Words: Absolute shielding, Chemical shifts, Chirality, Cluster models, Conformational dependence, Density functional theory, Disorder in crystals, Electron correlation, Four-component calculations, Gas phase NMR, Hydrogen bonds, Intra- and intermolecular effects, Isotope shifts, Medium effects, Molecular dynamics, NMR crystallography, Non-bonded interactions, Periodic boundary calculations, Polarizable continuum model, Polymorphs, Pseudopotentials, Relativistic calculations, Rovibrational averaging, Shielding surfaces, Structure determination, Temperature dependence, Tensor, Torsion angles, Two-component calculations

ABBREVIATIONS

AE all-electron
BO Born–Oppenheimer
BPPT Breit Pauli perturbation theory
CCSD coupled cluster singles and doubles
CFP charge field perturbation
CI configuration interaction
COSMO conductor-like screening model
CPMD Car-Parinello molecular dynamics
CSGT continuous set of gauge transformation
DFT density functional theory
DHF Dirac–Hartree–Fock
ECP effective core potential
EIM embedded ion method
EPR electron paramagnetic resonance
GAPW Gaussian and augmented plane-wave method
GGA generalized gradient approximation
GIAO gauge-including atomic orbitals
GIPAW gauge-including projector augmented wave
HAHA heavy atom heavy atom
HALA heavy atom light atom
HF Hartree–Fock
HOMO highest occupied molecular orbital
IGAIM individual gauge for atoms in molecules

KS Kohn–Sham
LAPW linear-augmented plane waves
LDA local density approximation
LHF-CEDA localized Hartree-Fock-common energy denominator Green's function approximation
LLH localized local hybrid
LMF local mixing function
LR-ESC linear response elimination of small component
LUMO lowest occupied molecular orbital
MAS magic angle spinning
MB-GIAO magnetically balanced gauge-including atomic orbitals
MC Monte Carlo
MD molecular dynamics
MM molecular mechanics
NAO numeric atomic orbital
NBO natural bond orbital
NICS nucleus independent chemical shift
NMR nuclear magnetic resonance
OEP optimized effective potential
OOD occupied-orbital dependent
PAW projector augmented wave
PBC periodic boundary conditions
PCM polarizable continuum model
PES potential energy surface
PW plane wave
QM quantum mechanics
RMB restricted magnetic balance
RPA random phase approximation
RSC relativistic small core
SCF self-consistent field
SCREEP surface charge representation of the electrostatic embedding potential
SO spin–orbit
SPARTA shift prediction from analogy in residue type and torsion angle
SPC simple point charge
SSNMR solid-state nuclear magnetic resonance
STO Slater-type orbitals
SWNT single-walled nanotube
USPP ultrasoft pseudopotential
XC exchange correlation
XRD X-ray diffraction
ZORA zeroth-order regular approximation

1. OVERVIEW OF THIS REVIEW

Monographs on shielding calculations have traced the advances in this field over the years: Nuclear Magnetic Shieldings and Molecular Structure (1993),[1] Modeling NMR Chemical Shifts: Gaining Insights into Structure and Environment (1999),[2] Calculation of NMR and EPR (electron paramagnetic resonance) Parameters: Theory and Applications (2004).[3] Reviews on shielding calculations have been published in various venues.[4–8] In addition, a review of *ab initio* shielding calculations as an emerging tool for protein structure determination[9] and of the PAW/GIPAW approach for the study of solids[10,11] have been published. The physical and theoretical aspects of nuclear shielding are reported on an annual basis in Specialist Periodical Reports on NMR.[12]

Early reviews of shielding calculations include the two reviews in this particular series of volumes (vol. 29, 1994).[13,14] Excellent recent reviews in this series have detailed the theoretical basis for the relativistic and density functional theory (DFT) methods for nuclear shielding computations.[15,16] We do not repeat a development of these theoretical foundations here. Rather we update with recent developments in exchange-correlation functionals (since the Wilson review in vol. 49, 2003) and in relativistic computations (since the Autschbach review in vol.67, 2009). To minimize duplication, we have limited this review primarily to papers published in 2004 and later.

A crucial role of theoretical calculations is for understanding physical systems, thus we stay connected to the concepts and motivations of experimentalists but use a limited number of examples which illustrate the quality and reliability of the information that calculations provide. For example, in part 2 of this review, we discuss how important are relativistic effects on shielding and which parts of the corrections are largest for what systems. We consider here the current thinking about which of the exchange and correlation functionals works best for which types of systems. In reviewing theoretical calculations in parts 3–6, we have grouped examples, such as to serve as a guide to approaches that have worked well for various types of systems. Thus, in part 3, we consider cases where single molecule calculations may be used, and cases where model fragments are the best systems for understanding the dependence on conformation separately from other factors, and cases where using supramolecular clusters including interacting neighbours is the most logical approach, especially when hydrogen bonding is involved. We review

various approaches in including subtle quantum effects such as electrostatic field effects from distant neighbours that influence the electron distribution of the local neighbour atoms and therefore affect the shielding of the nucleus in question. Local effects are paramount in understanding shielding in a majority of cases; thus, approaches that focus on local effects, using clusters and fragments and embedding them in a charge field may often be the most logical theoretical approach. On the other hand, some aspects of shielding in extended networks cannot be properly treated by using local approaches such as cluster and fragment models, and we have to consider the long-range effects of the entire network by doing calculations in periodic systems; this is especially true for covalent solids. Thus, in part 4, we discuss calculations which use methods which have been developed for these systems, theoretical methods that have become an important tool for experimentalists making measurements in the solid state. In part 5, we consider dynamic effects. For some systems, dynamic averaging is such a significant part of the observed chemical shift that calculations using a static geometry (atomic coordinates) do not provide the whole shielding story and may even lead to incorrect assignments of chemical structure. We consider both rovibrational averaging, which leads to isotope shifts and temperature dependence of shielding even in the gas phase, and dynamic averaging in condensed systems, notably in liquids. There are different approaches which have been used, and we consider which of the approaches is most logical for the type of system at hand. In the earlier parts, we discuss how the physical aspects of the system (bond length, bond angles, torsion angles, presence of neighbours, dynamics of bonded and non-bonded atoms, relativistic neighbours bonded and otherwise) have to be introduced into the model so as to carry out a proper calculation that can be compared with experimental measurements. In part 6, we discuss how to turn the information arrow the other way around: in favourable circumstances, what can the observed differential shieldings tell us about the nature of the physical system? Here, we provide some examples where theoretical calculations have been used to verify hypothetical information about the physical system under study.

2. ADVANCES IN METHODS OF CALCULATION

2.1. Relativistic calculations

In the calculations of nuclear magnetic shielding, the vector potential produced by the nuclear magnetic moment is very local and therefore affords a weighted sampling of the electronic wavefunction in the close vicinity of the

nucleus. Thus, the nuclear magnetic shielding in a molecular system is intrinsically an all-electron relativistic property. Methods and application of relativistic approaches to the calculation of nuclear shielding have been reviewed by Autschbach in this series of volumes in 2009. Therefore, in this review, we consider developments from 2009 on.

Conceptual and computational difficulties have conspired to delay the availability of fully four-component all-electron treatments at correlated levels using distributed gauge origins. However, the situation is largely clearing up. A difficulty particular to relativistic calculations of magnetic properties originates from the fact that the inclusion of a vector potential affects the balance between the large and the small components of the four-component spinors. This magnetic balance must be taken into account, explicitly or implicitly, in order to obtain accurate results for magnetic properties. An important difference between relativistic and nonrelativistic theory is the lack of an explicit diamagnetic term in the Hamiltonian in relativistic theory. However, the diamagnetic term enters through the contribution of negative energy states. The negative energy states are important for nuclear shielding because magnetic fields are introduced through operators which couple the large and small components, so the negative energy states cannot be neglected in relativistic treatment of magnetic properties, but it has been suggested that they may be treated in a simplified manner.[17] Extremely compact negative energy states require additional steep *s* and *p* functions in the basis set when highly accurate absolute NMR shieldings are sought. Effects of highly compact negative energy states essentially cancel out for relative shieldings (chemical shifts).[18] Kutzelnigg proposed a field-dependent unitary transformation of the four-component relativistic Hamiltonian in order to introduce an explicit diamagnetic term.[19] When magnetic balance between the small and large components is explicitly built in, the otherwise missing diamagnetism arises naturally[20] and the heavy demand on the basis sets of high angular momenta is also greatly alleviated.

Several groups considered a unified approach to four-component relativistic treatment of nuclear shielding nearly simultaneously. Kutzelnigg and Liu presented the formulation of a logical and systematic classification of existing methods of calculations of NMR parameters within relativistic quantum chemistry, together with new variants and presented new methods as well.[21] Various methods have been reported separately in this series over several years; the Kutzelnigg and Liu analysis puts all systematically in the proper context. They consider transformations at operator level versus matrix level, the possible formulations of the Dirac equation in a magnetic field,

traditional relativistic theory, field-dependent unitary transformation, bispinor decomposition, equivalence of the methods at operator level. They then consider relativistic theory in a matrix representation, expansion in unperturbed eigenstates, expansion in a kinetically balanced basis, and expansion in an extended balanced basis. The authors explore decomposition of the lower component, decomposition of the full bispinor, unitary transformation at the matrix level. They pay careful attention to singularities. First they discuss methods which are exact in the sense that their accuracy is only dependent on the quality of the chosen basis. In the limit of a complete basis, all these methods yield the same results, but the rate of convergence to the limit can be different.[21] Among these methods, they consider the ones best suited for each of the magnetic properties. For the case of nuclear magnetic shielding where one vector potential is due to an external field and one is due to a nuclear magnetic dipole, they suggest to discard the method based on the untransformed Dirac operator because it does not give the correct nonrelativistic limit. They also suggest to discard the method based on a unitary transformation of the full magnetic field because it is plagued by singularities. They offer the good choice as the method based on a unitary transformation of the external field only and formalisms equivalent to it because these lead to the correct nonrelativistic limit and are not plagued by singularities. They also recommend as a further possibility the method called FFUTm (full-field unitary transformation "at matrix level") by Xiao *et al.*,[22] where one starts formally from a unitary transformation at matrix level but evaluates the diamagnetic term exactly. They suggest that the restricted magnetic balance (RMB)[17] should be used. The performance of the various methods with respect to the basis set requirement has recently been investigated by Cheng *et al.*[18] The results differ very little, even for a small basis. Finally, Kutzelnigg and Liu[21] consider various approximations previously proposed which do not give the exact results in the limit of a complete basis, for example, see Xiao *et al.*[22] All of these approximations are based on methods which give the correct nonrelativistic limit and use a pseudo sum-over-states formulation with the restriction of the intermediate eigenstates to those with positive energy. Along the way, various commonly used approximations such as the Douglass-Kroll-Hess approximation[23] and the zeroth-order regular approximation (ZORA)[24] are discussed in context.

Cheng *et al.* showed that these variants of approaches using magnetic balance can all be recast into one unified form.[18] The various schemes previously proposed for incorporating the magnetic balance dependence are then shown to be equivalent to this new approach and therefore can be combined

with any level of theory for electron correlation. As mentioned in the analysis of Kutzelnigg and Liu, it has been recognized recently that the incorporation of the magnetic balance condition between the small and large components of the Dirac spinors is absolutely essential for four-component relativistic theories of magnetic properties. Cheng *et al.*[25] showed that the magnetic balance can be adapted to distributed gauge origins, leading to, for example, magnetically balanced gauge-including atomic orbitals (MB-GIAOs) in which each magnetically balanced atomic orbital has its own local gauge origin placed on its centre.[25] This MB-GIAO scheme can be combined with any level of theory for electron correlation.[26] Close inspection reveals that zeroth-order negative energy states are only important for the expansion of first-order electronic core orbitals. Their contributions to the paramagnetism are therefore transferable from atoms to molecule and are essentially cancelled out when taking shielding differences for chemical shifts.[25] As did Kutzelnigg and Liu, Cheng *et al.* also provided, in their introduction, critical remarks on the various schemes for relativistic calculations of NMR properties, classifying and comparing, noting where singularities occur and where numerical instabilities could occur, comparing various schemes to recover the relativistic diamagnetic contributions to the nuclear shielding, such as to guarantee the correct nonrelativistic limit.

Komorovsky *et al.* have also incorporated the gauge-including atomic orbitals (GIAO) approach in relativistic four-component DFT method for calculation of NMR shielding tensors using restricted magnetically balanced basis sets.[27] The authors carried out relativistic calculations for xenon dimer and the HX series (X = F, Cl, Br, I), where spin–orbit (SO) effects are known to be very pronounced for hydrogen shielding. It is not surprising that, when compared to shielding calculated at the four-component level with a common gauge origin, the results clearly demonstrate that the GIAO approach solves the gauge-origin problem in fully relativistic calculations as it does in the nonrelativistic case. Finally, what had been routine (use of GIAOs) for nonrelativistic calculations of shielding is becoming an integral part of four-component calculations of nuclear shielding. The formulation by Olejniczak *et al.*[28] is in many aspects similar to the one proposed by Komorovský *et al.*[17] except for a fully analytical approach and a possibility to use hybrid exchange-correlation (XC) functionals. To test their formalism, they carried out calculations of NMR shielding tensors for the HX series (X = F, Cl, Br, I, At), the Xe atom, and the Xe dimer.

In addition to the formulation of four-component relativistic theory of NMR parameters,[18] Cheng and co-workers[29] also presented an exact

two-component relativistic theory for nuclear magnetic shielding (and magnetizability and J coupling). This is obtained by first a single block-diagonalization of the matrix representation of the Dirac operator in a magnetic-field-dependent basis and then a magnetic perturbation expansion of the resultant two-component Hamiltonian and transformation matrices. They showed that all the problems (singularities, numerical instabilities) associated with the earlier attempts at an exact two-component treatment of NMR parameters can be avoided by going to a matrix formulation. That is, the matrix representation of the full Dirac operator in a magnetic-field-dependent basis can be block-diagonalized in a single step, just like the previous matrix formulation of the exact two-component algebraic Hamiltonians in the absence of magnetic fields. The resulting Hamiltonian and transformation matrices can then be expanded to obtain the expressions for NMR parameters. Such a matrix formulation is not only simple but also general in the sense that the various ways of incorporating the field dependence can be treated in a unified manner. The diamagnetic and paramagnetic terms agree individually with the corresponding four-component ones up to machine accuracy for any basis. The authors suggest that this formulation be adopted in lieu of quasi-relativistic theories that had been used previously.[29]

Polarization propagators have been successfully applied since the 1970s to calculate NMR parameters. They are special theoretical devices from which one can do a deep analysis of the electronic mechanisms that underlie any molecular response property from basic theoretical elements, such as molecular orbitals, electronic excitation energies, coupling pathways, entanglement, contributions within different levels of theory, etc. All this is obtained in a natural way in both regimes: relativistic and nonrelativistic. In a review article, Aucar *et al.*[30] discuss the new insights on magnetic shielding from relativistic polarization propagators, using model compounds CH_3X molecules (X = F, Cl, Br, I) and XH_n (X = Xe, I, Te, Sb, Sn; $n = 0$–4) as examples.

2.1.1 Four-component relativistic calculations

Maldonado *et al.* investigated the application of different magnetic kinetic balance prescriptions using the four-component polarization propagator approach in the calculation of nuclear magnetic shielding.[31] They find that, while working with relativistic polarization propagators, there is no formal requirement to enforce the application of magnetic kinetic balance prescription. The performance of various prescriptions was studied for molecules containing more than one heavy atom in order to examine the electronic

effects on the shielding of a heavy atom due to the presence of vicinal heavy atoms. The shieldings of X, Y, and H nuclei in XYH_3 molecular systems with X = C, Si, Ge, Sn and Y = Br, I were calculated thereby reproducing the HALA effect (vicinal heavy atom effect on the shielding of the light atom). The total shielding for ^{13}C in CH_3I is 235.57 ppm compared to ^{13}C in CH_4 where the total shielding is 195.55 ppm. Relativistic effects on the shielding of X due to heavy halogen atoms are larger for heavier X nuclei, which authors refer to as HAVHA + HAHA effects (heavy atom effects on the shielding of the vicinal heavy atom + heavy atom effects on its own shielding). The hydrogen shieldings exhibited an effect from the two-bond distant heavy atom Br or I; this effect is found to be more pronounced when the central atom is X = Si. All of these results are at the random phase approximation (RPA) level and so did not include electron correlation.[31]

Arcisauskaite *et al.*[32] investigated the importance of relativistic effects on NMR shielding tensors and chemical shifts of linear HgX_2 (X = Cl, Br, I, CH_3) compounds using three different relativistic methods: the fully relativistic four-component approach and the two-component approximations, linear response elimination of small component (LR-ESC), and ZORA. LR-ESC reproduces successfully the four-component results for the ^{13}C isotropic shielding value in $Hg(CH_3)_2$ within 6 ppm but fails to reproduce the ^{199}Hg shielding tensors and chemical shifts. The latter is mainly due to an underestimation of the change in SO contribution. Even though ZORA underestimates the absolute (relative to the bare nucleus) Hg NMR shielding values by ~2100 ppm, the differences between ^{199}Hg chemical shift values obtained using ZORA and the four-component approach without spin–density contribution to the exchange-correlation (XC) kernel are less than 60 ppm for all compounds using three different functionals, BP86, B3LYP, and PBE0. However, larger deviations (up to 366 ppm) occur for ^{199}Hg chemical shifts in $HgBr_2$ and HgI_2 when ZORA results are compared with four-component calculations.[32]

Relativistic calculations of NMR properties of RgH^+ ion (where Rg = Ne, Ar, Kr, Xe), ^{195}Pt shielding in platinum complexes, and ^{207}Pb shielding in solid ionic lead(II) halides have been reported.[33] For the Rg nucleus in the RgH^+ ions, four-component Dirac–Hartree–Fock (DHF), two-component (ZORA), nonrelativistic correlated, and nonrelativistic uncorrelated methods were used and results compared with each other. The difference between the DHF and HF (Hartree–Fock) calculations shows that for the Rg nucleus the relativistic effect on shielding scales with atomic number as $Z^{3.4}$. There are small effects on the shielding of the proton

in RgH^+ ion, 18.1, 5.2, 1.0, and 0.0 ppm in going from Xe to Ne, a trend similar to the one observed in the isoelectronic HX halides.[33] Seino and Hada likewise employed a four-component scheme to calculate the NMR shielding of the Hg atom.[34]

Relativistic four-component DFT-GIAO based calculations of ^{1}H NMR chemical shifts of a series of 3d, 4d, and 5d transition metal hydrides have revealed significant SO-induced heavy atom effects on the hydride shifts, in particular for several 4d and 5d complexes.[35] The SO effects provide substantial, in some cases even the dominant, contributions to the well-known characteristic high-field hydride shifts of complexes with a partially filled d-shell, thereby augmenting the Buckingham–Stephens model[36] of off-centre paramagnetic ring currents. In contrast, complexes with a $4d^{10}$ and $5d^{10}$ configuration exhibit large deshielding SO effects on their hydride ^{1}H NMR shifts.

2.1.2 Two-component calculations

Despite the new developments in four-component relativistic calculations of shielding described above, most relativistic shielding calculations are carried out with various two-component methods, DFT ZORA being the most commonly used method. Nuclear magnetic shieldings on the heavy atom for the systems $SnXH_3$ (X = H, F, Cl, Br, I), $SnXYH_2$ (X, Y = F, Cl, Br, I), and $PbXH_3$ (X = H, F, Br, I) were calculated using LR-ESC and compared to benchmark RPA calculations and then analyzed in order to determine the main trends and discuss the electronic origin of the shielding of two kinds of atoms involved in such systems: central and substituent atoms.[37] DFT ZORA calculations have been carried out with or without SO in a large number of systems, for example. ^{195}Pt shieldings in complexes,[38,39] ^{187}Os in osmium phosphines,[39] ^{207}Pb in cluster models of lead(II) halides,[40] ^{183}W in the polyoxometalates of W and Au,[41] ^{77}Se shielding in 40 molecules,[42] and for ^{195}Pt and ^{207}Pb in the $[Pt@Pb_{12}]^{2-}$ "superatom".[43]

Heavy atom effects on light atoms have also been demonstrated theoretically for ^{17}O in $[UO_2(OH)_4]^{2-}$,[44] ^{13}C in monohalo(F, Cl, Br, I) organic compounds,[45] ^{13}C and ^{14}N shielding in 6-halo(Cl, Br, I) purines,[46] ^{29}Si with Pd and Pt,[47] ^{13}C in methyl hydride complexes of Rh and Ir,[48] and ^{19}F in uranium chlorofluorides.[49]

2.2. Density functional calculations

The number of single point (one structure, usually the equilibrium structure) calculations of shielding reported annually[12] continues to grow. For single molecules, more important than the choice of functional is the use of an

energy-optimized geometry, preferably in the appropriate environment. The extreme sensitivity of shielding to bond lengths, angles, and torsions means that even X-ray diffraction (XRD) derived geometries need to be optimized. The widely accepted benchmarks for shielding calculations are the full-configuration interaction (CI) or coupled cluster singles, doubles, and triples calculations by Gauss *et al.*,[6,50,51] and they remain test systems against which any shielding calculation method should be checked. However, most systems of practical interest have larger numbers of electrons, therefore, for these systems, the method of choice has been DFT. There are many flavours of functionals in wide use, with or without admixture of exact exchange. When the perfect universal functional is found, no doubt the reliability of the results will be the same regardless of which part of the NMR Periodic Table is being investigated in organic, inorganic, or biomolecular systems. However, currently, some functionals perform better than others, depending on the nucleus of interest. Gauss's benchmarks only include molecules from which some reasonable absolute shielding scale has been developed, that is, where gas phase measurements have been done towards the isolated molecule limit. It is well known that cancellation of systematic errors can occur in calculating differences in shielding rather than absolute shielding (shielding in the system of interest relative to the bare nucleus). Therefore, the true test of a theoretical method is to be able to reproduce the full absolute shielding tensor as Gauss has done for light systems. Unfortunately, for many heavy nuclei this is not a possibility. Precisely for heavy atom nuclei, the identity that connects the spin rotation tensor and the shielding tensor,[52,53] in nonrelativistic theory does *not* hold in the relativistic domain. This has been proven experimentally by Wasylishen and co-workers by measuring the shielding tensors for XeF_2 in the solid state.[54] Here, there are well-defined shielding reference systems, the isolated Xe atom and the well-established ^{19}F absolute shielding scale (see a review of this proof in Ref. 55). Aucar et al. have carried out an analysis of the relativistic spin-rotation tensor and the nuclear magnetic shielding tensor by deriving in parallel the expressions for these tensors, considering relativistic electrons and non-relativistic nuclei for a molecule with a singlet ground state.[56] The coupling of the electronic distribution to the magnetic field is described by the vector product of the position and velocity operator, while the coupling of the electronic state and the rotational state is described by the total angular momentum operator. These quantities are simply related at the non-relativistic limit, but in relativistic quantum mechanics, the two operators couple the upper and lower components of the 4-component wavefunction very differently.

A combination of lack of gas phase absolute shieldings and the prevalent condensed phase environments, with attendant complexities of structural dependence on solution conditions, makes it difficult to judge which of the used functionals works best for calculations of transition metal shieldings, for example. At best, it is possible to observe whether the slope of calculated chemical shifts (usually using one of the compounds in the set as the reference) versus experimental chemical shifts is close to 1.0 for a wide range of compounds. Bühl has carried out many such comparisons for several transition metal nuclei, comparing the performance of different functionals. Hybrid functionals perform somewhat better for Ru chemical shifts, for example. This is in contrast to the situation for light, main-group nuclei where generalized gradient approximation (GGA) functionals (such as KT1 and KT2) can be more accurate than hybrid functionals.[57] For the present, the slope of the chemical shift plot for the whole range of compounds may be the best test, but it suffers from an inability to detect cancellation of systematic errors (in the treatment of core electrons, for example), and it could be misleading when the solution environment imposes differing amounts of environmental contributions for different compounds, as when a mix of neutral and charged complexes are included. Transition metal complexes that have net charge cannot be compared directly with uncharged carbonyl complexes, for example.

Since the Wilson review of this topic in this series (vol. 49, 2003), research on improvements on the currently available exchange-correlation functionals remains an important and active area of theoretical research. Despite the great success of global hybrid functionals, for example, B3LYP and PBE0, in predicting various molecular properties, they turned out not to be sufficiently flexible: It is usually not possible to find a unique constant for the amount of exact-exchange admixture that provides consistently high accuracy for different properties as well as for different classes of systems.

The Tozer group has been developing methods of devising corrections that improve the structure of the exchange-correlation potential, in particular, using the challenging diatomic molecules CO, N_2, and PN as the systems for testing.[58] They developed the KT1 and KT2 GGA functionals designed specifically to provide high-quality NMR shielding tensors. For shieldings in molecules of light main group elements, the results using KT1 and KT2 are encouraging; errors approach those of correlated wavefunction methods.[59] They also developed a new functional KT3 by an introduction of additional gradient-corrected exchange and correlation terms which preserve the high-quality shielding calculations of KT1 and KT2 and compared the performance with other GGAs.[60] For Se

compounds, they find that KT3 can simultaneously provide good quality geometries and ^{77}Se shielding tensors, without the inclusion of exact exchange, whereas the widely used B3LYP functional gave relatively poor results.[57] Tozer *et al*. have been studying the influence of optimized effective potential (OEP) and Coulomb-attenuation in DFT calculations of shielding and chemical shifts.[61]

Kaupp has been very active in constructing improved functionals that are still computationally efficient yet more accurate than existing ones. As he also has an active program in calculating NMR properties, the functionals he develops are tested for performance not only in thermochemistry and reaction barriers but also for NMR properties such as shielding and spin–spin coupling, in particular. Local hybrid functionals are a promising new generation of exchange-correlation functionals. In contrast to the constant exact-exchange admixture of global hybrids, local hybrids include exact exchange in a position-dependent way, governed by a "local mixing function" (LMF). Therefore, considerable effort has been spent recently in developing a hybrid function which determines the position-dependence of the exact-exchange admixture.[62] Recently, Arbuznikov and Kaupp reviewed the advances in hybrid functionals and discussed different strategies to construct LMFs (semiempirical vs. *ab initio*), different levels of the implementation of local hybrids (self-consistent vs. non-self-consistent), and some methodological aspects associated with the calculation of second-order magnetic properties (a coupled-perturbed scheme for general hyper-GGA functionals).[63] They provided some examples for the performance of local hybrids in the description of NMR properties. Localized local hybrid (LLH) potentials derived from corresponding local hybrid functionals with position-dependent exact-exchange admixture governed by appropriate LMFs were tested in calculations of nuclear shielding in molecules containing main-group nuclei and found to yield results that were comparable to those from global hybrid functionals, but this was achieved without generalized gradient corrections.[64] A more detailed examination of the performance of local hybrid functionals for NMR properties is given in Ref. 65 where recent work in the field of occupied-orbital dependent (OOD) exchange-correlation functionals in DFT is reviewed, with emphasis on the development of local hybrid functionals, and on the nontrivial self-consistent implementation of complex OOD functionals. Recently proposed LMFs have provided local hybrids of high accuracy in the computation of thermochemical data and with good performance for some magnetic resonance parameters. These local hybrids require very few semiempirical parameters. Two levels of the self-consistent implementation of

OOD functional are discussed: one may stop after the derivation of the functional derivatives with respect to the orbitals, leading to nonlocal potentials. This is discussed for local hybrids and for general OOD functionals up to and including the complicated B05 real-space model of nondynamical correlation. Alternatively, one may append an additional transformation to local and multiplicative potentials based on the OEP approach or of approximations to the OEP.[66] The localized Hartree–Fock-common energy denominator Green's function approximation (LHF-CEDA) to the OEP has been used to compute nuclear shielding tensors within an uncoupled Kohn–Sham (KS) framework.[67] The OEP approach has been tested with conventional hybrid functionals B3LYP and PBE0 for calculations of transition metal shieldings (Ti, Cr, Mn, V) in selected complexes and the results are an improvement over conventional hybrid values.[68] Numerical results for performance of local hybrid functionals for various properties including nuclear magnetic shielding have been reviewed.[65]

3. LOCAL EFFECTS ON SHIELDING: SINGLE MOLECULES, CLUSTERS, AND FRAGMENTS

That which makes the observed NMR chemical shift an extremely useful tool is the exquisite sensitivity of shielding to small differences in electronic environment. Of course, in turn, this means that theoretical calculation methods have to meet the challenge of explicitly including these factors. Our increasing ability to do quantum calculations for larger collections of atoms means that larger parts of the chemical environment can *a priori* be included in the theoretical system under study. Complete success would mean that we could reproduce measured values to experimental accuracy. Towards this goal, we have noted above that shielding calculations using four-component wavefunctions are beginning to be accessible and exchange–correlation functionals are being devised which are suitable for the demanding description that shielding calculations require more than does calculation of thermochemical data. Meanwhile, NMR practitioners still value the insight that can be gained by including various parts of the chemical environment of the nucleus, focusing on one or more factors at a time, thereby discovering what knowledge is largely transferable from one physicochemical system to another. In this section, we consider the current approaches to include various intra- and intermolecular effects on shielding. Even with increased computational capabilities, the use of small molecular fragment models or clusters to reproduce local effects, either via conformation or non-bonded interactions, continues to be a method

of choice. The information derived from these model calculations permits in most cases a decomposition of the NMR chemical shifts into its various contributing factors, and at times, fortunately provides one dominant element that determines the experimentally observed differences in NMR chemical shifts.

3.1. Conformational effects

With a firm basis supported by *ab initio* calculations that show convincingly that protein NMR shieldings are intimately dependent on backbone torsion angles, NMR chemical shifts are now widely recognized as important determinants of protein secondary structure. SPARTA (shift prediction from analogy in residue type and torsion angle) from Shen and Bax[69] is one example that utilizes a database of assigned protein chemical shifts and known X-ray structures. On the theoretical front, theoretical shielding surfaces that describe the dependence of NMR shielding on backbone torsion angles using *N*-formyl-$(Ala)_3$-NH_2 have been shown to be adequate in qualitatively describing backbone chemical shifts of all amino acid residues except Cys.[70] Taking into account motional averaging of $^{13}C^{\alpha}$ chemical shifts, thousands of computations can now be performed on model fragments, resembling hundreds of possible conformations, thereby allowing for the evaluation or validation of NMR-derived protein structures.[71] And as expected, one consequence of averaging is a reduction in the chemical shift anisotropy, as noted by Tang and Case[72] in their study of ^{15}N sites in peptides.

The success in understanding conformational effects on protein chemical shifts originates from the success in predicting these changes in small molecules. Confidence in this approach, as achieved in smaller systems, has led to its application to other larger systems, some of biochemical interest. With a fragment model consisting of a dimethyl phosphate and water molecules in the first solvation shell, a description of how ^{31}P shieldings in DNA are affected by the phosphate backbone torsion angle has been accomplished.[73] Other examples along this line of research involve studies on polymorphs,[74–81] confined molecules,[82] substituted calixarene systems,[83] sugars,[84,85] α, β-unsaturated carbonyl compounds,[86] and phase transitions.[87]

3.2. Neighbouring non-bonded atom effects

We consider (a) van der Waals contribution to the shielding which arise from the shielding response of the electrons of the neighbour atoms in interactions with the electrons of the atom in question and (b) the shielding contributions from the electrons of the neighbour atoms that would be

present even for a nuclear magnetic dipole at that position without its own electrons. The latter is independent of the nucleus under study, commonly referred to as NICS (nucleus independent chemical shift). The latter (NICS) is usually small compared to the former contribution to intermolecular shielding and is the same for all nuclei, so it is a relatively significant intermolecular effect only in the case of proton shielding. Also, NICS can be significant when aromatic rings are present, so it is often discussed in terms of "ring current" contributions.

In the field of intermolecular effects on NMR shielding, ^{129}Xe remains a nucleus of choice. The unsurpassed versatility of ^{129}Xe shielding is dramatically demonstrated in diastereomeric ^{129}Xe chemical shieldings, when Xe is placed inside a chiral cage, such as cryptophane-A, with a chiral compound attached to the cage. Calculations permit the assignment of the individual peaks in the diastereomeric sets.[88] Using O_2 as a model paramagnetic compound, even the changes in ^{129}Xe line shapes for Xe gas inside nanochannels containing paramagnetic impurities have been theoretically predicted.[89] Constitutive (CH_3, CH_2 contributions) solvent effects on ^{129}Xe shieldings of Xe dissolved in normal and cyclic alkanes have been theoretically determined,[90,91] again, with the use of model fragments.

Calculations of molecular shielding surfaces, the nuclear magnetic shielding at points in space around a molecule that would be experienced by a probe magnetic moment such as that of a neutron probe (sometimes referred to as NICS) provide visualization and quantification of the magnetic anisotropy effects arising from aromatic rings, C═C double bonds, or other groups. Ring currents can be an important factor in understanding and utilizing intermolecular NMR chemical shifts. For calculations of these contributions to shielding, there is likewise a need to take the appropriate cluster unit for the quantum calculations, for example, a trimer.[92] On account of the marked dependence of the ^{1}H chemical shift to ring currents arising from nearby aromatic rings, the calculated ^{1}H chemical shifts are found to be very sensitive to the stacking arrangement of the hexabenzocoronene molecules. Moreover, the ring current effect is found to be particularly long range, with a considerable influence of the second neighbour, at a distance of 700 pm, being observed. Modelled by a trimer structure, the shielding values for the molecule in the middle are then compared against experiment.

The visualization and interpretation of ring currents remains an active field of research. Ring currents have been shown, for example, to be dominated by contributions from the HOMO–LUMO virtual excitations,[93] as suggested by ipsocentric calculations on benzene, cyclooctatetraene,

borazine, coronene, and corrannulene. This approach has been extended to relatively large polycyclic aromatic compounds containing up to 438 carbon atoms.[94] Stagnation graphs displaying both vortices and saddle lines of the current density have also been drawn to explain general features in diatropic molecules.[95,96] Plots of magnetic shielding density combined with a visualization of the current density allow for a detailed interpretation of aromaticity and sigma ring currents, as exemplified in the simple model of a cyclopropane molecule.[97] Spatial models have been constructed likewise to display current densities around small molecules such as LiH, BeH_2, CO_2, C_2H_2, and C_2H_4.[98,99] Lastly, computations of magnetic shielding at points in space in the vicinity of small model molecules (NICS) are still widely used in quantifying anisotropy effects from aromatic rings and other groups containing a double bond. Examples include rigid cyclophanes and their derived carbocations,[100] inorganic clusters of boron,[101] highly congested hydrocarbons that contain alkene groups,[102] nitrate ion in complexes,[103] trisannelated benzenes,[104] fullerenes,[105] cyclobutadiene dianion derivatives,[106] calicene,[107] tetraazanapthalenes,[108] metallabenzenes,[109] and 9-arylfluorenes.[110]

3.3. Hydrogen-bonding effects

Hydrogen bonding, with its prevalence in nature, is an important factor for medium effects on NMR shielding. The most important effects are on the shielding of the donor atom, the acceptor atom, and the bridging H itself, but there are effects on neighbouring atoms of the donor and acceptor as well, especially when those atoms are themselves involved in hydrogen bonds. Duma *et al.* have recently summarized ways by which solid-state NMR can be used to characterize hydrogen bonding. These include not only a study of the shielding tensors of the non-hydrogen atoms (e.g. ^{13}C and ^{15}N) but also ^{1}H chemical shifts and relaxation times, which provide important clues with regard to not only the strength but also the dynamics of hydrogen bonding.[111] The least shielded and intermediate components of the ^{15}N shielding tensors are significantly affected by hydrogen-bond formation. By closely deciphering the observed ^{1}H and ^{13}C chemical shifts in anomeric maltose, Yates *et al.*[112] have found a quantitative correlation between the NMR chemical shifts and the geometry (distance and angle) of weak CH···O hydrogen bonds.

Cluster calculations are oftentimes seen necessary for reproducing hydrogen-bond effects on shielding. For example, explicit water molecules in the first solvation shell for *N*-formyl-alanyl-X amides (where X is one of the naturally occurring amino acids) appear to be consequential in

reproducing correctly the amide ^{15}N chemical shifts.[113] Likewise, taking hydrogen bonding into account in calculations of shielding for H, N, and O nuclei in amino acids, peptides, proteins, nucleic acids, DNA, sugars requires including each hydrogen-bonding partner or its surrogate donor or acceptor in the cluster. Using an approach previously used for interpreting ^{13}C chemical shifts in proteins by varying the torsion angles in a model cluster, the variation in the ^{31}P shielding tensor components as a function of DNA and RNA backbone conformations has been predicted from calculations on a solvated model cluster dimethyl phosphate.[114] The ^{31}P nucleus also serves as a probe for hydrogen bonding and ionization states in phosphorylated serine residues.[115] More accurate calculations necessitate including the next shell of hydrogen-bonding partners beyond those partners of the molecule in question. Some examples are ^{17}O shielding calculations in crystalline urea by Wu and co-workers.[116] It took six neighbouring urea molecules at the crystallographic positions to provide a suitable cluster for calculations that could reproduce the experimental ^{17}O shielding tensor in urea.[116]

The number of hydrogen bonds is particularly important in interpreting the shielding tensors for Cl^- ions in various amino acid—HCl salts.[117] As the chloride ion is usually present as a counter ion in amino acid salts, ^{35}Cl NMR measurements and shielding calculations have likewise been performed on these systems.[118] The ^{35}Cl shielding in these compounds is sensitive to the type of hydrogen-bonding present, which, in turn, depends on the type or identity of amino acid.

Calculations of the ^{1}H and ^{17}O shielding tensor components in liquid water itself are challenging. For this system, a hybrid approach, one that uses a small core of water molecules (about 10) treated quantum mechanically while adding a self-consistent reaction field that models the environment, has been applied.[119] This model makes it possible to incorporate dynamics and the following elements of *ab initio* computations; effects of electron correlation, gauge-origin independence, and type of semiempirical potentials, on the quality of the calculations can then be properly evaluated. Further discussion of shielding calculations for liquid water, a challenging system, is found in Section 5.3.4.2.

3.4. Electrostatic field effects

Approximations for including solvent effects on NMR shieldings are available. These approximations basically describe the environment provided by solvent molecules with an electrostatic potential. The simplest approach is an

implicit solvent model, that is, to use a reaction field approximation for the medium. No specific interactions of the cluster with the solvent molecules are included, a dielectric continuum is assumed. Methods in wide use for geometry optimization and shielding calculations incorporating solvent effects using continuum models are the conductor-like screening model (COSMO)[120] and polarizable continuum model (PCM).[121] Another approach is by embedding of the cluster in a point charge field. The representation of the crystal lattice with point charge arrays in quantum mechanical nuclear magnetic shielding calculations was pioneered by de Dios *et al.*[122–124] in the charge field perturbation (CFP) method which they applied to proteins. In these calculations, the shielding for the nuclei of interest in a given subject molecule are computed at a high *ab initio* quantum mechanical level, whereas the long-range contributions from beyond the subject molecule are simulated using AMBER point charges. Including charge distributions in the quantum chemical calculations does not significantly increase the computational costs, as the use of point charges does not require basis functions. A more formal approach is a self-consistent embedded ion method, EIM.[125] The method simulates the electrostatic crystal potential that is experienced by each atom in a given molecule or ion inside an infinite crystal lattice, the Madelung potential, with a large but finite array of point charges. A finite point charge array that reproduces the Madelung potential in a defined, central region of the array with the desired accuracy is obtained in an iterative procedure, that is, the embedding charges are determined by an SCF (self-consistent field) procedure. Subsequently, the nuclear magnetic shielding tensors of interest are calculated for a given ion or molecule embedded inside the point charge array, located inside its central region. Another method that gives comparable results to EIM is SCREEP (surface charge representation of the electrostatic embedding potential).[126] This method simulates the Madelung potential at a given subject molecule by a point charge distribution on a van der Waals surface surrounding the subject molecule. A direct comparison between using EIM and SCREEP for representing the electrostatic equivalent of the long-range intermolecular effects on ^{13}C and ^{15}N shielding tensors in Gly-Gly hydrochloride monohydrate, acetic acid, calcium formate, naphthalene, ammonium hydrogen oxalate hemihydrate, sucrose, and L-histidine monohydrate gives comparable results for the two methods.[127] An improvement over EIM is the extended embedded ion method (EEIM) of Weber *et al.*[128] It is similar to the EIM of Stueber *et al.*[125] in the manner of embedding the quantum chemically

treated part in an exact, self-consistent Madelung potential, and requires no empirical parameters. The comparison between EIM and EEIM is discussed by Weber *et al.*[128] A different way of choosing the embedding charges and a closer attention to the boundary between the cluster and the charge field gives the EEIM better agreement with experiment for ionic solids.[128] In the past, the EIM was mainly applied to organic compounds with relatively low ion charges. Deficiencies which gain importance when typical inorganic compounds with highly charged ions are involved are attended to in EEIM.

These approximations using point charge arrays and other similar approaches influence chemical shift computations in two ways, a direct and an indirect contribution. Calculating NMR shieldings with the perturbation of an electrostatic potential provides a direct contribution; this is a small effect and is determined by the values of the shielding derivatives with respect to electric fields, the so-called shielding polarizabilities and hyperpolarizabilities.[129] Calculations of shielding polarizabilities have been carried out at various levels of theory; they are notoriously dependent on basis set size and the level at which electron correlation is included.[130–132] The most accurate calculations at the highest coupled cluster levels indicate that the direct contribution of an electrostatic potential is usually small.[133] The Xe shielding in the presence of an electrostatic field from point charges representing the H and O atoms of crystalline clathrate hydrate cages is only 0.5 ppm lower shielding than in an isolated Xe atom.[134] As NMR shielding is extremely sensitive to local geometry, particularly bond length, geometry optimizations in the presence of the electrostatic field lead to a potentially significant indirect contribution to the calculated shielding. Using water to illustrate these two contributions, it has been shown that approximations have a greater effect on calculated shieldings via the structures that these charge field embedding approaches generate in the geometry optimization step, that is, the structure of the model system for the shielding calculation, rather than the level of electronic quantum calculations used in the shielding calculation itself.[135]

Some recent examples using continuum models are ^{195}Pt nuclear shielding in *cis* platin derivatives,[136] ^{183}W shielding in polyoxotungstates of different shapes and charges,[137] ^{31}P shielding in the phosphate head group of sphingomyelin,[138] ^{15}N and ^{13}C nuclear shieldings in halopurine nucleosides.[139] Examples of embedded clusters using EIM include the calculation of the ^{13}C chemical shift tensors in potassium carbonate, bicarbonate and related monomethyl derivatives,[140] the ^{13}C and ^{15}N chemical shift tensors in

adenosine, guanosine dihydrate, 2-deoxythymidine, and cytidine,[141] the ^{13}C chemical shift tensors in *p*-aminosalicylic acid, isaniazid, and pyrazinamide,[142] and also the ^{129}Xe shielding hypersurface for a xenon atom inside a cage of clathrate hydrate structures I and II.[134,143] EIM and EEIM results for ^{19}F and ^{31}P shielding tensors in NaF and in four different magnesium phosphates have been compared with experimental values from solid-state MAS (magic angle spinning) NMR. The improved agreement of EEIM results in comparison with experiments allows new signal assignments for the different P-sites in $Mg_2P_4O_{12}$, a-$Mg_2P_2O_7$, and MgP_4O_{11}.[128]

3.5. Intermolecular relativistic effects

Relativistic effects are significant for the absolute shielding of ^{129}Xe in an isolated atom,[144] but how important are relativistic contributions to intermolecular effects on ^{129}Xe shielding, that is, do the relativistic contributions remain largely unchanged as Xe atom comes close to another atom? In an attempt to answer this question,^{129}Xe shielding calculations have been performed at the BPPT (Breit Pauli perturbation theory) level with an uncontracted [29s25p24d2f] basis.[145,146] The relativistic calculations show that the BPPT contributions to the intermolecular shielding of ^{129}Xe in the Xe_2 dimer are about 10% at an internuclear distance of 3 Å, and 7% at the equilibrium separation of 4.36 Å. These differences are quite comparable in magnitude and opposite in sign to the contributions arising from electron correlation, as provided by the differences between calculations at the Hartree–Fock and CCSD(T) levels of theory.

A possible example of intermolecular relativistic effect is the large gas-to-solution shift of solutes in CH_nI_{4-n} solvent, becoming larger with the number of iodine atoms (Karol Jackowski, private communication). This phenomenon had been puzzling for some time, but no relativistic calculations have yet been carried out to determine how large the relativistic contributions are.

Both the intermolecular effects on shielding and those arising from non-bonded neighbour atoms in the secondary or tertiary structure of the same molecule can be reasonably reproduced via Hartree–Fock or density functional calculations for ^1H, ^{13}C, and other light nuclei, provided that heavy atoms are not present. Otherwise, relativistic corrections are necessary. For instance, in polyamine H_2O and alcohol complexes of transition metals Rh, Co, and Ir, SO contributions to ^1H shielding are found to be significant.[147]

Deprotonation of the H_2O or alcohol ligands in these systems depicts interesting trends such as SO-induced spin polarization, transmitted across at least three bonds from the central transition metal atom. In addition, the effects across increasing atomic numbers are unusual as these do not increase with the square of the atomic number in the series Rh, Co, and Ir. Also, a Karplus-like behaviour is observed in how the SO effects behave with changes in dihedral angle. This marked dependence holds promise in utilizing SO effects to probe the stereochemistry of these complexes.

3.6. Shielding and chirality

NMR shieldings are, in general, identical for a given set of enantiomers L and R in a magnetic field. Only the presence of chiral influences such as other chiral molecules, chiral potentials,[148] and/or parity violations[149] can give rise to a pseudoscalar addition to the shielding and thereby generate differences in the shielding between enantiomers in a magnetic field. Particular aspects of chirality and diastereomerism have been investigated, namely, chirality induced in an achiral system, that is, induction of a chiral response in an achiral molecule by a chiral environment, which may be called induced chirality.[148,150–152] This was done by studying the full nuclear magnetic shielding tensor of the Xe atom in a chiral environment and also in the chiral field of other asymmetric groups. Helices of neon atoms were used to model the chiral environment and a helical arrangement of point charges to model a chiral field. The findings were as follows: (1) The Xe shielding tensor components for the R and L systems are related by a rotation that changes the signs of the off-diagonal elements, but the eigenvalues of the symmetric matrix which provide the principal components of the Xe shielding tensor are identical. (2) The non-zero antisymmetric part of the shielding tensor is one measure of the induced chirality. Three principal components of the tensor and the directions of the principal axes system relative to the laboratory axes are a maximum of six quantities that can be determined from a single-crystal NMR experiment. At most three principal components can be obtained from a powder NMR spectrum. Only the isotropic shielding can be obtained from a solution NMR spectrum. The antisymmetric part is not observed in the usual NMR spectrum. Therefore, we can see that the R and the L systems produce the same Xe NMR spectrum in this model system. With the exception of the chiral point groups, D_n, T, and O, which forbid the existence of antisymmetric shielding,[153] chirality is a sufficient

condition for the existence of antisymmetry in the shielding but not a necessary condition.

The standard method of generating different magnetic responses for a given enantiomer is to create the diastereomer, where in a racemic mixture there would now be two resonances in the NMR spectrum, one corresponding to Ll+Rr, the other to Lr+Rl, as opposed to a single resonance for L and R. This is to be expected, as diastereomers are not mirror images of each other; hence, the magnetic responses from components of a diastereomeric set are not identical. On the other hand, the mirror images Ll and Rr are not distinguishable from each other by NMR, nor is Lr distinguishable from Rl. The shielding difference between the two components (say Ll vs. Lr) of a diastereomer is not necessarily small, as the structure and shape of the two can be significantly different; they are two different molecules after all. Thus, observed NMR chemical shifts have been used traditionally to distinguish diastereomers. An experimental example of induced chirality is Xe trapped in chiral cages such as cryptophanes.[154] The Xe atom acquires induced chirality, but the only way to observe it is to create diastereomers, for example, by placing the cage in a chiral medium or in the presence of a chiral group bound to one of the external faces of the cage. The ^{129}Xe shielding of an Xe atom in chiral cages such as those of cryptophanes has led to observation of diastereomeric signals.[154,155] Calculations have provided good estimates for the splittings of the signals and the assignments of one peak to Ll+Rr, the other to Lr+Rl.[154] Experimentally, the use of left-handed amino acids in the group chemically attached to a racemic mixture of cages, led to having only Ll and Rl systems in the sample, where the cage chirality is in upper case. Furthermore, for the chemical systems where the attached group had two asymmetric centres, the four peaks could be individually assigned to each one of (Ll_1l_2+Rr_1r_2), (Ll_1r_2+Rr_1l_2), (Lr_1r_2+Rl_1l_2), (Lr_1l_2+Rl_1r_2), where the cage chirality is in upper case and the chiral centres on the attached group are designated by lower case letters.[154] Again, in this case, the use of only left-handed amino acids in the synthesis led to having only Ll_1l_2, Ll_1r_2, Rl_1l_2, and Rl_1r_2 being present in the sample.

Under certain conditions, the application of a static or an AC electric field could remove the chiral blindness of conventional NMR.[156,157] Although demonstrated in principle, experimental realization is yet to be designed.

An example of a small diastereomeric shift is found for ^{3}H in the diastereomeric set (L-CHDT)-(α)-isosparteinium and (R-CHDT)-(α)-isosparteinium.

The L-CHDT group has a ^{3}H chemical shift that is 49 ppb downfield from the R-CHDT resonance.[158] The observed sign and magnitude of this diastereomeric shift is found to be in agreement with the values calculated from Hartree–Fock, DFT-B3LYP, and DFT-B3PW91 using the 6-311+G(2d,p) basis set. The shieldings of the three limiting positions (rotamers) were calculated and the mole fractions of each rotamer were also theoretically calculated. The three rotamers have distinct conformational energies. Weighting these limiting values with the populations yields the expected shielding difference between the diastereotopic methylene protons of the CHDT group. That such a small difference in chemical environment between the two diastereotopic sites could be observed is another confirmation of the extreme sensitivity of the shielding to the electron distribution at the nuclear site.

NMR shielding calculations have been carried out to help assign the stereochemistry in newly synthesized organic and natural products. Computations are made on several candidate structures in the gas phase with geometries previously optimized either by *ab initio* methods or MMs force field dynamics. Conformational distribution for each stereoisomer can be incorporated in these calculations by Boltzmann averaging over all low-energy conformers. This approach has been elegantly illustrated in the analysis of 16 diastereomeric stereopentads,[159] and the assignment of stereochemistry of 21 natural products, some of which had been previously incorrectly assigned.[160] It is in this pursuit that theoretical calculations may be able to aid in interpreting spectra, having in theory what shielding each specific diastereomer has and taking into account its distribution in the population.

4. SHIELDING IN EXTENDED NETWORKS

4.1. Approaches to extended networks

As we have described above, to apply the first-principles quantum mechanical calculation techniques to solid-state NMR, it had been necessary to devise finite clusters of atoms which model the local environment around a site of interest and embed the cluster in a charge field or other representation of the true extended structure, point charge embedding to model the long-range Coulomb interactions (e.g. EIM, Refs. 125,128). While this has led to unprecedented understanding of structure and neighbour influences on shielding, and successful predictions of NMR chemical shifts in systems such as molecular crystals,[161–165] ionic crystals[128,166,167] and supramolecular assemblies,[92] there are attendant difficulties particularly for covalent solids,

where capping of truncated covalent bonds may bring edge effects into play. Therefore, approaches are needed that inherently take account of the long-range effects in extended systems and also preserve the nuclear site symmetry by properly describing the periodic nature of the solid. For large systems, highly accurate quantum chemical calculations are prohibitively expensive and thus, only the computationally more affordable DFT can be used.

Several alternative DFT methods for periodic systems have been developed. These methods can be applied to crystalline and amorphous insulators under periodic boundary conditions (PBC), as well as to isolated molecules using a supercell technique. We refer to these methods collectively as PBC methods. (a) The most extensively used method originates from the first developed approach to shielding calculations in periodic solids by Mauri *et al.*[168] who overcame the inherent difficulty that the position operator which explicitly enters the perturbed Hamiltonian for NMR is not well defined for periodic systems. This original approach was adapted later via implementation of GIPAW,[169] gauge-including PAWs, which is a modification of PAW (projector augmented wave) for systems in an external magnetic field. GIPAW plays a role similar to GIAO in quantum chemistry techniques. The GIPAW algorithm reconstructs the all-electron wavefunction in the presence of a magnetic field. The code for this method is implemented in the CASTEP software suite,[170] in PARATEC,[171] and also in Quantum ESPRESSO.[172] All these software suites are based on density–functional theory, plane-wave (PW) representations, and pseudopotentials. (b) The method developed by Sebastiani[173] transforms Bloch states to localized Wannier orbitals to overcome the position operator problem. This is implemented in the CPMD (Car-Parinello molecular dynamics) suite of programs.[174] This approach has been extended by Weber *et al.*[175] to an all-electron description of the system with mixed Gaussian and augmented plane waves (GAPW), implemented in QUICKSTEP,[176] which is part of the CP2K suite.[177] (c) The converse approach of Thonhauser *et al.*[178,179] calculates shielding as the finite difference of orbital magnetization with respect to nuclear moment, thus without having to resort to linear response theory, and a later development uses GIPAW for pseudopotential augmentation.[180] The converse method is implemented in Quantum ESPRESSO.[172] (d) Ziegler *et al.* have developed a method of calculating shielding in periodic systems using atom-centred basis functions,[181,182] implemented in the BAND program suite.[183] In BAND the Bloch basis set is

constructed from Slater-type orbitals (STOs) and/or numeric atomic orbitals (NAOs). The electronic density matrix near the nuclei is very important for NMR shielding and both STOs and NAOs afford a potentially accurate description of the KS orbitals in this region; in particular some users prefer STOs because they satisfy the cusp at the origin. Atomic-centred basis functions allow for use of gauge-included atomic orbitals (GIAOs) to ensure gauge-invariant shielding results. (e) The linear-augmented plane waves (LAPW)[184] all-electron approach (implemented in the WIEN2k software package for electronic structure of solids)[185] has been extended to shielding calculations by Laskowski and Blaha.[186] We consider these methods in turn.

(a) Mauri *et al.* (1996, 2001, 2007)

In solids, the task of computing the induced current is complicated by the fact that the magnetic field breaks translational symmetry. Moreover, the position operator, which explicitly enters the perturbed Hamiltonian, is not well defined for periodic systems. The first method that overcame this difficulty was proposed by Mauri *et al.*, where the external magnetic field was modulated with a finite wave vector.[168] The response was then calculated taking the limit at infinite length of the modulation vector. Although this method was developed within an all-electron formalism, it has been applied using pseudopotentials. It can be shown that for finite systems PAW and GIPAW use special pseudopotentials which, by reconstructing all-electron density close to atomic nuclei, correctly account for electrons in this region. The response is calculated taking the limit at infinite length of the modulation vector. It has been shown that for finite systems the Mauri *et al.* method is equivalent to a variant of the continuous set of gauge transformations (CSGT) method.[187] The method of Mauri *et al.* has been derived and implemented for plane-wave (PW)-based pseudopotential codes; however, it neglects the effects of the wave functions that have been modified by the pseudopotentials on the induced current, which should be considerable in the core region of heavier atoms. It has been used for light elements and with the use of hard pseudopotentials in several applications, particularly for covalent solids,[188–191] and in ice and liquid water.[192] This drawback has been removed by Pickard and Mauri.[169] Their approach operates within the projector augmented-wave method (PAW)[193] and has defined the PAW transformations such that they ensure correct gauge (translational) symmetry of the pseudo-wavefunction in the presence of the external magnetic field. The method is referred to in literature as the GIPAW method. Within the framework of the pseudopotential approximation,

the GIPAW method is able to converge towards all-electron magnetic response calculations. One contributing factor to this success is the assumption of a rigid contribution to the shielding NMR parameters of core electrons, that is, the assumption of the validity of the frozen core approximation. Therefore, the all-electron atomic potential can be replaced by a pseudopotential which mimics the potential created by the nucleus surrounded by its inner electrons. The orthogonality condition between the valence and the core states being relaxed, the valence wave functions become smoother and easier to calculate using PW basis sets. For second and third row elements, the core-valence states separation is quite obvious and usual selections of core states are employed by the community for first-principle pseudopotential calculations. A large number of GIPAW shielding calculations in this form have been carried out on covalent solids such as boron carbide,[194] carbon nanotubes,[195] SiO_2,[196] silicate crystals and glasses,[197–199] aluminosilicates,[200,201] molecular crystals,[112,202–204] including polymorphs.[205,206] Difficulties appear for the fourth row elements, for example, for the 3d transition metals. First row elements, transition, and rare-earth metals require very large numbers of PWs to accurately describe the valence wave functions. As both the calculation time and the memory requirement scale as roughly the 3/2 power of the maximum plane-wave cutoff energy, it is desirable to use softer and hence more efficient pseudopotentials. Thus, the GIPAW approach has been reformulated such that it can be based on ultrasoft pseudopotential (USPP) calculations.[207] Vanderbilt's "ultrasoft" pseudopotentials are designed to be as soft as possible in the core region and require a minimum number of PWs for full convergence.[208] This softness is achieved at the cost of relaxing the property of norm conservation and so the pseudo-wavefunctions obey a generalized orthonormality condition. GIPAW with ultrasoft pseudopotentials has been applied to elements in various parts of the Periodic Table: in minerals such as kaolinite,[209] perovskites,[210] molecular crystals,[211–214] organic single crystals,[215] inorganic solids, for example, ^{95}Mo shielding in solid-state molybdenum compounds,[216] Br in alkaline earth bromides,[217] glasses, for example, ^{73}Ge correlation with Ge–O–Ge bond angle in vitreous GeO_2,[218] ^{19}F, ^{29}Si, ^{31}P, and ^{23}Na in bioactive glasses,[219] biomolecules in the solid state, for example, peptides.[220] Truflandier *et al.*[221] have designed ultrasoft pseudopotentials for 3d transition elements in GIPAW. In a further development, relativistic GIPAW operators have been included for shielding calculations in the ZORA,

and applied to ^{77}Se and ^{125}Te shieldings in a range of compounds.[222] Availability of reliable pseudopotentials has certainly greatly contributed to the quick widespread usage of the GIPAW method. There is a growing list of publications involving various applications.[223]

(b) Sebastiani *et al.* (2001, 2009)

An alternative method to calculate nuclear shieldings in extended systems under PBC was proposed by Sebastiani and Parinello.[173] The formalism relies on the exponential decay of KS-wavefunctions which are maximally localized in space, also called Wannier orbitals,[224] treat these localized orbitals as virtually isolated, combined with a saw-shaped "periodized" position operator,[173] such that the discontinuity due to the periodization appears in a region where the Wannier functions vanish. The main advantage of this method is that for large systems which in any event require large unit cells, such as *ab initio* molecular dynamics (MD) simulations of biological systems,[225] or extended disordered systems, it demands considerably lower computational efforts than GIPAW. For the gauge problem, a particular variant of the CSGT method[226] is adapted and applied to these localized orbitals. The original implementation by Sebastiani and Parinello used a pseudopotential plane-wave representation of the electronic structure in the frozen core approximation. The method is implemented in CPMD, a DFT pseudopotential suite of programs based on a PW representation.[174] The results by this approach has been compared directly to the Mauri *et al.*[168] results for the same systems and are found to agree within about 0.3 ppm[173] when using the same cutoff and the same level of theory (LDA) as Mauri *et al.* For systems that can be described by a small primitive cell, Sebastiani's method would have to use a supercell technique to obtain sufficiently localized Wannier functions, whereas the method of Mauri *et al.* works with the primitive cell only and is therefore more efficient for such cases. The improvement of the Sebastiani method by Weber *et al.* called GAPW[175] avoids the use of the pseudopotential approximation. The underlying idea in GAPW is that the electron density varies smoothly in the interstitial region and is therefore easily representable in a plane-wave basis, whereas the quickly varying electron density near the nuclei is more efficiently manipulated in terms of localized functions, in particular Gaussian-type functions, allowing for reduced complexity algorithms. Weber *et al.* use either of Keith and Bader's methods to circumvent gauge-origin problems, IGAIM (individual gauge for atoms in molecules)[227] or CSGT[226] methods. A direct comparison of IGAIM-GAPW with the original Sebastiani and Parinello implementation for isolated adenine

molecule shows that the calculated shieldings differ by tens of ppm for C and N nuclei. The differences can be attributed to the incomplete description of the core electron contributions. On the other hand, IGAIM-GAPW and GIPAW results are in good agreement.[175] It appears that this new implementation of the Sebastiani-Parinello method is a competitive alternative for Pickard and Mauri's GIPAW method. Recent applications of the Sebastiani method in hydrogen-bonded systems have been reported.[228–231]

(c) Thonhauser *et al.* (2009)

In most theoretical treatments, the external magnetic field is introduced as the initial perturbation, inducing a current density with which the second perturbation in the form of the nuclear magnetic dipole interacts. Nearly, all NMR software codes treat the two perturbations in this order. The converse approach by Thonhauser *et al.*[178] is fundamentally different from the other solid-state methods that calculate the induced magnetic fields at the nuclear positions in response to an applied, uniform magnetic field within a linear response framework.[168173] In the converse approach, the NMR shielding tensor of a particular nucleus is obtained from the total orbital magnetization induced by a magnetic dipole placed at the position of that particular nucleus.[232] In the converse approach, a linear response treatment of the electronic states is circumvented. The ground state Bloch functions of the perturbed Hamiltonian, that is, including the vector potential of the magnetic dipole, are calculated and their k-gradients are used to obtain the induced orbital magnetization[233] which is a ground state quantity. This method can be applied in the framework of the GIPAW, where it is used to calculate a pseudopotential contribution to the shielding tensor. As is done for the linear response methods, a PAW[193] reconstruction in the core region is needed to obtain accurate shieldings. The complete derivation of this converse approach in the GIPAW framework was recently presented by Ceresoli *et al.*[180] Converse calculations of σ could be implemented in other standard band structure codes, including all-electron methods. The disadvantage of the converse method is that it requires a supercell approach to ensure a proper separation of the localized dipoles. An example of its application is illustrated in polycyclic aromatic hydrocarbons.[179]

(d) Ziegler *et al.* (2010, 2011)

The method of Ziegler and co-workers[181,182] differs from the other solid-state methods in using the Bloch basis set constructed from atom-centred functions, STO or NAO. The atom-centred functions permit the use of GIAO to ensure gauge-invariant results. This method also treats the two perturbations in the converse order. Their method first evaluates the

current density induced by the three components of the nuclear magnetic moment, followed by the response of this induced current density to the three components of the external magnetic field. Initially, they determined the induced current density from a zero-order field-free calculation on a supercell large enough so that the induced current density vanishes at the supercell border.[181] This requirement was necessary to determine the interaction with the non-periodic constant magnetic field. Thus, the calculations considered an array of periodic supercells, each containing a magnetic dipole. They later found a more efficient scheme, which they call the single dipole method, as it considers the perturbation from the single magnetic dipole in a large crystal.[182] Use is still made of a supercell that is now extended to the entire crystal, but the determination of the induced current density over the entire crystal is based on zero-order KS orbitals from SCF calculations involving only a primitive unit cell. This is made possible by a combination of first-order analytic perturbation theory and the relationships for Bloch functions and their derivatives. In addition, use was made of the transformation relationships between the local representations of KS orbitals obtained with the whole crystal as the periodic unit and those of the crystal momentum. This transformation is specific to atom-centred basis sets. Relativistic effects within the scalar ZORA have been included in the new scheme. Only a few results are available as yet for this new method. Results for ^{15}N shielding calculations in boron nitride crystal (a diamond-like structure) give a chemical shift relative to the standard ^{15}N reference substance (nitromethane) equal to -359.8 ppm,[182] which is in very good agreement with the experimental value of -358.6 ppm and with an earlier calculation using the cluster method (an H-saturated cluster containing 71 atoms) which gave a value of -359.0 ppm. The calculated ^{67}Zn chemical shift in ZnS (zincblende) crystal was 1199 ppm relative to a free Zn atom, to be compared with the experimental chemical shift of 1068 ppm.

(e) Laskowski and Blaha (2012)

The NMR shielding calculations for the full-potential all-electron LAPW method has been implemented in the Wien2K code.[186] The implementation follows the GIPAW method, except that the integration of the current cannot be performed in reciprocal space only (as in GIPAW), so has inherently different integration of the induced all-electron current density in the presence of a uniform external magnetic field. In the LAPW method, the unit cell is partitioned into non-overlapping atomic spheres centred on

the nuclei and the interstitial region. The basis functions are PWs in the interstitial region that are augmented by a linear combination of functions inside each atomic sphere. The standard LAPW basis set is accurate for valence and lowest conduction bands. In order to cover a larger energy region, additional basis functions have to be supplied in the form of local orbitals (called NMR-LO functions) which vanish at the sphere boundary and at the interstitial region, so they are not coupled to the PWs. Most of the shielding is generated in the atomic sphere, but integration of the current density in the interstitial region and also in neighbour atomic spheres is of course necessary for accurate calculations of shielding. The disadvantage of the LAPW method for calculating shielding is that a large number of local orbitals have to be used to increase the flexibility of the basis. So far, only a comparison with Pickard and Mauri's GIPAW for isotropic ^{1}H, ^{13}C, ^{17}O, ^{19}F, ^{29}Si shieldings in small molecules, oxides, and fluorides from the literature has been carried out, finding reasonably good agreement between the two methods for small molecules; for ^{13}C in diamond, the difference is nearly 9 ppm and for oxides and fluorides it is as large as 20 ppm.

These PBC methods of calculating shielding are the methods of choice for covalent solids, ionic solids, strongly hydrogen-bonded solids, proton-conducting molecular crystals, and systems where slight differences in crystal packing forces create subtle differences in shielding and other properties for the same chemical compound composition, that is, polymorphs. In addition to the early success cases already mentioned above, we consider some examples below.

4.2. Crystalline materials

PBC methods for shielding calculations in solids are a natural choice in covalent solids like quartz, diamond, chalcogenides, or extended networks constituted with covalent bonds, not necessarily in three dimensions, such as carbon nanotubes. The prediction of NMR properties for these and many more systems may be found in the GIPAW list of references[223] because the methods developed by Mauri *et al.* came first and were accessible. Undoubtedly the other more recent methods discussed in Section 4.1 will catch up in terms of numbers of applications, as soon as solid-state NMR spectroscopists become more aware of them. Particularly useful is the ability to calculate both the shielding and the electric field gradient tensor, which becomes indispensable when dealing with the quadrupolar nuclei that inhabit most of the NMR Periodic Table.[234] Some interesting recent results include the

finding that the ^{13}C shielding in single-walled carbon nanotubes correlate with the tube diameter.[235] The linear relation found tends to asymptotically approach the line position expected in graphene. Those doing work in NMR crystallography are beginning to find the PBC methods to be very useful.[236] Interesting trends are found especially when both the shielding and quadrupolar tensors are interpreted together, for example, ^{35}Cl shielding and electric field gradient tensors in a series of alkali and alkaline earth chloride hydrates.[237] By doing calculations for ^{35}Cl, ^{81}Br, and ^{127}I, Bryce and coworkers have found that when an isostructural series of related compounds pack in the same space group, it has been possible to interpret trends in the NMR data in terms of the strength of the halogen bond.[238] For example, in the case of a series of haloanilinium bromides, they find the ^{81}Br shielding tensor span and isotropic value both decrease as the bond is weakened. Studies of Br^- ion in triphenylphosphonium bromides[239] provides trends of the chemical shift tensor components with the Br–P distance in the crystal structure, a clear neighbour effect that could just as well have been found by a cluster calculation. On the other hand, GIPAW calculations could distinguish between the two chemically similar bromine sites, which helped in the analysis. An example which clearly demonstrates the success of a periodic approach is the ^{17}O shielding tensor in three crystalline sodium phosphates[240]: sodium trimetaphosphate, $Na_3P_3O_9$, tripolyphosphate, $Na_5P_3O_{10}$, and pyrophosphate, $Na_4P_2O_7$. A cluster-based calculation, including either the anion or the first coordination sphere demonstrates that the first coordination sphere does not determine the ^{17}O shielding tensor; GIPAW calculations clearly show that the long-range structural organization influences the shielding. Only a PBC approach could reproduce the observed NMR spectra.

Some of the success stories are in studies of polymorphs, where the small differences in environment can lead to significant differences in physical properties in the solid state for the same compound that becomes one entity in solution. With the same chemical formula and chemical structure, polymorphs differ only in subtle bond length and bond angle differences, differences possibly imposed by packing forces in the solid state, yet they can have different physical properties such as solubility. Solid-state NMR is particularly suited to the discovery of the nature of these subtle differences. SSNMR can distinguish between polymorphs, and the PBC methods of calculating NMR properties help in understanding the slight differences in environment. Examples of such applications are ^{1}H, ^{13}C, and ^{19}F shieldings in a molecular crystal flurbiprofen,[202] ^{15}N shielding

tensors in *N*-benzoyl-L-phenyalanine,[241] ^{13}C in *N*,*N*″-diacetybiuret,[242] ^{13}C in prednisolone,[74] ^{13}C in the anticancer drug paclitaxel,[75] ^{17}O and ^{29}Si shielding tensors for six polymorphs of $MgSiO_3$,[76] α and β polymorphs of poly(*p*-xylylenes),[77] ^{17}O and ^{29}Si in Mg_2SiO_4 polymorphs,[243] polydiacetylenes,[244] vaterite $CaCO_3$ polymorph,[245] ^{17}O in glutamic acid polymorphs,[205] carbamazepine and its dihydrate,[206] oxybuprocaine hydrochloride,[211] and polymorphs of alumina,[246] ^{1}H and ^{13}C in thymol,[78] and ^{13}C in piroxicam.[81]

On the other hand, for the polymorphs of glycine, cluster calculations appear to have better agreement with experiment.[247] With the availability of ultrasoft potentials, shielding of nuclei such as ^{77}Se in inorganic and organoselenium systems[248] and Sn in organotin compounds[249] have also been studied, as well as ^{19}F in alkali, alkaline earth, and rare-earth fluorides,[250] and even transition metal shielding.[251]

Despite these successes, there are some issues which have been raised. We need to do better than the commonly used PBE for solids. For a given geometry, both LDA and common GGA functionals (PBE, Wu-Cohen, PBEsol) give a very similar description of NMR parameters. Usually, the agreement with experiment is reasonably good—a rough rule of thumb is that errors in the chemical shift are within 2–3% of the typical shift range for that element. There are, however, some notable exceptions: Several groups have shown[252] that while present functionals can predict the trends in ^{19}F chemical shifts, a graph of experimental against calculated shifts has slope significantly less than 1.0. Another example is the calculation of ^{17}O chemical shifts[201] in calcium oxide and calcium aluminosilicates. There are significant errors in the ^{17}O shifts which arise due to the failure of PBE to treat the unoccupied Ca 3d states correctly. In Ref. 201, it was found that a simple empirical adjustment of the Ca 3d levels via the pseudopotential was sufficient to bring the ^{17}O chemical shifts into good agreement with experiment. However, in both cases, it is clear that current GGAs do not describe all of the relevant physics of shielding in solids.

4.3. Non-crystalline materials, glasses

GIPAW represented a major step forward for the investigation of glass structure when combined with MD simulations (the MD-GIPAW approach).[198,201] The combination of MD simulations with GIPAW calculations has made it possible to study the dependence on distributions of structural parameters, such as those found in glasses. Mauri and

co-workers have shown that the combination of the CP simulations with NMR GIPAW calculations can be helpful to gain insight into the structural interpretation of the NMR parameters. For lithium and sodium tetrasilicate glasses, configurations were extracted from the CP simulations, and then relaxed to 0 K using the CPMD code. For one model, this relaxation of the atomic positions was done on a last configuration of the CP run, and the relaxed model presented a perfect SiO_4 network. For the other model, the starting configuration from the CP simulation presented a defective network and was extracted quite shortly after an observed topology change. Through the relaxation to 0 K, it became a non-defective model. Investigation of the strong sensitivity of ^{17}O and ^{29}Si NMR to the bond angles, in addition to the influence of the modifier cation environment, reveal that for T = Q(4), Q(3), Q(2), the dependence of $\sigma_{iso}(^{29}Si)$ on Si–O–T angle could be well described by means of a single (i.e. the same for both glasses) simple linear dependence.[253] The subsequent example of the analysis of how ^{29}Si, ^{17}O, and ^{23}Na shieldings depend on the environment in sodium silicate glasses is another good one.[254] The mean values and also the distributions of structural parameters can be obtained by the GIPAW-MD approach to glasses. The independent variation of the MD-GIPAW ^{29}Si isotropic shielding with the Si–O–Si angles of the *n*Si tetrahedral linkages in Q(1), Q(2), Q(3), Q(4) coordination types is convincing. The MD-GIPAW ^{17}O shielding variation with Si–O bond length for the bridging and non-bridging oxygens is less so.

Conventional diffraction studies do not provide sufficient information to determine the short-range order in chalcogenide Ge_x–Se_{1-x} glasses, which can include corner- and edge-sharing tetrahedral arrangements, under-coordinated and over-coordinated atoms, and homopolar bonds. ^{77}Se NMR studies obtained using MAS showed two large, but rather broad peaks. Two conflicting interpretations had been suggested: the first consists of a model of two weakly linked phases, one characterized by Se–Se–Se sites, the other Se–Ge–Se. The second model assumes a fully bonded structure with the contributions from Ge–Se–Se and Ge–Se–Ge linkages overlapping. To answer this question, Kibalchenko *et al.*[255] carried out first-principles calculations on several crystalline precursors of germanium selenide glasses ($GeSe_2$, Ge_4Se_9, and GeSe) to establish the range of chemical shifts associated with each type of Se site. This connection between local structure and observed NMR parameters provides a reliable interpretation of the ^{77}Se spectra of Ge_x–Se_{1-x} glasses, ruling out the presence of a bimodal phase and

supporting a fully bonded structure. Recent work in glasses include analysis of the structure and changes in vitreous silica,[256] borosilicate glass,[257] phosphate glasses,[258] and fluoride-containing bioactive glasses.[259]

4.3.1 Disordered systems

First-principle calculations and solid-state NMR have recently been used to study disorder in the fluorine substituted hydrous magnesium silicate clinohumite ($4Mg_2SiO_4{\cdot}Mg(F,OH)_2$). This mineral is of considerable interest as model for the incorporation of water within the Earth's upper mantle. Diffraction provides the overall crystal structure but gives no information on the ordering of the F^-/OH^- ions. The ^{19}F NMR spectrum reveals four distinct fluorine environments. Griffin *et al.* performed GIPAW calculations[252] on a series of supercells of clinohumite using F and OH substitutions to generate all possible local fluorine environments. From these, it was found that the computed ^{19}F NMR parameters were clustered into four distinct ranges depending on their immediate neighbours. The ranges correspond well to the observed peaks providing an assignment of the spectrum. Shielding calculations have assisted the probing of disorder in ceramics using ^{89}Y[260] and ^{119}Sn nuclei.[261]

4.4. NICS in periodic systems

Sebastiani has presented a pseudopotential PW approach in which the electronic current density and the NICS map are obtained from an inverse Fourier transformation of the induced magnetic field represented in reciprocal space.[262] This NICS contributes the same amount to every nucleus, but for protons this contribution to the shielding is relatively important. The calculated NICS surfaces can be used to calculate the most substantial part of proton shielding (added to that in the isolated molecule) for a molecule trapped within the CNT or hydrogen-bonded calixhydroquinone nanotubes at low loading. In a subsequent paper, selected guest molecules are observed in these nanotube hosts, but no averaging of guest positions have been carried out.[263]

4.5. Relativistic calculations in solids

Mauri and co-workers have included relativistic calculations for heavy nuclei using pseudopotentials and ZORA.[222] Using this method for ^{95}Mo in solid $Mo(CO)_6$,[264] and other molybdenum compounds,[216] relativistic effects were included for all elements during the USPP generation by solving the scalar-relativistic equation of Koelling and Harmon,[265] which omits SO

but retains all other relativistic kinematic effects such as mass-velocity, Darwin, and higher order terms. Most of the scalar-relativistic effects acting on core electrons are included in the USPP and on valence electrons through the interaction with the USPP. Then, no additional calculation is needed. Spin–orbit coupling effects were not taken into account in this work. Nevertheless, the linear correlation plot between the ^{95}Mo shielding differences and observed chemical shifts has a slope of 0.95. Another method that includes ZORA is that of Ziegler *et al.*,[181,182] which is a very promising method for solids because atom-centred basis functions are used, but no calculations are yet published using this option.

4.6. The case for retaining cluster approaches in our toolbox

Now that we have seen the proper treatment of extended networks using PBC calculations, are there any justifications/advantages of using the old embedded cluster methods? It had been the case that only LDA and GGA DFT approximations were available for NMR calculations in periodic boundary condition methods, although this is no longer true with the development of other PBC approaches like GAPW.[175] On the other hand, standard all-electron quantum QM (quantum mechanics) chemistry methods, which are widely available in many QM chemistry computer programs are very mature and can calculate nuclear shielding tensors with a range of approximations, using well-tested Gaussian-type orbital basis sets. In increasing order of computational cost, these methods range from DFT, HF, and hybrid methods, to correlated approximations such as second- and higher order Møller–Plesset perturbation and singles, doubles, triples coupled cluster methods. The persistence of cluster based models is mainly due to the advantage that understanding the dependence of the shielding on structural parameters (bond length, bond angle, torsion angles, etc.) is very easy with embedded cluster methods. These dependencies can also be treated by periodic boundary calculations, but *implementation of a systematic variation of a structural parameter is more difficult, due to the geometrical constraints of the periodic crystal structure* and the often limited range or variety of experimental values available in reference crystalline compounds. Also, incomplete atomic coordinates in the crystal structure, for example, omission of hydrogens on waters in XRD data, do not permit periodic boundary condition methods to be used. Finally, cluster methods, including embedded cluster methods, make use of the locality of NMR properties. Thus, the cluster approaches described in part 3 are not completely superseded by

the periodic approaches. Sometimes cluster calculations can provide insight (e.g. about the hydrogen-bonding network) that PBC approaches cannot, and at the same time, get results closer to experiment than is possible with PBC approaches. For example, natural bond orbital (NBO)[266] analysis can be carried out to assess the strengths of intermolecular interactions present, allowing the significant non-covalent interactions to be identified. Such insights are important, as there are typically a large number of non-covalent interactions involving the site of a given nucleus in a crystal structure, such that it may be difficult to discriminate the important structural factors that influence the observed chemical shift.[247]

An excellent example is afforded by the use of calculations in catechin 4.5-hydrate to refine the atomic coordinate positions in the crystal.[267] Because neighbouring moieties often suggest more than one orientation for the hydrogens in the O–H groups to optimize hydrogen bonding, calculations using model clusters are required. Intermolecular-hydrogen-bond-dictated orientations can be energetically less favourable than conformations obtained from geometry optimization of a single molecule under vacuum. Here, calculations in model clusters with variable >C–O–H conformations were used to determine the O–H proton orientations with respect to the aromatic ring, using the sensitivity of the ^{13}C tensor components to the C–C–O–H dihedral angle. Then, the initial structure, solved using XRD heavy atom positions and SSNMR OH hydrogen orientations, had excellent agreement with diffraction data but gave a poor fit of computed ^{13}C tensor principal values (sp^2 and sp^3 carbons) with experimental data. This large error in SSNMR fit indicated that further atomic coordinate refinement was possible. A significant improvement in the fit was obtained in the final refinement by adjusting bond lengths and valence angles computationally, while holding dihedral angles constant at XRD values, that is, adjusting positions of heavy atoms, not only hydrogens. As hydrogens were also optimized during the iterative refinement process described, a separate analysis was performed to determine what portion of the improvement was due to hydrogen optimization. Optimal hydrogen positions were determined by holding heavy atoms rigid at the initially determined XRD-determined positions (i.e. before any bond length or valence angle refinement) and allowing only hydrogens to adjust via energy minimization. ^{13}C tensors were then computed using the coordinates of the modified structure. This hydrogen refinement altered the computed error by only 0.48 ppm relative to the structure before refinement. It may therefore be concluded that roughly 93% of the improvement in the SSNMR error comes from

refinement of non-hydrogen atoms. Note that accurate work such as described in this work requires that complete tensor information from SSNMR measurements have to be used, rather than isotropic shielding values which hide compensating errors in the components within the isotropic average. The complete tensor refers to the six observable symmetric tensor elements. It is more convenient, when comparing two complete tensors, to use the icosahedral representation of the shielding tensor. The Grant group converts all computed and experimental tensor data to the icosahedral representation[268] before using any least-squares fitting procedures, so as to make full use of the entire symmetric shielding tensor, thereby using not only the principal components but including also the principal axis orientation information.

In the case of catechin discussed above, the geometry *in situ* was made consistent with both the full ^{13}C tensors from SSNMR and the XRD data, using embedded cluster calculations to carry out the geometry variations. When the local structural distortions are largely intramolecular, it is logical to invoke a cluster or even a single molecule calculation to assist a GIPAW shielding calculation in the crystal, because exploring the intramolecular distortions within the full solid-state environment with PBC can be too challenging. Intramolecular distortions can occur where each molecule is found in a nonequilibrium (relative to an isolated molecule) geometry stabilized by its crystalline environment, principally through steric effects. In bisphosphinoamine, the ^{31}P isotropic shielding could be assigned to the various crystallographic sites with GIPAW calculations but the elongation of the ^{31}P–^{31}P cross peaks parallel to the diagonal in the 2D NMR spectrum, as well as the thermal ellipsoids associated with the uncertainties on the atomic positions of the XRD structure indicated some structural distortion.[269] Single molecule vibrational mode calculations revealed modes of structural distortions (variations of a couple of degrees in bond and dihedral angles) which are consistent with the observed slight disorder in the crystal. The authors suggest this approach should be applicable to a broad range of solids with small amplitude structural disorder and will ultimately allow us to link this type of disorder to their macroscopic physical and chemical properties.

Another good example of embedded cluster approach is the study of the ^{17}O shielding dependence on structural parameters, B–O bond length and B–O–B angle, in ABO_3 transition metal perovskite crystals.[166] The authors use a cluster embedded in point charges to model the long-range Coulomb interactions in the ABO_3 materials. The target oxygen atom is fully

coordinated with QM atoms located at its nn and nnn sites. Second, the target atom's nn QM atoms are themselves fully coordinated with nn QM atoms. Finally additional QM atoms are added, as required by ideal perovskite symmetry. This procedure results in a 21 QM-atom cluster: $(A_4B_2O_{15})^{14-}$, where A = Sr, Ba, or Pb; B = Ti or Zr. All-electron treatments were used for the O and Ti atoms, while the other QM atoms were represented using scalar-relativistic small core (scalar-RSC) pseudopotentials also called effective core potentials (ECP). The QM cluster is embedded in the crystal environment by surrounding it with a large array of point charges. The purpose of the point charges is to better simulate the crystal environment by generating the correct crystalline electrostatic Madelung potential in the QM region. The finite point charge distribution is determined using the EWALD program.[270] The method calculates an array of point charges that reproduces the electrostatic potential of the infinite crystal within an accuracy usually < 1 μV in the interior of the quantum cluster. In the first step, EWALD calculates the Madelung potential with the Ewald method for PBC, using nominal ionic values (e.g. $Q_i = -2$ and $Q_i = +2$ for O^{2-} and Pb^{2+}, respectively) for the atoms placed at crystallographic positions of the targeted system. In the second step, EWALD retains the nearest $O(10^4)$ Q_i centred on the target atom, adjusting the values of the outermost Q_i to reproduce the Madelung electrostatic potential on and in the vicinity of the QM atoms. In this second step, the nearest ca. 500–750 Q_i are fixed at their nominal values, and in addition, the net monopole and dipole moments of the point charge distribution are constrained to vanish. The large ^{17}O shielding anisotropy is analyzed in terms of the hybridization between the O(2p) and virtual B-site d-states. The calculations identify an incorrect experimental assignment of two of the five inequivalent ^{17}O sites in $PbZrO_3$.

The crystalline amino acids are another good example in which cluster calculations can provide insight. Using NBO analysis in the cluster calculations, the high-frequency chemical shift observed for H_4 in the α polymorph of glycine, compared to H_5 in the α polymorph and to H_4 and H_5 in the γ polymorph, can now be attributed to intermolecular C—H···O close contacts.[247] These results suggest that, in spite of the relatively narrow span of ^1H NMR chemical shifts (ca. 10 ppm), computation of ^1H NMR chemical shifts can successfully distinguish small differences in chemical shifts between polymorphs and, furthermore, can provide insights into the reasons underlying differences in chemical shifts induced by differences in molecular geometry and crystal packing. Shielding calculations for amino acids in the

crystal state have been carried out using supermolecular clusters,[271] using embedded cluster method (EIM),[272] and also by GIPAW.[273] The supermolecule calculations by Chen *et al.* considered all possible hydrogen bonds with the given amino acid, that is, including all possible hydrogen bonds with side chain atoms, in addition to the hydrogen bonds with the carbonyl oxygen and amino hydrogen atoms.[271] This means that the cluster includes the amino acid of interest with up to 8 complete amino acids as neighbours in the crystal configuration. The principal values of ^{13}C shielding *tensors* in nine crystalline amino acids were included in this cluster study, and an r.m.s. deviation of 10.6 ppm was found for the correlation with experimental values, using B3LYP. Agreement with experimental isotropic shieldings is much better, of course. For the embedded cluster study by Strohmeier *et al.*[272] the cluster calculations on α glycine, γ glycine, and L-alanine were performed on clusters of complete molecules where atomic positions were taken from the known single-crystal neutron diffraction studies. The γ glycine and L-alanine clusters included seven and the α glycine cluster six complete molecules; L-asparagine and L-histidine were provided with all their hydrogen bonds using smaller molecules (water, acetamide, and glycine). The clusters of complete molecules were placed inside the final point charge array obtained from the EIM calculations. As described in Section 3.4, the electrostatic crystal potential that is experienced by each atom in a molecule in the infinite crystal lattice is simulated with a finite, self-consistent array of point charges, which are generated using the Ewald summation method and quantum mechanical partial atomic charge calculations.[125] Subsequently, using standard quantum mechanical methods, the NMR shielding tensors are calculated for the cluster embedded inside the point charge array. Strohmeier found that the principal components of the ^{13}C shielding tensors for the 5 amino acids studied had an r.m.s. of 4.0 ppm in the correlation with experimental values.[272] Prior to doing a GIPAW study, Zhen *et al.* carried out an ONIOM study on the principal values of ^{13}C shielding tensors of the carboxyl carbon in three crystalline amino acids. The r.m.s. was 5.9 ppm when the geometry optimization was first carried out on the original XRD coordinates.[274] When the same lab did the GIPAW study, they reduced the r.m.s. for the carboxyl principal tensor components to 4.85 and 10.0 ppm for all carbons in 12 amino acids and one dipeptide.[273] This is comparable to the r.m.s. deviation of 10.6 ppm using supermolecule clusters.[271] If in addition the supermolecules had been embedded in point charge arrays as in the EIM method, the results would probably have been even better. It appears that EIM-embedded cluster calculations are capable of

producing shielding tensors of high accuracy. Given that XRD data are available for the system under study, the unquestioned advantage of all the periodic methods is that one needs absolutely no chemical knowledge to carry out the calculations whereas cluster methods make use of a general knowledge about hydrogen-bonding donors and acceptors, ring currents, van der Waals radii, to make good decisions about constructing suitable clusters.

5. DYNAMIC AVERAGING OF SHIELDING

5.1. Why is averaging so important for nuclear shielding calculations?

Fragment and single molecule and cluster calculations discussed in part 3 have demonstrated the exquisite sensitivity of nuclear shielding to local configuration, that is, bond structure (bond lengths, bond angles, torsion angles) and arrangements of non-bonded neighbours, which means that any motional changes in these configurations is accompanied by changes in the nuclear shielding. Atoms in the observed system are always in motion, even if only zero-point motion is available, thus, effects of dynamic averaging (e.g. vibrations, conformational averaging, molecular aggregation) can be more significant than differences arising from choices of exchange-correlation functional or basis set sizes. Explicit experimental manifestation of dynamic averaging effects on shielding are isotope shifts and the temperature dependence of shielding that has been observed in the gas phase at the limit of zero density, in the limit of no intermolecular interactions, or else in mixtures of gases where averages from intermolecular interactions can be carried out in closed form and verified against density and temperature dependence. In situations, as in liquids, where the configurations of the neighbours change dynamically, the intermolecular contributions to shielding also change with changing configurations. Therefore, dynamic averaging needs to be taken into account in the theoretical modelling, even when there are no significant strong interactions such as hydrogen bonding. The size of systems that can be studied using first-principles calculations has rapidly increased with the use of DFT. As the size increases so does the number of degrees of freedom, so also does the time scale of the dynamics that these systems exhibit. This is particularly relevant for biological systems where hydrogen bonding and van der Waals interactions are controlling factors for the secondary and tertiary structure, the greater dynamical freedom permits sweeping through large regions on the shielding hypersurface of every

nucleus in the structure. As NMR calculations are performed on ever larger systems, it is therefore going to be increasingly necessary to explicitly include dynamical effects in the theoretical treatment.

5.2. Rovibrational averaging

The effects of rovibrational averaging of shielding are observed as isotope shifts and temperature dependence of chemical shifts, even in the absence of intermolecular interactions (as in the extremely dilute gas phase).

5.2.1 Isotope shifts

As variations in the average geometry depend on the magnitude of the change in the reduced mass of the nuclei that are in motion, deuterium substitution leads to more easily observable isotope chemical shifts and are therefore most often noted. Nevertheless, halogen isotope shifts such as those induced by $^{35}Cl/^{37}Cl$ and $^{79}Br/^{81}Br$ have been measured for ^{19}F chemical shifts in a series of fluorinated cyclopropanes and cyclopropyl ethers.[275] These secondary isotope shifts are in the order of a few ppb. The $^{17}O/^{18}O$ isotope effects on ^{13}C chemical shifts have been employed to examine in more detail the structure of benzyloxycarbonyl-Ala-Pro-Phe-glyoxal as it binds to chymotrypsin.[276] The more common deuterium-induced isotope effects have been utilized in characterizing Schiff bases,[277] compounds containing nitro- and acetyl groups,[278] systems with strong hydrogen bonds,[279–281] and sugars.[282] Deuterium-induced isotope effects can be affected by conformation and solvent. In the case of proteins, a range of deuterium isotope effects have been observed on backbone ^{15}N chemical shifts.[283] This observation certainly adds to the increasing set of NMR parameters that can be used to elucidate protein secondary structure. This, of course, is in addition to the fact that deuterium-induced isotope shifts can be used to pinpoint exchangeable protons in a protein, as illustrated in the study of Cys residues in the protein EPPIb.[284] Similar studies have been employed using deuterium-induced shifts on ^{19}F chemical shifts in fluorine-labelled tyrosine residues in calmodulin.[285]

Isotope shifts arise mainly from the change in the rovibrationally averaged geometry of the molecule upon isotope substitution. Its calculation requires knowledge of the potential surface and its accurate experimental determination, to remove intermolecular effects, requires extrapolation to zero density. In this arena, deuterium-induced secondary isotope effects on ^{13}C and ^{17}O chemical shifts of methanol[286] and to ^{1}H shielding in water[287] (e.g. difference between HOD and H_2O) have been measured.

Extrapolation to the isolated molecule limit has been afforded by employing fluoromethanes as buffer gas to pressure-narrow the observed resonances. Benchmark calculations have been performed for deuterium-induced isotope shifts on ^{1}H in H_2, ^{35}Cl in HCl, and ^{23}Na in NaH using coupled cluster singles and doubles (CCSD) level of theory and employing aug-cc-pVTZ basis functions. Beyond the Born–Oppenheimer (BO) approximation, Gaussians that specifically contain kinetic energy terms that depend on nuclear mass have been used to estimate deuterium-induced isotope shifts on ^{15}N chemical shifts in lysine residues.[288]

5.2.2 Temperature dependence of shielding

The dependence of chemical shifts on local geometry is likewise revealed in variable temperature measurements. The earliest work was in diatomic and other small molecules in the gas phase.[289,290] The temperature dependence of NMR chemical shifts in small molecules can be treated in a rigorous fashion. Calculations can be carried out with large basis sets and with a high level of theory while experiments can be made in the gas phase which allows for extracting and removing intermolecular effects from the measured shifts. A systematic and comprehensive study of ^{1}H and ^{13}C NMR chemical shifts in halomethanes is a recent example.[291] As the heavy halogens (Br and I) are included in this work, these calculations require relativistic contributions. In particular, scalar and SO-induced relativistic effects have been incorporated. Large gauge-including basis sets are employed to guarantee basis set convergence and electron correlations at various levels are applied. To determine the chemical shift at any given temperature, it is important to have a good description of how the shielding changes with geometry. For this purpose, hypersurfaces involving a large number of points (about 100 geometries suitably chosen in the vicinity of the equilibrium geometry) have been constructed and from these surfaces, the derivatives of the shielding with respect to the symmetry coordinates of the molecule are extracted. By transforming these derivatives to terms based on the vibrational normal coordinates Q_k of the molecule, and applying the average values of $\langle Q_k Q_l \rangle^T$ and $\langle Q_k \rangle^T$, obtained from harmonic and anharmonic force fields as well as centrifugal distortion, calculated shielding values can be converted from their equilibrium values to those that should correspond for a molecule at 300 K, for example. A direct comparison with experiment can then be made using absolute shielding values, and in this case, the agreement is indeed excellent for the entire series of methyl halides.

In complex systems, this temperature dependence has been used to examine phase transitions, local and collective motions, and polymorphism, as illustrated in NMR measurements of potassium ferrocyanide trihydrate,[292] triethyleneglycol-substituted perylenetetracarboxdiimides,[293] branched polyolefins,[294] semifluorinated alkanes,[295] supercooled confined water,[296] and L-selenomethionine.[297] For condensed phases, the observed temperature dependence of the chemical shift depends not only on vibrations but intermolecular interactions, which theoretical approaches are discussed below

5.3. Dynamic averaging in condensed phases

5.3.1 Approaches to dynamic averaging of shielding in condensed phases

The dynamic averaging may be carried out in various ways, but in general one needs a means of generating configurations over which the averages are taken and a means of generating the shielding for a given configuration. The means of generating configurations may be via a Monte Carlo (MC) process for canonical or grand canonical ensembles or via a MD trajectory. Both methods of generating configurations have been used for dynamic averaging of shielding. In most early and many current uses, the interaction potentials between the particles are functions of the inter-particle coordinates and may include pairwise, three-body, and higher order terms, whose functional forms are related to the nature of interactions and bonding in the system under study. These potentials are commonly determined by choosing a parameterized functional form on the basis of physical and chemical considerations and fitting the parameters to a set of experimental or theoretically calculated data. Many widely used combinations of potentials (or force fields) specifically developed for biological systems (AMBER, CHARMM, GROMOS, etc.) or systems consisting of organic molecules (OPLS) have been used extensively in dynamic averaging of shielding in solutions. As the potential parameters are unchanging during the process of generating configurations either via classical MD or MC schemes, the applicability is limited in those circumstances where the system evolves into regions of configuration space not covered by the fitted data. Beyond classical MD are Born–Oppenheimer molecular dynamics (BOMD) methods in which the interatomic interactions underlying the evolution of the nuclear degrees of freedom are generated concurrently and consistently as the simulation evolves. That is, the determination of the potential is an integral part of the simulation, but the evolution of the system is restricted to a single electronic potential energy

surface (PES). The electronic energy on this PES and the forces on the nuclei are calculated "on the fly" which can then be used in the integration of the classical equations of motion of the nuclei, advancing them by a small time step to a new configuration. For MD on the ground state BO surface, this method can be realized with any *ab initio* method, including hybrid methods such as QM/MM. In the same spirit as standard BOMD, but using quite a different approach, in addition to the classical equations of motion for the nuclei, CPMD method, which is DFT based, solves in addition, a fictitious dynamics of the electronic system by describing the time evolution of the KS wavefunctions connected with the atomic motion.[298] For example, for ionic liquids, Bagno *et al*. used CPMD to generate the snapshots.[299] For periodic systems, CPMD uses pseudopotentials and plane-wave basis set expansion and is probably the most popular of BO type of MD methods which has been used for averaging shielding.[300] The use of a supercell or repeating images of the system is not an intrinsic feature of a BOMD and therefore may be used for clusters which may have multipole moments.[301,302]

There are various means of generating the shielding for a given configuration. Obviously, this is based ultimately on quantum mechanical calculations of shielding. For the purpose of dynamic averaging, shielding may be calculated using PBC methods for a completely QM description of the entire system as represented by a supercell,[135,192,220,303,304] or a quantum system that includes different layers of description nevertheless, as in an ONIOM approach where the few atoms closest to the nucleus in question may be treated at a higher level of theory than the next shell of atoms, or a quantum system in a QM/MM approach.[119,305–307] In a cluster approach, only a finite number of molecules are included, the molecule in question plus some number of neighbours. The cluster method has been used for a rare gas atom in a zeolite cage[308] or an organic cage,[309] or a pair of molecules at various distances and orientations.[89,310,311] The number of molecules in the cluster could be two or more; for example, calculations of the shielding for water have included 5–64 molecules in the cluster.[135,312–315] An improvement is afforded by an embedded cluster approach. The cluster may be placed in a reaction field,[315] or the cluster may be embedded in a collection of point charges, using EIM[125] or EEIM[128] methods to determine the charge field that describes the periodic lattice. A systematic variation of geometry in a fragment of the system embedded in a charge field of the remainder of the system has been used to generate a shielding surface, for example, a peptide residue in a protein.[122]

Finally, the methods of doing the averaging are (a) in general, to select a series of configurations from MD or MC simulations, do quantum calculations of shielding for those snapshots and take the equally weighted average or (b) to use pre-calculated shielding hypersurfaces and do the averaging during the process of generating the configurations in an MD or MC simulation. We cite some examples in the following sections.

5.3.2 Use of pre-calculated shielding hypersurfaces in MD or MC simulations

For the interpretation of Xe distributions and chemical shifts, PBC Grand canonical MC simulations were carried out in various crystalline zeolites,[316–318] aluminium phosphate,[319] dipeptides,[320] clathrate hydrates,[134,143] and in constructed idealized crystalline materials containing paramagnetic centres,[89] also canonical simulations of Xe in an organic cage (cryptophane A).[309] These studies are deficient in that the cages are not vibrating, although long-range effects are included by using PBC for zeolites, aluminium phosphate dipeptides, and clathrates in the MC simulations. Pre-calculated Xe shielding surfaces were constructed from *ab initio* calculations using a large number of positions for the Xe atom within the cage, distributing the points in a manner guided by the sharp dependence of Xe shielding on atom–atom distance. The calculated shielding tensors were all fitted to suitable pairwise additive functional forms and fitting parameters were determined so as to reproduce the *ab initio* Xe shielding at each location. When more than a single Xe atom is present in the same cage or channel in the crystal, then the shielding contributions from other adsorbed gases are added in. The Xe-molecule shielding surface is likewise carried out for a large number of configurations for the Xe+other supermolecule. Like the Xe-clathrate hydrate calculation, for example, this too can be expressed as a mathematical function with parameters fitted so as to regenerate the *ab initio* values. The quality of the Xe shielding hypersurface for the Xe+other supermolecule was tested against temperature and density dependent Xe chemical shift measurements in gas mixtures. As it has been found experimentally that at modest densities the latter are additive (i.e. as a sum of Xe–Xe shielding contribution plus Xe-other contributions and linear with density), it is a good approximation to assume additivity of the shielding contributions from zeolite and from other adsorbed molecules. The latter assumption is found to be reasonably good, as has been found for Xe shielding calculations involving 3 or more Xe atoms, or a Xe atom and some number of rare gas atoms.[146,150] For Xe

adsorbed in solids, the Xe-molecule shielding contributions were considered additive to the Xe shielding contributions from interactions with the cage or channel atoms. During the grand canonical or canonical MC simulations, Xe shielding tensors were calculated from the shielding hypersurfaces, along with energies. Average tensor components observed in these systems were reproduced by the MC simulations.[318–320,143] For Xe in clathrate hydrates, the *ab initio* shielding values for one type of hydrate structure were fitted to a pairwise additive functional form involving Xe–O and Xe–H. Therefore, MC averaging was easily done for several new structures of clathrate hydrates. Calculations of the isotropic shielding on the fly during the MD trajectories in simulations of Xe solution in liquid water[321] used the same pre-calculated Xe shielding hypersurface from clathrate hydrates, and similar MD simulations for Xe in solution with solvents such as normal and cycloalkanes used the pre-calculated Xe shielding hypersurface for Xe–CH_4.[90,91] Using a cutoff distance together with the shielding functions, in MC or MD simulations using PBC, permits simulations to be carried out for the entire crystal or solution. The biggest weakness in using classical MC or MD simulations to obtain average electronic properties such as nuclear shielding arise from the intermolecular potential functions used in the simulations. It is therefore important that these be tested independently by reproducing other physical quantities such as adsorption isotherms or solubility, or else use quantum MD such as CPMD, which calculates all interactions quantum mechanically.

5.3.3 Quantum calculations from MD or MC snapshots

This is a commonly applied method of averaging in condensed phase. In this method, the snapshots are first generated and then the shielding calculation is done for each snapshot. For Xe in benzene solution, the highly anisotropic nature of the interaction between Xe and the benzene molecule makes it difficult to precisely express the set of calculated shielding values for Xe at various positions relative to a benzene molecule into an analytic mathematical form of the Xe shielding hypersurface. Instead, Standara *et al.*[322] carried out classical MD simulations of one Xe atom in a periodic box of benzene molecules and selected snapshots from the classical MD trajectory. Then the ^{129}Xe shielding was calculated for each snapshot and a straight average is used. This is the most commonly used approach. Applications differ only in the many approaches described above (Section 5.3.1) for choosing the system for which the shielding is calculated. For example, a supercell was used for liquid water,[192,303] the periodic simulation box was used in its

entirety for Xe dissolved in benzene.[322] A cluster approach was used for ^{1}H shielding in an ionic liquid,[299] and for ^{1}H and ^{13}C shielding of α-D-glucose in water.[85] An embedded cluster approach (EIM) was used for Xe in crystalline clathrate hydrates.[134,143] An ONIOM approach with QM/MM shells was used for adenine in aqueous solution,[305] a hybrid QM/MM was used by Sebastiani *et al.* for liquid water.[307] Clusters containing various numbers of water molecules solvating anionic Pt complexes were used for ^{195}Pt shielding in tetrahaloplatinate(II) complex and hexahaloplatinate (IV) complexes.[323] For convergence, the number of configurations sampled from the *ab initio* MD trajectories was 128, and the number of solvating molecules needed in the cluster calculation (using ZORA DFT) for convergence of the average shielding was 12 for the smaller tetrachloroplatinate (II) complex, while 14 seem to be required for the larger corresponding bromo complex. Both octahedral hexachloroplatinate (IV) and hexabromoplatinate (IV) complexes required less (about 8 water molecules).

5.3.4 Dynamic averaging of long-range effects

We consider the dynamic averaging of shielding in crystals and in liquids.

5.3.4.1 Crystals

Two approaches accounting for motional effects in solids can be considered: (a) DFT MD method and (b) force field method.

(a) MD method

Here, *ab initio* MD simulations are carried out to sample the configuration space of the system, and snapshots taken at regular time intervals, for example, 50 fs. Shielding values are averaged over these snapshots. Dume and Pickard[324] carried this out for β-L-aspartyl-L-alanine crystal and observed that the usefulness of such simulations is limited by their short duration. In another study of shielding in L-alanine crystal, two strategies were used to avoid correlation between configurations generated using MD.[325] First they use a DFT-based MD method. In this case, Langevin dynamics implemented within the DFT code CASTEP is used to sample efficiently the configuration space. Once a trajectory has been generated, configurations are sampled from it at a regular time interval (e.g. every 15 fs). Once an ensemble of N uncorrelated configurations has been obtained, DFT calculations are carried out to calculate the shieldings. The shieldings for each configuration are then averaged to find the mean and standard deviation of

the mean. After around 16 configurations the standard deviations decrease smoothly with $1/\sqrt{N}$, indicating well-behaved convergence. After 256 configurations, the errors have become reasonably small: carbons are converged to better than 0.2 ppm and hydrogens to 0.02 ppm for the molecular crystal L-alanine. However, the computational expense of DFT means that this does not scale well to larger systems.

An alternative to DFT MD is to do classical MD using standard potential energy terms. For consistency, the force field parameters are fitted to DFT-calculated forces. For validation, the parameterized force field is then used with a classical MD suite to attempt to reproduce the DFT MD result. The problem with this approach is that standard force fields in wide use for classical MD (AMBER, GROMOS, CHARMM, OPLS, for example) are useful in that they are parameterized to be generally transferable from one system to another containing similar atom bonding situations. Having to fit the force field parameters to DFT-calculated forces for each system to be studied defeats this advantage.

(b) Force field method

This method focuses on vibrational motion and allows for an assessment of the zero-point correction to shielding, which is found to be significant. In this method, the contribution of the curvature of the property surface is explicitly calculated, and the anharmonic vibrational effects are taken into account. Using a DFT-based PBC code such as CASTEP, the crystal cell vibrations are obtained within the harmonic or anharmonic approximations. The shielding at equilibrium, the first and second shielding derivatives with respect to the dimensionless mode coordinates, and the cubic and semi-diagonal quartic force constants are calculated by numerical differentiation. Vibrational wave functions are obtained using a vibrational potential constructed with up to quartic terms in the force field. The average shielding is then obtained as a vibrational average. This procedure is analogous to the vibrational averaging procedure used for molecules in the gas phase at the low density limit.

Vibrational averaging of the ^{13}C shielding values for β-L-aspartyl-L-alanine crystal was carried out in this manner.[324] Later, the shieldings of ^{13}C, ^{15}N, and ^{1}H nuclei in crystalline α-glycine was carried out in this manner.[326] First, the authors calculated first and second shielding derivatives and force field parameters. The numerical differentiation required more attention than for static computations on isolated molecules, because of the limited accuracy of the PW method. The calculated harmonic vibrational frequencies used for the averaging provided excellent agreement with the experimental Raman and inelastic neutron scattering data. A suitable choice

of the differentiation parameters enabled the correction of the equilibrium shielding by using the vibrational averaging and also to simulate their temperature dependence. Both the first and the second shielding derivatives were found important for the temperature dependence. Both quantum dynamic averaging and classical dynamic averaging were carried out and the results compared. First, at the "quantum" approaches, crystal cell vibrations are obtained within the harmonic or anharmonic approximations, and an approximate vibrational wave function is used to average the NMR parameters. This is in principle the more advanced method but many approximations had to be adopted in practical computations, in particular for the treatment of the variation of the shielding with vibrational coordinates. Instead of doing *ab initio* dynamics, the second method relies on classical BOMD simulations to sample the configuration space of the system via classical Newtonian motion of nuclei. This may miss some quantum effects; however, the direct averaging of BOMD clusters is computationally more robust than the quantum approach and may be quite appropriate for low-frequency vibrations. Because of the large contribution of the lowest-frequency vibrational motions (e.g. lattice modes and NH_3 rotation) for which the BOMD averaging is appropriate, the classical dynamics approach produced the most important experimentally observable trends reasonably well. Although the accuracy of both the NMR experiment and the computations was limited, the computed results are reasonably consistent with the previously published experimental values.[326] Incidentally, these results were also in agreement with the classical BOMD model based on a direct cluster averaging. In analogy to the averaging method used for molecules in the gas phase,[327,328] the temperature dependence of the shielding in crystalline α-glycine was obtained from

$$\langle\sigma\rangle^{\mathrm{T}} \approx \sigma_e + \sum_i \sigma_i/4\omega_i \sum_k C_{ikk} \coth(\hbar\omega_k/2k_{\mathrm{B}}T) + \sum_i (\sigma_{ii}/4\omega_i) \coth(\hbar\omega_i/2k_{\mathrm{B}}T)$$

In another application of the approach by Mauri and co-workers to rovibrational effects in solids, ^{17}O and ^{25}Mg NMR shieldings in MgO were calculated as functions of temperature.[329]

5.3.4.2 Liquids

In a QM/MM approach the smallest part for which the highest level of quantum calculation is carried out consists of the solute molecule and potentially a selection of a few specific solvent molecules, for example, the first

and possibly also the second solvation shell. The remainder of the system is treated classical MM. There have been a large number of applications in solutions using this standard approach. A hybrid QM/MM method was introduced by Sebastiani *et al.*[307] and applied to the ^{1}H and ^{17}O shielding calculation in liquid water. An additional short-ranged repulsive potential (a simple Gaussian shape) pushes the electrons out of those regions that would be occupied by neighbouring electrons of the surrounding classical atoms, but no polarization effects are included. In an improvement over this method, a hybrid QM/MM method introduced by Ruud *et al.*,[119] the smaller subsystem is treated using DFT and the rest is treated at the level of MM including explicit polarization effects. The solvent is described by assigning to each atom a partial point charge. In addition, this DFT/MM approach includes explicitly a microscopic description of the solvent polarization, for example, to each solvent molecule an electric dipole polarizability is assigned, giving rise to instantaneous induced dipole moments in the solvent, thereby increasing the accuracy for the long-range part. The energy of the total system is given as $E_{tot} = E_{DFT} + E_{DFT/MM} + E_{MM}$, where E_{DFT} is given by the usual expression for the energy of a molecule in vacuum, $E_{DFT/MM}$ is the interaction energy between the DFT and MM systems and E_{MM} is the energy of the molecules described using MMs. In this model, the molecules treated using MM are described by assigning partial point charges to the atomic sites and a point polarizability at the centre of mass of each molecule. In addition, a set of Lennard–Jones potentials is introduced in order to describe dispersion and short-range effects. In the calculation of $E_{DFT/MM}$, the interaction energy between two induced dipole moments in the MM part of the system has an implicit dependence on the QM system and that E_{MM} therefore also contributes to the effective KS operator. In each self-consistent-field iteration, the latter operator, which has the contributions due to the introduction of a polarizable environment, has to be updated. Solute–solvent configurations dumped during the MD simulations are then used as inputs to the calculations of the shielding tensors in a DFT/MM approach, including the polarization effects in the environment. This is a distinct improvement over the PCM and goes beyond the Sebastiani method[307] in including polarization in the MM part of the system. For liquid water, for both σ^{H} and σ^{O} a very broad distribution of the shielding is observed, indicating the importance of a proper statistical sampling over a large number of solute–solvent configurations, for example, at least 300 configurations with 10 water molecules in the QM system. The oxygen absolute shielding and liquid to vacuum shift values are well

represented using polarized SPC water model with 10 water molecules in the supramolecular cluster. In sharp contrast, with only *one* water molecule treated quantum mechanically, immersed in the MM liquid, the calculated liquid to vacuum shift is opposite in sign to experiment! This is not surprising. Changes of local chemical structure accompanying thermal motion is significant in hydrogen-bonded liquids such as liquid water, so a single water molecule in the MM liquid completely misses the important local interactions.

Using empirical force fields for the solute, the solvent and solute–solvent interactions in a classical MD approach is sometimes the practical choice especially when slow (nanosecond time scale) conformational dynamics take place. The size of the cluster to be used for the shielding calculations would be an important factor in obtaining accurate results. Quantum mechanical calculations using DFT have been performed for a series of structures of liquid water generated by MC and MD simulations by Fileti *et al.*[330] The dependence of the resulting average chemical shifts on the empirical potential used in the simulations, on the cluster size and on the functional chosen for the quantum chemical calculations were investigated.

Liquid water has also been considered in a completely quantum approach, where the dynamically fluctuating hydrogen-bond network is taken into account explicitly in generating configurations. CPMD has been used by several groups.[173,192,303,315] In one approach by Vaara *et al.*,[315] the CPMD trajectory is sampled by cutting out nearly spherical clusters of molecules from the simulated liquid-state trajectory and used as an input for the QC calculations (DFT-B3LYP) using a reaction field model for the remaining waters. Each cluster contained a central molecule and a suitable neighbourhoods of molecules around it. A distance criterion was used to determine the neighbours of the central molecule. The molecules that were included had at least one of their atoms inside a sphere (of a chosen radius) centred at the oxygen nucleus of the central molecule. The cluster was placed in a spherical cavity cut into a dielectric continuum. The radius of the cavity equalled the distance between the centre of mass of the cluster and its most distant atom plus the van der Waals radius of this atom. The dielectric constant 78.5, appropriate for water, was chosen for the continuum. In a later study by Vaara *et al.*,[331] sampling instantaneous configurations from a CPMD simulation in water for calculations of nuclear shielding reveals how the tensors evolve as the environment changes gradually from gas to liquid upon increasing the number of hydrogen bonds (based on a distance criterion) to the molecule of interest. Liquid state distributions of the instantaneous values of shielding

show a wide range of values for each case of the classified hydrogen-bonding species, with significant overlap between the different cases.

In a different approach to the QC shielding calculation, Pfrommer *et al.*[192] modelled liquid water by nine snapshots from a CPMD simulation at 300 K and used this to build a supercell of 32 water molecules for an extended network shielding calculation for ^{1}H and ^{17}O. As an early test of the Sebastiani and Parinello approach for PBC systems, the shieldings in liquid water were compared directly with these results.[173] A later study considered water under normal and supercritical conditions.[303] In a recent CPMD in liquid water, a random set of about 30 snapshots from the MD trajectories was sampled, and all ^{1}H shieldings were computed.[135] The average thus consisted of typically 2000 individual proton shifts (for a system of 32 water molecules); unfortunately, only the ^{1}H shielding was calculated in this last example, and not ^{17}O.

CPMD has also been used in the first-principles calculation of the ^{1}H NMR chemical shift distribution of an aqueous HCl solution as a function of concentration.[304] With the instantaneous shielding being very sensitively dependent on solute structure as well as hydrogen-bonding with the solvent, a quantum MD method such as CPMD is the method of choice, particularly when the solvation effects lead to changes in solute geometry and electronic structure. An example of this challenging case is the calculation of the ^{1}H and ^{13}C NMR spectra of α-D-glucose in water.[85] Here the relative stability of the various conformers in the isolated solute is significantly affected by solvation, and as the differences in energies of the conformers are small, quantum mechanical calculation of the equilibrium distribution of conformers is problematic. There are a large number of conformations of the glucose hydroxyl groups which in water form strong hydrogen bonds with water molecules. In a recent study, empirical potentials were used to generate a 10 ns MD trajectory which served as a source of configurations (one every 100 ps) for quantum mechanical calculations of ^{1}H and ^{13}C shieldings using a glucose and its first solvation shell of water molecules, and these were averaged over 100 snapshots.[85]

6. EXTRACTING INFORMATION FROM NMR CHEMICAL SHIFTS WITH THE HELP OF THEORETICAL CALCULATIONS

Twenty years ago, NMR shielding calculations faced the challenge of limited computer resources. Such limitation forced a piecewise analysis of shielding in the hope of arriving at an approach that would decompose

shielding into contributions that were more manageable. One benefit from this limitation was the required planning and resulting realization of how various factors might be influencing NMR chemical shifts. For diatomic molecules with only one internal coordinate, the observations of temperature dependence in the limit of zero density had a clear implication in terms of theoretical calculations.[289] Raynes and co-workers first evaluated how displacement coordinates of a polyatomic molecule affect shielding in small molecules like water[332] and methane.[333] These were followed by similar work on ammonia[334] and phosphine.[335] By working with these small molecules and coupled with gas phase NMR measurements, how the local geometry was affecting NMR chemical shifts became known to great detail. These small molecules contain only one heavy atom so the factors that may affect shielding are limited to bond lengths and bond angles. With the addition of a second heavy atom, a new internal coordinate, the dihedral angle, is introduced. It is in this area that proteins provided a good set of data to test shielding calculation methods. The use of model fragments in which only a specific dihedral angle is varied allowed for pinpointing exactly how shielding depends on the internal rotation about bonds. Through this, chemical shifts of the alpha carbon site in peptides and proteins have been shown to be strongly correlated with backbone dihedral angles.[122] How factors can be evaluated separately really went hand in hand with the computational limitations at that time.[123] The insights drawn from these studies not only demonstrated that theoretical reproduction of experimental results was possible, but, more importantly, origins of chemical shift differences were specifically identified. Now, both computational resources and methodology have allowed calculations for large systems, and in most cases, no longer requiring the design of model clusters or environment. Experimental chemical shifts in complex and condensed systems can be reproduced. However, the deeper understanding of the origins of chemical shift differences has unfortunately vanished inside a black box. Nevertheless, there are still excellent examples that have gone farther than just reproducing experimental NMR chemical shifts and selected examples are briefly mentioned in the following.

6.1. Shielding tensors as tools for NMR crystallography

The emerging field of NMR crystallography combines solid-state NMR together with computation with the aim of providing new insight, with atomic resolution, into structure, disorder and dynamics in the solid state. As theoretical methods have proven to be sufficient in reproducing not only

isotropic shielding values but also the entire shielding tensor for ^{13}C, calculated shielding tensors can now be used as filter for selecting computer-generated crystal structure candidates.[336] Applying this approach to methyl pyranosides of galactose, glucose, mannose, and xylose, calculated shielding tensors can eliminate as much as eighty percent of the structures suggested by energy calculations. And amazingly, the top-five structures that provide calculated shielding tensors that best agree with NMR data are the known structures of these sugar crystals. This is an example where the structural information provided by shielding calculations and chemical shift measurements is confirmed by pre-existing X-ray data. This is the case for many NMR crystallography publications on organic solids.[211,213,236,336–342] and for inorganic solids.[343,344] The ability of NMR chemical shifts to provide high-quality structural information is demonstrated in these instances where other approaches or methods are equally useful and agreement among the results provides corroboration. With the increased confidence in shielding interpretation, it is timely to show that NMR shielding tensors can indeed provide unique structural information. This is elegantly exemplified in the catechin example. In a case where only the positions of the heavy atoms can be determined by powder diffraction data, calculated ^{13}C chemical shift tensors compared to the experimental values can uniquely provide the unknown dihedral angles describing the orientation of the various —OH groups in catechin.[267] Catechin 4,5-hydrate forms powders unsuitable for high-resolution crystallography. Fortunately, NMR shielding tensors provide site-specific information, which enables the evaluation of the coordinates of each atom separately. Disagreement between experimental shielding values and those calculated from a given structure pinpoints errors within the vicinity of the nucleus concerned. As each nucleus presents six pieces of information in its shielding tensor, solid-state NMR spectroscopy really holds great promise in complementing diffraction studies. Shielding tensors have likewise been used to prove that the cyanides in the hydrazine adduct of CuCN are fully orientationally ordered.[344]

A decade and a half ago, the pioneering approach to protein structure via chemical shifts was pursued by mapping out the shielding surfaces in proteins through carrying out quantum mechanical calculations using fragments that include hydrogen-bonding partners and perturbing charge fields from the rest of the atoms in the protein.[122] Experiments such as those by Tjandra and Bax have nicely confirmed that large variations in $^{13}C^{\alpha}$ chemical shift indeed correlate with secondary structure.[345] In the previous decade,

theoretical calculations of nuclear shielding surfaces in amino acid residues indicated parts of the tensor that are much more sensitive to protein secondary structure.[346] These calculations also mapped how the principal axis system of shielding in these systems might be changing with the peptide backbone dihedral angles. It is expected that in the very near future these findings, with incorporation of motional averaging, will enable interpretation of protein NMR spectra with an emphasis on a much more dynamic rather than a static view of proteins in solution. More recently, the same approach is being applied to DNA. For example, using SOS-DFT-IGLO calculations on a solvated model of dimethyl phosphate, the changes in the ^{31}P shielding tensor components as a function of DNA and RNA backbone conformations have been predicted.[114] The dependence of ^{31}P shielding on the phosphate backbone torsion angle in DNA has been carried out using a model that consists of a dimethyl phosphate and water molecules found in the first solvation shell.[73] With MD simulations, the observed ^{31}P chemical shifts in B_I and B_{II} DNA can now be properly interpreted.[73]

Confidence in shielding tensor computations can also guide the design of novel NMR experiments. Knowing beforehand how the shielding tensor is affected by local geometry in a given system should provide inspiration for new experimental techniques that take advantage of trends that have been discovered from theoretical calculations. For example, with the knowledge gained from numerous shielding tensor calculations of carbonyl carbon sites, a solid-state NMR experiment that takes advantage of the interaction between anisotropy of the carbonyl carbon shielding and the dipolar vector C^{α}–H^{α} is now available, providing a direct measurement of the dihedral angle ψ in peptides and proteins.[339]

6.2. Details of local structure

The sensitivity of the shielding to local structure suggests that shielding tensors provide information about local structure. For example, refined structures for silica-ZSM-12, [343] and ITQ-4,[347] zeolites have been obtained by optimizing Si–O, O–O, and Si–Si distances to reach a closer agreement between calculated and experimental ^{29}Si chemical shift tensors. The ^{17}O and ^{29}Si shielding in $MgSiO_3$ and Mg_2SiO_4 have been studied by Ashbrook *et al.*, allowing for a full assignment of the ^{17}O sites and a deeper understanding of how the ^{17}O shielding depends on the Si–O bond length and coordination environment.[76,243] Isostructural analogs of zeolites, such as aluminium phosphate $AlPO_4$-15 are constituted of linked PO_4 tetrahedra

and AlO_6 octahedra which form channels. The channels are filled with ammonium cations and water molecules, both of which exhibit hydrogen bonds to the framework. There are two distinct P species, each coordinated by four O atoms. The two distinct Al species are coordinated by six O, four of which are bonded to P. Based on starting coordinates from a synchrotron X-ray single-crystal diffraction study carried out on the same sample as that used in solid-state NMR studies, the GIPAW calculations permitted the discrimination of the distinct Al and P environments and assignment of spectra to the distinct local structures.[348] With a combination of experimental and theoretical determinations of ^{109}Ag and ^{31}P chemical shift tensors, a dimer structure has been proposed for silver dialkylphosphite salts.[349]

The dependence of shielding on molecular conformation, as illustrated now by a wide array of calculations, paves the way for utilizing NMR chemical shifts in the determination of conformational distribution in the solid state, as well as to distinguish between polymorphs. Examples are studies on triphenylphosphite in two crystalline modifications,[350] polymorphs of the anti-rheumatic compound prednisolone,[74] the anticancer drug paclitaxel,[75] poly(*p*-xylylenes),[77] thiamin diphosphate,[351] ciprofloxacin-saccharinate,[79] piroxicam,[81] and the various perovskite phases of $NaNbO_3$. By making use of models, the physical basis behind the observed NMR chemical shift differences between polymorphs can be ascertained. For example, in piroxicam,[81] the difference is found to be not due to a conformational change, but to the formation of a zwitterion. The changes observed in the ^{13}C chemical shifts of hydrocarbons upon introduction to synthetic structure H gas hydrates have been shown to be mostly due to conformational changes.[82] And in the fast emerging field of self-assembly of inorganic compounds, ^{31}P solid-state NMR, *ab initio* calculations, and crystallography have afforded a detailed structural characterization of ligand complexes that serve as connecting moieties between metal cations.[352]

With the capability of predicting conformational effects on chemical shifts, shielding hypersurfaces can now be relied upon and applied to the study of local disorder in partially disordered solids. Calculated shielding tensors at various conformations combined with a set of possible local distortions yield spectra that can be compared against experimental 2D NMR lineshapes to determine which changes in local geometry are most likely present in the structural disorder in solids.[269] The ability to predict the dependence of shielding on local structure permits a more detailed interpretation of NMR results from variable temperature studies as well as

isotope-induced shifts. Combined with calculations, the temperature dependence of ^{207}Pb shielding tensors in Pb(II) compounds can now be explained by changes in bond lengths and deviation from octahedral symmetry.[353] On the other hand, ^{18}O/^{16}O isotope effects on ^{13}C chemical shifts in benzyloxycarbonyl-Ala-Phe-glyoxal have provided evidence that the glyoxal inhibitor binds to the active site serine hydroxyl group in chymotrypsin in a hemiketal fashion.[276]

6.3. Shielding as a probe for intermolecular interactions

Theoretical treatments that allow for a detailed examination of intermolecular interactions have likewise provided excellent opportunities for using chemical shifts to extract structural features that define these interactions. A difference in orientation between C═O and N—H bonds in the anti-parallel structure of the tripeptide Ala-Ala-Ala has been determined as the main reason for why this sample has two magnetically distinct ^{17}O sites in Ala-2 that differ by 32 ppm.[354] Calculations using a cluster of molecules have enabled the assignment of the observed proton resonances in hydroxylated MgO powders, in which the chemical shift dispersion is mainly due to differences in the number of hydrogen-bond partners.[355] GIPAW calculations can identify a specific intermolecular hydrogen-bonding arrangement for a pharmaceutical polymorph for which no crystal structure is available.[356] Proton irradiation on deuterated KH_2PO_4 results in an increase in its ferroelectric phase transition temperature, which is now explained by an increase in hydrogen-bond length, as suggested by both ^{2}H and ^{31}P NMR data.[357] These calculations can likewise rule out intermolecular interactions. For instance, while X-ray structures suggest that three of the six surfaced-exposed lysines of protein G form salt bridges, in solution, both the measured ^{15}N and ^{1}H chemical shifts and the deuterium-induced isotope effects are predicted by a simple hydrated amine model.[358] This leads to the conclusion that, in solution, unlike in the crystal, all lysine residues are not participating in salt-bridges. Taking advantage of intermolecular effects on chemical shifts, ^{1}H NMR data combined with *ab initio* calculations can now provide information regarding the location of guest molecules in host cavities.[340] *Ab initio* shielding calculations have made it possible to describe in detail how a Na^+ ion binds to a calix[4]arene–guanosine conjugate dimer.[359] In this system, the Na^+ ion lies above the G-quartet plane and is simultaneously coordinated to a water molecule in a square pyramidal geometry. Ring-current effects on ^{1}H and ^{13}C chemical shifts have been used to characterize two

crystallographically distinct host cavities within single crystals based on hexagonal frameworks comprising guanidinium ions and organomonosulfonates.[360] Likewise, effects of aromatic groups on chemical shifts have been used to assess how antimalarial drugs interact with a model porphyrin compound in which the paramagnetic Fe(III) centre has been replaced by diamagnetic Zn(II).[361]

The theoretical studies on ^{129}Xe started not even with a Xe atom, but with the use of a smaller noble gas atom, Ar, as a model.[362] With this model, in addition to reproducing successfully observed experimental intermolecular chemical shifts of ^{129}Xe in mixtures of gases where averaging is straightforward, important and useful insights were drawn on how and why ^{129}Xe NMR chemical shifts change with intermolecular interactions. The use of models that were designed not only to reproduce the experiment, but also, and perhaps, more importantly, to understand the origins and mechanism of intermolecular NMR chemical shifts, is one of the reasons why interpretation of ^{129}Xe chemical shifts has reached its current sophistication.

With the understanding of how ^{129}Xe NMR line shapes are influenced by intermolecular interactions,[363] ^{129}Xe NMR spectroscopy continues to be a powerful tool for characterizing porous materials and molecular cages. For example, knowing that systematic changes in ^{129}Xe chemical shifts with temperature are associated with the diameter of the channels leads to the conclusion that in the nanochannels formed by alanylisoleucine crystals, Xe atoms are unable to pass each other.[364] The absence of multiple peaks in ^{129}Xe NMR spectra of Xe inside nanochannels of aluminium napthalenedicarboxylate is deemed as an indication that the surface in these materials is homogeneous,[365] and phase transitions of van der Waals cages of *p-tert*-butylcalix[4]arene can now be easily monitored by ^{129}Xe NMR spectroscopy.[366]

6.4. Characterization of solids

The ability to calculate chemical shifts for infinite systems has definitely extended the usefulness of NMR data in characterizing systems in the solid state, as seen in the many examples mentioned in Section 4. ^{13}C NMR chemical shifts in single-walled carbon nanotubes (SWNTs) can now be used to study the diameter of these tubes,[367] the presence of functional groups such as –NH, $-NCH_3$, $-NCH_2OH$, $-CH_2NH_2$,[368] –F,[369] and the presence of Stone–Wales defects.[370] And in the case of $AlVO_4$, ^{51}V

shielding calculations that make use of the GIPAW method are accurate enough that errors in previous assignments of the three inequivalent ^{51}V sites can now be corrected.[251] The use of GIPAW has also introduced a new way of looking at shielding surfaces. In crystals, the shielding can be described as a function of lattice volume.[371] In this approach, the dependence of the shielding on both covalent and non-covalent distances can be examined. The application of any of the PBC methods which provide geometry optimization and calculate the shielding tensors (and the electric field gradient tensors for quadrupolar nuclei) provides the SSNMR spectroscopist with an indispensable tool for characterizing solids in terms of both local and long-range order, as we have seen in the many examples given here.

REFERENCES

1. Tossell JA, editor. *Nuclear magnetic shieldings and molecular structure*. Dordrecht: Kluwer Academic Publishers; 1993. 584 pp.
2. Facelli JC, de Dios AC, editors. *Modeling NMR chemical shifts: gaining insights into structure and environment*. *ACS symposium series*, vol. 732. Washington, DC: American Chemical Society; 1999. 384 pp.
3. Kaupp M, Bühl M, Malkin VG, editors. *Calculation of NMR and EPR parameters: theory and applications*. Weinheim: Wiley-VCH; 2004. 621 pp.
4. Jameson CJ. Understanding NMR chemical shifts. *Annu Rev Phys Chem* 1996;**47**:135–69.
5. Helgaker T, Jaszunski M, Ruud K. *Ab initio* methods for the calculation of NMR shielding and indirect spin–spin coupling constants. *Chem Rev* 1999;**99**:293–352.
6. Gauss J, Stanton JF. Electron-correlated approaches for the calculation of NMR chemical shifts. *Adv Chem Phys* 2002;**123**:355–422.
7. Vaara J. Theory and computation of nuclear magnetic resonance parameters. *Phys Chem Chem Phys* 2007;**9**:5399–418.
8. Casablanca LB, de Dios AC. *Ab initio* calculations of NMR chemical shifts. *J Chem Phys* 2008;**128**:052201.
9. Mulder FAA, Filatov M. NMR chemical shift data and *ab initio* shielding calculations: emerging tools for protein structure determination. *Chem Soc Rev* 2010;**39**:578–90.
10. Charpentier T. The PAW/GIPAW approach for computing NMR parameters: a new dimension added to NMR study of solids. *Solid State Nucl Magn Reson* 2011;**40**:1–20.
11. Harris RK, Hodgkinson P, Pickard CJ, Yates JR, Zorin V. Chemical shift computations on a crystallographic basis: some reflections and comments. *Magn Reson Chem* 2007;**46**:S174–86.
12. Jameson CJ, de Dios AC. Theoretical and physical aspects of nuclear shielding. In: *Nuclear magnetic resonance*. *Specialist periodical reports*, vol. 28–41. London: Royal Society of Chemistry; 1999–2012.
13. Chesnut DB. *Ab initio* calculations of NMR chemical shielding. *Annu Rep NMR Spectrosc* 1994;**29**:71–122.
14. de Dios AC, Jameson CJ. The NMR chemical shift. Insight into structure and environment. *Annu Rep NMR Spectrosc* 1994;**29**:1–69.
15. Autschbach J, Zheng S. Relativistic computations of NMR parameters from first principles: theory and applications. *Annu Rep NMR Spectrosc* 2009;**67**:1–95.

16. Wilson PJ. Density functional theory and its application to NMR shielding constants. *Annu Rep NMR Spectrosc* 2003;**49**:118–68.
17. Komorovsky S, Repisky M, Malkina OL, Malkin VG, Ondik IM, Kaupp M. A fully relativistic method for calculation of nuclear magnetic shielding tensors with a restricted magnetically balanced basis in the framework of the matrix Dirac–Kohn–Sham equation. *J Chem Phys* 2008;**128**:104101.
18. Cheng L, Xiao YL, Liu WJ. Four-component relativistic theory for NMR parameters: unified formulation and numerical assessment of different approaches. *J Chem Phys* 2009;**130**:144102.
19. Kutzelnigg W. Diamagnetism in relativistic theory. *Phys Rev A* 2003;**67**:032109.
20. Kutzelnigg W. Relativistic corrections to magnetic properties. *J Comput Chem* 1999;**20**:1199–219.
21. Kutzelnigg W, Liu WJ. Relativistic theory of nuclear magnetic resonance parameters in a Gaussian basis representation. *J Chem Phys* 2009;**131**:044129.
22. Xiao Y, Liu W, Cheng L, Peng D. Four-component relativistic theory for nuclear magnetic shielding constants: critical assessments of different approaches. *J Chem Phys* 2007;**126**:214101.
23. Hess BA. Relativistic theory and applications. In: von Rague´ Schleyer P, editor. *Encyclopedia of computational chemistry*. Chichester, NY: Wiley; 1998. p. 2499–508.
24. van Lenthe E, Baerends EJ, Snijders JG. Relativistic regular two-component Hamiltonians. *J Chem Phys* 1993;**99**:4597–610.
25. Cheng L, Xiao YL, Liu WJ. Four-component relativistic theory for nuclear magnetic shielding: magnetically balanced gauge-including atomic orbitals. *J Chem Phys* 2009;**131**:244113.
26. Xiao Y, Sun Q, Liu W. Fully relativistic theories and methods for NMR parameters. *Theor Chem Acc* 2012;**131**:1080.
27. Komorovsky S, Repisky M, Malkina OL, Malkin VG. Fully relativistic calculations of NMR shielding tensors using restricted magnetically balanced basis and gauge including atomic orbitals. *J Chem Phys* 2010;**132**:154101.
28. Olejniczak M, Bast R, Saue T, Pecul M. A simple scheme for magnetic balance in four-component relativistic Kohn–Sham calculations of nuclear magnetic resonance shielding constants in a Gaussian basis. *J Chem Phys* 2012;**136**:014108.
29. Sun Q, Liu W, Xiao Y, Cheng L. Exact two-component relativistic theory for nuclear magnetic resonance parameters. *J Chem Phys* 2009;**131**:081101.
30. Aucar GA, Romero RH, Maldonado AF. Polarization propagators: a powerful theoretical tool for a deeper understanding of NMR spectroscopic parameters. *Int Rev Phys Chem* 2010;**29**:1–64.
31. Maldonado AF, Aucar GA. The UKB prescription and the heavy atom effects on the nuclear magnetic shielding of vicinal heavy atoms. *Phys Chem Chem Phys* 2009;**11**:5615–27.
32. Arcisauskaite V, Melo JI, Hemmingsen L, Sauer SPA. Nuclear magnetic resonance shielding constants and chemical shifts in linear ^{199}Hg compounds: a comparison of three relativistic computational methods. *J Chem Phys* 2011;**135**:044306.
33. Cukras J, Sadlej J. Predicted NMR properties of noble gas hydride cations RgH^+. *Chem Phys Lett* 2008;**467**:18–22.
34. Seino J, Hada M. Magnetic shielding constants calculated by the infinite-order Douglas–Kroll–Hess method with electron-electron relativistic corrections. *J Chem Phys* 2010;**132**:174105.
35. Hrobárik P, Hrobáriková V, Meier F, Repiský M, Komorovský S, Kaupp M. Relativistic four-component DFT calculations of ^{1}H NMR chemical shifts in transition-metal hydride complexes: unusual high-field shifts beyond the Buckingham–Stephens model. *J Phys Chem A* 2011;**115**:5654–9.

36. Buckingham AD, Stephens PJ. Proton chemical shifts in the nuclear magnetic resonance spectra of transition-metal hydrides: octahedral complexes. *J Chem Soc* 1964;2747–59.
37. Melo JI, Maldonado A, Aucar GA. Relativistic effects on the shielding of SnH_2XY and PbH_2XY (X, Y = F, Cl, Br and I) heavy atom–containing molecules. *Theor Chem Acc* 2011;**129**:483–94.
38. Autschbach J, Zheng SH. Analyzing Pt chemical shifts calculated from relativistic density functional theory using localized orbitals: the role of Pt 5d lone pairs. *Magn Reson Chem* 2008;**46**:S45–55.
39. Krykunov M, Ziegler T, van Lenthe E. Implementation of a hybrid DFT method for calculating NMR shieldings using Slater-type orbitals with spin−orbital coupling included. Applications to ^{187}Os, ^{195}Pt, and ^{13}C in heavy-metal complexes. *J Phys Chem A* 2009;**113**:11495–500.
40. Dmitrenko O, Bai S, Dybowski C. Prediction of ^{207}Pb NMR parameters for the solid ionic lead(II) halides using the relativistic ZORA-DFT formalism: comparison with the lead-containing molecular systems. *Solid State Nucl Magn Reson* 2008;**34**:186–90.
41. Bagno A, Bini R. NMR spectra of terminal-oxo gold and platinum complexes: relativistic DFT predictions. *Angew Chem Int Ed* 2010;**49**:1083–6.
42. Nakanishi W, Hayashi S, Katsura Y, Hada M. Relativistic effect on ^{77}Se NMR chemical shifts of various selenium species in the framework of zeroth-order regular approximation. *J Phys Chem A* 2011;**115**:8721–30.
43. Le Guennic B, Autschbach J. $[Pt@Pb_{12}]^{2-}$ A challenging system for relativistic density functional theory calculations of ^{195}Pt and ^{207}Pb NMR parameters. *Can J Chem* 2011;**89**:814–21.
44. Wren JEC, Schreckenbach G. Neptunium(VII) in alkaline solutions: $[NpO_2(OH)_4]^{1-}$ or $[NpO_4(OH)_2]^{3-}$? *Can J Chem* 2009;**87**:1436–43.
45. Neto AC, Ducati LC, Rittner R, Tormena CF, Contreras RH, Frenking G. Heavy halogen atom effect on ^{13}C NMR chemical shifts in monohalo derivatives of cyclohexane and pyran. Experimental and theoretical study. *J Chem Theory Comput* 2009;**5**:2222.
46. Standara S, Malinakova K, Marek R, Marek J, Hocek M, Vaara J, et al. Understanding the NMR chemical shifts for 6-halopurines: role of structure, solvent and relativistic effects. *Phys Chem Chem Phys* 2010;**12**:5126–39.
47. Truflandier LA, Brendler E, Wagler J, Autschbach J. ^{29}Si DFT/NMR observation of spin–orbit effect in metallasilatrane sheds some light on the strength of the metal→silicon interaction. *Angew Chem Int Ed* 2011;**50**:255–9.
48. Bagno A, Saielli G. Relativistic DFT calculations of the NMR properties and reactivity of transition metal methane sigma-complexes: insights on C–H bond activation. *Phys Chem Chem Phys* 2011;**13**:4285–91.
49. Saielli G, Bini R, Bagno A. Computational ^{19}F NMR. 1. General features. *Theor Chem Acc* 2012;**131**:1140–50.
50. Auer AA, Gauss J, Stanton JF. Quantitative prediction of gas-phase ^{13}C nuclear magnetic shielding constants. *J Chem Phys* 2003;**118**:10407–17.
51. Harding ME, Lenhart M, Auer AA, Gauss J. Quantitative prediction of gas-phase ^{19}F nuclear magnetic shielding constants. *J Chem Phys* 2008;**128**:244111.
52. Ramsey NF. Magnetic shielding of nuclei in molecules. *Phys Rev* 1950;**78**:699–703.
53. Flygare WH. Spin-rotation interaction and magnetic shielding in molecules. *J Chem Phys* 1964;**41**:793–800.
54. Forgeron MAM, Wasylishen RE, Penner GH. Investigation of magnetic shielding in xenon difluoride using solid-state NMR spectroscopy and relativistic density functional theory. *J Phys Chem A* 2004;**108**:4751–8.
55. Jameson CJ, de Dios AC. Theoretical and physical aspects of nuclear shielding. In: Webb GA, editor. *Nuclear magnetic resonance*, vol. 38. London: Royal Society of Chemistry; 2009. p. 68–93 Chap. 2; 2012. p. 38–55 Chap. 2.

56. Aucar IA, Gómez SS, Ruiz de Azúa MC, Giribet CG. Theoretical study of the nuclear spin-molecular rotation coupling for relativistic electrons and non-relativistic nuclei. *J Chem Phys* 2012;**136**:204119.
57. Keal TW, Tozer DJ. Selenium chemistry with DFT: molecular structures and ^{77}Se NMR shielding constants. *Mol Phys* 2005;**103**:1007–11.
58. Keal TW, Tozer DJ. The exchange-correlation potential in Kohn–Sham nuclear magnetic resonance shielding calculations. *J Chem Phys* 2003;**119**:3015–24.
59. Keal TW, Tozer DJ, Helgaker T. GIAO shielding constants and indirect spin–spin coupling constants: performance of density functional methods. *Chem Phys Lett* 2004;**391**:374–9.
60. Keal TW, Tozer DJ. A semiempirical generalized gradient approximation exchange-correlation functional. *J Chem Phys* 2004;**121**:5654–60.
61. Peach MJG, Kattirtzi JA, Teale AM, Tozer DJ. Shielding constants and chemical shifts in DFT: influence of optimized effective potential and coulomb-attenuation. *J Phys Chem A* 2010;**114**:7179–86.
62. Perdew JP, Ruzsinszky A, Tao J, Staroverov VN, Scuseria GE, Csonka GI. Prescription for the design and selection of density functional approximations: more constraint satisfaction with fewer fits. *J Chem Phys* 2005;**123**:062201.
63. Arbuznikov AV, Kaupp M. Advances in local hybrid exchange-correlation functionals: from thermochemistry to magnetic-resonance parameters and hyperpolarizabilities. *Int J Quantum Chem* 2011;**111**:2625–38.
64. Arbuznikov AV, Kaupp M. Nuclear shielding constants from localized local hybrid exchange-correlation potentials. *Chem Phys Lett* 2007;**442**:496–503.
65. Kaupp M, Arbuznikov A, Bahmann H. On occupied-orbital dependent exchange-correlation functionals. From local hybrids to Becke's B05 model. *Z Phys Chem* 2010;**224**:545–7.
66. Arbuznikov AV, Kaupp M, Bahmann H. From local hybrid functionals to "localized local-hybrid" potentials: formalism and thermochemical tests. *J Chem Phys* 2006;**124**:204102.
67. Arbuznikov AV, Kaupp M. Coupled-perturbed scheme for the calculation of electronic g-tensors with local hybrid functionals. *J Chem Theory Comput* 2009;**5**:2985–95.
68. Teale AM, Cohen AJ, Tozer DJ. Transition metal NMR chemical shifts from optimized effective potentials. *J Chem Phys* 2007;**126**:074101.
69. Shen Y, Bax A. Protein backbone chemical shifts predicted from searching a database for torsion angle and sequence homology. *J Biomol NMR* 2007;**38**:289–302.
70. Czinki E, Csaszar AG. Empirical isotropic chemical shift surfaces. *J Biomol NMR* 2007;**38**:269–87.
71. Vila JA, Scheraga HA. Factors affecting the use of $^{13}C^{\alpha}$ chemical shifts to determine, refine, and validate protein structures. *Proteins* 2008;**71**:641–54.
72. Tang S, Case DA. Vibrational averaging of chemical shift anisotropies in model peptides. *J Biomol NMR* 2007;**38**:255–66.
73. Precechtelova J, Novak P, Munzarova ML, Kaupp M, Sklenar V. Phosphorus chemical shifts in a nucleic acid backbone from combined molecular dynamics and density functional calculations. *J Am Chem Soc* 2010;**132**:17139–48.
74. Suitchmezian V, Jess I, Sehnert J, Seyfarth L, Senker J, Nather C. Structural, thermodynamic, and kinetic aspects of the polymorphism and pseudopolymorphism of prednisolone (11,17 alpha,21-trihydroxy-1,4-pregnadien-3,20-dion). *Cryst Growth Des* 2008;**8**:98–107.
75. Heider EM, Harper JK, Grant DM. Structural characterization of an anhydrous polymorph of paclitaxel by solid-state NMR. *Phys Chem Chem Phys* 2007;**9**:6083–97.
76. Ashbrook SE, Berry AJ, Frost DJ, Gregorovic A, Pickard CJ, Readman JE, et al. ^{17}O and ^{29}Si NMR parameters of $MgSiO_3$ phases from high-resolution solid-state NMR spectroscopy and first-principles calculations. *J Am Chem Soc* 2007;**129**:13213–24.

77. Sroka-Bartnicka A, Olejniczak S, Ciesielski W, Nosal A, Szymanowski H, Gazicki-Lipman M, et al. Solid state NMR study and density functional theory (DFT) calculations of structure and dynamics of poly(p-xylylenes). *J Phys Chem B* 2009;**113**:5464–72.
78. Salager E, Day GM, Stein RS, Pickard CJ, Elena B, Emsley L. Powder crystallography by combined crystal structure prediction and high-resolution ^{1}H solid-state NMR spectroscopy. *J Am Chem Soc* 2010;**132**:2564–6.
79. Garro Linck Y, Chattah AK, Graf R, Romanuk CB, Olivera ME, Manzo RH, et al. Multinuclear solid state NMR investigation of two polymorphic forms of ciprofloxacin-saccharinate. *Phys Chem Chem Phys* 2011;**13**:6590–6.
80. Johnston KE, Griffin JM, Walton RI, Dawson DM, Lightfoot P, Ashbrook SE. ^{93}Nb NMR and DFT investigation of the polymorphs of $NaNbO_3$. *Phys Chem Chem Phys* 2011;**13**:7565–76.
81. Liu W, Wang WD, Wang W, Bai S, Dybowski C. Influence of structure on the spectroscopic properties of the polymorphs of piroxicam. *J Phys Chem B* 2010;**114**:16641–9.
82. Lee J, Lu H, Moudrakovski IL, Ratcliffe CI, Ohmura R, Alavi S, et al. ^{13}C NMR studies of hydrocarbon guests in synthetic structure H gas hydrates: experiment and computation. *J Phys Chem A* 2011;**115**:1650–7.
83. Bifulco G, Riccio R, Gaeta C, Neri P. Quantum mechanical calculations of conformationally relevant ^{1}H and ^{13}C NMR chemical shifts of N-, O-, and S-substituted calixarene systems. *Chem Eur J* 2007;**13**:7185–94.
84. Webber AL, Elena B, Griffin JM, Yates JR, Pham TN, Mauri F, et al. Complete ^{1}H resonance assignment of β-maltose from ^{1}H–^{1}H DQ-SQ CRAMPS and ^{1}H (DQ-DUMBO)–^{13}C SQ refocused INEPT 2D solid-state NMR spectra and first principles GIPAW calculations. *Phys Chem Chem Phys* 2010;**12**:6970–83.
85. Bagno A, Rastrelli F, Saielli G. Prediction of the ^{1}H and ^{13}C NMR spectra of α-d-glucose in water by DFT methods and MD simulations. *J Org Chem* 2007;**72**:7373–81.
86. Mocci F. Torsion angle relationship of the ^{17}O NMR chemical shift in α, β-unsaturated carbonyl compounds. *Magn Reson Chem* 2009;**47**:862–7.
87. Dong RY, Marini A. Conformational study of a bent-core liquid crystal: ^{13}C NMR and DFT computation approach. *J Phys Chem B* 2009;**113**:14062–72.
88. Ruiz EJ, Sears DN, Pines A, Jameson CJ. Diastereomeric Xe chemical shifts in tethered cryptophane cages. *J Am Chem Soc* 2006;**128**:16980–8.
89. Sears DN, Vukovic L, Jameson CJ. Xe NMR lineshapes in channels decorated with paramagnetic centers. *J Chem Phys* 2006;**125**:114708.
90. Yuan H, Murad S, Jameson CJ, Olson JD. Molecular dynamics simulation of Xe chemical shifts and solubility in n-alkanes. *J Phys Chem C* 2007;**111**:15771–83.
91. Yuan H, Jameson CJ, Gupta SK, Olson JD, Murad S. Prediction of Henry's constants of xenon in cyclo-alkanes from molecular dynamics simulations. *Fluid Phase Equil* 2008;**269**:73–9.
92. Ochsenfeld C, Brown SP, Schnell I, Gauss J, Spiess HW. Structure assignment in the solid state by the coupling of quantum chemical calculations with NMR experiments: a columnar hexabenzocoronene derivative. *J Am Chem Soc* 2001;**123**:2597–606.
93. Steiner E, Soncini A, Fowler PW. Full spectral decomposition of ring currents. *J Phys Chem A* 2006;**110**:12882–6.
94. Steiner E, Fowler PW, Soncini A, Jenneskens LW. Current-density maps as probes of aromaticity: global and π ring currents in totally resonant polycyclic aromatic hydrocarbons. *Faraday Discuss* 2007;**135**:309–23.
95. Pelloni S, Lazzeretti P. Magnetotropicity of five-membered heterocyclic molecules. *Theor Chem Acc* 2007;**117**:903–13.
96. Pelloni S, Faglioni F, Zanasi R, Lazzeretti P. Topology of magnetic-field induced current-density field in diatropic mono-cyclic molecules. *Phys Rev A* 2006;**74**:012506.

97. Pelloni S, Lazzeretti P, Zanasi R. Assessment of σ-diatropicity of the cyclopropane molecule. *J Phys Chem A* 2007;**111**:8163–9.
98. Pelloni S, Lazzeretti P, Zanasi R. Topological models of magnetic field induced current density field in small molecules. *Theor Chem Acc* 2009;**123**:353–64.
99. Pelloni S, Lazzeretti P. Ring current models for acetylene and ethylene molecules. *Chem Phys* 2009;**356**:153–63.
100. Okazaki T, Laali KK. Transannular π–π interactions in janusenes and in related rigid systems with cofacial aromatic rings; gauging aromaticity in the hydrocarbons and in model carbocations; a DFT study. *Org Biomol Chem* 2006;**4**:3085–95.
101. Corminboeuf C, King RB, Schleyer PV. Implications of molecular orbital symmetries and energies for the electron delocalization of inorganic clusters. *Chemphyschem* 2007;**8**:391–8.
102. Kleinpeter E, Koch A, Seidl PR. Visualization and quantification of the anisotropic effect of C=C double bonds on ^{1}H NMR spectra of highly congested hydrocarbons-indirect estimates of steric strain. *J Phys Chem A* 2008;**112**:4989–95.
103. Kleinpeter E, Koch A. Trisannelated benzenes–aromatic molecules or 1,3,5-cyclohexatriene derivatives subjected to magnetic properties. *J Mol Struct (Theochem)* 2008;**857**:89–94.
104. Kleinpeter E, Koch A, Sahoo HS, Chand DK. Anisotropic effect of the nitrate anion-manifestation of diamagnetic proton chemical shifts in the ^{1}H NMR spectra of NO_3-coordinated complexes. *Tetrahedron* 2008;**64**:5044–50.
105. Kleinpeter E, Mod S, Koch A. Endohedral and external through-space shieldings of the fullerenes C_{50}, C_{60}, C_{60}^{-6}, C_{70}, and C_{70}^{-6}–visualization of (anti)aromaticity and their effects on the chemical shifts of encapsulated nuclei. *J Org Chem* 2008;**73**:1498–507.
106. Kleinpeter E, Koch A, Shainyan BA. Cyclobutadiene dianion derivatives–planar 4c,6e or three-dimensional 6c,6e aromaticity? *J Mol Struct (Theochem)* 2008;**863**:117–22.
107. Shainyan BA, Fettke A, Kleinpeter E. Push-pull vs captodative aromaticity. *J Phys Chem A* 2008;**112**:10895–903.
108. Cuesta IG, Marin JS, de Meras AMJS. How nitrogen modifies the nuclear magnetic shielding in tetraazanaphthalenes. *Phys Chem Chem Phys* 2009;**11**:4278–85.
109. Periyasamy G, Burton NA, Hillier IH, Thomas JMH. Electron delocalization in the metallabenzenes: a computational analysis of ring currents. *J Phys Chem A* 2008;**112**:5960–72.
110. Kleinpeter E, Koch A. The anisotropic effect of functional groups in ^{1}H NMR spectra is the molecular response property of spatial NICS–the frozen conformational equilibria of 9-arylfluorenes. *Tetrahedron* 2011;**67**:5740–3.
111. Duma L, Abergel D, Tekely P, Bodenhausen G. Proton chemical shift anisotropy measurements of hydrogen-bonded functional groups by fast magic-angle spinning solid-state NMR spectroscopy. *Chem Commun* 2008;2361–3.
112. Yates JR, Pham TN, Pickard CJ, Mauri F, Amado AM, Gil AM, et al. An investigation of weak C–HO hydrogen bonds in maltose anomers by a combination of calculation and experimental solid-state NMR spectroscopy. *J Am Chem Soc* 2005;**127**:10216–20.
113. Cai L, Fushman D, Kosov DS. Density functional calculations of ^{15}N chemical shifts in solvated dipeptides. *J Biomol NMR* 2008;**41**:77–88.
114. Precechtelova J, Padrta P, Munzarova ML, Sklenar V. ^{31}P chemical shift tensors for canonical and non-canonical conformations of nucleic acids: a DFT study and NMR implications. *J Phys Chem B* 2008;**112**:3470–8.
115. Gajda J, Olejniczak S, Bryndal I, Potrzebowski MJ. Elucidation of structural restraints for phosphate residues with different hydrogen bonding and ionization states. *J Phys Chem B* 2008;**112**:14036–44.

116. Dong S, Ida R, Wu G. A combined experimental and theoretical ^{17}O NMR study of crystalline urea: an example of large hydrogen-bonding effects. *J Phys Chem A* 2000;**104**:11194–202.
117. Bryce DL, Sward GD, Adiga S. Solid-state $^{35/37}Cl$ NMR spectroscopy of hydrochloride salts of amino acids implicated in chloride ion transport channel selectivity: opportunities at 900 MHz. *J Am Chem Soc* 2006;**128**:2121–34.
118. Chapman RP, Bryce DL. A high-field solid-state $^{35/37}Cl$ NMR and quantum chemical investigation of the chlorine quadrupolar and chemical shift tensors in amino acid hydrochlorides. *Phys Chem Chem Phys* 2007;**9**:6219–30.
119. Kongsted J, Nielsen CB, Mikkelsen KV, Christiansen O, Ruud K. Nuclear magnetic shielding constants of liquid water: insights from hybrid quantum mechanics/molecular mechanics models. *J Chem Phys* 2007;**126**:034510.
120. Klamt A, Schüürmann G. COSMO: a new approach to dielectric screening in solvents with explicit expressions for the screening energy and its gradient. *J Chem Soc, Perkin Trans 2* 1993;799–805.
121. Miertuš S, Scrocco E, Tomasi J. Electrostatic interactions of a solute with a continuum. A direct utilization of ab initio molecular potentials for the pervision of solvent effects. *Chem Phys* 1981;**55**:117–29.
122. de Dios AC, Pearson JG, Oldfield E. Secondary and tertiary structural effects on protein NMR chemical shifts: an *ab initio* approach. *Science* 1993;**260**:1491–6.
123. de Dios AC, Oldfield E. Methods for computing nuclear magnetic resonance chemical shielding in large systems: multiple cluster and charge field approaches. *Chem Phys Lett* 1993;**205**:108–16.
124. de Dios AC, Laws DD, Oldfield E. Predicting carbon-13 nuclear magnetic resonance chemical shielding tensors in zwitterionic L-threonine and L-tyrosine via quantum chemistry. *J Am Chem Soc* 1994;**116**:7784–6.
125. Stueber D. The embedded ion method: a new approach to the electrostatic description of crystal lattice effects in chemical shielding calculations. *Concepts Magn Reson A* 2006;**28**:347–68.
126. Stefanovich EV, Truong TN. A simple method for incorporating Madelung field effects into *ab initio* embedded cluster calculations of crystals and macromolecules. *J Phys Chem B* 1998;**102**:3018–22.
127. Di Fiori N, Orendt AM, Caputo MC, Ferraro MB, Facelli JC. Modeling solid-state effects on NMR chemical shifts using electrostatic models. *Magn Reson Chem* 2004;**42**:S41–7.
128. Weber J, Schmedt auf der Günne J. Calculation of NMR parameters in ionic solids by an improved self-consistent embedded cluster method. *Phys Chem Chem Phys* 2010;**12**:583–603.
129. Buckingham AD. Solvent effects in nuclear magnetic resonance spectra. *Can J Chem* 1960;**38**:300–7.
130. Bishop DM, Cybulski SM. Ab-initio calculation of the nuclear magnetic shielding constants and shielding polarizabilities of the noble gases. *J Magn Reson A* 1994;**107**:99–101.
131. Cybulski SM, Bishop DM. Calculation of magnetic properties VII. Electron-correlated magnetizability polarizabilities and nuclear shielding polarizabilities for nine small molecules. *Mol Phys* 1998;**93**:739–50.
132. Pecul M, Saue T, Ruud K, Rizzo A. Electric field effects on the shielding constants of noble gases: a four-component relativistic Hartree-Fock study. *J Chem Phys* 2004;**121**:3051–7.
133. Gauss J. Shielding polarizabilities calculated at the coupled-cluster singles and doubles level augmented by a perturbative treatment of triple excitations. *J Chem Phys* 2002;**116**:869–77.

134. Stueber D, Jameson CJ. The chemical shifts of Xe in the cages of clathrate hydrate structure I and II. *J Chem Phys* 2004;**120**:1560–71.
135. Banyai DR, Murakhtina T, Sebastiani D. NMR chemical shifts as a tool to analyze first principles molecular dynamics simulations in condensed phases: the case of liquid water. *Magn Reson Chem* 2010;**48**:S56–60.
136. Truflandier LA, Sutter K, Autschbach J. Solvent effects and dynamic averaging of ^{195}Pt NMR shielding in *cis* platin derivatives. *Inorg Chem* 2011;**50**:1723–32.
137. Bagno A, Bonchio M, Autschbach J. Computational modeling of polyoxotungstates by relativistic DFT calculations of ^{183}W NMR chemical shifts. *Chem Eur J* 2006;**12**:8460–71.
138. Sugimori K, Kawabe H, Nagao H, Nishikawa K. *Ab initio* and DFT study of ^{31}P-NMR chemical shifts of sphingomyelin and dihydrosphingomyelin lipid molecule. *Int J Quantum Chem* 2009;**109**:3685–93.
139. Bai S, Dmitrenko O, Dybowski C. ^{15}N and ^{13}C NMR chemical shifts of 6-(fluoro, chloro, bromo, and iodo)purine 2'-deoxynucleosides: measurements and calculations. *Magn Reson Chem* 2010;**48**:61–7.
140. Stueber D, Orendt AM, Facelli JC, Parry RW, Grant DM. Carbonates, thiocarbonates, and the corresponding monoalkyl derivatives: III. The ^{13}C chemical shift tensors in potassium carbonate, bicarbonate and related monomethyl derivatives. *Solid State NMR* 2002;**22**:29–49.
141. Stueber D, Grant DM. ^{13}C and ^{15}N chemical shift tensors in adenosine, guanosine dihydrate, 2-deoxythymidine, and cytidine. *J Am Chem Soc* 2002;**24**:10359–551.
142. Barich DH, Clawson JS, Stueber D, Strohmeier M, Pugmire RJ, Grant DM. Determination of ^{13}C chemical shift tensors in the presence of hydrogen bonding and ^{14}N quadrupolar coupling: p-aminosalicylic acid, isaniazid, and pyrazinamide. *J Phys Chem A* 2002;**106**:11375–9.
143. Jameson CJ, Stueber D. The NMR lineshapes of Xe in the cages of clathrate hydrates. *J Chem Phys* 2004;**120**:10200–14.
144. Vaara J, Pyykkö P. Relativistic, nearly basis-set-limit nuclear magnetic shielding constants of the rare gases He–Rn: a way to absolute nuclear magnetic resonance shielding scales. *J Chem Phys* 2003;**118**:2973–6.
145. Hanni M, Lantto P, Illias M, Hansen HJ, Vaara J. Relativistic effects in the intermolecular interaction-induced nuclear magnetic resonance parameters of xenon dimer. *J Chem Phys* 2007;**127**:164313.
146. Hanni M, Lantto P, Vaara J. Pairwise additivity in the nuclear magnetic resonance interactions of atomic xenon. *Phys Chem Chem Phys* 2009;**11**:2485–96.
147. Hyvarinen M, Vaara J, Goldammer A, Kutzky B, Hegetschweiler K, Kaupp M, et al. Characteristic spin-orbit induced ^{1}H(CH_2) chemical shifts upon deprotonation of group 9 polyamine aqua and alcohol complexes. *J Am Chem Soc* 2009;**131**:11909–18.
148. Sears DN, Jameson CJ, Harris RA. Nuclear magnetic shielding and chirality IV. The odd and even character of the shielding response to a chiral potential. *J Chem Phys* 2004;**120**:3277–83.
149. Barra AL, Robert JR. Parity non-conservation and NMR parameters. *Mol Phys* 1996;**88**:875–86.
150. Sears DN, Jameson CJ, Harris RA. Nuclear magnetic shielding and chirality I. The shielding tensor of Xe interacting with Ne helices. *J Chem Phys* 2003;**119**:2685–90.
151. Sears DN, Jameson CJ, Harris RA. Nuclear magnetic shielding and chirality II. The shielding tensor of a naked spin in Ne helices. *J Chem Phys* 2003;**119**:2691–3.
152. Sears DN, Jameson CJ, Harris RA. Nuclear magnetic shielding and chirality III. The single electron on a helix model. *J Chem Phys* 2003;**119**:2694–701.

153. Buckingham AD, Malm S. Asymmetry in the nuclear magnetic shielding tensor. *Mol Phys* 1971;**22**:1127–30.
154. Ruiz EJ, Sears DN, Pines A, Jameson CJ. Diastereomeric Xe chemical shifts in tethered cryptophane cages. *J Am Chem Soc* 2006;**128**:16980–8.
155. Ruiz EJ, Spence MM, Rubin SM, Wemmer DE, Pines A, Winssinger N, et al. *43rd experimental NMR conference, April 14–19, Asilomar, CA*; 2002.
156. Buckingham AD, Fischer P. Direct chiral discrimination in NMR spectroscopy. *Chem Phys* 2006;**324**:111–6.
157. Harris RA, Jameson CJ. A note on chirality in NMR spectroscopy. *J Chem Phys* 2006;**124**:096101.
158. Allen BD, Cintrat JC, Faucher N, Berthault P, Rousseau B, O'Leary DJ. An isosparteine derivative for stereochemical assignment of stereogenic (chiral) methyl groups using tritium NMR: theory and experiment. *J Am Chem Soc* 2005;**127**:412–20.
159. Smith SG, Channon JA, Paterson I, Goodman JM. The stereochemical assignment of acyclic polyols: a computational study of the NMR data of a library of stereopentad sequences from polyketide natural products. *Tetrahedron* 2010;**66**:6437–44.
160. Smith SG, Goodman JM. Assigning stereochemistry to single diastereoisomers by GIAO NMR calculation: the DP4 probability. *J Am Chem Soc* 2010;**132**:12946–59.
161. Facelli JC, Grant DM. Determination of molecular symmetry in crystalline naphthalene using solid-state NMR data. *Nature* 1993;**365**:325–7.
162. Strohmeier M, Orendt AM, Alderman DW, Grant DM. Investigation of the polymorphs of dimethyl-3,6-dichloro-2,5-hydroxyterephthalate by ^{13}C solid-state NMR spectroscopy. *J Am Chem Soc* 2001;**123**:1713–22.
163. Hu JZ, Facelli JC, Alderman DW, Pugmire RJ, Grant DM. ^{15}N chemical shift tensors in nucleic acid bases. *J Am Chem Soc* 1998;**120**:9863–9.
164. Facelli JC, Pugmire RJ, Grant DM. Effects of hydrogen bonding in the calculations of ^{15}N chemical shift tensors: benzamide. *J Am Chem Soc* 1996;**118**:5488–9.
165. Anderson K, Merwin LH, Wilson WS, Facelli JC. ^{15}N chemical shifts in energetic materials: CP/MAS and ab initio studies of aminonitropyridines, aminonitropyrimidines, and their N-oxides. *Int J Mol Sci* 2002;**3**:858–72.
166. Pechkis DL, Walter EJ, Krakauer H. High sensitivity of ^{17}O NMR to p-d hybridization in transition metal perovskites: first principles calculations of large anisotropic chemical shielding. *J Chem Phys* 2009;**131**:184511.
167. Pechkis DL, Walter EJ, Krakauer H. First-principles calculations of ^{17}O nuclear magnetic resonance chemical shielding in $Pb(Zr_{1/2}Ti_{1/2})O_3$ and $Pb(Mg_{1/3}Nb_{2/3})O_3$: linear dependence on transition-metal/oxygen bond lengths. *J Chem Phys* 2011;**135**:114507.
168. Mauri F, Pfrommer BG, Louie SG. *Ab-initio* theory of NMR chemical shifts in solids and liquids. *Phys Rev Lett* 1996;**77**:5300–3.
169. Pickard CJ, Mauri F. All-electron magnetic response with pseudopotentials: NMR chemical shifts. *Phys Rev B* 2001;**63**:245101.
170. Clark SJ, Segall MD, Pickard CJ, Hasnip PJ, Probert MJ, Refson K, et al. *Zeit Kristallographie* 2005;**220**:567–70.http://www.castep.org/.
171. Canning A, Raczkowski D. Scaling first-principles planewave codes to thousands of processors. *Computer Physics Communications* 2004; 169: 449–453. PARATEC (PARAllel Total Energy Code) developed at Lawrence Berkeley National Laboratory by Pfrommer B, Raczkowski D, Canning A, Louie SG, (with contributions from F. Mauri, M. Côté, Y. Yoon, C. Pickard and P. Haynes) is heavily optimized for running on large parallel machines https://www.nersc.gov/users/software/applications/materials-science/paratec/. Accessed Aug. 14, 2012.
172. Giannozzi P, Baroni S, Bonini N, Calandra M, Car R, Cavazzoni C, Ceresoli D, Chiarotti GL, Cococcioni M, Dabo I, Dal Corso A, Fabris S, Fratesi G, de Gironcoli S,

Gebauer R, Gerstmann U, Gougoussis C, Kokalj A, Lazzeri M, Martin-Samos L, Marzari N, Mauri F, Mazzarello R, Paolini S, Pasquarello A, Paulatto L, Sbraccia C, Scandolo S, Sclauzero G, Seitsonen AP, Smogunov A, Umari P, Wentzcovitch RM. QUANTUM ESPRESSO: a modular and open-source software project for quantum simulations of materials. *J Phys Condens Matter* 2009;21:395502. Quantum ESPRESSO is available from http://www.quantum-espresso.org/. Accessed Aug. 14, 2012.

173. Sebastiani D, Parrinello M. A new ab-initio approach for NMR chemical shifts in periodic systems. *J Phys Chem A* 2001;**105**:1951–8.
174. J. Hutter, M. Parrinello, D. Marx, P. Focher, M. Tuckerman, W. Andreoni, A. Curioni, E. Fois, U. Roetlisberger, P. Giannozzi, T. Deutsch, A. Alavi, D. Sebastiani, A. Laio, J. VandeVondele, A. Seitsonen, S. Billeter, Computer code CPMD, version 3.5, Copyright IBM Corp. and MPI-FKF Stuttgart 1990–2002, http://www.cpmd.org. Accessed Aug. 14, 2012.
175. Weber V, Iannuzzi M, Giani S, Hutter J, Declerck R, Waroquier M. Magnetic linear response properties calculations with the Gaussian and augmented-plane-wave method. *J Chem Phys* 2009;**131**:014106.
176. VandeVondele J, Krack M, Mohamed F, Parrinello M, Chassaing T, Hutter J. Quickstep: fast and accurate density functional calculations using a mixed Gaussian and plane waves approach. *Comput Phys Commun* 2005;**167**:103–28.
177. The CP2K developers group, 2008, http:/cp2k.berlios.de/.
178. Thonhauser T, Ceresoli D, Mostofi AA, Marzari N, Resta R, Vanderbilt D. A converse approach to the calculation of NMR shielding tensors. *J Chem Phys* 2009;**131**:101101.
179. Thonhauser T, Ceresoli D, Marzari N. NMR shifts for polycyclic aromatic hydrocarbons from first-principles. *Int J Quantum Chem* 2009;**109**:3336–42.
180. Ceresoli D, Marzari N, Lopez MG, Thonhauser T. *Ab initio* converse NMR approach for pseudopotentials. *Phys Rev B* 2010;**81**:184424.
181. Skachkov D, Krykunov M, Kadantsev E, Ziegler T. The calculation of NMR chemical shifts in periodic systems based on gauge including atomic orbitals and density functional theory. *J Chem Theory Comput* 2010;**6**:1650–9.
182. Skachkov D, Krykunov M, Ziegler T. An improved scheme for the calculation of NMR chemical shifts in periodic systems based on gauge including atomic orbitals and density functional theory. *Can J Chem* 2011;**89**:1150–61.
183. P.H.T. Philipsen, G. te Velde, E.J. Baerends, J.A. Berger, P.L. de Boeij, J.A. Groeneveld, E.S. Kadantsev, R. Klooster, F. Kootstra, P. Romaniello, D.G. Skachkov, J.G. Snijders, G. Wiesenekker, T. Ziegler, BAND2012, SCM, Theoretical Chemistry, Vrije Universiteit, Amsterdam, The Netherlands, http://www.scm.com BAND, a periodic structure program for the study of bulk crystals, polymers, and surfaces in the Amsterdam Density Functional (ADF) package
184. Schwarz K, Blaha P, Trickey SB. Electronic structure of solids with WIEN2k. *Mol Phys* 2010;**108**:3147–66.
185. P. Blaha, K. Schwarz, G. Madsen, D. Kvasnicka and J. Luitz, WIEN2k, An Augmented Plane Wave Plus Local Orbitals Program for Calculating Crystal Properties, Institute for Materials Chemistry, Technical University Vienna. ©2001 by P. Blaha and K. Schwarz. Latest release December 14, 2007.
186. Laskowski R, Blaha P. Calculations of NMR chemical shifts with APW-based methods. *Phys Rev B* 2012;**85**:035132.
187. Gregor T, Mauri F, Car R. A comparison of methods for the calculation of NMR chemical shifts. *J Chem Phys* 1999;**111**:1815–22.
188. Mauri F, Pfrommer BG, Louie SG. *Ab initio* NMR chemical shift of diamond, chemical-vapor-deposited diamond, and amorphous carbon. *Phys Rev Lett* 1997;**79**:2340–3.
189. Yoon Y-G, Pfrommer BG, Mauri F, Louie SG. NMR chemical shifts in hard carbon nitride compounds. *Phys Rev Lett* 1998;**80**:3388–91.

190. Mauri F, Pfrommer BG, Louie SG. Signature of surface states on NMR chemical shifts: a theoretical prediction. *Phys Rev B* 1999;**60**:2941–5.
191. Mauri F, Pasquarello A, Pfrommer BG, Yoon Y-G, Louie SG. Si-O-Si bond-angle distribution in vitreous silica from first-principles ^{29}Si NMR analysis. *Phys Rev B* 2000;**62**:R4786–9.
192. Pfrommer BG, Mauri F, Louie SG. NMR chemical shifts of ice and liquid water: the effects of condensation. *J Am Chem Soc* 2000;**122**:123–9.
193. Blöchl PE. Projector augmented-wave method. *Phys Rev B* 1994;**50**:17953–79.
194. Mauri F, Vast N, Pickard CJ. Atomic structure of icosahedral B_4C boron carbide from a first principles analysis of NMR spectra. *Phys Rev Lett* 2001;**87**:085506.
195. Marques MAL, d'Avezac M, Mauri F. Magnetic response and NMR spectra of carbon nanotubes from *ab initio* calculations. *Phys Rev B* 2006;**73**:125433.
196. Profeta M, Mauri F, Pickard CJ. Accurate first principles prediction of ^{17}O NMR parameters in SiO_2: assignment of the zeolite ferrierite spectrum. *J Am Chem Soc* 2003;**125**:541–8.
197. Farnan I, Balan E, Pickard CJ, Mauri F. The effect of radiation damage on local structure in the crystalline fraction of $ZrSiO_4$: investigating the ^{29}Si NMR response to pressure in zircon and reidite. *Am Mineralogist* 2003;**88**:1663–7.
198. Charpentier T, Ispas S, Profeta M, Mauri F, Pickard CJ. First-principles calculation of ^{17}O, ^{29}Si, and ^{23}Na NMR spectra of sodium silicate crystals and glasses. *J Phys Chem B* 2004;**108**:4147–61.
199. Benoit M, Profeta M, Mauri F, Pickard CJ, Tuckerman ME. First-principles calculation of the ^{17}O NMR parameters of a calcium aluminosilicate glass. *J Phys Chem B* 2005;**109**:6052–60.
200. Gervais C, Profeta M, Babonneau F, Pickard CJ, Mauri F. *Ab-initio* calculations of NMR parameters of highly coordinated oxygen sites in aluminosilicates. *J Phys Chem B* 2004;**108**:13249–53.
201. Profeta M, Benoit M, Mauri F, Pickard CJ. First-principles calculation of the ^{17}O NMR parameters in Ca oxide and Ca aluminosilicates: the partially covalent nature of the Ca-O bond, a challenge for density functional theory. *J Am Chem Soc* 2004;**126**:12628–35.
202. Yates JR, Dobbins SE, Pickard CJ, Mauri F, Ghi PY, Harris RK. A combined first principles computational and solid-state NMR study of a molecular crystal: flurbiprofen. *Phys Chem Chem Phys* 2005;**7**:1402–7.
203. Gervais C, Dupree R, Pike KJ, Bonhomme C, Profeta M, Pickard CJ, et al. Combined first-principles computational and experimental multinuclear solid-state NMR investigation of amino acids. *J Phys Chem A* 2005;**109**:6960–9.
204. Ghi PY, Harris RK, Hammond RB, Ma C, Roberts KJ, Yates JR, et al. Solid-state NMR and computational studies of 4-methyl-2-nitroacetanilide. *Magn Reson Chem* 2006;**44**:325–33.
205. Yates JR, Pickard CJ, Payne MC, Dupree R, Profeta M, Mauri F. Theoretical investigation of oxygen-17 NMR shielding and electric field gradients in glutamic acid polymorphs. *J Phys Chem A* 2004;**108**:6032–7.
206. Harris RK, Ghi PY, Puschmann H, Apperley DC, Griesser UJ, Hammond RB, et al. Structural studies of the polymorphs of carbamazepine, its dihydrate, and two solvates. *Org Process Res Dev* 2005;**9**:902–10.
207. Yates JR, Pickard CJ, Mauri F. Calculation of NMR chemical shifts for extended systems using ultrasoft pseudopotentials. *Phys Rev B* 2007;**76**:024401.
208. Vanderbilt D. Soft self-consistent pseudopotentials in a generalized eigenvalue formalism. *Phys Rev B* 1990;**41**:7892–5.
209. Zhou B, Sherriff BL, Wang T. 27Al NMR spectroscopy at multiple magnetic fields and *ab initio* quantum modeling for kaolinite. *Am Mineralogist* 2009;**94**:865–71.

210. Ashbrook SE, Polles LL, Gautier R, Pickard CJ, Walton RI. ^{23}Na multiple-quantum MAS NMR of the perovskites $NaNbO_3$ and $NaTaO_3$. *Phys Chem Chem Phys* 2006;**8**:3423–31.
211. Harris RK, Cadars S, Emsley L, Yates JR, Pickard CJ, Jetti R, et al. NMR crystallography of oxybuprocaine hydrochloride, Modification II°. *Phys Chem Chem Phys* 2006;**9**:360–8.
212. Harris RK, Joyce SA, Pickard CJ, Cadars S, Emsley L. Assigning carbon-13 NMR spectra to crystal structures by the INADEQUATE pulse sequence and first principles computation: a case study of two forms of testosterone. *Phys Chem Chem Phys* 2006;**8**:137–43.
213. Webber AL, Emsley L, Claramunt RM, Brown P. NMR crystallography of Campho [2,3-c]pyrazole ($Z' = 6$): combining high-resolution ^{1}H-^{13}C solid-state MAS NMR spectroscopy and GIPAW chemical-shift calculations. *J Phys Chem A* 2010;**114**:10435–42.
214. Kücukbenli E, Sonkar K, Sinha N, de Gironcoli S. Complete ^{13}C NMR chemical shifts assignment for cholesterol crystals by combined CP-MAS spectral editing and *ab initio* GIPAW calculations with dispersion forces. *J Phys Chem A* 2012;**116**:3765–9.
215. Johnston JC, Iuliucci RJ, Facelli JC, Fitzgerald G, Mueller KT. Intermolecular shielding contributions studied by modeling the ^{13}C chemical-shift tensors of organic single crystals with plane waves. *J Chem Phys* 2009;**131**:144503.
216. Cuny J, Furet E, Gautier R, Le Polles L, Pickard CJ, d'Espinose de Lacaillerie CB. Density functional theory calculations of ^{95}Mo NMR parameters in solid-state compounds. *Chemphyschem* 2009;**10**:3320–9.
217. Widdifield CM, Bryce DL. Solid-state $^{79/81}$Br NMR and gauge-including projector-augmented wave study of structure, symmetry, and hydration state in alkaline earth metal bromides. *J Phys Chem A* 2010;**114**:2102–16.
218. Kibalchenko M, Yates JR, Pasquarello A. First-principles investigation of the relation between structural and NMR parameters in vitreous GeO_2. *J Phys: Condens Mat* 2010;**22**:145501.
219. Pedone A, Gambuzzi E, Malavasi G, Menziani MC. First-principles simulations of the ^{27}Al and ^{17}O solid-state NMR spectra of the $CaAl_2Si_3O_{10}$ glass. *Theor Chem Acc* 2012;**131**:1147.
220. De Gortari I, Portella G, Salvatella X, Bajaj VS, van der Wel PCA, Yates JR, et al. Time averaging of NMR chemical shifts in the MLF peptide in the solid state. *J Am Chem Soc* 2010;**132**:5993–6000.
221. Truflandier L, Paris M, Boucher F. Density functional theory investigation of 3d transition metal NMR shielding tensors in diamagnetic systems using the gauge-including projector augmented-wave method. *Phys Rev B* 2007;**76**:035102.
222. Yates JR, Pickard CJ, Payne MC, Mauri F. Relativistic nuclear magnetic resonance chemical shifts of heavy nuclei with pseudopotentials and the zeroth-order regular approximation. *J Chem Phys* 2003;**118**:5746–53.
223. http://www.gipaw.net.
224. Berghold G, Mundy C, Romero A, Hutter J, Parrinello M. General and efficient algorithms for obtaining maximally localized Wannier functions. *Phys Rev B* 2000;**61**:10040.
225. Piana S, Sebastiani D, Carloni P, Parrinello M. *Ab initio* molecular dynamics-based assignment of the protonation state of pepstatin A/HIV-1 protease cleavage site. *J Am Chem Soc* 2001;**123**:8730–7.
226. Keith TA, Bader RFW. Calculation of magnetic response properties using a continuous set of gauge transformations. *Chem Phys Lett* 1993;**210**:223–31.
227. Keith TA, Bader RFW. Calculation of magnetic response properties using atoms in molecules. *Chem Phys Lett* 1992;**194**:1–8.
228. Sebastiani D. Ab-initio calculations of NMR parameters In condensed phases. *Modern Phys Lett B* 2003;**17**:1301–19.

229. Sebastiani D, Goward G, Schnell I, Parrinello M. NMR chemical shifts in periodic systems from first principles. *Comput Phys Commun* 2002;**147**:707–10.
230. Sebastiani D, Goward G, Schnell I, Spiess HW. NMR chemical shifts in proton conducting crystals from first principles. *J Mol Struct (Theochem)* 2003;**625**:283–8.
231. Schmidt J, Hoffmann A, Spiess HW, Sebastiani D. Bulk chemical shifts in hydrogen-bonded systems from first-principles calculations and solid-state-NMR. *J Phys Chem B* 2006;**110**:23204–10.
232. Ceresoli D, Gerstmann U, Seitsonen AP, Mauri F. First-principles theory of orbital magnetization. *Phys Rev B* 2009;**81**:060409.
233. Ceresoli D, Thonhauser T, Vanderbilt D, Resta R. Orbital magnetization in crystalline solids. *Phys Rev B* 2006;**74**:24408.
234. Widdifield CM, Bryce DL. Solid-state ^{127}I NMR and GIPAW DFT study of metal iodides and their hydrates: structure, symmetry, and higher-order quadrupole-induced effects. *J Phys Chem A* 2010;**114**:10810–23.
235. Abou-Hamad E, Babaa M-R, Bouhrara M, Kim Y, Saih Y, Dennler S, et al. Structural properties of carbon nanotubes derived from ^{13}C NMR. *Phys Rev B* 2011;**84**:165417.
236. Pickard CJ, Salager E, Pintacuda G, Elena B, Emsley L. Resolving structures from powders by NMR crystallography using combined proton spin diffusion and plane wave DFT calculations. *J Am Chem Soc* 2007;**129**:8932–3.
237. Bryce DL, Bultz EB. Alkaline earth chloride hydrates: chlorine quadrupolar and chemical shift tensors by solid-state NMR spectroscopy and plane wave pseudopotential calculations. *Chem Eur J* 2007;**13**:4786–96.
238. Attrell RJ, Widdifield CM, Korobkov I, Bryce DL. Weak halogen bonding in solid haloanilinium halides probed directly via chlorine-35, bromine-81, and iodine-127 NMR spectroscopy. *Cryst Growth Des* 2012;**12**:1641–53.
239. Burgess KMN, Korobkov I, Bryce DL. A combined solid-state NMR and X-ray crystallography study of the bromide ion environments in triphenylphosphonium bromides. *Chem Eur J* 2012;**18**:5748–58.
240. Vasconcelos F, Cristol S, Paul J-F, Tricot G, Amoureux J-P, Montagne L, et al. ^{17}O solid-state NMR and first-principles calculations of sodiumtrimetaphosphate ($Na_3P_3O_9$), tripolyphosphate ($Na_5P_3O_{10}$), and pyrophosphate ($Na_4P_2O_7$). *Inorg Chem* 2008;**47**:7327–37.
241. Olejniczak S, Mikua-Pacboczyk J, Hughes CE, Potrzebowski MJ. ^{15}N and ^{13}C high-resolution solid-state NMR study of the polymorphism of the L-enantiomer of N-benzoylphenylalanine. *J Phys Chem B* 2008;**112**:1586–93.
242. Macholl S, Lentz D, Borner F, Buntkowsky G. Polymorphism of N, N″-diacetylbiuret studied by solid-state ^{13}C and ^{15}N NMR spectroscopy, DFT calculations, and X-ray diffraction. *Chem Eur J* 2007;**13**:6139–49.
243. Ashbrook SE, Le Polles L, Pickard CJ, Berry AJ, Wimperis S, Farnan I. First-principles calculations of solid-state ^{17}O and ^{29}Si NMR spectra of Mg_2SiO_4 polymorphs. *Phys Chem Chem Phys* 2007;**9**:1587–98.
244. Filhol J-S, Deschamps J, Dutremez SG, Boury B, Barisien T, Legrand L, et al. Polymorphs and colors of polydiacetylenes: a first principles study. *J Am Chem Soc* 2009;**131**:6976–88.
245. Bryce DL, Bultz EB, Aebi D. Calcium-43 chemical shift tensors as probes of calcium binding environments. Insight into the structure of the vaterite $CaCO_3$ polymorph by ^{43}Ca solid-state NMR spectroscopy. *J Am Chem Soc* 2008;**130**:9282–92.
246. Lizarraga R, Holmstrom E, Parker SC, Arrouvel C. Structural characterization of amorphous alumina and its polymorphs from first-principles XPS and NMR calculations. *Phys Rev B* 2011;**83**:094201.
247. Aliev AE, Mann SE, Rahman AS, McMillan PF, Corà F, Iuga D, et al. High-resolution solid-state ^{2}H NMR spectroscopy of polymorphs of glycine. *J Phys Chem A* 2011;**115**:12201–11.

248. Griffin JM, Knight F, Hua G, Ferrara J, Hogan S, Woollins JD, et al. ^{77}Se solid-state NMR of inorganic and organoselenium systems: a combined experimental and computational study. *J Phys Chem C* 2011;**115**:10859–72.
249. Caruso F, Chan EJ, Hanna JV, Marchetti F, Pettinari C, Di Nicola C, et al. The question of *cis* versus trans configuration in octahedral metal diketonates: an in-depth investigation on diorganobis(4-acyl-5-pyrazolonato)tin(IV) complexes. *Eur J Inorg Chem* 2012;1369–79.
250. Sadoc A, Body M, Legein C, Biswal M, Fayon F, Rocquefelte X, et al. NMR parameters in alkali, alkaline earth and rare earth fluorides from first principle calculations. *Phys Chem Chem Phys* 2011;**13**:18539–50.
251. Truflandier L, Paris M, Payen C, Boucher F. First-principles calculations within periodic boundary conditions of the NMR shielding tensor for a transition metal nucleus in a solid state system: the example of ^{51}V in $AlVO_4$. *J Phys Chem B* 2006;**110**:21403–7.
252. Griffin JM, Yates JR, Berry AJ, Wimperis S, Ashbrook SE. High-resolution ^{19}F MAS NMR spectroscopy: structural disorder and unusual J couplings in a fluorinated hydroxy-silicate. *J Am Chem Soc* 2010;**132**:15651–60.
253. Ispas S, Charpentier T, Mauri F, Neuville DR. Structural properties of lithium and sodium tetrasilicate glasses: molecular dynamics simulations versus NMR experimental and first-principles data. *Solid State Sciences* 2010;**12**:183–92.
254. Angeli F, Villain O, Schuller S, Ispas S, Charpentier T. Insight into sodium silicate glass structural organization by multinuclear NMR combined with first-principles calculations. *Geochim Cosmochim Acta* 2011;**75**:2453–69.
255. Kibalchenko M, Yates JR, Massobrio C, Pasquarello A. Structural composition of first-neighbor shells in $GeSe_2$ and $GeSe_4$ glasses from a first-principles analysis of NMR chemical shifts. *J Phys Chem C* 2011;**115**:7755–9.
256. Charpentier T, Kroll P, Mauri F. First-principles NMR structural analysis of vitreous silica. *J Phys Chem C* 2009;**113**:7917–27.
257. Soleilhavoup A, Delaye J-M, Angeli F, Angeli F, Caurant D, Charpentier T. Contribution of first-principles calculations to multinuclear NMR analysis of borosilicate glasses. *Magn Reson Chem* 2010;**48**:S159–70.
258. Forler N, Vasconcelos F, Cristol S, Paul JF, Montagne L, Charpentier T, et al. New insights into oxygen environments generated during phosphate glass alteration: a combined ^{17}O MAS and MQMAS NMR and first principles calculations study. *Phys Chem Chem Phys B* 2010;**12**:9053–62.
259. Pedone A, Charpentier T, Menziani MC. The structure of fluoride-containing bioactive glasses: new insights from first-principles calculations and solid state NMR spectroscopy. *J Mater Chem* 2012;**22**:12599–608.
260. Mitchell MR, Carnevale D, Orr R, Whittle KR, Ashbrook SE. Exploiting the chemical shielding anisotropy to probe structure and disorder in ceramics: ^{89}Y MAS NMR and first-principles calculations. *J Phys Chem C* 2012;**116**:4273–86.
261. Mitchell MR, Reader SW, Johnston KE, Pickard CJ, Whittle KR, Ashbrook SE. ^{119}Sn MAS NMR and first-principles calculations for the investigation of disorder in pyrochlore ceramics. *Phys Chem Chem Phys* 2011;**13**:488–97.
262. Sebastiani D. Current densities and nucleus-independent chemical shift maps from reciprocal-space density functional perturbation theory calculations. *Chemphyschem* 2006;**7**:164–75.
263. Brunklaus G, Koch A, Sebastiani D, Spiess HW. Selectivity of guest–host interactions in self-assembled hydrogen-bonded nanostructures observed by NMR. *Phys Chem Chem Phys* 2007;**9**:4545–51.
264. Cuny J, Sykina K, Fontaine B, Le Polle's L, Pickard CJ, Gautier R. ^{95}Mo nuclear magnetic resonance parameters of molybdenum hexacarbonyl from density functional theory: appraisal of computational and geometrical parameters. *Phys Chem Chem Phys* 2011;**13**:19471–9.

265. Koelling DD, Harmon BN. A technique for relativistic spin-polarized calculations. *J Phys C* 1977;**10**:3107–14.
266. E. D. Glendening, A. E. Reed, J. E. Carpenter, F. Weinhold, NBO, Version 3.1; Chemistry Department, University of Wisconsin: Madison, WI, 1995.
267. Harper JK, Doebbler JA, Jacques E, Grant DM, Von Dreele RB. A combined solid-state NMR and synchrotron X-ray diffraction powder study on the structure of the antioxidant (+)-catechin 4.5-hydrate. *J Am Chem Soc* 2010;**132**:2928–37.
268. Alderman DW, Sherwood MH, Grant DM. Comparing, modeling, and assigning chemical-shift tensors in the Cartesian, irreducible spherical, and icosahedral representations. *J Magn Reson A* 1993;**101**:188–97.
269. Cadars S, Lesage A, Pickard CJ, Sautet P, Emsley L. Characterizing slight structural disorder in solids by combined solid-state NMR and first principles calculations. *J Phys Chem A* 2009;**113**:902–11.
270. Klintenberg MK, Derenzo SE, Weber MJ. Accurate crystal fields for embedded cluster calculations. *Comput Phys Commun* 2000;**131**:120–8.
271. Chen X, Zhan C-G. First-principles studies of C-13 NMR chemical shift tensors of amino acids in crystal state. *J Mol Struct (Theochem)* 2004;**682**:73–82.
272. Strohmeier M, Stueber D, Grant DM. Accurate ^{13}C and ^{15}N chemical shift and ^{14}N quadrupolar coupling constant calculations in amino acid crystals: zwitterionic, hydrogen-bonded systems. *J Phys Chem A* 2003;**107**:7629–42.
273. Zheng A, Liu S-B, Deng F. ^{13}C Shielding tensors of crystalline amino acids and peptides: theoretical predictions based on periodic structure models. *J Comput Chem* 2009;**30**:222–35.
274. Zheng A, Yang M, Yue Y, Ye C, Deng F. ^{13}C NMR shielding tensors of carboxyl carbon in amino acids calculated by ONIOM method. *Chem Phys Lett* 2004;**399**:172–6.
275. Brey WS, Richardson D, Bechtel B, Aksenov A. Spin-spin coupling and substituent and halogen isotope shift effects in the fluorine NMR spectra of fluorinated cyclopropanes and cyclopropyl ethers. *Magn Reson Chem* 2007;**45**:205–19.
276. Spink E, Hewage C, Malthouse JPG. Determination of the structure of tetrahedral transition state analogues bound at the active site of chymotrypsin using ^{18}O and ^{2}H isotope shifts in the ^{13}C NMR spectra of glyoxal inhibitors. *Biochemistry* 2007;**46**:12868–74.
277. Rozwadowski Z. Deuterium isotope effect on ^{13}C chemical shifts of tetrabutylammonium salts of Schiff bases amino acids. *Magn Reson Chem* 2006;**44**:881–6.
278. West-Nielsen M, Dominiak PM, Wozniak K, Hansen PE. Strong intramolecular hydrogen bonding involving nitro- and acetyl groups. Deuterium isotope effects on chemical shifts. *J Mol Struct* 2006;**789**:81–91.
279. Chmielewski P, Ozeryanskii VA, Sobczyk L, Pozharskii AF. Primary H-1/H-2 isotope effect in the NMR chemical shift of $HClO_4$ salts of 1,8-bis(dimethylamino) naphthalene derivatives. *J Phys Org Chem* 2007;**20**:643–8.
280. Golubev NS, Detering C, Smirnov SN, Shenderovich IG, Denisov GS, Limbach HH, et al. H/D isotope effects on NMR chemical shifts of nuclei involved in a hydrogen bridge of hydrogen isocyanide complexes with fluoride anion. *Phys Chem Chem Phys* 2009;**11**:5154–9.
281. Golubev NS, Denisov GS, Macholl S, Smirnov SN, Shenderovich IG, Tolstoy PM. NMR study of blue-shifting hydrogen bonds formed by fluoroform in solution. *Z Phys Chem* 2008;**222**:1225–45.
282. Tiainen M, Maaheimo H, Soininen P, Laatikainen R. ^{13}C isotope effects on ^{1}H chemical shifts: NMR spectral analysis of ^{13}C-labelled D-glucose and some ^{13}C-labelled amino acids. *Magn Reson Chem* 2010;**48**:117–22.
283. Abildgaard J, Hansen PE, Manalo MN, LiWang A. Deuterium isotope effects on ^{15}N backbone chemical shifts in proteins. *J Biomol NMR* 2009;**44**:119–26.

284. Takeda M, Jee J, Terauchi T, Kainosho M. Detection of the sulfhydryl groups in proteins with slow hydrogen exchange rates and determination of their proton/ deuteron fractionation factors using the deuterium-induced effects on the ^{13}C NMR signals. *J Am Chem Soc* 2010;**132**:6254–60.
285. Kitevski-LeBlanc JL, Evanics F, Prosser RS. Approaches for the measurement of solvent exposure in proteins by ^{19}F NMR. *J Biomol NMR* 2009;**45**:255–64.
286. Makulski W. ^{1}H, ^{13}C and ^{17}O nuclear magnetic shielding of methanol and its deuterated isotopomers from gas phase measurements. *J Mol Struct* 2008;**872**:81–6.
287. Makulski W. An H-2(D) isotope shift in the H-1 NMR spectra of water in gaseous environment of fluoromethanes. *J Mol Struct* 2007;**839**:90–3.
288. Ullah S, Ishimoto T, Williamson MP, Hansen PE. *Ab initio* calculations of deuterium isotope effects on chemical shifts of salt-bridged lysines. *J Phys Chem B* 2011;**115**:3208–15.
289. Jameson CJ. Variation of chemical shielding with internal coordinates. Applications to diatomic molecules. *J Chem Phys* 1977;**66**:4977–82.
290. Jameson AK, Schuett K, Jameson CJ, Cohen SM, Parker H. The temperature dependence of chemical shielding in diatomic molecules: CO, F_2, ClF, HBr and HCl. *J Chem Phys* 1977;**67**:2821–4.
291. Kantola AM, Lantto P, Vaara J, Jokisaari J. Carbon and proton shielding tensors in methyl halides. *Phys Chem Chem Phys* 2010;**12**:2679–92.
292. Willans MJ, Wasylishen RE, McDonald R. Polymorphism of potassium ferrocyanide trihydrate as studied by solid-state multinuclear NMR spectroscopy and X-ray diffraction. *Inorg Chem* 2009;**48**:4342–53.
293. Hansen MR, Schnitzler T, Pisula W, Graf R, Mullen K, Spiess HW. Cooperative molecular motion within a self-assembled liquid-crystalline molecular wire: the case of a TEG-substituted perylenediimide disc. *Angew Chem Int Ed* 2009;**48**:4621–4.
294. Wei YY, Graf R, Sworen JC, Cheng CY, Bowers CR, Wagener KB, et al. Local and collective motions in precise polyolefins with alkyl branches: a combination of ^{2}H and ^{13}C solid-state NMR spectroscopy. *Angew Chem Int Ed* 2009;**48**:4617–20.
295. Lee YJ, Clark CG, Graf R, Wagner M, Mullen K, Spiess HW. Solid-state organization of semifluorinated alkanes probed by ^{19}F MAS NMR spectroscopy. *J Phys Chem B* 2009;**113**:1360–6.
296. Mallamace F, Corsaro C, Broccio M, Branca C, Gonzalez-Segredo N, Spooren J, et al. NMR evidence of a sharp change in a measure of local order in deeply supercooled confined water. *Proc Natl Acad Sci USA* 2008;**105**:12725–9.
297. Gajda J, Pacholczyk J, Bujacz A, Bartoszak-Adamska E, Bujacz G, Ciesielski W, et al. Structure and dynamics of L-selenomethionine in the solid state. *J Phys Chem B* 2006;**110**:25692–701.
298. Car R, Parinello M. Unified approach for molecular dynamics and density-functional theory. *Phys Rev Lett* 1985;**55**:2471–4.
299. Bagno A, D'Amico F, Saielli G. Computing the ^{1}H NMR spectrum of a bulk ionic liquid from snapshots of Car-Parrinello molecular dynamics simulations. *Chemphyschem* 2007;**8**:873–8.
300. Parrinello M. Simulating complex systems without adjustable parameters. *Comput Sci Eng* 2000;**2**:22–7.
301. Barnett RN, Landman U. Born Oppenheimer molecular-dynamics simulations of finite systems: structure and dynamics of $(H_2O)_2$. *Phys Rev B* 1993;**48**:2081–97.
302. Heine T, Vietze K, Seifert G. ^{13}C NMR fingerprint characterizes long time-scale structure of $Sc_3N@C_{80}$ endohedral fullerene. *Magn Reson Chem* 2004;**42**:S199–201.
303. Sebastiani D, Parrinello M. *Ab-initio* study of NMR chemical shifts of water under normal and supercritical conditions. *Chemphyschem* 2002;**3**:675–9.

304. Murakhtina T, Heuft J, Meijer EJ, Sebastiani D. First principles and experimental ^{1}H N MR signatures of solvated ions: the case of $HCl_{(aq)}$. *Chemphyschem* 2006;**7**:2578–84.
305. Komin S, Gossens C, Tavernelli I, Rothlisberger U, Sebastiani D. NMR solvent shifts of adenine in aqueous solution from hybrid QM/MM molecular dynamics simulations. *J Phys Chem B* 2007;**111**:5225–32.
306. Schiffmann C, Sebastiani D. Hydrogen bond networks: structure and dynamics via first-principles spectroscopy. *Phys Status Solidi B* 2012;**249**:368–75.
307. Sebastiani D, Rothlisberger U. Nuclear magnetic resonance chemical shifts from hybrid DFT QM/MM calculations. *J Phys Chem B* 2004;**108**:2807–15.
308. Jameson CJ, Lim H-M. *Ab initio* studies of the nuclear magnetic resonance chemical shifts of a rare gas atom in a zeolite. *J Chem Phys* 1995;**103**:3885–94.
309. Sears DN, Jameson CJ. Theoretical calculations of Xe chemical shifts in cryptophane cages. *J Chem Phys* 2003;**119**:12231–44.
310. Sears DN, Jameson CJ. The Xe shielding surfaces for Xe interacting with linear molecules and spherical tops. *J Chem Phys* 2004;**121**:2151–7.
311. Jameson CJ, Sears DN, de Dios AC. The ^{129}Xe nuclear shielding tensor surfaces for Xe interacting with rare gas atoms. *J Chem Phys* 2003;**118**:2575–80.
312. Chesnut DB, Rusiloski BE. A study of NMR chemical shielding in water clusters derived from molecular dynamics simulations. *J Mol Struct (Theochem)* 1994;**314**:19–30.
313. Malkin VG, Malkina OL, Steinebrunner G, Huber H. Solvent effect on the NMR chemical shieldings in water calculated by a combination of molecular dynamics and density functional theory. *Chem Eur J* 1996;**2**:452–7.
314. Vaara J, Lounila J, Ruud K, Helgaker T. Rovibrational effects, temperature dependence, and isotope effects on the nuclear shielding tensors of water: a new ^{17}O absolute shielding scale. *J Chem Phys* 1998;**109**:8388–97.
315. Pennanen TS, Vaara J, Lantto P, Sillanpää AJ, Laasonen K, Jokisaari J. Nuclear magnetic shielding and quadrupole coupling tensors in liquid water: a combined molecular dynamics simulation and quantum chemical study. *J Am Chem Soc* 2004;**126**:11093–102.
316. Jameson CJ, Jameson AK, Lim HM. Competitive adsorption of xenon and krypton in zeolite NaA. ^{129}Xe NMR and grand canonical Monte Carlo simulations. *J Chem Phys* 1997;**107**:4364–72.
317. Jameson CJ, Jameson AK, Kostikin P, Baello BI. Adsorption of xenon and CH_4 mixtures in zeolite NaA. ^{129}Xe NMR and grand canonical Monte Carlo simulations. *J Chem Phys* 2000;**112**:323–34.
318. Jameson CJ. The Xe chemical shift tensor in silicalite and SSZ-24 zeolite. *J Am Chem Soc* 2004;**126**:10450–6.
319. Jameson CJ. Calculations of Xe lineshapes in model nanochannels. Grand canonical Monte Carlo averaging of the ^{129}Xe NMR chemical shift tensor. *J Chem Phys* 2002;**116**:8912–29.
320. Moudrakovski I, Soldatov DV, Ripmeester JA, Sears DN, Jameson CJ. Xe NMR lineshapes in channels of peptide molecular crystals. *Proc Natl Acad Sci USA* 2004;**101**:17924–9.
321. Jameson CJ, Sears DN, Murad S. Molecular dynamics averaging of Xe chemical shifts in liquids. *J Chem Phys* 2004;**121**:9581–92.
322. Standara S, Kulha´nek P, Marek R, Hornı´cˇek J, Bourˇ P, Straka M. Simulations of ^{129}Xe NMR chemical shift of atomic xenon dissolved in liquid benzene. *Theor Chem Acc* 2011;**129**:677–84.
323. Truflandier LA, Autschbach J. Solvent effects and dynamic averaging of ^{195}Pt NMR Shielding in *cis* platin derivatives. *J Am Chem Soc* 2010;**132**:3472–83.
324. Dumez J-N, Pickard CJ. Calculation of NMR chemical shifts in organic solids: accounting for motional effects. *J Chem Phys* 2009;**130**:104701.

325. Robinson M, Haynes PD. Dynamical effects in *ab initio* NMR calculations: classical force fields fitted to quantum forces. *J Chem Phys* 2010;**133**:084109.
326. Drac˘´ınsky´ M, Bour P. Vibrational averaging of the chemical shift in crystalline α-glycine. *J Comput Chem* 2012;**33**:1080–9.
327. Jameson CJ. The dependence of 19F nuclear magnetic shielding on internal coordinates in CF_4, SiF_4, and BF_3. *J Chem Phys* 1977;**67**:2814–20.
328. Jameson CJ, Osten HJ. Theoretical aspects of the isotope effect on nuclear shielding. *Annu Rep NMR Spectrosc* 1986;**17**:1–78.
329. Rossano S, Mauri F, Pickard CJ, Farnan I. First-principles calculation of ^{17}O and ^{25}Mg NMR shieldings in MgO at finite temperature: rovibrational effect in solids. *J Phys Chem B* 2005;**109**:7245–50.
330. Fileti EE, Georg HC, Coutinho K, Canuto S. Isotropic and anisotropic chemical shifts in liquid water. A sequential QM/MM. *J Braz Chem Soc* 2007;**18**:74–84.
331. Pennanen TS, Lantto P, Sillanpää AJ, Vaara J. Nuclear magnetic resonance chemical shifts and quadrupole couplings for different hydrogen-bonding cases occurring in liquid water: a computational study. *J Phys Chem A* 2007;**111**:182–92.
332. Fowler PW, Riley G, Raynes WT. Dipole moment, magnetizability and nuclear shielding surfaces for the water molecule. *Mol Phys* 1981;**42**:1463–81.
333. Lazzeretti P, Zanasi R, Sadlej AJ, Raynes WT. Magnetizability and carbon-13 shielding surfaces for the methane molecule. *Mol Phys* 1987;**62**:605–16.
334. Jameson CJ, de Dios AC, Jameson AK. Nuclear magnetic shielding of nitrogen in ammonia. *J Chem Phys* 1991;**95**:1069–79.
335. Jameson CJ, de Dios AC, Jameson AK. The ^{31}P shielding in phosphine. *J Chem Phys* 1991;**95**:9042–53.
336. Harper JK, Grant DM. Enhancing crystal structure prediction with NMR tensor data. *Crystal Growth Design* 2006;**6**:2315–21.
337. Elena B, Emsley L. Powder crystallography by proton solid-state NMR spectroscopy. *J Am Chem Soc* 2005;**2005**(127):9140–6.
338. Elena B, Pintacuda G, Mifsud N, Emsley L. Molecular structure determination in powders by NMR crystallography from proton spin diffusion. *J Am Chem Soc* 2006;**128**:9555–60.
339. Mou Y, Tsai TWT, Chan JCC. Determination of the backbone torsion psi angle by tensor correlation of chemical shift anisotropy and heteronuclear dipole-dipole interaction. *Solid State Nucl Magn Reson* 2007;**31**:72–81.
340. Brouwer DH, Alavi S, Ripmeester JA. NMR crystallography of *p*-tert-butylcalix[4]arene host–guest complexes using ^{1}H complexation-induced chemical shifts. *Phys Chem Chem Phys* 2008;**10**:3857–60.
341. Salager E, Stein RS, Pickard CJ, Elena B, Emsley L. Powder NMR crystallography of thymol. *Phys Chem Chem Phys* 2009;**11**:2610–21.
342. Bradley JP, Velaga SP, Antzutkin ON, Brown SP. Probing intermolecular crystal packing in (γ-indomethacin by high-resolution ^{1}H solid-state NMR spectroscopy. *Cryst Growth Des* 2011;**11**:3463–71.
343. Brouwer DH. A structure refinement strategy for NMR crystallography: an improved crystal structure of silica-ZSM-12 zeolite from ^{29}Si chemical shift tensors. *J Magn Reson* 2008;**194**:136–46.
344. Aguiar PM, Kroeker S. Cyanide orientational ordering and copper electric field gradients in $CuCN{\cdot}N_2H_4$. *Phys Chem Chem Phys* 2009;**11**:834–40.
345. Tjandra N, Bax A. Large variations in ^{13}C chemical shift anisotropy in proteins correlate with secondary structure. *J Am Chem Soc* 1997;**119**:9576–7.
346. Walling AE, Pargas RE, de Dios AC. Chemical shift tensors in peptides: a quantum mechanical study. *J Phys Chem A* 1997;**101**:7299–303.

347. Brouwer DH, Moudrakovski IL, Darton RJ, Morris RE. Comparing quantum-chemical calculation methods for structural investigation of zeolite crystal structures by solid-state NMR spectroscopy. *Magn Reson Chem* 2010;**48**:S113–21.
348. Byrne PJ, Warren JE, Morris RE, Ashbrook SE. Structure and NMR assignment in AlPO-15: a combined study by diffraction, MAS NMR and first-principles calculations. *Solid State Sci* 2009;**11**:1001–6.
349. Chen F, Wasylishen RE. Structural characterization of silver dialkylphosphite salts using solid-state ^{109}Ag and ^{31}P NMR spectroscopy, IR spectroscopy and DFT calculations. *Magn Reson Chem* 2010;**48**:270–5.
350. Sehnert J, Senker J. A concerted approach for the determination of molecular conformation in ordered and disordered materials. *Chem Eur J* 2007;**13**:6339–50.
351. Paramasivam S, Balakrishnan A, Dmitrenko O, Godert A, Begley TP, Jordan F, et al. Solid-state NMR and density functional theory studies of ionization states of thiamin. *J Phys Chem B* 2011;**115**:730–6.
352. Scheer M, Gregoriades LJ, Zabel M, Bai J, Krossing I, Brunklaus G, et al. Self-assemblies based on $[Cp_2Mo_2(CO)_4(\mu,\eta^2\text{-}P_2)]$-solid-state structure and dynamic behaviour in solution. *Chem Eur J* 2008;**14**:282–95.
353. Dmitrenko O, Bai S, Beckmann PA, van Bramer S, Vega AJ, Dybowski C. The relationship between ^{207}Pb NMR chemical shift and solid-state structure in Pb(II) compounds. *J Phys Chem A* 2008;**112**:3046–52.
354. Yamauchi K, Okonogi M, Kurosu H, Tansho M, Shimizu T, Gullion T, et al. High field ^{17}O solid-state NMR study of alanine tripeptides. *J Magn Reson* 2008;**190**:327–32.
355. Chizallet C, Costentin G, Lauron-Pernot H, Che M, Bonhomme C, Maquet J, et al. Study of the structure of OH groups on MgO by 1D and 2D ^{1}H MAS NMR combined with DFT cluster calculations. *J Phys Chem C* 2007;**111**:18279–87.
356. Bradley JP, Pickard CJ, Burley JC, Martin DR, Hughes LP, Cosgrove SD, et al. Probing intermolecular hydrogen bonding in sibenadet hydrochloride polymorphs by high-resolution ^{1}H double-quantum solid-state NMR spectroscopy. *J Pharmaceutical Sci* 2012;**101**:1821–30.
357. Kim SM, Kim DH. Determination of the structure of 1,1'-diethyl-2,2'-carbocyanine iodide using NMR spectra and GIAO-HF/DFT calculations. *Dyes Pigment* 2008;**79**:1–6.
358. Tomlinson JH, Ullah S, Hansen PE, Williamson MP. Characterization of salt bridges to lysines in the protein G B1 domain. *J Am Chem Soc* 2009;**131**:4674–84.
359. Wong A, Kotch FW, Kwan ICM, Davis JT, Wu G. Probing the Na^+ binding site in a calix[4]arene–guanosine conjugate dimer by solid-state ^{23}Na NMR and quantum chemical calculation. *Chem Commun* 2009;2154–6.
360. Comotti A, Bracco S, Sozzani P, Hawxwell SM, Hu CH, Ward MD. Guest molecules confined in amphipathic crystals as revealed by X-ray diffraction and MAS NMR. *Crystal Growth Des* 2009;**9**:2999–3002.
361. Alumasa JN, Gorka AP, Casabianca LB, Comstock E, de Dios AC, Roepe PD. The hydroxyl functionality and a rigid proximal N are required for forming a novel non-covalent quinine-heme complex. *J Inorg Biochem* 2011;**105**:467–75.
362. Jameson CJ, de Dios AC. *Ab initio* calculations of the intermolecular chemical shift in nuclear magnetic resonance in the gas phase and for adsorbed species. *J Chem Phys* 1992;**97**:417–34.
363. Jameson CJ, de Dios AC. Xe nuclear magnetic resonance lineshapes in nanochannels. *J Chem Phys* 2002;**116**:3805–21.
364. Anedda R, Soldatov DV, Moudrakovski IL, Casu M, Ripmeester JA. A new approach to characterizing sorption in materials with flexible micropores. *Chem Mat* 2008;**20**:2908–20.

365. Comotti A, Bracco S, Sozzani P, Horike S, Matsuda R, Chen J, et al. Nanochannels of two distinct cross-sections in a porous Al-based coordination polymer. *J Am Chem Soc* 2008;**130**:13664–72.
366. Brouwer DH, Moudrakovski IL, Udachin KA, Enright GD, Ripmeester JA. Guest loading and multiple phases in single crystals of the van der Waals host *p*-tert-butylcalix[4]arene. *Cryst Growth Des* 2008;**8**:1878–85.
367. Zurek E, Pickard CJ, Walczak B, Autschbach J. Density functional study of the ^{13}C NMR chemical shifts in small-to-medium-diameter infinite single-walled carbon nanotubes. *J Phys Chem A* 2006;**110**:11995–2004.
368. Zurek E, Pickard CJ, Autschbach J. A density functional study of the ^{13}C NMR chemical shifts in functionalized single-walled carbon nanotubes. *J Am Chem Soc* 2007;**129**:4430–9.
369. Zurek E, Pickard CJ, Autschbach J. A density functional study of the ^{13}C NMR chemical shifts in fluorinated single-walled carbon nanotubes. *J Phys Chem A* 2009;**113**:4117–24.
370. Zurek E, Pickard CJ, Autschbach J. Density functional study of the ^{13}C NMR chemical shifts in single-walled carbon nanotubes with Stone-Wales defects. *J Phys Chem C* 2008;**112**:11744–50.
371. Vasconcelos F, Cristol S, Paul J-F, Montagne L, Mauri F, Delevoye L. First-principles calculations of NMR parameters for phosphate materials. *Magn Reson Chem* 2010;**48**: S142–50.

CHAPTER TWO

Pure Phase Encode Magnetic Resonance Imaging of Fluids in Porous Media

Colleen E. Muir[*,†], **Bruce J. Balcom**[*,†]

*MRI Research Centre, Department of Physics, University of New Brunswick, P.O. Box 4400, Fredericton, New Brunswick, Canada

†Department of Chemistry, University of New Brunswick, P.O. Box 4400, Fredericton, New Brunswick, Canada

Contents

Annual Reports on NMR Spectroscopy, Volume 77
ISSN 0066-4103
http://dx.doi.org/10.1016/B978-0-12-397020-6.00002-7

Abstract

Two classes of pure phase encoding MRI methods employed for imaging fluids in porous media, single point ramped imaging with T_1 enhancement (SPRITE) and spin echo single point imaging (SE-SPI), are reviewed. Centric scan SPRITE methods have simple signal equations and are robust in generating quantitative images with relatively short acquisition times and minimal gradient duty cycles. SE-SPI sequences are useful for measuring materials with moderate T_2 and short T_2*. T_2 mapping SE-SPI permits measuring spatially resolved T_2 distributions which provide important information about fluid occupancy of the pore space. Applications of pure phase encoding methods in porous media have been demonstrated in the measurement of static fluid content as well as in the measurement of dynamic processes.

Key Words: Magnetic resonance imaging, Porous media, Pure phase encoding, SPRITE, SE-SPI, Core analysis

1. INTRODUCTION

Quantitative measurements of fluids in porous media are important for understanding how much fluid is present and how those fluids can move throughout the void spaces. Porous media encompass a large number of materials, ranging from geological materials such as sedimentary rocks to living organisms such as skin and bone, to industrial materials such as paper and concrete.[1] Porous media are characterized by three important macroscopic parameters: porosity, saturation, and permeability. Porosity is a measure of the fraction of the bulk sample volume that is occupied by void space. Saturation is the ratio of the volume of fluid in the sample to the total accessible pore volume. Permeability is a measure of the ability of a fluid to flow through the porous sample.

Traditional methods of measuring porous media parameters are usually based on bulk measurements. Porosity can be determined through gravimetric analysis or through mercury injection. Saturation is typically measured through gravimetric analysis of the weight and volume of the sample. Permeability is determined through Darcy's law after careful measurement of flow through the sample. Many processes that occur in porous media are sensitive to the heterogeneous nature of the porous material. Therefore, resolution of sample heterogeneity is important for measuring pore characteristics. In this chapter, we review pure phase encode magnetic resonance imaging (MRI) methods applied to porous media.

MRI is best known for clinical imaging of the body but can be applied to imaging of fluids in the pore space of various porous media such as reservoir

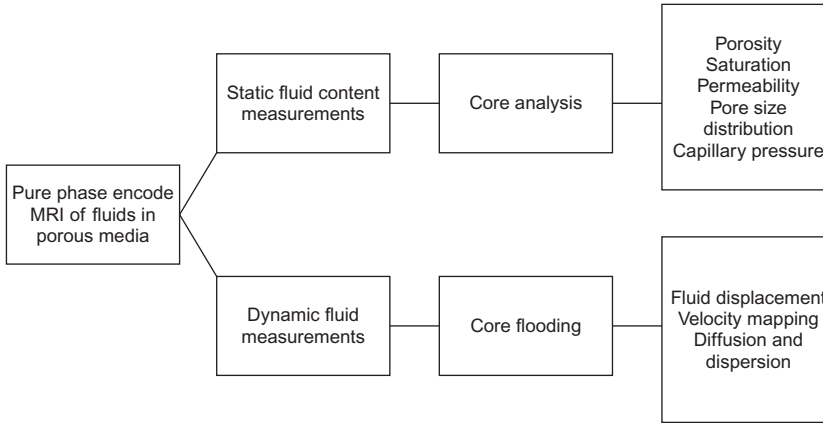

Figure 2.1 Outline of pure phase encode MRI of fluids in porous media topics.

rock cores. Another clinical imaging technique, X-ray computed tomography (CT), has been employed for imaging the pore matrix in rock cores. X-ray CT provides 2D or 3D images of opaque objects. However, the attenuation from an X-ray depends largely on atomic number. In a rock saturated with a fluid, such as water or oil, the rock matrix contains heavy nuclei, and the fluid contains lighter nuclei. Therefore, the X-ray attenuation and image contrast are much greater in the matrix than the fluid. X-ray CT is useful for imaging the matrix structure but is limited in its ability to directly image the fluids within a rock core.[2]

In contrast, MRI acquires signal from the fluids within the pore space. MRI is a nondestructive imaging method that can provide quantitative, spatially resolved images and can readily discriminate between water and oil. These features make it an effective method for imaging rock cores, as well as other porous materials. We focus this review on pure phase encode MRI methods that have been developed in our laboratory for imaging fluids in porous media (Fig. 2.1).

2. RELAXATION IN POROUS MEDIA

The spin–lattice and spin–spin relaxation times of fluids in a pore space are shorter than in a bulk fluid because the confined fluid interacts with the pore wall, leading to enhanced relaxation.[3,4] The rate of relaxation is related to the surface-to-volume ratio of the pore space. The spin–lattice relaxation time in the pore space is given by

$$\frac{1}{T_1} = \rho_1 \frac{S}{V} + \left(\frac{1}{T_1}\right)_B \quad [2.1]$$

where T_1 is the spin–lattice relaxation time, $(1/T_1)_B$ is the bulk spin–lattice relaxation time, ρ_1 is the spin–lattice surface relaxivity, and S/V is the surface-to-volume ratio.

Similarly for T_2, the spin–spin relaxation time is given by

$$\frac{1}{T_2} = \rho_2 \frac{S}{V} + \left(\frac{1}{T_2}\right)_B + \left(\frac{1}{T_2}\right)_D \quad [2.2]$$

where ρ_2 is the spin–spin surface relaxivity, $(1/T_2)_B$ is the bulk spin–spin relaxation time, and $(1/T_2)_D$, which describes signal loss due to diffusion in a magnetic field gradient, is given by Eq. (2.3).

$$\left(\frac{1}{T_2}\right)_D = \frac{D_0(\gamma G_i \mathrm{TE})^2}{12} \quad [2.3]$$

where D_0 is the self-diffusion coefficient of the fluid, γ is the gyromagnetic ratio, TE is the echo time, and G_i is the internal magnetic field gradient. Relaxation of fluid in bulk is usually much slower than relaxation of fluid in the pore space; therefore, the bulk terms in Eqs. (2.1) and (2.2) can be neglected. Therefore, Eq. (2.1) simplifies to

$$\frac{1}{T_1} = \rho_1 \frac{S}{V} \quad [2.4]$$

The internal gradient (G_i) in Eq. (2.3) is related to the magnetic susceptibility difference between the fluid in the pore and the matrix.[5]

$$G_i = \frac{\Delta\chi B_0}{d_g} \quad [2.5]$$

where $\Delta\chi$ is the magnetic susceptibility difference between the fluid filling the pore space and the grains of the matrix, B_0 is the static magnetic field, and d_g is the grain size of the rock matrix. When measurements are taken at low magnetic field, the internal magnetic field gradient is small, and when a short TE is employed, relaxation due to diffusion is negligible compared to relaxation due to surface relaxation.[5] Thus, Eq. (2.2) simplifies to

$$\frac{1}{T_2} = \rho_2 \frac{S}{V} \quad [2.6]$$

3. FREQUENCY ENCODING AND PHASE ENCODING

Traditionally, MRI of porous media has been undertaken with frequency encoding methods. Frequency encoding methods sample k-space by sampling the signal as a function of time during a constant gradient as illustrated in Fig. 2.2.

The pulse sequence illustrated in Fig. 2.2 is a Spin Echo imaging sequence with frequency encoding on the x-axis. An echo is collected after the application of a 90° and 180° pulse. The signal equation is given in Eq. (2.7), where M_0 is the sample magnetization, TE is the echo time, and TR is the repetition time. The image intensity is weighted by both relaxation terms T_1 and T_2. Two disadvantages arise from the T_1 and T_2 terms in the signal equation when measuring signal in porous media: (a) In porous media, the T_1 and T_2 relaxation terms are multi-exponential due to pore size distributions. The signal in frequency encoding methods cannot be readily quantified due to the multi-exponential relaxation times. (b) The T_2 relaxation time in porous media can be very short due to surface relaxation. Therefore, a significant portion of the signal may decay before the signal is collected.

$$S = M_0 \exp\left(\frac{-\mathrm{TE}}{T_2}\right)\left[1 - \exp\left(-\frac{\mathrm{TR}}{T_1}\right)\right] \qquad [2.7]$$

Phase encoding has proved to be a robust approach for imaging samples with short relaxation times, such as fluids in rock cores. While frequency encoding measures signal at a fixed gradient value and variable time, phase

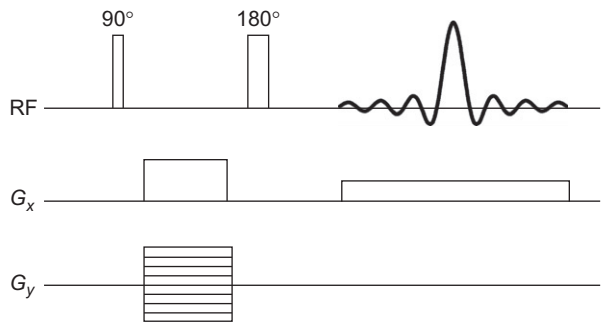

Figure 2.2 2D frequency encoded Spin Echo pulse sequence.

encoding employs changing gradient values with a fixed encoding time.[6] Phase encoding is immune to artefacts that arise from susceptibility effects, chemical shift, and B_0 inhomogeneity.[7] Further, pure phase encoding techniques avoid the linewidth restriction on resolution that arises in frequency encoding methods.[6,7]

3.1. Single point imaging and SPRITE

Pure phase encoding as a method of imaging solids was first introduced by Emid and Creyghton.[6] They employed a single point imaging (SPI) method, which begins with a 90° pulse followed by a free induction decay (FID) collected at a fixed time after the pulse. They repeated the SPI experiment, incrementing the gradients each time. No frequency encoding gradients were applied, and thus the images did not suffer from line broadening. Gravina and Cory illustrated the usefulness of the SPI method by employing a short RF pulse after the application of a gradient to produce 2D and 3D images of short $T_2\star$ samples.[7] SPI methods are also called constant time imaging because the signal is observed at a constant time with variable gradient strength. The SPRITE (single point ramped imaging with T_1 enhancement) imaging technique, developed by Balcom *et al.*,[8] introduced a ramped gradient to avoid intense, rapidly switched gradients employed in the SPI methods. SPRITE employs a short RF pulse and a ramped gradient to produce 1D, 2D, or 3D images of short $T_2\star$ samples.

Early SPRITE methods are based on sampling k-space from one extremity to the other, as illustrated in Fig. 2.3. These methods are known as standard SPRITE methods. At an encoding time, t_p, after the RF pulse, a single k-space point is acquired on the FID. After a repetition time, TR, the

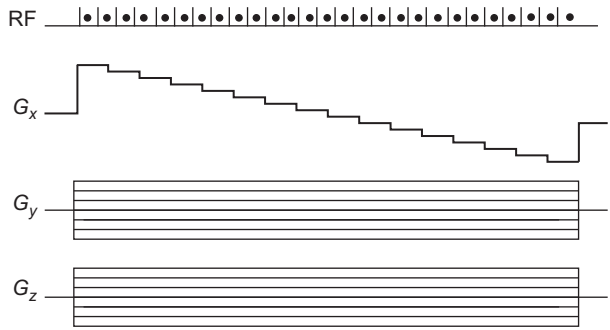

Figure 2.3 Standard SPRITE pulse sequence.

primary gradient, G_x, is incremented for 1D k-space sampling. For 2D and 3D k-space sampling, the G_y and G_z gradients are incremented after a complete cycle of G_x, leading to Cartesian sampling of 2D and 3D k-space. The signal equation for standard SPRITE imaging is given in Eq. (2.8):

$$S = M_0 \exp\left(\frac{-t_p}{T_2^*}\right)\left[\frac{1-\exp\left(-\frac{TR}{T_1}\right)}{1-\cos\alpha\,\exp\left(-\frac{TR}{T_1}\right)}\right]\sin\alpha \qquad [2.8]$$

where M_0 is the initial magnetization, t_p is the encoding time, TR is the repetition time, and α is the flip angle. The fundamental benefits of SPRITE imaging over traditional SPI methods are (a) in samples with a short T_1 relaxation time, a SPRITE experiment can be run quickly in a manner that SPI cannot (T_1 enhancement); (b) incrementing the gradients in a SPRITE experiment leads to a more rapid sampling of k-space as the repetition time is shortened; and (c) there are greatly reduced gradient vibrations due to impulsive Lorentz forces that are applied and released relatively slowly.[8] Whereas an SPI measurement can be painfully loud with violent gradient vibration, a SPRITE measurement is often completely inaudible despite essentially equivalent k-space sampling.

The disadvantages of the standard SPRITE method are (a) the longitudinal magnetization saturation leads to a diminution of available signal (b) the duty cycle is significant because many sequential points are acquired at the extremities of k-space where the gradient values are large, and (c) the signal equation, shown in Eq. (2.8), is complicated due to the T_1 contrast terms in the square brackets.[9] Centric scan SPRITE methods were developed to overcome these issues.[9] The T_1 dependence in the square bracket of Eq. (2.8) may be removed in the limit of long T_1 and short α, but this decreases the experimental sensitivity of standard SPRITE.

3.2. Single exponential T_2* decay

The effectiveness of the centric scan class of SPRITE techniques is significantly increased due to the single exponential behaviour of the $T_2\star$ decay frequently observed in porous media. The effective $T_2\star$ in porous media may be obtained by analysing the FID. The decay rate of the FID ($1/T_2\star$) is the sum of the spin–spin relaxation decay rate ($1/T_2$), the underlying magnetic field inhomogeneity ($1/T_{2m}$), and the susceptibility difference ($\Delta\chi$) between the pore-filling fluid and the solid matrix ($1/T_{2i}$),[10] as shown in Eq. (2.9).

$$\frac{1}{T_2^*} = \frac{1}{T_2} + \frac{1}{T_{2\mathrm{m}}} + \frac{1}{T_{2\mathrm{i}}} \qquad [2.9]$$

The $1/T_{2\mathrm{m}}$ term, associated with inhomogeneity in the magnet employed, is usually insignificant compared to other terms in Eq. (2.9), in realistic porous media. In most sedimentary rocks, the $T_2\star$ decay is dominated by the $T_{2\mathrm{i}}$ term due to a large susceptibility difference between the pore-filling fluid and the solid matrix because of paramagnetic impurities in the matrix. The result is a single exponential $T_2\star$ decay, which is commonly observed in both partially and fully saturated rocks.[10] In the limit of low B_0, we must recover the natural T_2 distribution in $T_2\star$ unless the magnet inhomogeneity driven $1/T_{2\mathrm{m}}$ dominates.

The decay rate of $T_{2\mathrm{i}}$ is given in Eq. (2.10), where γ is the gyromagnetic ratio, ΔB_{i} is the breadth of the magnetic field distribution due to the susceptibility difference, C is a proportionality constant, $\Delta\chi$ is the susceptibility difference between the pore-filling fluid and the rock matrix, and $f_0 = \gamma B_0/2\pi$ is the Larmor frequency.

$$\frac{1}{\pi T_{2i}} = \frac{\gamma \Delta B_i}{2\pi} = C\Delta\chi f_0 \qquad [2.10]$$

Single exponential $T_2\star$ decay implies that the magnetic field distribution is Lorentzian in the pore space. Chen *et al.*[10] illustrated the single exponential $T_2\star$ decay in a water-saturated Berea sandstone, as shown in Fig. 2.4. The data points were collected following a 90° pulse, then fitted to Eq. (2.11):

$$S = M_0 \exp\left(\frac{-t}{T_2{}^*}\right) \sin\alpha \qquad [2.11]$$

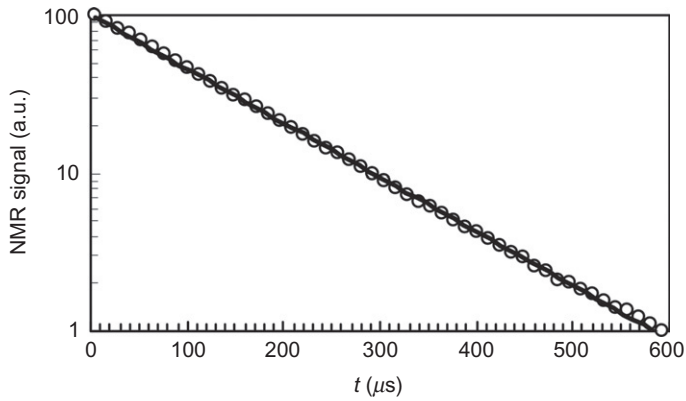

Figure 2.4 Semi-logarithmic plot of the FID signal from a water-saturated Berea sandstone, illustrating single exponential $T_2{}^*$ decay.

where S is the signal intensity, M_0 is the sample magnetization at equilibrium, t is the time after the RF pulse, and α is the flip angle. In this instance, the $T_2^\star$ was 127 μs. Previous work showed that the $T_2^\star$ remained single exponential when the water saturation was varied from 9.1% to 100%, while the T_1 and T_2 of the Berea core were both multi-exponential. Single exponential $T_2^\star$ decay has also been demonstrated in concrete.[11]

This simple but powerful feature of the $T_2^\star$ decay allows for quantitative imaging with the centric scan SPRITE methods. The sample magnetization, M_0, is of course directly related to the ^{1}H density and fluid content.

3.3. Centric scan SPRITE

Centric scan SPRITE techniques begin k-space sampling at the centre of k-space, which results in no T_1 weighting at the k-space origin. The image intensity for centric scan SPRITE techniques is given by

$$S = M_0 \exp\left(\frac{-t_p}{T_2^*}\right) \sin\alpha \qquad [2.12]$$

where S is the local image intensity, M_0 is the sample magnetization at equilibrium, t_p is the encoding time, and α is the flip angle. T_1 and TR are no longer intensity parameters in centric scan methods but are instead resolution parameters.[12] The image intensity depends on $T_2^\star$, a single-exponential parameter in porous media. If the encoding time, t_p, is significantly smaller than $T_2^\star$ and α is constant over the length of the sample, the signal is proportional to the magnetization, M_0.

Centric scan SPRITE experiments have been developed for imaging in 1D, 2D, or 3D. The centric scan methods are more commonly used than standard SPRITE methods and thus will be the focus of discussion in this review.

For 1D imaging, the double half k-space (DHK) SPRITE experiment is employed.[13] DHK SPRITE samples data in one half of k-space by incrementing the gradient, then after a relaxation delay of $5 \times T_1$, the data in the second half of k-space are sampled by incrementing the gradient in the opposite direction, as shown in Fig. 2.5. The two data sets are arranged in a single linear array, and the two $k = 0$ points are averaged prior to a Fourier transform.

Spiral SPRITE is the centric scan technique for imaging in 2D. Sampling starts at the centre of k-space at $k = 0$ and continues to the extremities of k-space following the shape of a gridded Archimedean spiral, as illustrated in Fig. 2.6. An RF pulse is applied for each gradient step, as shown in Fig. 2.7.

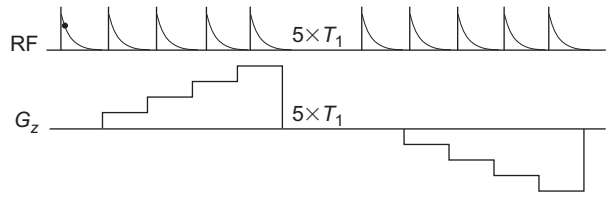

Figure 2.5 DHK SPRITE pulse sequence.

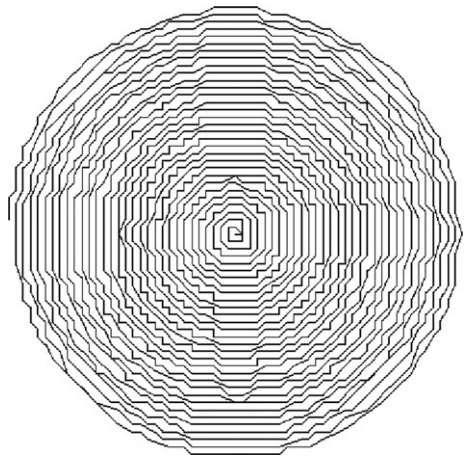

Figure 2.6 Generic spiral k-space trajectory. Sampling begins at $k=0$.

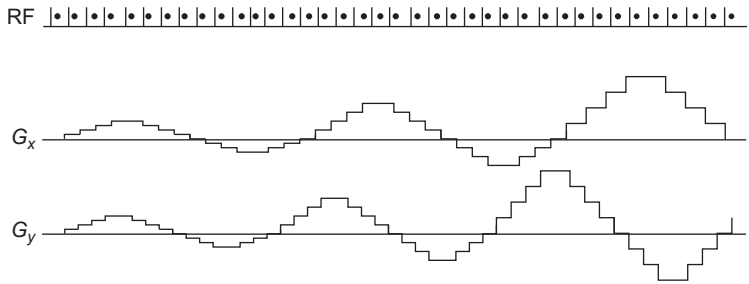

Figure 2.7 Spiral SPRITE pulse sequence.

The sampling density is high near the k-space origin and sparse in the extremities of k-space.[14] The acquired k-space points fall on a grid so that a conventional fast Fourier transform can be performed for image reconstruction. The spiral trajectory can be implemented with any number of spiral interleaves by changing the gradient waveform. Spiral k-space trajectories are commonly used in frequency encoding methods in biomedical imaging.

Conical SPRITE, the centric scan technique for imaging in 3D, is a simple extension of Spiral SPRITE with the addition of a third phase encode gradient. The X and Y gradients oscillate, as in the Spiral SPRITE method, while the Z gradient is ramped, as shown in Fig. 2.8. An RF pulse is applied at each gradient step. The method employs a series of spiral trajectories along conical surfaces to sample the 3D k-space. The first k-space point of each cone is collected in the absence of a gradient. Commonly, 39 cones are collected in the implementation of Conical SPRITE.[9] Sectoral SPRITE is an alternate centric scan technique for imaging in 2D and 3D. A small sector of k-space is sampled, and then the sampling is repeated at different orientations to cover all of k-space. It provides images with increased resolution and more robust contrast in magnetization preparation methods.[15]

The advantages of centric scan SPRITE methods over standard SPRITE include a simplified signal equation without T_1 contrast, inherent spoiling, reduced acquisition times and reduced gradient duty cycles.[9] The RF pulse train in a SPRITE sequence could lead to unwanted echo formation and image artefacts. However, the phase encoding gradients passively spoil any residual transverse magnetization. Each centric scan SPRITE method begins at the k-space origin where $G_x = G_y = G_z = 0$ G/cm, and then the gradients are incremented to reach the extremities of k-space. In standard SPRITE methods, active spoiling is required around the k-space origin when the gradient step duration (TR) is approximately equal to $T_2^\star$. Kaffanke *et al.*[16] have shown that phase cycling can be applied for suppression of residual magnetization in SPRITE measurements of long $T_2^\star$ samples ($TR \ll T_2^\star$), such as biological tissue.

The acquisition time is reduced in a centric scan sequence because the extremities of k-space, where the SNR is low, are omitted from centric scan

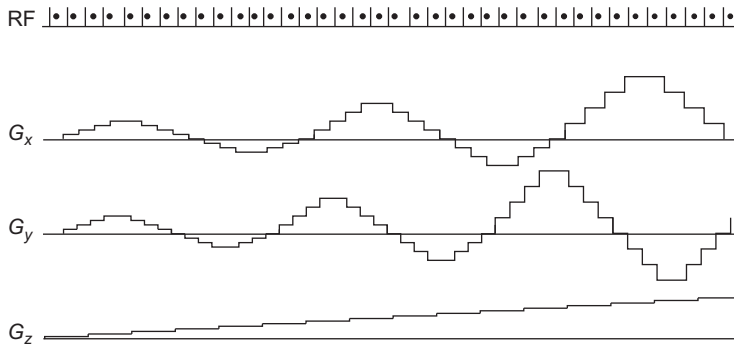

Figure 2.8 Conical SPRITE pulse sequence.

trajectories. In Spiral SPRITE, only ¾ of the full k-space matrix is acquired. In the case of Conical SPRITE, only ½ of the k-space matrix points are acquired.[9] k-space data points not acquired are zero filled.

The gradient duty cycle is reduced because less time is spent acquiring data at the peripheries of k-space where the gradient values are very high. Halse *et al.* calculated relative duty cycles for Conical SPRITE and 3D standard SPRITE experiments by summing the gradient values for each method within a period of interest and normalising by the total number of gradient steps. In a complete Conical-SPRITE experiment, the duty cycle was 29.7% for G_x and G_y and 33.8% for G_z. The gradient duty cycle for a complete standard SPRITE experiment was 50.8%.[9]

The gradient duty cycle is more appropriately considered in terms of gradient power deposition, as power is proportional to the square of the gradient current. Therefore, at the k-space periphery where the gradient current is high, the power deposited is large. There is a significant reduction in power from standard SPRITE experiments to Conical-SPRITE, and thus a significant reduction in gradient heating.[9] Centric scan SPRITE methods decrease the short duration gradient duty cycle by regularly returning to the k-space origin, with zero gradient, as data acquisition proceeds. Skipping k-space points also reduces the duty cycle.

3.4. Multiple FID point acquisitions

A disadvantage of SPRITE methods when compared to frequency encoding imaging techniques is that one k-space point is acquired per RF pulse with a SPRITE sequence, while an entire line of k-space is acquired per excitation with a frequency encoding sequence. This results in a low signal-to-noise ratio (SNR) for SPRITE sequences. In order to improve the SNR of a centric scan SPRITE experiment, multiple time-domain FID points can be collected and used by employing a Chirp z-Transform.[12] The Chirp z-Transform will scale and normalise the field-of-view (FOV) of images from the individual FID points. The resulting images can be combined to increase the SNR. Halse *et al.*[12] employed the Chirp z-Transform on multiple FID points to improve the SNR and to perform $T_2^\star$ mapping. We favour the use of multiple point acquisition (MPA) for SNR improvement rather than $T_2^\star$ mapping. There are two constraints when choosing the number of FID points that can be averaged to increase the SNR. The dwell time between successive FID points must be long enough to avoid noise correlation, and the FOV scaling must be limited to maintain an acceptable

spatial resolution. In an experiment with 64 k-space points and a FOV scaling limit, $Z_{\text{lim}} = 0.8$, the maximum number of FID points that can be averaged to increase the SNR is 9, giving a passive SNR improvement of 3.[12]

3.5. Relaxation time mapping

SPRITE methods can be used to obtain quantitative maps of T_1, T_2, and $T_2^\star$ relaxation times in samples with short relaxation times.[11] The T_1 and T_2 mapping methods rely on magnetization preparation to obtain images, which will be discussed below. The $T_2^\star$ mapping technique is simple because the signal intensity of a centric scan experiment is dependent on $T_2^\star$ and the sample proton density. By examining Eq. (2.12), it is evident that a $T_2^\star$ map can be obtained by repeating a SPRITE experiment with various t_p values.[11] Marica *et al.*[17] presented a noninvasive method for measuring local and global porosity in core samples through $T_2^\star$ mapping. The SPRITE $T_2^\star$ mapping technique was performed on a series of sandstone core plugs that varied in porosity and the degree of local heterogeneity due to bedding plane structure. Proton density values were extracted from the $T_2^\star$ maps through extrapolation of the decay curves to $t_p = 0$. The MRI-derived porosity values were in good agreement with gravimetric-derived porosity values. It was also shown that signal intensity might be low in a high porosity region of a core, where signal would be expected to be high, due to a short $T_2^\star$ value reducing the signal intensity, as shown in Eq. (2.12).

3.6. Magnetization preparation and SPRITE

An attractive feature of MRI is the ability to apply a number of different contrasts to the images. One method of applying contrast to a SPRITE image is through magnetization preparation. The magnetization will initially undergo a series of RF pulses and gradient applications to achieve the desired contrast. Then, the "prepared" magnetization is stored along the z-axis and spoiling gradient pulses are applied to destroy any magnetization that remains in the transverse plane. Finally, a SPRITE sequence is applied to spatially resolve the contrast. Magnetization preparation has been employed to achieve T_1 and T_2 contrast and to invoke diffusion contrast in SPRITE images.[18–20]

As mentioned above, magnetization preparation can be employed to obtain T_1 and T_2 maps. The T_1 mapping technique can be performed by either a saturation or an inversion recovery preparation, followed by a centric scan SPRITE readout. A T_2 map can be obtained with a spin echo

magnetization preparation followed by a SPRITE sequence.[20] The advantage of using SPRITE as the readout sequence is that it can map relaxation times of samples with short $T_2\star$ values.

Recently, Romanenko *et al.*[21] employed pulsed field gradient (PFG) prepared centric scan SPRITE to obtain 2D permeability maps in a capillary bundle, glass bead packs, and composite sandstones samples.[21] Permeability is the ability of porous media to transmit fluids and is an important measurement in studies of hydrocarbon recovery and groundwater flow in aquifers. Spatially resolved measurements of permeability are of particular importance for fluid dynamics studies. Such measurements were obtained by combining centric scan SPRITE for spatial resolution and a stimulated echo with a Cotts PFG scheme for velocity encoding, as shown in Fig. 2.9. SPRITE, as a pure phase encode method, is insensitive to velocity,[22] and therefore must be combined with magnetization preparation in porous media for velocity encoding. 2D permeability maps were based on independent measurements of porosity and velocity maps. The quantitative porosity maps were measured with centric scan SPRITE. In samples with short $T_2\star$, the quantitative porosity maps were obtained by acquiring a series of images with different t_p and then fitting to Eq. (2.12). Figure 2.10 shows results from

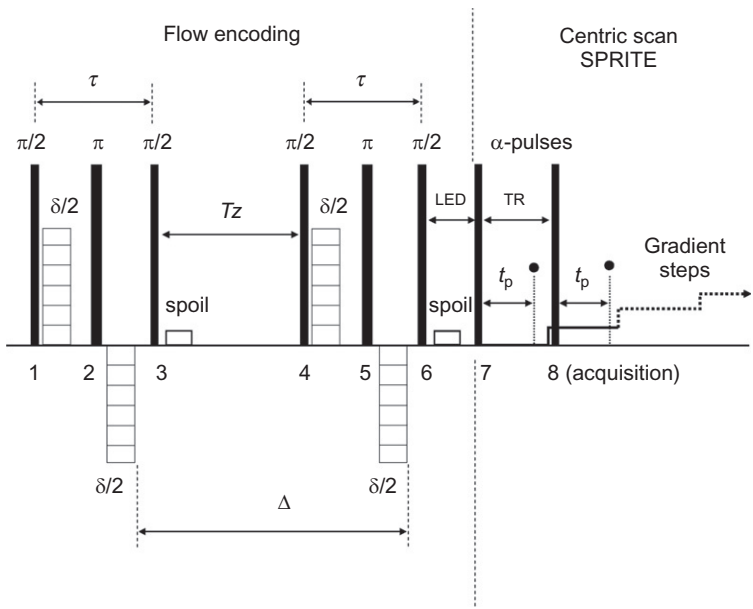

Figure 2.9 Pulse sequence employed for permeability mapping. Velocity encoding through Cotts PFG scheme, followed by spatial resolution with centric scan SPRITE.

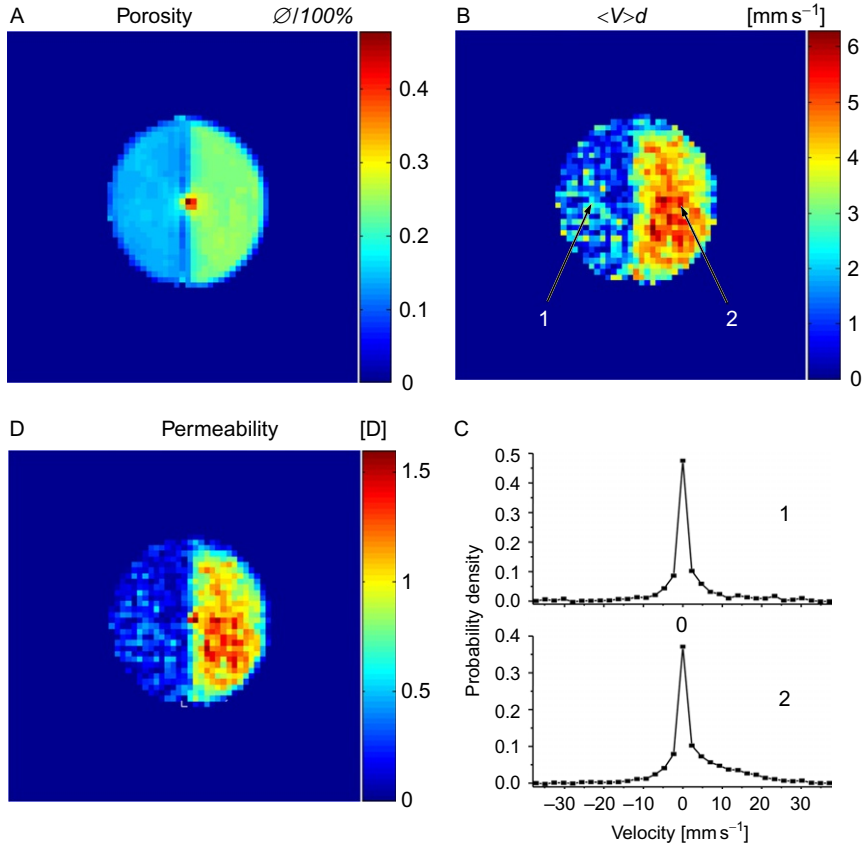

Figure 2.10 Composite sample of Bentheimer sandstone (right) and Pink Clashach (left). (A) Porosity map, (B) velocity map, (C) velocity distribution at pixels marked in (B), and (D) permeability map reconstructed from porosity and velocity maps.

a composite sample of a Bentheimer sandstone and a Pink Clashach sandstone glued together. The composite sample has two distinct permeability domains. The measurements of the composite sample, as well as those of the capillary bundle and bead packs, were in good agreement with traditional steady-state flow measurements and theoretical predictions. Rapid velocity maps in sandstone cores have been acquired with reduced acquisition time through echo sampling near the q-space origin.[23] Velocity maps may be converted to permeability maps given information on the corresponding pressure drop.

3.7. Performing a SPRITE experiment

We have presented a number of SPRITE methods for imaging fluids in porous media. SPRITE is typically a valuable method when imaging a sample with $T_2^\star < 1$ ms. To perform a good SPRITE experiment in 1D, 2D, or 3D, one must consider several acquisition parameters. A natural starting point is to choose an appropriate FOV of the image. The FOV should be set according to the size of the sample being imaged. Typically, a sample should take up about two-thirds of the FOV.

The FOV is inversely proportional to the sampling interval, Δk:

$$\mathrm{FOV} = \frac{1}{\Delta k} = \frac{2\pi}{\gamma \Delta G t_\mathrm{p}} \qquad [2.13]$$

The encoding time, t_p, is set according to the properties discussed below; therefore, the gradient step size, ΔG, determines the sampling interval, Δk.

The encoding time can be set based on the $T_2^\star$ of the sample and hardware properties such as the probe dead time. There are three methods of setting t_p to obtain quantitative density images: (1) Set $t_\mathrm{p} \ll T_2^\star$. The observed signal in this case is proportional to magnetization or proton density. (2) Set $t_\mathrm{p} \approx T_2^\star$ in a sample, where $T_2^\star$ is invariant throughout the sample. (3) Vary t_p and perform $T_2^\star$ mapping to determine magnetization or proton density. Typical t_p values range from 50 to 150 μs. The minimum t_p value is limited by the spectrometer and probe dead time, assuming sufficient gradient strength and is typically tens of microseconds.

To detect all frequencies present in the signal, the filter width (FW) must be set according to

$$\mathrm{FW} \geq \frac{n}{4t_\mathrm{p}} \qquad [2.14]$$

where n is the number of k-space points in 1D. The typical number of points collected in 1D to achieve a suitable balance between resolution, acquisition time, and gradient duty cycle is 64. In a DHK SPRITE experiment with $n = 64$ and $t_\mathrm{p} = 150$ μs, an FW of 125,000 Hz is appropriate.

In a SPRITE experiment, the RF pulse length is short and inversely proportional to the pulse bandwidth, as shown in Eq. (2.15).

$$\text{Pulse length} = \frac{1}{\text{pulse bandwidth}} \qquad [2.15]$$

The pulse bandwidth must be set to excite the entire sample, thus,

$$\text{Pulse bandwidth} > G_{\max} \times \text{sample length} \quad [2.16]$$

This is a very conservative limit because the k-space origin, which dominates the image, has a narrow bandwidth. When setting the flip angle, α, in a SPRITE experiment, one must also consider the repetition time, TR, of the experiment and the T_1 of the sample. A longitudinal steady state is reached in a SPRITE experiment after several successive RF pulses. The M_z magnetization decays as $exp(-n(\mathrm{TR}/T_{1\ \mathrm{app}}))$,[9] where

$$\frac{1}{T_{1\ \mathrm{app}}} = \frac{1}{T_1} - \frac{\ln(\cos\alpha)}{\mathrm{TR}} \quad [2.17]$$

In a centric scan SPRITE experiment, attenuation of the longitudinal magnetization and incomplete k-space sampling will lead to image blurring which is governed by the flip angle, TR, and T_1. TR influences the acquisition time of the sequence and is typically set to a few milliseconds. Therefore, the flip angle must be optimised to maximise SNR and minimise blurring. In the case of a Spiral SPRITE experiment, the choice of an appropriate flip angle depends on the TR/T_1 ratio and the number of spiral interleaves. Image blurring decreases as the number of interleaves and TR/T_1 are increased. Point spread functions (PSFs) of the centric scan SPRITE methods have been numerically simulated and verified experimentally.[12] When $\mathrm{TR}/T_1 > 1$, there is no significant blurring with large flip angles, so blurring effects do not need to be considered when choosing a flip angle. This occurs in some gas phase systems and some systems with extremely rapid spin–lattice relaxation such as concretes. Typical flip angles employed in centric scan SPRITE experiments are between 5° and 15°. The Ernst angle is generally a good choice for the excitation pulse flip angle since it provides a good compromise between image intensity and image resolution.[20]

4. APPLICATIONS OF SPRITE

4.1. Quantitative measurement of fluid content

Measuring fluid content with SPRITE has been demonstrated in a very wide variety of porous media. Porous media are solid materials containing voids, including wood, concrete, rocks, and bone.[1] Standard SPRITE has been employed to measure spatially and time-resolved moisture content in wood fibre systems. The SPRITE measurements showed dramatic improvement

over traditional frequency encoded spin echo measurements of low moisture content wood.[24]

The freeze–thaw cycle in concrete has been monitored using SPRITE. The cycle is detrimental to concrete because it will lead to cracking and eventual disintegration. The $T_2^\star$ of ice in concrete is so short (< 9 μs) that the proton signal will not be observed from ice, and therefore only unfrozen water will be imaged in a freeze–thaw experiment. Prado *et al.*[25] and Choi *et al.*[26] obtained spatially resolved SPRITE profiles of the freeze–thaw process in concrete. MRI is probably the only method that can provide quantitative spatially resolved data for water content in the freeze–thaw process.[27]

SPI and SPRITE have been employed to image the bone mineral phase of cortical bone.[28] In most clinical MRI images, the cortical bone appears as a signal void due to its short $T_2^\star$ signal lifetime. With SPRITE imaging, the bone can be visualised with a reasonable SNR and with no resolution loss. Magnetization preparation can be easily combined with centric scan SPRITE to suppress the signal from bone marrow when imaging cortical bone.

4.2. Mass transport in porous media

Pure phase encoding methods have been extensively employed for measuring mass transport processes in porous materials. SPRITE has been employed for quantitative measurements of fluid in rock cores.[29] Marica *et al.* measured the distribution of H_2O as it entered a deuterium oxide (D_2O)-saturated sandstone with Conical SPRITE. The quantitative, spatially resolved porosity data were used to determine diffusion coefficients in the rock core.[30] Diffusion has also been measured using SPRITE in a gel/reservoir system[31] and cement paste and mortars.[32] Muir *et al.* measured the diffusion of H_2O from an H_2O-based gel into a neighbouring D_2O reservoir. Quantitative spatial- and time-resolved profiles of the diffusion process were acquired using DHK SPRITE, as illustrated in Fig. 2.11. This naturally allowed for use of the differential form of Fick's second law to determine the diffusion coefficient, D. This technique is a simple alternative to a complicated integrated form of Fick's law for determining a diffusion coefficient.

4.3. Measuring capillary pressure in rock cores

SPRITE methods are now employed routinely for petroleum reservoir core analysis. Capillary pressure, P_c, is a measure of the pressure difference at the interface of two immiscible fluids. It is a useful measurement in rock cores because it allows for the determination of irreducible water saturation,

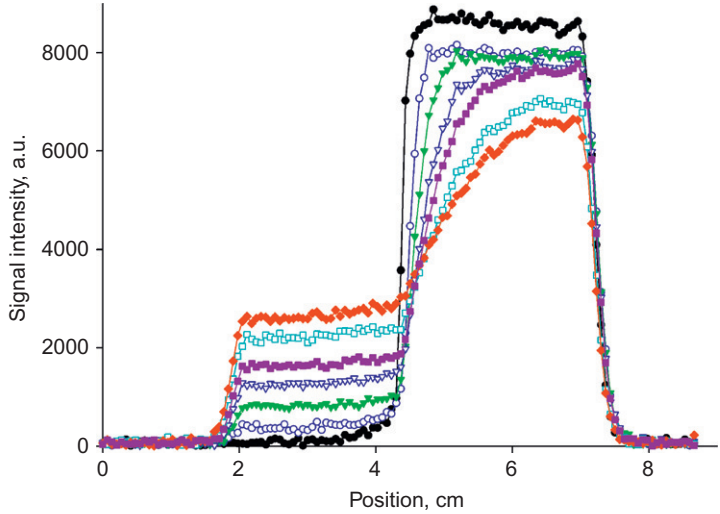

Figure 2.11 1D DHK SPRITE profiles of the diffusion of H_2O from an H_2O-based agarose gel (right) to a neighbouring well-mixed D_2O reservoir (left) at 0, 6, 32, 87, 156, 336, and 500 min after the D_2O reservoir was placed adjacent to the agarose gel.

residual oil saturation, and wettability. Traditionally, capillary pressure curves in rock cores are determined using mercury injection, porous plate, or centrifugation methods.[1] Mercury injection is a rapid method but uses a non-representative fluid, mercury, which is both toxic and destroys the core sample. Porous plate is recognised as the standard method but requires weeks or months to perform a complete measurement. A third method, centrifugation, is a compromise between mercury injection and porous plate. It employs representative reservoir fluids and permits more rapid measurement of capillary pressure. The traditional centrifugation method requires centrifugation at several different speeds to produce a capillary pressure curve. Chen *et al.*[33,34] and Green *et al.*[35] have combined the centrifugation method with DHK SPRITE imaging to obtain a simple, fast method of acquiring capillary pressure curves. The DHK SPRITE method allows a capillary pressure curve to be obtained after centrifugation at one speed or several speeds.

In the traditional method, a fluid-saturated rock core is placed in a core holder within a centrifuge and rotated at a number of different speeds. The core holder also contains another fluid, which displaces the wetting fluid until the two fluids reach equilibrium. The fluid displaced from the core plug is measured, and thus an average saturation for the core plug is known.

The capillary pressure, P_c, can be calculated using the Hassler–Brunner equation:

$$P_c(r) = \frac{1}{2}\Delta\rho\omega^2\left(r_1{}^2 - r^2\right) \qquad [2.18]$$

where $\Delta\rho$ is the density difference between the wetting and non-wetting fluids, ω is the angular rotation speed of the centrifuge, and r, r_1, and r_2 are the distances from the axis of rotation to any point along the core, the outlet face, and the inlet face as shown in Fig. 2.12. In conventional centrifuge methods, the saturation at the inlet face is approximated using the average fluid saturation. A point on the capillary pressure curve is obtained by plotting the inlet saturation against the capillary pressure obtained through Eq. (2.18). The centrifugation is repeated 7–10 times at different speeds to build a curve of 7–10 data points.

The DHK SPRITE method simplifies the traditional method because multiple points on a capillary pressure curve can be obtained at each centrifugation speed. The DHK SPRITE method is quantitative; therefore, the signal along the core is proportional to the quantity of saturating fluid along the core. After the centrifuge creates a distribution of the fluid in the rock, the fluid quantity along the rock can be measured directly with MRI. The positions r and r_1 can be measured and therefore the capillary pressure can be determined for various r positions using Eq. (2.18). The method can be repeated at different centrifuge speeds, which improves the range and resolution of the capillary pressure curves.

Green *et al.*[35] employed the MRI method of capillary pressure determination on a wide sampling of rock core plugs. They acquired air/brine capillary pressure curves, which showed close agreement to curves acquired with the porous plate method. They also acquired oil/brine capillary pressure curves by employing D_2O in place of H_2O in the brine solution. Deuterium yields

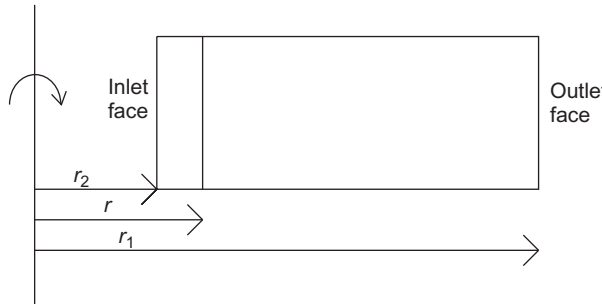

Figure 2.12 Schematic of a rock core plug in a centrifuge.

no signal in a ^{1}H MRI image, therefore, in an oil/D_2O-based brine system, ^{1}H signal arises from the oil only.

The DHK SPRITE centrifuge method has a number of advantages over the traditional centrifuge method for capillary pressure determination. Multiple points on a capillary pressure curve can be obtained after centrifugation at a single speed. The method is fast and employs realistic fluids. Most importantly, the fluid saturation can be directly determined through experiment.

5. SPIN ECHO SINGLE POINT IMAGING

SPRITE is a robust method for imaging fluid content in porous media with short $T_2^\star$ and T_2 values. When measuring porous materials that have a short $T_2^\star$ with moderate T_2, another method, Spin Echo Single Point Imaging (SE-SPI), may be advantageous. SE-SPI is similar to SPRITE in that it is a pure phase encoding method and therefore is immune to artefacts due to susceptibility variations and paramagnetic impurities and has no linewidth restriction on resolution. The advantages of employing an SE-SPI method for measuring moderate T_2 materials are (a) the contrast in SE-SPI methods is due to T_2, rather than $T_2^\star$; (b) several k-space points can be acquired per excitation in an SE-SPI experiment (Hybrid SE-SPI), resulting in increased sensitivity over SPRITE; (c) SE-SPI employs a relatively narrow signal bandwidth which also results in increased sensitivity over SPRITE.[36]

5.1. TurboSPI

Turbo Single Point Imaging, TurboSPI, was the first SE-SPI method developed at UNB.[37] TurboSPI is a modified Spin Echo sequence with pure phase encoding. It is based on the Fast Spin Echo class of imaging methods, specifically the RARE (Rapid Acquisition with Relaxation Enhancement) sequence. The measurement begins with a low flip angle pulse, followed by a series of 180° pulses interspersed with RARE-type bipolar gradients, as illustrated in Fig. 2.13. In order for the magnetization to return to equilibrium, a delay of $5 \times T_1$ would ordinarily be required. To decrease the acquisition time of TurboSPI, the signal can be acquired in a longitudinal steady state. The optimal flip angle for the excitation pulse is the Ernst angle, given by

$$\cos\alpha = \exp\left(\frac{-\mathrm{TR}}{T_1}\right) \qquad [2.19]$$

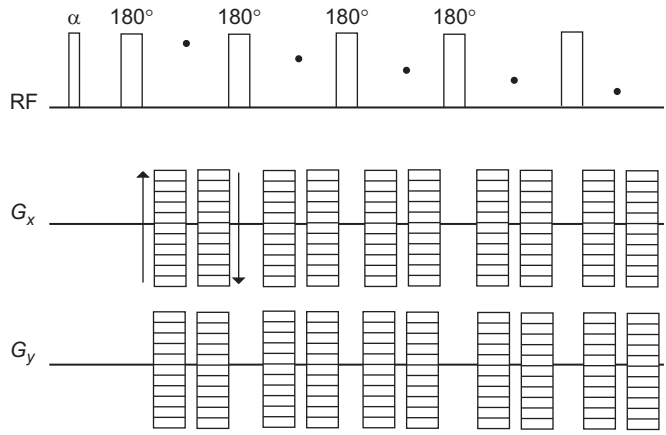

Figure 2.13 2D TurboSPI pulse sequence.

where TR is the repetition time, T_1 is the spin–lattice relaxation time, and α is the flip angle. However, when using a low flip angle in conjunction with spin echo trains, imperfect 180° pulses will scramble the y and z components of magnetization, which will then mix with different components of magnetization. To overcome this problem, the XY-8 or XY-16 RF pulse phase cycle can be employed.[37] The phase cycling preserves the magnetization and prevents any mixing of transverse magnetization with the longitudinal steady state.

The TurboSPI image intensity is given by

$$S = M_0 \exp\left[\frac{-n\mathrm{TE}}{T_2}\right]\left(\frac{1-\exp\left(-\frac{\mathrm{TR}}{T_1}\right)}{1-\cos\alpha\exp\left(-\frac{\mathrm{TR}}{T_1}\right)}\sin\alpha\right) \qquad [2.20]$$

where M_0 is the initial magnetization, TE is the echo time, and T_2 is the spin–spin relaxation time. The T_1 recovery period, TR, is the time between the end of the echo train and the next excitation. TurboSPI can be implemented with linear phase encode ordering or centric phase encode ordering. The dependence of T_2 contrast on the k-space coordinate, n, in Eq. (2.20) is important when a linear k-space trajectory is used rather than a centric ordered trajectory. The contrast in a TurboSPI sequence is due to the T_2 relaxation time. 2D TurboSPI images of four $CuSO_4$ doped agarose gels are shown in Fig. 2.14. The gels have T_2 values of 5, 10, 25, and 50 ms, respectively. The image in Fig. 2.14A was acquired with centric phase encode ordering, while the image in Fig. 2.14B was acquired with linear phase encode ordering. Images acquired with centric phase encode ordering have an effective echo time, $\mathrm{TE}_{\mathrm{eff}}$, equal to

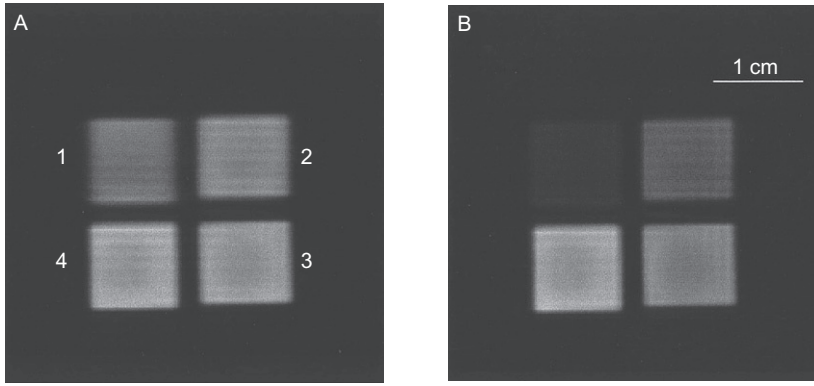

Figure 2.14 2D TurboSPI images of $CuSO_4$ doped agarose gels with $T_2 = 5, 10, 25, 50$ ms for gels 1, 2, 3, 4, respectively. (A) Images acquired with centric phase encode ordering ($TE_{eff} = TE = 1.3$ ms). (B) Images acquired with linear phase encode ordering ($TE_{eff} = 5 \times TE = 6.5$ ms).

TE. Images acquired with linear phase encode ordering have a TE_{eff} of approximately $5 \times TE$ because the central k-space data is acquired after the fourth and fifth echo in the echo train. The T_2 contrast is evident in both cases, however, is greater in the case of linear phase encode ordering due to a longer TE_{eff}.

5.2. Hybrid SE-SPI

The Hybrid SE-SPI pulse sequence is conceptually similar to TurboSPI in that individual echoes are phase encoded to provide different k-space data points. However, Hybrid SE-SPI is a 1D measurement where the k=0 point is determined from the 90° pulse FID. This results in a significant gain in sensitivity and removes the T_2 contrast of the TurboSPI method, allowing for true fluid content images. The pulse sequence begins with a 90° pulse, followed by a series of 180° pulses interspersed with phase-encoding gradients of equal strength but opposite sign. After a period of $5 \times T_1$, the second half of k-space is collected by employing gradients that are opposite of the sign in the first half of the acquisition, as illustrated in Fig. 2.15. The two sides of k-space are combined, and the $k = 0$ point is averaged prior to Fourier transformation. The signal intensity of a Hybrid SE-SPI image is given by Eq. (2.21):

$$S = M_0 \qquad [2.21]$$

where M_0 is the initial magnetization. The $k = 0$ point is assumed to be acquired promptly after the initial 90° pulse, without any $T_2^{\star}$ attenuation, so

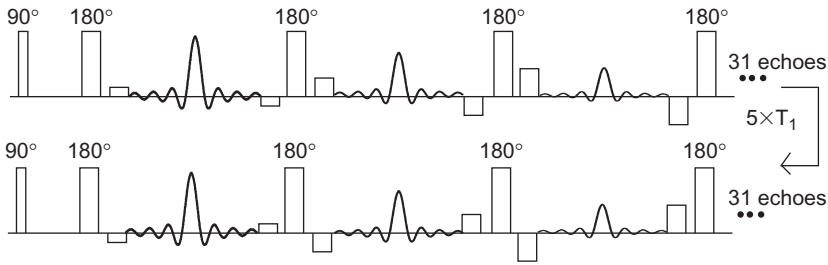

Figure 2.15 Hybrid SE-SPI pulse sequence.

the signal is directly proportional to the magnetization and thereby the ^{1}H density.

The Hybrid SE-SPI sequence suffers from a simple image blurring due to T_2 attenuation of the phase encoded echoes. In samples with a significant population of short T_2, the blurring may affect the quantification of the sequence. Generally in samples with a dominant T_2 population greater than 5 ms, the blurring will be minimal.[36] Samples with important short T_2 components can be measured using the T_2 mapping SE-SPI sequence.

5.3. T_2 mapping SE-SPI

Determination of the bulk T_2 of a porous material is the most common magnetic resonance measurement in porous media. The T_2 value is proportional to pore size; relaxation is faster in smaller pores. The T_2 mapping SE-SPI method allows for spatially resolved T_2 measurements in porous media. Therefore, a T_2 mapping SE-SPI experiment can provide spatially resolved pore size distributions in a porous medium. T_2 mapping SE-SPI begins with a 90° pulse, followed by the application of a gradient and a series of 180° pulses. The sequence provides a series of T_2 weighted profiles, which, after an inverse Laplace transformation, provide spatially resolved T_2 distributions. An early version of the T_2 mapping SE-SPI method developed by Li *et al.* employs RARE-type bipolar gradients between 180° pulses.[36] The magnetization is unwound before the application of the next 180° pulse, as shown in Fig. 2.16.

A later version of the T_2 mapping SE-SPI sequence developed by Petrov *et al.*, illustrated in Fig. 2.17, phase encodes the magnetization within the first pulse interval, then employs XY-16 phase cycling to preserve magnetization.[39] The advantages of this method are that the second and subsequent echoes have a shorter TE and there are fewer gradient applications which result in a lower duty cycle.

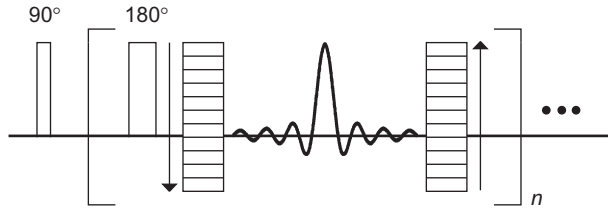

Figure 2.16 T_2 mapping SE-SPI pulse sequence with phase unwinding gradient.

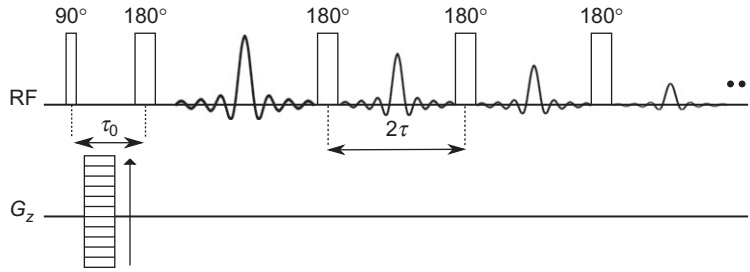

Figure 2.17 T_2 mapping SE-SPI pulse sequence with phase cycling.

The signal intensity, S, after the nth echo is given in Eq. (2.22):

$$S = M_0 \exp\left(\frac{-2\tau_0}{T_2}\right) \exp\frac{-(n-1)2\tau}{T_2} \qquad [2.22]$$

where M_0 is the initial magnetization, τ_0 is the period between the 90° and 180° pulses, τ is the refocusing period between 180° pulses in the pulse train, and T_2 is the spin–spin relaxation time. Acquiring multiple time-domain points on the echo can increase the SNR of the T_2 mapping SE-SPI sequence. The number of points is limited by the dwell time and the τ value.[39]

5.4. Performing a SE-SPI experiment

Implementing an effective SE-SPI sequence requires careful consideration of several acquisition parameters. In Hybrid SE-SPI, the $k=0$ data point is acquired at a near zero evolution time from the FID following the 90° pulse. The k-space origin point is density weighted, but the following k-space points will suffer from T_2 attenuation. Therefore, it is important to minimise the echo times with fast gradient switching. Echo times typically range from 500 μs to 1.6 ms depending on limits of the gradient set and the RF duty cycle. The delay between half k-space acquisitions is $5 \times T_1$.

The Hybrid SE-SPI sequence will lead to an attenuation of the k-space data and a blurring of the image. The amplitude modulation of the k-space data can be defined by an amplitude modulation function shown in Eq. (2.23), and the image blurring can be described by a PSF shown in Eq. (2.24).

$$\mathrm{MTF} = \mathrm{MTF}_{\mathrm{k-space}} \times \mathrm{MTF}_{\mathrm{diffusion}} \times \mathrm{MTF}_{T_2} \quad [2.23]$$

$$\mathrm{PSF} = \mathrm{PSF}_{\mathrm{k-space}} \otimes \mathrm{PSF}_{\mathrm{diffusion}} \otimes \mathrm{PSF}_{T_2} \quad [2.24]$$

$\mathrm{MTF}_{\mathrm{k-space}}$ is due to k-space sampling, MTF_{T_2} is due to signal decay with time constant T_2, and $\mathrm{MTF}_{\mathrm{diffusion}}$ is due to molecular diffusion through underlying magnetic field gradients. A typical number of k-space points in a Hybrid SE-SPI experiment is 64. The diffusion and T_2 modulation will be limited by a short echo time (TE). The blurring in the Hybrid SE-SPI image will depend significantly on the fraction of short T_2 components in the T_2 distribution and can be decreased with a short TE.

When imaging with T_2 mapping SE-SPI, it is beneficial to have the shortest echo time ($\mathrm{TE} = 2 \times \tau$) possible to reduce the signal attenuation due to T_2 decay. There are two τ times in the T_2 mapping SE-SPI sequence. The first τ_0 between the 90° and 180° pulses must accommodate the phase encoding gradient. Values can be set for the gradient ramp up time, the gradient plateau time, and the gradient ramp down time, the sum of which is typically 300–600 μs. The τ value, which is the refocusing period between 180° pulses in the pulse train, is limited by the RF duty cycle.

To increase the SNR of a T_2 mapping SE-SPI sequence, the number of time domain points collected on the echoes should be maximised for the given dwell time and τ time. The image intensity is roughly proportional to the number of time domain points collected on the echoes. A typical dwell time is 8 μs, and a typical number of time-domain echo points is 10–20.

To observe the complete signal decay, the number of echoes, or number of 180° pulses, must be balanced with the τ time. If the signal does not decay completely, the number of echoes may be increased or the τ time increased. A long train of RF pulses may heat the sample, in which case, the τ time should be increased and the number of echoes reduced.

Spatially resolved T_2 distributions can be obtained using the T_2 mapping SE-SPI sequence. After a Fourier transform, the sequence will provide a series of profiles that are T_2-weighted (Fig. 2.18A). Then, for a pixel in a region of interest (ROI), an echo decay is obtained (Fig. 2.18B), which after an inverse Laplace transformation, provides a T_2 distribution at that particular location (Fig. 2.18C).[36] This is repeated for each pixel in the ROI. The

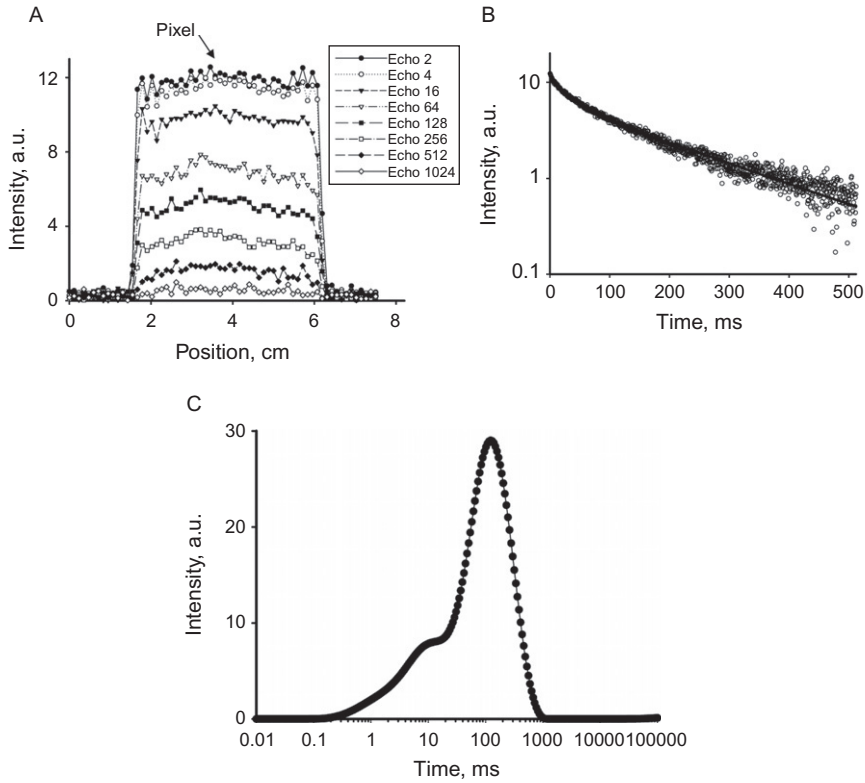

Figure 2.18 (A) T_2-weighted profiles of a sandstone core plug acquired with a T_2 mapping SE-SPI sequence. (B) Image intensity decay from the pixel marked in (A). (C) T_2 distribution of the marked pixel obtained after an inverse Laplace transform of the decay in (B).

area under the curve of each T_2 distribution can be summed to give a value representing the signal density at that position. Thus, when all of the T_2 distributions are summed and plotted according to their position, a density-weighted profile is produced. The T_2 mapping technique does not suffer from the T_2 blurring of the Hybrid SE-SPI technique.

6. APPLICATIONS OF SE-SPI

6.1. Quantification of superparamagnetic iron oxide

SE-SPI methods have been employed to quantify fluid content. TurboSPI has been employed in a biomedical imaging context for the quantification of labelled cells containing an iron oxide contrast agent. Relaxation rate mapping is often employed to monitor the distribution of implanted cells after

they have been injected with the contrast agent. Rioux *et al.* modified the TurboSPI sequence to acquire several hundred time points on the spin echo for each phase encode step.[38] This permitted robust relaxation rate mapping of iron concentrations over a large dynamic range. The relaxation rates measured by TurboSPI agreed with bulk measurements, indicating that the sequence is suitable for iron quantification in labelled cells.

6.2. Spatially resolved T_2 distributions in rock cores

Petrov *et al.* demonstrated the utility of T_2 mapping SE-SPI for obtaining spatially resolved T_2 distributions of realistic rock core samples.[39] A Wallace sandstone sample was a composite made of two cores: one saturated with water and the other saturated with heavy mineral oil. The SE-SPI profiles in Fig. 2.19 show a clear distinction between the water-saturated core and the oil-saturated core. Although both cores were saturated with equal amounts of fluid, there is less signal amplitude from the water-saturated core. This is due to a greater amount of diffusive attenuation of water than oil in the τ_0 period.

Petrov *et al.* also performed a flooding experiment in a Berea core plug. The plug was initially saturated with D_2O brine (23%) and dodecane (77%). D_2O was then flooded into one end of the core plug while the sample was in the magnet. T_2 mapping SE-SPI profiles were acquired every 30 min during

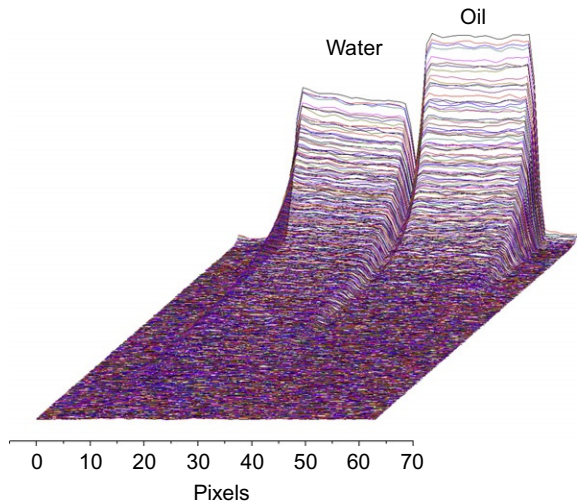

Figure 2.19 T_2 mapping SE-SPI profiles of two pieces of Wallace sandstone saturated with water (left) and oil (right).

the duration of the flooding experiment. T_2 distributions were compared at three different sites along the core plug: near the front face of the core, near the middle of the core, and near the rear face of the core as shown in Fig. 2.20. Distributions were also compared at an early time in the flooding process and at a late time. The distributions reveal information about the pore occupancy during the flooding process. As the residual dodecane level decreases, the arithmetic mean T_2 increases. The amplitude of the short T_2 peak decreases with time, while the long T_2 peak amplitude remains the same. This indicates that as D_2O enters the core, the dodecane is displaced from smaller pores first, while larger pores remain occupied. Such behaviour is expected for a non-wetting phase in a water-wet core sample.

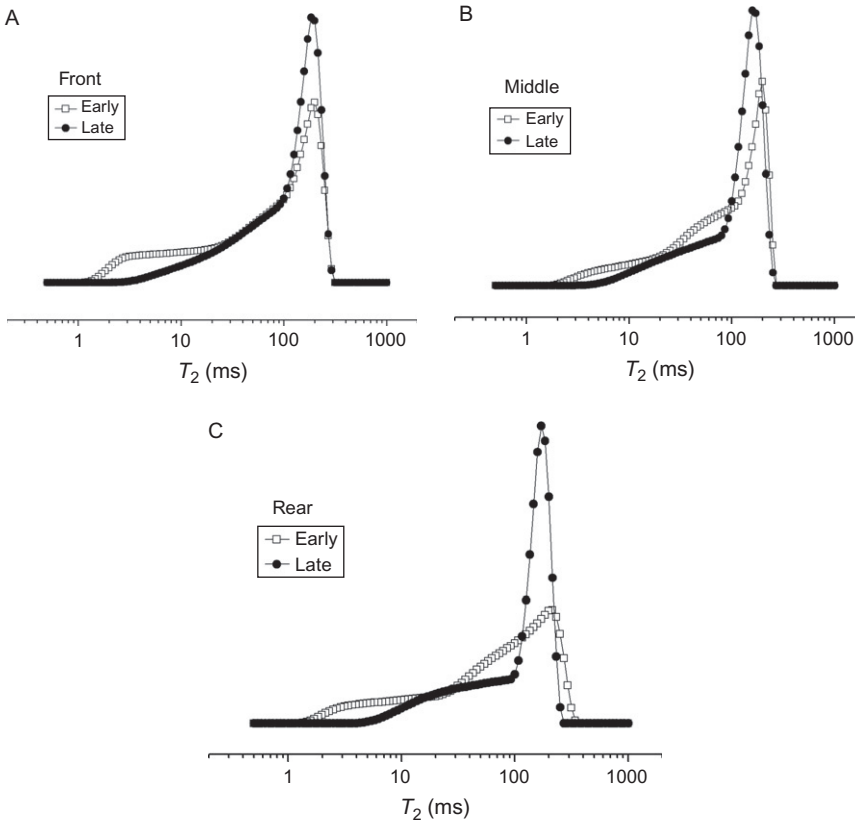

Figure 2.20 T_2 distributions of dodecane in Berea sandstone measured near the front face (A), the middle (B), and near the rear face (C) at early and late stages in the flooding experiment.

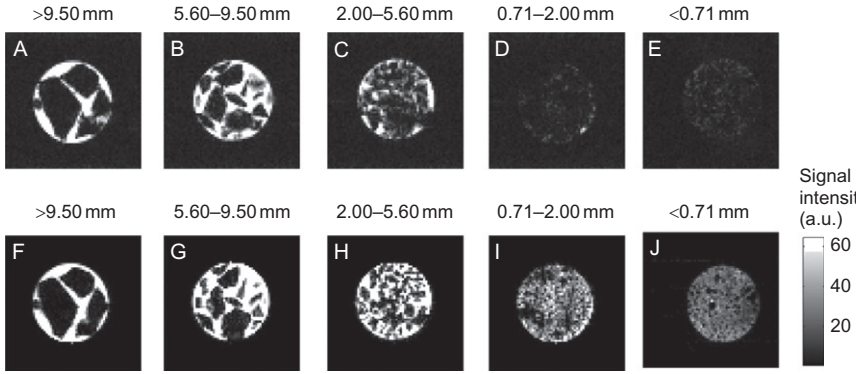

Figure 2.21 Images of saturated ore samples of different particle sizes acquired with SPI–MPA (A–E) and SE-SPI (F–J). The images (A–E) and (F–J) have been produced with the same intensity scales.

The T_2 mapping SE-SPI measurement is fast and provides spatially resolved pore size distribution information. It is a promising measurement for monitoring core flooding and other fluid flow processes.

6.3. Copper ore heap leaching

An SE-SPI method was used to image aqueous flow fields in low grade copper ore. Fagan *et al.* showed that a frequency encoded spin echo technique was not appropriate for imaging in ore systems due to magnetic susceptibility artefacts. Instead, images from SPI and SE-SPI methods were employed and compared with a high resolution X-ray image. The SPI method was a MPA technique where four points were collected on the FID. The SE-SPI method used a split gradient sequence where a gradient was applied after a 90° pulse and after the 180° pulse. Both the SPI-MPA and SE-SPI methods produced non-distorted images of the ore systems, but the SE-SPI images had a better SNR for equal total acquisition times (Fig. 2.21).[40]

7. CONCLUSIONS

Pure phase encode MRI methods have been proven to be effective for imaging fluids in porous media with short signal lifetimes. Phase encoding methods offer several advantages for imaging porous media over frequency encoding methods including immunity to susceptibility effects, chemical shift artefacts, B_0 inhomogeneity, and no linewidth restriction on resolution.

Centric scan SPRITE methods have simple signal equations and are robust in generating quantitative images with relatively short acquisition times and minimal gradient duty cycles. SPRITE sequences can be employed to generate quantitative $T_2^\star$ maps or combined with magnetization preparation sequences to apply T_1, T_2, or permeability contrast.

Spin Echo SPI sequences are a second class of pure phase encode methods that are useful for measuring materials with moderate T_2 and short $T_2^\star$. SE-SPI provides high sensitivity measurements due to a relatively narrow filter and multiple k-space point acquisition per excitation. T_2 mapping SE-SPI permits measuring spatially resolved T_2 distributions which provide important information about fluid occupancy of the pore space.

Applications of pure phase encode methods in porous media have been illustrated in the measurement of static fluid content as well as the measurement of dynamic processes. We have demonstrated how these methods provide spatially resolved information in heterogeneous samples and can easily be extended to other types of porous media. Quantitative measurement of fluid in rock core plugs is a promising area of application for SPRITE and SE-SPI methods for both core analysis and core flooding experiments.

ACKNOWLEDGMENTS

C.E.M. thanks colleagues at the UNB MRI Centre for their input and assistance in preparing this review, and NSERC of Canada for funding (PGS-D). B.J.B. thanks NSERC of Canada for a Discovery Grant and the Harrison McCain Foundation Visitorship Award for funding. B.J.B. thanks the faculty, staff and students at the Magnetic Resonance Research Centre, Cambridge, and Dr. Michael Johns for their discussions and motivation for this review.

REFERENCES

1. Dullien F. *Porous media: fluid transport and pore structure*. New York: Academic Press; 1991.
2. Kantzas A. Recent advances in the characterization of porous media using computer assisted tomography of X-rays. *CWLS J* 1995;**20**:99–111.
3. Korringa J, Seevers DO, Torrey HC. Theory of spin pumping and relaxation in systems with a low concentration of electron spin resonance centers. *Phys Rev* 1962;**127**:1143–50.
4. Kenyon WE. Nuclear magnetic resonance as a petrophysical measurement. *Nucl Geophys* 1992;**6**:153–71.
5. Kleinberg RL, Horsfield MA. Transverse relaxation processes in porous sedimentary rock. *J Mag Res* 1990;**88**:9–19.
6. Emid S, Creyghton JHN. High resolution NMR imaging in solids. *Physica* 1985;**128B**:81–3.
7. Gravina S, Cory DG. Sensitivity and resolution of constant-time imaging. *J Mag Res B* 1994;**104**:53–61.
8. Balcom B, MacGregor R, Beyea S, Green D, Armstrong R, Bremner T. Single-point ramped imaging with T_1 enhancement (SPRITE). *J Magn Res A* 1996;**123**:131–4.

9. Halse M, Goodyear DJ, MacMillan B, Szomolanyi P, Matheson D, Balcom BJ. Centric scan SPRITE magnetic resonance imaging. *J Mag Res* 2003;**165**:219–29.
10. Chen Q, Marble AE, Colpitts BG, Balcom BJ. The internal magnetic field distribution, and single exponential magnetic resonance free induction decay, in rocks. *J Mag Res* 2005;**175**:300–8.
11. Beyea SD, Balcom BJ, Prado PJ, Cross AR, Kennedy CB, Armstrong RL, et al. Relaxation time mapping of short $T_2^\star$ nuclei with Single-Point Imaging (SPI) methods. *J Mag Res* 1998;**135**:156–64.
12. Halse M, Rioux J, Romanzetti S, Kaffanke J, MacMillan B, Mastikhin I, et al. Centric scan SPRITE magnetic resonance imaging: optimization of SNR, resolution and relaxation time mapping. *J Mag Res* 2004;**169**:102–17.
13. Deka K, MacMillan MB, Ouriadov AV, Mastikhin IV, Young JJ, Glover PM, et al. Quantitative density profiling with pure phase encoding and a dedicated 1D gradient. *J Mag Res* 2006;**178**:25–32.
14. Szomolanyi P, Goodyear D, Balcom B, Matheson D. SPIRAL-SPRITE: a rapid single point MRI technique for application to porous media. *Mag Res Imag* 2001;**19**:423–8.
15. Khrapitchev AA, Newling B, Balcom BJ. Sectoral sampling in centric-scan SPRITE magnetic resonance imaging. *J Mag Res* 2006;**178**:298–306.
16. Kaffanke JB, Stöcker T, Romanzetti S, Dierkes T, Leach MO, Shah NJ. Phase-cycled averaging for the suppression of residual magnetisation in SPI sequences. *J Mag Res* 2009;**199**:117–25.
17. Marica F, Chen Q, Hamilton A, Hall C, Al T, Balcom BJ. Spatially resolved measurement of rock core porosity. *J Mag Res* 2006;**178**:136–41.
18. Mastikhin IV, Balcom BJ, Prado PJ, Kennedy CB. SPRITE MRI with prepared magnetization and centric k-space sampling. *J Mag Res* 1999;**136**:159–68.
19. Li L, Marica F, Chen Q, MacMillan B, Balcom BJ. Quantitative discrimination of water and hydrocarbons in porous media by magnetization prepared centric-scan SPRITE. *J Mag Res* 2007;**186**:282–92.
20. Khrapitchev AA, Newling B, Balcom BJ. Centric-scan SPRITE magnetic resonance imaging with prepared magnetisation. *J Mag Res* 2006;**181**:271–9.
21. Romanenko K, Balcom BJ. Permeability mapping in porous media by magnetization prepared centric-scan SPRITE. *Exp Fluids* 2011;**50**:301–12.
22. Newling B, Poirier CC, Zhi Y, Rioux JA, Coristine AJ, Roach D, et al. Velocity imaging of highly turbulent gas flow. *Phys Rev Lett* 2004;**93**:154503-1–4.
23. Romanenko K, Balcom BJ. Permeability mapping in naturally heterogeneous sandstone cores by magnetization prepared centric-scan SPRITE. *AIChE J* 2012. http://dx.doi.org/10.1002/aic.13778.
24. MacMillan MB, Schneider MH, Sharp AR, Balcom BJ. Magnetic resonance imaging of water concentration in low moisture content wood. *Wood Fiber Sci* 2002;**34**:276–86.
25. Prado PJ, Balcom BJ, Beyea SD, Armstrong RL, Bremner TW. Concrete thawing studied by single-point ramped imaging. *Solid State Nucl Mag Res* 1997;**10**:1–8.
26. Choi C, Balcom BJ, Beyea SD, Bremner TW, Grattan-Bellew PE, Armstrong RL. Spatially resolved pore-size distribution of drying concrete with magnetic resonance imaging. *J Appl Phys* 2000;**88**:3578–81.
27. Young JJ, Bremner TW, Thomas MDA, Balcom BJ. *Pure phase encode magnetic resonance imaging of concrete building materials. Nuclear magnetic resonance imaging in chemical engineering*. Weinheim, Germany: Wiley-VCH; 2006 285 p.
28. Mastikhin IV, Balcom BJ. Centric SPRITE MRI of biomaterials with short $T_2^\star$. *Encyclopedia of Magnetic Resonance*, eds-in-chief R. K. Harris and R. E. Wasylishen, John Wiley: Chichester. http://dx.doi.org/10.1002/9780470034590.emrstm1265 Published online 15 June 2012.

29. Chen Q, Rack FR, Balcom BJ. *Quantitative magnetic resonance imaging methods for core analysis. New techniques in sediment core analysis*. London: The Geological Society of London; 2006 193 p.
30. Marica F, Jofré SAB, Mayer KU, Balcom BJ, Al TA. Determination of spatially-resolved porosity, tracer distributions and diffusion coefficients in porous media using MRI measurements and numerical simulations. *J Contam Hydrol* 2011;**125**:47–56.
31. Muir CE, Lowry BJ, Balcom BJ. Measuring diffusion using the differential form of Fick's law and magnetic resonance imaging. *New J Phys* 2011;**13**:015005.
32. Feng X, Balcom BJ, Thomas MDA, Bremner TW. Na and Li ion diffusion in modified ASTM C 1260 test by magnetic resonance imaging (MRI). *Cement Concrete Res* 2008;**38**:1409–15.
33. Chen Q, Balcom B. Capillary pressure curve measurement using a single-moderate-speed centrifuge and quantitative magnetic resonance imaging, In: *International symposium of the society of core analysts*; 2005 SCA2005-44.
34. Chen Q, Hickey H, Balcom B. A single-shot method for determining drainage and imbibition capillary pressure curves, In: *International symposium of the society of core analysts*; 2006 SCA2006-12.
35. Green D, Dick J, McAloon M, Cano-Barrita PF de J, Burger J, Balcom B. Oil/water imbibition and drainage capillary pressure determined by MRI on a wide sampling of rocks, In: *International symposium of the society of core analysts*; 2008 SCA2008-01.
36. Li L, Han H, Balcom BJ. Spin echo SPI methods for quantitative analysis of fluids in porous media. *J Mag Res* 2009;**198**:252–60.
37. Beyea SD, Balcom BJ, Mastikhin IV, Bremner TW, Armstrong RL, Grattan-Bellew PE. Imaging of heterogeneous materials with a turbo spin echo single-point imaging technique. *J Mag Res* 2000;**144**:255–65.
38. Rioux JA, Brewer KD, Beyea SD, Bowen CV. Quantification of superparamagnetic iron oxide with large dynamic range using TurboSPI. *J Mag Res* 2012;**216**:152–60.
39. Petrov OV, Ersland G, Balcom BJ. T_2 distribution mapping profiles with phase-encode MRI. *J Mag Res* 2011;**209**:39–46.
40. Fagan MA, Sederman AJ, Johns ML. MR imaging of ore for heap bioleaching studies using pure phase encode acquisition methods. *J Mag Res* 2012;**216**:121–7.

CHAPTER THREE

Steroids and NMR

Martin Jaeger*, Ruud L.E.G. Aspers†

*DSM Nutritional Products Ltd., Analytical Research Center, Wurmisweg, Kaiseraugst, Switzerland
†Radboud University, Institute for Molecules and Materials, Biophysical Chemistry, Heyendaalseweg, Nijmegen, The Netherlands

Contents

Annual Reports on NMR Spectroscopy, Volume 77
ISSN 0066-4103
http://dx.doi.org/10.1016/B978-0-12-397020-6.00003-9

Abstract

In this chapter, the NMR spectroscopic investigation of steroids is analyzed from five different angles, yet the general stage, the steroid-specific aspect and the provision of an illustrative example are the common themes for each perspective. Firstly, steroids and NMR are placed in their chemical, analytical and pharmaceutical context. Secondly, the characteristic challenges of steroid structure elucidation and the aspects of specific moieties of steroidal compounds are described following chronological and also stereospecific lines. Subsequently, the application of NMR methodology is reviewed with respect to host–guest chemistry, impurity profiling and isotopic labelling, such as ^{3}H, ^{17}O and ^{19}F. Furthermore, the use of computer-assisted structure elucidation applied to the steroids using incremental systems, simple databases and the current sophisticated spectral prediction algorithms will be discussed and their applications compared for testosterone and tibolone. The most recently developed and also the rare, but nonetheless valuable, NMR methods will also be presented. These include covariance processing, residual dipolar couplings and high-sensitivity C—C INADEQUATE experiments. Finally, suitable experiment sets for steroid structure elucidation and structure confirmation are discussed. Tibolone is used as the common thread and serves as an illustrative example throughout this chapter.

Key Words: Steroids, Chemical shift assignment, Pharmaceutical NMR applications, Host–guest chemistry, Stable isotopes, Computer-assisted structure elucidation, Covariance processing, Residual dipolar couplings, Diffusion-ordered spectroscopy, Structure elucidation strategy

1. PROLOGUE

When invited to write a chapter on NMR of steroids, one immediately thinks of the classic treatises by Kirk et al.[1–3] succeeded by Kasal et al.[4] and the textbook by Croasmun and Carlson.[5] In the general steroid field, the masterpiece by Fieser and Fieser[6] is instantly memorable as are the autobiographical essays of Djerassi.[7,8] Our intention was therefore not to re-write the art of our predecessors but hope that our readers may let themselves get intrigued by the compilation and the illustration of contemporary and rare topics that have not been assembled previously.

2. AN INTRODUCTION TO STEROIDS

2.1. Classification of steroids

Steroidal chemical compounds possess a noticeable common feature. Their skeleton consists of four fused rings, most often one five-membered and three six-membered carbocycles, cf. Fig. 3.1. The unsubstituted carbohydrate scaffold with a total of 17 carbon atoms has been baptized gonane. Although this

structure does not actually exist in nature, it forms the basis of the chemical class of the steroids.

The number of carbon atoms, which is augmented by the substituents on the gonane (**1**) scaffold, determines the membership of the compound to the steroid subclass. Cholestanes comprise 27 carbon atoms; hence cholesterol (**2**) makes part of that series. The cholanes and pregnanes have 24 and 21 carbon atoms, respectively. Examples are cholic acid (**3**) and progesterone (**4**). Androstanes and estranes complete the sequence of steroid classes; testosterone (**5**) and estradiol (**6**) are the most well-known representatives of these classes, possessing 19 and 18 carbon atoms each. In parallel to this chemical classification, a historical nomenclature exists, which is based on the origin of the compound or its main natural source: progestagens, androgens, oestrogens, glucocorticoids and mineralocorticoids. Interestingly, within these classes, the number of carbon atoms remains unchanged, cf. Fig. 3.1 and Table 3.1. Of course, this fact is related to the enzymatic carbon bond formation or cleavage that determines the biological function of the steroids. The metabolic pathway of steroids and related compounds has thoroughly been sketched in the well-known scheme "Boehringer biochemical pathways". Closely related to the predominant location of the steroidal compounds in biology, the taxonomy and biological function provide a third scheme for the classification. Steroids are found in animals, plants and

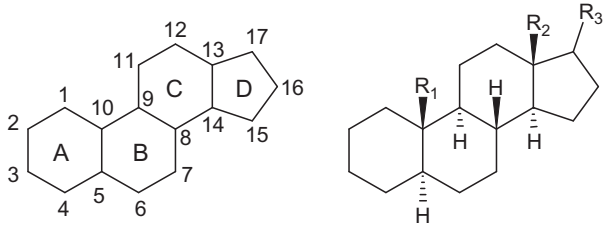

Steroidal compound	R1	R2	R3	Extra C atoms
Estrane	H	CH_3	H	
Androstane	CH_3	CH_3	H	
Pregnane	CH_3	CH_3	C_2H_5	2
Cholane	CH_3	CH_3	$CH(CH_3)–C_3H_7$	5
Cholestane	CH_3	CH_3	$CH(CH_3)–C_4H_7(CH_3)_2$	8
Ergostane	CH_3	CH_3	$CH(CH_3)–C_3H_5(CH_3)–CH(CH_3)_2$	9

Figure 3.1 Ring-lettering and carbon-numbering (left) and the basic systematic steroid structure classification (right, table). An atom or group attached to one of the rings is termed alpha (α) if it lies below or beta (β) if it lies above the steroidal plane. Alpha is shown in dashed lines, beta in thick, solid lines. R1 and R2 are generally methyl groups, 19-methyl and 18-methyl respectively; hydroxyl methyl groups or aldehyde groups are sometimes encountered, R3 may be absent.

Table 3.1 Overview of the steroid classes according to chemical and historical classification, corresponding structures are given in Figure 3.1

Number of carbon atoms	Chemical classification	Historical or functional classification	Biological function	Origin/source	Examples
27	Cholestanes	Cholesterol	Modulator of cell membrane fluidity; parent compound of steroid metabolism	Cholesterol: all normal animal tissues; gall stones	Cholesterol
24	Cholanes		Bile fluids, digestion, emulsifiers, cholesterol elimination	Bile fluids	Cholic acid
21	Pregnanes	Progestagens	Sex hormones	All tissues producing steroids	Progesterone
		Glucocorticoids	Regulators of metabolism and immune functions	Adrenal cortex; bovine bile acids, diosgenine, stigmasterol	Cortisol
		Mineralocorticoids	Regulators of blood volume and renal excretion	Adrenal cortex; bovine bile acids, diosgenine, stigmasterol	Aldosterone
19	Androstanes	Androgens	Sex hormones, anabolic steroids for bone and muscle synthesis	Male testes, female adrenal cortex	Testosterone
18	Estranes or formerly Oestranes	Oestrogens	Sex hormones	Developing follicles in the ovaries, the corpus luteum, and the placenta; secondary sources: liver, adrenal glands, and the breasts; pregnant mare's urine	Estradiol, estrone
17	Gonane				Non-natural structure

fungi. The latter are a source of ergosterols and vitamin D. In plants, phytosterols are found, among them ergosterol (**7**), sitosterol (**8**) and diosgenin (**9**). As late as 1979, brassinosteroids were discovered in plants; one of the four rings, the B-ring, is constituted of a seven-membered ring.

Animal steroids are divided into insect and vertebrate steroids. As insect steroids, ecdysteroids are widespread, with ecdysterone (**10**) as an example. Steroids in vertebrates usually serve as hormones. These are sex steroids, including androgens, oestrogens and progestagens that play various roles in sexual differentiation and reproduction. Further, there are the corticosteroids that regulate metabolism and immune functions, blood volume and excretion. Last but not least, there are anabolic steroids influencing muscle and bone synthesis. Finally, the parent compound of all vertebrate steroids is cholesterol, which is in itself a modulator of cell membrane fluidity and whose plaques may cause artheriosclerosis.

A comparative table on the classification of steroids is given in Table 3.1.

Chemical classification using the number of carbon atoms as its basis is particularly helpful for the side chain R3 at position 17, cf Fig. 3.1. Yet, this category does not reflect the structure–activity relation where the position of double bond or aromatic rings, alcohol or carbonyl functional groups plays an important role. It does not account for the synthetic alterations such as methylation or demethylation under conservation of the parent compound's activity. Tibolone (**11**) serves as an example.

Throughout this chapter, none of the classifications has been given preference and common trivial names will be used.

The number of known steroidal compounds is huge. The synthetic steroids and those extracted from plants that reside in databases of the pharmaceutical companies and remain unpublished cannot really be estimated. The number of steroids, whose NMR spectra have been investigated, while large in itself, is likely only a tiny fraction of the whole ensemble of known steroidal compounds.

Within the biochemical pathways illustrated in the famous Boehringer scheme,[9] 93 steroidal compounds alone are identified with an additional five compounds of vitamin D-type and squalene (**12**), which have partially or totally open ring structures. Vitamin D_2 (**13**), for example, is referred to as a secosteroid. Glucuronides and sulphates as metabolism endpoints are not counted. A more concise scheme has recently been published on the Internet.[10] It comprises 18 steroid structures.

The importance of and interest in single steroidal compounds originates, in the course of 235 years of steroid research, from various sources:

accessibility of material, such as cholic acid from bile fluid; biological activity, such as testosterone; the need for therapeutic activity, such as cortisone; the researcher's curiosity to synthesize compounds that surpass nature's own, such as dexamethasone; the structure elucidation, ranging from chemical constitution to the 3D structure, and its proof, such as cholesterol. Figure 3.2 presents an illustrative collection of steroidal structures that should guide the reader through this text and at the same time exemplify the traditional classes of steroids.

2.2. A history of steroids

Among the many possible ways to tell the story of the steroids, we, the grandchildren of the golden age of steroids, can free ourselves from personal perspectives of the fierce competitors in the race for the first structure elucidation, synthetic or medical fame or economic wealth. We can choose any perspective we like and point out minor details instead of the big issues. Finally, we may take the chance to transform the historical coordinates into a coordinate system suitable for our purposes, that of structure analysis, where the time axis will be our techniques and the data points shall be the steroid structures elucidated. As a tribute to those who participated in the heydays of the steroid chemistry and the days of the fierce race to be the first, we direct the reader's attention to a collection of reports and essays. These narrative reviews appeared in two special issues of *Steroids* in August and December 1992[11–25] followed by two contributions in August 1996.[26,27] In those papers, the pioneers and protagonists tell their story and that of their companies or institutions in their own ways.

Following the path of structure analysis, the 1930s marked a turning point in the perception of steroids. Not only were the first steroid chemical constitutions fully and correctly elucidated and published in 1932, for examples, see below, but it was also demonstrated that spectroscopy would greatly contribute to the future identification of steroids. In 1936, a systematic investigation of stereocentres using molecular rotation spectroscopy was published by Callow et al.[28] In 1939, an extensive study was conducted on the UV spectra of hundreds of steroids for comparison purposes to facilitate the identification of steroids.[29] The empirical collection of UV spectra contained 208 natural and synthesized steroids and vitamins containing conjugated systems since only wavelengths above 220 nm were attainable. The solvent dependency was exemplarily studied for testosterone. With increasing data collections, systematic alterations of the absorption maxima

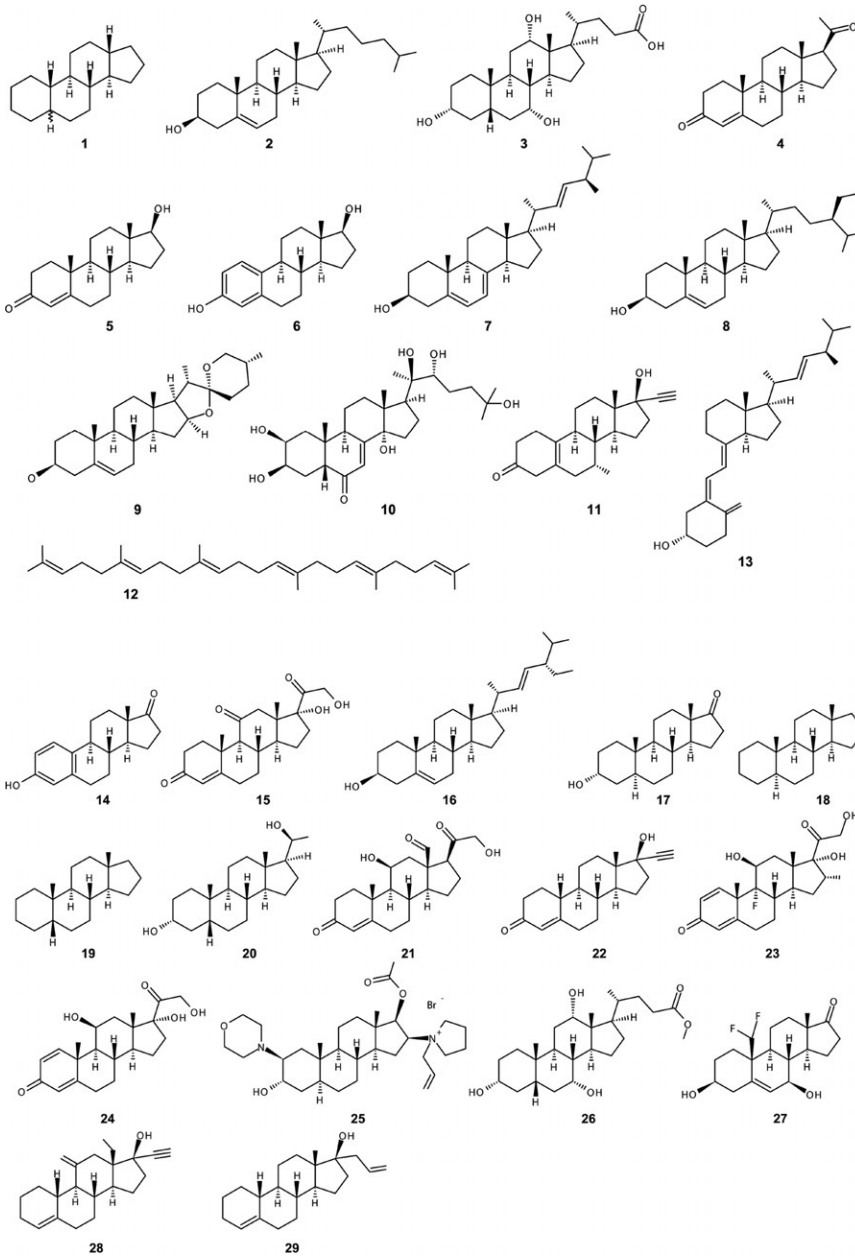

Figure 3.2 Selected steroidal structures from various classes of steroids, cf. Table 3.1: gonane (**1**), cholesterol (**2**), cholic acid (**3**), progesterone (**4**), testosterone (**5**), estradiol (**6**), ergosterol (**7**), sitosterol (**8**), diosgenin (**9**), ecdysterone (**10**), tibolone (**11**), squalene (**12**), vitamin D_2 (**13**), estrone (**14**), cortisone (**15**), stigmasterol (**16**), androsterone (**17**), 5α-androstane (**18**), 5β-androstane (**19**), pregnanediol (**20**), aldosterone (**21**), norethisterone (**22**), dexamethasone (**23**), prednisolone (**24**), rocuronium bromide (**25**), 3α,7α,12α-trihydroxymethylcholate (**26**), 19,19-difluoro-3β,7β-dihydroxy-androst-5-*en*-17-one (**27**), 13-ethyl-11-methylene-18,19-dinorandrost-4-ene-17-one, desogestrel (**28**), allylestrenol (**29**).

due to structural changes were readily identified. The influence of structure on the absorption of α,β-unsaturated ketones was described by Woodward et al. in 1941[30] and extended in 1942.[31] Spectral data were collected.[32] Mechanistic studies followed for more steroid classes.[33,34] In 1953, Dorfman reviewed the available spectra and the mechanistic interpretation approaches of varichromic effects.[35] The mathematical relations, where numerical values were attributed to substituents and added to the basis wavelength of a reference compound, were used to calculate absorption maxima of unsaturated steroids. At the end of the 1950s, when suitable instruments became available, saturated hydrocarbons were investigated in the far UV region.[36,37] Much later, when chromatography coupled to UV detectors paved its way towards a standard analytical technique, the spectrophotometric investigation of steroids continued,[38] the quantitative aspect being considered.[39]

For the characterization of stereocentres optical, rotatory power seemed to be a promising technique and became somewhat popular after its theoretical and practical description in 1935.[40] Research groups investigated the application of the technique during the mid 1930s until the late 1940s.[41–45] They tried to find relationships such as constant partial rotations[43,46] or investigated the concept of vicinal action.[47] In short, they searched for additivity or linearity, which means an increment system to relate structure and observables.[41] Yet, no relationship between structure and absolute values could be established,[48] but molecular rotation differences did provide a hint regarding the configuration analysis of a stereocentre.

The application of optical methods announced the dawn of a new era. Chemical reactions or degradations were still the primary means for structure identification, where the elucidation of cholanic acid (**3**),[49,50] testosterone (**5**),[51] estrone (**14**),[52,53] progesterone (**4**)[54,55] and cortisone (**15**)[56] were early milestones of the prespectroscopic area. Nevertheless, chemistry and the detailed knowledge of chemical reactions dominated the structural investigations.

The major sources of steroids were isolates from natural sources, such as bile fluids or their abnormal alteration, gallstones, or from urine extraction such as oestrogens. Yet, at all times, partial syntheses were carried out to obtain steroids from other steroids such as Ruzicka's synthesis of androsterone in 1934.[57] The first quest for large quantities of synthesis starting materials was investigated outside the vertebrate world, and thus natural product isolation was conducted at the end of the 1930s and the beginning of the 1940s. The search ended in the discovery of sapogenins and their transformation to sex hormones,[58–61] as a rich reservoir of starting material was opened from

Mexican plants, a species of which contained diosgenin (**9**). When the use of these natural resources became restricted later on, soy oil provided stigmasterol (**16**) as an alternate steroid starting material. For corticosteroid synthesis, bovine cholic acids were also used. With the new sapogenin resources and the knowledge in the pharmaceutical activity of cortisone, the race within the pharmaceutical industry regarding steroids entered a new dimension in the 1940s and culminated in the 1950s and 1960s with the development of the anticonception pill and lasted until the 1970s when clouds of side effects and misuse, such as thrombosis caused by the pill and anabolic steroid doping, began to overshadow the therapeutic effects of steroids.

For structure analytical purposes, X-ray crystallography had been available and was applied to steroid structure elucidation in 1944[62] when cholesteryl iodide was subjected to X-ray diffraction. Sources of X-rays at that time did not allow for the high resolution of modern diffractometers; the presence of the heavy atom iodine in the crystal simplified calculations and calculation methods for three-dimensional electron density had only recently become available. A sterol crystal survey showed that cholesteryl iodide had the most favourable properties. However, X-ray diffraction remained a non-standard technique in the field of steroid structure elucidation most likely due to the limited availability of X-ray crystallographic equipment and the complexity of the structure calculations that has only become routine very recently.[63] Among the milestones were the solution of the structure of epitestosterone in 1972[64] and cholesterol without heavy atom substituents in 1977.[65] The structure of testosterone was obtained including two conformations and all hydrogen atoms in 1973.[66] A collection of the published structures obtained by X-ray was given in the 1980s.[1,2] For steroids, the full structure elucidation of newly isolated or synthesized compounds and the progress in steroid analysis rested frequently upon other technologies.

While optical absorption spectroscopy had become a routine tool for the investigation of conjugated unsaturated carbon–carbon bonds, the 1950s saw the entry and application of infrared (IR) spectroscopy. Introduced into the steroid field in 1948, Jones et al. applied it to the analysis of functional groups.[67] The crystalline film technique, where the sample is obtained after solvent evaporation, was judged superior to the use of solvents for steroids. The spectra and the interpretation of vibrational assignments were collected as was or would become common for other spectroscopic techniques as well.[32] With the help of spectral tables, functional groups and their positions within the steroids could be identified without purely relying on the differential reactivity of certain positions as compared to others. The fingerprint

region of the IR spectrum was of great importance for steroids and especially the spectral comparison to authentic reference samples. Yet, the frequency correlation with molecular structure quickly progressed, and in 1952, methyl and methylene groups were described.[68,69] Furthermore, the intensities of the carbonyl bands were found useful to identify carbonyls within the steroid scaffold versus those located in the side chain.[70] All bands in an IR spectrum of a steroid could now be attributed to the structural moieties. A review by Jones and Herling attributes 460 absorption bands to the corresponding steroids.[71]

It should be noted that despite of the power of the physical methods, a relatively simple analytical technique, paper partition chromatography, introduced in 1948[72,73] and improved as reversed phase in 1950,[74,75] became very important for the separation and identification of steroids especially in the pharmaceutical field. The original publication by Burton, Zaffaroni and Keutman[72] contains retention factors, R_f, for the distinction of estrone (**14**), 0.53; progesterone (**4**), 0.16; and desoxycorticosterone, 0.92, whereas testosterone (**5**), androsterone (**17**) and dehydroisoandrosterone could not be separated, all of them having R_f values of 0.57 under the conditions chosen.

Since steroidal synthesis had grown to a highly busy terrain, stereochemistry had to be addressed not only in terms of chemical constitution but also in terms of chemical configuration, cf. 19-norsteroids or 5α-, versus 5β-androstane (**18** and **19**). In 1954 and 1955, the first contemporary optical rotatory dispersion (ORD) spectra of steroids were reported.[76,77] The development of the technique owes, in particular, to the group of Djerassi. The collection of spectra[78–80] and their comparison in search of systematic alterations upon the modification of stereocentres eventually allowed the determination of the absolute configuration of sesquiterpenes in 1957,[81] succeeded by α-halocyclohexanones.[82] A theoretical description sets the configuration determination by ORD on solid foundations.[83–85] The theory became known as the sector rules, the most famous of those being the octant rule.[86]

In 1956, the application of mass spectrometry was introduced by Mayo et al.[87] Due to the relatively strong ionization technique used, not only the molecular mass could be obtained from the mass-to-charge ratio, m/z, but also fragments that could quickly be related to the parent structure. This investigation was extended to bile acids and other steroids in 1958.[88] In the same year, Reed et al. published a systematic investigation,[89] analyzing the m/z fragments and comparing the effects of low and high ionization

energy spectra. Further studies on the fragmentation were soon undertaken.[90] First trials to address stereochemistry with mass spectrometry were reported.[91] Since electron ionization[92] was the standard technique of that time, spectra could be described by listing the major fragments in terms of m/z and their intensities, such that spectral comparison and mass libraries could be routinely used for steroid characterization. Molecular fragmentation patterns could be applied to elucidate the molecular constitution of steroids. The Djerassi group pioneered in this field.[93,94] Budzikiewicz et al. elucidated the respective fragmentation mechanisms in 1962.[95] More recently, the electrospray collision-induced dissociation of testosterone and testosterone analogues was investigated. The observed fragmentation mechanisms were compared to those discovered in electron-ionization studies reported earlier.[96] The topic of higher order electrospray ionization of pharmaceutical compounds has very recently been reviewed in detail including tandem mass spectra and the interpretation of the fragmentation pattern of 470 compounds.[97] As MS and steroids used to be a very active field of research and is still of interest today, the interested reader is referred to the specific literature in that field. Introductory reading may start from the recent reviews[98–100] or from the historical ones.[101,102] As a conclusion, from the early 1960s on, steroid analysis had another powerful structural technique at its disposition in the form of mass spectrometry, which provided the molecular mass, the access to the molecular formula thereby, the presence and kind of heteroatoms and connectivity information via the fragmentation.

This was the field and the stage when NMR started to slowly grow into the primary analytical tool for chemical constitution and stereochemistry elucidation that it is today.

2.3. NMR in steroid history

In 1958, Shoolery and Rogers published a remarkable collection of NMR spectra of approximately 50 steroids, recorded at 40 MHz.[103] The interested readers are referred to this chapter for an impression of what crowded NMR spectra look like at 40 MHz. To the same illustrative purpose, a 40-MHz 1D ^{1}H spectrum of 4,4-dimethyl-$\Delta^{5,10}$-3-ceto-estrenol is presented in Fig. 3.3.

The description of steroid NMR in the late 1950s and early 1960s was limited to a habitus or pattern description supported by a copy of the spectrum; due to the "hump" or "envelope" of the methylene and methine resonances, individual chemical shifts could only be determined for special

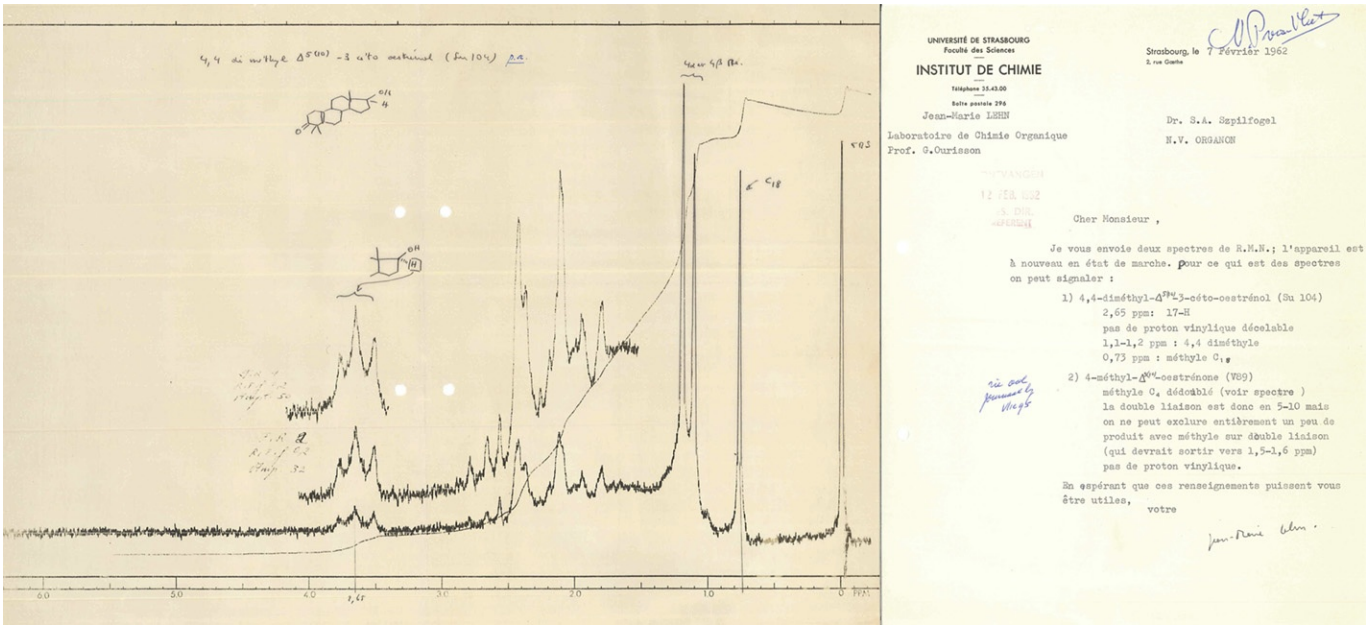

UNIVERSITÉ DE STRASBOURG
Faculté des Sciences

INSTITUT DE CHIMIE

Téléphone 35.43.00
Boîte postale 296

Jean-Marie LEHN

Laboratoire de Chimie Organique
Prof. G.Ourisson

Strasbourg, le 7 Février 1962
1, rue Goethe

Dr. S.A. Szpilfogel
N.V. ORGANON

Cher Monsieur ,

Je vous envoie deux spectres de R.M.N.; l'appareil est à nouveau en état de marche. Pour ce qui est des spectres on peut signaler :

1) 4,4-diméthyl-$\Delta^{5,10}$-3-céto-oestrénol (Su 104)
2,65 ppm: 17-H
pas de proton vinylique décelable
1,1-1,2 ppm : 4,4 diméthyle
0,73 ppm : méthyle C_{18}

2) 4-méthyl-$\Delta^{4,9}$-oestrénone (V89)
méthyle C_4 dédoublé (voir spectre)
la double liaison est donc en 5-10 mais on ne peut exclure entièrement un peu de produit avec méthyle sur double liaison (qui devrait sortir vers 1,5-1,6 ppm)
pas de proton vinylique.

En espérant que ces renseignements puissent vous être utiles,

votre

Jean-Marie Lehn

Figure 3.3 1D ^{1}H spectrum of 4,4-dimethyl-$\Delta^{5,10}$-3-ceto-estrenol, acquired at 40 MHz and the corresponding interpretation sheet. The spectrum was recorded for N.V. Organon at the University of Strassbourg and interpreted by the later Nobel laureate J.-M. Lehn. The original spectrum was kindly provided by M.B. Groen.

absorptions. In that respect, NMR at that time was comparable to IR spectroscopy. Shoolery and Rogers thus suggested to use the hump similar to the IR fingerprint region but stated that the chemical substitution of a single proton produced a marked and characteristic effect on the spectrum. In their discussion of the applicability of the NMR method to the elucidation of unknown steroids, they assured that "as a means of determining the number of methylgroups and to some extent their position, the NMR method may very well be unrivalled. Although based on empirical correlation with established known structures..." Nevertheless, the distinction of axial and equatorial protons was already mentioned. Using 60 MHz spectrometers in 1959, stereochemical aspects of sapogenins were investigated.[104] The investigations on steroids using NMR continued relying mainly on the methyl resonances and certain prominent signals. In 1961 and 1963, extensive reviews on steroid shift data were published by Zuercher[105,106] comprising 160 known and 100 new steroids. Derived from the analysis of the chemical shifts of the 18- and 19-methyl resonances, a system to calculate their chemical shifts depending on the substitution of the steroid skeleton was devised. A value was attributed to a substituent taking into account its chemical constitution and its relative position to the group whose chemical shift was to be calculated. For multiple substitutions, these increments could be added. The effect of symmetry of certain positions on the calculation of chemical shifts was considered as well.

It was not until the advent of FT-NMR around 1970 that NMR could be amended to the next level of important contributions to the steroid field. This achievement was not so much attained by the ^{1}H resolution increasing along with the magnetic field from 100 to 200 MHz too, but by the utilization of ^{13}C spectroscopy, where the apparently higher resolution is due to the larger spectral dispersion. The increase in resolution depending on the field strength is illustrated for tibolone (**11**) in Figs. 3.4 and 3.5.

Obviously, the 50-MHz $^{13}C\{^{1}H\}$ spectrum, corresponding to the one at 200 MHz proton Lamor frequency, provides superior and easier-to-collect information, cf. Figs. 3.4 and 3.5.

The molecular constitutional investigations could be carried out straight forward by means of ^{13}C NMR, first creating and then relying on the wealth of compiled reference data, cf. the compilation of 30 ^{13}C spectra,[107] the assignment of ketosteroids,[108] the distinction of 42 phytosterols[109] and the differentiation of C-24 isomeric sterols.[110] The assignment of the carbon chemical shifts was supported by selective decoupling techniques, chemical reactions, lanthanide shift reagents and selective and partial deuteration.[111]

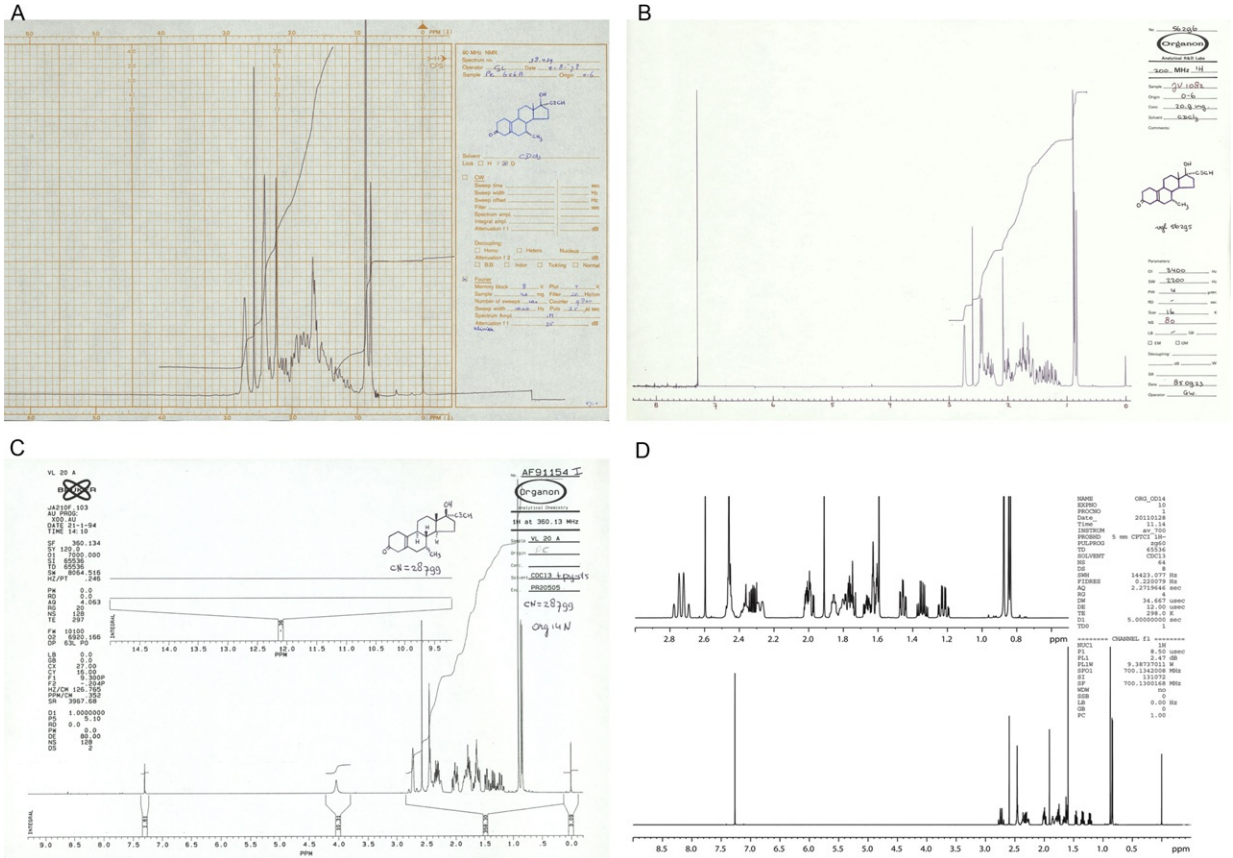

Figure 3.4 1D ^{1}H NMR spectra of tibolone (**11**) in $CDCl_3$ at different field strengths: (A) 90 MHz, (B) 200 MHz, (C) 360 MHz, (D) 700 MHz. Historically, all spectra are recorded with different spectral resolution and processed with different window functions. At 400 MHz, mathematical resolution enhancement by using a Gaussian window function was used, whereas no window function at all was applied at 700 MHz.

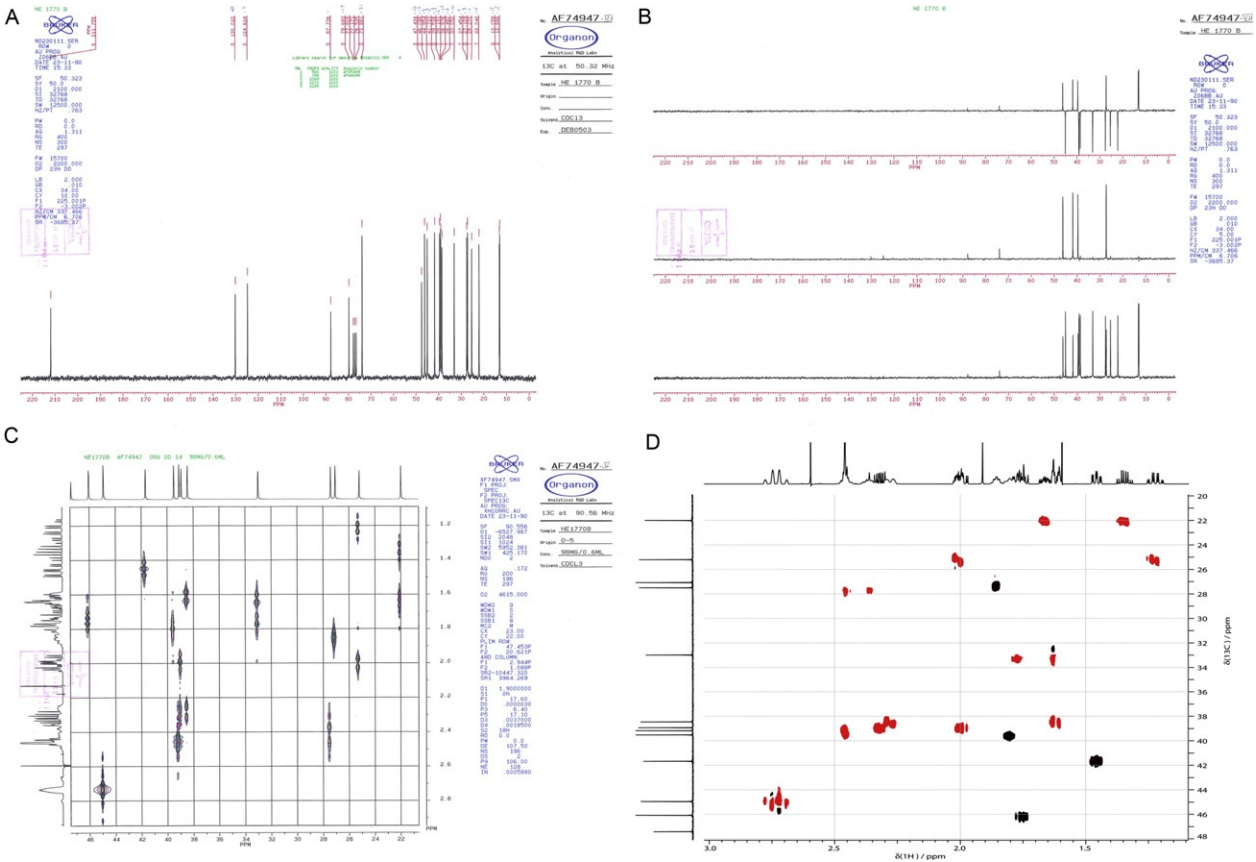

Figure 3.5 Direct and indirect ^{13}C detected spectra of tibolone (**11**) in $CDCl_3$ at different field strength: (A) 1D $^{13}C\{^1H\}$ at 50 MHz $\omega_L(^{13}C)$, (B) ^{13}C DEPT at 50 MHz $\omega_L(^{13}C)$, (C) C—H HETCOR at 90 MHz $\omega_L(^{13}C)$, (D) H—C HSQC at 700 MHz $\omega_L(^1H)$. Together with increasing field strength and instrument capabilities, the change in the standard experiment to extract ^{13}C related parameters is illustrated by the type of spectrum shown.

In 1977, Blunt and Stothers published a huge compilation with more than 400 steroids, also revising the assignments of earlier works.[112] As part of all reference compilations, there had been the establishment of a chemical shift increment system for the analysis and prediction of ^{13}C chemical shifts. The system was continuously extended, since the interpretation of chemical shifts remained a prime means for structure confirmation. The work by Blunt and Stothers also summarized the methods available at that time: shielding data interpretation, off-resonance decoupling, selective proton decoupling, spectral comparison, isotopic labelling, the use of lanthanide shift reagents and spin–lattice relaxation time measurements.

Yet, the issue of the complete elucidation of stereochemistry had remained unsolved. With field strength and thus resolution further increasing and the exploitation of nuclear Overhauser spectroscopy,[113] the assessment of the full 3D structure became possible from 1980 on. The conformation of 17α-acetoxy-6α-methylpregn-4-ene-3,20-dione was fully analyzed by Farrant et al.[114] using 2D NMR and NOE spectroscopy. While the one-dimensional techniques continued to be used, two-dimensional techniques became more and more common since the advent of 400 MHz spectrometers around 1980. The first full proton assignment was described by Hall and Sanders for 1-dehydrotestosterone indeed in 1980 and for 11β-hydroxyprogesterone a year later.[113,115] A first culmination of the description of 2D NMR applied to steroids occurred in 1985 when several research groups used homo- and heteronuclear correlation techniques such as COSY-90, COSY-45, heteronuclear-detected C—H correlation experiments, 2D *J*-resolved and C—C INADEQUATE experiments.[116–118] For the first time, the very importance of NMR with respect to the distinction of norethisterone was stated: "Two-dimensional NMR appeared to be superior to mass and IR spectroscopy in identifying the isomers".[119] By then, the principal experiments as considered essential for a full structure analysis according to today's standards were developed.

In the following years, instrumentation was further ameliorated, providing ever increasing field strength, gradient technology[120] and cryogenically cooled probes.[121] Experiments were adapted to the new technologies, taking advantage of inverse detection[122] and gradient-enhanced experiment versions.[123] Several strategies were available to approach stereochemistry. The original Karplus equation relating ^{3}J couplings to the dihedral angles of the coupling nuclei already dated from 1959.[124] It was refined in 1980 by Haasnoot et al.[125] On the other hand, nuclear Overhauser spectroscopy provided a complementary tool based on dipolar and thus through-space

mechanism. Its use for steroid stereochemistry elucidation has been pointed out above. In 1987, an investigation was dedicated to the A-ring conformation and the results as solution structure compared to X-ray crystallography representing the solid-state structure.[126,127] The dialectic of solution versus solid-state structure in conformational space remains—especially when structure–activity relations are discussed—a point of attention until today. For a thorough description of the methodology at that period, the reader is referred to a book chapter by Croasmun and Carlson.[128,5] As structure elucidation was not a routine task until the mid 1990s, strategies for steroid structure elucidation were discussed, based on the experiments available.[2,128–130]

Despite the availability of the principle techniques for a full chemical shift assignment in the mid 1980s, it was as late as 1990 that the full assignment of one of the best known steroids, testosterone, and 17α-methyltestosterone was published.[131,132] Remarkably, the publications contain interchanged proton assignments for H16α and H16β. The assignment of Kirk et al. turned out to be the correct one,[132] yet the supporting experiments were only published in 2011.[133]

Before concluding this historical overview on analytics and NMR, a brief look shall be taken in the view of chemical shift assignments as reflected by the journal Magnetic Resonance in Chemistry including former Organic Magnetic Resonance.

While in the starting years of the journal, assignments were as complex as to be elaborated on in full papers, two articles appeared in April and July 1981,[134,135] which were comparable to the later reference data format in so far that the strategy of signal assignment was no longer described in detail. In August 1982,[136] the first reference data article was published; in 1983, a section reference data and assignments were introduced, indicating that chemical shift assignment was considered important for publication but that the methodology had become standard and that no full description was necessary, cf. further steroid reference data.[137]

In the course of 2010, the reference data and spectral assignments section were destined to disappear from the journal, since chemical shift assignment has become a sufficiently simple task that the need for publishing reference data of new compounds has been considerably decreased.

It was by the 1980s that the interest in steroids of the pharmaceutical industry had dropped. The golden age of steroids had faded, although steroidal compounds still occupy their positions in the medical applications such as contraception and inflammation, cf. Table 3.2.

Table 3.2 Marketed drugs that contain steroidal compounds as sold on the US market in 2010 and according to worldwide sales as of 2009

Active ingredient	Drug name	Ranking w.r.t. prescription in the US (prescriptions in million units)	Ranking w.r.t. world wide sales 2009 in million USD	Company	Indication
Fluticasone and salmeterol	Advair, Seretide	9 16.6	4 8094	GSK	Asthma
Mometasone	Nasonex	18 8.8	68 1517	Merck & Co.	Nasal
Conjugated oestrogens	Premarin	24 7.7	138 833	Pfizer	Hypogonadism, absence or deficiency of endogenous testosterone in adult males
Norethindrone acetate and ethynyl estradiol	Loestrin 24 Fe	31 6.7		Warner Chilcott	Anticonception
Fluticasone propionate	Flurent HFA, Flixotide	44 5.1	83 1330	GSK	Asthma
Etonogestrel and ethynyl estradiol	Nuvaring	45 4.8		Merck & Co.	Anticonception
Drospirenone and ethynyl estradiol	Yaz	52 4.6	128 885	Bayer	Anticonception
Norgestimate and ethynyl estradiol	Ortho Tri Cyclen Lo	52 4.2		Ortho-McNeil	Anticonception

Budesonide and Formoterol	Symbicort	59 3.6	41 2353	AstraZeneca	Asthma
Dutasteride	Avodart	63 3.5	133 865	GSK	BPH products
Estradiol	Vivelle-Dot	75 2.8		Novartis	Oestrogen replacement
Conjugated oestrogens and medroxyprogesterone	Prempro	77 2.7		Pfizer	Menopausal symptoms
Desogestrel and ethynyl estradiol	Apri	87 2.4		Teva	Anticonception
Ciprofloxacin and dexamethasone	Ciprodex Otic	94 2.2		Alcon	Anti-infection and anti-inflammation
Testosterone	Androgel	103 2.0	166 708	Solvay	Hypogonadism, absence or deficiency in endogenous testosterone in adult males
Finasteride	Propecia, Proscar	138 1.3	177 663	Merck & Co.	Benign prostatic hypertrophy
Drospirenone and ethynyl estradiol	Yasmin	177 0.8	151 766	Bayer	Anticonception
Butenolide	Pulmicort	196 0.7	70 1505	AstraZeneca	Asthma

Source: http://cbc.arizona.edu/njardarson/group/top-pharmaceuticals-poster.

In addition, there are 15 more steroidal compounds among the drugs ranked 100–200 according to prescriptions in the United States in 2010.

Yet, due to the molecular properties, their availability, the wealth of data and their favourable NMR features, steroids continue to defend their place in NMR methodology development, such as NOE, inverse experiments, chirp pulses, 3D experiments, residual dipolar couplings (RDCs) or covariance methods.

As can easily be realized, the rather narrow selection of steroid analysis topics already yields a richness of information and historically interesting aspects. The references cited herein are only a fraction of the literature on the separation, synthesis, therapeutic and pharmacological aspects of steroids. It is far beyond the scope of this essay to review the literature regarding these topics. For the sake of a concise overview, a tabular representation of selected classical milestones in the filed of steroid synthesis shall be given in Table 3.3, such that the development of structural characterization and elucidation as described in this section can be set in perspective to the preparative and synthetic efforts and successes.

As a concluding remark of this section, it shall be mentioned that six Nobel prizes were received for work related to or based on steroids. The chemistry Nobel laureates were Heinrich Wieland in 1927, Adolf Windaus in 1928, Adolf Butenandt and Leopold Ruzicka in 1939, Derek Barton and Odd Hassel in 1969. For medicine and physiology, the Nobel Prize was awarded to Philip S. Hench, Edward C. Kendall, Tadeus Reichstein in 1950 and to Feodor Lynen and Konrad E. Bloch in 1964.

3. STRUCTURE ELUCIDATION OF STEROIDS

Through the eyes of a modern day NMR spectroscopist, the small technological steps paired with theoretical and empirical concepts may just seem history. Relying on 2D homo- and heteronuclear through-bond and through-space correlation experiments, even a moderately trained and experienced analytical or synthetic chemist of today is able to fully elucidate a steroid structure be it from a structure hypothesis or from a novel compound. Milestones of this methodological development were the advent of 400 MHz spectrometers, the 2D correlation experiments also in its inverse variants, and the exploitation of NOE spectroscopy during the 1980s. From this perspective, the scientific findings and the articles cited in the following section are divided—according to the authors' perception—into structure investigative studies, data collections of NMR spectroscopic parameters such as shifts and coupling constants and NMR method development with

Table 3.3 Anthology of discoveries in the steroid field

Year	Discovery	Reference	Available structure analytical technique
1769	Isolation of gall stone constituents	138	
1815	Isolation of cholesterol (**2**)	138	
1848	Elemental composition of cholic acid $C_{24}H_{40}O_5$ (**3**)	139	Chemical degradation, elemental analysis
1888	Elemental composition of cholesterol $C_{27}H_{46}O$ (**2**)	140	
<1900	Isolation of ergosterol		
1919	Structural work on cholic acid (**3**)	141–143	
1929	Isolation of estrone (**14**) (first sex hormone)	144, 145	
1930/1931	Preparation of pregnanediol (**20**), first steps towards constitution	146	
1932	Constitution proposal of testosterone and the steroidal compounds	51	
	Structure proposal for cholanic acid (**3**)	147	
	Constitution of estrone (**14**)	52,53	
	Constitution of cholanic acid (**3**)	49,50	
1934	Isolation and constitution of androsterone (**17**) from urine	148,149	
	Partial synthesis of androsterone (**17**)	150	
	Constitution of progesterone (**4**)	54, 55	
1934	Discovery of squalene (**12**) as precursor for steroids, proven in 1954	151–154	
1935	Isolation of testosterone (**5**) from steer testis	155	
	Partial synthesis and structure verification of testosterone	156, 57	

Continued

Table 3.3 Anthology of discoveries in the steroid field—Cont'd

Year	Discovery	Reference	Available structure analytical technique
1936	Description of cortisone (**15**) Constitution of cortisone (**15**) Discovery of oral activity of ethinyltestosterone	157–159 56 160	Molecular rotation
1939	Isolated, characterized, partially synthesized: estrone, androsterone, testosterone, progesterone		UV/Vis spectroscopy
1936–1942	Nore than 30 steroids are isolated		
1939/1940	Structure of sapogenins and synthetic route to sex hormones	58,59,161	
1940	Partial synthesis of estradiol (**6**)	162,163	UV as routine tool for conjugated unsaturated compounds
1944	Partial synthesis of cortisone (**15**)	164,165	
1948	Total synthesis of estrone (**14**) Total synthesis of the estrone series compounds	166 167	
1949	Application of cortisone (**15**) against rheumatoid arthritis	168	
1950	Total synthesis of estrone (**14**) and remaining stereoisomers	169	Paper partition chromatography IR spectroscopy, functional groups and fingerprint
1951	Total synthesis of cholesterol (**2**)	170	
1951	Total synthesis of androgenic hormones Total synthesis of cortisone (**15**)	171 172	

1952	Total synthesis of sterols	173	
	Discovery of microbiological oxidation at C-11	174,175	
1953	Total synthesis of epiandrosterone	176	ORD for molecular configuration
	Elucidation of the β-configuration of norprogesterone	177	
1954	Structure elucidation of aldosterone (**21**)	178	
	Norethisterone (**22**) synthesis	179	
1954–1958	Synthesis of 9α-fluoropregnanes (**23**) with superior activity		
1955	Synthesis of prednisolone (**24**) with superior activity	180	
	Postulation of the concept of contraception	181	
1956			Mass spectrometry (EI)
1956	Effects of certain 19-norsteroids on reproductive processes in animals	181	
	Effects of certain 19-norsteroids on the normal human menstrual cycle	190	
1957	Enovid combination against menstrual cycle disorders		
1957	Partial synthesis of vitamin D_2 (**13**)	182,183	
1958	Partial synthesis of calciferol and epicalciferol	184,185	
			Mass spectrometry fragmentation pattern analysis, applications to steroids
1958	Hormonal control of ovulation and early development through norsteroids (Enovid, Norlutin, Nivelar)	191	

Continued

Table 3.3 Anthology of discoveries in the steroid field—Cont'd

Year	Discovery	Reference	Available structure analytical technique
1959			^{1}H NMR for methyl resonances and certain prominent signals
1959	Effectiveness of an oral contraceptive	192	
1960	Approval of Enovid as contraception pill Microbiological 16β-hydroxylation of steroids	186	
1961	Synthesis of aldosterone from cortisone Constitution of clerodin	187 188	NMR, IR
1962	First anticonception pill by Organon (Lynestrol)		
1967	Discovery of the connection between anticonception pill and thrombosis		
1969			FT-NMR, ^{13}C, constitution and configuration
1974	Proof for thrombosis hypothesis		
1978	Total synthesis and characterization of calciferol	189	NMR
1980			Homonuclear 2D NMR, NOE spectroscopy
1982			Heteronuclear 2D spectroscopy
1985			Complete NMR assignments

steroid as examples. Since the data collections were often motivated by structure characterization or development of predictive systems such as increments, they are attributed to the section dealing with computer-assisted structure elucidation (CASE). In contrast, studies concerning the elucidation of the steroid structure or aspects thereof are reviewed in this section. Important NMR methodology progresses with minor emphasis on steroids themselves are placed where seeming appropriate.

3.1. NMR methods and structure elucidation of steroids

3.1.1 The early days of steroid NMR—1D ^{1}H NMR

For structure determination and signal assignment, the steroid skeleton may be assumed a rigid body in a first approximation. This is particularly true for ring B and C. It may further be taken for granted that in steroids from natural sources the configuration at the stereocentres C13, C8, C9 and C14 remains unchanged from chemical synthesis or metabolism, although the configuration inversion by synthetic chemistry on C13 and C14 has been investigated.[193,194] Rarely, an "unnatural" configuration is observed in natural steroidal compounds such as H14β in contignasterol.[195] Depending on the type of steroid, the configuration on C5 and C10, for example, androgens, may be considered invariant, so may C11 in cortisols and C17 in testosterone derivatives, if no chemical modifications such as oxidation or reduction as intermediate steps occur during synthesis. The complete synthetical inversion of all stereocentres has been described for ent-19-nortestosterone[196] according to Scheme 3.1.

Of course, oestrogens possess no stereocentres at C10 and C5. The norsteroids, well investigated for contraceptive medical applications, provided a comparatively long-term riddle concerning the stereochemistry after elimination of the methylgroup from the parent compound. Analogously, the substitution of a methylene proton leads to a new stereocentre with

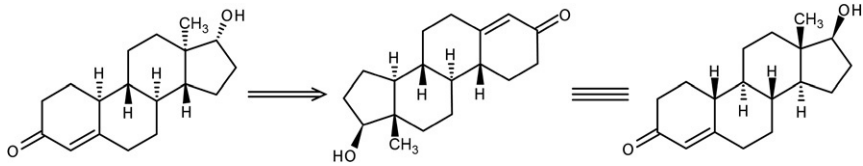

Scheme 3.1 Chemical synthesis strategy for the inversion of all stereocentres of 19-nortestosterone (right) to ent-19-nortestosterone (left). The synthesis consists of 19 steps and takes advantage of the pseudo-symmetry of the compound: removal/introduction of a methyl group and conversion of the A-ring into the D-ring and vice versa results in the total inversion of the stereochemistry.[196]

a demand for characterization. Along more systematic lines, the following paragraphs will summarize the picture of steroids from NMR spectroscopy.

Structure analysis of steroids as well as for all other compounds comprises the characterization of chemical constitution, configuration albeit relative and conformation. The latter includes potential flexibility, the presence of isomers with respect to a single bond at a given temperature or averaging on the time-scale of the analytical method.[197,198] It becomes quickly clear that, in general, the difficulty to spectroscopically master the unequivocal correlation between signal and structure to obtain a proof of structure increases along the sequence constitution, configuration, conformation for steroids, since the configuration can be derived from the configuration of known stereocentres within the scaffold. However, steroid studies strove—from early on—for the full exploitation of signals not only in terms of connectivity but also stereochemistry.[104,199–201] A fine example was given by Williamson et al.,[202] where the *cis* and *trans* forms of the isomers of androstane were deduced from the linewidth of the C19 methyl group signal. Until the utilization of ^{13}C NMR in the late 1960s, the strategy of structure elucidation by ^{1}H NMR went for hydroxysteroids from the analysis of resonance frequencies of methylgroup signals, via the interpretation of signals from CH-OR groups with respect to multiplicity and chemical shift, their presence or absence, the multiplicity analysis of hydroxyl protons to the interpretation of the chemical shift difference for equatorial and axial protons.[129]

As an early example, the configurations of six sapogenin isomers were deduced from the chemical shifts of the methyl resonances.[104] The chemical shift of the 27-methylgroup at C25 was interpreted in terms of the equatorial orientation, called iso form, and axial orientation, called normal form, if ring F assumes chair conformation, cf. Fig. 3.6. Thus, the stereochemistry of diosgenin (**I**), sarsasapogenin (**II**), smilagenin (**III**) and their neoforms (**IV**) could be deduced.

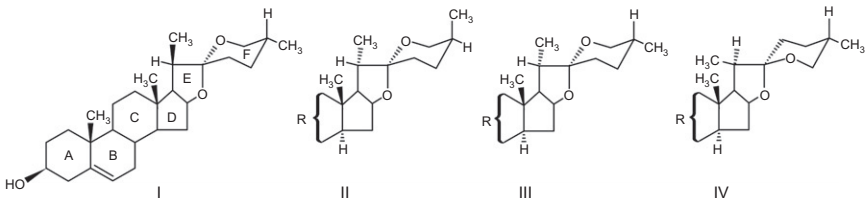

Figure 3.6 Structure and configuration of diosgenin (**I**) with R = $C_{13}H_{20}O$, sarsasapogenin (**II**), which belongs to the "normal" series sapogenins, smilagenin (**III**), which is part of the iso series sapogenin, both with R = $C_{13}H_{22}O$, and neosarsasapogenin (**IV**).[104] The full ^{1}H assignment was achieved in 1993[203] and the earlier findings thus confirmed.

Among the structural characterization challenges that could be addressed by NMR in the early 1960s, the stereochemistry of ring fusion, referred to as *cis* and *trans* isomerism, made part. From decaline systems, it was known that signals from axial protons were shielded as compared to signals from equatorial protons. Thereby, 5β,14α-androstane, *cis*-A/B, could be distinguished from 5α,14α-androstane, trans-A/B, as the 19-methyl chemical shift differed by 0.133 ppm.[200] In analogy, the 18-methyl resonance was found to shift by 0.300 ppm going from the *cis*-C/D androstane, 14β, to the trans-C/D androstane, 14α, with $\delta(H14\beta) > \delta(H14\alpha)$. The same analysis could be performed via linewidth measurements, cf. above. For the A/B-ring fusion, the linewidth at half-height was found larger within the 19-methyl signal for the *trans*-fusion than for the *cis*-fusion, with 0.084 ± 0.03 and 0.036 ± 0.07 Hz, respectively, as observed for androstane-3-one and cholestane-3-one type steroids.[202] This observation was interpreted in terms of unresolved long-range couplings, that is, *zig-zag* of W and M type, that had been observed for 11-keto steroids between the 12α proton and the 18-methyl signal.[204,205]

For decalins and steroids, the *trans* arrangement of the rings permits the occurrence of large W-couplings of 0.8 Hz with three protons, whereas only one large and four smaller M-couplings, 0.2 Hz, contribute to the splitting of the methyl signal in the *cis*-orientation. At field strengths where these signals were not resolved, the linewidth of the *trans* compound's signal appears therefore larger. With the values given above, the absolute linewidth determination or, at sufficient resolution, the multiplicity allows the identification of the configuration. Owing to the steroid skeleton, other long-range coupling pathways led to the observations of the respective splittings. Long-range proton–proton splittings were discovered arising, for example, from allylic, $^4J_{HH}$, and homoallylic, $^5J_{HH}$, arrangements.[206] Although the dihedral dependence of the magnitude of the coupling constants, which allows the distinction between cisoid and transoid arrangements, was said to be small to be useful,[200] the increase in spectral resolution in the following years made it a valuable tool in structure elucidation. Two decades later, the application of COSY and long-range COSY, that is, a COSY-45 with additional fixed delays, shone anew light on the topic and all pathways were systematically and thoroughly reviewed and classified for steroids by Platzer et al.[207] Long-range couplings of $^4J_{HH}$ type would be transmitted through coplanar or gauche arrangements and $^5J_{HH}$ through a zig-zag arrangement or bond proximity. A ^4J is maximal if the dihedral angle is close to 180°. Typical ^4J long-range couplings with a W-pathway in androstane type steroids are Me18 to H17α and H12α, and Me19 to H1α and H9. For hydrocortisones,

^4J W-pathways exist from Me18 to H12β and H12α, and from Me19 to H1α. Analogous ^5J pathways are usually observed from Me19 to H2β. Cholestane derivatives are known to still show W-pathways, cf. Fig. 3.7.

A lack of the expected long-range coupling between Me18 and H14 confirmed earlier observations.[207] Examples for non-W-couplings of ^4J distance are Me18 to H12β and Me19 to H1β, both gauche. *Zig-zag* ^5J couplings are H1β to H6α and H12β to H15α, both intercycle couplings. Through-space ^5J couplings of methyl groups with *syn* γ-protons were observed for Me19 to H2β, H6β and H8; Me18 to H8 and H11; Me4β to H6β and Me4α to H6α for the cholestane derivative of Fig. 3.7.

Apart from the homonuclear long-range splittings, heteronuclear proton–fluorine couplings up to six bond distances were observed. Values of 1.9–4.8 Hz for $^5J_{FH}$ between a fluorine nucleus and methyl protons and 3.8 Hz for a $^6J_{HF}$ coupling through six σ-bonds were reported.[208] The exceptionally distant long-range couplings were interpreted in terms of through-space and through-bond mechanisms.[208–210] The converging vector rule allows the prediction of long-range F–H splittings,[201] cf. Fig. 3.8. The rule is, however, not applicable for a separation of the nuclei over four σ-bonds.

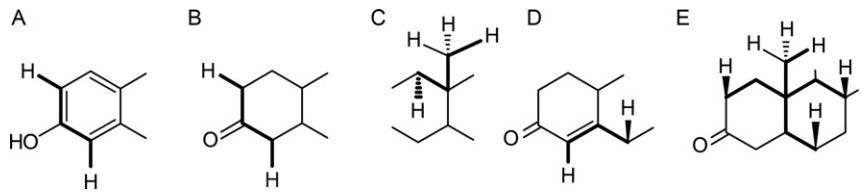

Figure 3.7 Typical W-pathways A–D leading to long-range correlations. The coupling ^4J (H4,H6β) amounts to approximately 0.5–2 Hz. Through-space ^5J couplings that can be observed in long-range COSY spectra are illustrated in structure E.[207]

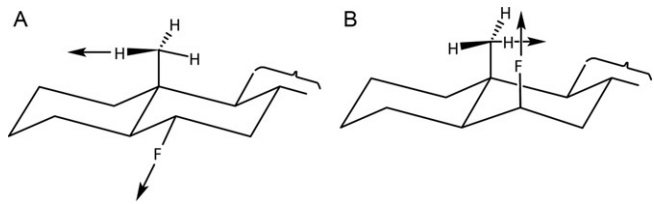

Figure 3.8 Illustration of the converging vector rule: orientation of the 19-methyl group with respect to the 6-fluoro substituent. Diverging vectors, A, do not lead to long-range couplings, converging vectors, B, do. Vectors point from carbon to hydrogen and from carbon to fluorine.

Not only long-range couplings but also geminal couplings were interpreted with respect to stereochemistry. Under the influence of a keto group or another π-bond, geminal splittings are smaller $^{2}J_{HH} \approx -12$ to -13 Hz if they are positioned on opposite sides of the p-orbital axis. The π-electron contribution between methylene group and p-orbital is low in this arrangement. Geminal couplings exhibit larger values, $^{2}J_{HH} \approx -16$ to -17 Hz if located on the same side of the p-orbital, cf. Fig. 3.9.

Examples of this effect are found for the 12-methylene group protons in 11-oxosteroids, with ^{2}J(H12α,H12β) ≈ −12–12.5 Hz, since the C-ring is slightly distorted form an ideal chair. In contrast, 12-methylene protons in 11-oxo-19-norsteroids exhibit a splitting of ^{2}J(H12α, H12β) = −16 Hz.[211]

Analysis of coupling constants followed from 1959 on the famous Karplus relation that relates the size of the coupling constant to the dihedral angle of the coupling nuclei.[124] The relation was soon described as "even if the dihedral angle dependence according to Karplus is only accurate within a few degrees, it belongs to the best quantitative methods of conformational analysis. . .".[200]

The application of the Karplus relation to steroids supported the assignment of α- and β-substituents, but gave further insight into the conformation of the steroid, as was described for 11α- and 11β-bromo-12-keto-cholanic acid.[200] The coupling values were determined as 4.4 Hz for ^{3}J(H9α, H11α) and 10.2 Hz for ^{3}J(H9α, H11β). Karplus analysis revealed that the dihedral angle between H9α and H11β is only 148° instead of 180°. This significant deformation was traced back to the strong interaction between the 11α-bromo and the 12-keto substituent as well as to the 1β-proton. The coupling analysis was also applied to structural problems that dated back 20 years before, such as the bromination of carbon 23 in monobromotigogenin.[199] Both synthetic C23 epimers were distinguished on the

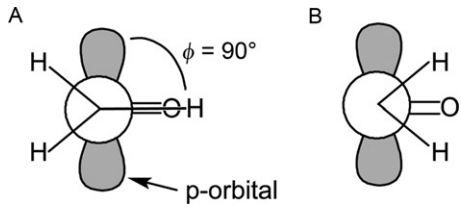

Figure 3.9 Geminal protons located on different sides of the p-orbital, A, and on the same side, B. Due to the lower π-electron contribution, the geminal couplings will be smaller for orientation A.[211]

basis of their $^{3}J_{HH}$ couplings. In the same study, the usefulness of increased field strength, 100 versus 60 MHz, was demonstrated. The D-ring conformations of 16 substituted pregnenes and 17α-pregnenes were analyzed with respect to the *J*(H16,H17) couplings, where the theoretical values of four possible stereoisomers calculated according to the Karplus relation were compared to the observed values. Additional support for the interpretation of the data was drawn from the 18-methyl shifts.[212]

Another example of the solution to an earlier question by NMR was the elucidation of (20*S*,22*R*)-and (20*S*,22*S*)-17α-20,22-trihydroxy cholesterol.[213] Based on the assumption of a pentacyclic ring via hydroxyl-hydrogen bonding, steric interactions were considered responsible for the chemical shift differences of the H22 proton of the two epimers. Multiplicity analysis yielded further support.

3.1.2 Lanthanide shift reagents

Due to resolution of the available spectrometers at that time, which was insufficient for the signals of the methane and methylene signals, sometimes called envelope or hump, methods were sought to alter the chemical shifts other than increasing the field strength.[109] As paramagnetic species cause changes in the chemical shift via contact or pseudo-contact interaction, the use of lanthanide complex reagents became a suitable means of broadening the spectral dispersion of steroids at the end of the 1960s into the 1970s. Although contact shifts are present within radicals, lead to hyperfine splitting of an ESR signal and cause line broadening in NMR spectra via longitudinal relaxation mechanisms, they induce shifts of a proton resonance to higher or lower fields as compared to the proton resonance of the diamagnetic species, when diamagnetically diluted.[198,214] Pseudo-contact shifts operate as through-space mechanism between a strongly anisotropic paramagnetic centre and the nucleus in question. The effect is distance dependent due to the dipolar nature of the interactions.[198,214]

Paramagnetic shifts in solutions of cholesterol upon addition of trisdipivalomethanatoeuropium(III), $Eu(DPM)_3$, in tetrachloromethane were investigated.[215] In agreement with the theoretical expectation, a lanthanide metal complex was formed with the cholesterol hydroxyl group, leading to paramagnetic shifts for protons. The change of the 1D ^{1}H spectrum of cholesterol upon addition of $Eu(DPM)_3$ is illustrated in Fig. 3.10. The lines did not show significant broadening.

Graphical analysis revealed the r^{-3} dependence, expected for pseudo-contact shifts, where *r* is the distance between the centre of complexation

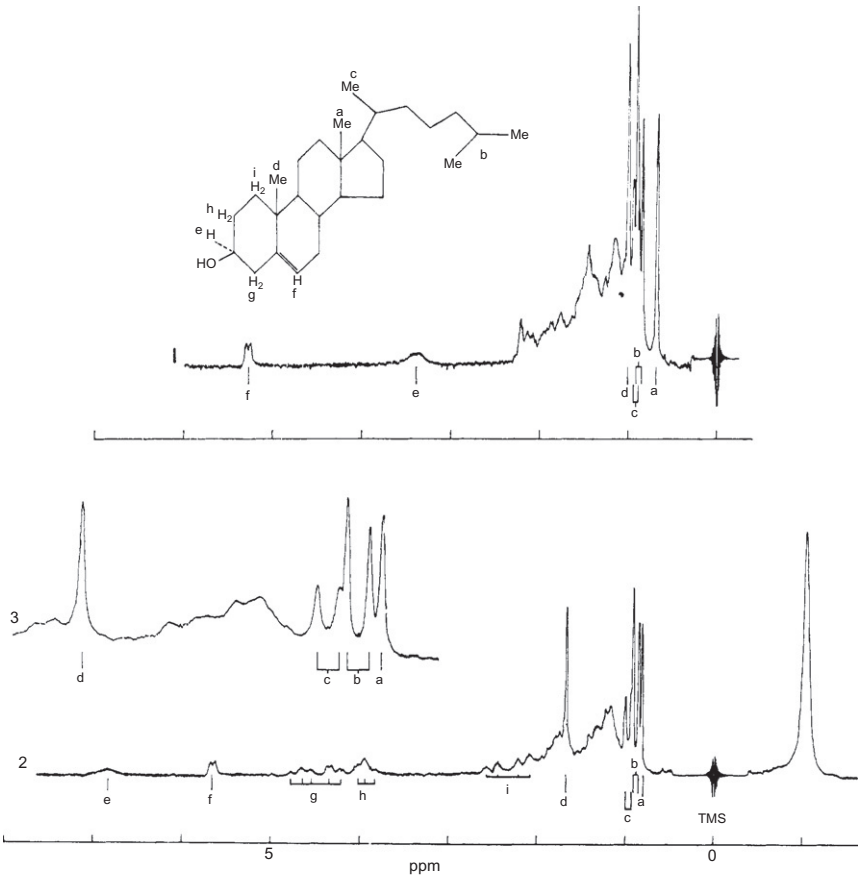

Figure 3.10 Spectrum 1 is of cholesterol monohydrate in CCl_4. Spectrum 2 is of a CCl_4 solution 0.05 M in $Eu(DPM)_3 \times 2$ py and 0.1 M in cholesterol monohydrate. Spectrum is an expansion of that region of spectrum 2 which includes the methyl resonances. Assignments are indicated by letter on the accompanying molecular diagram. The resonance 1 ppm upfield from tetramethylsilane (TMS) is due to the metal complex. Reprinted with permission from Hinckley et al.[215] Copyright 1969 American Chemical Society.

and the respective proton. Resonances up to 13 Å remote from the coordination site experienced paramagnetic shifts.[215] Since molecular modelling of sufficient quality was not commonly available, the use of Dreiding models became a standard for this type of distance analysis. Also the rigidity of the steroid skeleton proved favourable for these investigations. Further studies on steroids followed, for example, on 5α-androstan-2β-ol.[216,217] The presence of several complexation sites in one steroid was recognized to hamper the

simple shift analysis of graphical representations chemical shift difference $\Delta\delta$ versus difference r^{-3}.[218] The analysis of the graphs allowed the visualization of the uncertainties on the distances of the stereochemical model used. Vice versa, deviations between experimental and expected distance values could be interpreted in terms of conformations leading to different spatial proximities. By means of the dependence of the chemical shift on the lanthanide-steroid concentration ratio, specific chemical shifts could be assigned from the magnitude of the effect. In addition, complexation constants could be determined.[218,219] Deviations from the ideal r^{-3} relation were observed and found closer to r^{-2} or $r^{-2.2}$.[220] An investigation of the solvent dependence complexation-induced shifts[221] revealed that the complexation constant increased from chloroform over benzene, carbondisulfide, tetrachloromethane to cyclohexane, whereas the size of the lanthanide-induced shift increases from cyclohexane, carbondisulfide, chloroform, tetrachloromethane to benzene.

In conclusion, the lanthanide reagents provided an additional tool for the structure elucidation of steroids but were ultimately displaced by modern NMR experiments. As a rule of thumb, it may summarized that the use of europium(III) generally leads to downfield shifts of the affected protons, so does ytterbium, whereas praseodymium induces upfield shifts.[112,198] The size of the lanthanide-induced shift decreases with increasing distance from the complexation centre.

Solvent-induced chemical shifts were investigated for steroids in that époque as well. The methyl resonances in ketosteroids experienced an upfield shift when the chloroform as a solvent was replaced by benzene.[201] It was assumed that ketones form a solute–solvent collision complex in benzene leading to shielding and deshielding effects.[222]

3.1.3 Resolution enhancement—1D ^{13}C NMR

With respect to the exploitation of the chemical shift information, the data collection and the development of increment systems continued to grow,[103,105,106,129,223] cf. Section 5. Nevertheless, the use of methyl signals and distinguished protons, although supported by lanthanide shift reagents, reached soon its limitations. A complete connectivity picture of an arbitrary steroid was far from realization. That changed with the wider accessibility of ^{13}C NMR. In 1969, the first collection of chemical shifts of about 30 sterol and steroid hormones at 15.1 MHz carbon Larmor frequency was published by Reich et al.[107] Under conditions of complete proton decoupling, all signals were resolved. Their complete assignment

was achieved by using off-resonance proton decoupling, single-frequency proton decoupling, hydroxyl acetylation, deuteration and spectral comparison. These techniques should remain the standard toolbox for the following decade. As most of the proton shifts were not known, the single-frequency proton decoupling was not particularly useful, except for some prominent signals. Off-resonance decoupling led to spectra that contained no long-range C—H-couplings, and the magnitude of $^{1}J_{CH}$ splittings was reduced to about 20–40 Hz. The analysis of the data yielded several trends of resonance shift changes upon substitution of the steroid scaffold, such as the α-, β- and γ-effects. Upfield shifts were observed for carbons with γ-substituents, whereas β-hydroxyl and β-methyl groups induced downfield shifts. However, the assignment of signals to fully saturated A- and B-rings was not considered unequivocal due to very similar chemical shift values. Since signals were well resolved and the chemical shift was sensitive to the steroid structure, stereochemical questions could be addressed by ^{13}C NMR as had been previously by ^{1}H NMR. In 1972, the configuration of the A/B-ring junction was investigated through ^{13}C NMR.[224] A chemical shift difference of 11–12 ppm was observed for C5 in 5α- and 5β-steroids, thus *trans*- and *cis*-A/B-ring fusion, respectively. It was known from methyl cyclohexane that the methyl group in axial position absorbs at higher field, 6 ppm, than the one in equatorial position.[225] The orientation of the methyl group is called gauche with respect to carbons 3 and 5. As a general observation, gauche vicinal orientations relative to another atom lead to resonances shifted upfield in comparison to anti-vicinal arrangements. Applied to 5α- and 5β-steroids like androstane, gauche interactions between C19 and C2, C4 are observed for the 5α-isomer, whereas the 5β-isomer lacks these gauche interactions. Hence, the 19-methyl group within the 5β-isomer is less shielded and resonates thus at lower field. For a series of steroids, it was hence found that $\Delta\delta(\mathrm{C19}) = \delta(\mathrm{C19(5\beta)}) - \delta(\mathrm{C19(5\alpha)}) \approx 11.5$ ppm.[224]

Several monographs on ^{13}C NMR spectra of a variety of natural and synthetic compounds were published during the 1970s including steroids,[226–229] some of them are still being updated, as can be seen from inspection of the references. In the second half of the 1970s, a concise review was published by Blunt and Stothers,[112] summarizing in detail the status-quo of ^{13}C NMR on steroids, around 50 original articles at that time. The data of 400 steroids were tabulated and earlier assignments revised. Sapogenins and their glycosides, the saponins, were collected separately by Agrawal et al.[111,130] The collection contained more than

250 compounds by 1995. To the previous assignment strategy, isotopic labelling, in general, the use of lanthanide shift reagents and the determination of spin–lattice relaxation times were added.

Such T_1 spin–lattice relaxation times are in the range of 0.5–1.0 s for most skeleton carbons, more than 2 s for quaternary carbons and more than 1 s for angular methyl groups. Quaternary carbons could thus be identified by their low signal intensity from $^{13}C\{^1H\}$ spectra in a first approximation, but care has to be taken, since other slowly relaxing nuclei or fluorine-splitting may cause similar signal intensities. The precision of chemical shift determination was reported as 0.1 ppm relative to tetramethyl silane, but a change of the chemical shift on variation of the steroid concentration in deuterochloroform was also reported for hydroxyl and oxosteroids, albeit the more remote from oxygen substituent, the smaller the change.[112]

However, the most important assignment criterion remained the chemical shift. Within the shielding range of approximately 200 ppm, a quick assignment of progesterone would start from the non-conjugated carbonyl carbon C20 at 208 ppm, the more shielded, conjugated carbonyl C3 at 198.5 ppm. The next signals in the sequence stem from olefinic carbons, the more substituted carbon C5 at 169.5 ppm and the lower substituted C4 at 123.7 ppm. For the saturated carbons between 13.2 and 63.3 ppm, further strategies had to be selected. The then popular off-resonance decoupling became replaced by the DEPT technique and later by C—H and H—C correlation spectroscopy, yielding multiplicity information. The consideration of effects from polar, electron withdrawing or pushing subsitutents contributed to further signal assignment. An equatorial hydroxyl group would cause shift changes of +43.2 ppm on the α-carbon, +7.7 ppm as a β-effect and −2.5 ppm as a γ-effect. However, the introduction of a hydroxyl group at C5 of 5α-cholestane results in a downfield shift of 3.9 ppm for C19, which is in contrast to the expectation.

The complete assignment of 5α-androstane was achieved and described as an illustrative example of the combined use of all techniques.[108] In fact, the assignment was a revision of a previous one.[230] Table 3.4 presents a summary of the most important substituent effects. Note that, following the common definitions, a shielded nucleus experiences a high secondary magnetic field at the nucleus and the resonance appears at low applied field or frequency under pulse NMR conditions. Deshielding of a nucleus leads to a lower secondary field and a higher applied field. An increase in shielding is seen as an upfield shift but effectively shifts the resonance to a lower

Table 3.4 Most prominent substituent effects following references[112,232]

Effect	Irregular observations	Description of the effect
α-Effect		Largest shifts occur for carbons bound to polar substituent; causes deshielding
β-Effect		β-Carbons are less affected by polar substituents but also deshielded
	Exception	If a carbon is located both β- and eclipsed with respect to a C═O group, for example, C6 in 4-oxo-steroids, the β-carbon is γ to the carbonyl oxygen and eclipsed interactions of γ-nuclei result in upfield shifts relative to analogues with different geometries
γ-Effect		Carbons three bonds away from polar substituents tend to be shielded
	—OH substituent	Axial => gauche γ-carbon Equatorial => anti γ-carbon Both effects shift γ-carbons upfield, the effect is more pronounced for gauche γ-carbons
	Acetylation	Accentuates the α-effect and diminish the β-effect
	Anti-γ-effect	Causes deshielding in system in which both intervening carbons are fully substituted, for example, C19 in 5α-OH compounds although corresponding effects between substituents and carbons separated by two methane centres are shielding
Long-range effects	δ-Effects	*Syn*-axial arrangements of a substituent with a δ-carbon lead to a downfield shift of the δ-carbon, for example, C11 in 1β-OH, C19 in 2β-, 4β-, 6β- or 11β-OH derivatives

resonance frequency, and thus lower ppm values; deshielding causes a downfield shift and shifts the resonance to higher ppm values.[198,231]

It should be noted that steric crowding can give rise to shifts of a few parts per million and can be both up- and downfield. "As a rule of thumb, pronounced upfield deviations, i.e. experimental versus calculated values based on increment systems, arise from closely neighboring γ-substituents, while pronounced downfield deviations occur for closely neighboring δ-substituents. In both cases, the carbon bearing the interacting substituent exhibits the largest behavior."[112] Nevertheless, all effects were important for the elucidation of stereochemistry, for example, the determination of α- and β-positions through the gauche γ-effect.

Since ^{13}C was the leading NMR technique for structure elucidation not only in the steroid field, the general systematic of substituent effects on ^{1}H spectra began much later, although increment systems reflected the stereochemical effects on the chemical shift. But suitable probes were limited to angular methyl groups and protons in close neighbourhood of an electronegative substituent.[201,211] In 1985, Schneider et al. systematically analyzed stereochemical effects for ^{1}H NMR on the basis of steroids, relying on two-dimensional spectroscopy.[116]

It was found that the substituent effects were, in general, comparable to cyclohexanoid systems. In analogy to some ^{13}C shifts, shielding differences were observed to be often larger at the β- and γ-positions compared to the shifts at the substituent site. From the data, no notion of a general *syn*-upfield, anti-downfield effect of heterosubstituents on vicinal protons was found. Rather, the β-effect was always deshielding and, in more cases, stronger for the *syn*- than for the *anti*-proton. Equatorial substituents were seen to deshield the equatorial and axial vicinal protons to an unexpectedly differing degree, although the affected C—H bonds had the same *syn* relation to the C—X bond.[116] According to Schneider et al., the pronounced *syn* γ-H deshielding, which varies for all heterosubstituents between $+0.43$ and $+0.68$ ppm, would be the most reliable stereochemical probe. For hydrocarbon shifts, all equatorial protons resonated around 1.5 ± 0.2 ppm, except D-ring protons. The axial protons absorbed between 0.7 and 1.2 ppm, where the shielding increased with the number of other axial proton–carbon bonds. Carbonyl and halide effects were analyzed with respect to the contributions of electronic effects.

In following studies, the gauche γ-effect was compared for ^{13}C and ^{1}H nuclei.[233,234] Within the first investigation, 12-substituted-14β-hydroxy- and 14α-hydroxysteroids exhibited a linear correlation form $\delta(^{1}H)$ of H17 and $\delta(^{13}C)$ of C17. While the proton experienced a downfield shift, the carbon was shifted upfield. Both shifts resulted from the steric interactions with the 12-substituent, which was reported to decrease the electron density at H17 causing an increase in electron density of C17. Thus, H17 experienced a paramagnetic, C17 a diamagnetic shift. The same negative linear correlation was found for $\delta(^{1}H)$ of H12β and $\delta(^{13}C)$ of C12 for 17β-substituted steroids and for $\delta(^{1}H)$ of H14α and $\delta(^{13}C)$ of C14 in 7α-substituted steroids. The linearity was interpreted in terms of steric interactions as cause of the γ-effect.

The steric effects of fluorine on the ^{13}C chemical shifts were analyzed as well.[235] It was found for tertiary fluorosteroids that α- and β-carbons were

deshielded by 53–58 ppm, whereas γ-carbons were subjected to the gauche and anti-γ-effect. The latter induced a deshielding of the carbon atom by 2–5 ppm, the gauche γ-effect a shielding of 1–8 ppm. Couplings $^{3}J_{CF}$ were also found to vary between 0 and 3 Hz for gauche γ-carbons and 6 and 8 Hz for anti-γ-carbons. Couplings of 170–180 Hz were reported for α-carbons and approximately 20 Hz for β-carbons.[235]

Interestingly, the physical interpretation of the effects as being of stereochemical nature, that is, non-bonded interactions between the hydrogen atoms on the carbon in question and on the γ-substituent,[226,236] was questioned.[237,238] Beierbeck et al. assumed that the gauche γ-effect is a consequence of β-hydrogen elimination rather than γ-steric interaction. It was argued that a steric nature of the γ-effect should cause a $\Delta\delta$ of the methyl carbon atom in all three double bond isomers according to Fig. 3.11, which it effectively did not.

Yet, only the β,γ-isomer showed a downfield shift, which was assumed due to the deshielding effect of the electronic structure of the double bond. The authors elaborated, therefore, that the elimination of the β-hydrogen atom should lead to shielding and that the addition of the γ-group had no further effect, which in consequence meant that the γ-effect should not be considered a stereoeffect. A summary of the discussion is represented in Scheme 3.2.

More general descriptions of the steric effects can be found in textbooks and literature cited therein.[232]

The application of the available toolbox for ^{13}C chemical shift assignment, using extensive deuteration, led among others to the assignment of

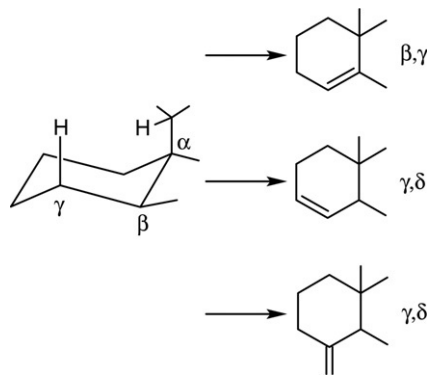

Figure 3.11 Elimination of a γ-hydrogen atom leading to a double bond according to Beierbeck et al.[237]

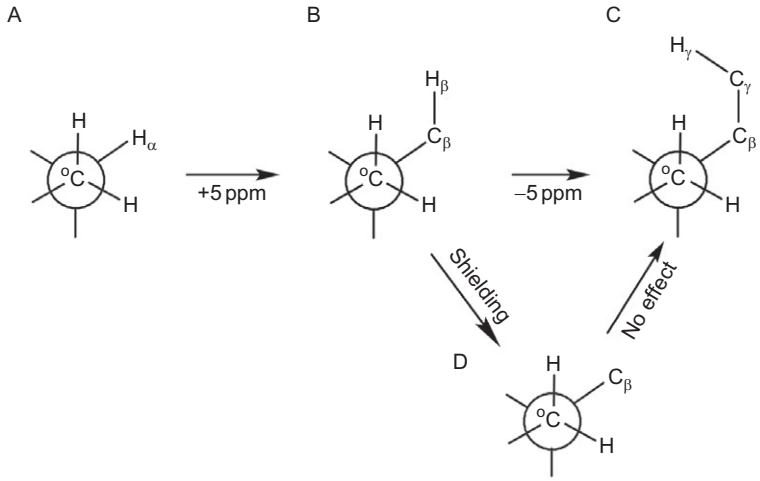

Scheme 3.2 Reasoning for β-hydrogen elimination instead of γ-steric interaction as the cause of the gauche γ-effect according to Beierbeck et al.[237,238] This explanation takes the observation into account—among others—that the gauche γ-effect is virtually independent of the nature of the γ-group.

stigmasterol and β-sitosterol.[239,240] In 1980, more steroids were assigned by the use of single-frequency off-resonance proton decoupling, termed SFORD, where the proton frequency range was irradiated at ±2 ppm.[241]

While the review by Blunt and Stothers marked a milestone of ^{13}C NMR on steroids in a pharmaceutical environment that was steadily withdrawing its forces from the steroid research, the challenge of the signal assignment of protons remained. During the 1970s, ^{13}C was clearly leading structure analysis by NMR, but proton studies continued. For 17-hydroxy-16-ethylestranes, coupling constants of J(H16α,H17α) = 9–11 Hz, J(H16β,H17α) = 6–8 Hz, J(H16β,H17β) = 5 Hz, and J(H16α,H17β) = 0–1 Hz were reported.[242] Yet, the finding that the coupling constants did not vary with the nature of the 16-substituent was not confirmed in other studies. The configurations of 16-substituted 17-hydroxysteroids were investigated by in-depth analysis of 160 compounds.[243,244] To this purpose, the $^3J_{HH}$ couplings, the chemical shift of the C13 methyl group and of the H17 protons as well as shift and multiplicity of H16 were found suitable. The large variety of data showed that in most cases of 17-hydroxysteroids the order J(H16α,H17β) < J(H16β,H17β) < J(H16β,H17α) < J(H16αH17α) was observed. A configuration determination from one isomer was considered possible only if $J > 8$ Hz, which is indicative for H16β and H17β orientation, or $J \leq 2$ Hz indicative for

H16β and H17α positions.[244] Nonetheless, the size of the coupling constant was reported to depend on the type of substituent. Similar rules were derived for 15,16,17-trisubstituted steroids, using also the downfield shift of protons geminal to hydroxygroups, caused by acetylation or *in situ* reaction with trichloroactylisocyanate.[245,246]

Despite the successes in the assignment of configurations and conformations, still no complete ^{1}H signal assignment of a steroid had been published by 1979.

3.1.4 Complete chemical shift assignment—1D NOE and 2D NMR

In 1980, Hall et al. published the first complete determination of proton chemical shifts and geminal and vicinal proton coupling constants for 1-dehydrotestosterone and 11β-hydroxyprogesterone.[247] In the succeeding communication, Hall and Sanders finally reported the assignment of all proton resonances of the two steroids.[113] This achievement took advantage of the techniques that had not been applied to steroids before. The chemical shift and the coupling determination owed to two-dimensional ^{1}H *J*-resolved spectroscopy,[248–250] since it transposed the overlapping multiplets into the second dimension. The assignment could then be achieved by NOE difference and decoupling difference techniques.[251,252] Especially, the use of difference techniques allowed the successful application of through-space and through-bond correlation spectroscopy. Although 2D C—H shift correlations were already available at that time,[253,254] Hall and Sanders did not opt to correlate their assignments to the carbon assignment.

One earlier attempt to use NOE spectroscopy for steroids is discussed in the 1973 issue of Topics in Stereochemistry,[255] referring to a lecture by Tori on using NOE spectroscopy on seven steroids. The α- and β-positions of substituents as well as the conformation of an 8β-formyl group could be determined. However, "the steroid group has received surprisingly little attention in NOE studies" was concluded, a statement that should hold true for another few years.

During their further study of 1-dehydrotestosterone and 11β-hydroxyprogesterone,[115,256] Hall and Sanders observed all axial–axial and also cross-ring through-space connectivities, such as those of H17α with H12α, H14, H16α and Me18 with H8, H12β, H15β, H16β and H11β, the latter for 1-dehydrotestosterone only. The exploitation of 2D *J*-resolved spectroscopy, in contrast, suffered from technical problems, such as artefacts from proton decoupling leading to off-centre singlets and

strong coupling leading to higher-order multiplets. How such strong-coupling artefacts could be interpreted in terms structure elucidation was shown for substituted dioxanes.[257] Alternatively, a remedy for their suppression was proposed and demonstrated for dehydroisoandrosterone,[258] cf. Fig. 3.12. The step in resolution for steroids can be best judged for 11β-hydroxyprogesterone where 11 multiplets occur between 1.0 and 2.5 ppm. By means of *J*-resolved spectra, each chemical shift could be identified. Long-range couplings were detected, such as *J*(H12α,H18), known from 11-ketosteroids, and *J*(H1α,H19). Yet, the lack of the seemingly equivalent coupling between H14 and H18 was remarked once again, which was later confirmed by Platzer et al.[207] In light of the new class of experiments, a strategy was proposed for the assignment of ^{1}H and

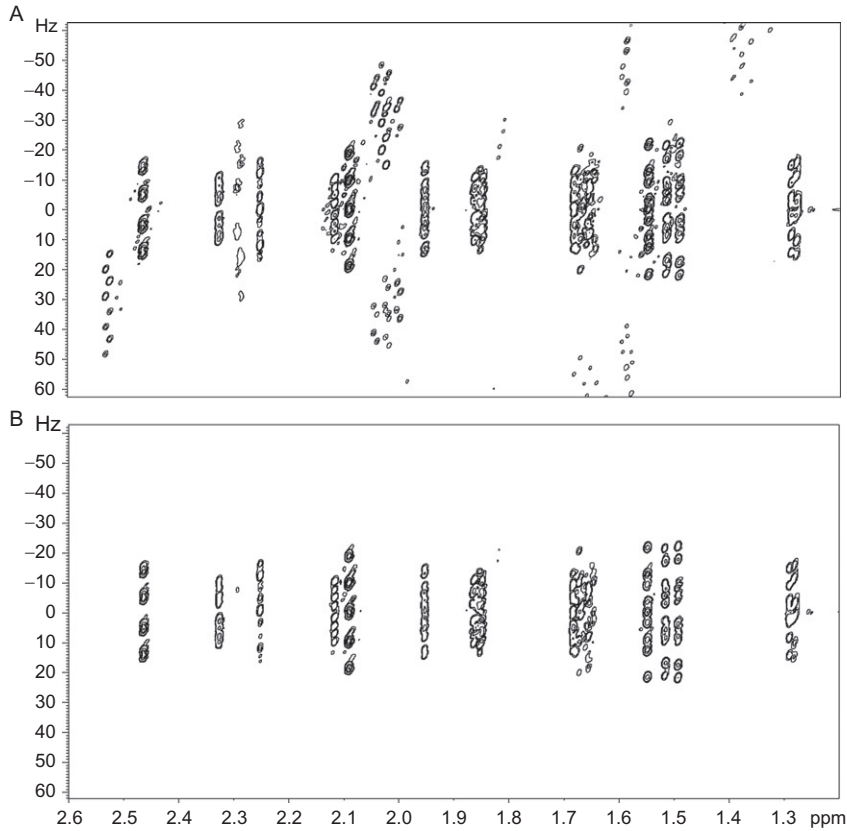

Figure 3.12 *J*-resolved spectra of dehydroisoandrosterone without suppression of strong-coupling artefacts (A) and with suppression (B). Reprinted from Thrippleton et al.,[258] Copyright 2005, with permission from Elsevier.

^{13}C signals of steroids, starting independently from obvious signal assignments within 1D ^{1}H and ^{13}C spectra, going to specialized experiments and achieving the total assignment via 2D C—H correlation experiments.[256]

With the ^{1}H assignment of the full steroid scaffold and the Karplus relation,[124] that was strongly refined for the electronegativity of substituents by Haasnoot et al.,[125] the investigation of the stereochemistry of all parts of the steroids could be attempted. In crystallographic studies of medroxyprogesterone acetate, MPA, that is, 17α-acetoxy-6α-methylprogesterone, the steroid showed an inverted half-chair conformation of the A-ring in agreement with its circular dichroism (CD). However, in solution, CD analysis suggested a normal half-chair conformation. Normal refers to the 1α,2β half-chair, inverted to the 1β,2α half-chair form, where the term "normal" includes the ring changes from 2β-sofa via 1α,2β half-chair to 1α-sofa, cf. Fig. 3.13.

The unsubstituted 17α-hydroxy-6α-methylprogesterone displayed a normal A-ring conformation in X-ray studies. Since MPA possessed unusually high progestational activity, the structure–activity relationship might have been interpreted in terms of the inverted A-ring. Also normal half-chair conformations were found for three other progesterone derivatives, only 2β-acetoxytestosterone-17-chloroacetate showed an inverted A-ring. The normal conformation of MPA was proven again by the combination of NOE difference, decoupling difference and 2D *J*-resolved spectroscopy.[259] The observation of NOE correlations between Me19 and H1β and H2β, the geminal coupling, was recognized by a 16-Hz coupling, cf. Fig. 3.9, and a W-coupling from M19 to H1α indicated the normal conformation.[114,259]

While these studies relied on proton homonuclear techniques, further studies tended to include the important C—H shift correlation experiments.

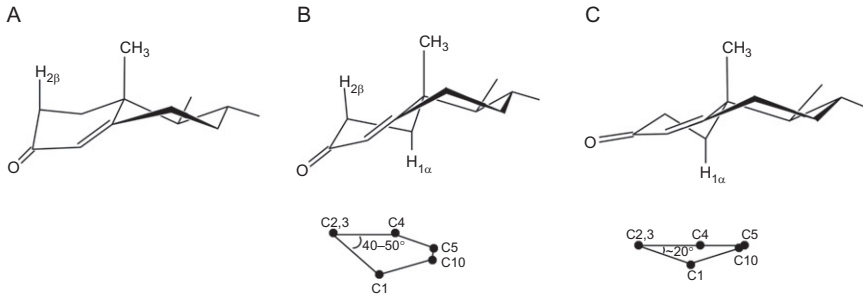

Figure 3.13 Normal half-chair conformations of the A-ring within 4-en-3-one steroids: 2β-sofa (A), 2β-half chair (B) and 1α-sofa (C).[211,259]

In the beginning of heteronuclear correlation experiments, magnetization was detected on the carbon nucleus. A carbon-detected heteronuclear *J*-resolved experiment, for example, was performed on a saturated solution of cholesterol in a 10-mm sample tube.[260] The experimental time amounted to 16 h. The information yielded C—H coupling constants in addition to the carbon multiplicity as compared to edited 1D methods such as INEPT,[261] DEPT[262] and SEMUT,[263] a spectral editing type of 1D ^{13}C NMR. The latter two were introduced on cholesterol and cholesteryl acetate, respectively. The DEPT was later extended to an edited direct-detected heteronuclear correlation experiment, again described on a cholesteryl acetate sample.[264] These methods were being developed during the period of the C—H correlation techniques. The experiment that correlates carbon and proton chemical shifts and provides thus the link between proton and carbon spectroscopy was introduced in 1978[265] and a year later applied for cholesterol.[266] In 1981, an improved version of the experiment using phase cycling[267] was tested on a 1.5-M solution of 5α-androstane. The spectrum was recorded within 30 min, which clearly demonstrated the advantages for structure elucidation purposes. As another important step for connectivity investigations, C—C INADEQUATE experiments had been introduced[268,269] and applied in the steroid field.[270] The INADEQUATE was even proposed as the basis for computer-based automated structure elucidation.[271] A contemporary study described the use of C—C correlations for the structure elucidation of cyclonervilasterol and its analogues; the natural products were isolated from an orchidaceae and were found to have a steroidal skeleton with a cyclopropyl bridge over the C5—C10 bond and a double bond from C9 to C11. However, due to its inherent insensitivity on account of the poor natural abundance of ^{13}C nuclei and thus adjacent ^{13}C nuclei, of long-relaxation times especially for two adjacent quaternary carbons and in the case of strongly coupled nuclei, the application of INADEQUATE spectra remained exotic.

In contrast, the carbon-detected C—H shift correlation spectroscopy was widely used, even though the more sensitive inverse, that is, proton, detected variants were already described such as the H—C HMQC experiment,[272] with improved sensitivity[273] or the HSQC.[274] The increase in sensitivity theoretically amounts to a factor of eight, resulting from the increase in resonance frequency for proton versus carbon for a given magnetic field strength. Yet, the inverse pulse schemes could not replace the direct detected experiment within the steroid field for quite some time,

as can be learned from the experimental sections of the references cited further below. Interestingly, the inverse detected long-range proton–carbon correlation or H—C HMBC,[275,276] in contrast, gained quickly popularity over the direct detected counterpart. The history and an overview of inverse detected experiments can be found in references[122,277] and for steroids in reference,[128] where also a brief review is given on the structure elucidation strategies for steroids, extended by the 2D methods.

3.1.5 The absolute structure elucidation

Taking widely advantage of the new instrumentarium and the angular dependence of coupling constants in its refined form,[125] the Haasnoot group dedicated several studies to the structure elucidation of norethisterone (**22**), mestranol and its photodegradants. At first, the assignment of ^{1}H and ^{13}C resonances for norethisterone was carried out straightforward at 500 MHz.[278] Due to the number of experimental data acquired, the unambiguous assignment was compared to an overdetermined matrix. To obtain the necessary connectivity information, the researchers relied on 2D spin–echo *J*-correlation experiments termed SECSY. The coupling network was sketched in a connectivity pathway diagram, as shown in Fig. 3.14, which the reader is asked to compare to the correlation matrix for through-bond and through-space connectivity in Fig. 3.40 at the end of this chapter.

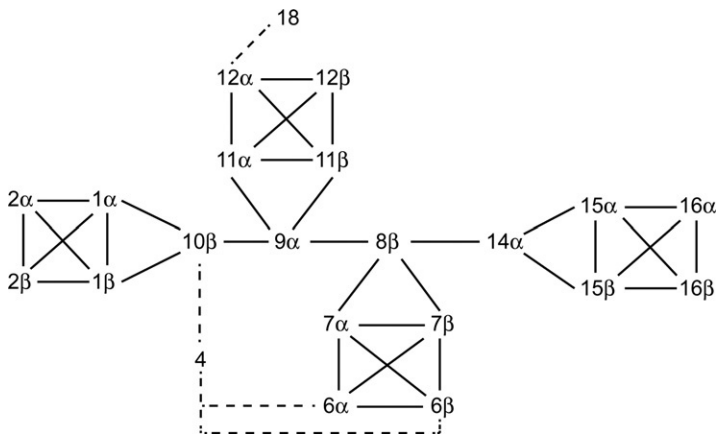

Figure 3.14 ^{1}H coupling network for the protons in norethisterone (**22**) according to Sedee et al.[278] Long-range couplings are illustrated as dashed lines. A generalization of this scheme containing a valuable collection of coupling and NOE parameters was devised by Kasal et al.[4]

The deviations from the Karplus relation observed for *J*(H8,H9) and *J*(H9,H11β) were not explained.

Consecutively, two photolytical and thermal reaction products of norethisterone were elucidated, revealing two isomeric photodegradants of 5α and 5β type. The same methodology was used as in the previous study.[119] Only the SECSY experiment was replaced by the more convenient H—H COSY to obtain proton connectivity information.

For 17β-hydroxy-19-nor-5α-17α-pregn-20-yn-3-one and its 5β-isomer, a conformational study was undertaken on the basis of the coupling constants[279] using structures from crystallography and MM2 force-field calculations. The application of the generalized Karplus equation, that is, the Haasnoot equation, yielded good results for rings A–C within 0.5 Hz accuracy. Deviations occurred again for ring D, in particular *J*(H15α, H16α), which was interpreted in terms of through-space interactions due to the C13β-envelope conformation of ring D in analogy to norbornane systems, cf. Fig. 3.15. A second deviation from the calculated values was observed for *J*(H8β,H9α), which amounted to 9.7 Hz experimentally versus 12.0 Hz calculated both for 5α- and 5β-isomers. This finding was traced back to the convexity of the steroid skeleton together with a small helical deformation, where the C1—C10—C9 fragment is bent slightly upwards as compared to its tentative position in a regular conformation, the C6—C7—C8 moiety appears somewhat planar. Mestranol and its photodegradants were subjected to a similar analysis.[117] Once again, ring D couplings were found deviating from expected values. Among the nine degradation products that were formed and analyzed by UV and MS, five structures could be confirmed by NMR, which demonstrated the power of NMR as an analytical technique. In the same year, a systematic study by Schneider et al.[116] furnished assignments, coupling constant analyses, ^{1}H increments and shielding mechanisms and, last but not least, conformational insight. To this purpose, a series of 5αH-androstanes and a

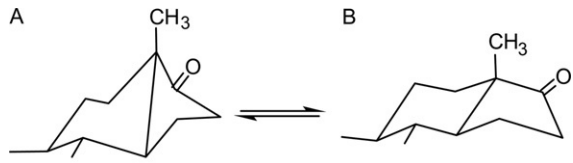

Figure 3.15 (A) C16 half-chair and (B) C14 envelope conformation for the D-ring of 17-oxosteroids.

progesterone analogue were analyzed. For the D-ring as the most flexible part of the skeleton, it was found that all conformations between a half-chair, C16, and the C14 envelope could be brought in agreement with the experimental coupling values. The half-chair and envelope conformations are illustrated for 17-oxosteroids in Fig. 3.15.

Earlier findings[114,259] with respect to the A-ring of Δ^4-3-oxosteroids were reinvestigated. According to the study by Schneider et al., the NMR spectroscopic data were in favour of the sofa conformation instead of the half-chair, cf. Fig. 3.13. Only *J*(H1β,H2) could not be matched, leading to an angular deviation of 12°.

For ring B, no couplings sufficiently accurate for computational use were obtained. For ring C, the values were in good agreement with the common chair conformation. The interpretation of the A-ring conformation as sofa was once again subjected to a study of 4-*en*-3-one steroids using systematic temperature variation.[127] The data were interpreted in terms of an equilibrium between the normal 1α,2β half-chair and the inverted 1α-sofa conformer. The half-chair was concluded to be the predominant form, the sofa conformer becoming more populated with increasing temperature but still remaining the less favourable conformer. Only a 2β-acetoxy substituent caused an inverted conformation, whereas substituents in 6-position did not influence the A-ring conformation. Discrepancies with the previous study were attributed to the presence of the equilibrium. The existence of the sofa form in the solid phase was explained in terms of crystal packing forces. A second study considered C2 monomethyl and dimethyl substituted 5α-androstane-3-ones. It was concluded that the 2α-methyl derivative existed with ring A in a regular chair conformation, while the 2β-methyl derivative assumed the inverted boat conformation with C2 and C5 at the bow-stern positions. Both forms were connected by an equilibrium.[126]

While the elucidation of stereochemical aspects continued and still continues, the ensemble of new methods was also utilized to demonstrate the efficient strategy of structure elucidation by NMR only, which had become possible. The 2D experiments were applied to numerous steroids in a straightforward manner to assign all ^{1}H and ^{13}C signals and hence close the proton assignment gap that had existed for many years. A few examples will be given.

In 1982, the 9α-hydroxyestrone methyl ether generated via a photochemical reaction was structurally investigated by H—H COSY, NOESY and *J*-resolved spectroscopy at 360 MHz.[280] The analysis of the assignment presented an all *trans*-connected ring system with the hydroxyl group in

α-position. A half-chair conformation was found for ring B. Interestingly, the ^{13}C assignment followed the old strategy including deuteration, lanthanide shift reagents and shift correlation diagrams supported by INEPT experiments. A series of polyhydroxylated 11α-hydroxysterols from marine invertebrates was elucidated by ^{1}H and ^{13}C assignments at 500 and 360 MHz.[281] The partial spectral assignment was achieved from 1D spectra and spectral comparison. The structure elucidation was supported by IR and UV spectroscopy and chemical reactivity.

The incomplete ^{1}H spectral assignment suggested that even with resolution compared to the previous decade signal crowding was sufficiently severe to prevent signal resolution adequate for full assignment. In contrast, the advantage of the resolution gained by disentanglement of the signals into two dimensions allowed the complete ^{1}H and ^{13}C assignment of 12 corticosteroids and related compounds at 400 MHz, using COSY-45, C—H HETCOR, COLOC and C—C INADEQUATE experiments.[118] The data obtained were analyzed with regard to the solvent-induced chemical shift mechanism for C20 carbonyl groups and stereoeffects on ^{1}H chemical shifts. A COSY-45 of tibolone, which was a particularly useful experiment for the distinction of methyl and methylene protons in the crowded spectra of steroids, is shown in Fig. 3.16 with tibolone (**11**) as example. According to current standards, the distinction can be made from H—C HSQC.

Linked by the basic full signal assignment, different studies elaborated on different aspects, for example, on stereochemistry or specific experimental techniques. In this respect, two studies pointed out the usefulness of long-range or relayed H—H coherence transfer experiments for steroids[207,282] as additions to the more standard set of experiments. The results of the first study have already been discussed for long-range coupling mechanisms above. The second study dealt with the assignment of 17β- and 17α-estradiol.[282] Exemplarily, relayed magnetization transfer appeared as a correlation signal between Me18 and H11α via the long-range coupling between Me18 and H12α. The long-range correlations were considered particularly useful during the assignment procedure, since they helped to identify chemical shifts within the methylene envelope to establish connectivity with well separate resonating protons, such as H17β. The effect of RELAY or TOCSY delays, 42 and 60 ms, on the spectra was compared, the latter found less useful due to sensitivity losses on account of relaxation. In 1990, the complete ^{1}H and ^{13}C assignment of testosterone and 17-methyltestosterone was undertaken at 600 MHz[131]; the attribution of the H16α and H16β shifts, which

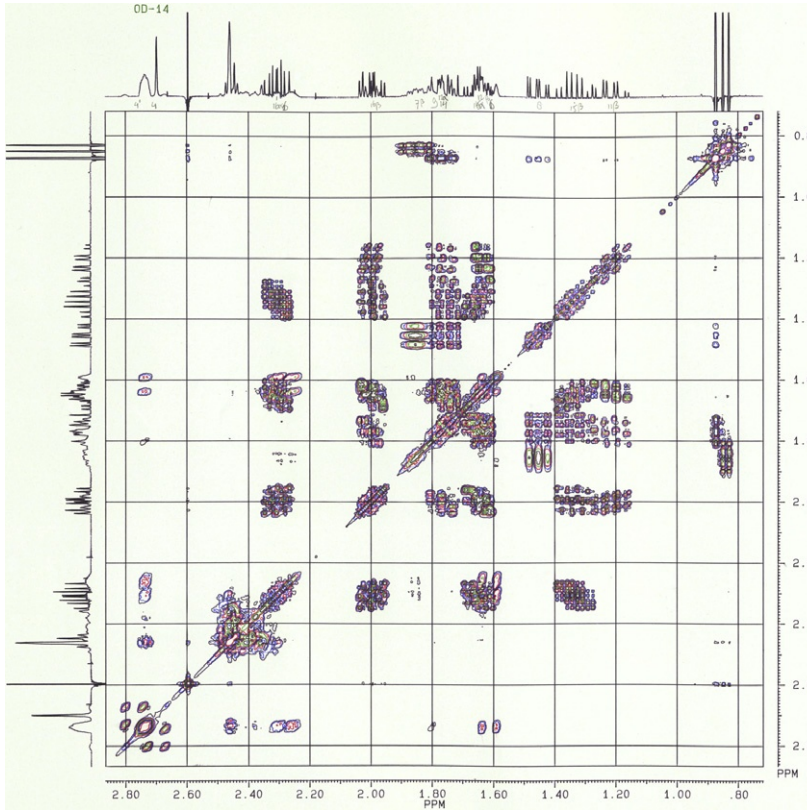

Figure 3.16 H—H COSY-45 of tibolone (**11**) in $CDCl_3$ at 360 MHz.

contradicts another analysis,[132] has been mentioned earlier. Experimental proof for the latter assignment was provided by H—C HSQC–NOESY spectra obtained from a 3D experiment and a 2D spectrum calculated from H—C HSQC and H—H NOESY by unsymmetrical indirect covariance (UIC) spectroscopy,[133] cf. Fig. 3.17. Nevertheless, the compound characterization of the 1990 study was carried out using H—H COSY, H—C shift correlation, H—H NOESY in the same way, as one would proceed in a modern analytical laboratory when a structure hypothesis is available.

In 1990, an overview was published of newly elucidated natural products among them steroidal alkaloids, pointing out the importance of the two long-range correlation techniques HOHAHA and HMBC.[283] Not only spectroscopists but also synthetic chemists made use of the 2D techniques.

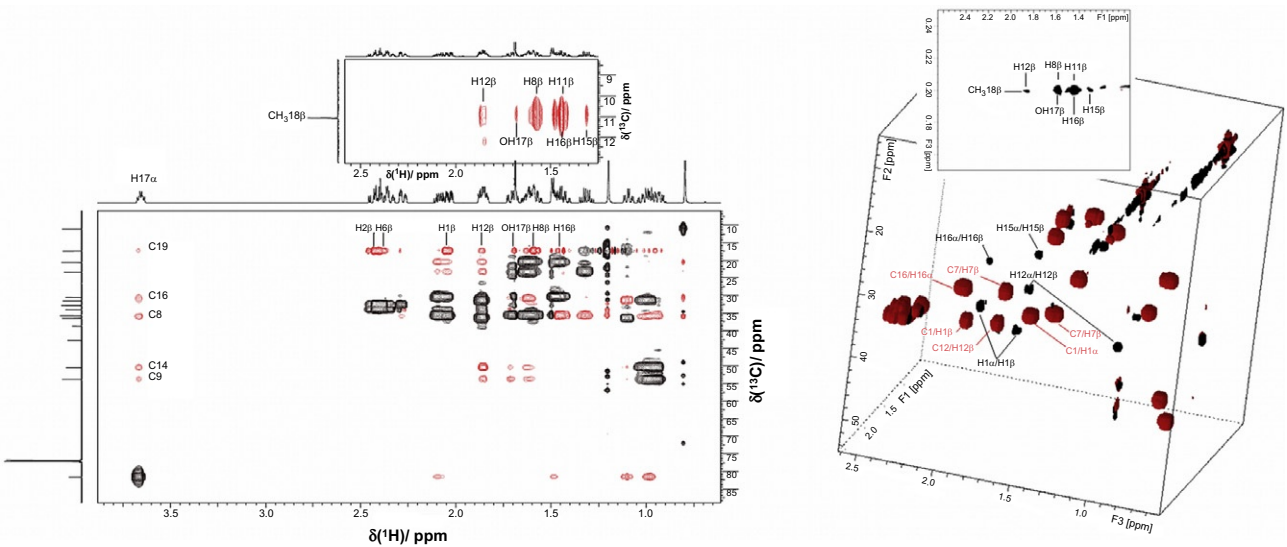

Figure 3.17 Comparison of H—C HSQC–NOESY spectra of testosterone (**5**). UIC 2D HSQC–NOESY from HSQC and NOESY (left), 3D HSQC–NOESY (right). Correlations used for the assignment of H16α and H16β resonances are indicated in the zoom regions. The F1–F3 plane (H—H plane) of the 3D cube is shown at carbon chemical shift of the 18-methyl resonance. Reprinted with permission from Aspers et al.[133] Copyright 2011 John Wiley & Sons Ltd.

Among these studies, the structure confirmation and configuration identification of 17α-hexanoic derivatives of testosterone and 5α-dihydrotestosterone obtained from chemical synthesis were achieved by NMR in combination with molecular rotation analysis.[22] The study was later continued by the same group for 17α-cyano, 17α-aminomethyl and 17α-alkylamidomethyl derivatives.[284] When, in 1992, tomatine, whose ^{13}C shifts had been previously assigned,[285] and tomatidine, the latter being the aglycone, were subjected to a complete assignment and conformational analysis,[286] it could be shown that the ensemble of NMR methods was almost self-consistent. The assignment could be carried out with a minimum of expert knowledge, that is, correlations and long-range correlations were able to substitute the prior knowledge of chemical shifts of structural fragments. The set of experiments used was enlarged by the equivalent of an H—C HMQC–TOCSY and a selective TOCSY–COSY experiment,[286] while coupling constants were extracted from E.COSY spectra. In 1993, the first complete assignment of diosgenin (**9**) together with solasodine was achieved.[203] The previous ^{13}C assignments[285,287,288] were confirmed. As entry points into the signal attribution, the double-bond carbons C5 and C6 were attributed and as always the separately absorbing protons H3, H6, H16 and H26α, H26β. The COSY pattern was followed via the long-range coupling Me18 to H12 and H6 to H4, H6 to H7. The stereochemistry of α- and β-orientations was derived from NOESY data. In a similar manner, the structures of new bitter saponins were elucidated.[289]

Reviews on the use of the 2D experimental techniques of that époque can be found for steroids in references[3,128] and for natural products in reference.[277] The application of NMR experiments towards the elucidation of conformation and configuration as driving force shall be briefly summarized in the following paragraphs.

The presence of conformational equilibria and its consequences for the A-ring coupling constants[126,127] has already been mentioned earlier. A special case of an equilibrium involving hydrogen bonding was investigated for 3α-hydroxy-2β-(4-morpholinyl)-5αH-androstan-17-one.[290] The A-ring conformation was the chair form in polar solvents such as DMSO, while apolar solvents favoured a twist-boat form. The interpretation was achieved from the Haasnoot equation and mainly based on the coupling values observed for J(H1α,H2α), J(H1β,H2α) and especially J(H2α,H3β). The twist-boat was assumed stabilized by a hydrogen bond involving the hydroxyl proton and the nitrogen as illustrated in Fig. 3.18.

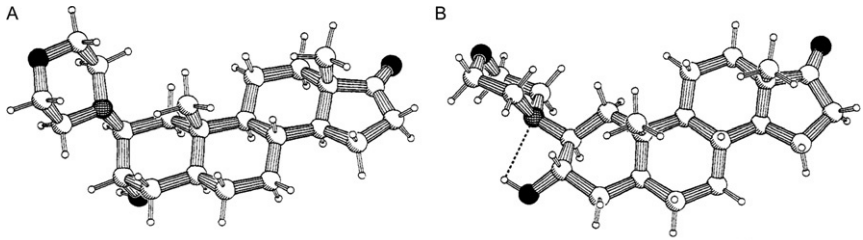

Figure 3.18 (A) Chair and (B) hydrogen bond stabilized twist-boat conformation for 3α-hydroxy-2β-(4-morpholinyl)-5αH-androstan-17-one. Geometries were calculated by molecular mechanics. *Adapted with permission from Fielding and Grant.*[290] Copyright 1991 American Chemical Society.

The polar solvent destabilizes the hydrogen bond by 1.5 kcal/mol, forcing the A-ring into the energetically favourable chair conformation. The detailed energetical consideration of the equilibrium[291] relied on the ^{13}C chemical shift of the 19-methyl group and on the coupling value of ^{3}J(H2α,H3β) and their changes upon solvent ratio variations. The latter ranged from 3.1 Hz in the chair arrangement to 9.5 Hz in the twist-boat conformation, allowing the populations to be derived from the actual observed value. The 19-methyl group experienced an upfield shift of about 4.0 ppm in the chair due to a release of sterical pressure. The population analysis, 88% chair in a DMSO environment versus 86% twist-boat in chloroform, was interpreted in terms of a preferred chair conformation for unsubstituted androstanes in solution. In the twist-boat conformation, H2α and H3β gave rise to pseudoaxial signals; in the chair form, they appeared clearly equatorial.[292] In addition, the shifts of H4α and H4β were found an exception to the rule that equatorial protons in six-membered rings are generally deshielded as compared to their axial counterparts, 1.16 ppm for H4α and 1.62 ppm for H4β.[292]

In their investigation of unnaturally configured 13-epi steroids, Fielding et al. sought for an easy distinction between both configurations.[193] They found the 18-methyl chemical shift indicative, 14 ppm for the 13β normal steroid versus 25 ppm for the 13α-epiandrosterone, which was interpreted as a release from the steric pressure two gauche γ-interactions in the normal configuration. For conformational analysis of the D-ring, couplings were only divided into large and small values, which proved sufficient for the investigation. While in regular isomers, the D-ring may occupy a continuum of states, the 13β,14α half-chair conformation often represents best the solution phase structure.[193] In the six 13-episteroid analyzed, where the

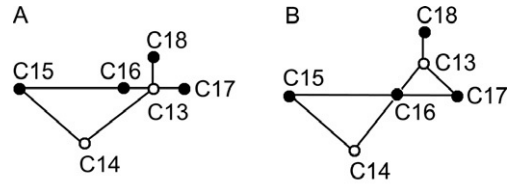

Figure 3.19 D-ring conformations, (A) and (B) for conventional 13β steroids, the 13β,14α half-chair, B, often represents best the solution conformation. For 13-epi steroids, the formulae may be mirror-imaged along a horizontal plane.

C/C-ring junction is *cis*, four steroids were found in the 13α,14β half-chair form, one was found to possess 17β-envelope and one 16β-envelope conformation. The ring geometries of the normal steroids are illustrated in Fig. 3.19, cf. also Fig. 3.15. The corresponding epigeometries can be obtained by constructing the mirror image with respect to a horizontal plane. The main technique used for the determination of coupling constants in that study was a 1D TOCSY; for the overall signal assignment, gradient versions of the COSY, NOESY and HSQC experiments were employed.

A further investigation of the morpholinyl steroidal compounds[293] showed that the configuration of 2-alkyl-morpholines could be determined. Since the 2-alkyl substituent at the morpholinyl moieties is always equatorial and the morpholine perpendicular to the steroid plane as was found from energy minimization calculations, the ***R***-configuration forces carbon C3 of the morpholine in a position above the β-face of the steroid and experiences thus a steric hindrance resulting in an upfield shift, 51 ppm (***R***) and 57 ppm (***S***). Carbon C5, in contrast, is situated above the β-face for the ***S***-configuration and is thus exposed to sterical compression leading again to an upfield shift, 45 ppm (***S***) versus 52 ppm (***R***). It was suggested that the steroid moiety served as chiral adjunct in analogy to Mosher's ester method.[293]

In 2007, the distinction of the absolute configuration of spirostanes and spirosolane glycosides among them disogenin, solasodine and tomatidine was studied.[294] The configuration at C22 could be distinguished by the chemical shifts of C23 and C26 laying around 7 and 3 ppm apart for C23 and C26, respectively. The difference was tentatively due to the steric interactions for the protons of C23 in the 22 (***S***) form. The study is an example for the solution of a contemporary stereochemical question by methods seemingly simple according to modern standards. However, the method is robust and accurate and could thus be applied easily for quality control

of pharmaceuticals. An epimerization was investigated very recently.[295] The acid-catalyzed conversion of the C17 stereocentre of 14β-hydroxy-20-ketopregnane glycosides was recognized by two distinct correlations in the 2D H—H ROESY, cf. Fig. 3.20. While the 17β-isomer displayed a ROE between H12α and H17α, the ROE was replaced by one from H12α to H16α, which was interpreted in terms of the 17α isomer. Configurations of 14 and 8 α- and β-3-methoxy-estra-1,3,5(10)-triene-7,17-diols are exemplarily illustrated in Fig. 3.21.

So far, we have described quantitative structure elucidation by using only scalar couplings and their dihedral dependence according to Karplus or Haasnoot.[124,125] Dipolar interactions appeared only in a qualitative manner. Nevertheless, NOEs are widely exploited quantitatively in biomolecular NMR.[296] Their use in the steroid field shall be discussed on the basis of an illustrative example.[297] It is known that conformational mobility, which steroids or parts thereof possess, demonstrates additional contribution of the scalar relaxation mechanism between indirectly or scalarly bound protons leading to an underestimation of NOE values in distance determinations.[298,299] In case of conformational averaging, the value of the scalar coupling $^3J_{HH}$ follows Eq. (3.1)

$$^3J_{HH}^{obs} = \sum P_i \, ^3J_{HH}^{i} \qquad [3.1]$$

where P_i is the population of the ith conformer, which introduces an uncertainty in the structure determination, if the populations are unknown. The source of uncertainty in NOE distance estimation arises from the scalar relaxation mechanism when the usual reference method according to Eq. (3.2) is used.

$$r_{ij} = r^{ref}\left(\frac{s^{ref}}{s_{ij}}\right)^{1/6} \qquad [3.2]$$

where r_{ij} is the internuclear distance, s^{ref} the NOE effect observed for a known reference distance r^{ref} and s_{ij} the NOE of the nuclei in question.[300] The equation is based on the assumption that the rotational correlation times τ_c^{ij} and τ_c^{ref} are equal, which is an approximation but strictly true only for spherical molecules.[301] For anisotropic molecules, Eq. (3.2) has to be corrected for the correlation times, yielding Eq. (3.3).

$$r_{ij} = r^{ref}\left(\frac{\tau_c^{ij}}{\tau_c^{ref}}\frac{s^{ref}}{s_{ij}}\right)^{1/6} \qquad [3.3]$$

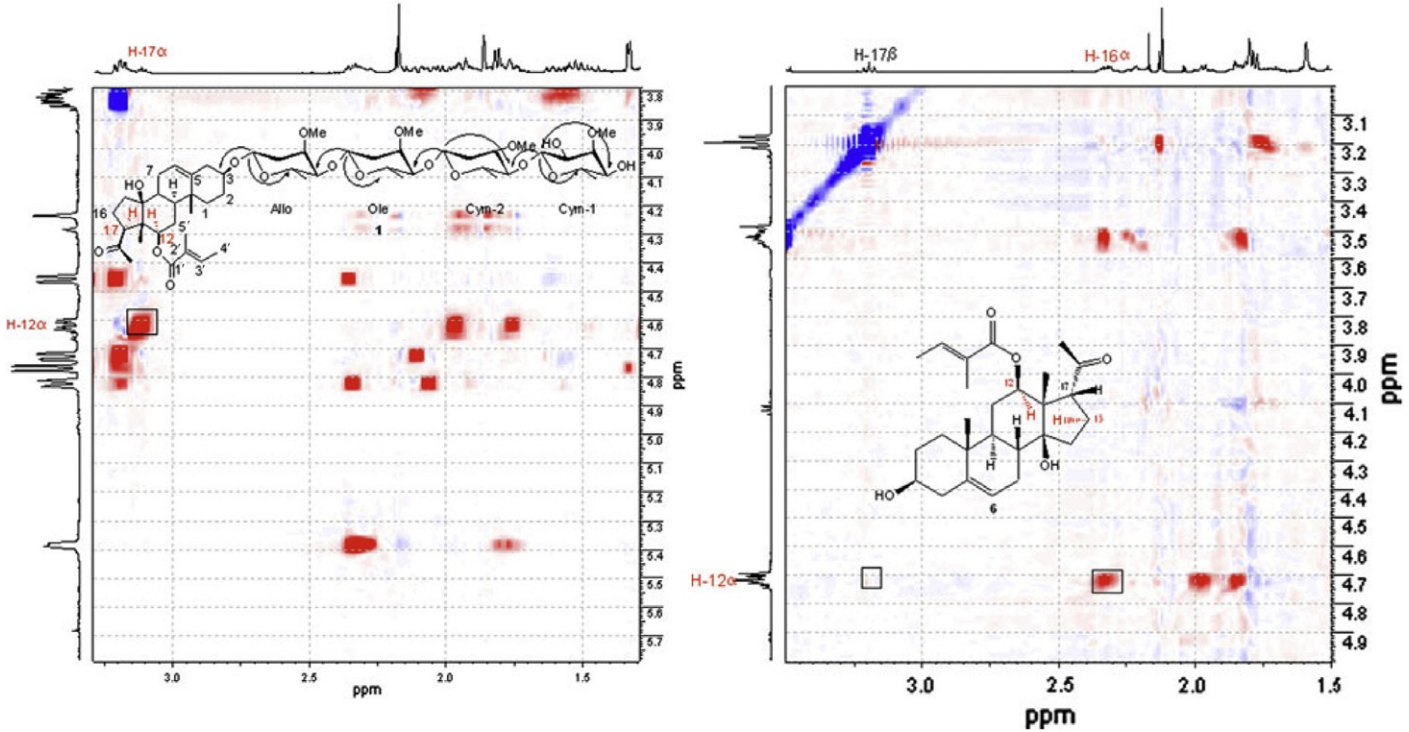

Figure 3.20 H—H ROESY spectra of 17β- and 17α-epimers of 14β-hydroxy-20-ketopregnanes, glycone and aglycone, in $CDCl_3$ at 500 MHz. Both isomers can be distinguished by their ROE correlations that are marked in the spectra according to Garcia et al.[295] The 17β-isomer spectrum is presented to the left, the 17α-isomer to the right. With kind permission from Springer Science + Business Media: Ref. 295, Figure 1 and 4.

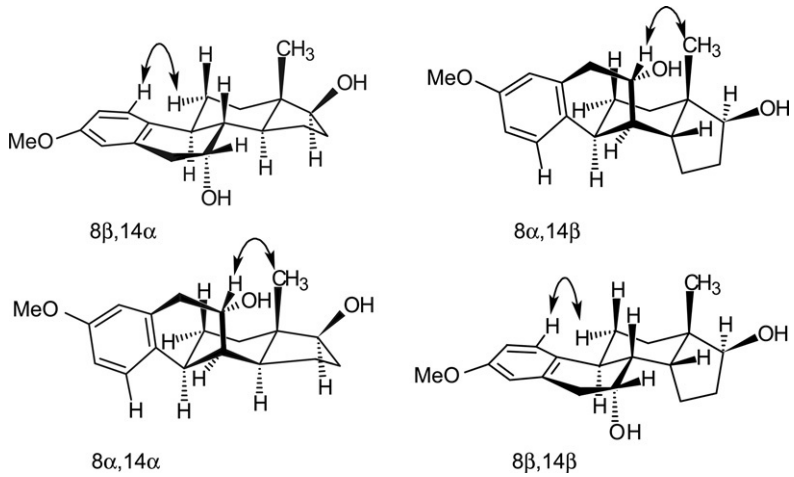

Figure 3.21 Steric arrangements of 3-methoxy-estra-1,3,5(10)-triene-7,17-diols with respect to the H8 and H14 protons. The arrows point to specific NOEs allowing the most straightforward distinction of the isomers.

Assuming that the vector of the reference distance r^{ref} is oriented orthogonal to the main inertial axis of the molecule and the measured vector parallel to that axis, the relative error of the r_{ij} determination cannot exceed 26%.[297] Nevertheless, it increases with increasing anisotropy, thus for steroids that are, in fact, anisotropic. Yet, estimation showed that the error for steroids should be around 18%. It was hence suggested by Selivanov et al.[297] to use Eq. (3.3) for steroids.

They carried out distance calculations using both models using a H—H distance of 1.77 Å for C7 and a reference angle of 80°. It was then demonstrated on 17β-acetoxy-3-methoxy-6-oxa-8-isoestra-1,3,5(10)-triene that the axially symmetric model, thus following Eq. (3.3), leads to a better agreement with data obtained from X-ray crystallography. In the same study, signals in the NOE spectrum that originated from exchange were analyzed. Two conformers of ring C were detected for 3-methoxy-D-homo-6-oxa-8,14-isoestra-1,3,5(10)-triene. Form A was interpreted as a conformation with H12α and H11β equatorial, thus staggered, while form B favoured H11β in an axial and H12β in an equatorial position, thus eclipsed, cf. Fig. 3.22. Form A was found the preferred conformer, 2:1 at 30°C. The interpretation was derived from the temperature dependence of the ratio of the integrals of cross and diagonal peaks in the NOESY spectrum of that compound, under the conditions of rapid ring conversion. Under the

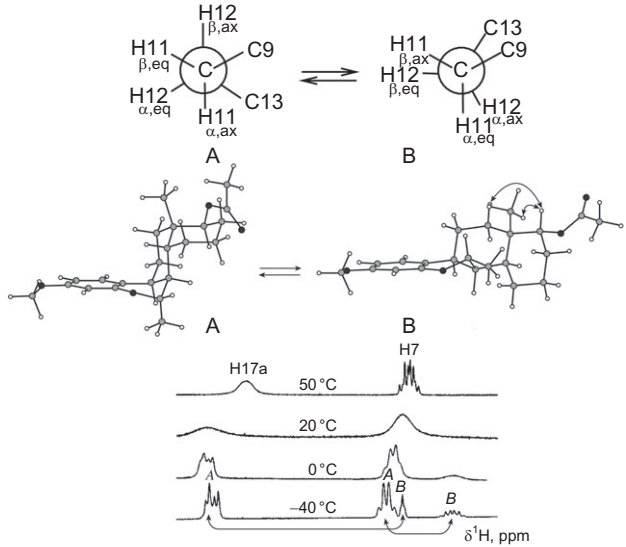

Figure 3.22 Newman projections (top) of the C-ring conformations of a non-naturally configured, conformationally flexible 6-oxasteroid analogue, form A being the energetically more stable conformation. Conformers of the steroid analogue (middle). 1D ^{1}H NMR spectra of the temperature-dependent equilibrium between conformer A and B (bottom). With kind permission from Springer Science + Business Media: Refv. 297, Figures 7 and 8.

conditions of exchange, the scalar relaxation mechanism interferes with the dipolar mechanism; hence distance determinations were not feasible.

The application of NOE spectroscopy together with Eq. (3.2) and coupling constant analysis to the conformation of 7α-methyl-8α-oestrogen analogues revealed an inversion equilibrium of ring B of these compounds.[302] The B-ring was found to assume boat shape. The conformational equilibrium depended on the type of atom in position 6. In case of oxygen at position 6, the population of the conformer with pseudoaxial orientation of the 7α-methyl group decreased as compared to its carbon counterpart, from a ratio of 80:20 to 64:36. The Newman projections of the —C6—C7— fragment for the two conformers are given in Fig. 3.23.

3.1.6 Elucidation of intermolecular properties—Diffusion ordered spectroscopy

Another aspect of structure analysis leads away from the individual molecule and aims at the investigation of intermolecular association or interactions such as cluster formation or hydrogen bonding. Upon association of

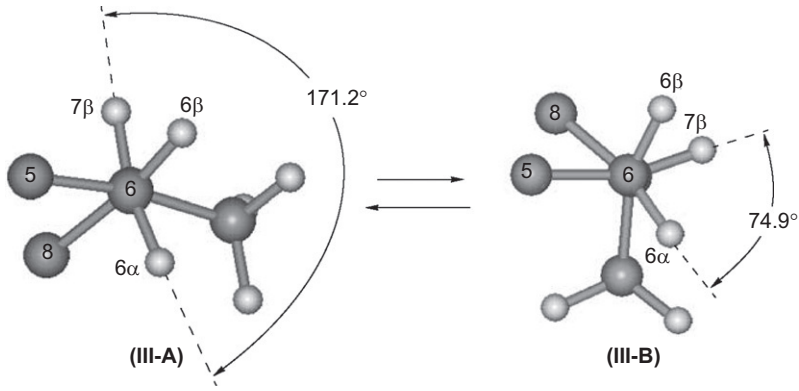

Figure 3.23 Newman projections of the ethane fragment —C6H$_2$—C7H(Me)— and dihedral angles θ(H6αH7β) in the two conformers, III-A and III-B, of the 7α-methyl-8α-oestrogen analogues. With kind permission from Springer Science + Business Media: Ref. 302, Figure 5.

molecules, their diffusion behaviour changes, that is the larger the aggregates the slower their self-diffusion becomes. Determining thus the diffusion rate of a compound, the presence of clustering or hydrogen bonding can be recognized. The application of gradient-enhanced or diffusion-edited spectroscopy to this purpose has been described.[303] In the field of steroids, a series of 12 compounds was investigated with respect to their diffusion behaviour and hydrogen bond formation.[304] The compounds, their molecular weights, molar volumes and diffusion rates are presented in Table 3.5. Only for progesterone and dehydroepiandrosterone acetate, no hydrogen bonding was found from plots of the diffusion coefficients versus molecular weight or molar volume. As can be seen from Table 3.5, the two non-hydrogen bond forming compounds exhibited faster diffusion behaviour. Yet, it was noted that from the diffusion measurements, strictly speaking, only the occurrence of clusters could be deduced. Its cause, that is, hydrogen bonding, was proven by other spectroscopic methods.[304]

It was our intention to show the reader that the investigation of the structure of steroidal compounds was a busy field and that research in this direction still continues. Yet, a significant decrease in the number of original work is due to the decrease in pharmaceutical interest. However, as described in the experimental technique-oriented paragraph, steroids are still being used as models for NMR method development. In a later section, the most recent NMR methodological studies using steroids shall be presented in light of recent progresses in NMR spectroscopy. Prior to doing that, we

Table 3.5 Diffusion rates of steroidal compounds as determined by pulsed-field gradient spectroscopy in methanol-d_3: deuteriumoxide 98:2 at 283 K and 10 mM sample concentrations[304]

Steroid	MW (Da)	Molar V_{calc} ($10^{-28}m^3$)	D_{obs} (10^{-10} m^2/s)
Progesterone (**4**)	314	2.25	6.98
Estrone (**14**)	270	1.81	6.29
Cortisone (**15**)	360	2.32	5.58
Hydrocortisone	362	2.36	5.18
Cholic acid (**3**)	408	2.84	4.54
Androsterone (**17**)	290	2.12	5.85
Norethisterone (**22**)	298	2.07	5.72
Dehydroepiandrosterone acetate	330	2.28	6.81
11α-Hydroxyprogesterone	330	2.28	5.38
Corticosterone	346	2.33	5.40
Prednisolone acetate	402	2.61	5.17
Cholic acid methylester	422	2.96	4.61

will report on two NMR applications within the chemical and pharmaceutical industry. Within the first study, NMR is used for the determination of host–guest binding properties, and secondly, NMR is used as hyphenated technology for impurity profiling.

4. APPLIED NMR METHODOLOGY IN STEROID ANALYSIS

Steroids and NMR spectroscopy were linked to each other by a rubber band, sometimes closer related and sometimes progressing separately as can be drawn as a conclusion from the previous section.

The 1950s and 1960s saw the golden age of pharmaceutical steroid research, NMR only appeared on the scene of structure investigation,[305] still far away from today's nearly automated capabilities. When, in the 1980s, NMR began to deploy its forces towards full elucidation of a molecule's three-dimensional structure without further help from other technologies and demonstrated its power in the field of steroids, steroid research had shrunk from a major general pharmaceutical business into separate smaller,

yet still important, specialty areas such as anticonception and inflammation, cf. Table 3.2.

Steroidal derivatives from natural sources, such as plants, marine or insect organisms,[306,307] still represent a field of activity of structure elucidation, nurtured by the interest in biological functions[308] or in search of new medicines[309,310] or adverse side effects.[311] Since numerous steroidal compounds are still marketed drugs, cf. Table 3.2, new formulations, new combinations or even novel molecular derivatives are developed; NMR plays a pivotal role in the structure elucidation, impurity profiling[312,313] and metabolite identification[314] as well as content determination in quantitative analyses.[315]

The next sections will deal with the applications of NMR methodology.

4.1. Host–guest steroid chemistry

The type and strength of binding to a target protein usually determines to a large extent the mode of action and the efficacy of a drug. This is certainly the case for steroidal compounds. Association or complex forming can also occur for any two compounds, provided complementary binding sites, for example, acetic acid dimers or Watson–Crick hydrogen bonded base pairs. While a target–ligand interaction is usually highly specific, small molecule interactions can be less specific and also weaker. Among the well-known complex forming or host structures, there are cyclodextrins (CDs), crown-ethers, cryptands and others.[316] The host–guest complex was the basic idea for a specific application in anaesthesia. During surgical procedures, neuromuscular blocking drugs are often used. It is sometimes desirable to finish the patient's neuromuscular block and thus paralysis prematurely, for example, at the end of the surgery. Following the current practice, an acetylcholinesterase inhibitor is administered to this purpose. However, these inhibitors may cause cardiovascular side effects.

For one of the neuromuscular blocking agents, rocuronium bromide (**25**), an aminosteroid, the complexation idea was pursued to find an alternative means to acetylcholinesterase inhibitors. Therefore, CDs were chosen as suitable compounds to reverse the muscle relaxation.[317,318] These cyclic oligosaccharides consist of a ring of α-1,4 linked D-glucosyl residues containing six, seven or eight CD units and are referred to as α-, β- and γ-CDs. The tertiary structure resembles a hollow, truncated cone. The smaller opening is often referred to as the primary side, and the larger side as the secondary side. Taking advantage of the central cavity of low polarity, CDs act as a host for the encapsulation of small molecules.[316,319] In contrast

to the low micromolar to nanomolar binding affinities of protein–ligand interactions, CDs form weaker complexes. A thorough review on CDs and their investigation with NMR was written by Schneider et al.[319]

Since for drug purposes the binding affinity of natural CDs is not strong enough, γ-dextrins were modified systematically by chemical synthesis and their association constants towards rocuronium bromide determined.[320,321]

In a first methodological study on the affinity determination of rocuronium bromide and CDs, Cameron and Fielding investigated the use of association constant, K_a, determination by single-point diffusion measurements as compared to the NMR titration method.[322] While for an equilibrium slow on the spectroscopic time scale distinct signals for all species may be observed, they appear as average observables weighted by the mole fractions for fast exchanging species.[323] For NMR spectroscopy, the signals of slowly exchanging species can be directly integrated, whereas the analysis of fast exchanging species follows Eqs. (3.4)–(3.6).

$$O_{obs} = \alpha_L O_L + \beta_{compl} O_{compl} \quad [3.4]$$

$$\beta_{compl} = \frac{O_L - O_{obs}}{O_L - O_{compl}} \quad [3.5]$$

where the observable O may be the chemical shift, coupling constant or diffusion coefficient for the ligand L, the complex, compl, and the actual observed value, obs. The actual mole fractions are labelled α and β. Usually, the observable of the completely complexed species cannot be detected and is obtained through parameter fitting of titration data. In case of diffusion experiments, it is generally assumed that the diffusion coefficient D, in the following referred to as diffusion rate since $[D] = m^2/s$, of the complex is equal to the receptor or host diffusion rate, since the receptor is usually a macromolecule. Substitution of Eq. (3.5) thus leads to Eq. (3.6).

$$K_a = \frac{\beta_{compl}}{\left(1 - \beta_{compl}\right)\left([R]_0 - \beta_{compl}[L]_0\right)} \quad [3.6]$$

With total concentrations of the receptor or host and ligand or guest $[R]_0$ and $[L]_0$, respectively. The association constant can hence be derived from a single-point measurement.

The study by Cameron and Fielding found that for cholic acid and β-CD the assumption that the diffusion rate varied as a function of complexation, thus the assumption $D_{compl} = D_R$ did not hold true for the molecular sizes of

the host–guest system in question.[322] In case of modest K_a values, they also observed that D_L dominated D_{obs} in the concentration range best suitable for NMR observations. When taking into account the dependence of the observed diffusion rate on the complexation, a K_a of 5900 ± 800 1/M was obtained for cholic acid and β-CD.[322]

The complex formation of bile acids with CDs was studied earlier by NMR[324] and calorimetry.[325] Selected complexation data from these studies are collected in Table 3.6 together with the rocuronium bromide binding parameters.[326]

In the studies preceding the one on rocuronium bromide and sugammadex, several bile acids were observed to generally form 1:1 complexes with β- and γ-CDs. Hydrophobic interactions were found as the main driving forces for association. Analysis of the complexation-induced

Table 3.6 Complexation constants K_a of steroids with cyclodextrins as derived from NMR and isothermal calorimetry[324–326]

Steroid	CD	K_a (1/M)	Reference
Cholate (**3**)	β	4.1×10^3	325
Deoxycholate	β	3.6×10^3	325
Chenodeoxycholate	β	1.8×10^5	325
Ursodeoxycholate	β	7.8×10^5	325
Lithocholate	β	1.9×10^6	325
Cholate	β	1488	324
	γ	362	324
Glycocholate	β	336	324
	γ	210	324
Glycochenodeoxycholate	β	371	324
	γ	239	324
Lithocholate	β	88	324
Rocuronium bromide (**25**)	β	$3.3 \pm 0.5 \times 10^3$	326
	γ	$1.8 \pm 0.2 \times 10^4$	326
	Sugammadex[a]	6×10^4 (NMR) 1.8×10^7 (ITC)	326
	Chemically modified γ-cyclodextrin[a]	2.0×10^6 and 1.3×10^3 for a second complex with 2:1 stoichiometry	326

[a]For chemical structure cf. Figure 3.24.

chemical shift (CIS) led to the interpretation that bile acid anions could only penetrate the β-CD cavity via the hydrophilic opening. Additional interactions of the cavity with ring C and D of the steroid were observed. For the larger γ-CDs, it was concluded that the bile acids can enter further into the cavity, while the side chain protrudes from the larger end. The CIS values of the methyl protons H18, H19 and H21 were most affected and thus most informative. The protons H12, H3 and H7 were of further help. Adding to the structural results of the NMR titration study,[324] the findings were supported by ROESY investigations.[327–329]

Cameron and Fielding reported further on the investigation of the thermodynamics and geometries of binding,[330] cf. also Table 3.7. While they detected 1:1 stoichiometry for almost all complexes, one synthetically modified γ-CD containing a para-thiophenyl carboxylate substituent at each glucosyl residue allowed a second rocuronium bromide to enter its cavity. The strong association complexes could not be quantified by NMR, since the necessary concentration ratios were outside the range of detection for NMR. However, isothermal microcalorimetry showed a biphasic behaviour. The interpretation in terms of a second weaker binding was then supported again by NMR, as a new set of signals occurred, which are attributed to the steroid in a 2:1 complex.[318] The increase in binding affinity for the pair rocuronium bromide–sugammadex resulted in a slowdown of the exchange rate, such that for this complex, distinct signals were observed at room temperature, cf. Fig. 3.24.[326]

Table 3.7 Molecular weights for rocuronium bromide, CD inclusion complexes based on 1:1 stoichiometry, and diffusion rates[330]

Molecule	Mass (Da)	K_a (l mol^{-1})	D (10^6 cm^2 s^{-1})
Rocuronium bromide (Roc)	610		4.09 ± 0.04
β-CD	1135		3.23 ± 0.07
γ-CD	1297		3.09 ± 0.05
Sugammadex	2178		2.45 ± 0.03
Roc@β-CD	1745	2600 ± 600	2.74 ± 0.07
Roc@γ-CD	1907	6000 ± 1000	2.61 ± 0.05
Roc@sugammadex	2685	$> 10^6$	2.30 ± 0.07

The parameters were determined after mixing of stock solutions containing 0.1 M phosphate-buffered deuteriumoxide at pH 7.5. The final sample concentrations were 0.5 mM each.

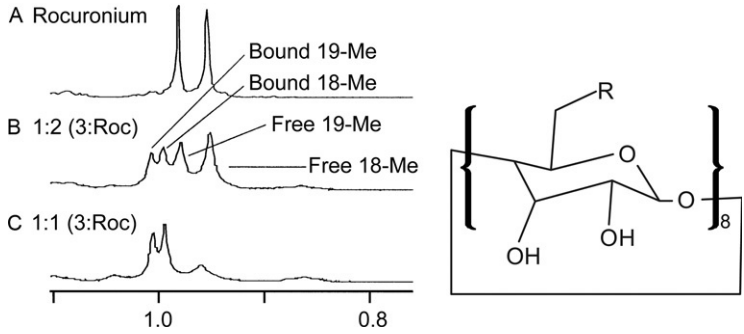

Figure 3.24 1D ^{1}H NMR of rocuronium bromide (**25**) and sugammadex at different molar ratios and structures of the two compounds.[318] The repeating unit of sugammadex is given on the right, where R = $S(CH_2)_2$ CO_2Na for sugammadex and R = p-S-C_6H_4-CO_2Na for the γ-CD in Table 3.6. The NMR spectra show signals of rocuronium bromide (**25**), (A), superposition of signals of free and bound species (B), and at equimolar ratio, only signals of bound rocuronium bromide, (C). The association equilibrium is thus in slow exchange. Reprinted (adapted) with permission from Cameron et al.[318] Copyright 2002 American Chemical Society.

For the elucidation of the complex geometry, CIS mapping was used as well as mapping of NOE or ROE contacts. Here, larger CIS and NOE/ROE intensity values were interpreted in terms of closer proximity and thus stronger interactions. If equatorial protons were more affected than axial ones, an edge-on arrangement of the steroid could be assumed or inversely a face-on geometry. However, the investigation of rocuronium bromide and a metabolite of another aminosteroid analogue, vencuronium bromide, proved difficult. For rocuronium bromide, intermolecular NOE correlations to ring A– C were found for β-CD, which was in agreement to the CIS values observed. Yet, no consistent picture could be obtained whether edge-on or face-on was the preferred orientation. For the γ-CD, the fit seemed looser since less pronounced CIS values were obtained, in general, <0.1 ppm versus 0.1–0.2 ppm for β-CD. The data suggested that ring B of the steroid occupied the centre of the cavity, but the findings could not be supported by NOEs due to the poor spectral dispersion at 400 MHz. For sugammadex, high CIS values were observed, larger than 0.1 ppm up to 0.31 ppm for H17α. But again due to the poor spectral resolution, no discernable NOEs could be used for structure elucidation. The findings were interpreted in terms of the steroid free rotation inside the CD cavity.[326] The vencuronium metabolite proved analogously difficult. Data suggested that binding to the secondary face of the β-CD took place, ring B and C were

buried inside the cavity of γ-CD and the signals of sugammadex could not be interpreted due to the broad resonances. Despite the NMR difficulties to overcome, the structure of the host–guest inclusion complex was determined. This structure obtained from X-ray crystallography is shown in Fig. 3.25.

Cameron and Fielding further investigated the diffusion behaviour of rocuronium bromide complexes.[330] The complexes displayed up to 15% lower diffusion rates than those of the free β- and γ-CDs alone. For the rocuronium bromide–sugammadex complex, a difference of only 6% and, for another modified but weaker complex forming γ-CD, 9% difference were observed. When the molecular masses were plotted against the determined diffusion rates, that is, D versus $1/(\mathrm{MW})^3$, a linear relation was obtained, as would be expected from the Stokes–Einstein equation. This finding independently confirmed the 1:1 complex stoichiometry.[330] The

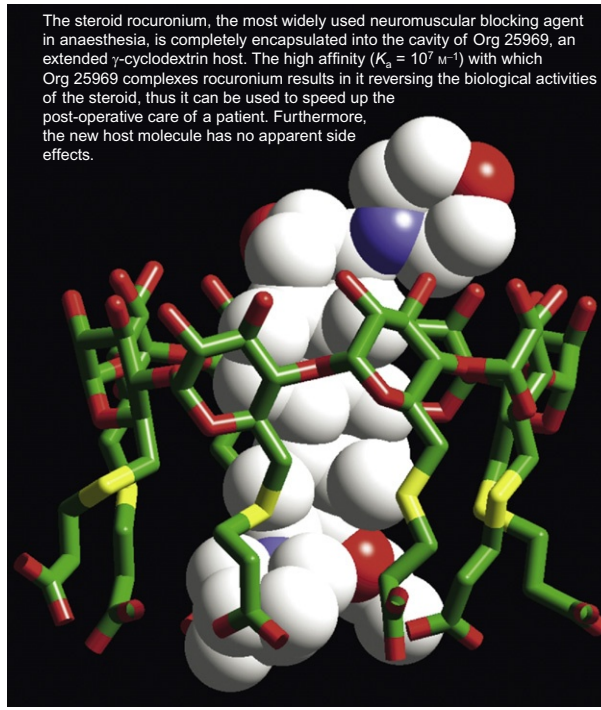

Figure 3.25 Structure of the inclusion complex rocuronium and sugammadex as revealed by X-ray crystallography. Reprinted with permission from Bom et al.[317] Copyright 2002 John Wiley & Sons Ltd.

diffusion data and the molecular masses for the compounds and complexes under investigation are given in Table 3.7. Further diffusion rates of steroids are collected in Table 3.5 following reference.[304]

Rocuronium bromide and sugammadex are both drugs, marketed as Zemeron or Esmeron and Bridion, respectively.

4.2. Impurity profiling

Impurity profiling was and is an important issue within the pharmaceutical industry.[331–333] Not only require regulatory authorities a statement of the presence and the kind of compounds other than the active pharmaceutical ingredient in drug substance or drug product but also the quantity and toxicity need to be known. Depending on the amount of such an impurity, either solely the quantity has to be announced or the identity must be proven or *de novo* elucidated. Impurities are categorized into solvents, related impurities and unrelated impurities such as salts or catalysts. The knowledge of the impurity profile is evenly important for the registration of a drug but also to have complete control over the manufacturing process, in particular, if the process drifts out of specifications or is changed totally. An impurity profile is subject to changes in the synthetic route, reaction conditions, source and quality of starting materials, reagents and solvents. The profile further depends on synthesis, purification steps, conditions of crystallization, drying, distillation and storage of bulk dry materials.[334] The same applies to drug formulations. While in later stages, that is, in production, the analytical instruments are mostly high-pressure liquid chromatography coupled to UV detection, since the data obtained are sufficient for substance identification and quantification, while a new peak indicates a deviation from the normal process. Yet, when in the development phase the synthesis process is evaluated, the proof of structure for an unknown compound often proceeded via re-synthesis. Since the structure characterization methods have significantly increased in sensitivity, impurities may also be elucidated using purely spectroscopic techniques preceded by isolation of the product. With the successful coupling of HPLC and NMR spectroscopy,[313,335] its modern extension by MS or solid phase extraction (SPE) to HPLC–MS–NMR or HPLC–SPE–NMR[336,337] in several variants, the capabilities to elucidate impurities, degradants from light or temperature exposure and metabolites at the 0.1 % level have become not only feasible but also fast and efficient.[338]

As a so-called hyphenated technique, NMR in HPLC–NMR coupling can be applied not only as a detector in analogy to UV or MS but also as the sophisticated spectroscopic tool for structure investigation.

In the area of steroids, applications reach back until 1991 when no hyphenated commercial instrument was yet available.[339] In a sample of ethynodiol diacetate, the *E*/*Z* isomers of 17α-ethynyl-4-oesteren-3β,17-diol-3-acetate-17-(3′-acetoxy-2′-butenoate) were identified. The identification was based on the chemical shifts of the 3′-acetoxygroup, an achievement that cannot be easily attained by any other method. In a sample of pipecuronium bromide, 2′-dehydro-pipecuronium bromide could be identified and quantified. It was found that not only the 16β-methylpiperazylring protons were shifted but also the D-ring signals.[339] The strategy of impurity profiling including LC–NMR in off-line mode was demonstrated.[340] Preparative HPLC was performed prior to NMR analysis such that sufficient amounts of the impurities were available. The process was carried out on two unsaturated impurities contained in allylestrenol (**29**). The distinction between the saturated educt and the unsaturated by-products was easily achieved. As a second example of that study, the impurity profile of mazipredone was recorded and all structures were identified by NMR. In the second half of the 1990s, LC–NMR instruments became commercially available. The chemical and analytical characterization of related organic impurities of steroids has been thoroughly and personally reviewed.[312] Although NMR does not play a role in the profiling, the synthetic routes and the interpretation where side products occur are described for hydrocortisone, prednisolone, ethynodiol diacetate, pipecuronium bromide and ethynylsteroids. Another case study deals with the elucidation of two impurities of norgestrel by combined, that is, chromatographic retention, UV and NMR, methods, the final proof was achieved by assignment of the NMR signals.[334]

4.3. Hyphenated NMR in steroid characterization

Hyphenated NMR was successfully applied to in a recent natural product elucidation study of steroidal compounds.[307] New cardenolides and related compounds were characterized from isolates from a rare firefly. Analyses were performed on partially purified samples. The mixtures contained up to three steroids, and 40 nmol of compound was sufficient for identification by means of capillary NMR spectroscopy (CapNMR). Thus, 13 new steroidal compounds were described.

4.4. NMR for batch release

A pharmaceutical relevant topic, where an NMR application was shown for steroids,[341] is batch approval, which often implies that the impurity profile matches the specifications. Yet, batches of certain compounds are released

through biological testing, heparin, estradurin, the phosphoric acid polyester of and estradiol derivative, are such examples. The biological assay is a duration test with ovarisectomized mice. The test starts on day 3 and continues until the mice reach the state of anoestrus.[341] Starting from ^{31}P spectra, multivariate data analysis, principal component analysis, discriminant projections to latent structures and pattern recognition were performed, yielding a correlation between the biological analyses and the ^{31}P spectra. This correlation demonstrates that NMR combined with mathematical tools is able to substitute the biological testing by a faster and less expensive manner.[341]

4.5. Steroids and isotopes

From an NMR perspective, one might consider the presence of an NMR active nucleus other than the naturally most abundant isotope already as isotopic labelling. Of course, all ^{13}C-related investigations would fall under the same definition as, for example, tritium labelling. The proper features of NMR in conjunction with the interest of medicinal chemistry shall instead be taken as a selection criterion for the choice of isotopes within the steroidal compound reviewed here.

For example, a chlorine substituent would alter the physico-chemical and pharmacological properties of a compound, thus of a steroid but would also be highly attractive for mass spectrometry studies due to the specific isotope pattern of ^{35}Cl and ^{37}Cl. For X-ray crystallography, chlorine would serve as a heavy atom allowing the configurational determination of the molecule. Yet, NMR spectroscopic investigation would only profit in a very limited manner. The isotopes considered in the following will therefore be tritium, ^{3}H, fluorine, ^{19}F, both introduced into the steroid via chemical synthesis, and oxygen, ^{17}O, which is present at natural abundance and after chemical synthesis.

4.5.1 ^{17}O NMR

Due to the unfavourable NMR properties of ^{17}O, such as its very low natural abundance, rather limited availability of ^{17}O starting material[342] and a nuclear spin of $-5/2$, ^{17}O studies remained mostly academic. In addition, the lack of interest from a medicinal chemistry or bioanalytical point of view discouraged the pursuit of ^{17}O NMR on steroids. Among the theoretical use of oxygen NMR, the investigation of structural and electronic effects of the compounds[343] and the configurational analysis of ether and ester substituents[344] were proposed and described for a few examples. As a potentially interesting pharmaceutical application, the study of aggregation of sterols

was suggested.[342] The recording of 1D ^{17}O NMR spectra proved nearly as laborious as the isotope enrichment with water-^{17}O. Solutions between 0.04 and 0.5 M were investigated at approximately 54 MHz field strength; corresponding to 400 MHz proton Larmor frequency, the ^{17}O nucleus allowed the use of relaxation delays of 50–90 μs and acquisition times of 45 ms. Signal-to-noise ratios above 50 were obtained after 100,000 accumulated scans on resonances with a linewidth between 200 and 900 Hz and sometimes more than 1500 Hz, cf. Fig. 3.26. In total, more than 120 steroids were described.[342–344] As a result, chemical shifts and linewidths could be used for the differentiation between hydroxyl containing isomers of steroids, the determination of the degree of substitution and the nature of the substituent, such as alcohols, ethers, ketones, carboxylic acids and esters. Twenty years after these studies, oxygen NMR has not further extended into the field of steroid research. Today's high-resolution mass spectrometry readily provides the molecular formula and thus the presence of oxygen. Higher order MS is able to indicate the position of the oxygen whether being within a substituent or a ring system of the scaffold. The technique only requires a few micrograms of compound in contrast to the sample quantities required for oxygen NMR. Furthermore, the position and stereochemistry of the oxygen substituent can mostly be deduced from NMR experiments other than ^{17}O NMR. A general compilation of ^{17}O NMR spectroscopy can be found in a textbook by Berger et al.[345]

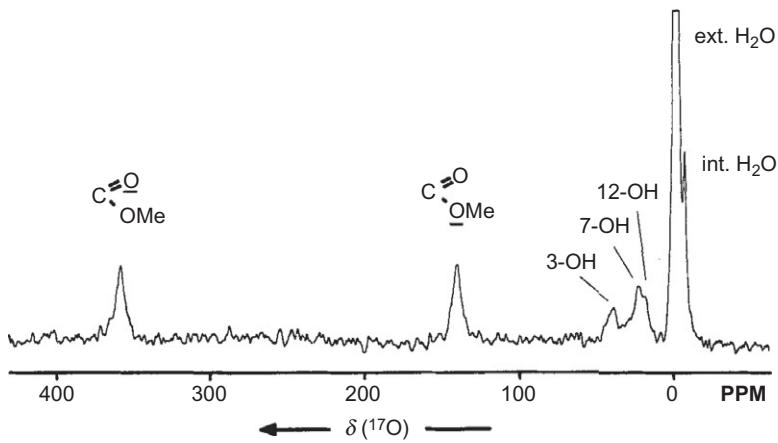

Figure 3.26 1D ^{17}O NMR spectrum of 3α,7α,12α-trihydroxymethylcholate (**26**) of a 0.5-M solution in acetonitrile 75 °C. Reprinted with permission from Kolehmainen et al.[344] Copyright 2011 John Wiley & Sons Ltd.

4.5.2 ^{19}F NMR

In contrast to ^{17}O NMR, fluorine NMR spectroscopy was much more frequently used for steroid structure analysis, although it does not seem to be as widely exploited as it could be.[346] Fluorine NMR profits from the favourable properties of the ^{19}F nucleus, that is, its receptivity being 83% of that of ^{1}H, and from the medicinal chemistry interest,[347,348] that is, improvement in biological activity and physico-chemical properties, such as activity enhancement as in 9α-fluorocortisol[16,349] alterations of the metabolic stability of a compound, changing basicity and lipophilicity and increasing binding affinity. Fluorine may be introduced into a compound during the pharmaceutical lead optimization process to protect the drug against oxidation or dealkylation by cytochrome P450 enzymes.[350] Through change in basicity, the bioavailability can be adjusted. The influence of a fluorine substituent on stereochemistry and electron distribution may exercise positive effects on target–ligand binding. Further, more recent applications of fluorine as a unique probe for metabolite investigations were described pointing out the advantage of the absence of interfering signals, since naturally occurring compounds usually lack fluorine substituents.[351–353] With pharmaceutical, chemical and spectroscopic interest in fluorinated steroids going together, a report on 19-hydroxy and 6β-hydroxymethyl cholestanes fluorinated at positions 3β and 5α was published by Lanet et al. in 1969.[354] Fluorine chemical shifts and proton–fluorine couplings were determined, the couplings related to the equatorial and axial positions of the fluorines. This is remarkable since in 1968, the resolution of proton spectra was, in general, insufficient to deduce the stereochemistry of the steroidal compound purely from NMR spectroscopy. The fluorine substituents caused a deshielding of the protons, which shifted their signals away from the crowded area of the methylene envelope. A systematic investigation on corticosteroids was conducted some 15 years later.[355] The study was carried out on a continuous wave spectrometer operating at 100 MHz ^{1}H Larmor frequency. Chemical shifts and coupling constants were related to the stereochemistry of the steroids. Due to its monoisotopic occurrence, fluorine–carbon couplings are easily observed in ^{13}C spectra that were of outmost importance for the characterization of steroids during the 1970s, cf. above. Therefore, effort to systematically investigate C—F couplings and stereochemistry was undertaken.[235] About the same time, 9α-fluorocortisol was investigated in detail[356] with C—H correlation spectroscopy, demonstrating the determination of J_{HF} and J_{CF} couplings

from the two-dimensional spectra. Not only the size but also the sign of the couplings was determined, the latter from the skew of the correlation signals. A long-range coupling in the order of $^{4}J(\mathrm{H12\beta,F}) = 2$ Hz was reported for proton H12β. Analysis of coupling values yielded the conformation of the A-ring. The findings were interpreted as evidence for an "abnormal" or inverted A-ring conformation, which is consistent with data from X-ray crystallography.

It was not until the 1990s that another systematic study was conducted on fluorinated steroids by Hughes et al. using fluorine detection.[357] From the two-dimensional techniques made widely available during the 1980s, the F—H COSY experiment was applied at a field strength of 500 ^{1}H Larmor frequency such that long-range couplings, ^{4}J and ^{5}J, were revealed. The analysis of the coupling values was compared to the energy-minimized molecular conformations of the 6 mono-, di-, and tri-fluorinated corticosteroids under investigation. Therefrom, all proton and fluorine chemical shifts and splittings could be assigned and detailed structures could be derived.

As in the pharmaceutical industry the need for polymorphism determination arose, solid-state NMR made its entry into chemical analyses. A feasibility study of ^{19}F NMR for proton containing solids was conducted in the mid 1990s,[358] pointing out the technical difficulties of high-power proton decoupling and a narrow dual probe for close proximity of the resonance frequencies of ^{1}H and ^{19}F. Cortisol derivatives were used as examples. Owing to the resolution achieved in the proton-decoupled fluorine spectrum, dipolar dephasing, rotational resonance and spin diffusion could be studied. To the knowledge of the authors of this chapter, ^{19}F solid-state NMR was routinely used at the Organon and later Schering-Plough analytical laboratories in Oss to study polymorphism of small molecule compounds.

The fading pharmaceutical interest in steroid research during the recent decades led to a steady decrease of large-scale NMR spectroscopic studies of steroidal compounds, which holds also true for fluorine NMR. In the development of novel experimental methods, the today well-known structure of the steroidal scaffold may still provide an illustrative model, as was the case in two recent investigations.

A three-dimensional F—H heteronuclear TOCSY filtered/edited experiment was used to characterize the individual steroids from a mixture of four dexamethasone (**23**) derivatives without prior separation.[359] The corresponding spectral cube is presented in Fig. 3.27. Pulse sequences were developed for F—H TOCSY edited H—H TOCSY and F—H TOCSY edited H—C HSQC experiments, which provide sufficient signals for

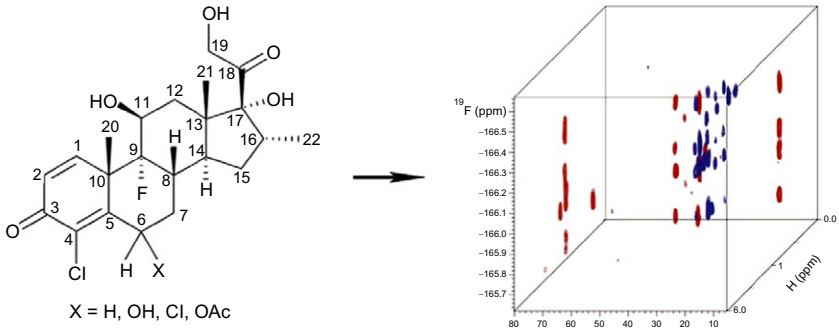

Figure 3.27 3D ^{19}F–^{1}H heteronuclear TOCSY edited, multiplicity edited ^{1}H-^{13}C HSQC. Positive and negative contours are plotted in red and blue, respectively. The spectrum was recorded at 25.0 °C on a 600 MHz spectrometer equipped with a 3-mm ^{1}H-^{19}F {^{1}H-^{19}F/^{13}C} PFG triple-resonance probe and *z*-gradient accessory. Reprinted with permission from Hu et al.[359] Copyright 2008 American Chemical Society.

compound identification. Hu et al., nevertheless, suggest that the experiment should be combined with LC–MS methods to increase confidence. As a drawback, the authors admit that in cases of a single fluorine substituent, which is often the case with steroids, all detectable magnetization stems form a single fluorine nucleus, resulting in a relatively low sensitivity of the experiment. However, the lack of fluorine in biological matrices may render this experiment attractive for metabolic studies.

In the second recent investigation, the use of a series of fluorine correlation spectra such as F—H and H—F HOESY, F—C HMQC was described for steroid configuration assignments.[346] The F—C HMQC for 19,19-difluoro-3β,7β-dihydroxy-androst-5-*en*-17-one (**27**) is exemplarily illustrated in Fig. 3.28, Due to the complexity and signal overlap in the ^{1}H spectra of fluorinated steroids under consideration, fluorine detection provided a superior and elegant manner to unequivocally assign diastereotopic fluorine nuclei and to determine the configuration of the carbon atoms C4 and C5 to which a cyclopropyl substituent was attached. Neither from the synthetic route nor from the molecular modelling could the configuration unequivocally be assigned, cf. Fig. 3.29. The F—H HOESY that was recorded for the purpose of configuration elucidation of the cyclopropyl-substituted steroid is presented in Fig. 3.30. The H—F or F—H HOESY experiments were thus reported as a sensitive and simple experiment for use in structure elucidation, if modern NMR instrumentation is available.

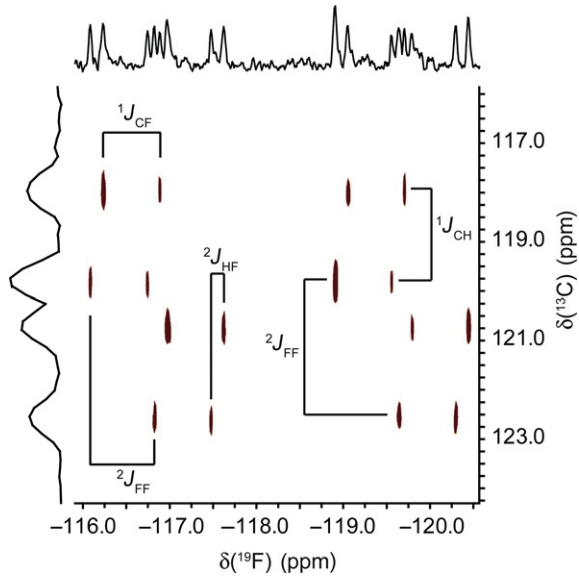

Figure 3.28 F–C HMQC of 19,19-difluoro-3β,7β-dihydroxy-androst-5-*en*-17-one (**27**) in DMSO-d_6 with couplings assigned. Reprinted with permission from Ampt et al.[346] Copyright 2011 John Wiley & Sons Ltd.

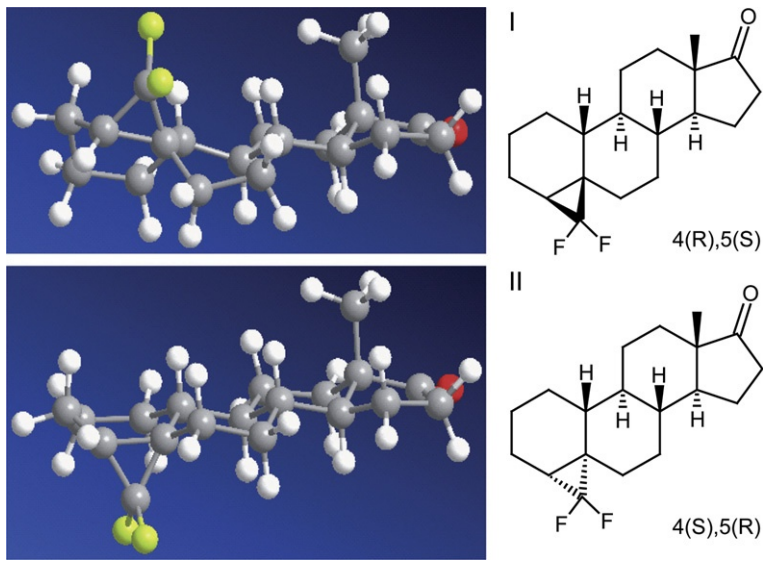

Figure 3.29 Calculated 3D models (left) of the steroids depicted (right). Minimization energy was calculated with ChemBiodraw MM2 force field. (I) 50.5 kcal/mol and (II) 48.5 kcal/mol. Reprinted with permission from Ampt et al.[346] Copyright 2011 John Wiley & Sons Ltd.

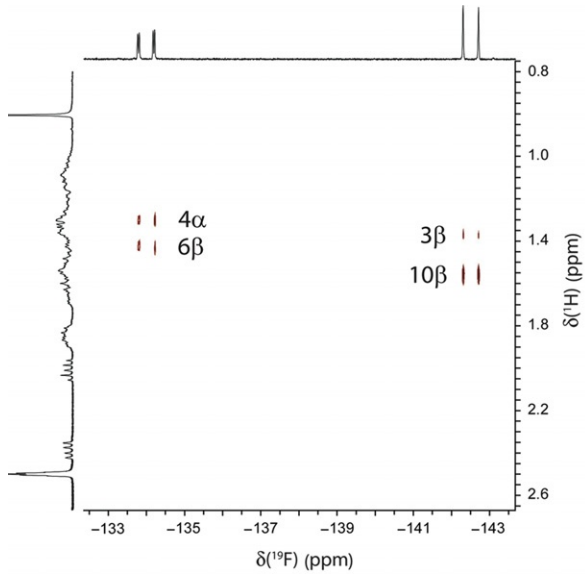

Figure 3.30 Configuration determination by F–H HOESY for the difluoro-cyclopropylandrostane derivative of Figure 3.29. After assignment of the ^{1}H signals to H4, H6 and H10, it can be easily deduced from the HOESY that the fluorine being *trans* to H4 is in close proximity to H10β and H3β, the *cis*-fluorine to H4α and H6β. Therefore, the cyclopropyl moiety is situated above the plane and H4 is oriented below the plan. The other stereocentres are defined by the naturally occurring steroid scaffold, the absolute configuration at C4 and C5 is ***S*** and ***R***, respectively. Reprinted with permission from Ampt et al.[346] Copyright 2011 John Wiley & Sons Ltd.

In the extension of that study, the full exploitation of the F—C HMQC experiment towards magnitude and sign of J_{HF}, J_{CF}, J_{CH} and J_{FF} couplings was demonstrated, cf. also Fig. 3.38, which may be of potential interest in structure analysis using RDCs.

4.5.3 ^{3}H NMR

Much less common to the NMR community, but frequently applied for radio studies, there is tritium as the smallest radioactive nuclide. Tritiated compounds are often used as tracers for metabolic and pharmacokinetic studies. Tritiated steroids, in particular, were encountered in radio-immunoassays and hormone receptor-binding studies, such as the determination of certain steroid receptor levels in human breast tumour biopsies.[360,361] Although substitutes have been found for the test based on tritiated steroids, the pharmaceutical demand clearly nurtured utilization of tritium NMR spectroscopy of steroids. The demand was high enough such that by

1980 a number of multiply labelled steroids were available from commercial sources.[361] The introduction of tritium into a molecule can solely be achieved via synthetic chemistry. There are five main routes to obtain tritiated molecules[361,362]:

1. exchange of hydrogen with $^3H_2$ gas on palladium-cole catalysts, for example, cholesterol and diosgenin;
2. reduction of double bonds with $^3H_2$ gas;
3. exchange with excess ^3H_2O in the presence of catalysts, reagents, etc.;
4. reduction of cabonylgroups with metal hydrides-^{3}H, for example, for bile acids;
5. catalyzed dehydrogenation by $^3H_2$ gas, for example, estradiols, oestrogens.

The questions to be answered by NMR were important with respect to the results of biological and medical studies. Since the label is mostly introduced by substitution reactions, the ratio of labelled versus unlabelled product, that is, the yield of the synthesis, needs to be determined. Secondly, relative quantities are to be measured when labelled material is re-diluted in cold material. The regio- and stereospecificity or at least the chemistry of the labelling reaction has to be elucidated. An example is the α/β ratio of 1-^{3}H androgens that needed quantification prior to their use as substrates in aromatase assays. Last but not least, NMR as a non-destructive method did not require additional sample to be synthesized.

In search of the answers to these questions, the access to the corresponding ^{1}H NMR data and the correlation was found essential.[361] The comparable NMR relevant features of ^{3}H and ^{1}H can be readily recognized from the typical properties. The nuclear spin of both isotopes is ½. The Larmor frequencies of ^{1}H and ^{3}H are 200 MHz and 213 MHz, respectively. The gyromagnetic ratio of ^{3}H is 28.53×10^7 rad s^{-1} T^{-1}. The molar receptivity of tritium is hence 121% relative to ^{1}H. The chemical shifts of both isotopes are almost equal, $\delta(^3H)$ approximately equal to $\delta(^1H)$. Tritium coupling constants can be calculated according to $J(^3H,^1H) = 1.07\, J(^1H,^1H)$ and $J(^3H,^3H) = 1.14\, J(^1H,^3H)$.[362] An example of ^{3}H and ^{3}H{^{1}H} is shown in Fig. 3.31. The chemical shift and coupling parameters determined from the spectrum are collected in Table 3.8.

The first report on ^{3}H NMR of steroids from 1976 addressed the issues of regio- and stereospecificity and the quantitative aspects of labelling.[363] The essential steroid hormones and their labelled isotopomers were investigated, for example, testosterone, progesterone, dehydroepiandrosterone, estrone, estriol and estradiol and their derivatives. Only the lack of observable NOEs

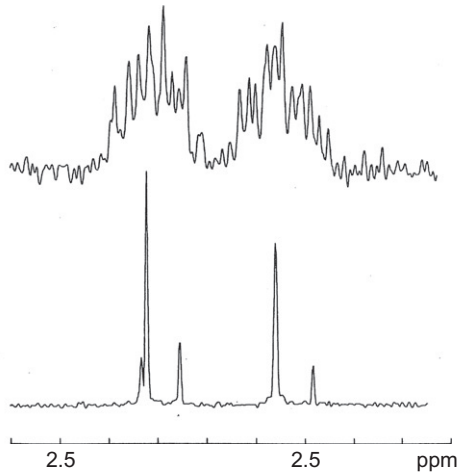

Figure 3.31 1D ^{3}H (top) and $^{3}H\{^{1}H\}$ (bottom) NMR spectrum of 13-ethyl-11-methylene-[16-^{3}H]18,19-dinorandrost-4-ene-17-one (**28**) in $CDCl_3$. Reproduced with permission from Funke et al.[362] Copyright 1983 John Wiley & Sons Ltd.

Table 3.8 NMR parameters of 13-ethyl-11-methylene-[16-^{3}H]18,19-dinorandrost-4-ene-17-one (**28**) extracted from the corresponding 1D ^{3}H NMR spectra in Fig. 3.31[362]

Chem. shift (ppm)[a]	Assignment[b]	Relative intensity[c]	$J(^{3}H,^{3}H)$[d]	$J(^{3}H,^{3}H)$[e]
2.04	16β (16α)	21	15.6	12.4
2.07	16β	34	–	15.0, 12.4
2.29	16α (16β)	21	15.1	9.6
2.33	16α	43	–	15.0, 10.6

[a]In ppm from the ghost reference, determined from the ^{1}H decoupled spectra.
[b]Based on chemical shifts and on $^{3}H—^{3}H$ splitting pattern.
[c]Calculated from (continuously) ^{1}H decoupled spectra.
[d]In Hz, determined from ^{1}H decoupled spectra.
[e]In Hz, estimated from—often degraded—$^{3}H—^{1}H$ splitting pattern.

in $^{3}H\{^{1}H\}$ was erroneously interpreted in terms of radioactive disintegration of tritium. A year later, NOEs were observed within testosterone and estradiol isotopomers,[364] bringing thus observation and expectation back to agreement. In consequence, quantitative ^{3}H NMR experiments require care not to choose pulse sequences that enable NOE signal enhancements through specific decoupling schemes.[364]

A systematic investigation from the steroid pharmaceutical industry described the synthetic tritiation of seven steroids at positions C1, C2, C6, C7,

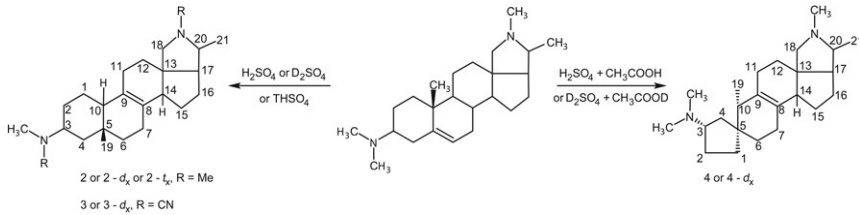

Scheme 3.3 The rearrangement of conessine, middle, to isoconessine, left, or neoconessine, right, via double bond and ring rearrangement according to Frappier et al.[365] The mechanism was elucidated by means of ^{13}C and ^{3}H NMR.

C9 and C16[362] and lists their ^{3}H NMR characteristics. A fundamental application of ^{3}H NMR in combination with ^{13}C NMR was published in 1982.[365] Further to the labelling itself, the mechanism of the backbone rearrangement of aminosteroids was investigated. The rearrangement of conessine to isoconessine and neoconessine via a double-bond rearrangement from C5—C6 to C8—C9 is illustrated in Scheme 3.3. The double-bond migration is followed by a methyl group shift from C10 to C5 yielding the isoform; when followed instead by an A-ring rearrangement to a pentacycle, the neo form of conessine results, cf. Scheme 3.3. The complete rearrangement was found to depend on the reaction conditions.

Radiolabelling studies with tritium are still conducted in the pharmaceutical industry, and might thus be performed for steroids as well. Both the chemistry of labelling and the techniques required for analysis including NMR are well-beaten paths today.

5. COMPUTER-ASSISTED STRUCTURE ELUCIDATION

After the excursion into the isotope and less frequently represented nuclei world in the steroid field, the following section shall deal with steroid data and computerized structure elucidation. The wealth of available steroid structures and their data is huge, such that computational chemistry, chemical shift prediction and basic analytical database research could rely and build on the accessible information. A closer look shall be taken on computation from databasing to automated structure elucidation.

In the beginning, reference spectra of steroids and later tables of reference data as a way to describe spectra were published for ^{1}H and ^{13}C recordings.[2,103,112] When data collections were transformed into computerized databases, algorithms were designed, using shift increments[105] and more

sophisticated models, such as the HOSE code[366] and artificial intelligence.[367,368] While those methods took stereochemistry into account via an empirical manner, that is, through the information contained in the collection of experimental chemical shifts, quantum-mechanical calculation provided a means to incorporate stereochemistry through *ab initio* calculations.[369] The result of these *ab initio* computations is hence determined by the quality of the structural modelling.

The most modern computer programs such as CASE systems are able to analyze a set of NMR data with respect to all chemically reasonable structures selected from all hypothetical structures of a given molecular formula.[370] The computer software would then compare the constraints from spectroscopic data, such as correlation signals with the structure, and exclude the mismatching structures. Finally, ranking of probable structures will be generated according to a set of criteria such as agreement between experimental and predicted ^{1}H or ^{13}C spectra.[371] More details will be presented below.

In summary, common CASE methods may be classified as shown in Table 3.9 following references.[367,372]

It should be noted that CASE is a research field of its own and that the scientific literature extends far beyond the scope of this assay. Therefore, the articles are selected on the grounds of their relevance to steroid research according to the authors' opinion. For recent reviews on the many aspects of computerized spectral interpretation, the reader may consider the given references as starting points.[370,373–375]

5.1. Spectra collections and increments

In 1958 when computers were still rather exotic parts of a laboratory and NMR had just taken off at 40 MHz ^{1}H Larmor frequency, the first collection of chemical shifts of some 48 steroids was published by Shoolery and Rogers,[103] cf. historical section. Only the methyl proton shifts of C18 and C19, called angular methyl groups, were reported and accompanied by some well separate signals, such as H17 for 17-hydroxysteroids, and other, olefinic protons. Nonetheless, figures of the 1D ^{1}H spectra were given in the literature, such that visual comparison could facilitate the identification of steroids from chemical synthesis. The following large collection of steroid chemical shifts was recorded at 60 MHz in 1961 and 1963 by Zuercher.[105,106] About 260 steroids were analyzed with respect to methyl proton shifts and predominant other signals. In line with Shoolery and

Table 3.9 Computer-assisted structure elucidation algorithms and program parts

Method/part of method	Characteristic features	Advantages/disadvantages/critical parameters
1. Database retrieval methods	Chemical shift prediction by finding the atom within the most similar environment	Description of atom, definition of descriptors; quality/diversity/similarity of database
2. Linear additivity relationship	Increment system: addition of chemical shift values according to type and proximity of substituent, for example, ChemDraw, Spectool; based on simple linear equations	Deviations from additivity of increments
3. Empirical modelling		
	3.1 Linear relation of shift to atom-based structural features, e.g. SpecInfo, ACD/CNMR, PredictIt NMR	No comparable reference for exotic molecules/moieties; performs better than neural networks for more exotic fragments[368]
	3.2 Neural network of shift to atom-based structural features	High computation speed after initial training; high accuracy; interactions of substituents are reflected in the training set; dependence on the quality, diversity and similarity of training set; database independent; performs better for chemical shifts closer to an average value
	3.3 Multivariate/statistical data treatment	
4. Quantum-chemical/*ab initio* calculations	Chemical shift calculation based on first principles using a model from molecular modelling, for example, Gaussian, Cosmos	Conformations and their populations need to be known; conformational flexibility
5. Structure generation	Generation of all theoretical structures; constraints from spectra yield hit list according to scoring function	Combinatorial explosion
6. Verification	Often based on ^{1}H and ^{13}C shift prediction	

Rogers, Zuercher recognized the influence of substituents on the chemical shifts of the methyl group nuclei; he also analyzed the additivity of the effects. In consequence, he derived an increment system for the calculation of chemical shifts. For deviations from additivity, steric influences were discussed such as substituent–substituent influences and deformations of the steroid skeleton, for example, for epoxides and double bonds. Despite the effort, the resolution of the spectrometers at that time did not account for unique identification on the grounds of tabulated chemical shifts but would help in the verification of synthetic modifications. In 1969, Reich et al.[107] published the complete ^{13}C chemical shift assignment for 24 steroids; the spectra were recorded at 15.1 MHz ^{13}C Larmor frequency. The larger spectral dispersion at ^{13}C provided sufficiently resolved spectra for the distinction of all signals. For the full assignment, the authors used specific single-frequency and off-resonance proton decoupling as spectroscopic methods. Hydroxyl acetylation and deuteration were applied as chemical methods. Last but not least, the analogy within the series and thus incremental substituent effects were considered for the "unambiguous assignment of all resonances encountered". At those field strengths, it is retrospectively obvious that "the carbon resonances are in general far more informative than proton resonances for structural analysis of steroids". As a forerunner of increment systems, the systematic signal changes were illustrated in chemical shift correlation schemes, cf. Fig. 3.32.

5.2. Chemical shift tables and increment systems

In 1970, 344 steroids were investigated by Bridgeman et al.[223] using proton magnetic resonance at 60 MHz. Androstane, pregnane and estrane derivatives were hydroxylated microbiologically. Further mild oxidation yielded the corresponding ketones. The structure elucidation was reported as starting from the 18- and 19-methylgroups chemical shifts of the ketone. Increment systems for the chemical shifts from the literature or from within the study were successively applied to deduce the structure of the microbiological transformation products. The characteristic features, that is, the chemical shift and the splitting pattern of the hydroxymethylene protons, were described and their spectra illustrated for future structure identification purposes.

Retrospectively, the comparative analysis of data would ultimately lead to the means for the structure elucidation of novel synthetic, metabolized or

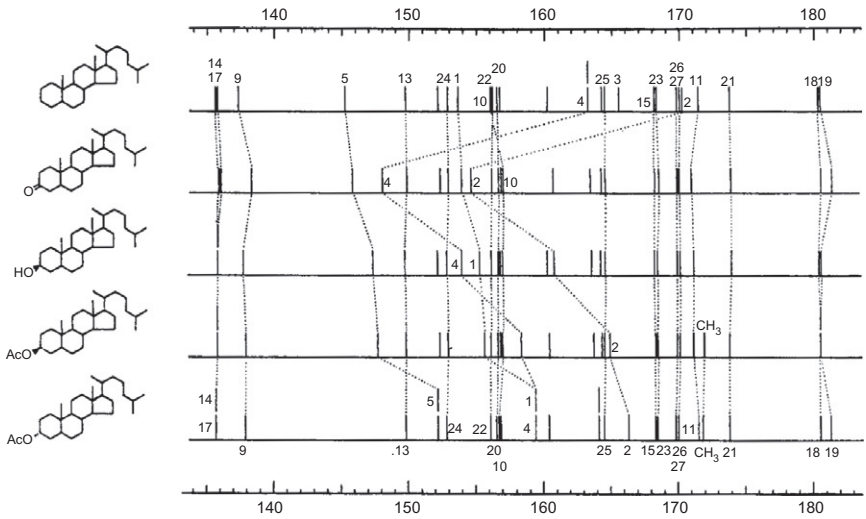

Figure 3.32 Chemical shift correlation schemes to visualize the frequency change upon chemical alteration of the steroidal compound. Compounds from top to down are cholestane, cholestan-3-one, cholestan-3β-yl acetate and cholestan-3α-yl acetate. Reprinted from Reich et al.[107] with permission. Copyright 1969 American Chemical Society.

otherwise obtained steroidal compounds. Yet, NMR at this point was not able to surpass IR or MS spectroscopy in the structural investigations other than the stereochemistry elucidation in the neighbourhood of the angular methyl groups or strongly chemical deshielding substituents, due to the missing resolution in the proton dimension and the lack of correlation experiments. Therefore, the technical advances mostly in the area of field strength fostered ^{13}C NMR for the study of steroids. In 1977, a survey over the ^{13}C chemical shifts of over 400 steroids was issued by Blunt and Stothers,[112] and revisions to previously published assignments were made when appropriate. With the help of this enormous amount of data, the increment system could be further refined, more insight in stereochemical effects on chemical shielding was gained, whose discussion is part of another section of this essay. Another collection of hormonal steroids was contributed by Hickey et al.[241]

Although reference data and spectral assignments continued to appear, cf. the historical section, the 1980s saw a change in the application of structure elucidation by NMR, in general, and for steroids as well. This was caused by the increase in field strength to about 400 MHz and thus increased spectral resolution and sensitivity, the advent of through-space spectroscopy,

such as NOE experiments and correlation techniques, such as C—H heteronuclear and *J*-resolved experiments.

Certainly, the data collections already described here were not the only ones undertaken. A brief overview of a few examples over nearly four decades will be given. Ketosteroids with androstane and cholestane skeleton were investigated using deuterium labelling.[108] The authors noted the isotope shift of the signal from deuterated ^{13}C as compared to proton bearing ^{13}C. Another study used isotope labelling with fluorine for ^{13}C chemical shift assignment, taking advantage of the C—F couplings, especially long-range ones, but recording of ^{19}F data was not considered. However, the spectral comparison of fluorinated and non-fluorinated steroids was applied for the assignment of the non-fluorinated compounds.[376] In 1977, a study was dedicated to the use of ^{13}C shifts for the determination of the glycosidation position of previously assigned aglycones.[377] Further investigations were added during the early 1980s, utilizing the established ^{13}C techniques for D-homoandrostane derivatives,[135] *N*-methylimidazol-substituted sterol esters,[134] methylated sterols[136] and steroids.[137]

5.3. 2D NMR versus stored knowledge

As a result of the remarkable progress of NMR correlation techniques, Duddeck et al.[118] assigned the ^{1}H and ^{13}C signals of about 12 corticosteroids using 2D techniques such as H—H COSY-45, C—H correlation, C—H COLOC and C—C INADEQUATE. While analyzing substituent effects for ^{1}H shielding rules, the authors were able to derive all shifts from the spectroscopic data recorded. In 1990, the ^{1}H chemical shifts of 166 steroidal compounds were published by Kirk et al.[132] as a survey of high-field NMR of the steroid hormones, their hydroxylated derivatives and related compounds. All assignments contained in the data collection were based on the available 2D experiments. Special emphasis was laid on the analysis of proton multiplets. As reference data, 15 fluorinated steroids were described including the fluorine chemical shifts in 1993.[378] Within the section reference data of the journal Magnetic Resonance in Chemistry, the assignments of steroids based on 2D methods continued to appear on a sporadic basis.[379–385] Some reports emphasized the contribution of mass spectrometry along with NMR or were aimed at chemical synthesis and the characterization of their products.[386,387] Other reports focused on pharmaceutical applications[388] or metabolic studies.[389]

In conclusion, the development of 2D correlation spectroscopy and the increased resolution and sensitivity of the NMR spectrometers rendered the

need for extensive data collections and increment tables less and less important for steroid research in the course of time. The tabulated shifts as a form of simple databases not only supported structure identification but were always intended as a tool for structure elucidation of unknowns as shown by the strive for continuously improved shift calculation systems. Still, the effect of substituents especially the effect of stereochemistry on the shielding required an expert knowledge to reliably interpret structure–property relation and thus the observed chemical shift. It is, therefore, obvious that much effort was put into the development of tools to store such knowledge and apply it to structure elucidation in a self-consistent manner. In this respect, the elaborate data collections of the past provided a valuable basis for the development of CASE.

An illustration of the early tools for spectral assignment is depicted in Fig. 3.33 and Tables 3.10–3.12.

5.4. Computerized spectral prediction using increments

The first attempts in the direction of calculated structure analytical tools were indeed the increment system. Starting from a well-assigned chemical shift of a nucleus in a parent compound, the alteration of the chemical shift upon changes in the chemical environment of the nucleus, be it of electronic or steric nature, is decomposed into contributions each of a certain size. The individual contributions are added. In search of a highly complete increment system, Englert et al. and Arnold et al. analyzed more than 1300 spectra of more than 750 9β,10α-retro and 9α,10β-steroids with respect to their 18- and 19-methyl ^{1}H shifts and obtained more than 250 and 290 increments, respectively.[390,392] Their system yielded an average accuracy of 0.01 ppm. Of course, they found deviations from additivity, which they explained in terms of changes in the skeleton geometry, electronic effects, for example, double bonds, and when two substituents would interact with each other. Deviations from the additivity had already been observed earlier for methyl proton shifts and interpreted in terms of conformational changes, for example, for 16β-methyl groups and ring D.[393] Thus, for the calibration of the methyl chemical shift, the skeleton, that is, the type of steroid, had to be known prior to the increment calculation, a problem that would persist for all empirical and semi-empirical predictive methods. Furthermore, it is easily recognized that the incremental calculation of shifts is rather laborious, especially when several structure hypotheses are to be compared. To automate such

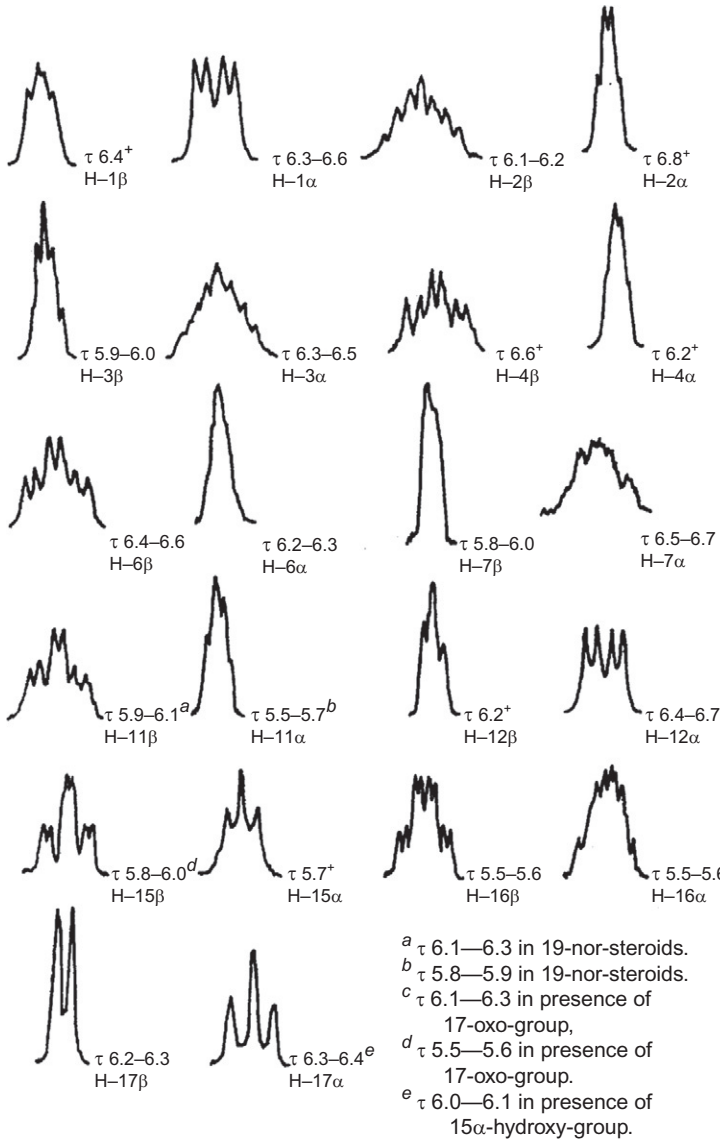

Figure 3.33 Illustration of the development of structure elucidation assistance tools. Graphical spectral representations: Pattern of proton signals geminal to hydroxyl substituents in 5a-steroids. Reprinted from Bridgeman et al.[223] Reproduced by permission of The Royal Society of Chemistry. Tabulated chemical shift values for ^{1}H and ^{13}C,[133] Table 3.10. Increment value tables for ^{1}H, Table 3.11, and for ^{13}C, Table 3.12.[390,391]

Table 3.10 Assignment for ^{13}C and ^{1}H resonances of tibolone ($CDCl_3$), allylestrenol ($CDCl_3$), dexamethasone (DMSO-d_6) and testosterone ($CDCl_3$)[133]

	Tibolone		Allylestrenol		Dexamethasone		Testosterone	
Carbon atom numbering	**δ(^{13}C) (ppm)**	**δ(^{1}H) (ppm)**	**δ(^{13}C) (ppm)**	**δ(^{1}H) (ppm)**	**δ(^{13}C) (ppm)**	**δ(^{1}H) (ppm)**	**δ(^{13}C) (ppm)**	**δ(^{1}H) (ppm)**
1	27.85	1.36 2.45	28.97	1.10 1.98	152.85	7.29 –	35.38	1.70 2.04
2	39.54	2.45 2.45	22.24	1.70 1.37	129.03	6.23 –	33.62	2.34 2.41
3	211.82	– –	25.63	1.93 1.93	185.33	– –	199.70	– –
4	45.37	2.73 2.73	120.08	5.40 –	124.11	6.01 –	123.41	5.74 –
5	125.09	–	140.58	–	167.12	–	171.80	–
6	38.91	1.62 2.27	35.65	2.21 2.01	30.30 2.62	2.32	32.59 2.37	2.27
7	27.51	– 1.86	32.01	0.86 1.69	37.30	1.35 1.77	31.31	1.01 1.85
8	42.14	1.46	41.95	1.28	33.66	2.34	35.34	1.58
9	39.95	1.81	50.40	0.63	101.27	–	53.68	0.93
10	130.42	–	42.11	1.78	47.98	–	38.43	–
11	25.65	2.01 1.22	26.11	1.85 1.21	70.73	4.14 (OH) 5.30	20.39	1.61 1.44
12	33.44	1.78 1.62	31.88	1.32 1.51	35.85	2.13 1.43	36.18	1.09 1.86

Continued

Table 3.10 Assignment for ^{13}C and ^{1}H resonances of tibolone ($CDCl_3$), allylestrenol ($CDCl_3$), dexamethasone (DMSO-d_6) and testosterone ($CDCl_3$)[133]—Cont'd

	Tibolone		Allylestrenol		Dexamethasone		Testosterone	
Carbon atom numbering	**δ(^{13}C) (ppm)**	**δ(^{1}H) (ppm)**	**δ(^{13}C) (ppm)**	**δ(^{1}H) (ppm)**	**δ(^{13}C) (ppm)**	**δ(^{1}H) (ppm)**	**δ(^{13}C) (ppm)**	**δ(^{1}H) (ppm)**
13	47.83	–	46.49	–	47.47	–	42.53	–
14	46.52	1.76	49.72	1.22	43.30	2.10	50.21	0.98
15	22.42	1.67 1.35	23.77	1.57 1.31	32.03	1.06 1.62	23.08	1.63 1.31
16	39.39	2.31 1.99	35.03	1.95 1.58	34.91	– 2.95	29.83	2.08 1.46
17	80.23	– (OH) 1.95	82.57	(OH) 1.61	90.18	(OH) 4.97 –	80.93	3.65 (OH) 1.67
18	13.21	0.88	14.54	0.93	16.69	0.87	10.92	0.80
19	–	–	–	–	22.93	1.49	17.14	1.20
20	87.95	– –	41.88	2.19 2.31	211.20	– –	–	– –
21	74.34	2.59 – –	135.08	6.00 – –	66.30 – –	4.07 4.49 (OH) 4.70	– –	– – –
22	13.41	0.84	119.24	5.16 5.20	15.34	0.78 –	–	– –
$CDCl_3$	77.16	7.27	77.16	7.27			77.16	7.27
DMSO-d_6					39.52	2.50		

For methylene groups, chemical shifts of protons with α-orientation are given first, those with β-orientation below.

Table 3.11 Substituent effects in ppm on ^{1}H chemical shifts of the 18-methyl and 19-methyl protons[390]

Number –	Substituent 5β, 9β, 10α-androstane	Quantity	18-Methyl protons 0.719	19-Methyl protons 0.944
1	1β-CH_3	4	−0.003	0.064
2	1β-OH	4	0.008	0.006
3	1α-OH	1	0.006	0.040
4	1β-O-ac	3	−0.005	0.070
5	1α-O-ac	1	−0.015	0.062
6	1β-Cl	1	0.002	0.314

calculations, computerization had already been described a decade before the investigation of Englert et al. and Arnold et al. The first examples in the steroid field were introduced by Cohen and Rock in 1964.[394] In search of coefficients that could be added or subtracted from the chemical shift of the angular methyl groups, it was recognized that the introduction of a substituent at two positions causes the same change in the chemical shift of the methyl resonance if the two positions are linked by symmetry, that is, C2 and C4 or C6 and C11 in an androstane scaffold. This was found valid for steroids with *trans*-A/B-ring fusion, but not for *cis*-A/B annealing due to symmetry breaking.[395] To solve the problem of deviations from simple additivity, Cohen and Rock used a linear regression model to correlate the data of 292 steroids and to analyze the influence of substituents. The findings were in agreement with those of Zuercher.[105,106]

Since at that time ^{13}C NMR was not restricted to the observation of only very few distinct signals and the ^{13}C shifts were found also less solvent dependent, research was undertaken in ^{13}C increment systems. In 1976, 31 monohydroxylated androstanes, cholestanes and their acetoxy derivatives were thus analyzed.[108] Substituent effects for α, β, γ and δ carbons relative to the hydroxyl groups were derived, all of them interpreted in terms of stereochemical nature. Shift prediction on the basis of the increment system yielded values of 2.0 and 1.0 ppm for α and β carbons, respectively. It was stated that for a rigid conformation the prediction was more reliable since conformational averaging affecting the chemical shifts could be excluded. The predictive systems were tested against dihydroxysteroids in 1977.[396] Again steric interaction, which occurred in 1,2- and 1,3-

Table 3.12 Hydroxyl substituent effects in ppm[391a]

Hydroxyl position	α-Carbon	β-Carbon[b]	γ-Carbon[b,c]
1β	40.1	11.0 (2); 6.2 (10)	−2.2 (3) t; −0.9 (5) t; 0.3 (9) g; −5.5 (19) g
1α	32.7	6.6 (2); 3.7 (10)	−6.7 (3) g; −8.1 (5) g; −7.7 (9) g; 0.7 (19) t
2α	45.7	9.4 (1); 9.4 (3)	−1.5 (4) t; 1.2 (10) t
2β	45.7	6.4 (1); 7.0 (3)	−5.3 (4) g; −0.3 (10)g
3β	44.4	9.3 (2); 9.1 (4)	−1.7 (1) t; −2.2 (5) t
3α	39.6	6.8 (2); 6.7 (4)	−6.5 (1) g; −7.9 (5) g
4α	41.2	9.4 (3); 7.1 (5)	−1.8 (2) t; −6.4 (6) g; 1.3 (10) t
4β	43.2	7.0 (3); 3.0 (5)	−5.3 (2) g; −3.1 (6) g; −0.1 (10) g
5α	26.0	5.2 (4); 5.4 (6); 3.0 (10)	−7.2 (1) g; −6.2 (3) g; −5.9 (7) g; −8.7 (9) g; 0.0 (19) t
6α	40.8	6.7 (5); 9.5 (7)	−6.4 (4) g; −1.3 (8) t; 0.6 (10)t
6β	43.3	2.7 (5); 7.4 (7)	−3.1 (4) g; −5.3 (8) g; 0.0 (10) g
7β	43.0	9.5 (6); 8.0 (8)	−3.0 (5) t; −1.8 (9) t; −0.8 (14) g
7α	36.0	7.6 (6); 4.1 (8)	−7.9 (5) g; −8.5 (9) g; −5.9 (14) g
11α	48.3	6.1 (9); 11.5 (12)	−0.6 (8) t; 2.0 (10) g; 0.4 (13) t
11β	47.7	3.9 (9); 8.8 (12)	−4.3 (8) g; 0.1 (10) g; −0.9 (13) g
12β	40.7	9.0 (11); 5.5 (13)	1.2 (9) t; -1.4 (14) t; -2.3 (17) g; -5.8 (18) g

12α	33.7	7.5 (11); 4.5 (13)	−6.8 (9) g; −8.3 (14) g; −7.5 (17) g; 1.1 (18) t
15α	50.0	7.2 (14); 12.4 (16)	−0.5 (8); 1.2 (13); −2.4 (17)
15β	47.0	4.9 (14); 13.5 (16)	−4.1 (8); −0.2 (13); −0.1 (17)
16α	51.3	11.8 (15); 11.7 (17)	1.1 (13); −2.4 (14)
16β	51.4	11.8 (15); 11.0 (17)	−0.5 (13); −0.4 (14)
17α	39.5	12.0 (16); 4.5 (13)	−7.4 (12); −5.8 (14); −0.9 (15); −0.4 (18)
17β	41.6	10.1 (16); 2.3 (13)	−2.1 (12); −3.4 (14); −2.1 (15); −6.4 (18)

[a]The numbers given are the chemical shift differences, δ(ROH)–δ(RH) for corresponding carbon atoms; a negative sign signifies an upfield shift.
[b]Carbon atom number given in parentheses.
[c]g and t designated gauche and *trans* γ interactions.

dihydroxylated compounds for equatorial–equatorial and axial–axial substituents, did not follow the principle of additivity of increments. Apart from substituent interactions, the increments were applied to monounsaturated compounds.[397] Yet, no reliable predictions could be obtained due to severe changes in the stereochemistry, that is, the conformation, in comparison to the saturated steroids that were used as reference compounds. In other words, saturated steroids did not provide good reference systems or calibrants for unsaturated compounds. But, the need for a suitable reference forms the basic idea for a spectral database. As has been stated above, input data for databases were widely and readily available. The problem to be solved remained how to encode the chemical structures, that is, how to correlate chemical shift and structural features, and how to use the relation for the prediction of chemical shifts for previously unknown structures or structural moieties.

5.5. Chemical shift databasing and computational methods

Among the successful attempts and still employed solutions for such structure–property relation descriptions, the HOSE code occupies an important place.[366] A carbon atom was defined by its hybridization and by its neighbours that were organized in spheres. Thus, similar HOSE codes led to similar chemical shifts. An example is presented in Table 3.13.

However, these descriptors did not incorporate any stereochemical information. This important property was later introduced via a substructure code where the three-dimensional arrangement was encoded within a four-bond radius with regard to δ-substituent effects.[398] The structure–property relationship was computerized and examples for the steroid chemistry were shown.

To include stereochemical effects, a complementary approach was designed. A code to describe absolute and relative configurational and conformational information, termed CAST, was linked to a database of dihedral angle information.[399] The ^{13}C chemical shifts of 20-hydroxyecdysone could thus be accurately predicted.

For flat structures such as many heterocyclic compounds, the negligence of stereochemistry does not have any severe impact on the chemical shift prediction. But for steroids, where shielding and deshielding are largely exercised by steric interactions, the chemical shift prediction based on increment systems often yields better results than similarity prediction using

Table 3.13 Segment from the HOSE code register with averaged chemical shifts, standard deviations, number of entries and highest/lowest values[366]

HOSE code	Average shifts (ppm)	Standard number of entries	Highest and lowest value (ppm)
CCC(C, CC/C, C, CC&, C	136.0 # 0.4	2 lines	136.3 and 135.7
CCC(C, CC /O, O, O&	125.2 # 0.	1 line	125.2 and 125.2
CCC(C, CC, O/O&, C, CCC	173.1 # 0.5	2 lines	173.5 and 172.8
CCC(C, C, /C, C/C, CCO)	137.4 # 2.3	3 lines	139.4 and 134.9
CCC(C, C, /C, C/C, CC)	136.9 # 2.5	3 lines	139.8 and 135.5

The first three rows illustrate different ^{13}C shifts due to different HOSE codes, and the following two rows indicate similar chemical shifts due to similar HOSE codes.

HOSE type codes. In search of the most reliable relation to link structure and spectroscopic properties, linear relations were succeeded by neural networks. An introduction into the topic of neural networks can be found in references[367,372,400] with the latter illustrating, in general, structure–property relationships in chemistry. Anker et al. elaborate in depth on the application of layer neural networks, with a simple architecture of input, hidden, and output layers, on the ^{13}C chemical shift prediction of ketosteroids.[372] A schematic diagram of the artificial neural network used in the study is represented in the top part of Fig. 3.34. A more sophisticated network is sketched in the bottom part of the same figure.[367] By use of the simple network, an accuracy of 0.1 ppm was achieved for steroids based on a set of 24 ketosteroids.

5.6. Chemical shift calculations based on molecular structure models

The quantum mechanical or *ab initio* calculation methods do not need any experimentally derived data. Signals observable in NMR spectra are derived from first principles; therefore, the calculation of the correct conformation or the most frequently occurring conformation is of prime importance. Such calculations were described for testosterone, epitestosterone and androstenedione,[401] for estradiol, epiestradiol and estrone,[369] for pregnanolones[402] and for norethisterone and its 5α-derivatives.[403]

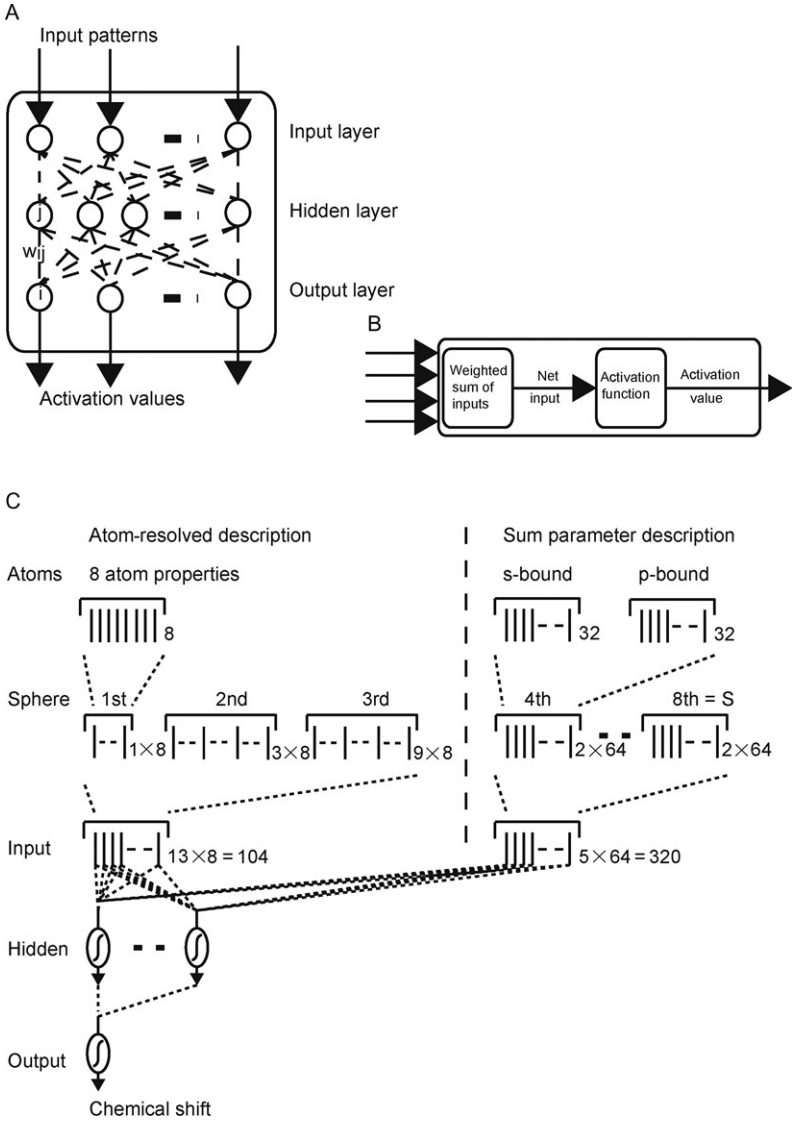

Figure 3.34 Schematic diagrams of a feed-forward artificial neural network (A) and of an artificial neuron (B). The architecture consists of one input, one hidden and one output layer. Adapted with permission from Anker et al.,[372] Copyright 1992 American Chemical Society. A more complex architecture is given in (C): The atom environment is illustrated by a single substituent on an "atom" level and on a "sphere" level. Eight parameters per atom form the "atom-resolved description" in the first three spheres. The following four spheres and an additional sum-sphere receive a "sum parameter description". Atoms are classified into 32 types and are counted twice. The first count reckons all atoms, and the second count includes only atoms that are part of the same π-electron system as the atom considered. The atoms of the first three spheres are subjected each to eight input neurons, resulting in 104 input units. One sphere is coded by 64 input values. For spheres 4–7 and the sum-sphere, 320 parameters are thus obtained. Since every substituent of a carbon atom is exposed to this input vector, input units vary in numbers. The resulting data are processed by a hidden layer. Finally, the chemical shift values are computed and output by one neuron. There are 32 hidden neurons in all classes except for allyl carbon atoms with only 8 neurons. Reprinted from Meiler et al.,[367] Copyright 2002, with permission from Elsevier.

The generation of structure proposals as interpretational help, see Table 3.9, has not been discussed until now. Of course, a structure can be proposed by a human expert, but attempts to generate structure proposals by computers were made long ago, although not in the steroid area. Acyclic molecules containing carbon, hydrogen, nitrogen and oxygen atoms were constructed by "artificial intelligence".[404] Since functional groups helped to reduce the number of possible structures, the concept of a good list and a bad list was programmed. The concept of automated structure generation was later refined to use input from spectroscopic constraints in the program GENOA.[271] Connectivity constraints were derived from C—C INADEQUATE data and, if not available, other spectral information could be incorporated as substructures.

5.7. Spectral prediction and chemical shift assignment using CASE

The combination of all aspects of structure–property relationships is realized in today's most advanced CASE systems. Some of the computer programs are commercially available, others are freeware. It is beyond the scope of this work to review the manifold of software. They are reviewed in references.[370,373] Aiming at the same goal, automated structure elucidation, programs differ in the type of input data, spectral databases, the structure–property descriptors, the prediction functions, the structure generator and the way to circumvent the combinatorial explosion of structures and last but not least in the method to select the most probable candidate structures. Selected examples are a system based on ^{13}C data and an extensive database only.[405] The novelties of this approach have been discussed in succeeding articles.[406,407] The functionality of the program was demonstrated on the steroidal compound 23,24-dihydro-15-oxocurcurbacitin F. A contrasting approach purely relying on 2D correlations and thus connectivity information instead of chemical shifts was described in 2006[408] for the successful application to a steroid, which had been isolated from the soft coral Sinularia dissecta and had the sum formula $C_{29}H_{44}O_3$. Assuming an ergostane skeleton as substructure, 54 structures were computed. Assignment of signals from rings A and B reduced the manifold to 15 structures. With C18 identified as part of a lactone group, two solutions were obtained. Both solutions represented the same structure but with different shift assignments.

The importance of generating all possible, but reasonable, structures according to chemical understanding was pointed out[409] in order not to miss

an exotic type of molecule or molecular moiety. The problem lies then in the reduction of all *N*-1 structures that do not comply with the data, where *N* are all hypothetical structures. Positive constraints, such as hybridization and heteroatom neighbours, and negative constraints, such as ring sizes, and bond orders were introduced, similar to the good list and the bad list. The system and its features are fully described.[370,410] A comparative test of the system's ^{13}C prediction capabilities was undertaken for steroids as well, where the importance of including stereochemical descriptors was emphasized.[411] Interestingly, the development of CASE systems led to a cross-fertilization towards the experimental side of NMR. The use of ^{13}C data asked for higher sensitivity, since the amount of sample is usually determined by chemistry or the abundance in natural sources. To automate the establishing of correlation maps, connectivity information needed to be derived from 2D experiments. The ambiguity of H—C HMBC data with respect to $^{2}J_{CH}$ and $^{3}J_{CH}$ or even higher long-range correlations was known to lead to contradictory connectivity information.[410] Therefore, experiments such as 1,1-ADEQUATE or H—C H2BC were considered to be preferred to H—C HMBC data.[373] A potential disadvantage of the 1,1-ADEQUATE its limited use for proton-deficient compounds[412] do not apply to steroids. In contrast, the observation of strong long-range correlations, $^{4}J_{HH}$ and $^{5}J_{HH}$, is very common in steroid spectra. The connectivity determination is, therefore, expected to suffer from contradictions when structures with ^{n}J, $n < 4$, are prioritized as compared to those with ^{n}J, $n \geq 4$.[412] The introduction of fragments in the structure generation and analysis algorithms, as has been proposed,[412] should be very helpful for steroids in contrast to unknown natural compounds. Analogously, structure elucidation should not suffer from a bias that might be introduced by fragments. The use of ^{13}C data or its prediction as a filter for relative stereochemistry determination[413] was demonstrated successfully for two steroidal compounds, where the calculation of isomers and its chemical shift prediction based on HOSE code yielded the best agreement with the correct stereoisomer. It was the agreement of predicted and experimental data that determined the structure candidate selection or short list. In this case, but also, in general, the fit of experimental versus predicted ^{13}C and ^{1}H spectra acts as the criterion for the validation of the structure proposal from a list of candidates.[373]

A comparison of experimental versus calculated chemical shifts is presented for tibolone and testosterone in Tables 3.14a and 3.14b. The calculations were carried out using ChemNMR, ACDLabs and Mestrelab software.

Table 3.14a Comparison of experimental (exp.) versus calculated chemical shifts for tibolone (**11**) using ChemNMR, ACDLabs and Mestrelab software

Compound							**Tibolone**					
Nucleus							^{1}H					
Software		ChemNMR	Mestrelab	ACD/labs				ChemNMR	Mestrelab	ACD/labs		
Shift numbering	**Exp. (ppm)**	**Shift (ppm)**	**Shift (ppm)**	**Shift (ppm)**	**Av. exp. (ppm)**	**N. net (ppm)**	**Exp. (ppm)**	**Shift (ppm)**	**Shift (ppm)**	**Shift (ppm)**	**Av. exp. (ppm)**	**N. net (ppm)**
1	27.85	24.9	28.48	29.47	27.40	30.17	2.36 2.45	2.24 2.24	2.38 2.38	2.44 2.50	2.38–2.67 2.39–2.78	2.02 2.02
2	39.54	39.0	42.23	39.23	39.00	36.88	2.45 2.45	2.49 2.49	2.51 2.51	2.44 2.39	2.47–2.88 2.38–2.66	2.35 2.35
3	211.82	210.0	209.25	211.23	211.1	210.26	– –	– –	– –	– –	– –	– –
4	45.37	44.6	36.62	45.45	44.70	42.74	2.73 2.73	3.12 3.12	2.80 2.80	2.57 2.57	2.77–2.78 2.76–2.77	2.70 2.70
5	125.09	126.8	125.94	129.52	126.40	124.19	–	–	–	–	–	–
6	38.91	36.5	35.18	33.07	26.93–36.08	40.28	1.62 2.27	2.04 1.79	2.10 2.01	2.44 2.05	2.00–2.68 1.70–2.25	2.06 2.06
7	27.51	31.2	29.54	26.79	26.98–27.32	31.41	– 1.86	– 1.84	– 2.34	– 1.46	– 1.34–2.50	– 1.96
8	42.14	36.1	42.13	41.74	41.7	43.11	1.46	1.44	1.65	1.44	1.67–1.97	1.21
9	39.95	38.4	37.98	37.85	39.48–39.82	40.87	1.81	2.11	2.13	2.08	1.91–2.52	1.90
10	130.42	130.8	132.87	131.52	131.10	135.75	–	–	–	–	–	–
11	25.65	24.9	24.50	25.34	25.30	26.32	2.01 1.22	1.56 1.31	1.52 1.44	1.81 1.44	1.60–2.06 1.19–1.76	1.81 1.81

Continued

Table 3.14a Comparison of experimental (exp.) versus calculated chemical shifts for tibolone (**11**) using ChemNMR, ACDLabs and Mestrelab software—Cont'd

Compound		**Tibolone**										
Nucleus		^{13}**C**					^{1}**H**					
Software		**ChemNMR**	**Mestrelab**	**ACD/labs**				**ChemNMR**	**Mestrelab**	**ACD/labs**		
Shift numbering	**Exp. (ppm)**	**Shift (ppm)**	**Shift (ppm)**	**Shift (ppm)**	**Av. exp. (ppm)**	**N. net (ppm)**	**Exp. (ppm)**	**Shift (ppm)**	**Shift (ppm)**	**Shift (ppm)**	**Av. exp. (ppm)**	**N. net (ppm)**
12	33.44	29.2	31.28	33.25	33.08–33.22	33.09	1.78 1.62	1.56 1.31	1.56 1.49	1.28 1.81	0.94–1.53 1.46–2.05	1.52 1.52
13	47.83	47.8	47.95	47.45	47.38–47.52	47.18	–	–	–	–	–	–
14	46.52	46.0	49.91	46.63	46.18–46.32	47.45	1.76	1.40	1.45	1.34	0.94–1.54	1.66
15	22.42	23.5	24.06	21.41	22.10	24.73	1.67 1.35	1.60 1.35	1.56 1.48	1.73 1.32	1.57–1.98 1.14–1.58	1.73
16	39.39	35.4	36.77	39.00	39.00	37.55	2.31 1.99	1.92 1.67	2.20 1.75	2.28 2.05	2.11–2.25 1.92–1.98	2.20 2.20
17	80.23	81.4	79.45	79.85	79.78–79.92	80.21	– (OH) 1.95	– 3.65	– 1.25	– 1.98	– 1.98	– 3.39
18	13.21	13.0	14.80	12.90	12.90	12.54	0.88	1.04	0.85	0.96	0.64–1.10	0.90
19	–	–	–	–	–	–	–	–	–	–	–	–
20	87.95	87.6	86.43	87.85	87.78–87.92	87.08	–	–	–	–	–	–
21	74.34	74.0	74.44	73.75	73.68–73.82	73.89	2.59	3.52	2.29	2.97	2.39–2.54	2.70
22	13.41	19.5	17.76	12.59	12.89–13.01	15.5	0.84	0.96	0.91	0.96	0.83–1.00	1.03
CDCl3	77.36						7.26					

Table 3.14b Comparison of experimental (exp.) versus calculated chemical shifts for testosterone (**5**) using ChemNMR, ACDLabs and Mestrelab software

Compound					**Testosterone**							
Nucleus					^{13}**C**					^{1}**H**		
Software		**ChemNMR**	**Mestrelab**	**ACD/labs**					**ChemNMR**	**Mestrelab**	**ACD/labs**	
Shift numbering	**Exp. (ppm)**	**Shift (ppm)**	**Shift (ppm)**	**Shift (ppm)**	**Av. exp. (ppm)**	**N. net (ppm)**	**Exp. (ppm)**	**Shift (ppm)**	**Shift (ppm)**	**Shift (ppm)**	**Av. exp. (ppm)**	**N. net (ppm)**
1	35.38	35.2	36.26	35.81	35.52–36.10	35.33	1.70 2.04	1.24 1.49	1.51 1.76	1.70 2.03	1.70 2.03	1.65 1.65
2	33.62	34.1	34.42	33.95	33.79–34.10	34.32	2.34 2.41	2.89 2.99	2.74 2.77	2.42 2.35	2.42 2.35	2.39 2.39
3	199.7	196.9	199.97	199.00	198.00–200.00	199.25	– –	– –	– –	– –	– –	– –
4	123.41	124.0	123.81	123.88	123.57–124.20	124.06	5.74 –	5.85 –	5.78 –	5.73 –	5.73 –	5.72 –
5	171.80	170.2	170.55	170.92	170.40–171.43	172.05	–	–	–	–	–	–
6	32.59	32.5	32.35	32.75	32.68–32.82	32.47	2.27 2.37	1.91 2.01	2.21 2.24	2.29 1.85	2.29 1.85	2.23 2.23
7	31.31	31.6	31.28	31.75	31.30–32.20	32.47	1.01 1.85	1.17 1.42	1.38 1.46	0.96 1.03	1.00 1.00	1.12 1.12
8	35.34	35.7	36.30	35.59	35.00–36.18	35.7	1.58	1.41	1.18	1.57	1.57	1.54
9	53.68	53.7	50.84	54.14	53.69–54.60	53.91	0.93	1.44	1.17	0.93	0.93	0.95
10	38.43	38.6	38.43	38.76	38.51–39.00	38.46	–	–	–	–	–	–
11	20.39	21.1	22.01	20.82	20.43–21.20	20.37	1.61 1.44	1.52 1.27	1.50 1.42	1.60 1.43	1.60 1.43	1.59 1.59

Continued

Table 3.14b Comparison of experimental (exp.) versus calculated chemical shifts for testosterone (**5**) using ChemNMR, ACDLabs and Mestrelab software—Cont'd

Compound							**Testosterone**					
Nucleus			^{13}C					^{1}H				
Software		ChemNMR	Mestrelab	ACD/labs				ChemNMR	Mestrelab	ACD/labs		
Shift numbering	**Exp. (ppm)**	**Shift (ppm)**	**Shift (ppm)**	**Shift (ppm)**	**Av. exp. (ppm)**	**N. net (ppm)**	**Exp. (ppm)**	**Shift (ppm)**	**Shift (ppm)**	**Shift (ppm)**	**Av. exp. (ppm)**	**N. net (ppm)**
12	36.18	26.7	35.52	36.65	36.19–37.10	36.84	1.09 1.86	1.31 1.56	1.26 1.57	1.10 1.86	1.10 1.86	1.14 1.14
13	42.53	43.1	43.19	42.91	42.61–43.20	44.17	–	–	–	–	–	–
14	50.21	50.5	52.15	50.66	50.23–51.10	51.33	0.98	1.40	1.04	0.98	0.98	0.96
15	23.08	23.3	22.95	23.45	23.09–23.80	23.2	1.63 1.31	1.60 1.35	1.49 1.41	1.62 1.31	1.62 1.31	1.59 1.59
16	29.83	30.9	30.92	30.40	30.10–30.71	30.99	2.08 1.46	1.78 1.53	1.74 1.65	2.09 1.48	2.09 1.48	1.77 1.77
17	80.93	81.7	81.26	81.29	81.00–81.57	81.65	3.65 (OH) 1.67	3.22 3.58	3.85 1.28	3.65 1.97	3.65 1.69–4.98	3.61 2.99
18	10.92	12.0	15.00	11.12	10.94–11.30	11.24	0.80	1.04	0.94	0.80	0.80	0.80
19	17.14	19.0	18.10	17.36	17.26–17.44	17.88	1.20	1.30	1.02	1.19	1.19	1.19
20	–	–	–	–	–	–	–	–	–	–	–	–
21	–	–	–	–	–	–	–	–	–	–	–	–
22	–	–	–	–	–	–	–	–	–	–	–	–
CDCl3	77.36						7.26					

For steroids, intense research has been carried out on ^{13}C chemical shift data; they have been translated into increment systems, including stereochemical refinement approaches. The predictive power of this system is very good—provided access to the data is available, cf. Table 3.14a and 3.14b. Any type of fragment description as an addition to the steroid skeleton has been found to work well due to the resemblance of steroids scaffolds. Since a synthetic modification of a given steroid may be recognized by a single signal, for example, a certain NOE, or the change of a multiplet, for example, fluorine versus proton coupling, any algorithm that incorporates the knowledge specific to steroidal compounds contributes greatly to the automated structure elucidation of steroids. Nevertheless, this means that this expert knowledge is stored as substructure information specific for the steroid compound class, not in form of a generic algorithm suitable for all types of compounds. In this way, that part of a CASE system tends to resemble a human expert who narrows structural variants down until the correct structure remains. The proton chemical shift dependence on solvents is nowadays equalized by the H—C correlation experiments, thus opening the proton connectivity pattern via a reliable assignment entry point in principal independent of the absolute proton chemical shift value. Therefore, automated structure analysis is likely to suffer little from more difficult to predict proton chemical shift errors, as would have been the case 40 years ago.

A great deal of steroid structure elucidation is concerned with stereochemistry. Today, NOESY or ROESY spectra are easily accessible; hence, the 3D structure is readily elucidated, provided sufficient resolution. Due to frequent long-range couplings resulting from steroid chemistry, the use of a H—H NOESY for proton assignment will probably give better results than connectivity information from H—H COSY or TOCSY experiments. Nevertheless, both for human and for computer analysis, a good 3D model is a prerequisite, be it an old-fashioned Dreiding model, a crystal structure or a computed model stemming from the most sophisticated quantum-mechanical calculation.

6. MODERN AND RARE NMR METHODS IN THE STEROID FIELD

6.1. Recent general NMR developments

So far, we were concerned with the structure elucidation of steroidal compounds, their constitution, relative and absolute configuration and their conformation. We reviewed classical studies as well as investigations of

focused interest, such as radioisotope labelling and its NMR analyses. This section entitled Modern and Rare Methods shall not only point out the most recent methodological studies on steroids but also remind of some examples of experiments that have not been often applied to steroids.

Although quite a few steroidal compounds are still successfully marketed drugs, cf. Table 3.2, the liaison between steroids and modern NMR developments has cooled down in recent years. Nevertheless, newly developed experiments and technologies are implemented in laboratories that study steroids and are applied for structure elucidation purposes. Only, the results are not consistently made public. For those spectroscopists who are just entering the field of small molecules, there is a variety of textbooks and reviews to choose suitable experiments from. These experiments work well for steroids, too. As a few examples of experimentally oriented publications may serve the compilation of experiments by Berger[414] containing very generic experimental parameters to start successfully with the experiment. There is the critical experiment and parameter review by Reynolds et al.[415] demonstrating the optimization of modern experiments. A qualitative overview of current 1D and 2D experiments was collected and illustrated by Martin et al.[416] A very practical comparison of structure elucidation by older and more recent methods including the application of cryogenic probes was carried out as well.[417] Among the textbooks, the recent one by Claridge might be found helpful for providing experimental details.[418] Kwan and Huang proposed a selection of experiments as standard set for structure investigations.[419] With respect to instrumental and hardware developments, many of the once state-of-the-art devices are now widely and routinely available, such as gradient equipment,[123] small volume probes[420,421] and cryogenically cooled probes.[121,422] A very promising tool for structure elucidation of small molecules will be the ^{13}C sensitive cryoprobes that allow ^{13}C direct detected and especially C—C INADEQUATE experiments on only a few milligrams of sample in less than a day.[423,424]

Advances in not only sensitivity but also sophisticated experimental set-ups add to the instrumentarium of the spectroscopist. Special attention was paid to fast NMR spectroscopic methods.[423–426] These methods are either constituted of experimental techniques, where several experiments are combined into one sequence,[427,428] time-shared experiments or parallel acquisition and detection.[429–433] Other fast methods make use of non-linear or statistical sampling of data points in multidimensional experiments[434,435] or rely on computational techniques, such as covariance processing.[436–441]

6.2. Covariance NMR and steroids

Covariance NMR is of special interest in the case of environments allowing only limited experimental time, since the spectral computation involved in covariance processing does not require further or extended experiments but mathematically improves the visualization of information by enhancing spectral resolution in sparsely sampled spectral dimensions[438,439] or by linking and transforming heterogeneous data sets.[436,442] It is the power of covariance spectroscopy that UIC processing allows to access low-sensitivity or time-consuming correlation experiments, for example, HSQC–NOESY or C—C COSY.[436,437,442] The higher sensitivity of UIC hyphenated spectra, for example, HSQC–TOCSY, as compared to the fully experimental counterparts stems from the component spectra, here HSQC and TOCSY, which are more sensitive than their combined pulse sequence.[436,443] For steroids, the revelation of long-range couplings resulting from the enhanced sensitivity of the UIC method[444] would be of special interest in the steroid field.

Aspers et al.[133] studied four steroids to investigate the effect of spectral congestion on the usefulness of UIC processing of spectral data. The signal density and thus spectral congestion increased from dexamethasone over testosterone and allylestrenol to tibolone. Experimental and UIC-computed hyphenated spectra, such as HSQC–TOCSY and HSQC–NOESY, were compared. Depending on the signal crowding, the computed spectra proved superior with regard to sensitivity and fast accessibility. In the case of the heavily congested spectra of tibolone, artefacts from residual noise and spectral overlap hampered the distinction between true correlations and artefacts. The usefulness for structure elucidation was thus considered less important. The recording of 3D HSQC–NOESY data was not regarded really advantageous for steroids, since the necessary information could be derived from 2D spectra or UIC 2D-HSQC–NOESY. Covariance transformation of hyphenated experiments resulted in CH_m—CH_n COSY and CH_m—CH_n NOESY spectra. Although applicable for structure verification in case of low and moderate spectral density, they were regarded inferior to a C—C INADEQUATE experiment with respect to readily available structure information. While the HSQC–TOCSY and HSQC–NOESY were found very useful in general, as they were quickly derived with sufficient quality from data recorded in screening mode, the use of CH_m—CH_n COSY and NOESY was recommended only for special purposes. The effects of spectral noise and insufficient experimental parameter optimization on the computed spectra were demonstrated as well.

The NOESY, HSQC and UIC HSQC–NOESY spectra of tibolone are given in Fig. 3.35. Exemplarily, the true signal C15H16 and the artefact C1H4 were analyzed. True correlations, such as C15H16, and artefacts, such as C1H4, are labelled in the spectra of Fig. 3.35. The NOE cross-peak H15H16 was correlated to C15H15 in the HSQC spectrum during covariance processing. After this transformation, the peak C15H16 was

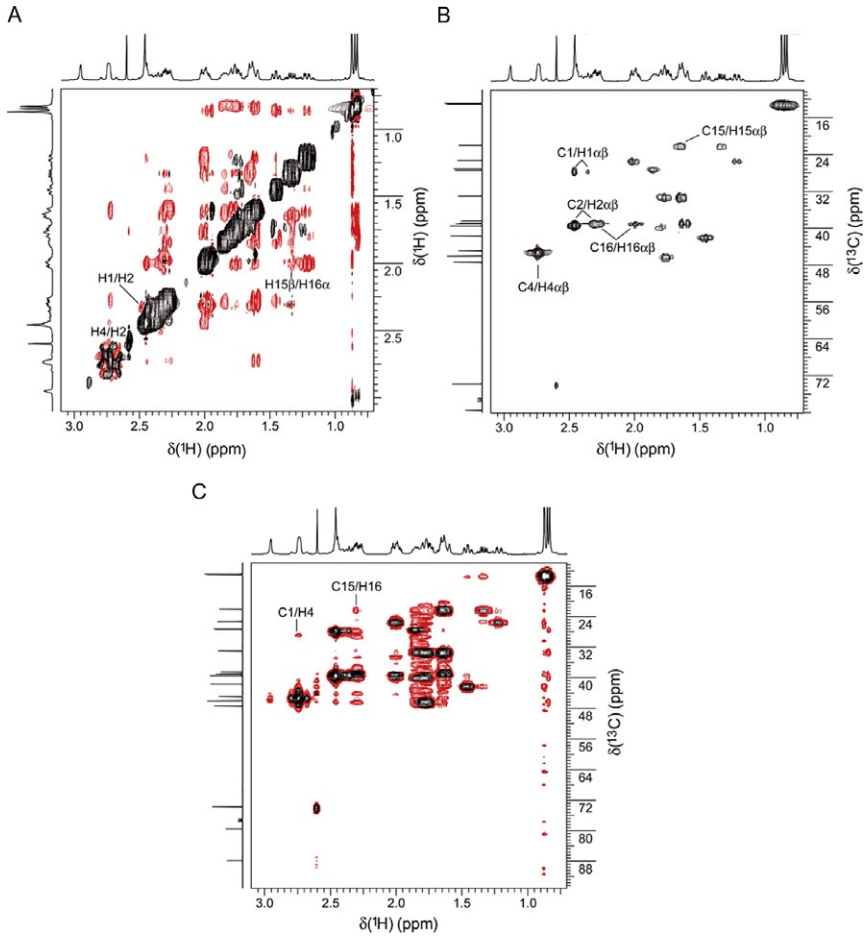

Figure 3.35 UIC generated H—C HSQC–NOESY spectrum (C) from H—H NOESY (A) and H—C HSQC (B) of tibolone. The signals leading to the true signal C15H16 and the artefact C1H4 in the UIC HSQC–NOESY are indicated in the NOESY and HSQC spectrum. The t_1-noise in the UIC spectrum is a remainder from the NOESY acquired with generic parameters without sample optimization. Reprinted with permission from Aspers et al.[133] Copyright 2011 John Wiley & Sons Ltd.

obtained in the HSQC–NOESY spectrum. The artefact C1H4 observed in the UIC spectrum could analogously be traced back to the NOE signals H1H2 and H2H4: The signals of H1 and H2 overlapped in the proton dimension of the HSQC; they, hence, interfered during covariance transformation and caused the false correlation C1H4. In the UIC HSQC–NOESY, direct H—C correlations can be distinguished from H—C NOE correlations by their opposite phases, indicated as different colours within the spectra in Fig. 3.35.

On the basis of the spectra in Fig. 3.35, the effects of *t*1-noise, the range of NOE intensities and the use of non-optimized experiment parameters were discussed for structure elucidation and structure verification. Since NOESY spectra were found to suffer from these effects more than COSY or TOCSY data, the optimization of experimental parameters was claimed a prerequisite for further covariance treatment.

The combinations that result from using phase-sensitive and magnitude-mode spectra as component spectra for UIC transformations were compiled and discussed with respect to the obtainable information. The attractiveness of covariance-computed spectra for routine laboratories arises from its fast availability. When a more frequent use is considered, it was suggested to choose an experiment's phase sensitivity according to a potential future covariance treatment.[133]

In the field of steroids, the challenge becomes less to develop a new experiment to allow access to the solution of the specific problem but to choose the most suitable experiment and not to fall into a trap to interpret data in a vicious circle. Sitosterol (**8**) may serve as such an example.[415] The C7 methylene and C8 methine signals overlap in a 1D ^{13}C experiment leading to deceptive interpretation of $^{13}C\{^{1}H\}$, ^{13}C DEPT and APT spectra. The problem is of course not encountered when utilizing edited H—C HSQC spectra.

In the following paragraph, we will point out the studies in which techniques were applied that seemed to us not to have been exploited to their full potential.

6.3. The HSQC–TOCSY experiment

When relying on modern NMR instrumentation, the somewhat low sensitivity of the HSQC–TOCSY experiment may be overcome such that experiments can be recorded on a few milligrams within a few hours[133,445] and the utilization of this experiment in natural product structure elucidation will

continue to grow.[446] As particular interesting variants of HSQC–TOCSY, phase-sensitive spectra have been described, which allow the distinction of direct C—H correlations from relayed ones[445,447] or the discrimination of C—H multiplicities.[448] The use of the latter was demonstrated on a dimeric cholesten derivative, where all resonances could be assigned on the basis of the phase-sensitive HSQC–TOCSY experiment. Although the multiplicity information can in principal be derived from 1D techniques such as DEPT or APT, the edited HSQC–TOCSY will be helpful to decrease signal density in strongly crowded spectra or spectral regions, as is the case for androstane, tibolone and others. The HSQC–TOCSY with inverted-direct responses or correlations, IDR-HSQC–TOCSY, was shown to enhance resolution as well.[447] Its greater strength lies in the separation of direct from relayed responses and the interpretatory help therein. Nevertheless, this experiment has not been described for use with steroids. The successful covariance construction of IDR-HSQC–TOCSY spectra was reported.[436] A method to enhance the spectral dispersion by spreading the resonances into three dimensions was termed 3D MAXY–HMQC for maximum-quantum correlation spectroscopy.[449] Exemplarily, the separation of the CH_n resonances of dexamethasone was successfully demonstrated. The experiment was shown to provide essentially the same sensitivity as other 3D HMQC or HSQC experiments.

6.4. ^{13}C detected experiments

A different class of experiments profits greatly from the hardware developments mentioned above: the heteronuclear direct detected methods, and for steroids especially the ^{13}C detected methods. An update on edited 1D ^{13}C NMR was recently given for the DEPTQ experiment.[450,451] Improved sensitivity was exemplarily demonstrated on cholesterol in one study. In light of the high-sensitivity cryoprobes, the C—C INADEQUATE experiment will be considered more often in future analyses. Versions and practical aspects were reviewed in 2002.[452] More recently, the INADEQUATE was investigated with respect to problems, artefacts and their solutions.[453] Among other non-steroidal compounds, 17α-ethinylestradiol was studied. Due to the magnificent signal-to-noise ratio, not only direct C—C correlations but also long-range correlations up to three bonds could be visualized, cf. Fig. 3.36. This visualization was achieved by variation of the interpulse delay within the spin–echo part of the pulse sequence from values of 0.005 to 0.05 s, corresponding to a J_{CC}

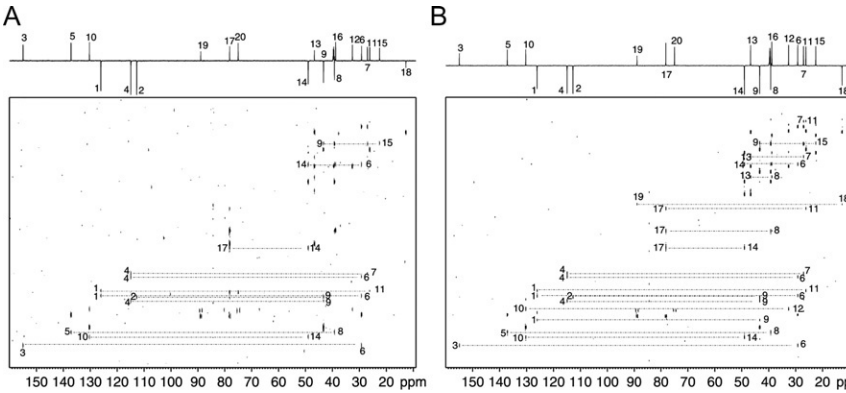

Figure 3.36 Comparison of the INADEQUATE spectra of 17α-ethinylestradiol: (A) the standard experiment recorded with $\tau = 0.005$ s from $\tau = 1/(4\ J_{CC})$ where $J_{CC} = 50$ Hz and (B) the long-range version recorded with $\tau = 0.05$ s from $\tau = 1/(4\ J_{CC})$ where $J_{CC} = 5$ Hz. The dashed lines indicate correlations arising from two- and three-bond C—C coupling interactions. Reprinted with permission from Bain et al.[453] Copyright 2011 John Wiley & Sons Ltd.

equal to 50 Hz and an $^{n}J_{CC}$ equal to 5 Hz. While most of the direct correlations were observed at a delay τ equal to $1/(4\ J_{CC})$ with $J = 50$ Hz, the missing ethinyl correlations C19—C20 and C19—C17 could be detected at $\tau = 3/(4\ J_{CC})$, since the couplings magnitude is $J_{C19C20} = 163$ Hz and $J_{C19C17} = 72.1$ Hz.

The long-range correlations $^{n}J_{CC}$ were observed at $\tau = 0.05$ s; they can be recognized from the dashed lines in Fig. 3.36. The spectra were obtained from overnight experiments on 10–25 mg of sample.

6.5. 1D methods

In many routine laboratories, the use of maximally generic experiment sets sometimes prevents specific experiments from being considered. A 2D experiment is often believed to provide all information from which the necessary parts can be extracted. Occasionally, the application of selective experiments may lead to a more straightforward, problem-oriented solution and also to an answer more reliable with respect to data quality. In 1997, the accuracy of 1D pulsed-field gradient NOE experiments, PFG–NOE, was analyzed and NOE enhancements of 0.02% could be reliably measured.[454] Based on the high-quality data thus obtained, the initial linear part of the NOE build-up curve could be determined, from which intermolecular distances could be derived. The steroid, 11β-hydroxyprogesterone, served as

an example. In another study, selective excitation in combination with pulsed-field gradients was also used for the chemical shift assignment of stigmasterol (**16**).[455] The complete proton assignment succeeded, solely based on the 1D selective COSY, relayed COSY, TOCSY and NOESY. As an advantage of the 1D methods, the high resolution allowing the direct determination of coupling constants was emphasized.

Next to NOE data, scalar coupling constant analysis remains a central pillar of conformational structure elucidation. In the field of steroids, the reduction of spectral overlap is hence a motor for the search of experiments suitable for the determination of coupling constants. Proton–proton and one-bond proton–carbon splittings of chenodeoxycholic acid were determined from phase-sensitive H—C HMQC spectra.[456] Further and more recent experiments for the measurement of $^{n}J_{CH}$ coupling constants have been compiled as well.[457]

6.5.1 High-resolution 1D ^{1}H NMR

Despite its valuable use in structure elucidation, coupling constants also create complexity rendering the identification and interpretation of signals a challenging task especially in crowded spectra such as those of many steroids. While heteronuclear decoupling was successfully applied early within ^{13}C NMR to reduce signal complexity, homonuclear decoupling was used as a selective decoupling mode prior to the advent of two-dimensional techniques. Decoupling over the whole spectral range remained impossible.

In the study of steroids, three attempts resulted in the equivalent of a full-range ^{1}H{^{1}H} NMR, also referred to as a pure-shift spectrum.

In 1999, Guenneau et al. reported on the application of a *J*-resolved experiment for the determination of relaxation times.[458] The method proved unsuccessful for transverse relaxation times due to pulse imperfections and non-resolved long-range *J*-couplings. In contrast, longitudinal and rotating frame relaxation times could be determined, provided an appropriate preparation period preceded the 2D spin–echo sequence of the *J*-resolved experiment. Lorentzian lines were obtained in the power spectra, which were found suitable for the estimation of ^{1}H relaxation parameters. By this method, these parameters were obtained for androstane. The authors concluded as well that fully decoupled spectra could be obtained from spin–echo experiments although in a non-quantitative manner. Due to the 2D character, the experiments proved rather time consuming for a pure shift spectrum.

In 2007, Pell and Keeler applied 2D *J*-spectroscopy in order to observe homonuclear decoupled spectra.[459] They introduced the Zangger–Sterk

pulse sequence[460] into the *J*-resolved experiment with the result that absorption-mode line shapes were obtained. Although the spectral sensitivity was found low, the lines retained their natural intensities. The resolving power of this experiment was demonstrated—among others—for dehydroisoandrosterone. The regular and the decoupled ^{1}H NMR spectrum of the steroidal compound are presented in Fig. 3.37.

In 2011, Kolkman et al.[461] developed a method based on reconstruction. Selectively decoupled spectral regions were summed up to yield the full-range spectrum. The experiment may be considered a development of the decoupling using spatial encoding through gradient pulses.[462] The improvements consist of the full utilization of the sample size as compared to the original sample slicing, further of the fast pulse repetition and on the sensitivity increase while retaining quantitative information. The experiment was applied to blood plasma samples and testosterone.

Fully decoupled or pure shift ^{1}H NMR experiments are expected to assume an important future role in the identification of compounds in mixtures, in particular, when the compounds themselves provide complex or crowded spectra. Two features might be considered essential for this future role: a reasonable experiment time and the signals being quantifiable.

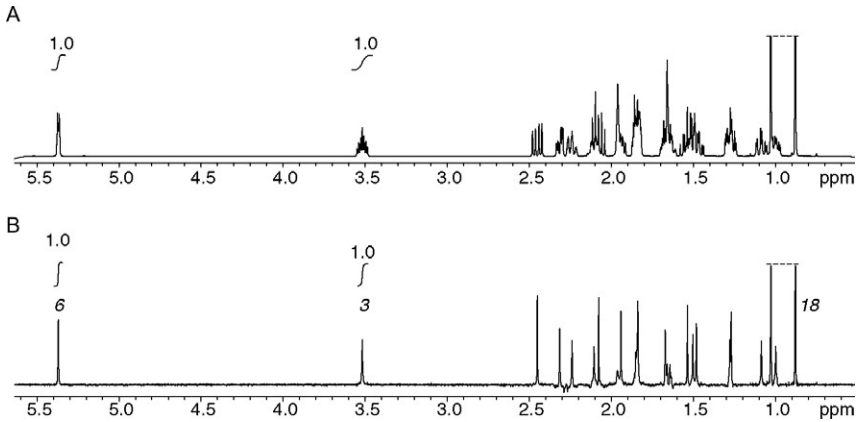

Figure 3.37 The 1D ^{1}H spectrum (A) and projection of the absorption-mode *J*-spectrum (B) of dehydroisoandrosterone. In (A) is shown the conventional spectrum of the full chemical shift range. The *J*-spectrum was acquired with 44 scans per t_1 increment. The spectral widths in ω_1 and ω_2 are 100 and 2561 Hz, respectively. The acquisition time in t_2 was 1.6 s; 200 t_1 increments were recorded, giving a maximum value of t_1 of 2.0 s. *Reproduced from Pell and Keeler[459] Copyright 2007, with permission from Elsevier.*

6.6. Fully coupled 2D ^{19}F NMR

A recent investigation was devoted to the determination of homonuclear and heteronuclear coupling constants involving diastereotopic fluorine nuclei.[463]

In the steroidal compound (**27**), cf. Fig. 3.29, all fluorine atoms were found magnetically and chemically inequivalent, their F–F coupling 280 Hz. Figure 3.38 D shows the expanded region of the fully coupled ^{19}F—^{13}C HMQC spectrum of compound (**27**). As is easily recognized from the figure, an E.COSY like pattern is displayed. The study further elaborated on the full analysis of the F1—C19 correlation signal. From the theoretical possible 32 cross-peaks, only a reduced multiplet with 8 correlations was observed due to E.COSY type cancellations. A simplified view of how the cross-peaks cancel out is presented in Fig. 3.38. The approach to spectral interpretation was based on spin states.

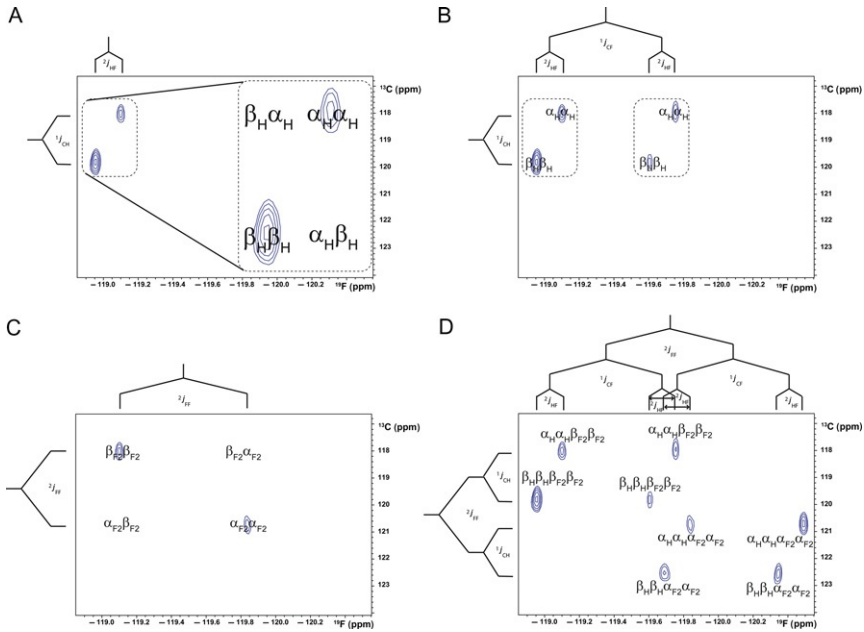

Figure 3.38 Zoomed-in region of the correlation between C19 (120.2 ppm) and F1 (−119.6 ppm) of the fully coupled HMQC of 19,19-difluoro-3β,7β-dihydroxy-androst-5-*en*-17-one (**27**) with the coupling tree displayed on the axes, (A) effect of passive spin H (6.22 ppm) on this correlation, where α and β represent the spin state of passive spin H, (B) effect of the CF coupling in the fluorine dimension, (C) effect of the homonuclear F1F2 coupling on this correlation, where α and β represent the spin state of F2, (D) resulting spectrum.[463]

Cross-peaks within a given multiplet were thus observed when the passive spin had the same spin state in both dimensions (αα or ββ). The sign of a coupling was derived from the slope or tilt of the cross-peak pattern. The size of the coupling constant $^{1}J_{CF}$, $^{1}J_{CH}$, $^{2}J_{HF}$ and $^{2}J_{FF}$ was determined from the splittings and the displacements of the peaks.

6.7. Residual dipolar couplings

RDCs have established themselves as a third pillar of stereochemical structure elucidation,[464] and with ever improving experimental ease of handling,[465] they will become even more widespread.[466] Due to the dipolar interaction mechanism, the size of a RDC depends on the length and the angle of the magnetic field and the internuclear vector of the two nuclei that are coupled to each other. The RDC contribution of the observed coupling is superimposed onto the scalar coupling and can be derived as the difference between the scalar coupling and the observed splitting.[467] To this purpose, the molecule is oriented in a weakly aligning medium, such as bicelles, phages, polymers[468–470] depending on the solubility of the compound and the desired strength of alignment.[467] The splitting, for example, H—H, C—H or N—H, is obtained from suitable *J*-resolved spectra. The scalar coupling may be measured from the same type of spectra recorded in the isotropic phase. The orientation of the molecule with respect to the magnetic field is computed by rotating a structural model, for example, from X-ray diffraction data or molecular modelling, with respect to a magnetic field axis such that the best agreement between calculated and observed RDCs is obtained.[471,472] Structure elucidation is achieved via comparison of a number of models with regard to their matching of calculated and observed RDCs. Using this approach, the conformation of a given compound can be deduced[473,474] as well as its relative configuration.[475–478] The determination of the absolute configuration was reported exemplarily, reliably when a stereocenter of known configuration is available as reference.[479,480] Recently, the use of RDCs for molecular constitution elucidation was described.[481] RDCs have great potential for structure elucidation especially when NOEs are not detectable due to the lack of suitable nuclei in proximity, or if coupling constants cannot be reliably analyzed according to Karplus or Haasnoot.

In 2002, the method was applied to configuration analysis of sodium cholate.[482] The resulting RDCs were compared to models of sodium cholate and several of its epimers. The analysis revealed that indeed only the correct epimer yielded a match allowing the unambiguous assignment of the stereocentres under study.

Kummerloewe et al. described[483] how RDCs can be used to distinguish diastereomers of 5α-cholestan-3-one and cholesterol by cross-fitting. Cross-fitting implies the comparison of RDCs computed from structural models of the diastereoisomers versus their experimentally determined counterparts and vice versa. The method included the transfer of structural information, the alignment tensors, cross-fitting of the anisotropic parameters of steroids, which have similar overall structure, and allowed thus the use of reduced subsets of RDCs. It was also shown that RDCs could be transferred between steroidal compounds in flexible moieties that are sufficiently similar in structure and dynamic behaviour. An example of spectra recorded in alignment medium and isotropic phase is given in Fig. 3.39 presenting 5α-cholestan-3-one. For the spectra in the anisotropic phase, 16 mg of the steroid were dissolved in a mixture of poly-dimethylsiloxane (PDMS) and chloroform. The resulting gel was stretched using a mechanical device. The corresponding isotropic coupling constants were determined in chloroform.

Within a study of testosterone and 17α-epitestosterone,[484,485] cross-fitting was performed for the distinction of both epimers. Comparison of experimental and calculated data presented good agreement between both isomers, as can be recognized from Fig. 3.40. On inspection of the quality factors within Table 3.15, it can be seen that only RDCs calculated for the correct epimer match the corresponding experimental data. Scalar coupling constants were determined in isotropic solution of chloroform; the corresponding RDCs were derived from aligned samples using poly-γ-benzyl-L-glutamate and chloroform. In contrast to the weaker alignment caused by PDMS gels, poly-glutamates generally induce stronger alignment, which, in turn, leads to larger RDCs. As a consequence, higher order effects often hamper the interpretation of proton-detected spectra. The recording of ^{13}C-detected spectra provides a suitable remedy. In the described study, 1D ^{13}C and carbon detected *J*-resolved experiments were used. From Fig. 3.40, it can be readily recognized that the largest deviations between experimental and calculated RDCs occurred for the stereocentre C17 and the adjacent carbon C16, indicating the specificity of the method. This observation is in line with the finding of Kummerloewe et al. that a reduced data set can be used for similar compounds. It is remarkable that even for stereocentres in the rather flexible D-ring of steroids, RDCs allowed not only the distinction of two epimers, when both epimers were studied, but also the absolute configuration assignment. The quality of the fit is superior for the correct stereoisomer, such that the configurations of the

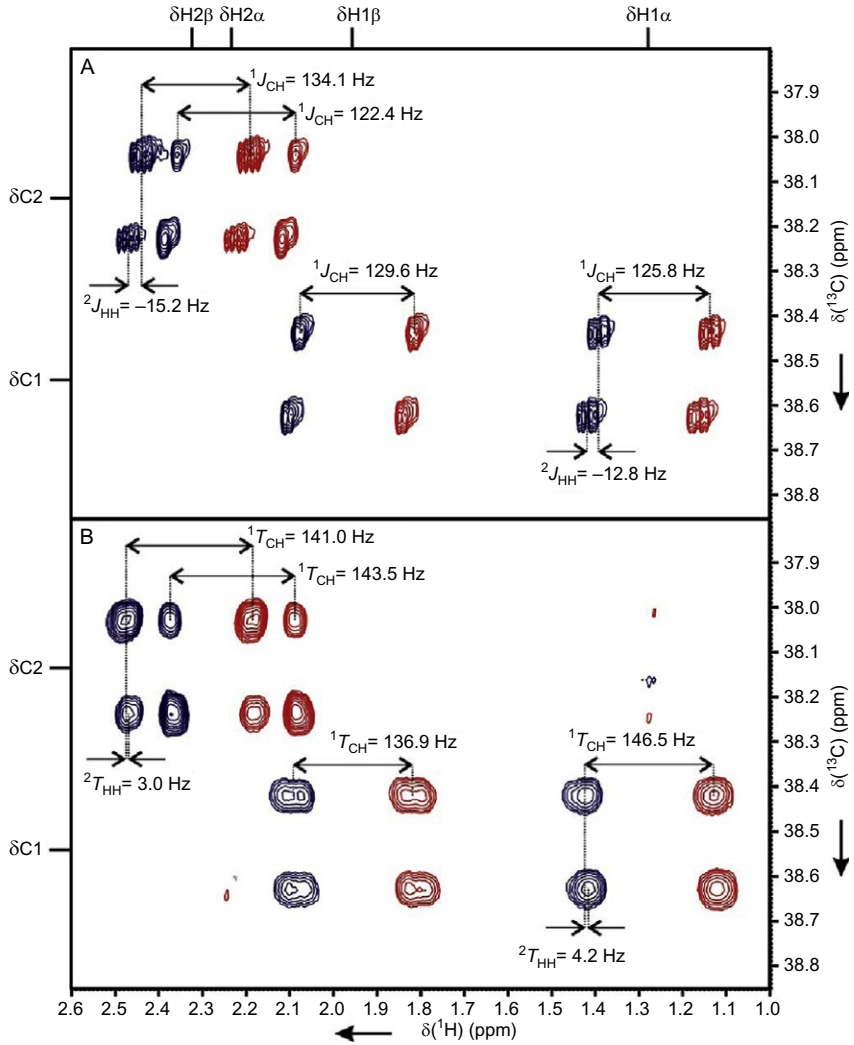

Figure 3.39 Details of P.E.-HSQC spectra acquired on 5α-cholestan-3-one in a chloroform solution (A) and in a stretched PDMS/$CDCl_3$ gel (B), showing the multiplets of the methylene groups at C1 and C2. One-bond C—H-couplings and geminal H—H-couplings are assigned in the spectra. Note that the sign-information of the homonuclear couplings is given by the tilt of the multiplet and that this tilt changes upon alignment in stretched PDMS gel as the negative $^2J_{HH}$-couplings (A) are compensated by the larger positive D_{HH}-couplings of both methylene groups in the aligned spectrum (B). Reprinted with permission from Kummerloewe et al.,[483] as published in The Open Spectroscopy Journal, 2010.

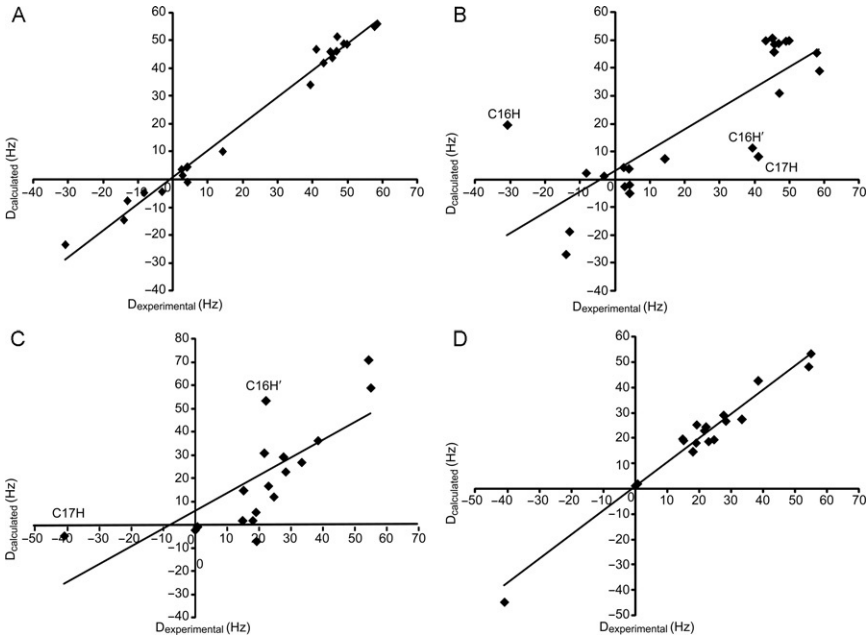

Figure 3.40 Scatterplots of experimental versus calculated RDC values, $D_{experimental}$ versus $D_{calculated}$: testosterone RDCs against a molecular model of testosterone (A) and of epi-testosterone (B); C, epi-testosterone RDCs against a model of testosterone (C) and of epi-testosterone (D).[484,485]

Table 3.15 Cross-fitting of RDC data obtained for testosterone and epitestosterone with the number of RDCs used for fitting, $n = 23$ for testosterone and $n = 18$ for epitestosterone

RDC input	Model testosterone	Model epitestosterone
Testosterone	RMS = 3.289	RMS = 15.871
	$n/\chi^2 = 0.350$	$n/\chi^2 = 0.020$
	$r = 0.993$	$r = 0.820$
Epitestosterone	RMS = 15.101	RMS = 3.649
	$n/\chi^2 = 0.016$	$n/\chi^2 = 0.242$
	$r = 0.740$	$r = 0.984$

The abbreviations RMS, n/χ^2 and r are used following the common statistical conventions.

steroids can be elucidated on the basis of a single epimer. A stereomodel obtained from basic molecular modelling proved sufficient for configuration investigations within this study. Both conclusions are in agreement with the earlier findings for sodium cholate.[482]

6.8. Mixture analysis by DOSY

For mixture analysis, diffusion-oriented spectroscopy (DOSY) has been applied for more than a decade.[486] As has been mentioned for CD inclusion complexes, cf. above, the relative diffusion rates can be determined by pulsed-field gradient experiments and analyzed with respect to solvent viscosity, complex formation constants or aggregation. The acronym DOSY usually refers to signal separation of compounds in the same sample on the grounds of their individual diffusion behaviour. Polyethyleneglycol was used as an additive to enlarge the range of diffusion rates and thus enhance the resolving power the DOSY method.[487] While the ^{1}H DOSY signals of testosterone (**5**) and estradiol (**6**) in a chloroform sample (600 µl) showed complete overlap, since their diffusion rates were essentially the same, the addition of 150 mg of polyethyleneglycol led to a change of the diffusion behaviour, $D_{\text{testosterone}}/D_{\text{estradiol}} \approx 2$, and hence to a good separation of the two sub-spectra.

Although it might be argued that with the assignment of first all carbon and later all proton signals at 400 MHz by 1980, the big challenges of structure elucidation of steroids were met and advances were only minor; there remains a continuing interest in method development on the basis of and for steroids. The demonstration was the goal of this and the previous sections. Due to the steroid skeleton and the manifold of correlation signals, steroids are very well suitable for method validation and, as can be seen from the past decade of publication, there are still aspects of the steroid structure to be discovered.

7. CONCLUSION AND CONSIDERATIONS

Structure elucidation of steroids by NMR using today's set of experiments[415,416,419] is mostly a routine task of moderate complexity, while in the 1980s, assignment strategies on the basis of the then new 2D techniques were discussed with respect to the specific properties of steroids.[111,128,256,488] The variety of currently available experiments provides ample choice of the most suitable route to assign all signals and thus arrive at the full structure. The task has been compared to solving an overdetermined matrix.[278] Straightforward

signal assignment is usually hampered only in case of strong signal crowding or overlap as for tibolone (**11**)[133] or in cases of limited availability of experimental time, which may lead to parameter choices resulting in insufficient resolution in two-dimensional data sets or a reduced set of spectral data. As a second cause for more difficult spectral interpretation, the availability of only submicrogram amounts of sample may be seen, for example, for metabolites or natural product isolates.

Structure elucidation needs to take two aspects into account, provided the steroid skeleton itself does not deviate totally from its natural chemical constitution and configuration as represented in Scheme 3.1. This holds very often true, although a few exceptions are known, such as the completely inverted ent-19-nortestosterone,[196] unnaturally configured 13-episteroids[193] or the brassinosteroids that were discovered as late as 1979.[489,490] The two questions to rise are indeed: What spectra or experiments are needed to assign all signals, that is, mostly from ^{1}H and ^{13}C, more rarely ^{19}F, establish the connectivity and describe the stereochemistry with respect to conformation and configuration? In principle, this question refers to *de novo* structure elucidation. Secondly, what spectra or experiments are the minimal set in terms of type and recording time needed to characterize a structural hypothesis? This aspect refers to verification or falsification of a structure proposal be it from chemical synthesis or purification or hit identification after screening of compound libraries.

Since the space of NMR experiments and pulse sequences has been reviewed elsewhere, cf. previous section, we will only discuss a preselection of experiment types regarding the investigation of steroids. The principal aspects of steroid structure to be taken into account are the signal assignment of ^{1}H and ^{13}C to describe skeleton and substituents, establish proof of connectivity, identify α and β positions of substituents including hydrogen isotopes and recognize the conformational preferences or flexibility. When a structure proposal is to be verified, these issues may be reduced to a certain part or moiety of the steroidal compound. A somewhat different task is the identification of a steroid in total based on a reduced data set, as will be explained below.

Within the structure elucidation protocol, the determination of the molecular formula should be most conveniently left to high-resolution mass spectrometry from a few nano- or micrograms. It should not be forgotten that the number of double bonds can be derived from MS data as well.[491] The identification of all heteroatoms by proton and carbon NMR is an indirect method, and might be supported by direct detected fluorine or

phosphorus NMR, but requires more work as compared to MS. After the determination of the molecular formula, the acquisition of NMR spectra usually starts with 1D ^{1}H, while a ^{13}C spectrum is often omitted for sensitivity reasons. Yet, the authors consider a composite-pulse decoupled 1D ^{13}C very valuable due to the superior resolution and its independence of coupling constants that might lead to unexpected or missing responses. The composite-pulse decoupling is preferable when edited versions, such as APT or DEPTQ, lead to underrepresented quaternary carbon signals, for example, in alkinyl or fluorinated steroids. When modern cryogenic probe technology allowing high-sensitivity carbon direct detection is available, 1D ^{13}C spectra can be recorded within a few hours on only some 100 μg per sample. As the next step, the easiest link between ^{1}H and ^{13}C spectrum may be achieved via an H—C HSQC. To our experience, the gradient multiplicity-edited HSQC provides excellent results at good sensitivity and delivers the H—C correlations and also all carbon multiplicities when compared to the 1D ^{13}C spectrum. At this point, signal assignment can already start, if there are a structure hypothesis and expert knowledge available. This knowledge might stem from a human expert, from electronic or paper databases or prediction of any kind. Even simple rules of thumb as given in Table 3.16 provide good starting points.

When operator time allows spectral parameter optimization for a steroid sample, a few considerations may furnish better results. In the proton dimension of 2D experiments, the size of the smallest coupling constant desired usually determines the necessary resolution. For the carbon dimension,

Table 3.16 ^{13}C chemical shifts of methyl, methylene and methine moieties and H—H coupling constants of steroids

Fragment	δ(^{13}C) (ppm)	Fragment with H—H connectivity	$^{n}J_{HH}$ (Hz)
Primary alkyl carbons	12–24	—CH_2— (geminal)	−14 to −12
Secondary alkyl carbons	20–21	—CH—CH— (vicinal)	
Tertiary alkyl carbons	35–57	Axial–axial	10–14
Quaternary carbons	65–91	Axial–equatorial	3.5–5
Olefinic carbons	119–172	Equatorial–equatorial	2.5–4
Carbonyl carbons	177–220	5-Membered ring	Depending on conformation
Carbons with fluorine	88–102		

overlap or similar shifts need to be taken into account. This is, however, of lesser concern due to the reduction of signal density by the second dimension. Nevertheless, if, for example, methyl resonances exhibit severe overlap, the C—H HETCOR equipped with a BIRD filter was shown to provide the highest resolution for CH resonances, 0.001 ppm in each frequency dimension, also in the case of steroids.[492,493] For a variety of small molecules, the resolution of a H—H COSY in magnitude mode was suggested to be set to 4 Hz per point,[415] since maximum signal intensity is obtained if the resolution equals J but can *in praxi* be five times bigger than the splitting; the presence of multiple long-range couplings within steroids often demands for higher resolution, which is easily achieved with modern spectrometers.

With respect to stereochemistry, it might be safely assumed that equatorial protons resonate at lower field than axial protons. For the concordance of α and β to axial and equatorial orientations, a model proves helpful. Nevertheless, there are several ways to establish direct proton–carbon bonding and multiplicity. The connectivity of the CH_n fragments can be made visible via the proton network through-bond or through-space, via the carbon network or via a combination of all. The first way is easily addressed by a H—H COSY type experiment. The use of a H—H TOCSY should be given more consideration on account of a high number of correlation signals, which could be observed and which would render the spectrum rather crowded. Because of the significant number of long-range H—H correlations in steroids, a TOCSY experiment with mixing times above 25 ms may already result in a high number of correlation peaks.[133] The common analysis of the proton pathway often follows the generic connectivity diagrams described exemplarily for norethisterone and 5α-androstane.[4,278] For the assignment, a connectivity and through-space proximity matrix proved useful. Examples of such correlation matrices are presented for dexamethasone and tibolone in Fig. 3.41.

Alternatively, the proton network can be mapped by NOESY spectroscopy. Since the stereochemistry of the rings can vary with the type of steroid, for example, 5α versus 5β or 14α versus 14β, nor- or episteroid, standard correlation diagrams often refer to the 5α-androstane as the generic skeleton. However, the NOE parameters have to be chosen carefully not to excite spin diffusion and create transferred NOEs or give rise to COSY or TOCSY artefacts in NOESY or ROESY spectra, which may cause contradictions especially during *ab initio* structure elucidation.

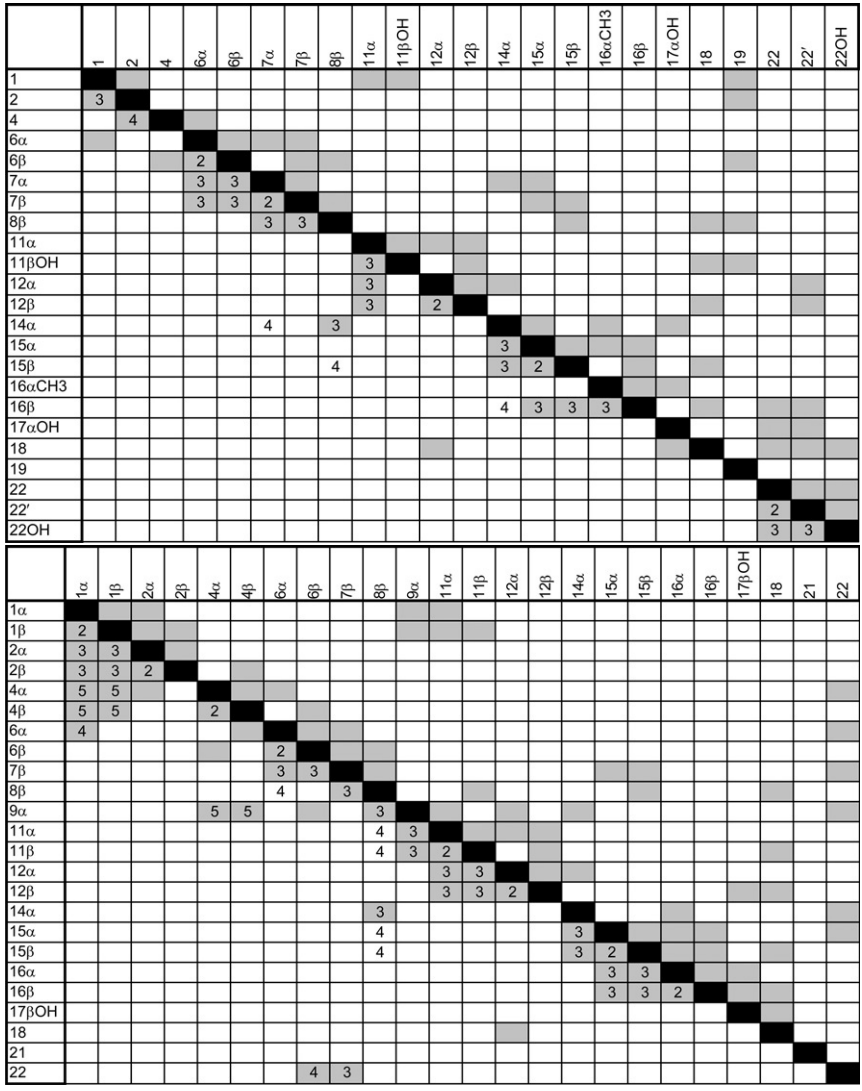

Figure 3.41 COSY, TOCSY connectivity and NOESY correlation matrices for dexamethasone (**23**), top, and tibolone (**11**), bottom. The NOESY correlations are marked above the diagonal, COSY and TOCSY correlations below. Numbers indicate the type of *J*-coupling. Mixing times were set to 18 ms for TOCSY and 500 ms for NOESY experiments.

A pure carbon network experiment is of course the C—C INADEQUATE. In recent example studies, using cryoprobe technology at 600 MHz, high-quality spectra were obtained on 10–20 mg samples within approximately 24 h recording time.[133,453,494] The superiority of INADEQUATE information is undoubted and will not be further discussed. An example is given in Fig. 3.42 for tibolone (**11**).

Among the mixed nuclei pathways, the inverse detected, that is, ^{1}H detected, experiments have proven their advantage over their heteronuclear-detected variants, although the latter may have the advantage of higher resolution.[415] For steroids, a lack of resolution may be compensated for by extracting the necessary information from another experiment. Still, the heteronuclear-detected experiments may experience a revival if dynamic nuclear polarization techniques[495,496] become more widespread, since the sensitivity gain should be larger on the time scale of carbon detection than of proton detection due to the longer carbon relaxation times.

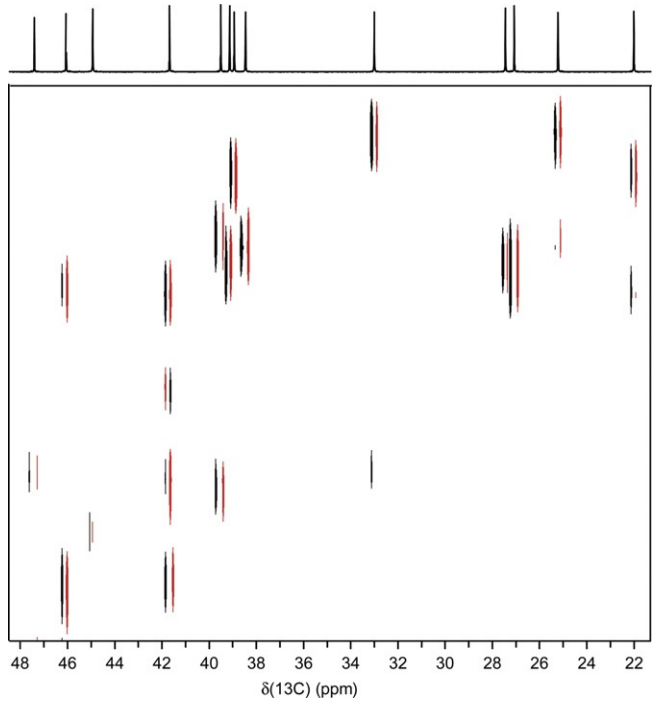

Figure 3.42 C—C INADEQUATE of tibolone (**11**) in $CDCl_3$. The delay was set for $J_{CC} = 50$ Hz.

Among the inverse detected long-range correlation experiments, the H—C HMBC is the most commonly used despite its disadvantages to distinguish between $^{2}J_{CH}$ and $^{3}J_{CH}$ splittings. This can be found for unsaturated steroids, for example, A-ring correlations in estradiol. More recently, H—C H2BC spectra were proposed as a remedy.[497] Spectral editing was subsequently included to reduce overlap, for example, in the spectra of prednisolone (**24**).[498] Few more reports applying H2BC to steroids were published up till now, among them saponins,[499] sapogenins[500] and bile acids.[501,502] For tibolone, the assignment strategy using the combination of HSQC and H2BC is illustrated in Fig. 3.43.

In the discussion of spectra suitable for CASE systems as a remedy to the distinction problem for two and three bonds, 1,1-ADEQUATE spectra were reinvestigated.[503,504]

As can be seen from Fig. 3.43, only $^{n}J_{CH}$ correlations were observed. Again, most recent cryoprobe technology allows the recording of a 1,1-ADEQUATE spectrum within a few hours on a few milligrams of sample. A common feature of HMBC and ADEQUATE experiments is that reasonable results can be obtained for steroids without the necessity of individual optimization of parameters such as delays corresponding to C—H-couplings. Both H2BC and 1,1-ADEQUATE are expected to bear the potential for significant contributions to problem-oriented as well as to automated structure analysis.

After the molecular constitution is established, the stereochemistry has to be addressed. Of course, H—H NOESY or H—H ROESY experiments are the means of choice. In cases of fluorinated steroids, H—F or F—H HOESY experiments have been applied successfully[346] for the fast assignment of diastereotopic fluorines and to determine the configuration two carbon atoms bearing a cyclopropyl substituent. As to H—H Overhauser

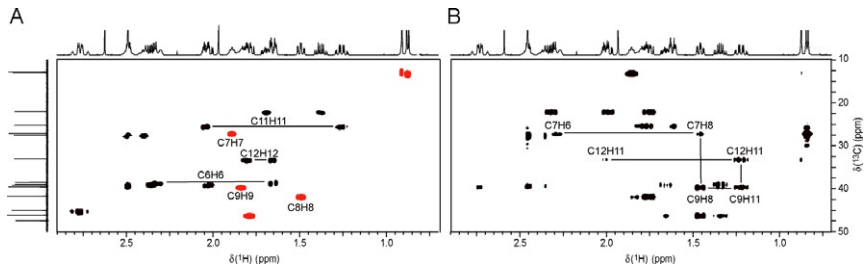

Figure 3.43 H—C HSQC (A) and H2BC (B) spectrum of tibolone (**11**) in $CDCl_3$ at 600 MHz.

spectroscopy, the NOESY experiment usually works fine for steroids in chloroform solution at 400 and 600 MHz according to the authors' experience. For steroids having large substituents, such as cholestane and ergostane, field strengths of 400 MHz proved preferable. Although the theoretical advantages of ROESY were well known, this type of experiment was rarely used in the authors' laboratory. Again to the authors' experience, the gradient version of the H—H NOESY gave in most cases of routine application reliable results with a better signal-to-noise ratio than the ROESY experiment.

In analogy to the COSY pathway, the stereochemical assignment and, in consequence, the stereochemical characterization often start from a distinct proton signal such as H8, H9, H14, CH_3-18, CH_3-19 or a proton geminal to a hydroxyl substituent of known configuration. As the reader certainly expects, this method is very robust. Only signal overlap or insufficient resolution may obstruct the straightforward assignment. The protons at C16 in testosterone represent illustrative examples,[131–133] as described earlier. When increasing the spectral resolution does not resolve the signal overlap, other experiments, such as hyphenated pulse sequences, need to be performed. This combination of pulse sequences such as HSQC and NOESY or HSQC and TOCSY allow the introduction of additional resolution via heteronuclear editing, even if the spectra are recorded in 2D variants.[277,416] The application of an HSQC–NOESY in 2D and 3D mode to the assignment of H16α and H16β in testosterone was demonstrated.[133]

Since NOE data are easily generated with NMR spectrometers of the past two decades, detailed analyses of coupling constants for qualitative assignment purposes seemed to have become somewhat redundant in the steroid field also owing to the rigidity of the steroid skeleton. This is in contrast to the 1980s when *J*-resolved spectroscopy was an important tool for structure elucidation, cf. Section 3.

In conclusion, today's standard set of experiments shall prove sufficient for structure analysis of steroids.

What experiments shall now be considered the spectroscopic minimum? A high-resolution mass-spectrum and a 1D ^{1}H NMR are non-disputable. Both H—H COSY and H—C HSQC require shorter experiment times than 1D ^{13}C but present only a selection of signals, whereas the H—H COSY reflects the connectivity network of protons over the steroid scaffold and the HSQC provides the necessary information over the carbon atoms without the quaternary carbons. In principle, COSY information may be

read out of the 1D ^{1}H, but will be difficult for steroids, since strong signal crowding is observed in the proton only domain for steroids. Clearly, C—C INADEQUATE, 1,1-ADEQUATE, H—C HMBC and any 3D spectroscopy are too time consuming or otherwise too insensitive to be considered for fast routine application in high-throughput mode. As a whole lot of structural information of the HSQC is contained in the chemical shifts, expert knowledge either in form of a human expert or of computerized data is to be combined with the spectroscopic data recorded in order to achieve structure confirmation. The experiment worthwhile to consider would be the H—C HSQC–TOCSY. Proton connectivity information and carbon shift information is combined in this hyphenated experiment. The TOCSY part should be recorded with short mixing times, for example, around 20 ms, to avoid signal crowding due to long-range coupling transferring magnetization too widely over the steroid scaffold. An HSQC–TOCSY is shown for tibolone in Fig. 3.44. The spectrum was recorded with a mixing time of 60 ms. While the correlations appear well separated, almost all signals are related to each other, providing not as much help for interpretation as could be achieved with shorter mixing times. To our experience, recording times of 1.5–4.5 h are needed on a few milligrams of a steroid.[133] Yet, indirect covariance transformation processing techniques[441] can generate this type of spectra within a few seconds from COSY or TOCSY and HSQC spectra.[436] It has been found that due to the higher sensitivity of the individual experiments as compared to the hyphenated sequence, the signal-to-noise ratio of the computed spectrum is superior to the experimental one.[133,436,444] A comparison of experimental and UIC-computed HSQC–TOCSY spectra of allylestrenol is presented in Fig. 3.45. It seems, therefore, worth trying to base structure confirmation of steroids on an H—C HSQC–TOCSY data set.

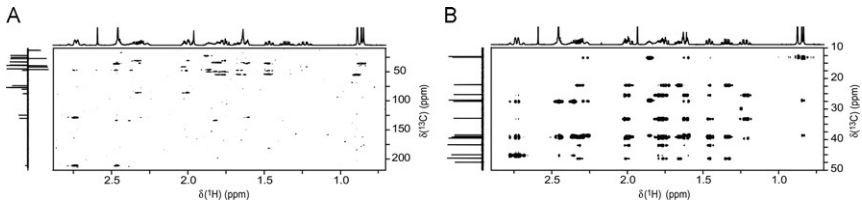

Figure 3.44 1,1-ADEQUATE of tibolone (**11**) in $CDCl_3$ at 298 K recorded at 500 MHz using a H,C sensitive cryoprobe (left). H—C HSQC–TOCSY of tibolone in $CDCl_3$ at 298 K recorded at 500 MHz and a mixing time of 60 ms (right).

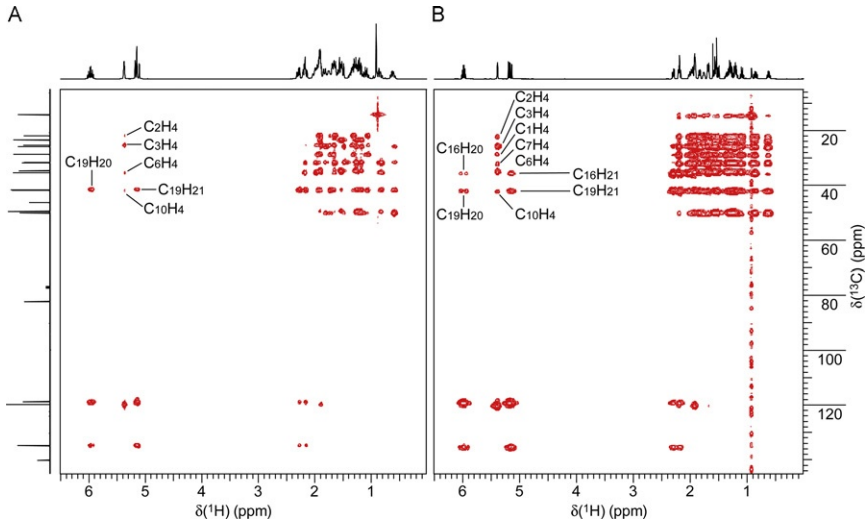

Figure 3.45 H—C HSQC–TOCSY spectra of allylestrenol (**29**) in $CDCl_3$. (A) Experimental spectrum, (B) spectrum computed from H—H TOCSY and H—C HSQC by unsymmetrical indirect covariance transformation. *Adapted with permission from Aspers et al.*[133] *Copyright 2011 John Wiley & Sons Ltd.*

Philosophically, one might ask: When the presence of a correlation in a spectrum which is due to a through-bond coupling is considered a direct proof of a chemical bond,[505] may the correlation that originates from a mathematical treatment of spectra be considered a proof of that bond, too?

A structural problem arising from a synthetic modification may be answered by other methods more specifically, such as COSY, NOESY or HMBC for introduction of a double bond, for a methylation in α- or β-position or an acetylation of a hydroxyl group, respectively. As was illustrated above, gradient-selective 1D experiments are powerful tools to address this specific type of issues, in particular, since they provide the high-resolution of 1D NMR spectra. For the recognition of the aromatization of the A-ring, a simple 1D ^{1}H might be sufficient. In metabolite investigations, COSY and TOCSY experiments play the most prominent role to identify position and configuration of the hydroxyl group.

In conclusion, steroids as nay other small molecule may be investigated following the general strategies how to verify structural hypotheses in the quickest and in the most generic manner. The spectroscopist imagination, creativity and experience will choose or devise the experiment to the most direct structure elucidation.

During the editorial process, a critical assessment on the methodology of enantiomer assignment by means of RDCs was kindly brought to our attention by C. Griesinger and C.M. Thiele prior to publication.[506] We expect that this communication will greatly impact further studies towards the determination of absolute configurations using alignment media.

ACKNOWLEDGMENTS

The authors are gratefully indebted to their former colleagues from N.V. Organon, Schering-Plough and Merck & Co. for many a fruitful discussion. They are especially thankful to L. Fielding, P.J.A.v. Tilborg, F.M. Kaspersen, G.N. Wagenaars, M. Honing, M.A. Lunenburg, C.A.A.v. Boeckel, F.T.L. Brands and G.E. Martin. Their heartfelt gratitude is due to Marinus B. Groen for sharing his experience and providing the 40 MHz spectrum of 4,4-dimethyl-$\Delta^{5,10}$-3-ceto-estrenol signed by J.-M. Lehn.

REFERENCES

1. Kirk DN. Steroids: physical methods. *Nat Prod Rep* 1986;**3**:505.
2. Kirk DN. Steroids: physical methods. *Nat Prod Rep* 1989;**6**:393.
3. Kirk DN, Gaskell SJ, Marples BA. *Spectroscopic methods of steroid analysis*. Makin HLJ, Gower DB, Kirk DN, editors. *Steroid analysis*. London, Glasgow, Weinheim, New York, Tokyo, Melbourne, Madras: Blackie Academic & Professional, an Imprint of Chapman & Hall; 1995. p. 25.
4. Kasal A, Budesinsky M, Griffiths WJ. *Spectroscopic methods of steroid analysis*. Makin HLJ, Gower DB, editors. *Steroid Analysis,* 2nd edition. Dordrecht, Heidelberg, London, New York: Springer; 2010. p. 27.
5. Croasmun WR, Carlson RMK. *Two-dimensional NMR spectroscopy. Applications for chemists and biochemists*. Weinheim: VCH; 1987.
6. Fieser LF, Fieser M. *Steroids*. New York: Reinhold Publishing Corporation; 1959.
7. Djerassi C. *Steroids made it possible (profiles, pathways, and dreams: autobiographies of eminent chemists)*. Washington, DC: American Chemical Society; 1990.
8. Djerassi C. *The pill, pygmy chimps, and Degas' horse*. New York: Basic Books; 1992.
9. Michal G. *Biochemical pathways (poster)*. Penzberg: Boehringer Mannheim; 1993.
10. *Human Steroidogenesis* Wikipedia http://en.wikipedia.org/wiki/Steroid.
11. Bernstein S. Historic reflection on steroids: Lederle and personal aspects. *Steroids* 1992;**57**:392.
12. Birch AJ. Steroid hormones and the Luftwaffe. A venture into fundamental strategic research and some of its consequences: the Birch reduction becomes a birth reduction. *Steroids* 1992;**57**:363.
13. Bloch K. Sterol molecule: structure, biosynthesis, and function. *Steroids* 1992;**57**:378.
14. Colton FB. Steroids and "the Pill": early steroid research at Searle. *Steroids* 1992;**57**:624.
15. Djerassi C. Steroid research at Syntex: "the Pill" and cortisone. *Steroids* 1992;**57**:631.
16. Fried J. Hunt for an economical synthesis of cortisol: discovery of the fluorosteroids at Squibb (a personal account). *Steroids* 1992;**57**:384.
17. Herzog H, Oliveto EP. A history of significant steroid discoveries and developments originating at the Schering Corporation (USA) since 1948. *Steroids* 1992;**57**:617.
18. Hirschmann R. The cortisone era: aspects of its impact. Some contributions of the Merck Laboratories. *Steroids* 1992;**57**:579.

19. Hogg JA. Steroids, the steroid community, and Upjohn in perspective: a profile of innovation. *Steroids* 1992;**57**:593.
20. Jones ERH. Early English steroid history. *Steroids* 1992;**57**:357.
21. Lehmann F. PA. Early history of steroid chemistry in Mexico: the story of three remarkable men. *Steroids* 1992;**57**:403.
22. Mappus E, Renaud M, Rolland de Ravel M, Grenot C, Cuilleron CY. Synthesis and characterization by 1H and 13C nuclear magnetic resonance spectroscopy of 17 alpha-hexanoic derivatives of 5 alpha-dihydrotestosterone and testosterone. *Steroids* 1992;**57**:122.
23. Nakanishi K. Past and present studies with ponasterones, the first insect molting hormones from plants. *Steroids* 1992;**57**:649.
24. Rosenkranz G. From Ruzicka's terpenes in Zurich to Mexican steroids via Cuba. *Steroids* 1992;**57**:409.
25. Zaffaroni A. From paper chromatography to drug discovery: Zaffaroni. *Steroids* 1992;**57**:642.
26. Heusler K, Kalvoda J. Between basic and applied research: Ciba's involvement in steroids in the 1950s and 1960s. *Steroids* 1996;**61**:492.
27. Szpilfogel SA, Zeelen FJ. Steroid research at Organon in the golden 1950s and the following years. *Steroids* 1996;**61**:483.
28. Callow RK, Young FG. Relations between the optical rotatory power and constitution in the steroids. *Proc R Soc Lond Ser A* 1936;**157**:194.
29. Dannenberg H. The ultraviolet absorption spectra of the steroids. *Abhandl preuss Akad Wiss Math-nat Klasse* 1940;**21**:68.
30. Woodward RB. Structure and the absorption spectra of a, b-unsaturated ketones. *J Am Chem Soc* 1941;**63**:1123.
31. Woodward RB. Structure and absorption spectra. IV. Further observations on a, b-unsaturated ketones. *J Am Chem Soc* 1942;**64**:76.
32. Jones RN. Characterization of sterol hormones by ultraviolet and infrared spectroscopy. *Recent Prog Horm Res* 1948;**2**:3.
33. Wilds AL, Beck LW, Close WJ, Djerassi C, Johnson Jr. JA, Johnson TL, Shunk CH. Ultraviolet absorption spectra of a, b-unsaturated ketones conjugated with an aromatic nucleus. *J Am Chem Soc* 1947;**69**:1985.
34. Djerassi C, Ryan E. Ultraviolet absorption spectra of steroidal dinitrophenylhydrazones. *J Am Chem Soc* 1949;**71**:1000.
35. Dorfman L. Ultraviolet absorption of steroids. *Chem Rev* 1953;**53**:47.
36. Turner DW. Far-ultraviolet light absorption by saturated hydrocarbons. *Chem Ind* 1958;626.
37. Turner DW. Spectrophotometry in the far ultraviolet region. II. Absorption spectra of steroids and triterpenoids. *J Chem Soc* 1959;30.
38. Sharma M, Georgian V. Syntheses and ultraviolet absorption of aza-steroids. *Steroids* 1976;**27**:225.
39. Khayam-Bashi H, Boroumand M. Spectrophotometric estimation of 17β-estradiol progesterone, and testosterone. *Biochem Med* 1975;**14**:104.
40. Lowry TM. *Optical rotatory power*. London: Longmans, Green and Co.; 1935.
41. Bernstein S, Kauzmann WJ, Wallis ES. The relationship between optical rotatory power and constitution of the sterols. *J Org Chem* 1941;**6**:319.
42. Bernstein S, Wilson Jr. EJ, Wallis ES. The relationship between optical rotatory power and constitution of the sterols. II. *J Org Chem* 1942;**7**:103.
43. Barton DHR. Application of the method of molecular rotation differences to steroids. I. Naturally occurring sterols and their simple derivatives. *J Chem Soc* 1945;813.
44. Bernstein S, Hicks Jr. EM, Clark DM, Wallis ES. The relationship between optical rotatory power and constitution of the sterols. III. *J Org Chem* 1946;**11**:646.

45. Barton DHR, Cox JD. Application of the method of molecular rotation differences to steroids. IV. Optical anomalies. *J Chem Soc* 1948;783.
46. Barton DHR. Application of the method of molecular rotation differences to steroids. II. Unsaturated sterols and their derivatives. *J Chem Soc* 1946;512.
47. Barton DHR, Klyne W. A survey of steroid molecular rotations. *Chem Ind* 1948;755.
48. Barton DHR. Optical rotation and molecular structure of the steroids. *Angew Chem* 1949;**61**:57.
49. Wieland H, Dane E. The constitution of the bile acids. L. The structure of the entire framework and the nature of ring D. *Z Physiol Chem* 1933;**216**:91.
50. Wieland H, Dane E, Martius C. The constitution of the bile acids. XLIX. Stereochemistry of bile acids and sterols. *Z Physiol Chem* 1933;**215**:15.
51. Butenandt A. Chemical constitution of the follicular and testicular hormones. *Nature* 1932;**130**:238.
52. Butenandt A, Weidlich HA, Thompson H. Neue Beiträge zur Konstitution des Follikel-Hormons (Vorläuf. Mitteil1). *Ber Dtsch Chem Ges (A and B Series)* 1933;**66**:601.
53. Butenandt A, Westphal U. Beitraege zur Konstitutionsermittlung des Follikelhormons. II. Ueber den Saettigungsgrad und den aromatischen Charakter des Follikelhormons. Untersuchungen ueber das weibliche Sexualhormon, 11. Mitteilung. *Z Physiol Chem* 1934;**223**:147.
54. Slotta KH, Ruschig H, Fels E. Reindarstellung der Hormone aus dem Corpus luteum (II. Mitteil.). *Ber Dtsch Chem Ges (A and B Series)* 1934;**67**:1624.
55. Wintersteiner O, Allen WM. Crystalline progestin. *J Biol Chem* 1934;**107**:337.
56. Reichstein T. ber Cortin, das Hormon der Nebennierenrinde. I. Mitteilung. *Helv Chim Acta* 1936;**19**:29.
57. Ruzicka L, Wettstein A. Sexualhormone VII. Über die künstliche Herstellung des Testikelhormons Testosterone (Androsten-3-on-17-ol). *Helv Chim Acta* 1935;**18**:1264.
58. Marker RE, Rohrmann E. Sterols. LXXXI. Conversion of sarsasapogenin to pregnanediol-3-(α),20(α). *J Am Chem Soc* 1939;**61**:3592.
59. Marker RE. Sterols. CXIII. Sapogenins. XLII. The conversion of the sapogenins to the pregnenolones. *J Am Chem Soc* 1940;**62**:3350.
60. Marker RE. Sterols. CV. The preparation of testosterone and related compounds from sarsasapogenin and diosgenin. *J Am Chem Soc* 1940;**62**:2543.
61. Marker RE, Rohrmann E. Sterols. LXXXVIII. Pregnanediols from sarsasapogenin. *J Am Chem Soc* 1940;**62**:518.
62. Crowfoot D. X-ray crystallography and sterol structure. *Vitam Horm* 1944;**2**:409.
63. Deschamps JR, George C. Advances in X-ray crystallography. *TrAC Trends Anal Chem* 2003;**22**:561.
64. Isaacs NW, Motherwell WDS, Coppola JC, Kennard O. Crystal and molecular structure of 17α -hydroxyandrost-4-en-3-one (epitestosterone). *J Chem Soc Perkin Trans 2* 1972;2335.
65. Shieh HS, Hoard LG, Nordman CE. Crystal structure of anhydrous cholesterol. *Nature* 1977;**267**:287.
66. Roberts PJ, Pettersen RC, Sheldrick GM, Isaacs NW, Kennard O. Crystal and molecular structure of 17β-hydroxyandrost-4-en-3-one (testosterone). *J Chem Soc Perkin Trans 2* 1973;1978.
67. Jones RN, Williams VZ, Whalen MJ, Dobriner K. Steroid metabolism. IV. Characterization of carbonyl and other functional groups in steroids by infrared spectrometry. *J Am Chem Soc* 1948;**70**:2024.
68. Jones RN, Cole ARH. Characterization of methyl and methylene groups in steroids by infrared spectrometry. I. Correlations of bending frequencies with molecular structure. *J Am Chem Soc* 1952;**74**:5648.

69. Jones RN, Cole ARH, Nolin B. Characterization of methyl and methylene groups in steroids by infrared spectrometry. II. Methyl and methylene bending frequencies in steroids labeled with deuterium. *J Am Chem Soc* 1952;**74**:5662.
70. Jones RN, Ramsay DA, Keir DS, Dobriner K. The intensities of carbonyl bands in the infrared spectra of steroids. *J Am Chem Soc* 1952;**74**:80.
71. Jones NR, Herling F. Characteristic group frequencies in the infrared spectra of steroids. *J Org Chem* 1954;**19**:1252.
72. Burton RB, Zaffaroni A, Keutmann EH. The application of paper partition chromatography to ketosteroids. *J Clin Endocrinol Metab* 1948;**8**:618.
73. Zaffaroni A, Burton RB, Keutmann EH. The application of paper partition chromatography to steroid analysis; ketosteroids. *J Biol Chem* 1949;**177**:109.
74. Zaffaroni A, Burton RB, Keutmann EH. Adrenal cortical hormones: analysis by paper partition chromatography and occurrence in the urine of normal persons. *Science* 1950;**111**:6.
75. Kritchevsky TK, Tiselius A. Reversed phase partition chromatography by steroids on silicone-treated paper. *Science* 1951;**114**:299.
76. Brand E, Washburn E, Erlanger BF, Ellenbogen E, Daniel J, Lippmann F, Scheu M. Rotatory dispersions of some steroids, amino acids and peptides using a new photoelectric spectropolarimeter. *J Am Chem Soc* 1954;**76**:5037.
77. Djerassi C, Foltz EW, Lippman AE. Optical rotatory dispersion studies. I. The androstane series. *J Am Chem Soc* 1955;**77**:4354.
78. Foltz EW, Lippman AE, Djerassi C. Optical rotatory dispersion studies. II. Steroid hormones. *J Am Chem Soc* 1955;**77**:4359.
79. Lippman AE, Foltz EW, Djerassi C. Optical rotatory dispersion studies. III. The cholestane series. *J Am Chem Soc* 1955;**77**:4364.
80. Djerassi C, Closson W, Lippman AE. Optical rotatory dispersion studies. V. The effect of isolated carbonyl groups and double bonds in the cholestane series. *J Am Chem Soc* 1956;**78**:3163.
81. Djerassi C, Osiecki J, Herz W. Optical rotatory dispersion. XIII. Assignment of absolute configuration to members of the guaianolide series of sesquiterpenes. *J Org Chem* 1957;**22**:1361.
82. Djerassi C, Klyne W. Optical rotatory dispersion studies. X. Determination of absolute configuration of a-halocyclohexanones. *J Am Chem Soc* 1957;**79**:1506.
83. Djerassi C, Klyne W. Recording and nomenclature of optical rotatory dispersion. *Proc Chem Soc Lond* 1957;55.
84. Djerassi C. *Optical rotatory dispersion; application to organic chemistry*. New York, Toronto, London: McGraw-Hill; 1960.
85. Crabbe P. *Applications of optical rotatory dispersion and optical circular dichroism in organic chemistry*. San Francisco: Holden-Day; 1968.
86. Moffitt W, Woodward RB, Moscowitz A, Klyne W, Djerassi C. Structure and the optical rotatory dispersion of saturated ketones. *J Am Chem Soc* 1961;**83**:4013.
87. De Mayo P, Reed RI. Application of the mass spectrometer to steroid and terpenoid chemistry. *Chem Ind* 1956;1481.
88. Bergstrom S, Ryhage R, Stenhagen E. Mass spectrometric studies on bile acids and other steroid derivatives. *Acta Chem Scand* 1958;**12**:1349.
89. Reed RI. Electron impact and molecular dissociation. I. Some steroids and triterpenoids. *J Chem Soc* 1958;3432.
90. Friedland SS, Lane Jr. GH, Longman RT, Train KE, O'Neal Jr. MJ. Mass spectra of steroids. *Anal Chem* 1959;**31**:169.
91. Biemann K, Seibl J. Application of mass spectrometry to structure problems. II. Stereochemistry of epimeric, cyclic alcohols. *J Am Chem Soc* 1959;**81**:3149.
92. Ryhage R, Stenhagen E. Mass spectrometry in lipide research. *J Lipid Res* 1960;**1**:361.

93. Budzikiewicz H, Djerassi C. Mass spectrometry in structural and stereochemical problems. I. Steroid ketones. *J Am Chem Soc* 1962;**84**:1430.
94. Gilbert B, Ferreira JM, Owellen RJ, Swanholm CE, Budzikiewicz H, Durham LJ, Djerassi C. Mass spectrometry in structural and stereochemical problems. II. Pyrifoline and refractidine. *Tetrahedron Lett* 1962;**3**:59.
95. Budzikiewicz H, Wilson JM, Djerassi C. Mass spectrometry and its application to structural and stereochemical problems. XV. Steroidal sapogenins. *Monatsh Chem* 1962;**93**:1033.
96. Williams TM, Kind AJ, Houghton E, Hill DW. Electrospray collision-induced dissociation of testosterone and testosterone hydroxy analogs. *J Mass Spec* 1999;**34**:206.
97. Niessen WMA. Fragmentation of toxicologically relevant drugs in positive-ion liquid chromatography–tandem mass spectrometry. *Mass Spec Rev* 2011;**30**:626.
98. Griffiths WJ. Tandem mass spectrometry in the study of fatty acids, bile acids, and steroids. *Mass Spec Rev* 2003;**22**:81.
99. Budzikiewicz H. Selected reviews on mass spectrometric topics—CXIV. *Mass Spec Rev* 2005;**24**:121.
100. Thevis M, Schaenzer W. Mass spectrometry in sports drug testing: structure characterization and analytical assays. *Mass Spec Rev* 2007;**26**:79.
101. Budzikiewicz H, Djerassi C, Williams DH. *Mass spectrometry of organic compounds*. San Francisco: Holden-Day; 1967.
102. Djerassi C. Mass spectrometric investigation in the steroid, terpenoid and alkaloid fields. *Pure Appl Chem* 1963;**6**:575.
103. Shoolery JN, Rogers MT. Nuclear magnetic resonance spectra of steroids. *J Am Chem Soc* 1958;**80**:5121.
104. Rosen WE, Ziegler JB, Schabica AC, Shoolery JN. The stereochemistry of steroidal sapogenins. III. Nuclear magnetic resonance spectra. *J Am Chem Soc* 1959;**81**:1687.
105. Zuercher RF. Protonenresonanzspektroskopie und Steroidstruktur I. Das C-19-Methylsignal in Funktion der Substituenten. *Helv Chim Acta* 1961;**44**:1380.
106. Zuercher RF. Proton (magnetic)resonance spectroscopy (N.M.R.) and steroid structure. II. The position of the C-18- and C-19-methyl signal and its dependence on substituents in the steroid framework. *Helv Chim Acta* 1963;**46**:2054.
107. Reich HJ, Jautelat M, Messe MT, Weigert FJ, Roberts JD. Nuclear magnetic resonance spectroscopy. Carbon-13 spectra of steroids. *J Am Chem Soc* 1969;**91**:7445.
108. Eggert H, Djerassi C. Carbon-13 nuclear magnetic resonance spectra of keto steroids. *J Org Chem* 1973;**38**:3788.
109. Rubinstein I, Goad LJ, Clague ADH, Mulheirn LJ. The 220 MHz NMR spectra of phytosterols. *Phytochemistry* 1976;**15**:195.
110. Thompson MJ, Dutky SR, Patterson GW, Golden EL. NMR spectra of C-24 isomeric sterols. *Phytochemistry* 1972;**11**:1781.
111. Agrawal PK, Jain DC, Gupta RK, Thakur RS. Carbon-13 NMR spectroscopy of steroidal sapogenins and steroidal saponins. *Phytochemistry* 1985;**24**:2479.
112. Blunt JW, Stothers JB. ^{13}C n.m.r. spectra of steroids—a survey and commentary. *Org Magn Reson* 1977;**9**:439.
113. Hall LD, Sanders JKM. Complete assignment of proton NMR spectra of steroids using nuclear Overhauser enhancement-difference and decoupling-difference techniques. *J Chem Soc Chem Commun* 1980;368.
114. Farrant RD, Kirk DN, Mersh JD, Sanders JKM. Recent applications of NMR to the investigation of steroid structures. *J Steroid Biochem* 1983;**19**:181.
115. Hall LD, Sanders JKM. Analysis of the proton nuclear magnetic resonance spectrum of 11b-hydroxyprogesterone by one- and two-dimensional methods. Some implications for steroid and terpenoid chemistry. *J Org Chem* 1981;**46**:1132.

116. Schneider HJ, Buchheit U, Becker N, Schmidt G, Siehl U. Proton NMR analyses, shielding mechanisms, coupling constants, and conformations in steroids bearing halogen, hydroxy, and oxo groups and double bonds. *J Am Chem Soc* 1985;**107**:7027.
117. Sedee AGJ, Beijersbergen van Henegouwen GMJ, De Vries ME, Erkelens C. Mestranol: the assignment of its proton and carbon-13 NMR spectra by means of two-dimensional NMR spectroscopy, and its photochemical decomposition. *Steroids* 1985;**45**:101.
118. Duddeck H, Rosenbaum D, Hani M, Elgamal A, Fayez MBE. High-field 1H and 13C NMR spectroscopy of some corticosteroids and related compounds. *Magn Reson Chem* 1986;**24**:999.
119. Sedee AGJ, Beijersbergen van Henegouwen GMJ, Guijt W, Haasnoot CAG. Structure elucidation of two isomeric steroids: photolytical and thermal reaction products from norethisterone studied by two-dimensional nuclear magnetic resonance. *Pharm Weekbl Sci Ed* 1985;**7**:202.
120. Martin GE, Guido JE, Robins RH, Sharaf MHM, Schiff Jr. PL, Tackie AN. Submicro inverse-detection gradient NMR: a powerful new way of conducting structure elucidation studies with <0.05 mmol samples. *J Nat Prod* 1998;**61**:555.
121. Martin GE. Cryogenic NMR probes: applications. *Encycl Nucl Magn Reson* 2002;**9**:33.
122. Bax A. *Two-dimensional nuclear magnetic resonance in liquids*. Dordrecht, Holland: D. Reidel Publishing Company; 1982.
123. Parella T. Pulsed field gradients: a new tool for routine NMR. *Magn Reson Chem* 1998;**36**:467.
124. Karplus M. Contact electron-spin coupling of nuclear magnetic moments. *J Chem Phys* 1959;**30**:1.
125. Haasnoot CAG, de Leeuw FAAM, Altona C. The relationship between proton-proton NMR coupling constants and substituent electronegativities-I : an empirical generalization of the karplus equation. *Tetrahedron* 1980;**36**:2783.
126. Marat K, Templeton JF, Gupta RK, Kumar VPS. Ring A conformation in steroids. 2. NMR study of C-2 monomethyl- and dimethyl-substituted 5a-androstan-3-ones. *Magn Reson Chem* 1987;**25**:730.
127. Marat K, Templeton JF, Kumar VPS. An NMR study of A-ring conformation in some 4-en-3-one steroids. *Magn Reson Chem* 1987;**25**:25.
128. Croasmun WR, Carlson RMK. Steroid structural analysis by two-dimensional NMR. *Methods Stereochem Anal* 1987;**9**:387.
129. Smith LL. Recognition of structure in hydroxy steroids. II. Nuclear magnetic resonance spectra. *Steroids* 1964;**4**:395.
130. Agrawal PK, Jain DC, Pathak AK. NMR spectroscopy of steroidal sapogenins and steroidal saponins: an update. *Magn Reson Chem* 1995;**33**:923.
131. Hayamizu K, Ishii T, Yanagisawa M, Kamo O. Complete assignments of the proton and carbon-13 NMR spectra of testosterone and 17α-methyltestosterone and the proton parameters obtained from 600 MHz spectra. *Magn Reson Chem* 1990;**28**:250.
132. Kirk DN, Toms HC, Douglas C, White KA, Smith KE, Latif S, Hubbard RWP. A survey of the high-field proton NMR spectra of the steroid hormones, their hydroxylated derivatives, and related compounds. *J Chem Soc Perkin Trans 2* 1990;1567.
133. Aspers RLEG, Geutjes PETJ, Honing M, Jaeger M. Using indirect covariance processing for structure elucidation of small molecules in cases of spectral crowding. *Magn Reson Chem* 2011;**49**:425.
134. Wilk M, Schmitt K. Carbon-13 NMR spectra of N-methylimidazole-substituted sterol esters. *Org Magn Reson* 1981;**15**:329.
135. Marcano D, Rojas A, Mendez B, De Mendez J. Carbon-13 nuclear magnetic resonance spectra of D-homoandrostane derivatives. *Org Magn Reson* 1981;**16**:205.

136. Iida T, Kikuchi M, Ishikawa T, Tamura T, Matsumoto T. Carbon-13 NMR spectra of some c-4 methylated sterols and their derivatives. *Org Magn Reson* 1982;**19**:228.
137. Iida T, Tamura T, Matsumoto T. Carbon-13 NMR spectra of some c-6 methylated steroids. *Magn Reson Chem* 1987;**25**:558.
138. Olson RE. Discovery of the lipoproteins, their role in fat transport and their significance as risk factors. *J Nutr* 1998;**128**:439S.
139. Strecker A. Untersuchung der Ochsengalle. *Ann Chem* 1848;**67**:1.
140. Reinitzer F. Beitraege zur Kenntniss des Cholesterins. *Monatsh Chem/Chemical Monthly* 1888;**9**:421.
141. Wieland H, Boersch E. Untersuchungen ueber die Gallensaeuren. V. Mitteilung. Die Reduktion der Dehydrocholsaeure und der Dehydrodesoxycholsaeure. *Z Physiol Chem* 1919;**106**:190.
142. Windaus A. Untersuchungen über Cholesterin. *Arch Pharm* 1908;**246**:117.
143. Windaus A, Neukirchen K. Die Umwandlung des Cholesterins in Cholansäure. (28. Mitteilung über Cholesterin.). *Ber Dtsch Chem Ges (A and B Series)* 1919;**52**:1915.
144. Doisy EA, Velor CD, Tayer S. Folliculin from urine of pregnant women. *Am J Physiol* 1929;**90**:329.
145. Butenandt A. Ueber "Progynon" ein krystallisiertes weibliches Sexualhormon. *Naturwissenschaften* 1929;**17**:879.
146. Butenandt A, Hildebrandt F, Brucher H. Pregnandiol, a new sterol derivative from gravid urine. II. *Ber Dtsch Chem Ges B* 1931;**64B**:2529.
147. Rosenheim O, King H. The ring-system of sterols and bile acids. *J Soc Chem Ind* 1932;**51**:464.
148. Butenandt A, Tscherning K. Androsterone, a crystalline male sex hormone. I. Isolation and purification from male urine. *Z Physiol Chem* 1934;**229**:167.
149. Butenandt A, Tscherning K. Androsterone, a crystalline male sex hormone. II. Its chemical characterization. *Z Physiol Chem* 1934;**229**:185.
150. Ruzicka L, Goldberg MW, Meyer J, Brungger H, Eichenberger E. Sex hormones. II. The synthesis of testicular hormone (androsterone) and its stereoisomers. *Helv Chim Acta* 1934;**17**:1395.
151. Robinson R. On the mechanism of the conversion of squalene to sterols. *J Soc Chem Ind* 1934;**53**:1062.
152. du Feu EC, McQuillin FJ, Robinson R. Synthesis of substances related to the sterols. XIV. A simple synthesis of certain octalones and ketotetrahydrohydrindenes which may be of angle-methyl-substituted type. A theory of the biogenesis of the sterols. *J Chem Soc* 1937;53.
153. Popjak G. Biosynthesis of squalene and cholesterol in vitro from acetate-1-C14. *Arch Biochem Biophys* 1954;**48**:102.
154. Cornforth JW, Popjak G. Studies on the biosynthesis of cholesterol. 3. Distribution of 14C in squalene biosynthesized from (Me-14C)-acetate. *Biochem J* 1954;**58**:403.
155. David K, Dingemanse E, Freud J, Laqueur E. Crystalline male hormone from testes (testosterone), more active than androsterone prepared from urine or cholesterol. *Z Physiol Chem* 1935;**233**:281.
156. Butenandt A, Hanisch G. Ueber Testosteron. Umwandlung des Dehydro-androsterons in Androstendiol und Testosteron; ein Weg zur Darstellung des Testosterons aus Cholesterin. *Z Physiol Chem* 1935;**237**:89.
157. Winersteiner O, Pfiffner JJ. Chemical Studies of the adrenal cortex: III. Isolation of two new physiologically inactive compounds. *J Biol Chem* 1936;**116**:291.
158. Pfiffner JJ, Wintersteiner O. Proceedings of the American Society of Biological Chemists: thirtieth annual meeting. *J Biol Chem* 1936;**114**:iii.
159. Mason HL, Myers CS, Kendall EC. The chemistry of crystalline substances isolated from the suprarenal gland. *J Biol Chem* 1936;**114**:613.

160. Inhoffen HH, Logemann W, Hohlweg W, Serini A. Untersuchungen in der Sexualhormon-Reihe. *Ber Dtsch Chem Ges (A and B Series)* 1938;**71**:1024.
161. Marker RE, Shabica AC. Sterols. XCIX. Sterols from various sources. *J Am Chem Soc* 1940;**62**:2523.
162. Inhoffen HH. The transformations of sterols into aromatic compounds. *Angew Chem* 1940;**53**:471.
163. Inhoffen HH, Zuhlsdorff G. Transformation of sterols into aromatic compounds. VI. Preparation of the follicular hormone estradiol from cholesterol. *Ber Dtsch Chem Ges B* 1941;**74B**:1911.
164. Sarett LH. A new method for the preparation of 17α-hydroxy-20-ketopregnanes. *J Am Chem Soc* 1948;**70**:1454.
165. Sarett LH. Preparation of pregnane-17α,21-diol-3,11,20-trione acetate. *J Am Chem Soc* 1949;**71**:2443.
166. Anner G, Miescher K. Steroids. LXXIII. Total synthesis of natural estrone. *Experientia* 1948;**4**:25.
167. Anner G, Miescher K. Steroids. LXXXIII. The synthesis of natural estrone. Total syntheses in the estrone group. 3. *Helv Chim Acta* 1948;**31**:2173.
168. Hench PS, Kendall EC, Slocumb CH, Polley HF. The effect of a hormone of the adrenal cortex (17-hydroxy-11-dehydrocorticosterone: compound E) and of the pituitary adrenocorticotropic hormone on rheumatoid arthritis. *Mayo Clin Proc* 1949;**24**:181.
169. Johnson WS, Banerjee DK, Schneider WP, Gutsche CD. Total synthesis of estrone and the remaining stereoisomers. *J Am Chem Soc* 1950;**72**:1426.
170. Woodward RB, Sondheimer F, Taub D. The total synthesis of cholesterol. *J Am Chem Soc* 1951;**73**:3548.
171. Cardwell HME, Cornforth JW, Duff SR, Holtermann H, Robinson R. Total synthesis of androgenic hormones. *Chem Ind* 1951;389.
172. Woodward RB, Sondheimer F, Taub D. The total synthesis of cortisone. *J Am Chem Soc* 1951;**73**:4057.
173. Woodward RB, Sondheimer F, Taub D, Heusler K, McLamore WM. The total synthesis of steroids. *J Am Chem Soc* 1952;**74**:4223.
174. Peterson DH, Murray HC. Microbiological oxygenation of steroids at carbon 11N 11. *J Am Chem Soc* 1952;**74**:1871.
175. Peterson DH, Murray HC, Eppstein SH, Reineke LM, Weintraub A, Meister PD, Leigh HM. Microbiological transformations of steroids. I. Introduction of oxygen at carbon-11 of progesterone. *J Am Chem Soc* 1952;**74**:5933.
176. Johnson WS, Bannister B, Bloom BM, Kemp AD, Pappo R, Rogier ER, Szmuszkovicz J. Total synthesis of epiandrosterone. *J Am Chem Soc* 1953;**75**:2275.
177. Djerassi C, Miramontes L, Rosenkranz G. Steroids. XLVIII.1 19-norprogesterone, a potent progestational hormone. *J Am Chem Soc* 1953;**75**:4440.
178. Simpson SA, Tait JF, Wettstein A, Neher R, Von Euw J, Schindler O, Reichstein T. The constitution of aldosterone, the new mineral corticoid. *Experientia* 1954;**10**:132.
179. Djerassi C, Miramontes L, Rosenkranz G, Sondheimer F. Steroids. LIV.1 Synthesis of 19-Nov-17α-ethynyltestosterone and 19-Nor-17α-methyltestosterone2. *J Am Chem Soc* 1954;**76**:4092.
180. Herzog HL, Payne CC, Jevnik MA, Gould D, Shapiro EL, Oliveto EP, Hershberg EB. 1-Oxygenated steroids. XIII. Synthesis and proof of structure of 1,4-pregnadiene-17α,21-diol-3,11,20-trione and $\Delta^{1,4}$-pregnadiene-11β,17α,21-triol-3,20-dione. *J Am Chem Soc* 1955;**77**:4781.
181. Pincus G, Chang MC, Hafez ESE, Zarrow MX, Merrill A. Effects of certain 19-norsteroids on reproductive processes in animals. *Science* 1956;**124**:890.

182. Inhoffen HH, Quinkert G, Hess HJ. Partial synthesis of vitamin D2. *Naturwissenschaften* 1957;**44**:11.
183. Inhoffen HH, Irmscher K, Hirschfeld H, Stache U, Kreutzer A. Partial synthesis of vitamins D2 and D3. *J Chem Soc* 1959;385.
184. Harrison IT, Lythgoe B. Partial synthesis of calciferol and of epicalciferol. I. *Proc Chem Soc Lond* 1957;261.
185. Harrison IT, Lythgoe B. Calciferol and its relatives. III. Partial synthesis of calciferol and of epicalciferol. *J Chem Soc* 1958;837.
186. Herzog HL, Gentles MJ, Basch A, Coscarelli W, Zeitz MEA, Charney W. Microbiological transformation of steroids. VIII. 16β-Hydroxylation and other transformations of testosterone by Wojnowicia graminis. *J Org Chem* 1960;**25**:2177.
187. Barton DHR, Beaton JM. Synthesis of aldosterone acetate. *J Am Chem Soc* 1961;**83**:4083.
188. Barton DHR, Cheung HT, Cross AD, Jackman LM, Martin-Smith M. The constitution of clerodin. *Proc Chem Soc Lond* 1961;76.
189. Lythgoe B, Moran TA, Nambudiry MEN, Tideswell J, Wright PW. Calciferol and its relatives. Part 22. A direct total synthesis of vitamin D2 and vitamin D3. *J Chem Soc Perkin Trans 1* 1978;590.
190. Rock J, Pincus G, Garcia CR. Effect of certain 19-nor steroids on the normal human menstrual cycle. *Science* 1956;**124**:891.
191. Pincus G. The hormonal control of ovulation and early development. *Postgrad Med* 1958;**24**:654.
192. Pincus G, Garcia CR, Rock J, Paniagua M, Pendleton A, Laraque F, Nicolas R, Borno R, Pean V. Effectiveness of an oral contraceptive; effects of a progestin-estrogen combination upon fertility. *Science* 1959;**130**:81.
193. Fielding L, Diepeveen Y, Fletcher D, Hamilton N. Unnaturally configured 13-epi steroids: full ^{1}H and ^{13}C assignments and ring C-D conformations from ^{1}H, ^{1}H vicinal couplings. *Magn Reson Chem* 2001;**39**:323.
194. Anastasia M, Allevi P, Fiecchi A, Oleotti A, Scala A. Stereochemical course of the hydroboration of highly hindered steroidal olefins. A ready synthesis of 14[beta]- and 8[alpha], 14[beta]-steroids. *Steroids* 1986;**47**:131.
195. Burgoyne DL, Andersen RJ, Allen TM. Contignasterol, a highly oxygenated steroid with the unnatural 14β configuration from the marine sponge Petrosia contignata Thiele. *J Org Chem* 1992;**57**:525.
196. Teerhuis NM, Huisman IAM, Groen MB. Synthesis of ent-19-nortestosterone from its naturally occurring antipode. *Tetrahedron Lett* 2001;**42**:2869.
197. Kessler H. Detection of hindered rotation and inversion by NMR spectroscopy. *Angew Chem Internat Ed* 1970;**9**:219.
198. Guenther H. *NMR spectroscopy. Basic principles, concepts, and applications in chemistry*. Chichester: John Wiley & Sons Ltd.; 1995.
199. Kutney JP, Cretney W, Pettit GR, Knight JC. Steroids and related natural products. XXIII. Structure and stereochemistry of the monobromotigogenins. *Tetrahedron* 1964;**20**:1999.
200. Zuercher RF. Configuration and conformation analysis using proton-spin resonance, demonstrated by using steroids as examples. *Chimia* 1964;**18**:349.
201. Bhacca NS, Williams DH. *Applications of NMR spectroscopy in organic chemistry. Illustrations from the steroid field*. San Francisco: Holden-Day; 1964.
202. Williamson KL, Howell T, Spencer TA. Nuclear magnetic resonance line widths of angular methyl groups in decalins, steroids, and N-methylquinolizidinium ions. Determination of ring fusion stereochemistry. *J Am Chem Soc* 1966;**88**:325.
203. Puri R, Wong TC, Puri RK. Solasodine and diosgenin: ^{1}H and ^{13}C assignments by two-dimensional NMR spectroscopy. *Magn Reson Chem* 1993;**31**:278.

204. Wehrli H, Heller MS, Schaffner K, Jeger O. ber Steroide und Sexualhormone. 223. Mitteilung. UV.-Bestrahlung von 11-Oxo-Steroiden I Die Darstellung von 11β, 19-Cyclo-, 9β, 19-Cyclo- und 19-Hydroxy-5α-pregnan-Verbindungen. *Helv Chim Acta* 1961;**44**:2162.
205. Bhacca NS, Gurst JE, Williams DH. Spin-spin coupling between hydrogen and steroid angular methyl protons. *J Am Chem Soc* 1965;**87**:302.
206. Barfield M, Chakrabarti B. Long-range proton spin-spin coupling. *Chem Rev* 1969;**69**:757.
207. Platzer N, Goasdoue N, Davoust D. Long-range proton coupling interactions: identification of different pathways by 2D NMR δ-δ correlated spectroscopy. Applications in structural analysis. *Magn Reson Chem* 1987;**25**:311.
208. Cross AD, Landis PW. Steroids. CXCVII.1a spectra and stereochemistry. Part II. 1b Long-range spin-spin coupling between fluorine and steroid angular methyl protons. *J Am Chem Soc* 1962;**84**:1736.
209. Cross AD. Steroids. CCLXII.1a Spectra and stereochemistry. XVI.1b A study of the mechanism of long-range 19-proton-6β-fluorine coupling in 6β-fluorosteroids. *J Am Chem Soc* 1964;**86**:4011.
210. Contreras RH, Barone V, Facelli JC, Peralta JE. Advances in theoretical and physical aspects of spin-spin coupling constants. *Annu Rep NMR Spectrosc* 2003;**51**:167.
211. Page JE. Nuclear magnetic resonance spectra of steroids. *Annu Rep NMR Spectrosc* 1970;**3**:149.
212. Cross AD, Crabbe P. Spectra and stereochemistry. IX.1,2 A nuclear magnetic resonance spectral study of some 16-substituted pregnenes and 17α-pregnenes. *J Am Chem Soc* 1964;**86**:1221.
213. Wittstruck TA. Determination of C-22 epimers in steroids using nuclear magnetic resonance spectroscopy. *J Org Chem* 1973;**38**:1426.
214. Carrington A, McLachlan AD. *Introduction to magnetic resonance with applications to chemistry and chemical physics*. New York: Harper & Row; 1967.
215. Hinckley CC. Paramagnetic shifts in solutions of cholesterol and the dipyridine adduct of trisdipivalomethanatoeuropium(III). A shift reagent. *J Am Chem Soc* 1969;**91**:5160.
216. Demarco PV, Elzey TK, Lewis RB, Wenkert E. Paramagnetic induced shifts in the proton magnetic resonance spectra of alcohols using tris(dipivalomethanato)europium(III). *J Am Chem Soc* 1970;**92**:5734.
217. Demarco PV, Elzey TK, Lewis RB, Wenkert E. Tris(dipivalomethanato)europium (III). Shift reagent for use in the proton magnetic resonance analysis of steroids and terpenoids. *J Am Chem Soc* 1970;**92**:5737.
218. Hinckley CC, Klotz MR, Patil F. Applications of rare earth nuclear magnetic resonance shift reagents. III. Graphical analysis of paramagnetic shifts for systems having two coordination sites. Testosterone and 17.alpha.-methyltestosterone. *J Am Chem Soc* 1971;**93**:2417.
219. Wittstruck TA. Analysis of steroid nuclear magnetic resonance spectra using paramagnetic shift reagents. *J Am Chem Soc* 1972;**94**:5130.
220. Ius A, Vecchio G, Carrea G. Use of tris(dipivaloylmethanato)europium(III) with bifunctional molecules. Additivity of the induced chemical shift changes in the NMR spectrum. *Tetrahedron Lett* 1972;**13**:1543.
221. Bouquant J, Chuche J. NMR lanthanide shift reagents. II. Solvent effects. *Tetrahedron Lett* 1973;**14**:493.
222. Casy AF. *PMR studies of compounds of pharmacological interest: further examples*. London, New York: Academic Press; 1971 240p.
223. Bridgeman JE, Cherry PC, Clegg AS, Evans JM, Jones ERH, Kasal A, Kumar V, Meakins GD, Morisawa Y, Richards EE, Woodgate PD. Microbiological

hydroxylation of steroids. Part I. Proton magnetic resonance spectra of ketones, alcohols, and acetates in the androstane, pregnane, and oestrane series. *J Chem Soc C Org* 1970;250.
224. Gough JL, Guthrie JP, Stothers JB. Stereochemical assignments in steroids by carbon-13 nuclear magnetic resonance spectroscopy. Configuration of the A/B ring junction. *J Chem Soc Chem Commun* 1972;979.
225. Anet FAL, Bradley CH, Buchanan GW. Direct detection of the axial conformer of methylcyclohexane by 63.1 MHz carbon-13 nuclear magnetic resonance at low temperatures. *J Am Chem Soc* 1971;**93**:258.
226. Stothers JB. *Carbon-13 NMR spectroscopy*. New York: Academic Press; 1972.
227. Breitmaier E, Voelter W. *Carbon-13 NMR spectroscopy*. Weinheim: VCH Verlagsgesellschaft mbH; 1990.
228. Breitmaier E, Voelter W. *Carbon-13 NMR spectroscopy*. Weinheim: Verlag Chemie; 1974.
229. Breitmaier E, editor. *Atlas of carbon-13 NMR data*. London: Heyden; 1975.
230. Balogh B, Wilson DM, Burlingame AL. Carbon-13 NMR study of the stereochemistry of steranes from oil shale of the Green River formation (Eocene). *Nature* 1971;**233**:261.
231. van de Ven FJM. *Multidimensional NMR in liquids*. New York: Wiley-VCH; 1995.
232. Kalinowski H-O, Berger S, Braun S. *13C-NMR-Spektroskopie*. Stuttgart: Georg Thieme Verlag; 1984.
233. Hammann PE, Habermehl GG, Kluge H. γ-Gauche effects in the ^{1}H and ^{13}C NMR spectra of steroids. *Magn Reson Chem* 1988;**26**:85.
234. Hammann PE, Kluge H, Habermehl GG. The γ-gauche effects in the proton and carbon-13 NMR spectra of steroids. II. *Magn Reson Chem* 1991;**29**:133.
235. Rozen S, Ben-Shushan G. Carbon-13 NMR of tertiary fluoro steroids as a stereochemical probe. *Magn Reson Chem* 1985;**23**:116.
236. Grant DM, Cheney BV. Carbon-13 magnetic resonance. VII. Steric perturbation of the carbon-13 chemical shift. *J Am Chem Soc* 1967;**89**:5315.
237. Beierbeck H, Saunders JK. A reinterpretation of beta, gamma, and delta substituent effects on carbon-13 chemical shifts. *Can J Chem* 1976;**54**:2985.
238. Beierbeck H, Saunders JK, ApSimon JW. The semiempirical derivation of carbon-13 nuclear magnetic resonance chemical shifts. Hydrocarbons, alcohols, amines, ketones, and olefins. *Can J Chem* 1977;**55**:2813.
239. Holland HL, Diakow PRP, Taylor GJ. Carbon-13 nuclear magnetic resonance spectra of some C-19-hydroxy, C-5,6-epoxy, C-24-ethyl, and C-19-norsteroids. *Can J Chem* 1978;**56**:3121.
240. Holland HL, Thomas EM. Carbon-13 nuclear magnetic resonance spectra of some halosteroids, 6-ketosteroids, and related compounds. *Can J Chem* 1979;**57**:3069.
241. Hickey JP, Butler IS, Pouskouleli G. Carbon-13 NMR spectra of some representative hormonal steroids. *J Magn Reson* 1980;**38**:501.
242. Goto G, Yoshioka K, Hiraga K, Miki T. A stereoselective synthesis and nuclear magnetic resonance spectral study of four epimeric 17-hydroxy-16-ethylestranes. *Chem Pharm Bull* 1977;**25**:1295.
243. Schoenecker VB, Tresselt D, Ponsold K. Steroide–XLIV: 1H-NMR-untersuchungen. Konfigurationszuordnung 16,17-disubstituierter Steroide. *Tetrahedron* 1975;**31**:2845.
244. Schoenecker B, Tresselt D, Draffehn J, Ponsold K, Engelhardt G, Zeigan D, Schneider G, Weisz-Vincze I, Dombi G. Steroide. LIII. ^{1}H-NMR-Untersuchungen. Konfigurationszuordnung von 16-substituierten 17-Hydroxy-Steroiden. *J Prakt Chem* 1977;**319**:419.
245. Schoenecker B, Tresselt D, Schubert G, Ponsold K. Steroide. 66. ^{1}H-NMR-Untersuchungen. Konfigurationszuordnung 15, 16, 17-trisubstituierter Steroide. *J Prakt Chem* 1981;**323**:207.

246. Schoenecker B, Tresselt D, Schubert G, Kohout L, Fajkos J. Proton-NMR investigations. Application of trichloroacetyl isocyanate to the structure determination of 3-, 6-, 7-, 7a- and 17-hydroxy steroids. *Collect Czech Chem Commun* 1978;**43**:2609.
247. Hall LD, Sanders JKM, Sukumar S. Measurement of the vicinal and geminal proton coupling constants of steroids using proton two-dimensional *J* spectroscopy. *J Chem Soc Chem Commun* 1980;366.
248. Aue WP, Karhan J, Ernst RR. Homonuclear broad band decoupling and two-dimensional *J*-resolved NMR spectroscopy. *J Chem Phys* 1976;**64**:4226.
249. Nagayama K, Bachmann P, Wuthrich K, Ernst RR. The use of cross-sections and of projections in two-dimensional NMR spectroscopy. *J Magn Reson* 1978;**31**:133.
250. Bodenhausen G, Freeman R, Niedermeyer R, Turner DL. Double Fourier transformation in high-resolution NMR. *J Magn Reson* 1977;**26**:133.
251. Richarz R, Wuethrich K. NOE difference spectroscopy: a novel method for observing individual multiplets in proton NMR spectra of biological macromolecules. *J Magn Reson* 1978;**30**:147.
252. Kuo M, Gibbons WA. Total assignments, including four aromatic residues, and sequence confirmation of the decapeptide tyrocidine A using difference double resonance. Qualitative nuclear overhauser effect criteria for beta turn and antiparallel beta-pleated sheet conformations. *J Biol Chem* 1979;**254**:6278.
253. Bodenhausen G, Freeman R. Correlation of chemical shifts of protons and carbon-13. *J Am Chem Soc* 1978;**100**:320.
254. Hall LD, Morris GA, Sukumar S. Resolution and assignment of the 270-MHz proton spectrum of cellobiose by homo- and heteronuclear two-dimensional NMR. *J Am Chem Soc* 1980;**102**:1745.
255. Bell RA, Saunders JK. Chemical applications of the nuclear Overhauser effect. *Top. Stereochem.* 1973;**7**:1.
256. Hall LD, Sanders JKM. Complete analysis of proton NMR spectra of complex natural products using a combination of one- and two-dimensional techniques. 1-Dehydrotestosterone. *J Am Chem Soc* 1980;**102**:5703.
257. Traficante DD, Meadows MD. Strong coupling effects in 2D J, δ spectra: an application for the determination of the conformational isomers of some 1,4 disubstituted dioxanes. *Conc Magn Reson* 1997;**9**:359.
258. Thrippleton MJ, Edden RAE, Keeler J. Suppression of strong coupling artefacts in *J*-spectra. *J Magn Reson* 2005;**174**:97.
259. Barrett MW, Farrant RD, Kirk DN, Marsh JD, Sanders JKM, Duax WL. The solution conformation of 17α-acetoxy-6α-methylprogesterone ('medroxyprogesterone acetate'): use of circular dichroism, nuclear overhauser effect difference and two-dimensional *J* spectroscopy. *J Chem Soc Perkin Trans 2* 1982;105.
260. Turner DL, Freeman R. The proton-coupled carbon-13 spectrum of cholesterol. *J Magn Reson* 1978;**29**:587.
261. Morris GA, Freeman R. Enhancement of nuclear magnetic resonance signals by polarization transfer. *J Am Chem Soc* 1979;**101**:760.
262. Doddrell DM, Pegg DT, Bendall MR. Distortionless enhancement of NMR signals by polarization transfer. *J Magn Reson* 1982;**48**:323.
263. Bildsoe H, Doenstrup S, Jakobsen HJ, Soerensen OW. Subspectral editing using a multiple quantum trap: analysis of *J* cross-talk. *J Magn Reson* 1983;**53**:154.
264. Bendall RM, Pegg DT. ^{1}H-^{13}C two-dimensional chemical shift correlation spectroscopy using DEPT. *J Magn Reson* 1983;**53**:144.
265. Freeman R, Morris GA. Experimental chemical shift correlation maps in nuclear magnetic resonance spectroscopy. *J Chem Soc Chem Commun* 1978;684.
266. Freeman R, Morris GA. Two-dimensional Fourier transformation in NMR. *Bull Magn Reson* 1979;**1**:5.

267. Bax A, Morris GA. An improved method for heteronuclear chemical shift correlation by two-dimensional NMR. *J Magn Reson* 1981;**42**:501.
268. Bax A, Freeman R, Kempsell SP. Natural abundance carbon-13-carbon-13 coupling observed via double-quantum coherence. *J Am Chem Soc* 1980;**102**:4849.
269. Bax A, Freeman R, Kempsell SP. Investigation of ^{13}C-^{13}C long-range couplings in natural-abundance samples. *J Magn Reson* 1980;**41**:349.
270. Bax A, Freeman R, Frenkiel TA. An NMR technique for tracing out the carbon skeleton of an organic molecule. *J Am Chem Soc* 1981;**103**:2102.
271. Lindley MR, Shoolery JN, Smith DH, Djerassi C. Application of the computer program GENOA and two-dimensional NMR spectroscopy to structure elucidation. *Org Magn Reson* 1983;**21**:405.
272. Mueller L. Sensitivity enhanced detection of weak nuclei using heteronuclear multiple quantum coherence. *J Am Chem Soc* 1979;**101**:4481.
273. Bax A, Subramanian S. Sensitivity-enhanced two-dimensional heteronuclear shift correlation NMR spectroscopy. *J Magn Reson* 1986;**67**:565.
274. Bodenhausen G, Ruben DJ. Natural abundance nitrogen-15 NMR by enhanced heteronuclear spectroscopy. *Chem Phys Lett* 1980;**69**:185.
275. Bax A, Summers MF. Proton and carbon-13 assignments from sensitivity-enhanced detection of heteronuclear multiple-bond connectivity by 2D multiple quantum NMR. *J Am Chem Soc* 1986;**108**:2093.
276. Lerner L, Bax A. Sensitivity-enhanced two-dimensional heteronuclear relayed coherence transfer NMR spectroscopy. *J Magn Reson* 1986;**69**:375.
277. Martin GE, Crouch RC. Inverse-detected two-dimensional NMR methods: applications in natural products chemistry. *J Nat Prod* 1991;**54**:1.
278. Sedee AGJ, Beijersbergen van Henegouwen GMJ, Guijt W, Haasnoot CAG. Assignment of the proton and carbon-13 nuclear magnetic resonance spectra of norethisterone using two-dimensional nuclear magnetic resonance spectroscopy. *J Chem Soc Perkin Trans 2* 1984;1755.
279. Sedee AGJ, Van Henegouwen GMJB, Guijt W, Haasnoot CAG. Conformational analysis of steroids in solution: 17β-hydroxy-19-nor-5α,17α-pregn-20-yn-3-one and its 5β-isomer studied by nuclear magnetic resonance. *J Org Chem* 1985;**50**:4182.
280. Leibfritz D, Haupt E, Feigel M, Hull WE, Weber W-D. Strukturnachweis von 9α-Hydroxyöstronmethylether durch zweidimensionale Protonen-FT-NMR und ^{13}C-NMR-Spektroskopie. *Annu Chem* 1982;**1982**:1971.
281. Jagodzinska BM, Trimmer JS, Fenical W, Djerassi C. Sterols in marine invertebrates. 49. Isolation and structure elucidation of eight new polyhydroxylated sterols from the soft coral Sinularia dissecta. *J Org Chem* 1985;**50**:1435.
282. Hughes DW. Application of relayed coherence transfer two-dimensional nuclear magnetic resonance spectroscopy to the assignment of proton chemical shifts in steroids. *Magn Reson Chem* 1988;**26**:214.
283. Atta ur R, Qureshi MM. Applications of modern 2D-NMR techniques in structure elucidation of natural products. *Pure Appl Chem* 1990;**62**:1385.
284. Mappus E, Chambon C, de Ravel MR, Grenot C, Cuilleron CY. Synthesis and characterization by ^{1}H and ^{13}C nuclear magnetic resonance spectroscopy of 17α-cyano, 17α-aminomethyl, and 17α-alkylamidomethyl derivatives of 5α-dihydrotestosterone and testosterone. *Steroids* 1997;**62**:603.
285. Weston R, Gottlieb H, Hagaman E, Wenkert E. Carbon-13 nuclear magnetic resonance spectroscopy of naturally occurring substances. LI. *Solanum* glycoalkaloids. *Austr J Chem* 1977;**30**:917.
286. Willker W, Leibfritz D. Complete assignment and conformational studies of tomatine and tomatidine. *Magn Reson Chem* 1992;**30**:645.
287. Eggert H, Djerassi C. ^{13}C NMR spectra of sapogenins. *Tetrahedron Lett* 1975;**16**:3635.

288. Bird G, Collins D, Eastwood F, Exner R, Romanelli M, Small D. The synthesis of (25R)-22a-N-[15C, 17a2H2]-spirosol-5-en-3β-ol ([15C,17a-2H2] solasodine) and assignment of the ^{13}C N.M.R. Spectra of solasodine and its derivatives. *Austr J Chem* 1979;**32**:783.
289. Tinto WF, Reynolds WF, Seaforth CE, Mohammed S, Maxwell A. New bitter saponins from the bark of Colubrina elliptica: ^{1}H and ^{13}C assignments by 2D NMR spectroscopy. *Magn Reson Chem* 1993;**31**:859.
290. Fielding L, Grant GH. Conformational equilibria in amino steroids. 1. A proton and carbon-13 NMR spectroscopy and molecular mechanics study of 3α-hydroxy-2β-(4-morpholinyl)-5αH-androstan-17-one. *J Am Chem Soc* 1991;**113**:9785.
291. Fielding L, Grant GH. Conformational equilibria in amino steroids. 2. Energetics of the chair/twist-boat equilibrium in ring A of 3α-hydroxy-2β-(4-morpholinyl)-5αH-androstan-17-one. *J Am Chem Soc* 1993;**115**:1902.
292. Fielding L, Hamilton N, McGuire R. Conformations of anaesthetic steroids: a ^{1}H and ^{13}C NMR Study of (2β,3α,5α)-2-[(2R)-ethyl-4- morpholinyl]-3-hydroxypregnane-11,20-dione and (2β,3α,5α)-2-[(2S)-ethyl-4-morpholinyl]- 3-hydroxypregnane-11,20-dione. *Magn Reson Chem* 1997;**35**:184.
293. Fielding L, Hamilton N, McGuire R, Maidment M, Campbell AC. Determination of absolute stereochemistry of 2-alkylmorpholines by a ^{13}C NMR study of steroid derivatives. *Magn Reson Chem* 1996;**34**:59.
294. Matsushita S, Yanai Y, Fusyuku A, Ikeda T, Ono M, Nohara T. Distinction of absolute configuration at C-22 of C-23-hydroxyspirostane and C-23-hydroxyspirosolane glycosides. *Chem Pharm Bull* 2007;**55**:1079.
295. García V. Acid epimerization of 20-keto pregnane glycosides is determined by 2D-NMR spectroscopy. *J Biomol NMR* 2011;**50**:91.
296. Prestegard JH, Bougault CM, Kishore AI. Residual dipolar couplings in structure determination of biomolecules. *Chem Rev* 2004;**104**:3519.
297. Selivanov SI, Shavva AG. An NMR study of the spatial structure and intramolecular dynamics of modified analogues of steroid hormones. *Russ J Bioorg Chem* 2002;**28**:194.
298. Neuhaus D, Williamson MP. *The nuclear overhauser effect in structural and conformational analysis*. London: John Wiley & Sons; 1992.
299. Egorov MS, Selivanov SI, Shavva AG. Study by NMR spectroscopy of particular spatial structure of B,19-bisnortestosterone 9,10-isoanalogs. *Russ J Org Chem* 2002;**38**:200.
300. Andersen NH, Eaton HL, Lai X. Quantitative small molecule NOESY. A practical guide for derivation of cross-relaxation rates and internuclear distances. *Magn Reson Chem* 1989;**27**:515.
301. Genest D, Simorre JP. Method for evaluating the reliability of distances and rotational correlation times deduced from 2D ^{1}H NMR NOESY experiments. *Magn Reson Chem* 1990;**28**:21.
302. Selivanov SI, Solov'ev AY, Morozkina SN, Shavva AG. An NMR study of the conformational mobility of steroid estrogen 7α-methyl-8α analogues. *Russ. J. Bioorg. Chem.* 2007;**33**:302.
303. Wu D, Chen A, Johnson CS. An improved diffusion-ordered spectroscopy experiment incorporating bipolar-gradient pulses. *J Magn Reson Ser A* 1995;**115**:260.
304. Shikii K, Seki H, Sakamoto S, Sei Y, Utsumi H, Yamaguchi K. Intermolecular hydrogen bonding of steroid compounds: PFG NMR diffusion study, cold-spray ionization (CSI)-MS and X-ray analysis. *Chem Pharm Bull* 2005;**53**:792.
305. Becker ED. *Anal Chem* 1993;**65**:295A.
306. Jayasuriya H, Herath KB, Ondeyka JG, Guan Z, Borris RP, Tiwari S, de Jong W, Chavez F, Moss J, Stevenson DW, Beck HT, Slattery M, Zamora N, Schulman M, Ali A, Sharma N, MacNaul K, Hayes N, Menke JG, Singh SB. Diterpenoid, steroid,

and triterpenoid agonists of liver X receptors from diversified terrestrial plants and marine sources. *J Nat Prod* 2005;**68**:1247.
307. Gronquist M, Meinwald J, Eisner T, Schroeder FC. Exploring uncharted terrain in nature's structure space using capillary NMR spectroscopy: 13 steroids from 50 fireflies. *J Am Chem Soc* 2005;**127**:10810.
308. Dufourc EJ. The role of phytosterols in plant adaptation to temperature. *Plant Signal Behav* 2008;**3**:133.
309. Aoki S, Watanabe Y, Sanagawa M, Setiawan A, Kotoku N, Kobayashi M. Cortistatins A, B, C, and D, anti-angiogenic steroidal alkaloids, from the marine sponge corticium simplex. *J Am Chem Soc* 2006;**128**:3148.
310. Rhen T, Cidlowski JA. Antiinflammatory action of glucocorticoids, new mechanisms for old drugs. *N Engl J Med* 2005;**353**:1711.
311. John S, Sorokin AV, Thompson PD. Phytosterols and vascular disease. *Curr Opin Lipid* 2007;**18**:35.
312. Goeroeg S. Chemical and analytical characterization of related organic impurities in drugs. *Anal Bioanal Chem* 2003;**377**:852.
313. Albert K, editor. *On-line LC-NMR and related techniques*. Chichester: John Wiley & Sons, Ltd; 2002.
314. Spraul M, Hofmann M, Dvortsak P, Nicholson JK, Wilson ID. High-performance liquid chromatography coupled to high-field proton nuclear magnetic resonance spectroscopy: application to the urinary metabolites of ibuprofen. *Anal Chem* 1993;**65**:327.
315. Holzgrabe U, Wawer I, Diehl B, editors. *NMR spectroscopy in pharmaceutical analysis*. Amsterdam: Elsevier; 2008.
316. Lehn J-M. *Supramolecular chemistry—concepts and perspectives*. Weinheim: VCH Verlagsgesellschaft mbH; 1995.
317. Bom A, Bradley M, Cameron K, Clark JK, van Egmond J, Feilden H, MacLean EJ, Muir AW, Palin R, Rees DC, Zhang M-Q. A novel concept of reversing neuromuscular block: chemical encapsulation of rocuronium bromide by a cyclodextrin-based synthetic host. *Angew Chem Int Ed* 2002;**41**:265.
318. Cameron KS, Clark JK, Cooper A, Fielding L, Palin R, Rutherford SJ, Zhang MQ. Modified γ-cyclodextrins and their rocuronium complexes. *Org Lett* 2002;**4**:3403.
319. Schneider H-J, Hacket F, Ruediger V, Ikeda H. MR studies of cyclodextrins and cyclodextrin complexes. *Chem Rev* 1998;**98**:1755.
320. Adam JM, Bennett DJ, Bom A, Clark JK, Feilden H, Hutchinson EJ, Palin R, Prosser A, Rees DC, Rosair GM, Stevenson D, Tarver GJ, Zhang M-Q. Cyclodextrin-derived host molecules as reversal agents for the neuromuscular blocker rocuronium bromide: synthesis and structure-activity relationships. *J Med Chem* 2002;**45**:1806.
321. Tarver GJ, Grove SJA, Buchanan K, Bom A, Cooke A, Rutherford SJ, Zhang M-Q. Substituted cyclodextrins as reversal agents for the neuromuscular blocker rocuronium bromide. *Bioorg Med Chem* 2002;**10**:1819.
322. Cameron KS, Fielding L. NMR diffusion spectroscopy as a measure of host-guest complex association constants and as a probe of complex size. *J Org Chem* 2001;**66**:6891.
323. Zerbe O, editor. *BioNMR in drug research*. Weinheim: Wiley-VCH; 2002.
324. Tan ZJ, Zhu XX, Brown GR. Formation of inclusion complexes of cyclodextrins with bile salt anions as determined by NMR titration studies. *Langmuir* 1994;**10**:1034.
325. de Jong MR, Engbersen JFJ, Huskens J, Reinhoudt DN. Cyclodextrin dimers as receptor molecules for steroid sensors. *Chem Eur J* 2000;**6**:4034.
326. Cameron KS, Fletcher D, Fielding L. An NMR study of cyclodextrin complexes of the steroidal neuromuscular blocker drug rocuronium bromide. *Magn Reson Chem* 2002;**40**:251.

327. Mucci A, Schenetti L, Vandelli MA, Forni F, Ventura P, Salvioli G. One- and two-dimensional NMR study of complexation of ursodeoxycholic acid with β-cyclodextrin. *J Chem Soc Perkin Trans 2* 1996;2347.
328. Ramos Cabrer P, Alvarez-Parrilla E, Meijide F, Seijas JA, Rodriguez Nunez E, Vazquez Tato J. Complexation of sodium cholate and sodium deoxycholate by β-cyclodextrin and derivatives. *Langmuir* 1999;**15**:5489.
329. Mucci A, Schenetti L, Vandelli MA, Ruozi B, Salvioli G, Forni F. Comparison between Roesy and ^{13}C NMR complexation shifts in deriving the geometry of inclusion compounds: a study on the interaction between hyodeoxycholic acid and 2-hydroxypropyl-β-cyclodextrin. *Supramol Chem* 2001;**12**:427.
330. Cameron KS, Fielding L. NMR diffusion coefficient study of steroid–cyclodextrin inclusion complexes. *Magn Reson Chem* 2002;**40**:S106.
331. Goeroeg S. The importance and the challenges of impurity profiling in modern pharmaceutical analysis. *TrAC Trends Anal Chem* 2006;**25**:755.
332. Baertschi SW. Analytical methodologies for discovering and profiling degradation-related impurities. *TrAC Trends Anal Chem* 2006;**25**:758.
333. Goeroeg S. The changing face of pharmaceutical analysis. *TrAC Trends Anal Chem* 2007;**26**:12.
334. Goeroeg S. 2.1. Strategies in impurity profiling. *Prog Pharm Biomed Anal* 2000;**4**:67.
335. Behnke B, Schlotterbeck G, Tallarek U, Strohschein S, Tseng L-H, Keller T, Albert K, Bayer E. Capillary HPLC-NMR coupling: high-resolution ^{1}H NMR spectroscopy in the nanoliter scale. *Anal Chem* 1996;**68**:1110.
336. Seger C, Godejohann M, Tseng L-H, Spraul M, Girtler A, Sturm S, Stuppner H. LC-DAD-MS/SPE-NMR hyphenation. A tool for the analysis of pharmaceutically used plant extracts: identification of isobaric iridoid glycoside regioisomers from harpagophytum procumbens. *Anal Chem* 2004;**77**:878.
337. Sandvoss M, Bardsley B, Beck TL, Lee-Smith E, North SE, Moore PJ, Edwards AJ, Smith RJ. HPLC–SPE–NMR in pharmaceutical development: capabilities and applications. *Magn Reson Chem* 2005;**43**:762.
338. Lindon JC, Nicholson JK, Wilson ID. Directly coupled HPLC-NMR and HPLC-NMR-MS in pharmaceutical research and development. *J Chromatogr B Biomed Sci Appl* 2000;**748**:233.
339. Gorog S, Balogh G, Gazdag M. Analysis of steroids. XLIII. Estimation of impurity profiles of drugs and related materials. VIII. Combined application of high-performance liquid chromatography and NMR spectroscopy in the impurity profiling of drugs. *J Pharm Biomed Anal* 1991;**9**:829.
340. Goeroeg S, Babjak M, Balogh G, Brlik J, Csehi A, Dravecz F, Gasdag M, Horvath P, Lauko A, Varga K. Drug impurity profiling strategies. *Talanta* 1997;**44**:1517.
341. Thelin B, Lundstedt T, Lundgren R, Olsson A, Batra S. Classification of Estradurin® batches: correlation between ^{31}P NMR and a biological duration test for batch approval. *Chemometr Intell Lab* 1995;**27**:135.
342. Smith LL, Herz JE, Ezell EL. Oxygen-17 nuclear magnetic resonance spectra of steroids. *Steroids* 1993;**58**:260.
343. Kaehlig H, Robien W. ^{17}O NMR spectroscopic investigation of steroids at natural abundance. *Magn Reson Chem* 1994;**32**:608.
344. Kolehmainen E, Kaartinen M, Kauppinen R, Kotoneva J, Lappalainen K, Lewis PT, Seppaelae R, Sundelin J, Vatanen V. Substituted methyl 5β-cholan-24-oates—a ^{17}O NMR spectral characterization. *Magn Reson Chem* 1994;**32**:441.
345. Berger S, Braun S, Kalinowski H-O. *NMR spectroscopy of the non-metallic elements*. Chichester: John Wiley & Sons; 1997.
346. Ampt KAM, Aspers RLEG, Jaeger M, Geutjes PETJ, Honing M, Wijmenga SS. Application of fluorine NMR for structure identification of steroids. *Magn Reson Chem* 2011;**49**:221.

347. Kirk KL. Fluorine in medicinal chemistry: recent therapeutic applications of fluorinated small molecules. *J Fluorine Chem* 2006;**127**:1013.
348. Kirk KL. Selective fluorination in drug design and development: an overview of biochemical rationales. *Curr Top Med Chem* 2006;**6**:1447.
349. Fried J, Sabo EF. Halogenated corticoids. I. 9-Halogen derivatives of cortisone and hydrocortisone. *J Am Chem Soc* 1957;**79**:1130.
350. Morgenthaler M, Schweizer E, Hoffmann-Röder A, Benini F, Martin RE, Jaeschke G, Wagner B, Fischer H, Bendels S, Zimmerli D, Schneider J, Diederich F, Kansy M, Müller K. Predicting and tuning physicochemical properties in lead optimization: amine basicities. *ChemMedChem* 2007;**2**:1100.
351. London RE, Gabel SA. Fluorine-19 NMR studies of fluorobenzeneboronic acids. 2. Kinetic characterization of the interaction with subtilisin Carlsberg and model ligands. *J Am Chem Soc* 1994;**116**:2570.
352. Luck LA, Vance JE, O'Connell TM, London RE. ^{19}F NMR relaxation studies on 5-fluorotryptophan- and tetradeutero-5-fluorotryptophan-labeled E. coli glucose/galactose receptor. *J Biomol NMR* 1996;**7**:261.
353. Martino R, Gilard V, Desmoulin F, Malet-Martino M. Fluorine-19 or phosphorus-31 NMR spectroscopy: a suitable analytical technique for quantitative in vitro metabolic studies of fluorinated or phosphorylated drugs. *J Pharm Biomed Anal* 2005;**38**:871.
354. Lanet JC, Mousseron-Canet M. Fluorinated steroids. NMR study of 19-hydroxy steroids. *Bull Soc Chim Fr* 1969;1751.
355. Joseph-Nathan P, Espneira J, Santillan RL. ^{19}F-NMR study of fluorinated corticosteroids. *Spectrochim Acta A Mol Spectrosc* 1984;**40**:347.
356. Wong TC, Rutar V, Wang JS. Study of proton chemical shifts and couplings with -fluorine-19 in 9α-fluorocortisol. Application of a novel proton-carbon-13 chemical shift correlation technique with homonuclear decoupling. *J Am Chem Soc* 1984;**106**:7046.
357. Hughes DW, Bain AD, Robinson VJ. NMR analysis of fluorinated corticosteroids related to fluocinonide: detection of long-range ^{1}H–^{19}F couplings using the heteronuclear equivalent of the COSY experiment. *Magn Reson Chem* 1991;**29**:387.
358. Carss SA, Scheler U, Harris RK, Holstein P, Fletton RA. *Magn Reson Chem* 1996;**34**:63.
359. Hu H, Kulanthaivel P, Krishnamurthy K. Simultaneous characterization of a mixture of fluorochemicals using three-dimensional ^{19}F-^{1}H heteronuclear TOCSY filtered/edited NMR experiments. *J Org Chem* 2007;**72**:6259.
360. Manni A. Hormone receptors and breast cancer. *N Engl J Med* 1983;**309**:1383.
361. Cabell M. The preparation of tritium-labeled steroids. *Isot Phys Biomed Sci* 1991;**1**:71.
362. Funke CW, Kaspersen FM, Wallaart J, Wagenaars GN. Tritium NMR spectroscopy of steroids. *J Labelled Compd Radiopharm* 1983;**20**:843.
363. Al-Rawi JMA, Bloxsidge JP, Elvidge JA, Jones JR, Chambers VEM, Chambers VMA, Evans EA. Tritium nuclear magnetic resonance spectroscopy. Part VI. Tritiated steroid hormones. *Steroids* 1976;**28**:359.
364. Altman LJ, Silberman N. Tritium nuclear magnetic resonance spectroscopy. Distribution patterns and nuclear Overhauser enhancements in some tritiated steroids. *Steroids* 1977;**29**:557.
365. Frappier F, Audinot M, Beaucourt JP, Sergent L, Lukacs G. Mechanism of the backbone rearrangement of amino steroids. A carbon-13 and tritium nuclear magnetic resonance spectroscopic study of isoconessine, neoconessine and the corresponding polydeuterated and polytritiated species. *J Org Chem* 1982;**47**:3783.
366. Bremser W. HOSE—a novel substructure code. *Anal Chim Acta* 1978;**103**:355.
367. Meiler J, Maier W, Will M, Meusinger R. Using neural networks for ^{13}C NMR chemical shift prediction-comparison with traditional methods. *J Magn Reson* 2002;**157**:242.

368. Smurnyy YD, Blinov KA, Churanova TS, Elyashberg ME, Williams AJ. Toward more reliable ^{13}C and ^{1}H Chemical shift prediction: a systematic comparison of neural-network and least-squares regression based approaches. *Chem Inf Model* 2008;**48**:128.
369. Kubli-Garfias C. Comparative study of the electronic structure of estradiol, epiestradiol and estrone by ab initio theory. *J Mol Struc THEOCHEM* 1998;**452**:175.
370. Elyashberg ME, Williams AJ, Martin GE. Computer-assisted structure verification and elucidation tools in NMR-based structure elucidation. *Prog Nucl Magn Reson Spectrosc* 2008;**53**:1.
371. Elyashberg M, Blinov K, Molodtsov S, Smurnyy Y, Williams AJ, Churanova T. Computer-assisted methods for molecular structure elucidation: realizing a spectroscopist's dream. *J Cheminf* 2009;**1**:1–26.
372. Anker LS, Jurs PC. Prediction of carbon-13 nuclear magnetic resonance chemical shifts by artificial neural networks. *Anal Chem* 1992;**64**:1157.
373. Steinbeck C. Recent developments in automated structure elucidation of natural products. *Nat Prod Rep* 2004;**21**:512.
374. Meiler J, Kock M. Novel methods of automated structure elucidation based on 13C NMR spectroscopy. *Magn Reson Chem* 2004;**42**:1042.
375. Abraham RJ, Mobli M. *Modelling ^{1}H NMR spectra of organic compounds. Theory, applications and NMR prediction software.* Chichester: John Wiley & Sons Ltd.; 2008.
376. Lukacs G, Lusinchi X, Hagman EW, Buckwalter BL, Schell FM, Wenkert E. Carbon-13 nuclear magnetic resonance of natural products and the related compounds XII and IV. Fluorinated steroids. *C R Acad Sci Ser C* 1972;**274**:1458.
377. Tori K, Seo S, Yoshimura Y, Arita H, Tomita Y. Glycosidation shifts in carbon-13 NMR spectroscopy: carbon-13 signal shifts from aglycone and glucose to glucoside. *Tetrahedron Lett* 1977;**18**:179.
378. Nelson JT, Kurz LJ. Proton, carbon-13 and fluorine-19 NMR spectral data for fifteen fluorinated steroids. *Magn Reson Chem* 1993;**31**:203.
379. Iida T, Chang FC, Mushiake K, Goto J, Nambara T. Complete ^{1}H and ^{13}C resonance assignments of stereoisomeric 3α,6,7,12α-tetrahydroxycholanoic acids by two-dimensional shift-correlated NMR. *Magn Reson Chem* 1993;**31**:645.
380. Mesko E, Schneider G, Dombi G, Zeigan D. Carbon-13 NMR data for methylated steroids. *Magn Reson Chem* 1994;**32**:565.
381. Ruiz Garcia JA, Verdecia Navarro FA, Velez Castro HT. ^{13}C NMR spectroscopy of some 20-ketopregnanes. *Magn Reson Chem* 1994;**32**:547.
382. Korde SS, Katoch R, Udasi RA, Trivedi GK. Total assignment of ^{1}H and ^{13}C NMR spectra of pregnenolone and progesterone haptens using 2D NMR spectroscopy. *Magn Reson Chem* 1999;**37**:594.
383. Ciuffreda P, Casati S, Manzocchi A. Complete ^{1}H and ^{13}C NMR spectral assignment of 17-hydroxy epimeric sterols with planar A or A and B rings. *Magn Reson Chem* 2004;**42**:360.
384. Sievanen E, Noponen V, Kral V, Briza T, Kolehmainen E. ^{1}H, ^{13}C, ^{19}F NMR, and ESI mass spectral-characterization of two geminal difluorosteroids. *Magn Reson Chem* 2008;**46**:392.
385. Takács M, Simon A, Liktor-Busa E, Báthori M, Zsila F, Bikádi Z, Horváth P, Veress G, Gergely A, Tóth G. Structure and stereochemistry of novel ecdysteroids from the roots of Serratula wolffii. *Magn Reson Chem* 2010;**48**:386.
386. De Brabandere VI, Thienpont LM, Stoeckl D, De Leenheer AP. ^{13}C-NMR and mass spectral data of steroids with a 17,17-dialkyl-18-nor-13(14)-ene substructure. *J Lipid Res* 1997;**38**:780.
387. Dionne P, Ngatcha BT, Poirier D. D-ring allyl derivatives of 17β- and 17α-estradiols: chemical synthesis and ^{13}C NMR data. *Steroids* 1997;**62**:674.

388. Midelfart A, Dybdahl A, Muller N, Sitter B, Gribbestad IS, Krane J. Dexamethasone and dexamethasone phosphate detected by ^{1}H and ^{19}F NMR spectroscopy in the aqueous humour. *Exp Eye Res* 1998;**66**:327.
389. Choudhary MI, Shah SAA, Atta ur R, Khan S-N, Khan MTH. Alpha-glucosidase and tyrosinase inhibitors from fungal hydroxylation of tibolone and hydroxytibolones. *Steroids* 2010;**75**:956.
390. Englert G, Arnold W, Els H, Fürst A, Meier A, Meister W. Substituent increments for the ^{1}H-NMR. Chemical shifts of the 18- and 19-methyl protons of steroids. Part I: 9β, 10α(retro)-steroids. *Helv Chim Acta* 1974;**57**:1549.
391. Eggert H, VanAntwerp CL, Bhacca NS, Djerassi C. Carbon-13 nuclear magnetic resonance spectra of hydroxy steroids. *J Org Chem* 1976;**41**:71.
392. Arnold W, Meister W, Englert G. Substituent increments for proton NMR. Chemical shifts of the 18- and 19-methyl protons of steroids. II. 9α,10β(normal)-steroids. *Helv Chim Acta* 1974;**57**:1559.
393. Cross AD, Beard C. Steroids. CCLXIX.1 spectra and stereochemistry. XVII.2 Non-additivity of Angular methyl proton frequency shifts and ring D conformational changes in 16-methyl steroids. *J Am Chem Soc* 1964;**86**:5317.
394. Cohen AI, Rock S. Anisotropy of substituents on the proton resonance of C-18 and C-19 methyl groups. Evaluation by computer regression. *Steroids* 1964;**3**:243.
395. Malinowski ER, Manhas MS, Muller GH, Bose AK. Effect of symmetry on C19 N.M.R. shifts in steroids. *Tetrahedron Lett* 1963;**4**:1161.
396. Van Antwerp CL, Eggert H, Meakins GD, Miners JO, Djerassi C. Additivity relations in carbon-13 nuclear magnetic resonance spectra of dihydroxy steroids. *J Org Chem* 1977;**42**:789.
397. Eggert H, Djerassi C. Carbon-13 nuclear magnetic resonance spectra of monounsaturated steroids. Evaluation of rules for predicting their chemical shifts. *J Org Chem* 1981;**46**:5399.
398. Gray NAB, Nourse JG, Crandell CW, Smith DH, Djerassi C. Stereochemical substructure codes for ^{13}C spectral analysis. *Org Magn Res* 1981;**15**:375.
399. Satoh H, Koshino H, Uzawa J, Nakata T. CAST/CNMR: highly accurate ^{13}C NMR chemical shift prediction system considering stereochemistry. *Tetrahedron* 2003;**59**:4539.
400. Halberstam NM, Baskin II, Palyulin VA, Zefirov NS. Neural networks as a method for elucidating structure-property relationships for organic compounds. *Russ Chem Rev* 2003;**72**:629.
401. Kubli-Garfias C. Ab initio comparative study of the electronic structure of testosterone, epitestosterone and androstenedione. *J Mol Struc THEOCHEM* 1998;**422**:167.
402. Kubli-Garfias C. Comparative study of the electronic structure of pregnanolones by ab initio theory. *Int J Quant Chem* 1999;**71**:433.
403. Kubli-Garfias C, Vàzquez R, Cooney AJ, Larrea F. Ab initio electronic structure of the progestogen norethisterone and its 5α-derivatives. *J Steroid Biochem Mol Biol* 2002;**82**:385.
404. Lederberg J, Sutherland GL, Buchanan BG, Feigenbaum EA, Robertson AV, Duffield AM, Djerassi C. Applications of artificial intelligence for chemical inference. I. Number of possible organic compounds. Acyclic structures containing carbon, hydrogen, oxygen, and nitrogen. *J Am Chem Soc* 1969;**91**:2973.
405. Will M, Fachinger W, Richert JR. Fully automated structure elucidation—a spectroscopist's dream comes true. *J Chem Inf Comp Sci* 1996;**36**:221.
406. Carabedian M. SpecSolv: artificially intelligent or artificially innovative? *J Chem Inf Comp Sci* 1997;**37**:402.
407. Will M, Richert J. SpecSolvAn innovation at work. *J Chem Inf Comp Sci* 1997;**37**:403.
408. Nuzillard J-M, de Paulo Emerenciano V. Automatic structure elucidation through data base search and 2D NMR spectral analysis. *NPC* 2006;**1**:57.
409. Elyashberg M, Blinov K, Williams A. A systematic approach for the generation and verification of structural hypotheses. *Magn Reson Chem* 2009;**47**:371.

410. Elyashberg ME, Blinov KA, Williams AJ, Martirosian ER, Molodtsov SG. Application of a new expert system for the structure elucidation of natural products from their 1D and 2D NMR data. *J Nat Prod* 2002;**65**:693.
411. Militao JSLT, Emerenciano VP, Ferreira MJP, Cabrol-Bass D, Rouillard M. Structure validation in computer-supported structure elucidation: ^{13}C NMR shift predictions for steroids. *Chemom Intell Lab Syst* 2003;**67**:5.
412. Blinov KA, Carlson D, Elyashberg ME, Martin GE, Martirosian ER, Molodtsov S, Williams AJ. Computer-assisted structure elucidation of natural products with limited 2D NMR data: application of the StrucEluc system. *Magn Reson Chem* 2003;**41**:359.
413. Elyashberg ME, Blinov KA, Williams AJ. The application of empirical methods of ^{13}C NMR chemical shift prediction as a filter for determining possible relative stereochemistry. *Magn Reson Chem* 2009;**47**:333.
414. Berger S, Braun S. *200 and more NMR experiments—a practical course*. Weinheim: Wiley-VCH; 2004.
415. Reynolds WF, Enriquez RG. Choosing the best pulse sequences, acquisition parameters, postacquisition processing strategies, and probes for natural product structure elucidation by NMR spectroscopy. *J Nat Prod* 2002;**65**:221.
416. Martin GE, Hadden CE, Russell DJ. Solution NMR spectroscopy. *Handb Spectrosc* 2003;**1**:209.
417. Martin GE, Russel DJ, Blinov KA, Elyashberg ME. Applications and advances in cryogenic NMR probes and computer-assisted structure elucidation. *Annu Magn Reson* 2003;**1**:1.
418. Claridge TDW. *High-resolution NMR techniques in organic chemistry*. Oxford: Elsevier Ltd.; 2009.
419. Kwan EE, Huang SG. Structural elucidation with NMR spectroscopy: practical strategies for organic chemists. *Eur J Org Chem* 2008;2671.
420. Martin GE. Small-volume and high-sensitivity NMR probes. *Annu Rep NMR Spectrosc* 2005;**56**:1.
421. Martin GE. Microprobes and methodologies for spectral assignments: applications. *Encycl Nucl Magn Reson* 2002;**9**:98.
422. Kovacs H, Moskau D, Spraul M. Cryogenically cooled probes–a leap in NMR technology. *Prog NMR Spectrosc* 2005;**46**:131.
423. Bermel W, Bertini I, Felli IC, Pierattelli R. Speeding up ^{13}C direct detection biomolecular NMR spectroscopy. *J Am Chem Soc* 2009;**131**:15339.
424. Felli IC, Brutscher B. Recent advances in solution NMR: Fast methods and heteronuclear direct detection. *Chemphyschem* 2009;**10**:1356.
425. Atreya HS. NMR methods for fast data acquisition. *J Indian Inst Sci* 2010;**90**:87.
426. Freeman R, Kupce E. New methods for fast multidimensional NMR. *J Biomol NMR* 2003;**27**:101.
427. Kupce E, Freeman R. High-resolution NMR correlation experiments in a single measurement (HR-PANACEA). *Magn Reson Chem* 2010;**48**:333.
428. Kupce E, Freeman R. Molecular structure from a single NMR sequence (fast-PANACEA). *J Magn Reson* 2010;**206**:147.
429. Fisher G, Petucci C, MacNamara E, Raftery D. NMR probe for the simultaneous acquisition of multiple samples. *J Magn Reson* 1999;**138**:160.
430. Frydman L, Scherf T, Lupulescu A. The acquisition of multidimensional NMR spectra within a single scan. *Proc Natl Acad Sci USA* 2002;**99**:15858.
431. Kupce E, Freeman R, John BK. Parallel acquisition of two-dimensional NMR spectra of several nuclear species. *J Am Chem Soc* 2006;**128**:9606.
432. Parella T, Nolis P. Time-shared NMR experiments. *Conc Magn Reson Part A* 2010;**36A**:1.
433. Webb AG, Sweedler JV, Raftery D. *Parallel NMR Detection*. Albert K, editor. *On-line LC-NMR and related techniques*. Chichester: John Wiley & Sons Ltd; 2002. p. 259.

434. Maciejewski MW, Stern AS, King GF, Hoch JC. Nonuniform sampling in biomolecular NMR. *Mod Magn Reson* 2006;**2**:1287.
435. Mobli M, Stern AS, Hoch JC. Spectral reconstruction methods in fast NMR: reduced dimensionality, random sampling and maximum entropy. *J Magn Reson* 2006;**182**:96.
436. Blinov KA, Larin NI, Williams AJ, Mills KA, Martin GE. Unsymmetrical covariance processing of COSY or TOCSY and HSQC NMR data to obtain the equivalent of HSQC-COSY or HSQC-TOCSY spectra. *J Heterocycl Chem* 2006;**43**:163.
437. Blinov KA, Williams AJ, Hilton BD, Irish PA, Martin GE. The use of unsymmetrical indirect covariance NMR methods to obtain the equivalent of HSQC-NOESY data. *Magn Reson Chem* 2007;**45**:544.
438. Bruschweiler R. Theory of covariance nuclear magnetic resonance spectroscopy. *J Chem Phys* 2004;**121**:409.
439. Bruschweiler R, Zhang F. Covariance nuclear magnetic resonance spectroscopy. *J Chem Phys* 2004;**120**:5253.
440. Snyder DA, Bruschweiler R. Generalized indirect covariance NMR formalism for establishment of multidimensional spin correlations. *J Phys Chem A* 2009;**113**:12898.
441. Snyder DA, Bruschweiler R. *Multidimensional NMR methods for the solution state*. Chichester, UK: John Wiley & Sons Ltd.; 2010 97pp.
442. Zhang F, Bruschweiler R. Indirect covariance NMR spectroscopy. *J Am Chem Soc* 2004;**126**:13180.
443. Martin GE, Hilton BD, Irish PA, Blinov KA, Williams AJ. Using unsymmetrical indirect covariance processing to calculate GHSQC-COSY spectra. *J Nat Prod* 2007;**70**:1393.
444. Martin GE, Hilton BD, Blinov KA, Williams AJ. Unsymmetrical indirect covariance processing of hyphenated and long-range heteronuclear 2D NMR spectra-enhanced visualization of $^{2}J_{CH}$ and $^{4}J_{CH}$ correlation responses. *J Heterocycl Chem* 2008;**45**:1109.
445. Hilton BD, Martin GE. Investigation of the experimental limits of small-sample heteronuclear 2D NMR. *J Nat Prod* 2010;**73**:1465.
446. Martin GE, Crouch RC. Inverse-detected 2D-NMR applications in alkaloid chemistry. *Mod Methods Plant Anal* 1994;**15**:25.
447. Hadden CE, Martin GE, Luo JK, Castle RN. A comparison of the hyphenated experiments GHMQC-TOCSY and GHSQC-TOCSY. *J Heterocycl Chem* 1999;**36**:533.
448. Bigler P, Mueller C. Assignment of ^{1}H signals in complex overlapping spectral regions using proton-detected 2D heteronuclear shift correlation spectroscopy. *Spectrochim Acta Part A* 1994;**50A**:297.
449. Liu M, Mao X-A, Ye C, Nicholson JK, Lindon JC. Three-dimensional maximum-quantum correlation HMQC NMR spectroscopy (3D MAXY-HMQC). *J Magn Reson* 1997;**129**:67.
450. Bigler P. Fast ^{13}C-NMR spectral editing for determining CH_n multiplicities. *Spectrosc Lett* 2008;**41**:162.
451. Bigler P, Kuemmerle R, Bermel W. Multiplicity editing including quaternary carbons: improved performance for the 13C-DEPTQ pulse sequence. *Magn Reson Chem* 2007;**45**:469.
452. Buddrus J, Lambert J. Connectivities in molecules by INADEQUATE: recent developments. *Magn Reson Chem* 2002;**40**:3.
453. Bain AD, Hughes DW, Anand CK, Nie Z, Robertson VJ. Problems, artifacts and solutions in the INADEQUATE NMR experiment. *Magn Reson Chem* 2010;**48**:630.
454. Stott K, Keeler J, Van QN, Shaka AJ. One-dimensional NOE experiments using pulsed field gradients. *J Magn Reson* 1997;**125**:302.
455. Forgo P, Kover KE. Gradient enhanced selective experiments in the ^{1}H NMR chemical shift assignment of the skeleton and side-chain resonances of stigmasterol, a phytosterol derivative. *Steroids* 2004;**69**:43.

456. Yang D, Xu X, Ye C. Application of HMQC to the measurement of *J*(H, H) homonuclear coupling constants. *Magn Reson Chem* 1992;**30**:711.
457. Marquez BL, Gerwick WH, Thomas Williamson R. Survey of NMR experiments for the determination of nJ(C, H) heteronuclear coupling constants in small molecules. *Magn Reson Chem* 2001;**39**:499.
458. Guenneau F, Mutzenhardt P, Grandclaude D, Canet D. Measurement of longitudinal and rotating frame relaxation times through fully *J*-decoupled homonuclear spectra. *J Magn Reson* 1999;**140**:250.
459. Pell AJ, Keeler J. Two-dimensional *J*-spectra with absorption-mode lineshapes. *J Magn Reson* 2007;**189**:293.
460. Zangger K, Sterk H. Homonuclear broadband-decoupled NMR spectra. *J Magn Reson* 1997;**124**:486.
461. Kolkman AJ, Draaisma J, Wijmenga SS, Tessari M. *Spectral simplification by collapsing J-multiplet structures: an improved technique for dilute samples*. Frankfurt: EUROMAR; 2011.
462. Aguilar JA, Faulkner S, Nilsson M, Morris GA. Pure shift ^{1}H NMR: a resolution of the resolution problem? *Angew Chem Int Ed* 2010;**49**:3901.
463. Ampt KAM, Aspers RLEG, Dvortsak P, van der Werf RM, Wijmenga SS, Jaeger M. Determination of size and sign of hetero-nuclear coupling constants from 2D ^{19}F-^{13}C correlation spectra. *J Magn Reson* 2011;**49**:221.
464. Thiele CM. Residual dipolar couplings (RDCs) in organic structure determination. *Eur J Org Chem* 2008;5673.
465. Luy B, Kobzar K, Kessler H. An easy and scalable method for the partial alignment of organic molecules for measuring residual dipolar couplings. *Angew Chem Int Ed* 2004;**43**:1092.
466. Kummerloewe G, Luy B. Residual dipolar couplings as a tool in determining the structure of organic molecules. *TrAC-Trends in Analytical Chemistry* 2009;**28**:483.
467. Thiele CM, Berger S. Probing the diastereotopicity of methylene protons in strychnine using residual dipolar couplings. *Org Lett* 2003;**5**:705.
468. Kummerloewe G, Luy B. Residual dipolar couplings for the configurational and conformational analysis of organic molecules. *Annu Rep NMR Spectrosc* 2009;**68**:193.
469. Freudenberger JC, Spiteller P, Bauer R, Kessler H, Luy B. Stretched poly (dimethylsiloxane) gels as NMR alignment media for apolar and weakly polar organic solvents: an ideal tool for measuring RDCs at low molecular concentrations. *J Am Chem Soc* 2004;**126**:14690.
470. Zweckstetter M, Bax A. Characterization of molecular alignment in aqueous suspensions of Pf1 bacteriophage. *J Biomol NMR* 2001;**20**:365.
471. Zweckstetter M. NMR: prediction of molecular alignment from structure using the PALES software. *Nat Protoc* 2008;**3**:679.
472. Losonczi JA, Andrec M, Fischer MWF, Prestegard JH. Order matrix analysis of residual dipolar couplings using singular value decomposition. *J Magn Reson* 1999;**138**:334.
473. Stevensson B, Landersjo C, Widmalm G, Maliniak A. Distribution function of a disaccharide in a liquid crystalline phase determined using NMR spectroscopy. *J Am Chem Soc* 2002;**124**:5946.
474. Landersjo C, Stevensson B, Eklund R, Ostervall J, Soderman P, Widmalm G, Maliniak A. Molecular conformations of a disaccharide investigated using NMR spectroscopy. *J Biomol NMR* 2006;**35**:89.
475. Sarfati M, Lesot P, Merlet D, Courtieu J. Theoretical and experimental aspects of enantiomeric differentiation using natural abundance multinuclear NMR spectroscopy in chiral polypeptide liquid crystals. *Chem Commun* 2000;2069.
476. Sarfati M, Lesot P, Merlet D, Courtieu J. First successful enantiomeric discrimination of chiral alkanes using NMR spectroscopy. *Chem Commun* 2000;2069.

477. Aroulanda C, Boucard V, Guibe F, Courtieu J, Merlet D. Weakly oriented liquid-crystal NMR solvents as a general tool to determine relative configurations. *Chem Eur J* 2003;**9**:4536.
478. Gil RR, Gayathri C, Tsarevsky NV, Matyjaszewski K. Stretched poly(methyl methacrylate) gel aligns small organic molecules in chloroform. Stereochemical analysis and diastereotopic proton NMR assignment in ludartin using residual dipolar couplings and ^{3}J coupling constant analysis. *J Org Chem* 2008;**73**:840.
479. Marathias VM, Tawa GJ, Goljer I, Bach AC. Stereochemical identification of (R)- and (S)-ibuprofen using residual dipolar couplings. *Chirality* 2007;**19**:741.
480. Ziani L, Lesot P, Meddour A, Courtieu J. Empirical determination of the absolute configuration of small chiral molecules using natural abundance ^{2}H NMR in chiral liquid crystals. *Chem Commun* 2007;4737.
481. Kummerloewe G, Crone B, Kretschmer M, Kirsch SF, Luy B. Dipolare Restkopplungen als effektives Instrument der Konstitutions- analyse: die unerwartete Bildung tricyclischer Verbindungen. *Angew Chem* 2011;**123**:2693.
482. Mangoni A, Esposito V, Randazzo A. Configuration assignment in small organic molecules via residual dipolar couplings. *Chem Commun* 2003;154.
483. Kummerloewe G, Schmitt S, Luy B. Cross-fitting of residual dipolar couplings. *Open Spectrosc J* 2010;**4**:16.
484. Wijten P. Structure elucidation and chiral discrimination of small molecules using Residual Dipolar Couplings, Thesis Wageningen University; 2010.
485. Jaeger M, Aspers RLEG, Wijten P, Wagener M. Towards Chiral Discrimination Using RDCs. EUROMAR 2012 Dublin; 2012.
486. Johnson Jr. CS. Diffusion ordered nuclear magnetic resonance spectroscopy: principles and applications. *Prog NMR Spectrosc* 1999;**34**:203.
487. Kavakka JS, Parviainen V, Wähälä K, Kilpeläinen I, Heikkinen S. Enhanced chromatographic NMR with polyethyleneglycol. A novel resolving agent for diffusion ordered spectroscopy. *Magn Reson Chem* 2010;**48**:777.
488. Duddeck H. Strategies and tactics in structure elucidation of unknown natural products structures by modern NMR. *Nat Prod Anal [Symp]* 1998;105.
489. Grove MD, Spencer GF, Rohwedder WK, Mandava N, Worley JF, Warthen JD, Steffens GL, Flippen-Anderson JL, Cook JC. Brassinolide, a plant growth-promoting steroid isolated from Brassica napus pollen. *Nature* 1979;**281**:216.
490. Adam G, Marquardt V. Brassinosteroids. *Phytochemistry* 1986;**25**:1787.
491. Hesse M, Meier H, Zeeh B. *Spektroskopische Methoden in der Organischen Chemie*. Stuttgart: Georg Thieme Verlag; 1991.
492. Reynolds WF, Yu M, Enriquez RG. Investigating the sensitivity limits of ^{13}C-detected ^{1}H–^{13}C chemical shift correlation sequences with modern microprobe and microtube technology. *Magn Reson Chem* 1997;**35**:614.
493. Reynolds WF, McLean S, Jacobs H, Harding WW. Assignment of 1H and 13C spectra fro polyprenol-12, a molecule with sever ^{1}H and ^{13}C spectral crowding, with the aid of high-resolution, 13C-detected, 13C-1H shift correlation spectra. *Can J Chem* 1999;**77**:1922.
494. Aspers RLEG, Jaeger M. At the sensitivity limit when C-C magnetization transfer is involved? in preparation.
495. Ardenkjaer-Larsen JH, Fridlund B, Gram A, Hansson G, Hansson L, Lerche MH, Servin R, Thaning M, Golman K. Increase in signal-to-noise ratio of $>$ 10,000 times in liquid-state NMR. *Proc Natl Acad Sci USA* 2003;**100**:10158.
496. Song C, Hu K-N, Joo C-G, Swager TM, Griffin RG. TOTAPOL: a biradical polarizing agent for dynamic nuclear polarization experiments in aqueous media. *J Am Chem Soc* 2006;**128**:11385.
497. Nyberg NT, Duus JO, Sorensen OW. Heteronuclear two-bond correlation: suppressing heteronuclear three-bond or higher NMR correlations while

enhancing two-bond correlations even for vanishing ^{2}J(CH). *J Am Chem Soc* 2005;**127**:6154.
498. Nyberg NT, Duus JO, Sorensen OW. Editing of H2BC NMR spectra. *Magn Reson Chem* 2005;**43**:971.
499. Kicha AA, Ivanchina NV, Huong TTT, Kalinovsky AI, Dmitrenok PS, Long PQ. Minor asterosaponin archasteroside C from the starfish Achaster typicus. *Russ Chem Bull* 2010;**59**:2133.
500. Uhlig S, Wisloff H, Petersen D. Identification of cytotoxic constituents of Narthecium ossifragum using bioassay-guided fractionation. *J Agr Food Chem* 2007;**55**:6018.
501. Holm R, Madsen JC, Shi W, Larsen KL, Staede LW, Westh P. Thermodynamics of complexation of tauro- and glyco-conjugated bile salts with two modified β-cyclodextrins. *J Incl Phen Macrocycl Chem* 2011;**69**:201.
502. Schoenbeck C, Westh P, Madsen JC, Larsen KL, Staede LW, Holm R. Methylated β-cyclodextrins: influence of degree and pattern of substitution on the thermodynamics of complexation with tauro- and glyco-conjugated bile salts. *Langmuir* 2011;**27**:5832.
503. Cheatham SF, Kline M, Sasaki RR, Blinov KA, Elyashberg ME, Molodtsov SG. Enhanced automated structure elucidation by inclusion of two-bond specific data. *Magn Reson Chem* 2010;**48**:571.
504. Martin GE, Hilton BD, Willcot III MR, Blinov KA. SQC-ADEQUATE—an investigation of data requirements. *Magn Reson Chem* 2011;**49**:350.
505. Levitt MH. *Spin dynamics. Basics of nuclear magnetic resonance*. Chichester: John Wiley & Sons, Ltd.; 2001.
506. Berger R, Courtieu J, Gil RR, Griesinger C, Koeck M, Lesot P, Luy B, Merlet D, Navarro-Vazquez A, Reggelin M, Reinscheid UM, Thiele CM, Zweckstetter M. Is Enantiomer Assignment Possible by NMR Spectroscopy Using Residual Dipolar Couplings from Chiral Nonracemic Alignment Media? - A Critical Assessment. *Angew Chem Int Ed* 2012;**51**:8388.

CHAPTER FOUR

Structural Characterization of Zeolites by Advanced Solid State NMR Spectroscopic Methods

Luís Mafra[*,†], **José Alejandro Vidal-Moya**[‡], **Teresa Blasco**[‡]

[*]Department of Chemistry, CICECO, University of Aveiro, Aveiro, Portugal
[†]Departamentos de Química Física y Analítica y Química Orgánica e Inorgánica, Universidad de Oviedo, Oviedo, Spain
[‡]Instituto de Tecnología Química (UPV-CSIC), Universidad Politécnica de Valencia-Consejo Superior de Investigaciones Científicas, Avda. de los Naranjos, s/n, Valencia, Spain

Contents

Abstract

This review overviews the application of solid state NMR spectroscopy to the structural characterization of silicate, and acidic aluminosilicate and borosilicate zeolites focusing on the utilization of new developed methods. We summarize recent results on the investigations of the distribution of silicon atoms into the zeolite framework, as well as the location of F^- anions and formation of pentacoordinated silicon species in zeolites synthesized in fluoride medium. Special attention is paid here to the characterization of framework and extraframework boron and most specially aluminium species and the

Annual Reports on NMR Spectroscopy, Volume 77
ISSN 0066-4103
http://dx.doi.org/10.1016/B978-0-12-397020-6.00004-0

acid sites in zeolites. In Section 6 of this review, we present the basis and practical aspects of advanced NMR experiments used in the characterization of microporous solids paying special attention to quadrupolar nuclei and other methods based on dipolar interactions.

Key Words: Zeolite, Zeotype, ^{27}Al MAS NMR, ^{11}B MAS NMR, ^{29}Si MAS NMR, ^{19}F MAS NMR, Extraframework aluminium, Quadrupolar nuclei, Solid state NMR

1. INTRODUCTION

Catalysis is essential in industry and is used in the production of more than 90% of chemicals.[1,2] Increasing environmental concerns is forcing the development and improvement of large-scale processes and the substitution of homogeneous for greener heterogeneous catalysts.[3,4] This policy is directed to decrease the energy consumption to better profit natural resources, diminish the formation of sub-products and eliminate contaminants.[3] Among the heterogeneous catalysts, zeolites are the most used in industry,[5] especially in the field of oil refining (Fluid Catalytic Cracking, isomerization, alkylation, oligomerization, etc.)[6] and petrochemical industry (alkylation of aromations, cumene production, etc.) but also for the production of fine chemicals.[7,8]

The successful industrial use of zeolites resides on the combination of their micropore structure of molecular dimensions, unique physical–chemical properties which can be tailored changing the chemical composition, and their thermal and hydrothermal stability. Although catalysis is the most important application of zeolites from the economy point of view, they are also used in large scale as adsorbents and in the formulation of detergents. The possibility of tuning their pore aperture opens the possibility of using them as molecular sieves for adsorption or separation processes. The limited size of their pores is also used in catalysis to what is called the "shape selectivity" of "reactant" or "products" by limiting the diffusion of large molecules present in the feed or formed in the reaction, so that the zeolite acts as a real molecular sieve, and/or the "shape selectivity of transition states" as only intermediate species of adequate size and/or shape will be formed, directing the product selectivity of the reaction.[5] Most of industrial catalytic processes uses one of the "big five" zeolites, that is, Y (FAU-type), ZSM-5 (MFI), Mordenite (MOR), Beta (BEA), and Ferrierite (FER) because of their high performance and low cost production. However, there is a great interest in the synthesis of large or extralarge pore zeolites for catalysis[9–13] especially in the field of fine chemicals and emerging applications.[4,14]

Typically, zeolites are defined as microporous aluminosilicate crystalline materials formed by cross linking TO_4 (T = Si or Al) tetrahedra sharing corners which give rise to channels and cavities of molecular dimensions, able to allocate exchangeable cations and organic molecules. Conceptually, they are considered as a silicate network, where the substitution of a Si^{4+} by an Al^{3+} atom generates a negative charge that must be compensated by organic or inorganic cations, which are placed within the zeolite pores or by protons linked to bridging oxygen atoms (Al–OH–Si). But they can also uptake neutral molecules within the pores such as water when they are under ambient conditions. A simplified formula of aluminosilicate zeolite is

$$M^{n+}_{x/n}Al_xSi_{1-x}O_2 \cdot yX$$

where $0 \leq x \leq 0.5$ and M^{n+} represent the cation and X neutral molecules, which can also be occluded inside the pores. Al–O–Al linkages are not formed in zeolites following what is known as the Lowenstein's rule,[15] so that the Si/Al = 1 molar ratio is the minimum possible in zeolites.

In aluminium rich (low Si/Al molar ratio) as-synthesized zeolites, M^{n+} are typically alkaline or alkaline–earth cations, which can be ion exchanged by any other metal cation. Aluminium rich zeolites compensated by alkaline cations have potential application in basic catalyzed reactions, as the framework oxygen atoms are Lewis basic sites.[16,17] In as-synthesized high silica zeolites (with high Si/Al molar ratio) the M^{n+} are organic cations, usually quaternary alkyl amines, which act as organic structure directing agent (SDA) towards the crystallization of specific structures. Calcination of zeolites synthesized using organic SDAs or NH_4^+ exchanged leave protons that compensate the negative framework charge generating Brønsted acid sites SiOHAl, liberating the pores for the reactant molecules to enter and react on the active site.

Zeolite structures are usually described as a function of the size, geometry, and connectivity of their pore systems. The pore sizes of zeolites are given by the number *n* of tetrahedral member forming the ring of the pore opening or window, which will control the access of the molecules into the void volume; a ring (R) containing *n* tetrahedra is referred to *n*R. According the pore sizes, zeolites are defined as small (8R, around 4 Å pore opening), medium (10R windows, 5.5 Å opening), large (12R, 7 Å opening), and extralarge (14R-18R, apertures > 7.5 Å). Figure 4.1 depicts the structure of typical zeolites. The channels may be regular or not (elliptical) and intersect with other channels to form cavities or cages which are delimited by windows. The pore architecture can be one dimensional (1D, unconnected channels),

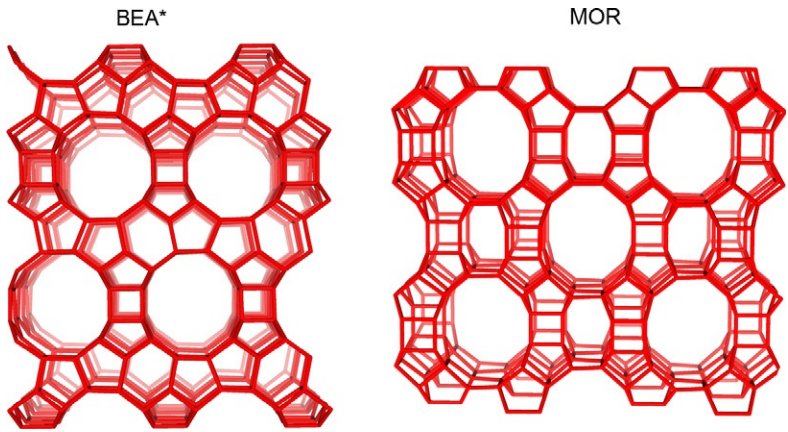

Figure 4.1 Structures of BEA* and MOR type zeolites.

bidimensional (2D, two pore systems interconnected), or three-dimensional (3D, interconnection of three pore systems).

Nowadays, there exist about 145 different topologies when only silicates are considered, and 201 for microporous tetrahedral frameworks of all compositions. The framework topology is depicted by a three letters code, which is assigned to a unique framework type by the International Zeolite Association (IZA). It is important to note that this code refers to framework type, not to a specific material. A list of all known structures can be found on the web page of the IZA, with all details on the crystalline structure, connectivity, and dimensions, as well as the chemical composition and materials with that structure type.[18]

The primary building blocks of the zeolite framework are the TO_4 tetrahedra, and the framework topology is defined by the secondary building units (SBUs) and composite building units (CBUs). There are 23 SBUs, which are the smallest (up to 16 T atoms) topological entities from which the entire framework may be built using only one type of SBU, being a ring (*n*R) the simplest SBU. The next level of complexity is linking together SBUs to form polyhedral cages, which are the CBUs, and chains. These units, frequently found in zeolite structures, are useful in identifying relationships between them. Cages can be described by the rings, or by the number of edges on each face, and the number of faces as superscript. As an example, a double four ring cage can be denoted as D4R or $[4^6]$. Figure 4.2 represents the MFI structure type characteristic of ZSM-5 (aluminosilicate) and silicalite (silicate) zeolites with the SBUs and the CBUs for this topology.

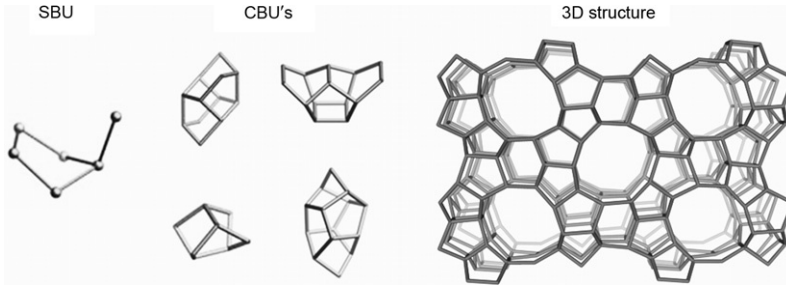

Figure 4.2 SBUs and CBUs of MFI topology.

Although the most common zeolites are silicates or aluminosilicates, they present a large variety of chemical composition by incorporating "heteroatoms" other than silicon or aluminium into tetrahedral framework positions, introducing active sites for specific catalytic reactions. Some heteroatoms incorporated to zeolites are Sn^{4+}, Ti^{4+}, Mg^{2+}, Be^{3+}, Ge^{4+}, Ga^{3+}, etc., giving substituted zeolites, which receive the general name of zeotypes. The discovery of aluminophosphates ($AlPO_4$) zeotypes by UOP in 1982 constituted the major expansion of composition of ordered microporous materials.[19] AlPOs consist of strict alternation of AlO_4 and PO_4 tetrahedra, giving rise to 3D structures similar to zeolites, and their composition has been largely varied in order to incorporate active sites for catalytic reactions by the introduction of one or more heteroatoms into substitutional framework sites.

The close relationship between zeolite structure and catalytic properties has motivated active research on the structural characterization and determination of physical–chemical properties of zeolites by a variety of techniques. Amongst them, solid state NMR plays a very special role, as it provides direct information on the local surrounding of atoms, some of them directly involved in the catalytic active sites. Zeolites have been widely studied by an array of NMR techniques by observing a variety of magnetically active nuclei to investigate the structure of framework and extraframework species, the acid sites,[20–24] the crystallization process,[25] the acid-base properties using probe molecules,[26] the catalytically active sites and reaction mechanisms using *in situ* techniques,[27–33] host–guests interactions, dynamics of adsorbed molecules,[34] or location of compensating cations into the zeolite channels.[35,36]

In this review, we provide an overview on the application of solid state NMR to structural characterization of zeolites mostly in its protonic form, paying special attention to new methodologies developed in the past years. The information provided by ^{29}Si MAS NMR and the application of 2D

J-coupling methods to determine the silicon connectivity is briefly described, highlighting the last developments made in the so-called NMR crystallography of zeolites. Fluoride anions incorporated into small zeolite cages give rise to pentacoordinated silicon, which has been detected by solid state NMR and characterized by using heteronuclear dipolar coupling techniques. Special attention is paid to the application of multiple-quantum MAS (MQMAS) NMR experiments to study ^{27}Al and ^{11}B framework and extraframework species and the zeolite acidity. Section 6 introduces the theoretical and practical experimental bases of the advanced NMR experiments applied to zeolites describing in more detail NMR experiments employed to study quadrupolar nuclei.

2. ^{29}Si NMR: STRUCTURAL CHARACTERIZATION OF ZEOLITES

Structure resolution by means of X-ray diffraction (XRD) is especially difficult when single crystals are not available and it is necessary to work with powdered samples, as this is usually the case of zeolites. ^{29}Si NMR spectroscopy is a powerful complement for the elucidation of the crystal structure determined by the analysis of the XRD data. ^{29}Si nuclei can be envisaged as an NMR probe of local arrangements exploiting a large set of nuclear spin interactions contained in the experimental spectrum such as isotropic chemical shift and chemical shift anisotropy (CSA), ^{29}Si–^{29}Si and ^{29}Si–^{27}Al dipole–dipole coupling, and the two bond isotropic indirect spin–spin scalar J^2 (^{29}Si–O–^{29}Si) coupling between covalently bonded Si species, which have been used in 2D NMR correlation analysis.

In zeolites, silicon is coordinated to four framework oxygen atoms in a tetrahedral SiO_4 coordination. The ^{29}Si NMR spectra of aluminosilicate zeolites with a Si/Al ratio up to 10 give typically a series of peak which correspond to SiO_4 tetrahedra in five different possible environments corresponding to different number of AlO_4 tetrahedra connected to the silicon via oxygen. For simplicity, these sites will be denoted ignoring the oxygen atoms as Si (nSi, 4-nAl), where $n \leq 4$; for instance, Si (4Si) will be used instead of $Si(OSi)_4$. Figure 4.3 shows the ^{29}Si chemical shifts ranges for these species. Alternatively, they can be named following the Q notation as Q^n sites, where n denotes the number of linked SiO_4 tetrahedra, so that Si(4Si) environments corresponds to Q^4, Si (3Si, 1Al) to Q^3, and so on. Simulation of experimental spectra with individual peaks allows to calculate the framework Si/Al molar ratio from the relative intensity of the Si (nSi, 4-nAl) peaks.[21,22]

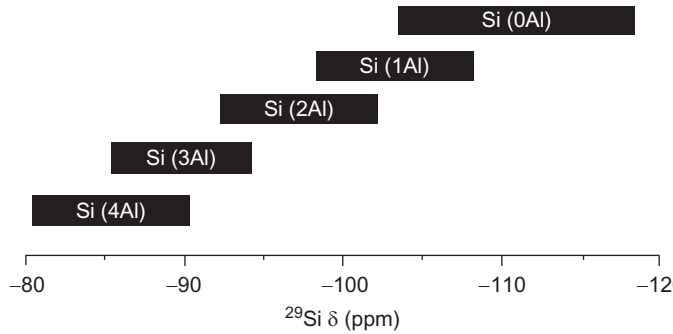

Figure 4.3 ^{29}Si NMR chemical shifts ranges of Si (*n*Al) species.

Si(4Si) sites are the predominant silicon surroundings in siliceous and highly siliceous zeolites, and the ^{29}Si NMR spectra usually consist of a series of sharp peaks, which can be as narrow as ca. 5 Hz in highly crystalline samples. The number of peaks present in the ^{29}Si NMR spectra of siliceous zeolites gives information on the number, and the intensity on the relative population of the non-equivalent crytallographic sites. Further structural information can be directly extracted from the 1D ^{29}Si NMR spectra making use of a series of mathematical expressions, which correlates δ ^{29}Si with structural parameters describing the local environment of the SiO_4 tetrahedral site from XRD structural resolution.[37] The quality of the correlations is improved using data obtained for single crystals or after lattice energy-minimization calculations.[37]

Two dimensional homonuclear correlation ^{29}Si solid state NMR techniques have been used for the assignment of individual peaks to specific crystallographic sites of the zeolite structure, by comparing the sites connectivity obtained experimentally by NMR with those predicted by the XRD structural data. COSY based on dipolar or J- coupling, and INADEQUATE experiments have been applied to a number of zeolites, as summarized in Table 4.1.

2.1. NMR crystallography

A new approach so-called NMR crystallography uses the data obtained by solid state NMR spectroscopy combined with powder XRD to obtain the crystal structure solution of pure silica zeolites.[47,49–52]

In general, the elucidation of crystal structures by XRD consists of three different steps: (1) determination of unit cell parameters and possible of the space group from the diffractogram, (2) the *structure solution*, that is, to propose a model which is consistent with the NMR data, and (3) refinement of

Table 4.1 Connectivity of Si crystallographic sites in zeolites investigated by 2D solid state NMR methods

Zeolite	Pulse sequence used
ZSM-29,[38] Dodecasil-3D[38]	COSY, DQF COSY, Spin Diffusion
ZSM-12,[39] KZ-2[39]	COSY, INADEQUATE
ZSM-5[40,41]	COSY, INADEQUATE, CP-INADEQUATE
DD3R[42]	COSY, INADEQUATE
Mordenite[43]	COSY
ZSM-11[44]	INADEQUATE
ZSM-23[45]	INADEQUATE
Ferrierite[46]	INADEQUATE
Sigma-2[47]	INADEQUATE, DQ-Homonuclear dipolar recoupling
ITQ-12[48]	DQ-Homonuclear dipolar recoupling

the proposed model against the diffraction data using the Rietveld method. The structure solution, step 2, is the most difficult for microcrystalline solids, especially if they have a complicated structure with many crystallographic sites as it may be the case of zeolites. In NMR crystallography, NMR data are directly used for the structure solution.

Direct information about the number and population of non-equivalent sites in the unit cell is directly obtained from the ^{29}Si MAS NMR spectra of pure or high silica zeolites. Moreover, several nuclear spin interactions have been used in NMR crystallography to obtain structural information: (i) ^{29}Si–^{29}Si dipole–dipole couplings, (ii) CSA, (iii) the two-bond isotropic indirect spin–spin scalar J^2 (^{29}Si–O–^{29}Si) coupling between covalently bonded Si species. Information on zeolite structure by exploiting ^{29}Si–^{29}Si dipolar interactions is obtained by means of the homonuclear dipolar recoupling $SR26_4^{11}$ pulse sequence in a 2D double quantum (DQ) correlation experiment (see Section 6.2.5).[49] This experiment is carried out on ^{29}Si natural abundance materials by transferring the magnetization through cross-polarization from the protons of the organic molecule used as SDA in the synthesis. The use of this pulse sequence to extract information on ^{29}Si–^{29}Si connectivity has several advantages over the classical INADEQUATE (based in J^2 ^{29}Si–^{29}Si scalar coupling): (i) the 2D spectrum contains all the

connectivity, including symmetry related sites in the diagonal; (ii) the intensity of the cross peaks is higher as a result of the stronger dipolar interactions, about one order the magnitude larger (160 Hz) than J coupling (10–15 Hz); and (iii) it is possible to probe long range of ^{29}Si—^{29}Si dipolar interactions, up to about 8 Å distance, by increasing the recoupling time τ. This is illustrated in Fig. 4.4 for zeolite Sigma-2.[47]

The experimental procedure followed to extract the long-range information from the spectra is depicted in Fig. 4.5 for zeolite Sigma-2.[47] The intensities of every Si–Si cross peaks in the 2D spectra are plotted against the recoupling time, yielding DQ buildup curves for each pair of Si–Si correlation cross peaks. Figure 4.5A shows these DQ buildup curves for three pairs of the Si–Si connectivity peaks of zeolite Sigma-2, and Fig. 4.5B reflects the high sensitivity of these curves with the Si–Si distances. The shape of the curve reflects the distribution of the Si–Si distances for a given pair of T sites, while the maximum intensity of the curve represents the number of Si–Si neighbours within the range of 8 Å, as it becomes evident by comparing with the distribution plots of the three crystallographically distinct Si–Si nuclear pairs, depicted in Fig. 4.5B. The number and occupancy of the silicon sites,

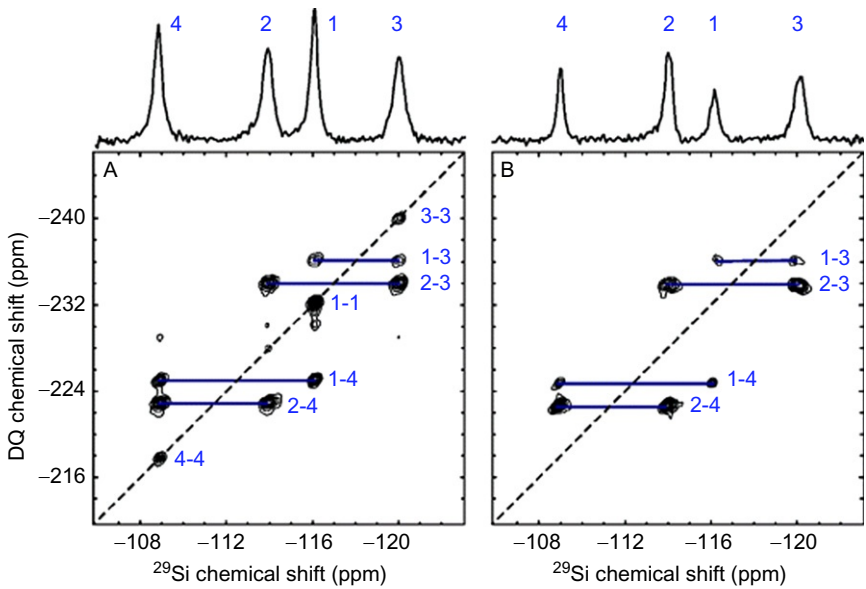

Figure 4.4 ^{29}Si QD correlation spectra of zeolite Sigma-2 obtained by using (A) the $SR26_4^{11}$ dipolar recoupling sequence and (B) the J-coupling based INADEQUATE. *Reprinted with permission from Ref. 47. Copyright (2005) American Chemical Society.*

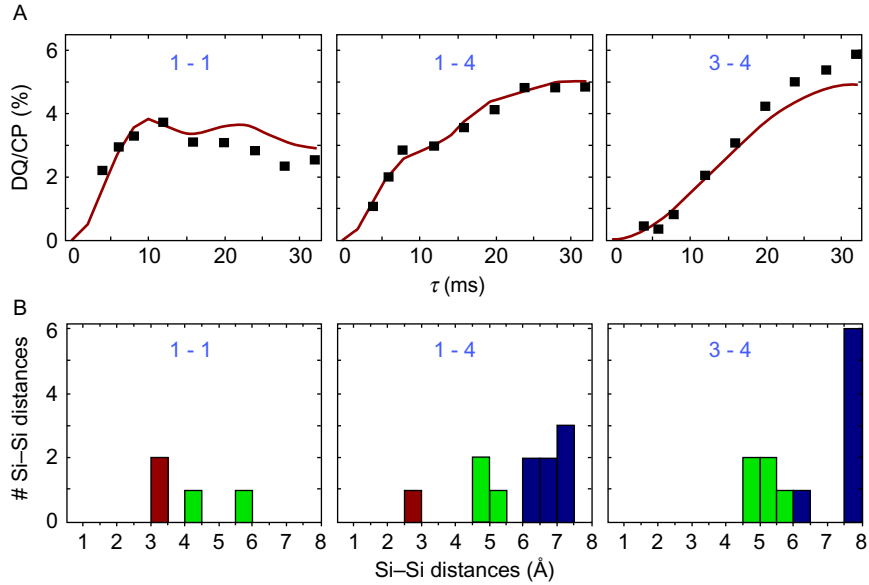

Figure 4.5 (A) ^{29}Si DQ buildup curves obtained by integration of the correlation peaks obtained in a series of 2D SR26$_4^{11}$ DQ correlation spectra. The solid lines are simulations of the DQ buildup curves taken into account ^{29}Si–^{29}Si spin pairs at a distance less than 8 Å. (B) Histograms of Si–Si distance distributions in zeolite Sigma 2. *Reprinted with permission from Ref. 47. Copyright (2005) American Chemical Society.*

the inter-site connectivity and the long-range Si–Si distance information provided by ^{29}Si solid state NMR, is combined with the unit cell parameters and space group determined by powder XRD to optimize the Si atomic coordinates in the asymmetric unit of the zeolite structure (see Fig. 4.6).[49] The atom coordinates are optimized by using an algorithm, which fit the experimental DQ curves with theoretical curves simulated from the Si–Si distances calculated for a given arrangement of silicon atoms. The algorithm combines a "grid" search with subsequent least square minimization. This methodology has been successfully used to solve the crystal structures of pure siliceous zeolites ITQ-4 (IFR topology) and ferrierite (FER topology).[49]

The position of the oxygen atoms remains unknown in structures after solution by powder XRD, which may lead to non-accurate determination of atom coordinates. This limitation can be overcome by measuring the CSA tensor of the ^{29}Si resonances, which reflects the silicon environment and supports the determination of the position of oxygen atoms in SiO_4 tetrahedra with much higher precision. The measurement of the CSA is

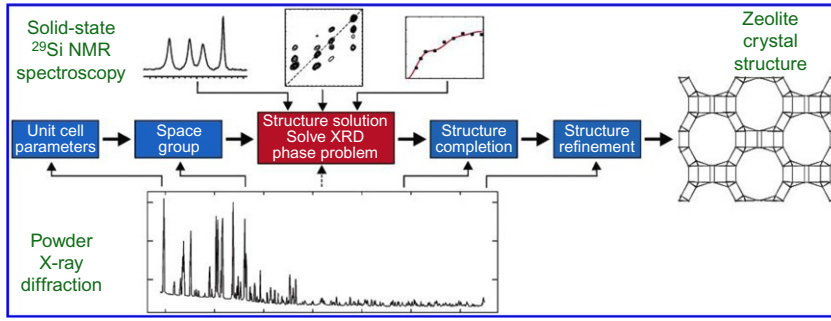

Figure 4.6 Strategy for the determination of zeolite structures by a combination of solid state NMR spectroscopy and powder X-ray diffraction. *Reprinted with permission from Ref. 49. Copyright (2005) American Chemical Society.*

challenging because of the small anisotropy of tetrahedral $^{29}SiO_4$ sites and the superimposition of the multiple crystallographic sites and their sideband patterns in the spectra acquired at low spinning rates make difficult the observation of the CSA envelope. These limitations are overcome with the utilization of very high magnetic fields which leads to the enhancement of the CSA, and the application of pulse sequences that refocuses the CSA on a second dimension of a 2D NMR experiment, yielding quasi-static spectra. This 2D experiment is illustrated in Fig. 4.7 for the zeolite Sigma-2, which also shows the simulation of the CSA slices of four Si sites. The experiment was carried out using a static magnetic field of 21.1 T.[51]

The principal components of the chemical shift tensor can be calculated using *ab initio* methods and the quality of the result strongly depend on the accurate determination of the silicon site geometry. The high sensibility of the CSA against the structure has been used to improve the quality of the crystal structure solutions. The structure obtained after optimization using the DQ-curves is refined to give the best agreement between ^{29}Si CSA tensors calculated by DFT calculations, and those obtained experimentally. The incorporation of CSA optimization into the algorithm which involves the use ^{29}Si DQ NMR data, improves the crystal structure determination. The obtained structure was in very good agreement with the measured X-ray single crystal structure. This strategy has been tested for zeolites Sigma 2, ZSM-12, and ITQ-4.[52]

Solid state 2D refocused INADEQUATE ^{29}Si{^{29}Si} NMR has been used to measure the two bonds scalar J^2 (^{29}Si–O–^{29}Si) coupling constants of Si–Si pairs in zeolite structures[53] with high accuracy for values as small as 6.3 Hz.

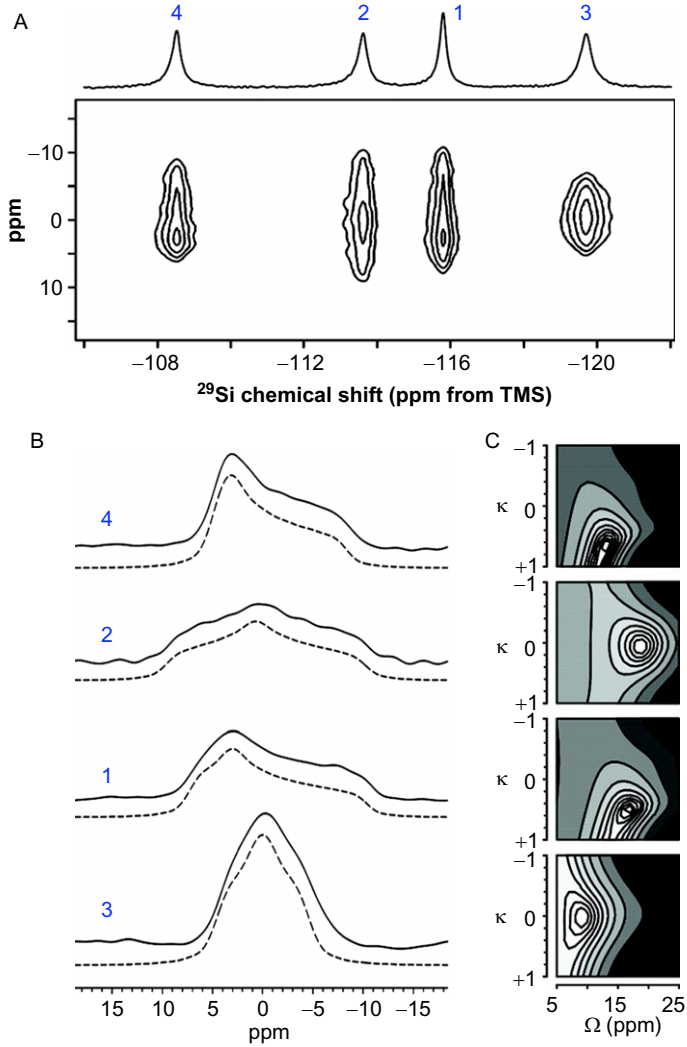

Figure 4.7 (A) 2D ^{29}Si CSA recoupling spectrum for zeolite Sigma-2, (B) experimental (solid line) and simulated (dashed lines) quasi-static CSA recoupled line shapes extracted from the 2D spectrum for the indicated Si sites, and (C) contour of the quality of fit. *Reprinted with permission from Ref. 51. Copyright (2008) American Chemical Society.*

Although J^2 (^{29}Si–O–^{29}Si) values cannot be correlated simply with geometrical parameters, they are very sensitive to local structure and agree with values calculated by DFT using zeolite structures known with accuracy. Therefore, measurements of J^2 (^{29}Si–O–^{29}Si) is a promising tool to probe and refine local structure when integrated in an iterative search protocol.

2.2. Zeolites synthesized in fluoride medium: Pentacoordinated silicon

Zeolites synthesis requires the addition of a strong base or HF as mineralizing agents to dissolve the reactants used as source of silicon and other T atoms (Al, Ge, Ga, etc.) depending on the chemical composition. When high or pure silica zeolites are synthesized in strong basic media, the positive charge of the organic SDA is compensated by framework SiO^- groups yielding materials with high concentration of defective silanol groups. However, when HF is used in the synthesis, fluoride anions are incorporated into the smallest cages of the zeolite structure compensating the positive charge introduced by the occluded organic SDA cations.

^{19}F NMR chemical shift of fluorine in silica zeolites covers a range between −30 and −80 ppm depending on its location, following the general trend of shifting to low field as the size of the cage decreases, as illustrated in Fig. 4.8 and Table 4.2. Table 4.2 collects the $\delta^{19}F$ of anions inside the various cages of pure silica, and Ge-containing zeolites. In this sense, the $\delta^{19}F$ of F^- inside D4R cage is about −38 ppm in the siliceous samples, while it is −14 ppm for GeO_2 composition. The results reported in this Table indicate that $\delta^{19}F$ mainly depend on F^- location in the zeolite and the local

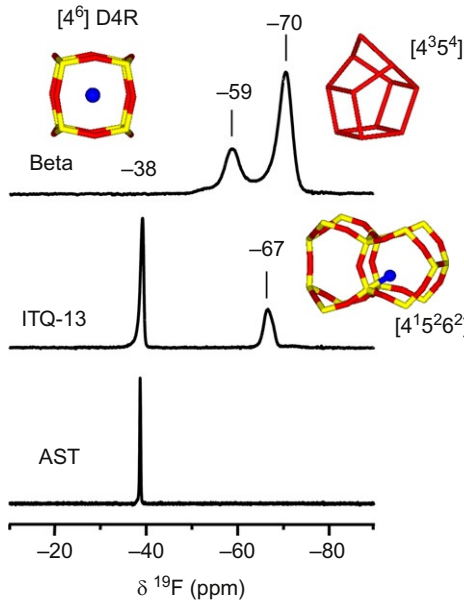

Figure 4.8 ^{19}F MAS NMR spectra of the fluoride anions located inside the cages of the pure silica zeolites indicated in the figure.

Table 4.2 Location of fluoride anions in small cages in zeolites and the corresponding chemical shift. Si and Ge denotes SiO_4 ant GeO_4 tetrahedra.

Cage (pure silica)	$\delta^{19}F$	Zeolite
$[4^6]$ D4R	−38 to −40	Octadecasil,[62] ITQ-7,[58] ITQ-13,[61] ITQ-21,[60] Beta,[63,64] ITQ-12,[65] ITQ-29,[66] ITQ34,[67] ITQ24,[68] ITQ43,[56] ITQ39[55]
	−31.6	ITQ-27[69]
$[4^35^4]$	−68, −70, −59	Beta,[63,70,64] SSZ-23,[63] ITQ39[55]
$[4^15^26^2]$	−64 to −67	Silicalite-1,[63] ITQ-13,[61] ITQ-34[67]
$[4^15^26^2]$	−78.1, −79.2	STF (SSZ-35,[71] MU-26[72])
$[4^15^26^2]$	−67, −80	MFI[73]
$[4^15^46^2]$	−76, −78	Nonasil,[74] ITQ-32[75]
$[5^4]$	−56	Ferrierite[76]
$[4^66^2]$ D6R	−64	Chabacite[76]
$[4^35^26^1]$	−68	ITQ-4[63]
$[4^35^4]$proposed	−69	ITQ-3[63]
$[4^25^4]$, $[4^26^2]$	−59, −81	ITQ-24[68]
Unknown	−78, −84	ZSM-12[63]
D4R composition in Ge-containing zeolites		
[7Si,1Ge]	−20	ITQ-13,[61] ITQ-7,[58] ITQ-17,[59] ITQ-21,[60] Octadecasil,[77] ITQ43,[56] ITQ24[68]
[5Si, 3Ge] [4Si, 4Ge]	−7, −9	ITQ-13,[61] ITQ-7,[58] ITQ-17,[59] octadecasil,[77] ITQ-21,[60] ITQ-40,[11] ITQ43,[56] ITQ24,[68] ITQ37[10]
[8Ge]	−14, −15	Octadecasil,[77] ITQ-21[60]
Other cages containing Ge atoms in Ge-containing zeolites		
$[4^35^4]$	−46	Beta[64]
$[4^15^46^2]$	−55	ITQ-13[61]
$[4^25^4]$, $[4^26^2]$	−52, −70	ITQ-24[68]

chemical composition. However, it must be noted that for purely siliceous zeolites, $\delta^{19}F$ of fluoride placed in the $[4^15^26^2]$ cage varies between -64 and -80 ppm in different structure types (silicalite-1, ITH, STF, SFF), suggesting the contribution of other factors, as supported by recently published results for MFI.[54] The substitution of Ge for Si into zeolite frameworks favours the formation of structures containing D4R units. This synthesis approach has resulted in a great number of novel zeolites with open structures, many of them synthesized in fluoride medium.[9,11,55–57] ^{19}F MAS NMR has been proved to be a powerful tool to investigate the distribution of Ge into the framework and to prove the preferential incorporation of Ge to the T crystallographic sites involved in the D4R units. Thus fluoride acts as a NMR probe of the local chemical composition.[58–61]

Fluoride ions placed in the centre of the smallest cage D4R gives a distance $d(F–Si) = 2.6$ Å, which is relatively long, as F^- is usually placed near silicon. Indeed, fluoride bonds silicon atoms in 4R ($d(F–Si) = 1.7$ Å) giving rise to pentacoordinated silicon $SiO_{4/2}F^-$ detectable by ^{29}Si NMR,[63,71,74] characterized by signals appearing in the range -125 to -150 ppm, at higher field than typical Si(4Si) environments (range -105 to -120 ppm). According to theoretical calculations,[78] silicon is bonded to four shared framework oxygen and one fluoride atom, resulting in trigonal bipyramidal configuration. The chemical shift and the shape of the ^{29}Si NMR signals depend on the disorder in the fluoride location and or dynamics effects.

Pentacoordinated silicon was first observed by ^{29}Si NMR in siliceous nonasil (NON) and silicalite (MFI topology) zeolites,[74] and in other pure silica zeolites such as ZSM-12, ITQ-3, Beta, SSZ-23, silicalite-1, and ITQ-4.[63] The structure of the $SiO_{4/2}F^-$ sites has been investigated by combining ^{29}Si and ^{19}F MAS NMR. Analysis of the spinning sideband pattern of the ^{19}F resonance allows to determine the span ($\Omega = \delta_{11} - \delta_{33}$) parameter, which gives information on the symmetry environment of fluorine atoms.[63] The ^{29}Si signal of 5-coordinated silicon appears at about -145 ppm in zeolite nonasil, as well as ITQ-3, Beta, ZSM-12,[63] zeolite type STF (SSZ-35,[71] Mu-26[72]), and SSZ-44.[79] The span of the corresponding ^{19}F NMR signal is approximately 80–90 ppm in these zeolites, indicating strong Si–F interaction and low motion of F^- among the Si sites. Meanwhile, pentacoordinated ^{29}Si resonance in other zeolites such as silicalite[74] and SSZ-23[63] gives a broad signal centred at -125 ppm and a smaller ^{19}F span of around 50–70 ppm. However, when the ^{19}F spectra of these zolites, i.e. silicalite and SSZ-23, are recorded at 140 K, the signal of pentacoordinated ^{29}Si resonance shifts to -147 ppm and splits into a doublet separated by 165 Hz due to the ^{29}Si–^{19}F

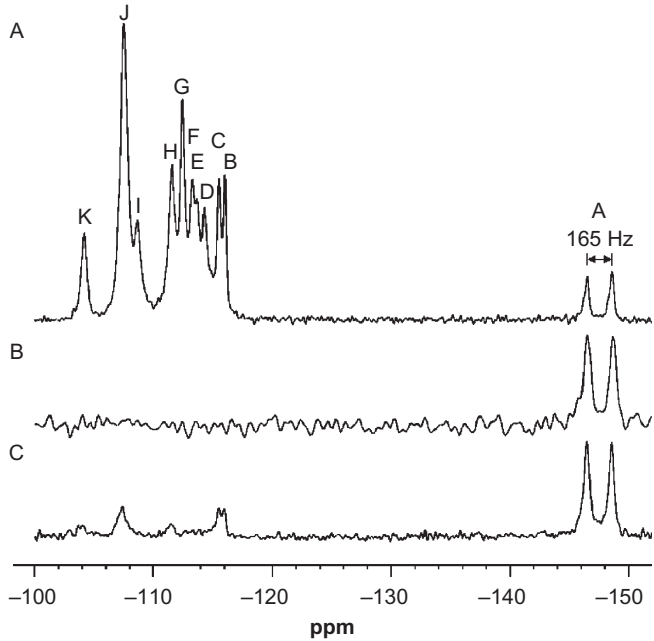

Figure 4.9 Fast spinning ^{29}Si NMR spectra of zeolite type STF, (A) $^{1}H \rightarrow {}^{29}Si$ CP MAS spectrum, 15 kHz spinning rate, and 3 ms contact time (B) $^{19}F \rightarrow {}^{29}Si$ rotor-synchronized refocused INEPT experiment, (C) $^{19}F \rightarrow {}^{29}Si$ CP MAS spectrum, 15 kHz spinning rate, and 0.4 ms contact time. *Reprinted with permission from Ref. 71. Copyright (2002) American Chemical Society.*

J coupling, and the span of the ^{19}F signal increases to ca. 80 ppm. The changes of the spectra as a function of the recording temperature indicate dynamic motion of F^- in the structure of silicalite and SSZ-23 zeolites at room temperature that decreases when the sample is cooled down to 140 K. The signal of pentacoordinated silicon sharply increasing under ^{19}F to ^{29}Si cross-polarization reflecting strong ^{29}Si–^{19}F dipolar interactions, and consequently, a short Si–F distance.[63,74] The assignment of the signal at − 145 ppm to Si atoms bounded to F was confirmed by applying the $^{19}F \rightarrow {}^{29}Si$ refocused INEPT sequence to zeolite STF(see Fig. 4.9).[71] The INEPT experiment, in which polarization is transferred via the through-bond *J*-coupling, displayed in Fig. 4.9b, shows only the doublet corresponding to pentacoordinated silicon NMR evidencing the covalent Si–F bond.

Dipolar based sequences such as cross-polarization dynamics, REDOR (rotational echo double resonance), and TEDOR (transferred echo double resonance), depicted in Section 6.2, have been used to measure Si–F distances in zeolites Octadecasil,[80,81] Silicalite-1 (MFI),[82] STF,[71] and

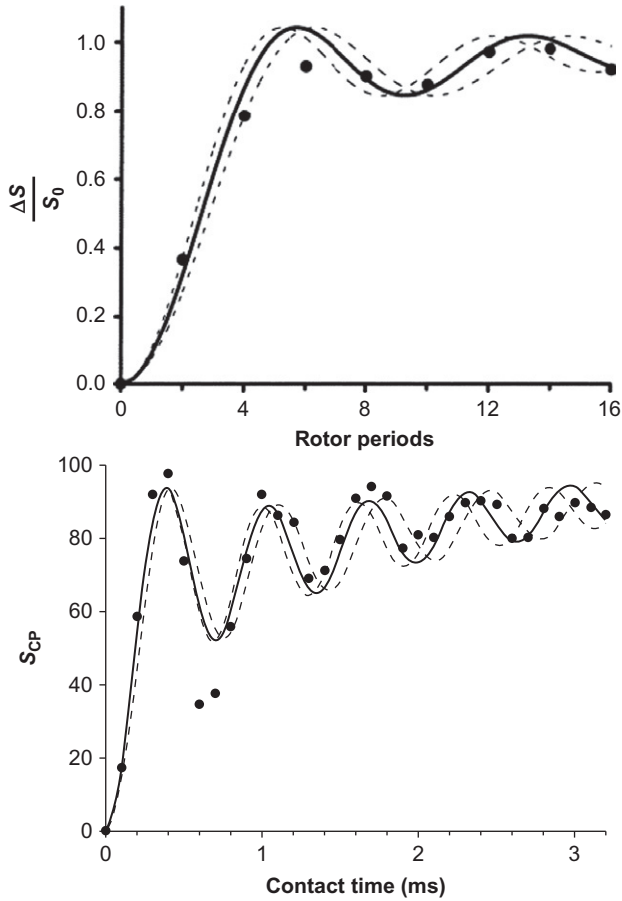

Figure 4.10 Experimental and simulated $^{19}F/^{29}Si$ CP REDOR curves for silicon peak Si3 (top); and experimental and simulated $^{19}F \rightarrow {}^{29}Si$ CP curves for peak Si3 (bottom). The data were fitted with a F–Si internuclear distance of 1.72 Å. The solid lines are the best fit and the dashed lines represent the estimate of the error limits. *Adapted with permission from Ref. 71. Copyright (2002) American Chemical Society.*

SSZ-44(SFF).[79] Figure 4.10 (bottom) represents the evolution of cross-polarized ^{19}F to ^{29}Si signal at different contact times for STF zeolite.[68] The curve shows an oscillation with a frequency, which is proportional to the ^{19}F–^{29}Si dipolar coupling. The method for adjusting the curve and calculate the dipolar coupling has been described by Fyfe *et al.*[79] Fig. 4.10 (top) shows the REDOR curve for zeolite STF. More details on REDOR pulse sequence and other recoupling schemes commonly applied to zeolites are depicted in Section 6.2.

The ^{19}F–^{29}Si distances obtained by NMR methods and XRD are in good agreement for octadecasil, while major discrepancies are found for zeolites MFI and STF due to the effects of fluorine dynamic motion, and static disorder on the XRD data.[71] The fact that only some silicon atoms in equivalent T sites are linked to F, produces an average between four- and five-coordination silicon. A good agreement is obtained when this is introduced in the XRD structural refinement.[71]

3. ^{27}Al NMR OF ZEOLITES

The presence of aluminium into framework sites of zeolites generates a negative charge that can be compensated by protons producing bridging ≡Si–OH–Al≡ hydroxyl groups, which are Brønsted acid sites. As mentioned in Section 1, acid properties of zeolites are responsible for their most important petrochemical and chemical industrial applications as catalysts, promoting the structural investigation of aluminium sites and of acid properties, being these of the most important topics on the application of solid state NMR in the field of zeolites.

^{27}Al ($I=5/2$) is a quadrupolar nucleus which produces NMR spectra commonly affected by the second-order quadrupolar interaction to an extent that depends on the local Al chemical environment and the strength of the external magnetic field used. The availability of high magnetic external fields and the use of the MQMAS experiment help to reduce or remove this broadening interaction and has provided the tools to obtain useful structural information on aluminium and other quadrupolar nuclei.[83–88]

In the following sections we address the most relevant results on the research activity on the characterization of aluminium sites in zeolites. The discussion is divided in four different aspects: (i) distribution of aluminium atoms within the zeolite framework (section 3.1), (ii) reversible framework octahedral aluminium (section 3.2), (iii) invisible aluminium (section 3.3) and (iv) extraframework aluminium (EFAL) species (section 3.4).

3.1. Distribution of aluminium atoms within the zeolite framework

Although the $Al(OSi)_4$ is the only aluminium environment in zeolites framework because of the Lowenstein rule,[15] the usually featureless ^{27}Al NMR spectra, mainly due to overlapping of quadrupolar broadened signals and site heterogeneity, make difficult the resolution of non-equivalent crystallographic positions and site occupancy. However, the distribution of

aluminium atoms amongst the non-equivalent crystallographic positions of the zeolite framework and its proximity are very important features as they determine the location of protons and then their acid strength, besides the thermal and chemical stability of the zeolite. Moreover, the exchange properties of zeolites by transition metal ions and metal oxo complexes representing the active sites for oxidation reactions may require the close proximity of aluminium atoms and of the framework negative charges to be balanced by cations with valence two or higher. Therefore, the distribution of aluminium atoms in the zeolite framework determine their catalytic performance[89,90] and adsorption properties.[91]

Determination of Al sitting in zeolites by XRD is not possible because its scattering properties are similar to those of Si. Lattice energy-minimization calculations give very small energy differences for Al atoms located in different crystallographic positions, suggesting that if there is preferential occupation, it must be kinetically rather than thermodynamically controlled. This implies that the aluminium distribution can be governed by the synthesis method and the organic SDA used.

The distribution of aluminium atoms in the zeolite framework has been mainly investigated by solid state NMR following two different approaches: (i) the analysis the ^{29}Si MAS NMR spectra taking advantage of its higher resolution; (ii) the analysis of the ^{27}Al NMR spectra, usually performing MQMAS experiments in combination with theoretical calculation of ^{27}Al NMR parameters.

3.1.1 ^{29}Si MAS NMR

The relative intensity of the signals of Si(*n*Al) environments in the ^{29}Si MAS NMR spectra of aluminosilicate zeolites gives direct information on the second neighbouring atoms (Si, Al) of silicon sites and their relative population. Comparison with the silicon environments obtained by modelling the sitting of aluminium atoms in the framework provides information on the distribution of aluminium. This procedure is especially useful for aluminium rich zeolites, as the NMR signals of Si (*n*Al) are very weak or negligible for high silica zeolites. The relative population of the Si (*n*Al) species for different models of aluminium distribution can be calculated using three different methodologies: (i) analyze quantitative contributions of aluminium in periodical building units of the zeolite,[90,92–94] (ii) apply standard statistical methods for random sitting of aluminium in the zeolite,[95] and (iii) the use of Monte Carlo simulations.[95]

The influence of the preparation procedure on the aluminium distribution is evident by comparison of the ^{29}Si MAS NMR spectra of zeolites Y (Si/Al = 1.7–7.9) with similar aluminium content crystallized in the presence of crown ethers or prepared by dealumination,[68,73,74] thus, explaining the differences in their catalytic activity.[90] Aluminium is randomly distributed (obeying the Lowenstein rule) in the dealuminated zeolites,[90,95,96] whereas fitting the experimental ^{29}Si NMR spectra of the zeolites prepared with the crown ethers requires heterogeneous aluminium sitting induced by the Na-crown ether complexes.[96] Experimental results of faujasite zeolites with Si/Al = 2.6–19.5 were fitted using double six rings as periodic building units, locating the aluminium atoms as far as possible from each other, allowing fulfil the Dempsey rule, which minimizes the number of Al next nearest Al–O–Si–O–Al neighbours.[94] A similar approach concluded a different dealumination mechanism for Beta and mordenite zeolites.[93]

3.1.2 ^{27}Al MAS NMR

^{27}Al MAS NMR has been used to study the aluminium distribution within the zeolite framework, especially after the development of the MQMAS NMR experiment. This technique allows complete characterization of the ^{27}Al NMR signals, providing the isotropic chemical shift and quadrupolar parameters. The assignment of specific framework crystallographic sites or group of sites in zeolite is usually performed by applying the empirical expression $\delta(\mathrm{Al}) = -0.50\theta + 132$ (ppm)[97] or by combination with quantum mechanic/molecular mechanic (QM/MM) calculations.[98–101] This expression correlates δ_{iso} ^{27}Al with structural parameters of the AlO_4 site, in this case with the average T–O–T angle (θ). Comparison with the mean T–O–T angle calculated for every crystallographic site of the zeolite structure resolved by XRD allows assigning every ^{27}Al signals to a site or group of sites. We must note that XRD does not discern Al from Si atoms and the average T–O–T angle of a crystallographic position is not specific for Si–O–Al but also includes Si–O–Si angles. This approach has been used to interpret the ^{27}Al NMR spectra of zeolites Beta and ZSM-5. The ^{27}Al MQMAS spectra of zeolite Beta allows to distinguish two signals of tetrahedral aluminium, which have been attributed to sites T1–T2 and T3–T9.[102,103] The relative intensities of the two peaks, and consequently, the relative occupancy of the crystallographic sites, changes with the Si/Al molar ratio, indicating that the distribution is non-random.[102] A different conclusion was reached for zeolites

ferrierite[104] and ZSM-5,[105] for which the combination of ^{29}Si NMR and ^{27}Al MQMAS led to the conclusion that aluminium is randomly distributed within the framework.

^{27}Al MQMAS has been combined with QM/MM theoretical calculations to investigate the distribution of aluminium atoms in the framework of zeolites ZSM-5 (MFI)[98–100] and ferrierite (FER).[101] Sitting of aluminium in MFI topology was investigated using a set of eleven Na–ZSM-5[98] or eighteen Li-, Na-, or H–ZSM-5[99] zeolites synthesized in different conditions, with Si/Al molar ratio in the range Si/Al = 14–140.[98,99] ^{27}Al MQMAS NMR spectra were analyzed and selected spectral slices in the F1 and F2 dimensions were simulated assuming three to four signals per sample. This is illustrated in Fig. 4.11 for sample ZSM-5. This procedure allowed the identification of a total of 10 resonances in a chemical shift range of 13.6 ppm for all the samples of MFI-type.[98] Previous to the calculation of δ^{27}Al by DFT methods, the geometry of the 24 AlO_4 crystallographic sites of the MFI topology was optimized, and then five shells clusters Al–O–Si–O–Si–H_{link} of the optimized structure were used to calculate the nuclear magnetic resonance parameters of ^{27}Al. The absence of Al–O–Si–O–Al– sequence was confirmed by the non-appearance of ^{29}Si(2Si 2Al) resonances in the

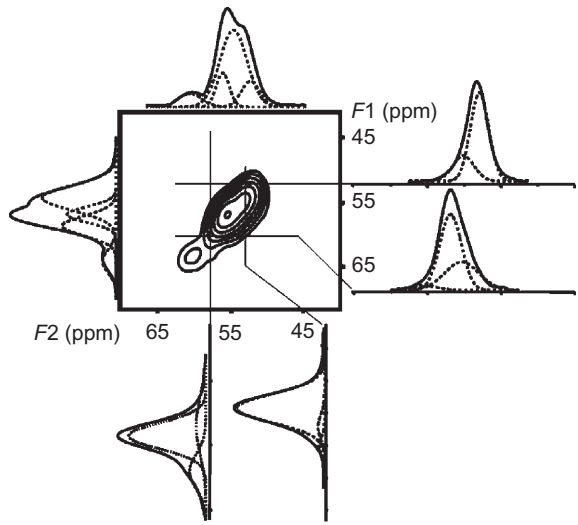

Figure 4.11 2D plot of the ^{27}Al 3QMAS NMR sheared spectrum of Na/ZSM-5, F1 and F2 projections, and selected normalized slices with simulations (dotted lines). *Reprinted from Ref. 98 with permission. Copyright 2007 Wiley-VCH.*

^{29}Si NMR spectra, and the non-occurrence of Al–O–Si–O–Si–O–Al– environments by the lack of exchange by $Co(H_2O)_6^{2+}$ cations. Calculations of ^{27}Al nuclear parameters of atoms in the 24 T sites give a shift range of $\Delta\delta = 14.1$ ppm, in good agreement with the experimental value $\Delta\delta = 13.6$ ppm. The assignment of experimental resonances to specific sites by comparison with theoretical values, with the smallest deviation of chemical shift, involves the non-occupancy of some crystallographic sites. Samples with similar Si/Al molar ratios prepared by different methods exhibit different site occupancies pointing out that the Al distribution is governed by kinetics and that it can be determined by the synthesis procedure. The δ_{iso} ^{27}Al calculated theoretically indicated that there is not a simple linear relationship between the isotropic δ_{iso} ^{27}Al and the average Al–O–Si angle, questioning the empirical expression proposed by Lipmaa *et al.*[97] It is concluded that the aluminium atoms are not randomly distributed in the zeolite and that it is not controlled by a simple rule, but it depends on the synthesis procedure of the zeolite.

A similar methodology was used to evaluate the influence of the presence of next nearest and next–next nearest aluminium atoms, that is, the sequences Al–O–Si–O–Al and Al–O–Si–O–Si–O–Al on the geometry of the AlO_4 site in ZSM-5 and then on their nuclear magnetic properties.[106] The results indicated that the presence of aluminium atoms affects the geometry of the AlO_4 tetrahedra and then the isotropic chemical shift up to 4 ppm, but it is not possible to predict the sense of the shift without carrying out theoretical calculations.[106] As the δ_{iso} ^{27}Al can be modified by the presence of AlO_4 tetrahedra in its proximity, the proper assignment of the ^{27}Al resonances in the MQMAS NMR spectra requires to know if AlO_4 atoms are isolated in the zeolite framework or if Al–O–Si–O–Al and Al–O–Si–O–Si–O–Al sequences are present in the sample.

A methodology, depicted in Fig. 4.12, has been developed to study aluminium sitting having into account the presence of Al–O–Si–O–Al and Al–O–Si–O–Si–O–Al sequences, using zeolite ferrierite (FER) as a case study.[101] A set of five differently synthesized samples with Si/Al in the range Si/Al = 10–30 were used. First, ^{29}Si NMR spectra are recorded to probe that Si(2Si 2Al) (Al–O–Si–O–Al– sequences) sites are negligible, which is usual in zeolites with a Si/Al molar ratio > 8. Then, samples are exchanged by $[Co(H_2O)]_6^{2+}$ and if the exchange level is significant, visible spectroscopy of the bare Co(II) in the dehydrated zeolites allows to identify rings with two close Al atoms. The zeolites studied possessed either isolated AlO_4 tetrahedra or isolated AlO_4 and Al–O–Si–O–Si–O–Al pairs in the

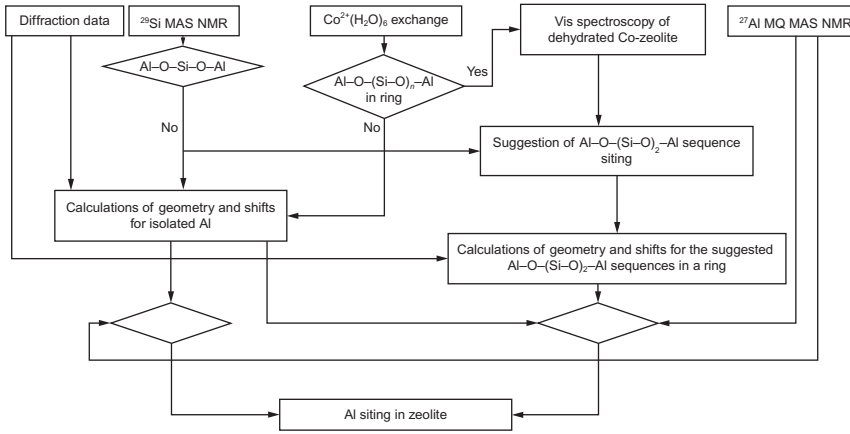

Figure 4.12 Strategy for the analysis of Al site in silicon-rich zeolites. *Reprinted with permission from Ref. 101. Copyright (2011) American Chemical Society.*

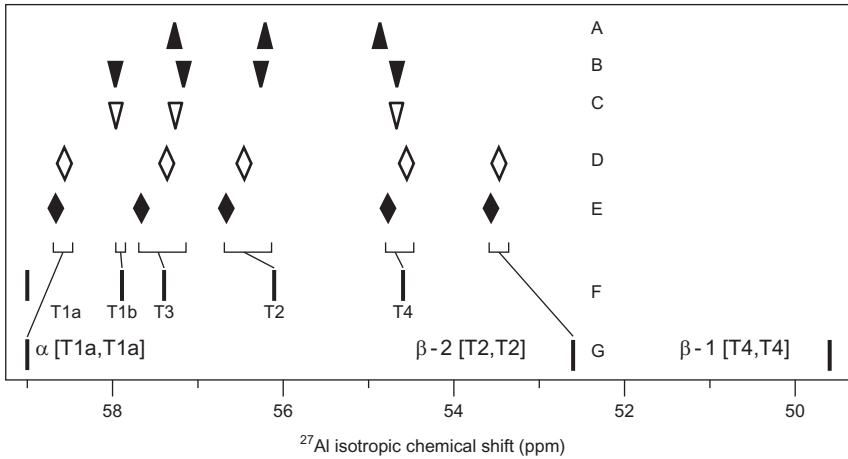

Figure 4.13 Comparison of the observed (A–E) and calculated (F,G) ^{27}Al δ_{iso} for zeolite ferrierite (FER) and the assignment to specific crystallographic T sites. ^{27}Al δ_{iso} was calculated for isolated Al atoms (F) and for Al–O–(Si–O)$_2$–Al sequences in the α and β cationic sites (G). *Reprinted with permission from Ref. 101. Copyright (2011) American Chemical Society.*

rings.[101] If Si(2Si 2Al) is not found, the isotropic chemical shifts of isolated AlO_4 and aluminium Al–O–Si–O–Si–O–Al pairs in the rings of the α and β cationic positions are calculated using DFT methods. The ^{27}Al MQMAS NMR spectra are then simulated taking into consideration that FER topology possesses four crystallographic sites. Figure 4.13 compares the calculated and observed δ_{iso} ^{27}Al, with a good agreement. It is concluded that the Al

sitting in the samples studied is not random but strongly depends on the zeolite synthesis conditions.[101]

3.2. Reversible octahedral framework aluminium

Although AlO_6 is usually associated with EFAL species, the formation of reversible octahedral species linked to the framework was first reported for zeolite beta (BEA topology)[103,107–110] and later on for zeolites ZSM-5 (MFI)[111] and Y (FAU),[112–114] as well as in less crystalline materials such as amorphous silica–alumina, indicating that this is typical of aluminosilicates and not only of zeolites.[114]

The ^{27}Al NMR spectra of protonic zeolites show signals of tetrahedral Al in the region of 50–65 ppm and usually one or more contributions of octahedral aluminium at about 0 ppm. Upon adsorption of basic molecules such as NH_3 or pyridine, or exchanged with alkaline cations such as K^+ or Na^+, hexacoordinated aluminium reverts to tetrahedral, indicating that these sites are linked to the zeolite network.[103,107–114] The extent of reversibility in aluminium coordination depends on the zeolite treatment, as the linkages to the network can be hydrolyzed under sever calcination conditions giving NMR invisible aluminium.[107]

The ^{27}Al MQMAS NMR spectra recorded before and after the adsorption of ammonia on zeolite H–USY, shown in Fig. 4.14, illustrate the changes experienced by aluminium depending on the sample atmosphere.[114] The use of the MQMAS experiment allows the identification of several aluminium sites, which is not obvious when the single pulse sequence is used. The MQMAS NMR spectrum of zeolite H–USY (Fig. 4.14A) shows the presence of two AlO_4 and three AlO_6 aluminium sites, with the NMR parameters summarized in Table 4.3.[114] According to δ_{iso} values, the weak signal appearing at 35 (Fig. 4.11A) is attributed to pentacoordinated AlO_5 species. The AlO_{6a} resonance corresponds to species with a very small quadrupolar interaction, while the signal AlO_{6c} deviates more from the diagonal indicating a large anisotropic quadrupolar shift and broadening. Figure 4.14B shows the ^{27}Al MQMAS NMR spectrum recorded after the adsorption of NH_3.[114] Signals AlO_{6a} and AlO_{6c} disappear and those of tetrahedral aluminium increase without changing the overall intensity of the spectrum, indicating the transformation of octahedral into tetrahedral aluminium. The signal of pentacoordinated AlO_5 disappears too, probably because it is also converted to tetrahedral Al.[114]

^{27}Al MAS NMR spectroscopy studies have shown that reversible tetrahedral–octahedral aluminium is formed in silica–alumina and not in

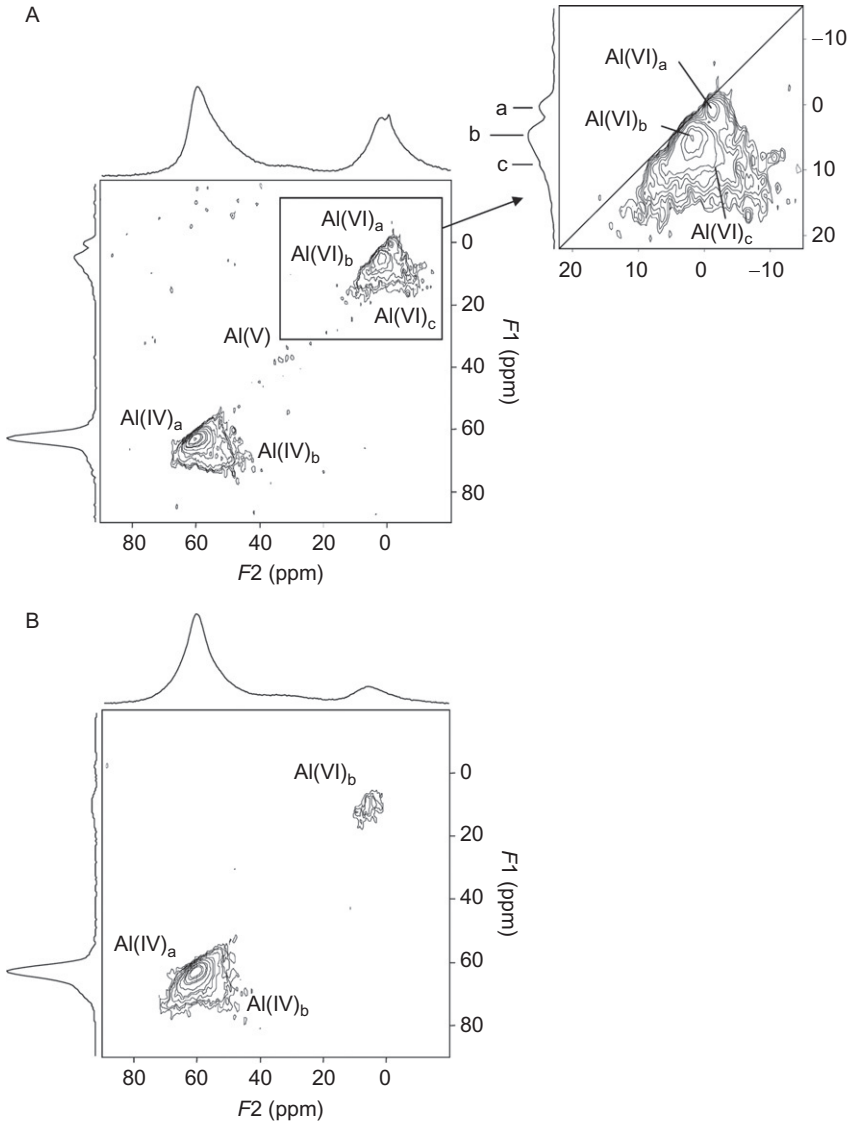

Figure 4.14 ^{27}Al MQMAS NMR spectra of (A) H–USY and (B) H–USY–NH_3. The top spectrum is the 1D 27Al MAS NMR spectrum. Al (IV), Al(V) and Al (VI) notations refers to tetrahedral (AlO_4), pentacoordinated (AlO_5) and octahedral (AlO_6) aluminium. The projection along the F1 axis is the isotropic spectrum. The insert shows magnification of the octahedral region. *Reprinted with permission from Ref. 114. Copyright (2003) American Chemical Society.*

γ-Al_2O_3.[114] This means that reversible aluminium species are not necessarily located into the zeolite framework, but that they can also be involved in an extraframework silica–alumina phase, the formation of which will depend on the severity of the zeolite treatment.[103,114] Nevertheless, the quadrupolar coupling constant (C_Q) value of reversible AlO_6 is larger in silica–alumina than in zeolites.[114] Then the resonance corresponding to AlO_{6c} sites of octahedral aluminium (Al(VI)c in Fig. 4.14A), and the presence of some non-reversible octahedral aluminium in sample H–USY (see Fig. 4.14B) is explained by the formation of extraframework silica–alumina (reversible AlO_6) containing alumina domains (non-reversible AlO_6).[114]

The application of the MQMAS technique to zeolite Beta steamed at 550 °C revealed two signals of $AlO_6$with very different CQ's constants; one of 1.6 MHz assigned to framework species and another of 5.5 MHz attributed to non-framework or less connected reversible octahedral Al, respectively.[103] These two species correspond to different steps in the process of hydrolysis of the Si–O–Al bonds during dealumination. ^{27}Al MQMAS spectra allowed to resolve AlO_4 in T1 and T2 from the other T3–T9 non-equivalent crystallographic sites,[102,103] and the quantitative analysis showed that atoms in positions T1 and T2 do not adopt an octahedral coordination and resist dealuminization.[103] This result support the idea that stability and catalytic behaviour of zeolites may depend on the synthesis procedure as far as it can determine the distribution of aluminium atoms in the framework.

The structure of the zeolitic reversible octahedral aluminium sites is not well established yet. This was first represented by a distorted framework aluminium linked to four lattice oxygen atoms, plus the oxygen of a hydronium and the oxygen of a water molecule.[107] In the dehydrated state, Al

Table 4.3 Properties of the ^{27}Al NMR signals of different species in zeolite H-Y

	δ_{iso} (ppm)	Av. C_Q (MHz)	H–USY (%)	H–USY–NH_3 (%)
AlO_{4a}	61.3	2.3	25	27
AlO_{4b}	63.7	6.6	31	56
AlO_5	35	3.2	5	–
AlO_{6a}	0	2	2	–
AlO_{6b}	2	2.6	20	17
AlO_{6c}	4.5	3.7	17	–

Data adapted with permission from Ref. 114. Copyright (2003) American Chemical Society.

becomes tetrahedral and the bridging hydroxyl group formed is able to protonate a strong base or to be exchanged by alkaline cations.[107] An alternative model for the formation of reversible framework AlO_6 involves partial hydrolysis of the Si–O–Al linkage to the network giving rise to connected Al–OH species, which are able to host water molecules to give octahedral coordination and a signal in the spectrum at 0 ppm.[103,110–114] The subsequent adsorption of basic molecules such as ammonia or pyridine or the exchange with alkaline cations converts this octahedral aluminium back to tetrahedral geometry. This model is supported by the appearance of a peak at 3.1 ppm in the ^{1}H spin-echo NMR spectrum, corresponding to protons connected to ^{27}Al, as indicated by the $^{1}H(^{27}Al)$ spin-echo double resonance experiment shown in Fig. 4.15.[112] The protons connected to aluminium can be seen in the difference spectrum displayed in Fig. 4.15C. This contains peaks at 4.6 and 3.7 ppm of Brønsted acid sites, at 2.4 ppm of EFAL species, and the signal at 3.1 ppm.[112]

According to experimental results, octahedral framework aluminium can only be created in the presence of water relaxing the distortion of some framework AlO_4 induced by the high electron affinity of protons in acid

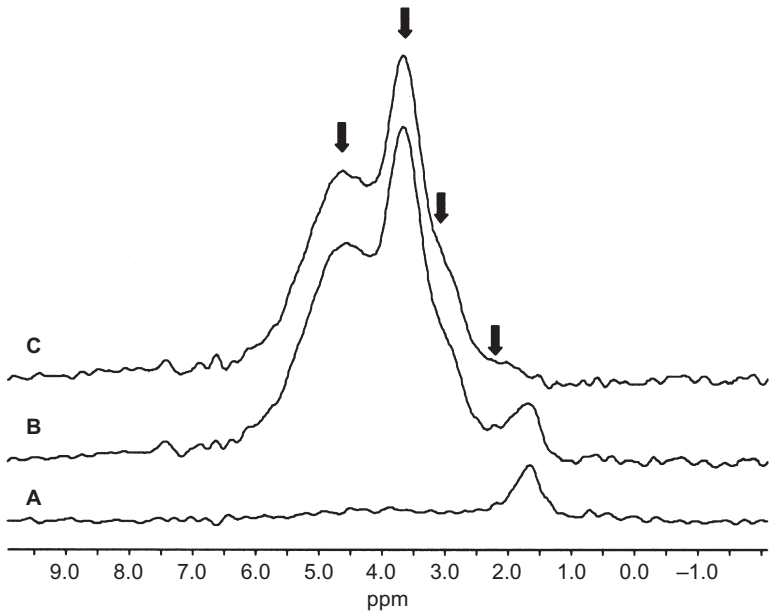

Figure 4.15 ^{1}H {^{27}Al} spin-echo double resonance MAS NMR of zeolite Y: (A) with ^{27}Al irradiation, (B) without ^{27}Al irradiation, and (C) the difference spectrum. *Reprinted with permission from Ref. 112. Copyright (1998) American Chemical Society.*

zeolites.[107] An alternative explanation is that the attraction of water molecules reduces the strong electric fields generated by the acid protons in the framework, which could be accompanied by partial hydrolysis of the Si–O–Al linkages.[103] Reversible AlO_6 is no longer detected once protons are re-exchanged by other cations (strong bases or alkaline cation).

Therefore, the ^{27}Al NMR signal of AlO_6 around 0 ppm, originated by framework but also by extraframework species in a relative concentration, which will depend on the extent of framework dealumination. Reversible framework species involving the hydrolysis of one Al–O–Si linkage are considered as intermediate in the formation of EFAL species. When increasing the severity of the treatment, the Si–O–Al linkages will be progressively hydrolyzed generating more distorted octahedral aluminium until losing chemical bonds with framework oxygen atoms.

3.3. Invisible aluminium

Resonances of ^{27}Al nucleus submitted to intense electric field gradients (EFG), give rise to severe quadrupolar broadening effects in the Al resonances observed in the NMR spectra. In drastic cases the resonances may be so broadened that they become undetectable by NMR, giving rise to the so-called "invisible aluminium", which is especially found in dehydrated acidic zeolites.[83–88] The fact that second-order quadrupolar broadening cannot be completely averaged-out by MAS has made difficult the observation of ^{27}Al NMR signals of dehydrated zeolites.

The effect of hydration degree on the ^{27}Al MAS NMR spectra of zeolites is illustrated in Fig. 4.16 left for dealuminated H-Beta (Si/Al = 9.1 submitted to hydrothermal treatment to a final Si/Al = 13.1 framework molar ratio determined by ^{29}Si MAS NMR).[83] Fig. 4.16 left shows much lower intensity of the signals in the spectrum of the dehydrated zeolite (Fig. 4.16a left) indicating the presence of "invisible" aluminium species. The magnified spectrum, drawn in Fig. 4.16a right, shows a very broad band superimposed to three peaks at 54 ppm of framework AlO_4, and at 30 and 0 ppm attributed to penta- and hexacoordinated EFAL species, respectively.[83]

Hydration of the zeolite provokes a sensitivity enhancement of the three narrower signals, especially that of framework AlO_4 at 54 ppm, at the expense of the broad hump (Fig. 4.16b–d).[83] Figure 4.17 shows the 3Q MAS NMR spectra of a dealuminated H–Y zeolite with increasing degree of hydration.[88] Besides the signals of framework AlO_4 (signal I) and of extraframework AlO_5 (signal III) and AlO_6 (signal IV) an additional signal of AlO_4 with larger C_Q,

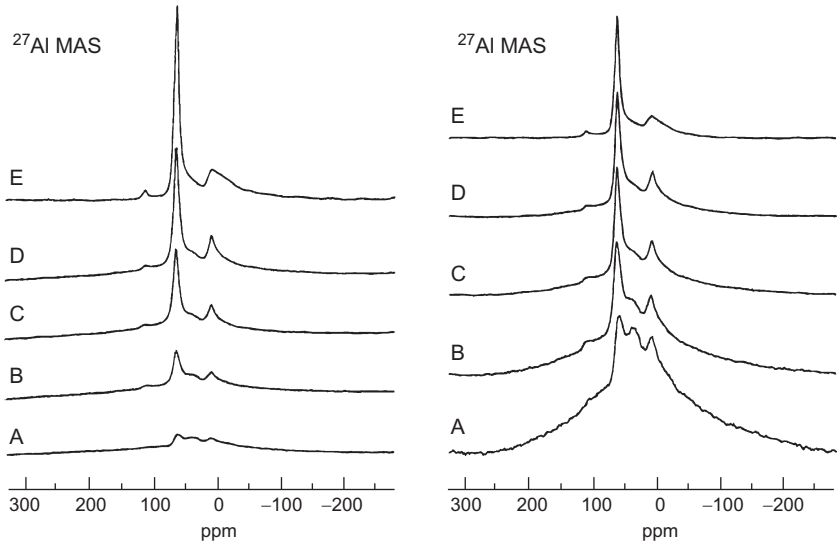

Figure 4.16 ^{27}Al MAS NMR spectra of zeolite H-Beta treated with saturated vapour at 540 °C increasing the degree of hydration from a to e, corresponding the spectrum e to fully hydrated zeolites. The spectra on the left were drawn the in a normalized intensity mode and those on the right in absolute mode. *Reprinted with permission from Ref. 83. Copyright (1998) American Chemical Society.*

probably due to EFAL species, is observed. In the experiments of Figs. 4.16 and 4.17, adsorption of water progressively decreases the C_Q value of the ^{27}Al nuclei making the signals more symmetrical.[88]

The observation of a broad resonance line associated with ^{27}Al nuclei showing large quadrupole coupling constant and the detection of total aluminium present in the sample requires the use of high fields (see Section 6.1). This is illustrated in Fig. 4.18, which compares the ^{27}Al MAS NMR spectra of steamed (hydrated) zeolite H-Y recorded at two different fields, 9.4 T (104.26 MHz) and at 18.8 T (208.43 MHz).[85] The spectrum recorded at lower field not only displays large contribution of broad resonances but also shows differences in intensity distribution and fails in detecting all aluminium present in the sample. Meanwhile, integrated intensity of the spectrum recorded at high field accounts for the total aluminium content and the signals are narrower and less affected by quadrupolar broadening effects.[85]

The large C_Q values of Al resonances observed in bare zeolites is explained by the strong EFG induced in the ^{27}Al nucleus by the proton of the bridging hydroxyl groups bonded to one of the oxygen atoms of the AlO_4 tetrahedra, leading to "invisible aluminium" signals.[23,84–86] It is

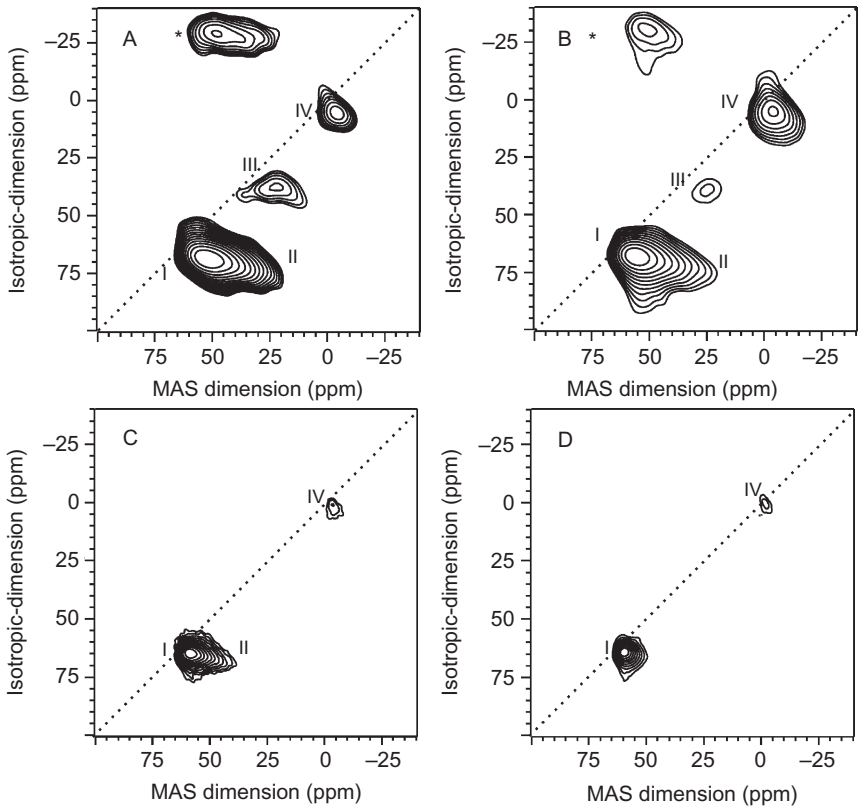

Figure 4.17 ^{27}Al 3Q MAS NMR spectra of zeolite H-Y with increasing degree of hydration from (A) to (D). *Reproduced from Ref. 88 with permission of the PCCP Owner Societies.*

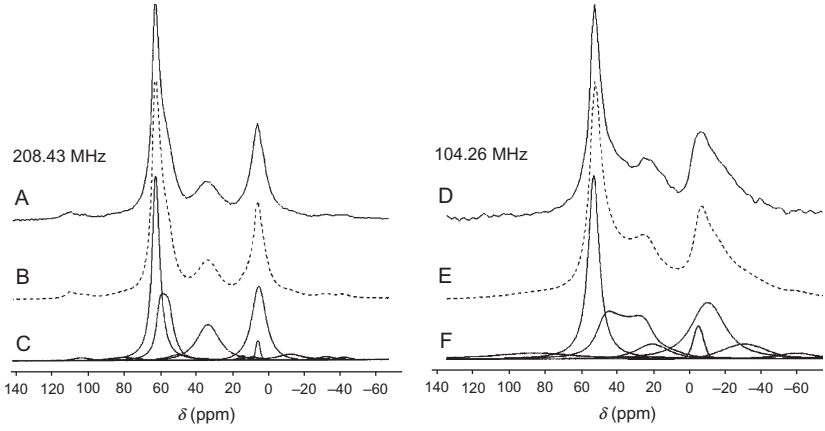

Figure 4.18 (A and D) ^{27}Al single pulse MAS NMR spectra of USY recorded at different external magnetic fields, (B and E) simulations, and (C and F) deconvolution. *Adapted from Ref. 85 with permission of The Royal Society of Chemistry.*

Table 4.4 Properties of the ^{27}Al NMR signals of different species observed in hydrated and non-hydrated zeolites[87,117]

	Hydrated		Non-hydrated		
Site	**δ_{iso} (ppm)**	**Av. C_Q (MHz)**		**δ_{iso} (ppm)**	**Av. C_Q (MHz)**
AlO_4	60–63	2–3	AlO_4H^+	70	16–18
AlO_4 distorted	60–63	6.5–7	AlO_4Na^+	60	5.5–8
AlO_5	30–35	3–4	AlO_4Al^{x+}	70	15
AlO_6	0–2	2	Al^{x+}	35	7.5
AlO_6	4.5	3.7			

assumed that hydration leads to the transfer of the proton of the Brønsted acid sites to the water molecules to form positively charged hydroxonium ions. Proton donation is accompanied by an increase in the symmetry around the Al atoms and, thus, by a decrease of the line widths.[23] It is worth mentioning that, according to theoretical calculations, one water molecule is not able to deprotonate the Brønsted acid site and that the formation of a hydroxonium requires the cooperative hydrogen bonding occurring in water clusters, and at least two water molecules in contact with the zeolite acid site.[115] The C_Q of ^{27}Al experiences a sharp decrease from 16 to 3.8 MHz upon adsorption of basic molecules, which are protonated on the acid site of the zeolite, while it only decreases to 9.4 MHz when the adsorbed molecules interacts with Brønsted acid sites by hydrogen bonds.[116] Table 4.4 summarizes typical isotropic δ_{iso} ^{27}Al and quadrupolar parameters of aluminium species in dehydrated and hydrated zeolites. This table also includes the parameters of the AlO_4 sites compensated by extraframework Al^{x+} or by Na^+ cations.[87]

3.4. Framework and extraframework aluminium species

As shown in the spectra of Figs. 4.16 and 4.17, thermal/hydrothermal treatment of zeolites usually releases aluminium atoms from the framework giving rise to EFAL species. This is usually accompanied by the appearance of Lewis acidity, which has also been associated with the occurrence of three-coordinated framework aluminium.[118,119] The formation of EFAL species plays an important role as it improves the zeolite thermal stability and catalytic performance. The latter effect has been explained by the creation of Lewis acid sites or by an increase

of the Brønsted acidity due to the influence of close EFAl species.[118,120–122] Moreover, various cationic AlO^+, $Al(OH)_2^+$, or $Al(OH)^{2+}$, and neutral entities such as AlOOH and $Al(OH)_3$ have been proposed as EFAl species.[123,124]

Recently, the application of 2D ^1H and ^{27}Al DQMAS NMR techniques in combination with theoretical calculations has proved the proximity of Brønsted/Lewis acid sites in dealuminated zeolites and has allowed to propose the reaction mechanism depicted in Fig. 4.19.[124–127] The use of 2-^{13}C-acetone as a NMR probe molecule[124,125,127] demonstrated an enhancement of the Brønsted acid strength, strongly supporting that its origin is the proximity of Lewis/Brønsted acid sites. The methodology used is illustrated in Figs. 4.20–4.25[124–127] for zeolite H-Y (framework Si/Al = 2.8 molar ratio in the parent zeolite and Si/Al = 3.5 after dealumination, determined by ^{29}Si NMR). This is based on the use of 2D DQMAS ^1H and ^{27}Al NMR experiments briefly described in Section 6.2.5.

The single pulse and spin-echo ^1H NMR spectra of zeolite Y, displayed in Fig. 4.20A and B, show two signals at 5.0 and 4.3 ppm assigned to SiOHAl Brønsted acid sites in the sodalite and supercage cavities respectively. Two more peaks are observed at 2.8 and 1.0 ppm, assigned to AlOH hydroxyl groups of EFAL associated with Lewis acid sites. This assignment is supported by the increase of the relative intensity of the peaks at 2.8 and 1.0 ppm in the ^1H

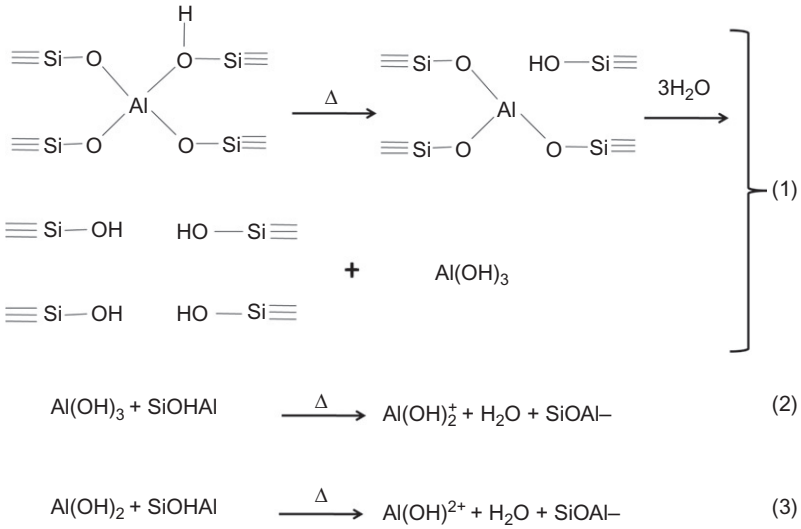

Figure 4.19 Dealumination mechanism proposed for zeolite H-Y. *According to Ref. 126 with permission. Copyright 2010 Wiley-VCH.*

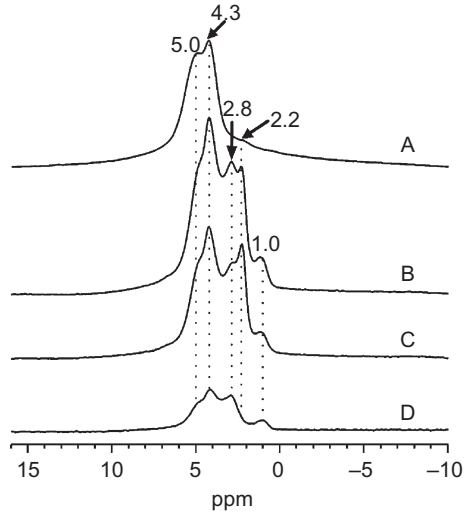

Figure 4.20 ^{1}H MAS spectra of (A) zeolite H-Y, single pulse; and 1H spin-echo MAS spectra of dealuminated zeolite HY (B-D) (B) without ^{27}Al irradiation, (C) with ^{27}Al irradiation, and (D) difference spectra of parts B and C. *Reprinted with permission from Ref. 124. Copyright (2007) American Chemical Society.*

spectrum recorded with ^{27}Al irradiation (see Fig. 4.20 B-D and Section 6.2.3). 2D ^{1}H DQ NMR (Fig. 4.21), is used here as an indirect method to investigate the proximity of Brønsted and Lewis acid sites through the ^{1}H–^{1}H dipolar interactions between the SiOHAl and AlOH species, producing DQ coherences for distances below 5 Å.[124] The ^{1}H DQ NMR spectrum of Fig. 4.21 reveals the proximity among the various Brønsted and Lewis acid sites in dealuminated zeolite H-Y. It must be noted the absence of an autocorrelation peak of the resonance at 1.0 ppm, suggesting its assignment to species containing only one proton $(Al(OH)^{2+}$ or AlOOH). Combination of experimental results with theoretical DFT calculations led to the conclusion that the preferred EFAL Lewis acid sites formed in the supercage are $Al(OH)_3$ and $Al(OH)^{2+}$ and the ones present in the sodalite cage correspond to $Al(OH)^{2+}$ species.[124]

Figure 4.22 shows the 3QMAS NMR spectra of zeolite H-Y parent and after calcination at 500, 600, and 700 °C.[126] Only framework aluminium AlO_4 species are present in the zeolite HY. Meanwhile, the spectra of the zeolite calcined at increasing temperature show the progressive formation of EFAL species: octahedral AlO_6 attributed to $Al(OH)_3{\cdot}3H_2O)$ (0 ppm), pentacoordinated AlO_5 due to $(O_F)_2{---}Al(OH)_2^{+}{\cdot}H_2O$ (30 ppm) and tetrahedral AlO_{4b} to $(O_F)_2---Al(OH)^{2+}\dot{H}_2O$ (56 ppm), where O_F represents framework oxygen atoms in close proximity to the Brønsted acid site.

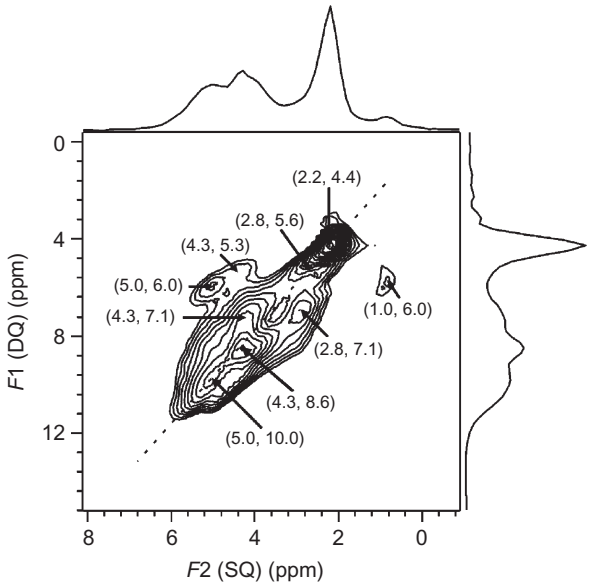

Figure 4.21 ^{1}H DQ MAS NMR spectra of dealuminated H-Y. *Reprinted with permission from Ref. 124. Copyright (2007) American Chemical Society.*

These assignments have been made on the basis of DFT calculations, which furthermore suggest changes in the number of coordination of the EFAL species upon water removal. Thus, in the absence of water, the $AlOH^{2+}$ species move to the centre of the 4R coordinating the four framework oxygen and thus changing to fivefold, while $Al(OH)_2^{+}$ and $Al(OH)_3$ would become four coordinated by bonding to two and one framework oxygen, repectively.

Figure 4.23 shows the 2D DQMAS ^{27}Al NMR spectra of hydrated zeolite H-Y calcined at increasing temperature (in the hydrated state).[126] Analysis of the spectra shows that the three types of aluminium species, framework AlO_4 (around 60 ppm), and EFAL penta- (around 30 ppm) and hexa- (around 0 ppm) coordinated are in close proximities (below 6 Å), being more intense the correlation between the four coordinated framework SiOHAl and the pentacoordinate $Al(OH)_2^{+}$ aluminium species. The analysis of the spectrum of the zeolite calcined at 700 °C shows an additional signal of tetrahedral $AlOH^{2+}$, which correlates with framework (SiOHAl). Interestingly, there is no special correlation between the fourfold ($AlOH^{2+}$) and the sixfold $Al(OH)_3$ EFAL species.

2-^{13}C-acetone was used as a probe molecule to check if Brønsted acidity is enhanced by the close proximity of the EFAL sites. The bridging hydroxyl group of the zeolite form hydrogen bonds with the oxygen atom of the

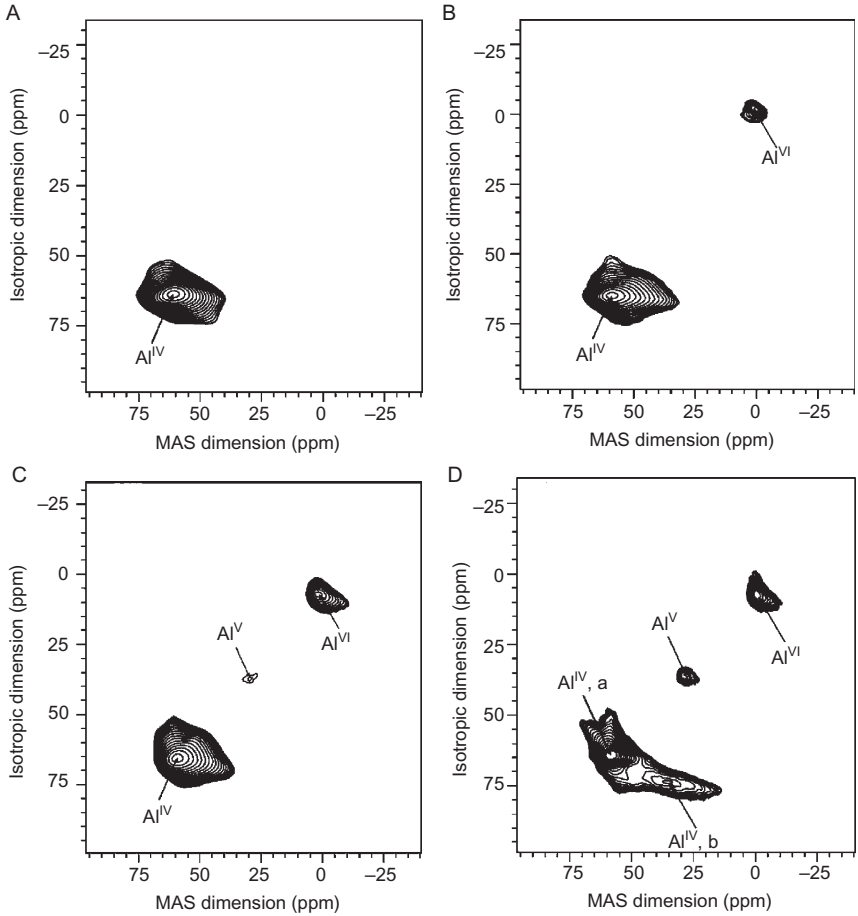

Figure 4.22 ^{27}Al 3QMAS NMR of zeolite H-Y, (A) parent, and calcined at (B) 500 °C, (C) 600 °C, and (D) 700 °C. Spectra recorded on hydrated samples. *Reprinted from Ref. 126 with permission. Copyright 2010 Wiley-VCH.*

carbonyl group of 2-^{13}C-acetone and shifts the δ^{13}C (^{13}CO) to low field in an amount, which depends on the acid strength. This is illustrated in Fig. 4.24 for the adsorption on dealuminated H–ZSM-5 zeolite, also possessing close Lewis/Brønsted acid sites similar to those depicted above for dealuminated zeolite H-Y.[124,126] The spectra recorded after adsorption on the parent (H–ZSM-5) and dealuminated zeolites (H–ZSM-5-600) show a peak at 220 ppm due to 2-^{13}C-acetone adsorbed on a Brønsted acid site. However, the dealuminated H–ZSM-5-600 zeolite shows a signal at 233 ppm attributed to an ^{13}C-acetone molecule interacting with a Brønsted acid sites in close proximity to EFAL, and the peak at 240 ppm to the direct

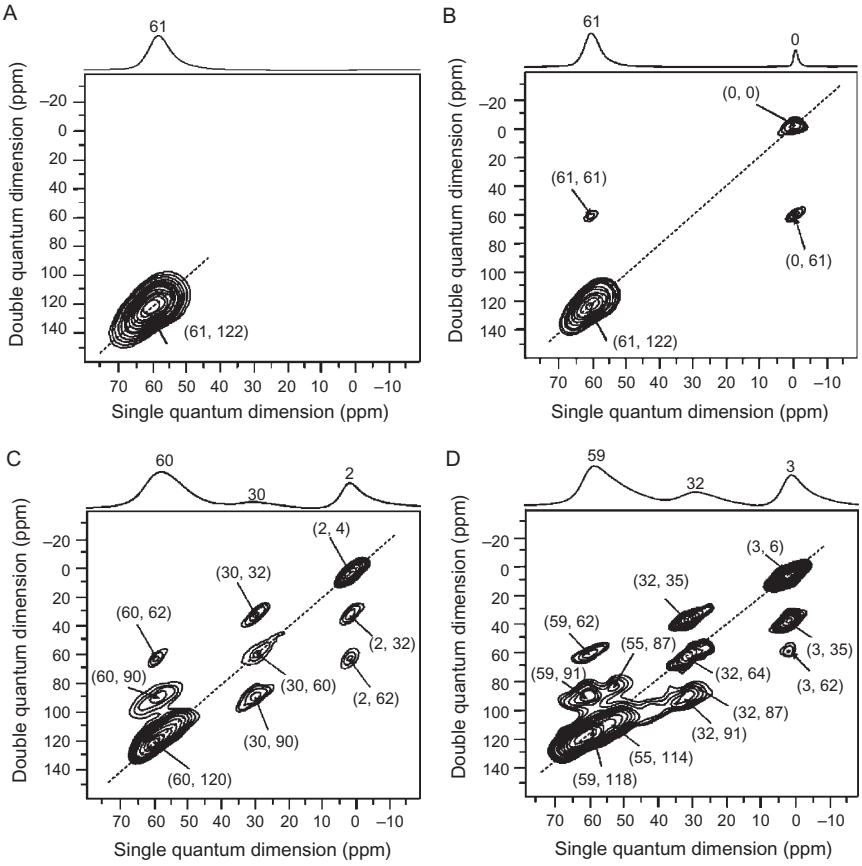

Figure 4.23 ^{27}Al MAS and DQMAS NMR spectra of zeolite H-Y (A) parent and calcined at (B) 500 °C, (C) 600 °C, and (D) 700 °C. 1D spectra are plotted on top of the 2D spectra. *Reprinted from Ref. 126 with permission. Copyright 2010 Wiley-VCH.*

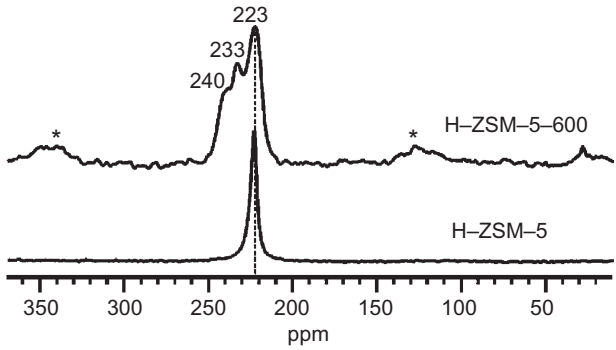

Figure 4.24 ^{13}C CPMAS NMR spectra of 2-^{13}C-acetone adsorbed on parent H-ZSM-5 and dealuminated H-ZSM-5-600 zeolites. *Adapted with permission from Ref. 127. Copyright (2011) American Chemical Society.*

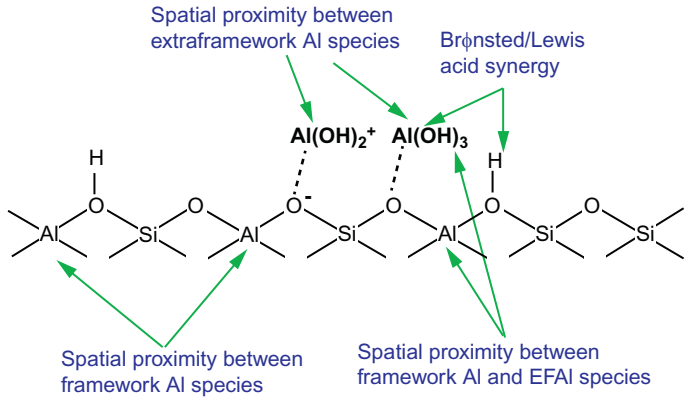

Figure 4.25 Scheme of Brønsted/Lewis acid synergy and experimentally observed spatial proximities of various species for dealuminated Zeolite H-MOR. *Adapted with permission from Ref. 127. Copyright (2011) American Chemical Society.*

adsorption of the EFAL site, as supported by DFT calculations.[124] The most relevant conclusion is that the coordination of the Lewis acid site to the oxygen atom nearest to the Brønsted acid site is able to enhance the acidity, although there is no direct interaction between them (see Fig. 4.19).[117,124–127]

The relative situation of the different species is summarized in Fig. 4.25 and the dealumination mechanism proposed is depicted in Fig. 4.19.[126,127] The first step would involve the formation of framework tricoordinated aluminium (Lewis acid site), which coordinates to three water molecules becoming octahedral and reverts to tetrahedral upon dehydration.

4. ^{11}B NMR OF BORON CONTAINING ZEOLITES: TRIGONAL BORON

Silicon atoms in zeolites can be isomorphycally substituted by boron generating the family of borosilicate materials possessing weaker acidity than the aluminosilicates, with potential applications as catalysts in less acidity demanding reactions. Boron is easily removed from the zeolites framework and substituted by aluminium by postsynthesis treatments offering the possibility of preparing of isostructural aluminosilicate that cannot be obtained by direct synthesis. Framework boron can be in tetrahedral or trigonal coordination depending on the charge compensating cation, changing its anchoring to framework with the sample environment. Cooordination of boron in borosilicate zeolites has been investigated by solid state NMR, taking advantages of the high natural abundance of the ^{11}B ($I=3/2$) nucleus and its sensitivity to discriminate three- and four-coordinated boron environments.

^{11}B MAS NMR spectra of as-synthesized B-zeolites, in where the negative charge is compensated by the organic SDA or alkaline cations, consists of a symmetric signal at −3 or −4 ppm of tetrahedral boron. In its acidic form, the negative charge induced by boron is compensated by protons and the ^{11}B NMR spectrum depends on the degree of hydration of the zeolite. The spectra of calcined zeolites shows a symmetric peak corresponding to a tetrahedral boron resonance at −4 ppm. Additional signals showing a typical quadrupolar powder pattern are listed in Table 4.5 together with their corresponding quadrupolar parameters.

Table 4.5 ^{11}B chemical shift and quadrupolar parameters of the boron species anchored in zeolites[129,131]

B site	δ_{iso} (ppm)	C_Q (MHz)	η
B(OSi)4, B[4]	−1 to −4	0.8	0
$B(OSi)_3$, B[3]-III	10–12	2.4–2.6	0.1–0.2
$B(OSi)_2OH$, B[3]-IIa $BOSi(OH)_2$, B[3]-IIb	14–16	2.4–2.6	0.1
$B(OH)_3$, B[3]-I	18.5-–19.5	1.8–2.2	0.1

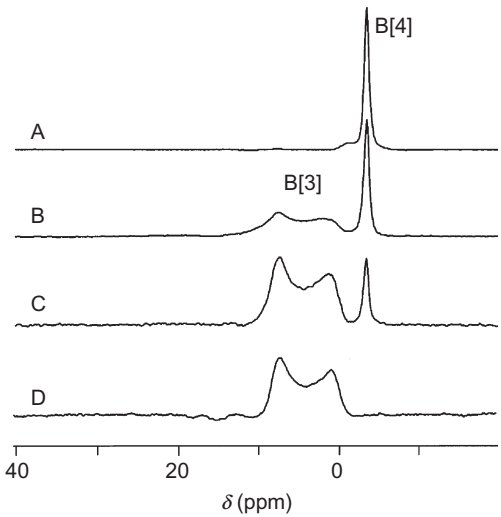

Figure 4.26 ^{11}B MAS NMR spectra of $[Na_x^+, H_{1-x}^+]$[B,Si-BEA], where x denotes the fraction of sodium ions in the ion-exchange solution (A) $x=1$, (B) $x=0.75$, (C) $x=0.25$, and (D) $x=0$. *Reproduced from Ref. 128 with permission of the PCCP Owner Societies.*

Figure 4.26 shows the ^{11}B MAS NMR spectra of zeolite B-Beta with different degrees of Na^+ exchange $[Na_x{}^+H_{1-x}{}^+]\,[B,Si-Beta]$.[128] The ^{11}B spectrum of the acidic $[H^+][B,Si\text{-}Beta]$ zeolite (Fig. 4.26D) shows a signal exhibiting quadrupolar shape with $\delta_{iso} = 9.5$ ppm, attributed to trigonal boron anchored to the zeolite framework through three –OSi bonds. The spectrum of the totally exchanged $[Na^+][B,Si\text{-}Beta]$ zeolite, consists of the peak at -4 ppm, assigned to tetrahedrally coordinated boron (see Fig. 4.26A). Similar spectrum showing only tetrahedral boron is obtained for $[Li^+][B,Si\text{-}Beta]$ and for $[NH_4{}^+]\,[B,Si-Beta]$ formed upon adsorption of NH_3 on dehydrated $[H^+][B,Si\text{-}Beta]$. These assignments were done by carrying out $^{11}B\{^{23}Na$, and $^{11}B\{^1H\}$ REDOR experiments in partially exchanged $[Na_x{}^+H_{1-x}{}^+]\,[B,Si-Beta]$ (see Section 6.2).

^{11}B MAS NMR spectra of H-B-zeolites change reversibly with the degree of hydration of the zeolite.[129–131] ^{11}B MQMAS spectra allowed the identification and characterization of the contributing signals collected in Table 4.5.[131] The ^{11}B MAS NMR spectrum of B-Beta dehydrated at 923 K gives a signal of trigonal boron anchored to the zeolite through three –OSi bonds, B[3]-III. After storing the sample in a closed vial for long periods, the ^{11}B spectra recorded showed trigonal boron species with different degree of anchoring to the zeolite framework (see Table 4.5) by progressive hydrolysis of the Si–O–B bonds and the formation of SiOH and BOH. Upon exposure to ambient, $B(OH)_3$, as well as tetrahedral B[4] generated by interaction of the trigonal species with water clusters $H^+(H_2O)_n$, are formed. Depending on the hydration conditions, total hydrolysis to $B(OH)_3$ can be achieved generating large amounts of silanol nests (detected by ^{29}Si NMR); however, this process is completely reversibly if zeolite is not exhaustively washed out, as described in Fig. 4.27. ^{11}B MAS NMR spectrum recorded after boron extraction from zeolite $[Na_x{}^+H_{1\text{-}x}{}^+][B,Si\text{-}Beta]$ by washing with water showed only tetrahedral B[4] associated with Na^+, indicating that this cation stabilizes framework boron.[129,131]

In order to interpret the ^1H NMR spectra of B-zeolites, ^1H to ^{11}B CP MAS and $^1H\,\{^{11}B\}$ REDOR experiments were carried out on samples with different degree of hydration.[128–130] The ^1H–^{11}B heteronuclear correlation spectra showed a cross peak between the signals of B[3] and ^1H at 2–3 ppm, of Si–OH groups adjacent to boron. Meanwhile, a ^1H signal at 1.7–2.0 ppm did not correlate with boron being assigned to Si–OH defect groups.[130]

^{11}B MAS NMR was used to monitor the changes of coordination of boron upon adsorption of a series of probe molecules in B-zeolites.[132]

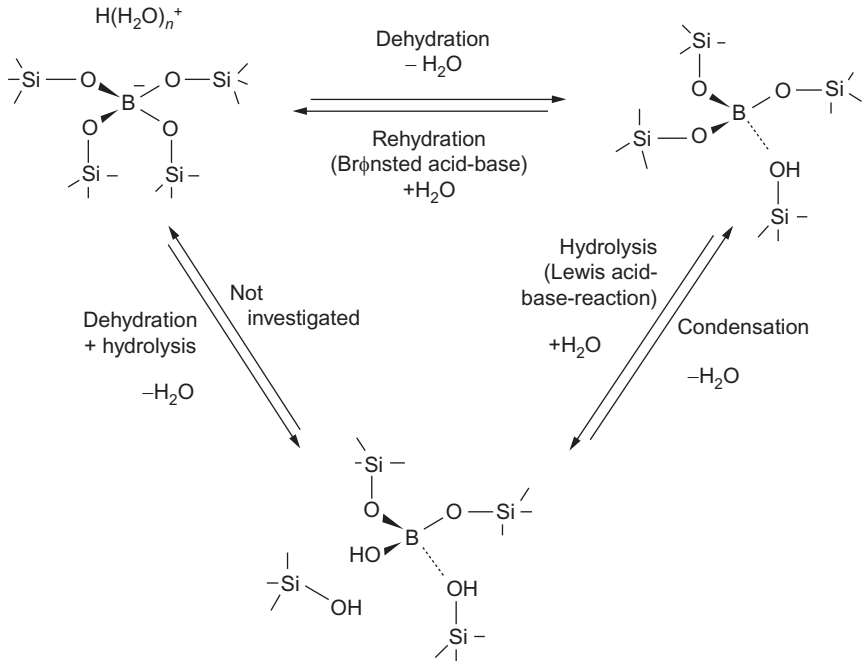

Figure 4.27 Proposed model for reversible conversion of B[4] and of the different B[3] species in boron containing zeolites. *Reprinted from Ref. 129, Copyright (2005) with permission of Elsevier.*

Probe molecules with a sufficiently high proton affinity are protonated upon adsorption on the Brønsted acid site, forming cationic species and provoking a change in the coordination of ^{11}B to tetrahedral, according to Fig. 4.28 path b. However, if the proton affinity of the molecule is not high enough, it will interact with the hydrogen of the adjacent Si–OH group remaining the boron in trigonal coordination (see Fig. 4.28 path a). Table 4.6 lists the probe molecules tested and its proton affinity, and the properties of the ^{11}B NMR signals. Observation of Table 4.6 indicates that only molecules with proton affinity PA $\geq$ 854 kJ mol^{-1} are able to be protonated by extracting the proton of the SiOH···B(OSi)$_3$ group, giving rise to a cation compensating tetrahedral boron. In this line, ^{11}B NMR was used to elucidate the nature of the active site for the Beckmann rearrangement reaction of oximes to amides using H–B-zeolites.[133] ^{1}H/^{15}N CP MAS NMR spectra indicated that the oximes is protonated and that this is accompanied by a change in the ^{11}B coordination from trigonal to tetrahedral. A good agreement was observed between theoretical and experimental ^{11}B chemical shifts.

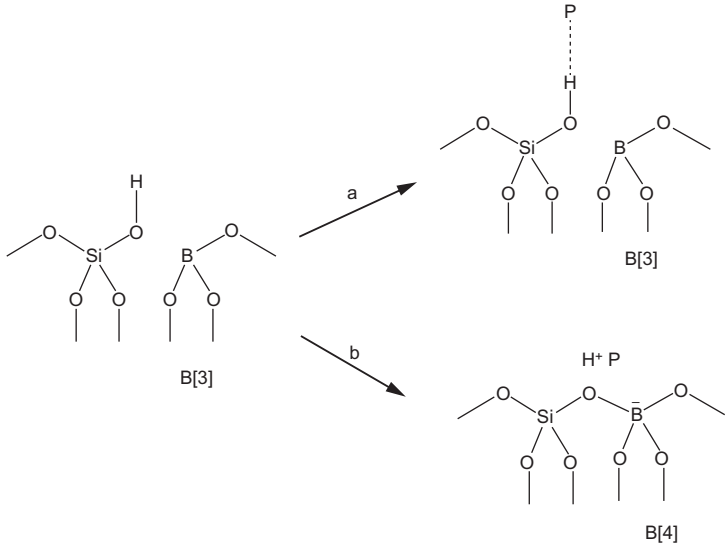

Figure 4.28 Local structure of boron atoms upon adsorption of probe molecules with proton affinities of (a) PA < 849 kJ mol^{-1} and (b) PA > 849 kJ mol^{-1}. *Reprinted from Ref. 132, Copyright (2007) with permission of Elsevier.*

Table 4.6 Proton affinities of probe molecules and nuclear properties of ^{11}B NMR signals[132]

		B[3]		B[4]	
Probe molecule	**Proton affinity (kJ mol^{-1})**	**C_Q (MHz)**	**η**	**C_Q (MHz)**	**η**
Pyridine	930	2.65	0.10	0.85	0.00
Dimethyl sulfoxide	884	2.75	0.10	0.85	0.00
Acetamide	864	2.65	0.10	0.85	0.00
Ammonia	854	2.70	0.10	0.85	0.00
Tetrahydrothiophene	849	2.07	0.10	–	–
Acetone	812	2.65	0.10	–	–
Nitrogen	494	2.65	0.10	–	–

Reprinted from Ref. 132, Copyright (2007) with permission of Elsevier.

5. ^{1}H NMR SPECTROSCOPY: ZEOLITE BRØNSTED ACID SITES AND THE USE OF PROBE MOLECULES

^{1}H MAS NMR spectroscopy has been applied to the investigation of the Brønsted acidity and the characterization of structure defect sites in zeolites. Zeolites, specially the more hydrophilic aluminosilicate and the

pores usually contain water molecules are readily hydrated at room temperature, under ambient conditions. Rapid exchange between the different proton species of the sample produces a peak at an average chemical shift position, precluding the identification of the proton species of the zeolite. The characterization of hydroxyl groups requires dehydration of the zeolite sample and filling the rotor under a controlled atmosphere to avoid the contact with air. Table 4.7 summarizes typical proton chemical shifts of different groups commonly encountered in zeolites.[134]

As shown in Table 4.7, δ^1H of Brønsted acid in zeolites is within the range 3.6–5.2 ppm. In principle, δ^1H should reflect the acid strength of Si–OH–Al bridging hydroxyl group, shifting to low field as the polarization of the O–H bond, and thus the acid strength, increases. However, δ^1H can be strongly affected by hydrogen bonds to framework oxygen atoms, thus giving rise to ^{1}H resonances displaced at low fields. For instance, the ^{1}H NMR spectra of dehydrated zeolite H,Na–Y give two signals of bridging hydroxyl groups, one at δ^1H = 3.6–4.0 ppm (protons located in the large supercage volume), and a second one at δ^1H = 4.8–5.2 ppm (Si–OH–Al in small sodalite cages). The larger chemical shift of this second species is due to the interaction through hydrogen bonding with framework oxygen sites in its proximity. Indeed, even weak acidic SiOH groups can appear at δ^1H higher than Brønsted sites because of hydrogen bonding. This behaviour was reported for as-synthesized zeolites presenting ^{1}H signal at δ^1H = 10.2 ppm from silanol groups.[135]

Table 4.7 ^{1}H NMR chemical shifts typical for hydroxyl groups in zeolites[134]

δ^1H (ppm)	Group	Assignment
−0.5–0.5	Metal-OH	Non-hydrogen bonding metal OH groups
1.3–2.2	Si–OH	Silanol groups at the external surface or at framework defects in zeolites
2.4–3.6	Metal OH, AlOH	Metal OH groups involved in hydrogen bonding such as AlOH extraframework aluminium species in zeolites
2.8–6.2	Cation OH CaOH LaOH	Small cages or channels with hydrogen bonding
3.6–4.3	SiOHAl	Large cavities
4.6–5.2	SiOHAl	Confined environments
5.2–8.0	SiOHAl	Hydrogen bonding
10–16	Si–OH	Silanols involved in strong hydrogen bonding

An alternative method to get information on the acid properties of zeolites is the use of basic molecules as NMR probes. Some examples on the use of different probe molecules to characterize zeolite acidity have been given in Sections 3 and 4 of this review. A list of the most used probe molecules in zeolites is described elsewhere.[134]

The coexistence of different hydroxyl groups in zeolites, the usually very typical broadening of the peaks, and the narrow chemical shift range of ^{1}H give rise to overlapping signals, which therefore complicate the interpretation of the spectra. However, a number of techniques based on homonuclear (2D DQ ^{1}H NMR) and heteronuclear dipolar interactions (CP MAS, REDOR, TRAPDOR, etc.) have been applied to investigate zeolites. The application of relevant techniques using protons for the structural investigation of acidic zeolites have been mentioned in the previous paragraphs and the theoretical bases will be depicted in Section 6.

6. ADVANCE METHODS: THEORETICAL AND PRACTICAL ASPECTS

Porous materials and in particular zeolites have been widely studied by an array of NMR techniques and a variety of magnetically active nuclei. Apart from the most exploited ^{1}H, ^{13}C, ^{27}Al, and ^{29}Si nuclei, other spin 1/2 nuclei such as ^{31}P, ^{15}N, ^{133}Cs, ^{129}Xe, ^{19}F, ^{109}Ag, ^{113}Cd, and ^{207}Pb have been monitored as well as the quadrupolar nuclei ^{2}H, ^{6}Li, ^{7}Li, ^{23}Na, ^{11}B, ^{95}Mo, ^{17}O, ^{69}Ga, ^{71}Ga, and ^{139}La. Some techniques are able to characterize the structure of the acid sites, monitor host–guest and cation–sorbate interactions, local dynamics of adsorbed molecules, pore dimensions and geometries, and the local environment of framework or extraframework species; some are suitable for probing internuclear distances, such as the distance between a nucleus on a Brønsted acid site and a nucleus in a probe molecule or measuring proximities between Brønsted and Lewis acid sites in zeolites.

Most of the zeolites contain quadrupolar nuclei and obtaining useful structural insights from their spectra is of much interest. Therefore, various examples of high-resolution NMR techniques, which are the most relevant to the study of zeolites are listed in Table 4.8 and outlined in the next sections giving emphasis to NMR applications involving quadrupolar nuclei. This section is not intended to address all types of NMR methods used to characterize zeolites but rather as a highlight of the most sophisticated and popular NMR methods in the field.

Table 4.8 Advanced NMR techniques and their potential application for the study of zeolites and zeotypes[136]

Technique	Nucleus	References
High-resolution methods for spin >½		
2D 3QMAS	^{27}Al	85–87,100,117, 137–147
	^{23}Na	36,148,149
	^{11}B	130
	^{17}O	150–153
2D 5QMAS	^{17}O	150,151
	^{27}Al	154,155
DOR	^{17}O	150,151,156
	^{23}Na	157–159
	^{27}Al	160
Methods based on CP		
2D CP-HETCOR	^{1}H–^{29}Si	161,162
	^{27}Al–^{29}Si	162,163
	^{1}H–^{27}Al	161
	^{1}H–^{11}B	130
	^{27}Al–^{31}P	164
	^{11}H–^{17}O	165
2D RAPT-CP-HETCOR-CPMG	^{27}Al–^{29}Si	163
CPMAS of uncommon spin pairs	^{19}F–^{29}Si	71,72,82
	^{27}Al–^{19}F	166
J-mediated methods		
2D INADEQUATE	^{29}Si–^{29}Si	34,167
2D COSY		
2D HMQC/INEPT	^{1}H–^{27}Al/^{23}Na–^{31}P/^{27}Al–^{31}P	168
	^{1}H–^{13}C	169

Table 4.8 Advanced NMR techniques and their potential application for the study of zeolites and zeotypes[136]—cont'd

Technique	Nucleus	References
Recoupling methods		
REDOR/CP-REDOR	^{23}Na–^{1}H	170,171
	^{29}Si–^{31}P	172
	^{7}Li–^{1}H	171
	^{11}B–^{23}Na/^{11}B–^{1}H	128
	^{17}O–^{1}H	165
	^{27}Al–^{29}Si	173
	^{1}H–^{19}F–^{29}Si	82
	^{13}C–^{11}B	174
	^{2}H–^{29}Si	175
TRAPDOR	^{27}Al–^{31}P	172
	^{15}N–^{27}Al/^{15}N–^{23}Na	176
	^{1}H–^{27}Al	177–180
	^{31}P–^{27}Al	178
	^{17}O–^{23}Na	153
REAPDOR	^{15}N–^{27}Al/^{15}N–^{23}Na	181
DQMAS	^{27}Al–^{27}Al	126,182
	^{29}Si–^{29}Si	49
	^{1}H–^{1}H	117
CSA recoupling	^{29}Si–^{29}Si	51
Methods to probe molecular dynamics and pore structure		
EXSY	^{129}Xe	183
	^{2}H	176
Wideline	^{2}H	170,171,184
Hyperpolarized	^{129}Xe	183,185,186
In situ	Various	30,32,185–195

In Sections 6.1.1–6.1.4, the theoretical basis of manipulating quadrupolar spins are reviewed in a nutshell providing only the key expressions necessary to understand the quadrupolar broadening nature. The most popular line-narrowing strategies to remove the second-order quadrupolar anisotropy are also addressed. Understanding some phenomena requires some knowledge on the underlying theory of manipulating spin $> 1/2$ nuclei, so that the spectroscopist is aware of the advantages and disadvantages of using a given method and capable of selecting the ideal technique for resonance assignment or to obtain reliable quantitative information. Section 6.2 deals with double- and triple-resonance dipolar recouping NMR experiments. These family of methods are also covered, as they are important to measure nuclear proximities between framework and extraframework species described in Section 3 and to access the Brønsted and Lewis acidity measuring interactions between framework acid sites and probe molecule atoms. Finally, Section 6.2.4 covers a set of other outstanding NMR techniques used in zeolites that were reported in recent years but not yet, or at least poorly, addressed in other reports.

Along the discussion of the NMR techniques an effort is made to also address relevant practical aspects such as typical experimental values employed in a given NMR technique and the relevant practical aspects, pitfalls, and solutions to consider when using a particular experiment comparing with other variants when applicable.

6.1. Quadrupolar interaction

6.1.1 The quadrupolar interaction

Unlike in liquids, structural information obtained from NMR spectra of solids is obscured by anisotropic line broadening from a number of interactions. Quadrupolar nuclei (spin $> 1/2$) account for ca. 75% of the Periodic Table and may experience large anisotropic interactions with local EFG, which are not completely averaged-out by MAS. To obtain high-resolution spectra of quadrupolar nuclei with half-integer spins, the central transition (CT) ($1/2 \leftrightarrow -1/2$), unaffected by the very large first-order ($\hat{H}_{\mathrm{Q}}^{(1)}$) quadrupolar interaction, is usually observed. This transition is affected only by second-order ($\hat{H}_{\mathrm{Q}}^{(2)}$) quadrupole interactions resulting, for polycrystalline solids, in a characteristic asymmetric line-broadening (or powder pattern) induced by the quadrupolar coupling constant (C_{Q}) and the asymmetry parameter, η. In addition, the second-order quadrupolar interaction also scales the centre of gravity of the experimental line, $\delta_{\mathrm{CG}}^{\mathrm{exp}}$, thus precluding the direct determination of the isotropic chemical shift (δ_{CS}). The C_{Q} value is given in frequency units,

$e^2qQ/\hbar$, and measures the strength of the quadrupolar interaction experienced by a particular nucleus and is characteristic of the molecular environment; eQ denotes the quadrupolar moment; eq is the magnitude of the EFG and e is the elementary charge. η describes the deviation of the EFG tensor, $\boldsymbol{V}$, from axial symmetry. Therefore, measuring the true chemical shift (δ_{CS}) of the CT will depend on these parameters as shown by Eq. (4.1)[196]:

$$\delta_{CS,(-1/2,1/2)} = \delta^{exp}_{CG,(-1/2,1/2)} + \frac{1}{30}\left(1+\frac{1}{3}\eta^2\right)\left[I(I+1)-\frac{3}{4}\right]\left[\frac{3C_Q}{2I(2I-1)\omega_0}\right]^2 \quad [4.1]$$

The value of δ^{exp}_{CG}, C_Q, and η can be derived using various methods including spectral simulations of the powder pattern. The former can also be directly determined from experimental evidence using DAS (dynamic angle spinning) or DOR (double rotation) techniques.[197–199]

The interaction of a quadrupolar nucleus under the influence of a magnetic field, $\boldsymbol{B}_0$, oriented along the z-axis may be described by the sum of the Zeeman and quadrupolar Hamiltonian operators, excluding additional interactions:

$$\hat{H}_{total} = \hat{H}_Q + \hat{H}_Z \quad [4.2]$$

In the laboratory (LAB) frame, $\hat{H}_Z$ is described as

$$\hat{H}_Z = -\omega_0\hat{I}_Z \quad [4.3]$$

The spherical tensor representation of $\hat{H}_Q$ in its principal axis system (PAS) may be written as

$$\hat{H}_Q = \frac{eQ}{4I(2I-1)\hbar}\sum_{q=-2}^{2}(-1)^q V_q^{(2)} T_{-q}^{(2)} \quad [4.4]$$

where $V_q^{(2)}$ and $T_{-q}^{(2)}$ are the second-rank irreducible spherical tensors for the space and spin parts of the quadrupolar interaction (with $q=-2,-1,0,1,2$). The expressions for the five spin tensor elements $T_{-q}^{(2)}$ take the form

$$\begin{aligned} T_0^{(2)} &= \frac{\sqrt{6}}{3}\left[3\hat{I}_Z^2 - I(I+1)\right] \\ T_{\pm1}^{(2)} &= \mp\hat{I}_Z\hat{I}_\pm \mp \hat{I}_\pm\hat{I}_Z \\ T_{\pm2}^{(2)} &= \hat{I}_\pm\hat{I}_\pm \end{aligned} \quad [4.5]$$

The five $V_q^{(2)}$ components defined in the PAS ($V_q^{(2)} = V_q^{(2),\mathrm{PAS}}$) of the EFG tensor and their relation with the three Cartesian tensor components (V_{XX}, V_{YY}, and V_{ZZ}) are given elsewhere.[196,200]

By substituting the $V_q^{(2)}$ and the $T_{-q}^{(2)}$ values given in Eq. (4.4), $\hat{H}_\mathrm{Q}$ becomes

$$\begin{aligned}\hat{H}_\mathrm{Q} = &\frac{eQ}{4I(2I-1)\hbar}\frac{\sqrt{6}}{3}\left[3\hat{I}_\mathrm{Z}^2 - I(I+1)\right]V_0^{(2)} + \left(\hat{I}_E\hat{I}_+ + \hat{I}_+\hat{I}_\mathrm{Z}\right)V_{-1}^{(2)} \\ &-\left(\hat{I}_\mathrm{Z}\hat{I}_- + \hat{I}_-\hat{I}_\mathrm{Z}\right)V_1^{(2)} + \hat{I}_+^2 V_{-2}^{(2)} + \hat{I}_-^2 V_2^{(2)}\end{aligned} \quad [4.6]$$

$\hat{H}_\mathrm{Q}$ can usually be treated as a perturbation of the Zeeman interaction by means of average Hamiltonian theory.[201,202] Therefore, it is very convenient to transform the quadrupolar interaction to the Zeeman interaction frame or LAB frame by applying to $\hat{H}_\mathrm{Q}$ a rotation at the Larmor angular frequency and generate the time-dependent $\hat{H}_\mathrm{Q}(t)$

$$\hat{H}_\mathrm{Q}(t) = \mathbf{e}^{\left(\mathbf{i}\omega_0\hat{I}_\mathrm{Z}t\right)}\hat{H}_\mathrm{Q}\mathbf{e}^{\left(-i\omega_0\hat{I}_\mathrm{Z}t\right)} \quad [4.7]$$

$\hat{H}_\mathrm{Q}(t)$ may be averaged over one Larmor period ($2\pi/\omega_0$) and generate high-order terms by means of the Magnus expansion to obtain the time-independent first- and second-order terms of the quadrupolar interaction in Eq. (4.8).[196]

$$\hat{\bar{H}}_\mathrm{Q}(t) = \hat{H}_\mathrm{Q}^{[1]} + \hat{H}_\mathrm{Q}^{[2]} \quad [4.8]$$

with

$$\hat{H}_\mathrm{Q}^{[1]} = \frac{eQ}{4I(2I-1)\hbar}\frac{\sqrt{6}}{3}\left[3\hat{I}_\mathrm{Z}^2 - I(I+1)\right]V_0^{(2)} \quad [4.9]$$

and

$$\begin{aligned}\hat{H}_\mathrm{Q}^{[2]} \approx &\frac{1}{\omega_0}\left[\frac{eQ}{4I(2I-1)\hbar}\right]^2 \\ &\times\left\{\begin{array}{l} 2V_{-1}^{(2)}V_1^{(2)}\hat{I}_\mathrm{Z}\left[4I(I+1) - 8\hat{I}_\mathrm{Z}^2 - 1\right] \\ +2V_{-2}^{(2)}V_2^{(2)}\hat{I}_\mathrm{Z}\left[2I(I+1) - 2\hat{I}_\mathrm{Z}^2 - 1\right]\end{array}\right\}\end{aligned} \quad [4.10]$$

$\hat{H}_\mathrm{Q}^{[1]}$ and $\hat{H}_\mathrm{Q}^{[2]}$ are approximate equation since only the secular terms are retained (i.e. terms that commute with $\hat{I}_\mathrm{Z}$). Higher-order terms can be neglected, as they do not have, in general, influence in the spectrum. In opposite to $\hat{H}_\mathrm{Q}^{[1]}$, $\hat{H}_\mathrm{Q}^{[2]}$ is inversely proportional to the ω_0, and therefore the stronger the $\boldsymbol{B}_0$ field employed the weaker will be the second-order quadrupolar broadening contribution (see Fig. 4.18).

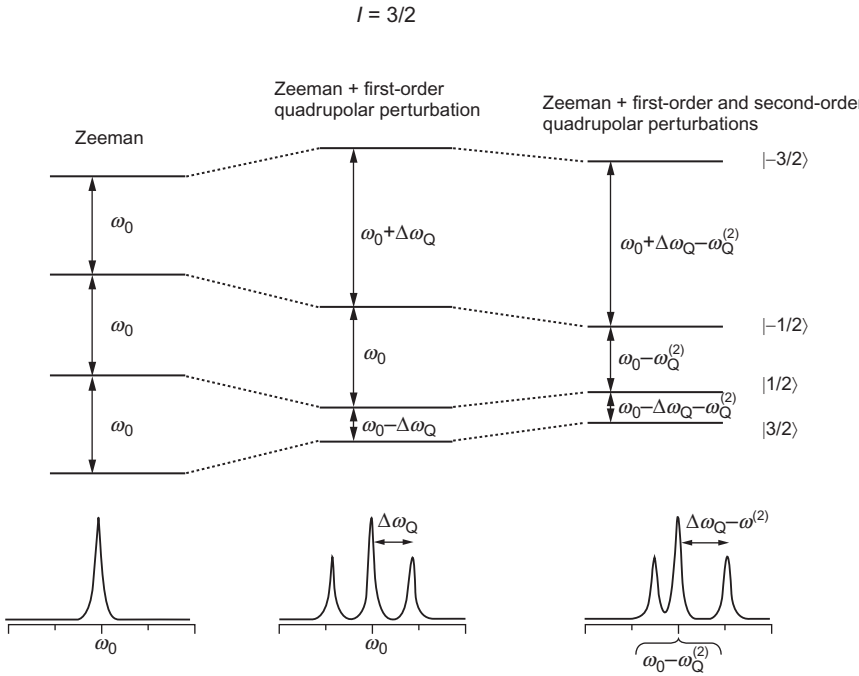

Figure 4.29 Energy-level diagram of a spin-3/2 nucleus. $\Delta\omega_Q$ is the orientation dependent quadrupolar splitting due to the first-order contribution (see Eqs. 4.16 and 4.20 for the static and MAS regimes). $\omega_Q^{(2)}$ is the orientation dependent second-order contribution to the CT and ST energy levels. In the bottom, model spectra of a single crystal are sketched, corresponding to the three different energy diagram situations.

$\hat{H}_Q^{[1]}$ splits the spectrum of a half-integer quadrupole spin system, in a single crystal, into 2I-1 satellite lines and one single central line, which remains at ω_0 (Fig. 4.29). The additional effect of $\hat{H}_Q^{[2]}$ is to shift further all the lines, including the central line. When the sample is a powder, it is generally the CT line, which is observed and its lineshape becomes asymmetric when $\hat{H}_Q^{[2]}$ is large. In certain cases the spinning sidebands from the powder pattern satellite transitions may be observed employing MAS.

The position or the transition energy in angular frequency of the spectral line associated with the transition $(m-1 \leftrightarrow m)$ resonates at

$$\omega_{(m-1\leftrightarrow m)} = \underbrace{\omega^{Z}_{(m-1\leftrightarrow m)}}_{\omega_0} + \omega^{Q,[1]}_{(m-1\leftrightarrow m)} + \omega^{Q,[2]}_{(mm-1\leftrightarrow m)} \qquad [4.11]$$

with m values representing the magnetic quantum numbers, which identify the energy levels in Fig. 4.29 for the case of a nuclear spin $I=3/2$ such as

^{23}Na or ^{11}B nuclei. The expressions for $\omega^{Q,[1]}_{(m-1\leftrightarrow m)}$ and $\omega^{Q,[2]}_{(m-1\leftrightarrow m)}$ in which the sample is either a static or a spinning (at the magic-angle) single crystal are given in sections 6.1.2 and 6.1.3.

6.1.2 Spectrum of a quadrupolar nucleus under static conditions

For a static single crystal, all the resonance frequencies can be determined by defining the $V^{(2),\mathrm{LAB}}$ components in the LAB frame as a function of the $V^{(2),\mathrm{PAS}}$ tensor components in the PAS of the quadrupolar tensor. This is accomplished by rotating the EFG tensor defined in the PAS to the LAB frame using a set of three Euler angles α, β, and γ to correlate both frames. The following formula is used for this axis transformation[200,203,204]:

$$V_i^{(2),\mathrm{LAB}} = \sum_{j=-2}^{2} D^{(2)}_{j,i}(\Omega_{\mathrm{PL}})\, V_j^{(2),\mathrm{PAS}} \qquad [4.12]$$

where $D^{(2)}_{j,i}(\Omega_{\mathrm{PL}})$ is the Wigner rotation matrix defined elsewhere[200,204] using the Euler angles $\Omega_{\mathrm{PL}} = (\alpha, \beta, \gamma)$. The subscripts P and L mean PAS and LAB, respectively, and indicate the sense of axis rotation that is, the PAS of the EFG tensor is the starting point and LAB is the final frame, $\mathrm{PAS} \xrightarrow{\Omega_{\mathrm{PL}}=(\alpha,\beta,\gamma)} \mathrm{LAB}$.

Multiplying the spatial tensor components $V_0{}^{(2),\mathrm{PAS}}$ of $\hat{H}_{\mathrm{Q}}^{[1]}$ (Eq. 4.9) by the rotation matrix expressed in Eq. (4.12), $V_0{}^{(2),\mathrm{LAB}}$ may be obtained, and Eq. (4.9) becomes

$$\hat{H}_{\mathrm{Q}}^{[1],\mathrm{static}} = \frac{1}{3}\omega_{\mathrm{Q}}(\alpha,\beta,\eta)\left[3\hat{I}_{\mathrm{Z}}^2 - I(I+1)\right] \qquad [4.13]$$

with

$$\omega_{\mathrm{Q}}(\alpha,\beta,\eta) = \underbrace{\frac{3e^2qQ}{4I(2I-1)\hbar}}_{\omega_{\mathrm{Q}}}\left[\frac{1}{2}\left(3\cos^2\beta - 1\right) + \eta\sin^2\beta(\cos)2\alpha\right] \qquad [4.14]$$

Note that the last geometrical term in squared brackets is derived from the calculation of $V_0{}^{(2),\mathrm{PAS}}$ in $V_0{}^{(2),\mathrm{LAB}}$ using the relation of Eq. (4.12):

$$V_0^{(2),\mathrm{LAB}} = \underbrace{\sqrt{\frac{3}{2}eq}}_{V_0^{(2),\mathrm{PAS}}}\left[\frac{1}{2}\left(3\cos^2\beta - 1\right) + \eta\sin^2\beta\cos 2\alpha\right] \qquad [4.15]$$

Using Eq. (4.13), the first-order transition frequencies are then given by

$$\begin{aligned}\omega^{\mathrm{Q},[1],\mathrm{static}}_{(m-1\leftrightarrow m)} &= \left\langle m-1\left|\hat{H}^{[1]}_{\mathrm{Q}}\right|m-1\right\rangle - \left\langle m\left|\hat{H}^{[1]}_{\mathrm{Q}}\right|m\right\rangle \\ &= (1-2m)\omega_{\mathrm{Q}}(\alpha,\beta,\eta)\end{aligned} \qquad [4.16]$$

One of the consequences of Eq. (4.16) is that the satellite transitions (e.g. the transition of the $m=\pm 3/2$ to $m=\pm 1/2$) are split by $2\omega_{\mathrm{Q}}(\alpha, \beta, \eta)$ by the first-order perturbation (Fig. 4.29), while the CT is unaffected, as Eq. (4.16) gives 0 for $m=1/2$. For the sake of simplicity, we refer to the first-order quadrupolar splitting, $2\omega_{\mathrm{Q}}(\alpha, \beta, \eta)$, as $\Delta\omega_{\mathrm{Q}}$.

Similarly, the second-order transition frequencies of a static single crystal, may also be derived expressing Eq. (4.10) in the LAB frame by obtaining the $V_0^{(2),\mathrm{LAB}}$ components through Eq. (4.12).[196]

$$\begin{aligned}\omega^{\mathrm{Q},[2],\mathrm{static}}_{(-1/2\leftrightarrow 1/2)} &= \left\langle -1/2|\hat{H}^{[2]}_{\mathrm{Q}}|-1/2\right\rangle - \left\langle 1/2|\hat{H}^{[2]}_{\mathrm{Q}}|1/2\right\rangle \\ &= \frac{1}{6\omega_0}\left[\frac{3C_{\mathrm{Q}}}{2I(2I-1)}\right]^2\left[I(I-1)-\frac{3}{4}\right] \\ &\times\left[F_1(\alpha,\eta)\cos^4\beta + F_2(\alpha,\eta)\cos^2\beta + F_3(\alpha,\eta)\right]\end{aligned} \qquad [4.17]$$

$F_n(\alpha,\eta)$ refers to long trigonometric factors including the angular functions resulting from applying the Wigner matrix rotations (4.12) and describe the orientation dependence of the second-order quadrupolar broadening under static conditions. Their explicit values may be found in Refs.196,200. These factors illustrate the complex nature of the orientation dependence of the CT when affected by second-order quadrupole broadening. If the EFG tensor has axial symmetry ($\eta=0$), Eq. (4.17) can be simplified as follows:

$$\begin{aligned}\omega^{\mathrm{Q},[2],\mathrm{static}}_{(-1/2\leftrightarrow 1/2)} &= \frac{1}{6\omega_0}\left[\frac{3C_{\mathrm{Q}}}{2I(2I-1)}\right]^2\left[I(I-1)-\frac{3}{4}\right] \\ &\times\frac{8}{3}\left(1-\cos^2\beta\right)\left(9\cos^2\beta-1\right)\end{aligned} \qquad [4.18]$$

6.1.3 Spectrum of a quadrupolar nucleus under MAS conditions

Under MAS conditions, the contribution of the first-order quadrupolar Hamiltonian to the frequency of the central and satellite transitions may be given by representing the Hamiltonian $\hat{H}^{[1]}_{\mathrm{Q}}$ of Eq. (4.9) in the LAB frame

by applying a transformation involving an additional coordinate system compared to the static condition. Another set of Euler angles must be used to make a PAS $\xrightarrow{\Omega_{PR}=(\alpha_{PR},\beta_{PR},\gamma_{PR})}$ ROTOR $\xrightarrow{\Omega_{RL}=\alpha_{RL},\beta_{RL},\gamma_{RL}}$ LAB transformation. The Euler angles $\boldsymbol{\Omega}_{PR}$ describe the rotation from the PAS of the EFG tensor to the ROTOR frame, which is followed by a second transformation to the LAB axis system using the Euler angles $\boldsymbol{\Omega}_{RL}=(\omega_R t,\theta_m,0)$. $\omega_R t$ defines the rotor phase with respect to $\boldsymbol{B}_0$, and θ_m is the magic-angle inclination between the rotor axis and the z-axis of the LAB frame.

Again, these space rotations may be executed calculating the $V_0^{(2),LAB}$ tensor spatial components using:

$$V_i^{(2),LAB}=\sum_{j=-2}^{2}\sum_{k=-2}^{2}D_{k,j}^{(2)}(\boldsymbol{\Omega}_{PR})D_{j,i}^{(2)}(\boldsymbol{\Omega}_{RL})V_k^{(2),PAS} \qquad [4.19]$$

The expression for the first-order transition frequencies under MAS yields:

$$\omega_{(m-1\leftrightarrow m)}^{Q,[1],MAS}=\left(\frac{1}{2}-m\right)\underbrace{\omega_Q(\alpha,\beta,\eta)\left(3\cos^2\theta_m-1\right)}_{\omega_Q'} \qquad [4.20]$$

Through analysis of Eq. (4.20), it is evident that the orientation dependence of $\omega_Q{}'$ is such that there is no resonance shift for any of the transitions when the crystal rotates exactly at the magic angle, $\theta_m=Arc\cos\left(1/\sqrt{3}\right)\approx 54.74°$, thus, completely removing the first-order powder broadening.

Note that the Euler angle γ, coming from the rotor modulation, does not appear in Eq. (4.20) because this treatment corresponds to NMR experiments undergoing a fast rotation regime and therefore no rotor modulation terms from Ω_{RL} were included in Eqs. (4.20) and (4.22) (for the second-order contribution under MAS). These MAS modulation terms may be incorporated by also adding the $V_{\pm 1}^{(2),LAB}$ and $V_{\pm 2}^{(2),LAB}$ terms and obtain these through Eq. (4.19) to express Eq. (4.20) as a Fourier series where the MAS modulation becomes evident by the presence of complex exponential containing the $\gamma+\omega_R t$ phase as follows:

$$\omega_{(m-1\leftrightarrow m)}^{Q,[1],MAS}(t)=\left(\frac{1}{2}-m\right)\underbrace{\sum_{q=-2}^{q}\omega_Q^q(\alpha,\beta,\theta_m,\eta)e^{iq(\omega_R t+\gamma)}}_{\omega_Q(t)}$$

$$\omega_Q(t)=\frac{\omega_Q}{2}\left[-\sqrt{2}\sin 2\beta\cos\left(\omega_R t+\gamma\right)+\sin^2\beta\cos 2(\omega_R t+\gamma)\right] \qquad [4.21]$$

Spinning a powdered sample at a rate comparable to the magnitude of the anisotropic interaction will generate a time-dependent signal, which is translated in the presence of a manifold of spectral spinning sidebands for the various satellite transitions centered at $\left(\frac{1}{2}-m\right)\omega_{\mathrm{Q}}$ and separated by ω_{R} as illustrated in Fig. 4.30.[205] This time-dependence is included in $\omega_{\mathrm{Q}}(t)$ assuming a $\eta=0$.

The second-order transition frequency of the CT under fast rotation regime shows a similar form as for the static case (Eq. 4.18).

$$\begin{aligned}\omega_{(-1/2\leftrightarrow 1/2)}^{\mathrm{Q},[2],\mathrm{MAS}} &= \langle -1/2|\hat{H}_{\mathrm{Q}}^{[2]}|-1/2\rangle - \langle 1/2|\hat{H}_{\mathrm{Q}}^{[2]}|1/2\rangle \\ &= \frac{1}{6\omega_0}\left[\frac{3C_{\mathrm{Q}}}{2I(2I-1)}\right]^2\left[I(I-1)-\frac{3}{4}\right] \\ &\quad G_1(\alpha,\eta)\cos^4\beta + G_2(\alpha,\eta)\cos^2\beta + G_3(\alpha,\eta)\end{aligned} \qquad [4.22]$$

Only the form of the spatial factors $G_n(\alpha,\eta)$ changes due to the distinct orientation dependence of the fourth-rank tensor spatial functions when rotating the EFG tensor in the direction PAS → ROTOR → LAB. Expression for these terms may also be found elsewhere.[196,200,204]

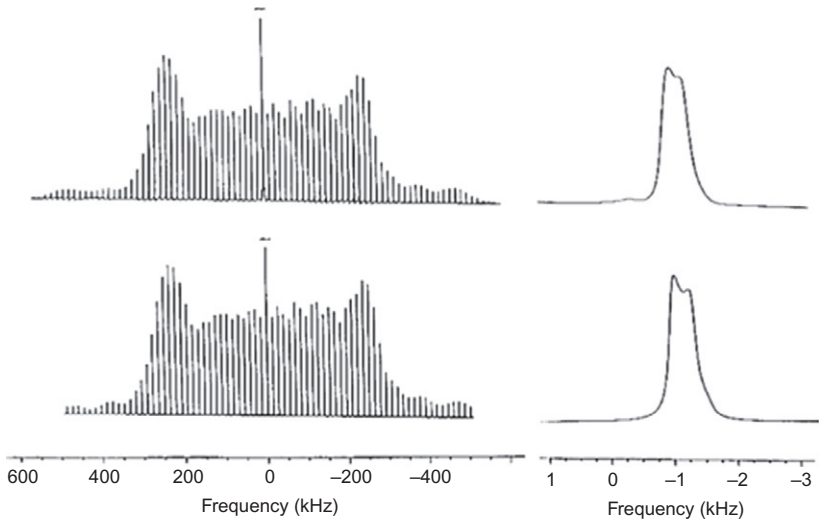

Figure 4.30 ^{23}Na spectrum of a sample of $NaNO_2$ showing the satellite transition sidebands (left) and the expanded CT resonance (right). The top trace is experimental and the bottom trace is a result of numerical simulation. From both the experimental and simulated spectra the quadrupolar parameters were estimated as $C_{\mathrm{Q}}=1.1\pm0.03$ MHz and $\eta=0.10\pm0.03$. Adapted from Ref. 205, Copyright (1999), with permission from Elsevier.

6.1.4 Effect of MAS in the central transition

The most important task in NMR of quadrupolar spins is the ability to observe the CT and retrieve information from its resonance position and lineshape. Unfortunately, unlike first-order effects such as the CSA, dipolar interaction and the first-order quadrupolar splitting, the anisotropy of the second-order quadrupolar interaction cannot be described by a second-rank tensor and applying MAS alone does not yield high-resolution spectra. The second-order quadrupolar broadening of the CT is described by a fourth-rank tensor instead, which has a complex angular dependence with respect to the $\boldsymbol{B}_0$ field. This may be observed by comparing the spectral lines at $\omega^{\mathrm{Q},[1],\mathrm{MAS}}_{(-1/2\leftrightarrow 1/2)}$ and $\omega^{\mathrm{Q},[2],\mathrm{MAS}}_{(-1/2\leftrightarrow 1/2)}$, which depend on the geometric factors $\propto \omega'_{\mathrm{Q}}$ (Eq. 4.20) and $\propto G_n(\alpha,\eta)$ (Eq. 4.22), respectively. Such geometric terms also correspond to the second- $P_2(\cos\theta)$ and fourth-order $P_4(\cos\theta)$ Legendre polynomials, respectively.

$$\omega'_{\mathrm{Q}} \propto P_2(\cos\theta) = 1/2\left(3\cos^2\theta - 1\right) \tag{4.23}$$

$$\begin{aligned} &G_1(\alpha,\eta)\cos^4\beta + G_2(\alpha,\eta)\cos^2\beta + G_3(\alpha,\eta) \propto P_4(\cos\theta) \\ &\quad = 1/8\left(35\cos^4\theta - 30\cos^2\theta + 3\right) \end{aligned} \tag{4.24}$$

The zero-order Legendre polynomials refer to the isotropic components and are not considered, as it does not influence the lineshape of the spectrum.

Nevertheless, one can see that setting the spinning rotor at $\theta = 54.74°$ in $P_4(\cos\theta)$ still reduces the linewidth of the second-order powder pattern in a polycrystalline sample by a factor of ~ 3. Thus, rotating the sample is always advantageous. Indeed, depending on the value of η, the CT line-narrowing effect may be improved by a factor between 3 and 4 under MAS. Figure 4.31 compares the simulated powder pattern of the CT under MAS and static conditions to access the line-narrowing capability of a rotating sample. Furthermore, the fine structure of the sidebands due to second-order shifts and sideband envelopes can be analyzed to obtain detailed information on the spin system.

In addition, an isotropic second-order quadrupolar shift $\omega^{\mathrm{iso}}_{\mathrm{Q},(m-1\leftrightarrow m)}$ of the centre of gravity of the powder pattern is given by[196]

$$\begin{aligned} \omega^{\mathrm{iso}}_{\mathrm{Q},(m-1\leftrightarrow m)} &= \frac{1}{4\pi}\int_0^{\pi} \mathbf{d}\beta \sin\beta \int_0^{2\pi} \mathbf{d}\alpha\, \omega^{\mathrm{Q},[2],\mathrm{MAS}}_{(m-1\leftrightarrow m)} \\ &= \frac{3}{40\omega_0}\left[\frac{C_{\mathrm{Q}}}{I(2I-1)}\right]^2 \left(1+\frac{1}{3}\eta^2\right) \times \left[I(I+1) - 9m(m-1) - 3\right] \end{aligned} \tag{4.25}$$

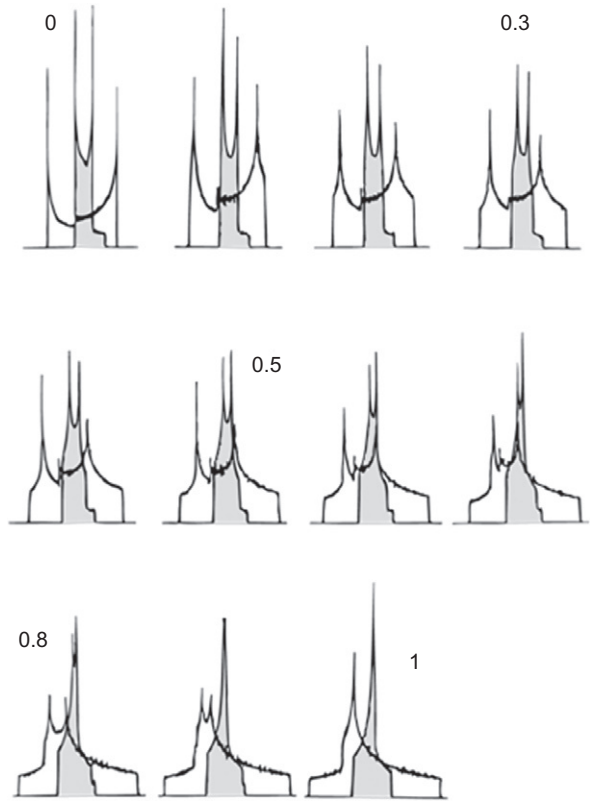

Figure 4.31 Superposition of simulated powder patterns of the resonance corresponding to the central transition during static and MAS (shaded spectra) experiments for increasing values of the asymmetry parameter η from 0 to 1 in steps of 0.1. *Reprinted with permission from Ref. 196.*

The true chemical shift may be expressed as

$$\delta_{\mathrm{iso},(m-1\leftrightarrow m)} = \delta^{\mathrm{exp}}_{\mathrm{CG},(m-1\leftrightarrow m)} - \underbrace{\frac{\omega^{\mathrm{iso}}_{q,(m-1\leftrightarrow m)}}{\omega_0}}_{\delta^{[2]}_{\mathrm{Q}}} \qquad [4.26]$$

For the CT ($m=1/2$), the Eq. (4.26) can be rearranged, and the final expression for $\delta_{\mathrm{iso},(-1/2\leftrightarrow 1/2)}$ becomes Eq. (4.1).

The second-order quadrupolar shift can displace the NMR resonances away from the typical chemical shift ranges observed for given chemical environments. This shift becomes more important for larger C_{Q} values and sometimes the line position may appear well outside the expected region thus making difficult the peak assignment. The second-order quadrupolar broadening can most of the times make Al sites in zeolites invisible

(see Section 3.3). It is well known that five-coordinated or distorted four-coordinates Al sites may sometimes present a very large C_Q and become invisible. This may be an important drawback in obtaining reliable quantification analysis in ^{27}Al MAS NMR studies and has been the subject of debate in the study of extraframework Al species in zeolites or Brønsted acid sites in dehydrated zeolites (see Sections 3.3 and 3.4). The best solution to overcome resolution/sensitivity problems related with broad lines or invisible sites consists in using high-resolution techniques at the highest $\boldsymbol{B}_0$ field possible, as the second-order quadrupolar interaction decreases at increasing magnetic fields (see Fig. 4.18).

Section 6.1.6 deals with the most popular line-narrowing NMR techniques to obtain high-resolution spectra of quadrupolar spins.

6.1.5 Effect of rf pulses in quadrupolar spins

6.1.5.1 Selective versus non-selective pulses: Quantification aspects

For spin-1/2 nuclei, the rf field interaction with the nucleus is much larger than the other internal interactions, which may thus be neglected. However, the manner in which the rf pulses affect quadrupolar spins in a high magnetic field is much more complicated and depends on the relative magnitudes of three parameters: (i) the rf amplitude (ω_1) generated by the pulse; (ii) the magnitude of first-order quadrupolar interaction, and (iii) the irradiation offset ($\Delta\omega_0$), that is, the difference between the resonance frequency and the carrier frequency of the rf pulse.

The first-order quadrupolar interaction (parameter ii) is often larger than the rf pulse interaction with the nucleus and cannot be neglected during the duration of a pulse. Consequently, under rf irradiation, the general behaviour of quadrupolar nuclei may be summarized by considering the following three cases[206]:

A. $\omega_1 \gg \Delta\omega_Q$: this corresponds to the application of a hard rf pulse resulting in a non-selective excitation of all transitions. The resonances are effectively on-resonance, and the offset and quadrupole terms need not to be considered. Under non-selective irradiation, the nutation frequency (ω_{nut}) of the CT is given by $\omega_{nut} = \omega_1$, meaning that in such condition the system behaves similarly to the case of an isolated spin-1/2 nucleus and that the evolution of each transition as a function of the pulse length is sinusoidal with angular frequency ω_1.

B. $\Delta\omega_Q \gg \omega_1$: a selective excitation occurs by applying an on-resonance rf irradiation. No irradiation of the other transitions is assumed so that only the on-resonance frequency line corresponding to the transition

$(m-1 \leftrightarrow m)$ is considered, as if these were the only existent two nuclear spin levels.

A fictitious spin operator is used to calculate its evolution as a function of the flip angle.[207] Under selective irradiation, the nutation frequency may be expressed as

$$\omega_{\text{nut}} = \sqrt{I(I+1)} - m(m+1)\omega_1 \qquad [4.27]$$

For the CT ($m=-1/2$) of a half-integer quadrupolar spin, Eq. (4.27) may be rewritten as

$$\omega_{\text{nut}} = \kappa \times \omega_1 \qquad [4.28]$$

with $\kappa=(I+1/2)=2$, 3, 4 for nuclear spins $I=3/2$, 5/2, and 7/2, respectively. This shows that the response of quadrupolar spins to a selective pulse has an associated scaling factor, which depends on the nuclear spin. At an experimental point of view, this means that a certain flip-angle pulse applied to a quadrupolar spin requires a shorter pulse length compared to a non-selective pulse or compared to a spin-1/2 nucleus, which has no quadrupolar interaction. As an example, Eq. 4.29 shows the relation between a selective and non-selective $\pi/2$ flip angle pulse:

$$\left(\frac{\pi}{2}\right)_{\text{selective}} = \frac{1}{\kappa} \times \left(\frac{\pi}{2}\right)_{\text{non-selective}} \qquad [4.29]$$

Figure 4.32 shows how the CT signal intensity of spin-3/2 and -5/2 nuclei behave as a function of the pulse flip angle, for distinct ω_Q/ω_1 ratios.[208] Note that for higher ω_Q/ω_1 ratios (approaching the selective irradiation) the maximum intensity ($\pi/2-$flip angle) is consistent with Eq. (4.29). For example, for the nutation curve with $\omega_Q/\omega_1=40$, the maximum signal intensities correspond to flip angle of $\sim 45°$ ($\kappa=2$) and $\sim 30°$ ($\kappa=3$) for a spin-3/2 and -5/2, respectively. For the case of a non-selective irradiation, the ω_Q/ω_1 values decrease and approach the situation of a "conventional" nutation curve (case A) with a maximum signal intensity at 90° ($\kappa=1$).

For quantitative comparison between different signals, it is crucial to work with excitation pulses of sufficiently small flip angle to ensure that the signal intensity does not depend on the nutation behaviour of the CT, which depends on ω_Q. According to Fig. 4.32, the largest deviation is between purely selective and non-selective ($\omega_Q/\omega_1=0$) excitations. Vega mentioned that to keep the deviation under 5%, the nominal flip angle (i.e. the nutation angle if the pulse was applied to a liquid sample) must be smaller than 18°, 11°, and 8° for $I=3/2$, 5/2, and 7/2, respectively. For deviations less than 10%, the flip angles must be limited to 25°, 15°, and 11°, respectively.[206]

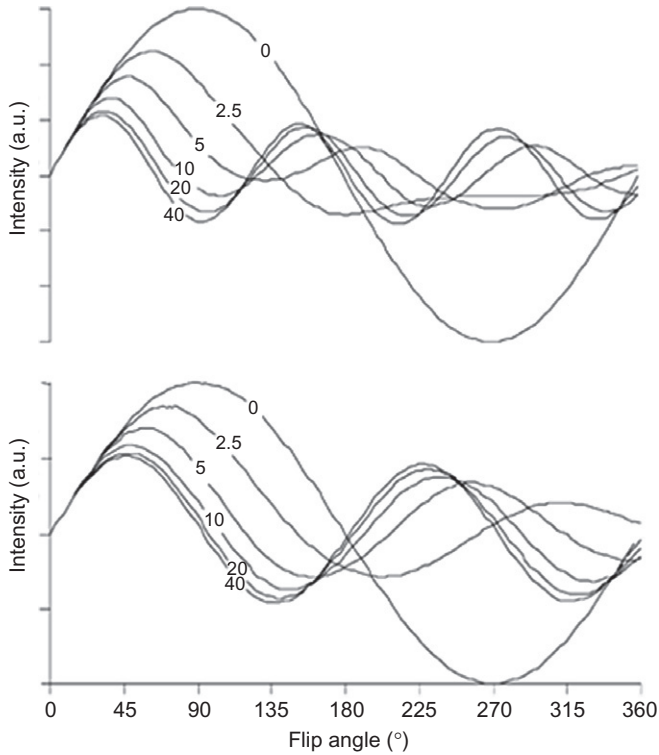

Figure 4.32 CT signal intensity of spins $I = 3/2$ (bottom) and $I = 5/2$ (top) under rf irradiation for different values of C_Q. The numerical values shown on the graphics denote the ω_Q/ω_1 ratios.

C. $\Delta\omega_Q \approx \omega_1$: the degree of excitation depends on ω_1, ω_Q, and on the molecular orientation in the applied $\boldsymbol{B}_0$ field. The response of the spin system to rf amplitudes that are intermediate between selective and non-selective excitation is more complex than in the limiting cases. In this situation the evolution of the system is not periodic, and in this case, it is possible to excite multiple-quantum coherences with a single pulse. The rf excitation becomes less dependent on ω_Q as the length of the pulse decreases and its amplitude increases. Usually, a relatively small flip angle ($\pi/4I+2$) is employed to excite homogeneously all the quadrupolar nuclei, which also allows to obtain a quantitative spectrum.

6.1.5.2 Intricacies of CPMAS spin-locking in quadrupolar spins

The ability to adequately spin-lock quadrupolar spins is an important matter to successfully make use of cross-polarization or 2D CP-based HETCOR

experiments to probe proximities between spin pairs of relevance in solid. For zeolites, in particular, ^{1}H–^{11}B, ^{1}H–^{27}Al, ^{1}H–^{23}Na, ^{29}Si–^{27}Al, ^{19}F–^{27}Al, ^{19}F–^{27}Al are the most useful and commonly exploited spin pairs for CPMAS related experiments involving one quadrupolar nucleus.

CP is the transfer of spin-locked magnetization from nuclei I to neighbour nuclei S during a contact time period by simultaneous rf irradiation of the two spin systems under matched conditions of the two rf amplitudes $\omega_{1,I}$ and $\omega_{1,S}$. When both I and S are spins-1/2, the matching requirement for a static sample is the so-called Hartmann–Hahn (HH) condition, defined as

$$\omega_{1,I} = \omega_{1,S} \qquad [4.30]$$

Equation (4.30) is also valid for quadrupolar nuclei if $\omega_{1,S} \gg \Delta\omega_Q$.

Under static conditions, the satellite transitions for large C_Q's are unaffected by the CP spin-lock field $\omega_{1,S}$, as the quadrupolar spin S (observation channel) is usually at selective regimes (i.e. $\omega_{1,S} \ll \Delta\omega_Q$). Under this condition, only S-spin magnetization buildup from the CT occurs using the following HH condition:

$$\omega_{1,I} = \omega_{nut,S} = (S+1/2)\omega_{1,S}, \quad \omega_{1,S} \ll \Delta\omega_Q \qquad [4.31]$$

However, the most useful applications employing CP are performed under MAS conditions. In such case, performing a CP between a I spin-1/2 (e.g. ^{1}H or ^{19}F) and half-integer quadrupolar spin S presents a considerable challenge due to the very complex spin dynamics involved in both the spin-locking of quadrupolar nuclei under MAS and the CP process itself.[209–213]The complications can be so severe under MAS that inefficient CP may result, even setting the correct HH condition. These arise from the periodic time-dependence of the first-order quadrupolar splitting $\omega_Q(t)$ imposed by the MAS perturbation (see Eq. 4.21). This time dependence is related to the continuously changing Euler angle β_{PR} (angle between the z-axes of the quadrupolar PAS and ROTOR frames) and implies that the time average of $\omega_Q(t)$ vanishes for nearly every S spins in the sample, as they experience two or four sign changes of $\Delta\omega_Q$ per rotor period.[214] Figure 4.33 illustrates the sign changes of the first-order quadrupolar splitting, $\omega_Q(t)$ for two β_{PR} angles.

As reported by Vega,[206] there are two limiting cases for the MAS-induced zero-crossing of $\Delta\omega_Q$ on which the performance of CPMAS spin-locking depends for a weak-field limit ($\omega_{1,S} \ll \Delta\omega_Q$):

1. Adiabatic zero-crossing ($\alpha \gg 1$)
2. Sudden zero-crossing ($\alpha \ll 1$)

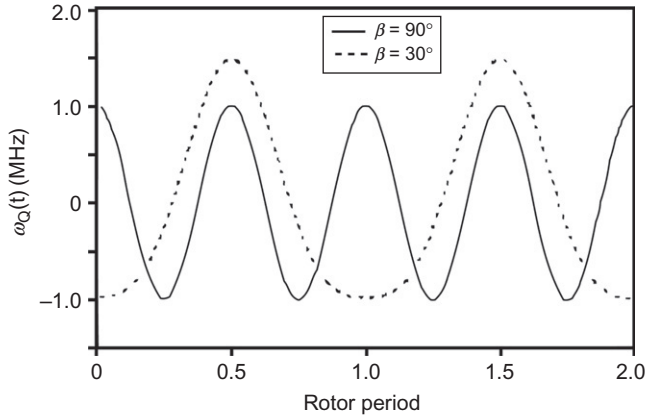

Figure 4.33 Plots of the variation of $\omega_Q(t)$ as a function of the rotor period, for $\omega_Q = 1$ MHz, and two different values of β; $\eta = 0$ and the initial orientation of the quadrupolar tensor at time = 0 is chosen such that the rotation axis, $\boldsymbol{B}_0$, and V_{zz} all lie in the same plane.

Vega introduced an adiabaticity parameter, α, (Eq. 4.32) as a practical way to classify regimes **1**. and **2**. purely based on the experimental parameters ω_Q, ω_R, and $\omega_{1,S}$. The formula for α is[206]

$$\alpha = \frac{\omega_{1,S}^2}{d\Delta\omega_Q/dt} \approx \frac{\omega_{1,S}^2}{\omega_R \omega_Q} \qquad [4.32]$$

The influence of the two regimes in changing the population distribution across the spin-locking eigenstates and the energy levels for a $I = 3/2$ energy-level diagram, at a point in the rotor period when $\omega_Q(t) < 0$ and at a later point $\omega_Q(t) > 0$, is shown in Fig. 4.34.

In Fig. 4.34A, the population difference across the $|1>$ and $|2>$ levels corresponds to the $|1/2> \leftrightarrow |-1/2>$ CT coherence when $\omega_Q(t) > 0$ but corresponds to the $|3/2> \leftrightarrow |-3/2>$ 3Q coherence when $\omega_Q(t) < 0$. This illustrates a rotor-driven adiabatic interconversion of $I = 3/2$ 1Q CT and 3Q coherences. In regime 2, the zero-crossing occurs very rapidly and the populations of the individual eigenstates are conserved. For example, Fig. 4.34B shows that the population difference across the $|1>$ and $|2>$ levels becomes a population difference across the $|3'>$ and $|4'>$ levels after zero-crossing. As $|1> = |3'>$ and $|2> = |4'>$, this indicates that the levels involved correspond always to a $|1/2> \leftrightarrow |-1/2>$ CT, before and after a zero-crossing, therefore leaving populations unchanged in their original states.

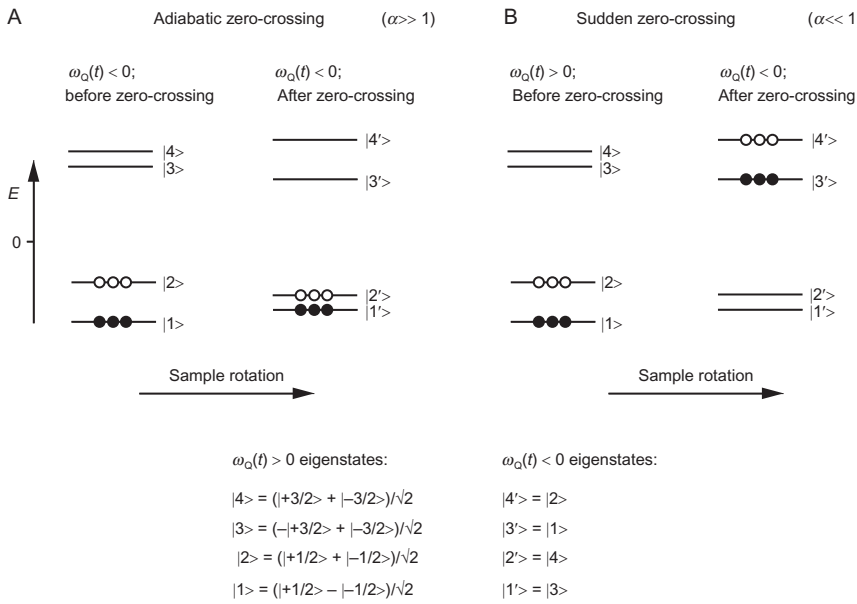

Figure 4.34 Schematic spin $I = 3/2$ energy-level diagrams in the weak-field spinlocking eigenbasis at points in the MAS rotor period when $\omega_Q(t) < 0$ and $\omega_Q(t) > 0$. The fate of a typical population difference is shown for the case of (A) an adiabatic zero-crossing and (B) a sudden zero-crossing. *Reprinted with permission from Ref. 214, Copyright (2004), American Institute of Physics.*

In the intermediate regime ($\alpha \sim 1$) CP will result in rapid decay of the spin-locked magnetization on a time scale $\sim 1/\omega_R$ and inefficient or no CP. In both cases, the adiabatic and sudden regimes, the quadrupolar S nucleus can be spin-locked; it is, however, usually much easier to perform CP experiments in the sudden regime because the rf spin-lock irradiation of the S spin, in most cases, obey to the condition $\omega_{1,S} \ll \Delta\omega_Q$. This condition is also necessary for a selective excitation of the CT. In addition, the fast spinning limit also favours the sudden regime. Under the sudden regime, the on-resonance CPMAS transfer to the CT is observed under the following HH condition[210,215]:

$$\varepsilon\omega_{1,I} \cong (S + 1/2)\omega_{1,S} + n\omega_R (\varepsilon = \pm 1;\ \ n = \pm 1,\ \ n = \pm 2) \qquad [4.33]$$

with $n = 0$ corresponding to the static case (where only $\varepsilon = -1$ is allowed), and ± 1, ± 2 to fast MAS with $\varepsilon = \pm 1$. $\varepsilon = -1$ and $\varepsilon = +1$ correspond to *flip–flip* and *flop–flop* transfers in the interaction frame, respectively. *Flop–flop* transfers can be observed only at very low values of $\omega_{1,I}$ and $\omega_{1,S}$

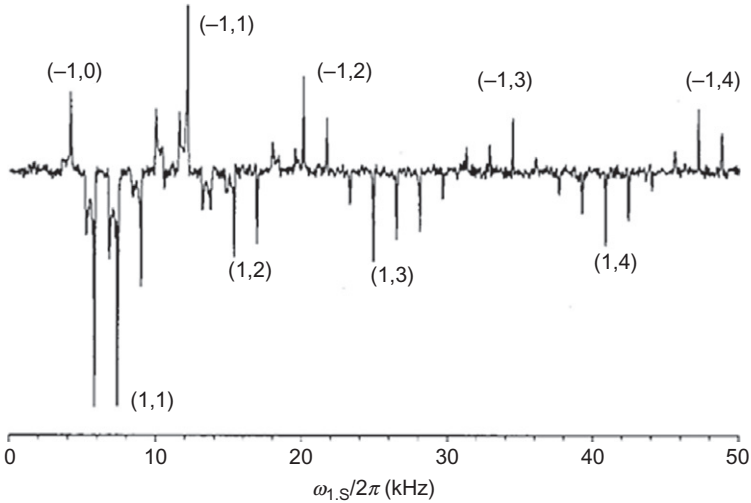

Figure 4.35 HH matching curve of a ^{1}H–^{11}B 1Q-CPMAS NMR experiment in borax ($Na_2B_4O_7{\cdot}10H_2O$) as a function of $\omega_{1,S}$. The ^{11}B spectra were acquired on-resonance, using $\omega_{1,I} = 6$ kHz, contact time = 300 μs and $\omega_R = 20$ kHz. Values in parenthesis depict the various HH conditions (n, ε). *Reprinted from Ref. 215, Copyright (2002) with permission of Taylor & Francis Ltd.*

and thus are of little practical importance in the case of spin-1/2 pairs but relevant in quadrupolar systems as will be demonstrated ahead.

Interpreting Eq. (4.33) is not always obvious because of the combination of ε and n, but Fig. 4.35 clearly shows the HH matching curve, measured on-resonance for both $I = {}^{1}H$ and $S = {}^{11}B$ spins, as a function of $\omega_{1,S}$. Numerous matches are observed with positive (*flop–flop*) and negative (*flip–flip*) amplitudes for the various n values. The intensity of these matching conditions decrease for increasing $\omega_{1,S}$ values due to the loss of spin-lock efficiency. It is worth mentioning that all the matching frequencies observed in Fig. 4.35 follow Eq. (4.33) with the (n, ε) values in perfect agreement with each positive and negative $\omega_{1,S}$ amplitudes.

An expression for the calculation of the HH condition to excite the MQ coherences directly through CP in quadrupolar spins is also available elsewhere[212,216] and will not be covered in this review as MQ-CP experiments are not very efficient and have not been applied to zeolites.

For further details on the theory of the spin-locking phenomena in quadrupolar nuclei, the reader is referred to the work of Vega[210,211] and other comprehensive reports.[214,215,217,218]

6.1.6 Line narrowing methods and practical aspects

It was shown that in order to remove the second-order quadrupolar interaction and consequently obtain a high-resolution spectra of quadrupolar spins, an experimental strategy is needed to find an angle θ such that $P_2(\cos\theta) = P_4(\cos\theta) = 0$ is satisfied.

Sophisticated methods such as DOR,[197,199] DAS,[198] MQMAS,[200,219,220] and satellite transition MAS (STMAS)[221,222] NMR consist as the major approaches to remove the second-order quadrupolar broadening. The first two methods involve real space averaging of the second-order quadrupolar interaction through mechanical rotational of the sample holder, while the latter two methods are 2D experiments based on the spin space manipulation making use of the distinct second-order quadrupolar broadenings of: (i) the single-quantum (SQ) CT and the MQ transitions (for MQMAS) or of (ii) the SQ CT and SQ ST (for STMAS). STMAS has not been as popular as MQMAS in zeolite applications but those interested in the method are referred to a detailed review.[223] The MQMAS method was a real breakthrough in the characterization of zeolites, since its invention in 1995 and has now replaced DOR and DAS, becoming the most widely used high-resolution NMR method to observe half-integer quadrupolar spins in materials. Explaining the basic principles and theory of all these methods is beyond the scope of this review, as several contributions dedicated to this subject already exist.[196,204,206,220,224] We restrict our discussion to a brief overview of the MQMAS method, which is the only method widely used in characterization of zeolites.

6.1.6.1 MQMAS principle

MQMAS is a 2D experiment starting with a hard rf pulse that excites non-observable MQ coherences during the t_1 evolution. The following rf pulses will convert the MQ transitions into observable SQ coherences during t_2, which combined with MAS will remove the quadrupolar anisotropy and an isotropic lineshape is obtained. For this purpose, only the symmetric $p/2 \leftrightarrow -p/2$ ($p = 2m$ with $m = -I, -I+1, \ldots, I$) coherences corresponding to pQ transitions are selected, as these are not influenced by the first-order broadening effects (only second-order is present for symmetrical transitions). The phase development $\varphi(t)$ of the observable SQ (p_2) and the non-observable MQ (p_1) coherences can be expressed as follows

$$\varphi^{\text{static}}_{p/2\leftrightarrow -p/2}(t_1,t_2)=\left\{p\Delta\omega+\sum_{k=0,2,4}V_k^{(2)}(\Omega_{\text{PL}})T_k^{(2)}(I,p_1)\right\}t_1 +\left\{p\Delta\omega+\sum_{k=0,2,4}V_k^{(2)}(\Omega_{\text{PL}})T_k^{(2)}(I,p_2)\right\}t_2 \quad [4.34]$$

The contributions for the chemical shift and the resonance offset are included in $\Delta\omega$. The terms $T_k{}^{(2)}(I,p)$ are the zero-, second-, and fourth-rank spin factors for $k=0$, 2, and 4, respectively. The zero-rank term refers to the isotropic term of the quadrupolar interaction. The $V_k{}^{(2)}(\Omega_{\text{PL}})$ terms refer to the geometric factor including the PAS → LAB transformation.

Under fast MAS [$P_2(\cos\theta)=0$], the second-rank term $T_2{}^{(2)}(I,p)$ vanishes and Eq. (4.34) becomes

$$\varphi^{\text{MAS}}_{p/2\leftrightarrow -p/2}(t_1,t_2) =\left[p\Delta\omega+V_0^{(2)}(\Omega_{\text{PR}})T_0^2(I,p_1)+P_4(\cos\theta_{\text{m}})V_4^2(\Omega_{\text{PR}})T_4^2(I,p_1)\right]t_1 +\left[p\Delta\omega+V_0^{(2)}(\Omega_{\text{PR}})T_0^2(I,p_1)+P_4(\cos\theta_{\text{m}})V_4^2(\Omega_{\text{PR}})T_4^2(I,p_1)\right]t_2 \quad [4.35]$$

The remaining second-order anisotropic broadening arises from the $P_4(\cos\theta_{\text{m}})V_4{}^{(2)}(\Omega_{\text{PR}})T_4{}^{(2)}(I,p)$. This term can be averaged out if the times t_1 and t_2 on the quantum levels pQ and -1Q fulfil the condition:

$$T_4^{(2)}(I,p_1)t_1+T_4^{(2)}(I,p_2)t_2=0 \quad [4.36]$$

p_1 and p_2 are the coherence orders evolving during t_1 and t_2, respectively with $p_2=-1$ (the observed coherence).

Rearranging Eq. (4.36) yields[204,225]

$$t_2=\frac{T_4^{(2)}(I,p_1)}{T_4^{(2)}(I,-1)}t_1=p_1\frac{36I(I+1)-17p_1^2-10}{36I(I+1)-27}t_1=k(I,p_1)t_1 \quad [4.37]$$

p_1 can be 3 and 5 for a 3Q and 5Q coherence pathways. Equation (4.37) is orientation independent meaning that all the crystal orientations are refocused at the same time $t_2=k(I,p_1)t_1$, giving rise to the MQMAS isotropic echo. After a double Fourier transform in t_2 and t_1, the NMR resonances appear along the anisotropic axis A with a slope $k(I,p_1)$. The projection of the spectrum onto an axis perpendicular to A, using a shearing transformation, yields an isotropic spectrum.[200]

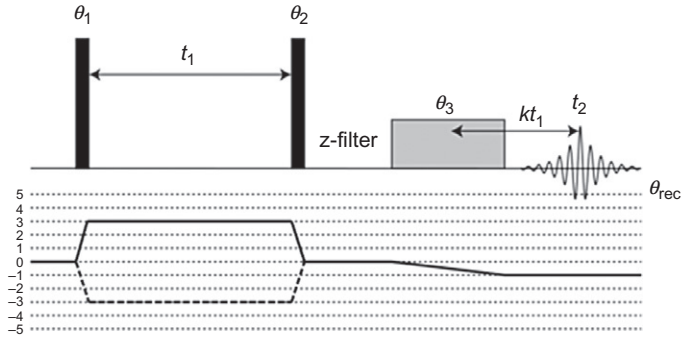

Figure 4.36 Pulse sequence and coherence transfer pathway for the amplitude-modulated z-filter acquisition scheme for a 3QMAS NMR experiment in a spin-5/2 nucleus. The coherence transfer pathways for 3QMAS NMR experiments is depicted at the bottom. Echo and antiecho pathway signals are represented by solid and dashed lines, respectively. The phase cycling is: $\theta_1 = 0°$, 60°, 120°, 180°, 240°, 300°; $\theta_2 = 0°$; $\theta_3 = \{0°\}_6$, $\{90°\}_6$, $\{180°\}_6$, $\{270°\}_6$; $\theta_{rec} = \{0°\ 180°\}_3$, $\{90°\ 270°\}_3$, $\{180°\ 0°\}_3$, $\{270°\ 90°\}_3$.

Several pulse sequences may be used to generate an isotropic echo. In the following, we discuss pulse sequences based on the z-filter experiment, which are the most popular high-resolution schemes for zeolites.

6.1.6.2 z-filter MQMAS scheme

Figure 4.36 shows a z-filter pulse sequence proposed by Amoureux *et al.*,[226] for a spin-5/2 nucleus, which consists of a three-pulse scheme. The method is robust and very easy to optimize. The first two hard pulses (3Q excitation and $\pm 3 \rightarrow -1$ coherence conversion) are followed by a short z-filter delay during which the magnetization is stored along the z-axis as 0Q coherences and then transferred into observable 1Q coherences using a soft (selective) $\pi/2$ pulse to only excite the CT. The symmetric coherence transfer pathway ($p = 0 \rightarrow \pm 3 \rightarrow 0$) assures that the echo ($p = 0 \rightarrow +3 \rightarrow 0$) and the antiecho ($p = 0 \rightarrow -3 \rightarrow 0$) signals lead to an amplitude-modulated FID and therefore a pure absorption spectra. Typically, the rf field strength of the hard pulses should be set to the highest power level achievable by the probe head. A z-filter delay of 10–20 μs and a final soft pulse field strength of about $\upsilon_1 = 10$–20 kHz is usually employed. When possible, the t_1 dwell time can be rotor-synchronized if the States, or States-TPPI scheme is employed to increase spectral sensitivity by folding the spinning sidebands into the centre band. In this condition, a larger F1 spectral window is obtained by increasing the sample rotation.

6.1.6.3 Split-t_1 z-filter MQMAS scheme

From the z-filter MQMAS scheme (Fig. 4.36), the projection of the 2D spectrum onto the F1 axis does not directly yield an isotropic spectrum as stated previously. An interesting alternative acquisition scheme, which avoids the need for using the shearing transformation, is the MQMAS split-t_1 method,[227] which splits t_1 into MQ and SQ evolution periods for a time fraction of $kt_1/[1+k(I, p_1)]$ and $t_1/[1+k(I, p_1)]$, respectively. This strategy will refocus the second-order anisotropic broadening at the end of the t_1 period and thus the echo will always appear at the same t_2 time. After a 2D Fourier transform, the anisotropic axis A appears parallel to the F2 axis (see Fig. 4.37).

6.2. Dipolar recoupling methods: Double- and triple-resonance MAS NMR

6.2.1 The time-dependent dipolar interaction

We shortly describe the dipolar interaction under MAS conditions, so that it becomes easier to understand how the dipolar interactions can be reintroduced using REDOR-like pulse sequences by combining real space and spin space manipulation in specific NMR method described below.

The heteronuclear dipolar interaction has the same orientation dependence (Eq. 4.23) as the first-order quadrupolar or the CSA interactions as it is also described by a second-rank tensor. The heteronuclear dipolar Hamiltonian for an isolated pair of spins I and S under MAS may be written as

$$\hat{H}_{IS}^{MAS}(t) = \omega_D(t)\hat{I}_Z\hat{S}_Z \qquad [4.38]$$

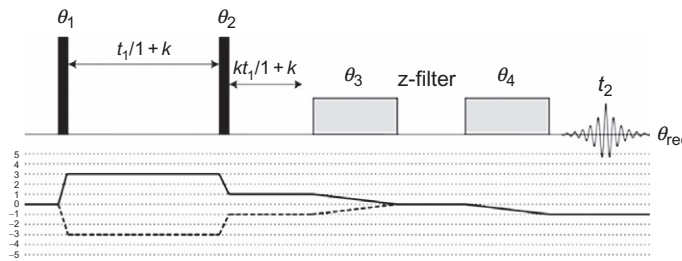

Figure 4.37 Pulse sequence and coherence transfer pathway for the split-t_1 z-filter acquisition scheme for a 3QMAS NMR experiment in a spin-5/2 nucleus. The coherence transfer pathways for 3QMAS NMR experiments is depicted at the bottom. Echo and antiecho pathway signals are represented by solid and dashed lines, respectively.

with

$$\omega_D(t) = \omega_D\left[\sin^2\beta\cos 2(\omega_R t+\gamma) - \sqrt{2}\sin 2\beta\cos(\omega_R t+\gamma)\right],$$
$$\omega_D = \frac{\gamma_I\gamma_S\hbar}{r^3} \qquad [4.39]$$

Equation (4.39) shows the space factor that depends on the MAS rate (ω_R), and also on γ and β, which are the azimuthal and the polar angles describing the relative orientation of the I–S internuclear vector (the z-axis of the PAS of the dipolar tensor) with respect to the spinning axis of the ROTOR frame. γ_I and γ_S are the magnetogyric ratios of the I and S nuclei. This time-dependent dipolar frequency, $\omega_D(t)$, term is averaged to zero integrating Eq. (4.39) over a full rotor period. This means that MAS removes the dipolar anisotropy as expected for a second-rank tensor. The following section deals with different strategies adopted to manipulate this time-dependent spatial term using rf pulses periodically spaced in order to induce a "counter-rotation" in spin space relative to MAS rotation in real space and avoid that the integral of this function averages to zero. Emphasis on recoupling methods to measure proximities between a spin-1/2 (I) and a quadrupolar (S) nuclei will be given as these are the type of spin pairs of most interest to study zeolites. Experimental and basic theoretical concepts regarding the different methods will be given in context with their applications.

6.2.2 REDOR and TEDOR

REDOR NMR is the most used NMR method to measure dipolar couplings between two spatially close spins I and S. Dipolar couplings are proportional to $1/r^3$ (r = internuclear distance), and therefore it may be used to measure internuclear distances, which is a powerful structural information for all domains of chemistry. Techniques like REDOR are called "recoupling" NMR methods, as they are able to recover or reintroduce the "lost" dipolar couplings during sample rotation at the magic angle as discussed in Section 6.2.1. A plethora of REDOR-like variants are available for this purpose, and they all rely on perturbing the averaging process of spinning the sample by means of periodic interference using a series of rotor-synchronized π pulses on the I channel during a certain time. The effect of applying a train of these π pulses on the irradiating I channel will prevent the dipolar interaction to be completely refocused by MAS at the end of the experiment. Thus, a dipolar echo is formed at the S channel with reduced intensity after a certain amount of dephasing π pulses depending on the

dipolar strength of each spin pair. In other words, the purpose of these π pulses is to cause the effects of the heteronuclear dipolar-induced dephasing accumulate. The major differences between the different REDOR-like methods lie on how these train of π pulses are arranged (cf. Figs. 4.38–4.40).

Figure 4.38 shows three typical equivalent REDOR pulse sequences to use between spin-1/2 (*I*) and quadrupolar spins (*S*). In all the schemes presented, a basic block of two π pulses per rotor period (τ_R) are applied sequentially at $\tau_R/2$ and τ_R on the I channel. A rotor-synchronized spin-echo is then applied to the S channel. In Fig. 4.38A, a simple REDOR experiments is shown, where, for example, I = ^{1}H or ^{19}F and S = ^{27}Al, ^{23}Na, ^{11}B, etc., Fig. 4.38B is equivalent but uses a CP block to polarize an S nucleus if necessary, which may or not be quadrupolar. Fig. 4.38C is a triple resonance CP-REDOR method usually used to measure ^{19}F(I)···^{29}Si(S) dipolar couplings while decoupling during the ^{1}H (I) channel. As the ^{29}Si isotope is a dilute nucleus it should be placed at the S channel to be cross-polarized by ^{1}H. The sequence illustrated in Fig. 4.38C has been used for ^{19}F–^{29}Si CP-REDOR experiments in tandem with ^{19}F–^{29}Si CPMAS experiments by Fyfe *et al.* to study F···Si distances in order to locate the fluoride ion in tetrapropylammonium fluoride silicalite-1 (see Section 2.2) ([TPA]-F-[Si-MFI]).[82] ^{13}C–^{11}B REDOR methods using the sequences shown in Fig. 4.38 were also employed to investigate the relative orientation of SDA in the zeolite channels towards the heteroatoms in two borosilicate zeolites.[174] The cation–sorbate(toluene) interactions were probed by ^{7}Li–^{1}H and ^{23}Na–^{1}H REDOR in LiNa–Y zeolite cavities. A ^{23}Na–^{7}Li REDOR was also used to measure inter-cationic distances in the same material.[171]

6.2.2.1 Understanding the recoupling idea in REDOR

The averaged dipolar Hamiltonian changes its sign every $\tau_R/2$ due to the sinusoidal modulation induced by MAS. Hence, the average Hamiltonian in four half-cycles can be represented by the sequence

$$\hat{\bar{H}}_{IS}^{MAS}, -\hat{\bar{H}}_{IS}^{MAS}, \hat{\bar{H}}_{IS}^{MAS}, -\hat{\bar{H}}_{IS}^{MAS} \qquad [4.40]$$

In the absence of dephasing I-spin π pulses every $\tau_R/2$, the effect of the dipolar interaction is zero and thus an echo signal, S_0, is formed at the end of the REDOR experiment at $2n\tau_R$ (Fig. 4.38) reaching its maximum intensity. However, the sign of the average Hamiltonian can be changed by manipulating the bilinear operator, $\hat{I}_Z\hat{S}_Z$, every time a π pulse is applied

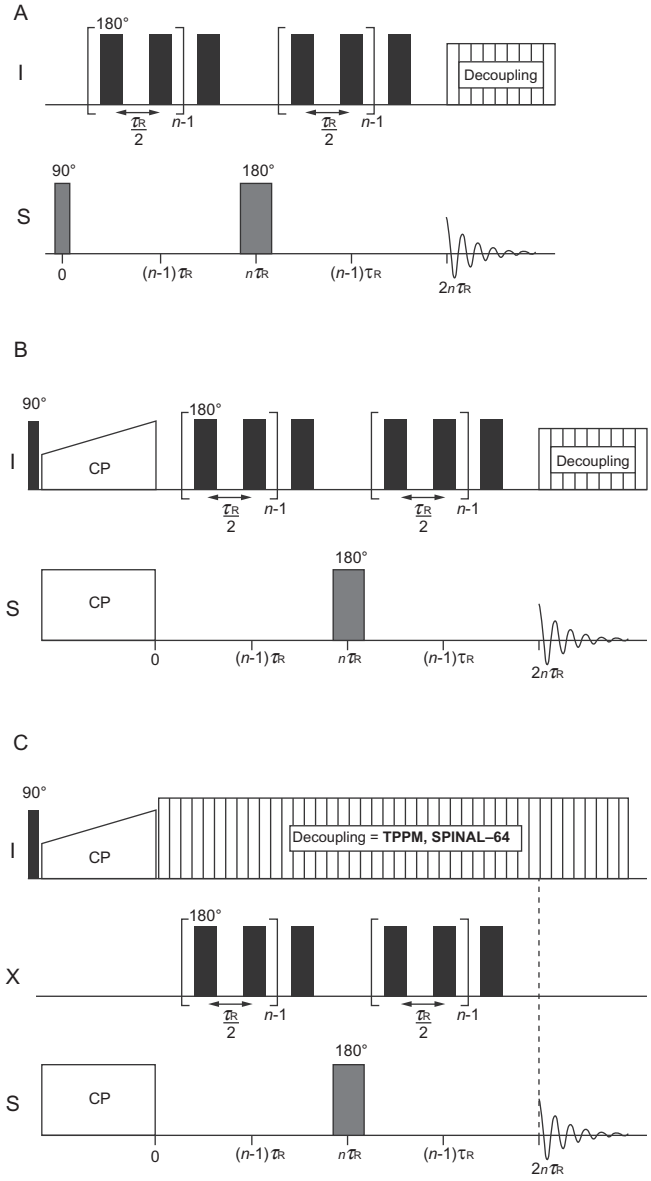

Figure 4.38 Example of NMR pulse sequences of the most commonly used schemes in zeolites. Conventional I–S REDOR sequences (A) without and (B) with CP, where the S channel should be used for the quadrupolar nucleus. (C) CP-REDOR sequence used for a pair of spin-1/2 nuclei to measure I···S internuclear distances with ^{1}H decoupling.

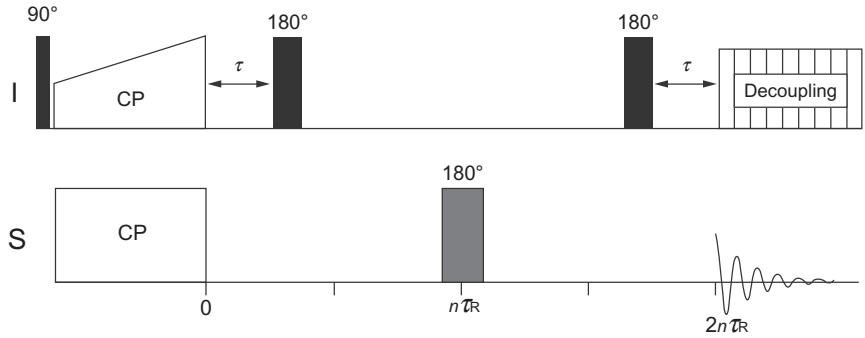

Figure 4.39 I–S CP-REDOR pulse sequence with shifted π pulses. The I shifted π pulses are omitted in the control experiment.

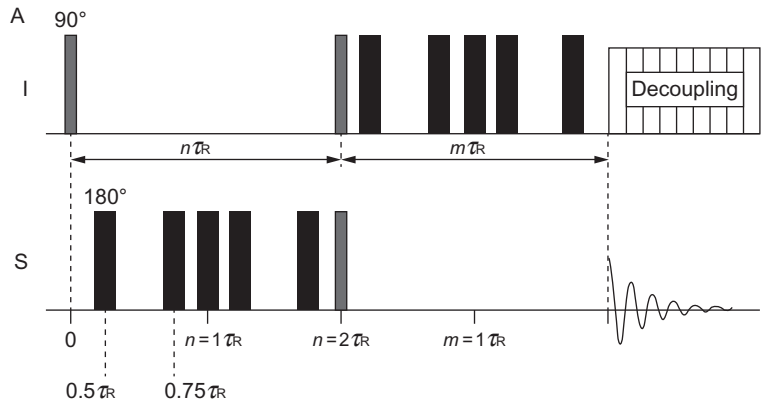

Figure 4.40 I–S TEDOR NMR pulse sequence with dephasing pulses on the observed S-spins before coherence transfer, and on the unobserved I-spins after coherence transfer. A series of experiments are acquired with *n* held constant and *m* varied or vice versa, and the π pulses at the midpoint of each half of the sequence ensure that the chemical shifts are refocused.

on the I channel. Therefore, the combined effect of the rotor-synchronized π pulses applied every $\tau_R/2$ over two rotor periods leads to

$$\hat{\bar{H}}_{IS}^{MAS}, \quad \hat{\bar{H}}_{IS}^{MAS}, \quad \hat{\bar{H}}_{IS}^{MAS}, \quad \hat{\bar{H}}_{IS}^{MAS} \qquad [4.41]$$

in the interaction frame. Under the effect of π pulses, the averaged Hamiltonian will affect the formation of each rotational echoes and at the end of the REDOR experiment a reduced signal, S_R, will result due to the incomplete refocusing caused by the dephasing π pulses. In practice, REDOR consists in two experiments. The first experiment is a control, which omits any π pulses on the I channel and is used to take into account the T2 decay,

producing an S_0 signal. The I-spin π pulses are activated in the second experiment to produce a dipolar dephased signal S_R. The ratio S_R/S_0 is the normalized dipolar dephased signal, and it is used to provide the commonly referred REDOR fraction or normalized REDOR difference [$\Delta S/S_0$, with $\Delta S = (S_0 - S_R)$]. The REDOR fraction is obtained at different numbers of rotor cycles ($N\tau_R$) to yield a buildup REDOR curve. This curve is then analyzed to obtain the internuclear distances.

Using zero-order average dipolar Hamiltonian, the net dephasing angle, $\phi(0, \tau_R)$, caused by the π pulse in one rotor period may be defined as

$$\phi(o, \tau_R) = \int_0^{\tau_R/2} \omega_D(t)\mathrm{d}t - \int_{\tau_R/2}^{\tau_R} \omega_D(t)\mathrm{d}t \qquad [4.42]$$

where the negative sign arises from the I-spin π pulse. The result of Eq. (4.42) yields

$$\phi(0, \tau_R) = \frac{\tau_R \omega_D}{\pi}\sqrt{2}\sin 2\beta \sin\gamma \qquad [4.43]$$

The total phase accumulation after N rotor periods in a REDOR experiments will just multiply Eq. (4.43) by N, which takes the form

$$\phi(0, N\tau_R) = \frac{N\tau_R \omega_D}{\pi}\sqrt{2}\sin 2\beta \sin\gamma \qquad [4.44]$$

The normalized dipolar dephased signal, S_R/S_0, is just given by $S_D(\gamma, \beta, N\tau_R) = \cos[\phi(0, N\tau_R)]$, for an isolate I–S spin pair. For a powder sample, all internuclear orientations (γ and β) need to be considered and summed over. Therefore, the S_R/S_0 signal ratio for a powder is[228,229]

$$S_R/S_0 = (2\pi)\int_\beta\int_\gamma S_D(\gamma, \beta, N\tau_R)\sin\beta \mathrm{d}\gamma \mathrm{d}\beta \qquad [4.45]$$

$S_D(\gamma, \beta, N\tau_R)$ may be expressed as a single cosine term for a spin-1/2 nucleus or a sum of cosine terms with different arguments $(2I - 2n)\phi(0, N\tau_R)$ depending on the nuclear spin I. The general formula for $S_D(\gamma, \beta, N\tau_R)$ may be written as

$$S_D(\gamma, \beta, N\tau_R) = \sum_{n=0}^{I-1/2} \frac{1}{2I - 2n}[(2I - 2n)\cos\phi(0, N\tau_R)] \qquad [4.46]$$

with $\phi(0, N\tau_R)$ given in Eq. (4.44). The $2I - 2n$ argument represents the different population transfers "Δm" affected by the π pulses among the

symmetric transitions available for a given nuclear spin *I*. For example, a spin-1/2 will present only one cosine term, as only the symmetric transition $\Delta m = -1/2 \leftrightarrow 1/2$ is available. For a spin-7/2, four symmetric transitions are available and the sum shown in Eq. (4.46) produces a sum of four cosine terms with arguments $\phi(0, N\tau_R)$, $3\phi(0, N\tau_R)$, $5\phi(0, N\tau_R)$, and $7\phi(0, N\tau_R)$.

The integration of Eq. (4.45), using the adequate expression for the dipolar dephased signal in Eq. (4.46), may be expressed as Bessel function products of the first kind, which are available in Ref. 228 for both spin-1/2 and quadrupolar nuclei. These functions give a universal analytical representation of the REDOR fraction curve and provide a fast approach to fit REDOR curves and therefore determine the internuclear distances.

Another variation of the REDOR/CP-REDOR pulse sequence (Fig. 4.39) has been used to estimate $^{1}H\cdots^{17}O$ internuclear distances of bridging hydroxyl groups in zeolites H–Y and H–ZSM-5 in high magnetic fields.[165,230] This mirror symmetric REDOR pulse sequence involves the continuous shift of two π pulses between $t = 0$ and $t = \tau_R$ as depicted in Fig. 4.39. Hence, the REDOR fraction is measured as a function of *t*. The sequence does not employ a series of increasing *n* rotor periods during the spin-echo delays, which render this sequence less sensitive to T2 decay. Instead, the evolution intervals are kept constant during two rotor periods.

In the TEDOR experiment[231–233] (Fig. 4.40), the π pulses are applied at $\tau_R/4$ and $3\tau_R/4$. As with REDOR, the purpose of these π pulses is to cause the effects of the heteronuclear dipolar-induced dephasing to accumulate during the experiment.

In opposite to REDOR, TEDOR experiment involves coherence transfer; the initial $\pi/2$ pulse is applied to the I spins followed by two π pulses per rotor cycle applied to the S nuclei. This sequence avoids the background signals from uncoupled nuclei, observed in REDOR experiment; as spectrum acquired with a TEDOR sequence shows only resonances of dipole coupled nuclei, the technique may be used as a complement to REDOR. After *n* rotor periods, coherence transfer is achieved by simultaneous $\pi/2$ pulses to both nuclei. The signal of the S nuclei is observed following a further *m* rotor periods where two π pulses per rotor cycle are applied to the I spins. TEDOR curves can be obtained by variation of either *n* with a fixed value of *m* or by holding *n* constant and varying *m*. TEDOR experiments have also been used in zeolite studies to measures various internuclear distances, for example, $^{19}F\cdots^{29}Si$,[82] $^{27}Al\cdots^{29}Si$.[173] Sections 6.2.2.2 – 6.2.2.4 addresses practical issues of REDOR, as this is the most employed recoupling method.

6.2.2.2 REDOR in quadrupolar nuclei

The application of the REDOR (and TEDOR) sequences to quadrupolar nuclei is very limited as the finite rf field strength of the π pulses are usually not strong enough to excite the overall width of the quadrupolar powder pattern, which can be very large. For integer quadrupolar S-spins like ^{2}H, REDOR performs satisfactorily.[234] However, for half integer quadrupolar S-spins with very large $C_Q/\omega_{1,S}$ ratios, REDOR is inefficient due to the extreme difficulty in exciting the frequencies corresponding to the spin transitions of the highest Δm values. In other words, the π pulses, in this case, will cause only a small fraction of the population to change states associated with large Δm transitions. As a consequence, the highest Δm terms in Eq. (4.46) are under-represented leading to a failure in the fitting of the REDOR fraction curve. Figure 4.41 shows the dramatic effect of increasing the C_Q in the numerical simulations of the REDOR fraction curves for a $I=1/2$, $S=3/2$ REDOR experiment using distinct C_Q's for a constant $\omega_{1,S}=50$ kHz.

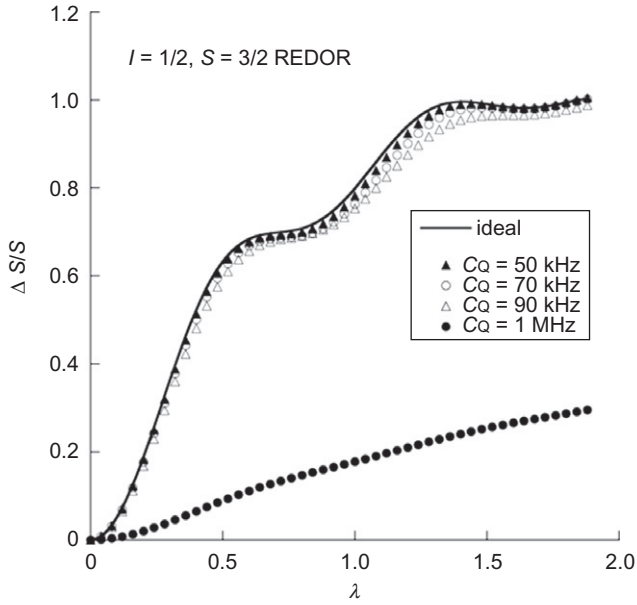

Figure 4.41 Numerical simulation of the REDOR fraction $\Delta S/S_0$ dependence on $\lambda=\gamma_I\gamma_S h/4\pi r^3 N\tau_R$ for the $I=1/2$, $S=3/2$ REDOR experiment. The solid curve labelled "ideal" assumes ideal π pulses. The remaining symbols are from simulations using 50 kHz rf field strengths for the I and S channels, spinning rate of 5 kHz, and quadrupole coupling constants C_Q indicated in the figure. *Reprinted from Ref. 228, Copyright (2005), with permission from Elsevier.*

The excitation problem becomes evident when observing the curve corresponding to the $C_Q = 1$ MHz; the recoupling effect of REDOR loses its dipolar dephasing efficiency. Operating at high magnetic fields may help to decrease the $C_Q/\omega_{1,S}$ ratios and enable the correct use of REDOR. Most of the applications in zeolites have used ^{7}Li, ^{23}Na, and ^{2}H quadrupolar spins in the observation S channel as these nuclei present, in general, very weak C_Q's in zeolites. It is possible to reduce the complexity of manipulating quadrupolar nucleus in REDOR by selectively irradiating the CT inverting the population difference of the quantum states $|1/2>$ and $|-1/2>$ while keeping all other spin states unchanged. However, if the population of higher Δm order are not inverted the extent of dephasing is reduced to $(S+1/2)^{-1}$; for a spin-5/2 only 1/3 the signal of the detected spin will be affected by the dipolar interaction for example.[228,235]

Note that when a quadrupolar nucleus is involved, the S channel (Fig. 4.38) should be used and not the I channel. Owing to the complexity related with pulsing in quadrupolar nuclei, it is always preferable to set spin $> 1/2$ nuclei to the channel containing less pulses (S channel). More robust methods, such as TRAPDOR (transfer of populations in double resonance) and REAPDOR (rotational echo adiabatic passage double resonance), especially developed to handle quadrupolar spins are briefly discussed in the following sections.

6.2.2.3 T2 decay

REDOR is a spin-echo sequence and thus highly sensitive to T2. Sometimes the rate of T2 decay of the resonance of interest is too fast to allow for measurable dipolar dephasings over a reasonable number of N rotor cycles to obtain a suitable REDOR fraction curve. Short T2 leads to a rapid disappearance of the signal, making it even more difficult to get an accurate measurement. In most cases, applying a simultaneous ^{1}H decoupling during the REDOR experiment may increase coherence life-times. Increasing the rf power may help to gain additional resolution and to decrease the rate of T2 relaxation. However, for weak dipolar coupling, a long train of π pulses spanning over several milliseconds may be necessary and if the decoupling power level surpasses a certain level during REDOR dephasing and signal acquisition, the probe can be damaged.

6.2.2.4 rf pulse imperfections

The train of π pulses applied during the spin-echo delays of REDOR must be phase cycled to minimize adverse effects caused by resonance offsets, amplitude imbalance of pulses with differing phases, imperfect phase settings, and pulse

transients. Gullion has showed that it is essential to phase cycle the π pulses during the REDOR experiment using the well-known supercycles XY-4 and XY-8.[228,229] Without any kind of phase cycling on the π pulses, the experiment become extremely dependent on the irradiation offset for these pulses. The effect of the pulse-length misset on the REDOR experiments is also relevant. REDOR tolerates a ±10% pulse-length misset from the ideal π pulse length. Larger missets will result in smaller values of $\Delta S/S_0$.[229]

6.2.3 Transfer of populations in double resonance

TRAPDOR[236–238] (and REAPDOR) sequences have been designed to facilitate recoupling involving spins in Zeeman states other than $|\pm 1/2>$. TRAPDOR exploits this fact making use of a long dephasing pulse, applied to the quadrupolar S-spin during the first half of the rotor-synchronized echo period, while a regular spin-echo experiment is performed on the detected spin-1/2 (*I*) (Fig. 4.42A). To measure dipolar

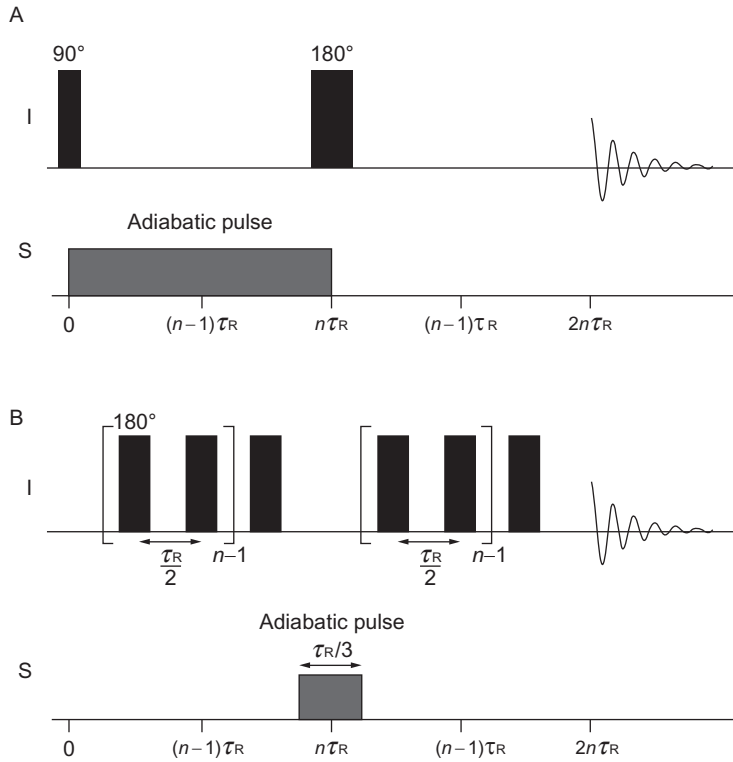

Figure 4.42 Pulse sequences for (A) TRAPDOR and (B) REAPDOR experiments.

coupling, two experiments S_R and S_0 are recorded, as usual, and a dephasing curve is obtained in the same way as in the case of REDOR and REAPDOR. As an example, in a ^{1}H–^{27}Al TRAPDOR experiment, the ^{27}Al irradiation prevents refocusing of the ^{1}H spin-echo, causing a TRAPDOR effect, which translates in a reduced ^{1}H echo signal. The stronger are the ^{1}H–^{27}Al dipolar couplings the stronger become this effect. This TRAPDOR effect relies on the adiabatic passage between the Zeeman eigenstates induced by MAS. As discussed previously, spinning the sample will make the quadrupolar splitting $\omega_Q(t)$ (Eq. 4.21) oscillate between negative and positive values. The population of the high-order Zeeman levels $|\pm m>$ are only efficiently inverted or transferred when $\omega_Q(t)$ passes slowly through the zero-crossings, which is accomplished under an adiabatic regime, $\alpha \gg 1$ (Eq. 4.32). A slow spinning speed further improves the adiabaticity condition. When a given crystallite is close to a zero-crossing, the spin system is, for a short time, in a condition $\omega_{1,S} \gg \Delta\omega_Q$, during which all the Zeeman energy states, involving the different Δm transitions, are mixed and population transfer may occur under adiabatic conditions.

This experiment has been widely used to measure ^{1}H–^{27}Al proximities as a probe to Brønsted acidity in zeolites. A typical ^{1}H–^{27}Al TRADOR experiment uses a ^{27}Al rf field strength of about 50–60 kHz using a MAS rate of ~4 kHz. TRAPDOR depends heavily on the size of the quadrupolar frequency and on its orientation with respect to the dipolar vector orientation. In addition to internuclear distance measurements, the experiment has also been used to indirectly measure the quadrupole coupling constant of the invisible aluminium spins in zeolite HY of the ^{27}Al spin via modulation of the rf offset value.[236] TRAPDOR has several drawbacks, among them, the previous knowledge on the relative orientation between the EFG tensor and the internuclear I–S vector (the Euler angles correlating both interaction frames are not easily accessible by experiments)[228] and the requirement for very long irradiation times and an induced phase shift on the detected spin-1/2.[235] Nevertheless several applications of ^{1}H–^{27}Al TRAPDOR were used to assign ^{1}H MAS NMR resonances of AlOH and bridging OH groups (SiOHAl) in dehydrated zeolite H-Beta[239] and to prove that hydroxyl protons bound to extraframework Al species.[108,240–242] The local structure of adsorbate complexes consisting of TMP coordinated at Lewis acid sites in dehydroxylated zeolite H,Na-Y was investigated by ^{31}P–^{27}Al TRAPDOR NMR experiments.[243] Recently, ^{27}Al–^{14}N TRAPDOR NMR was employed to support that two tetrahedral peaks observed in

the ^{27}Al MAS/3Q-MAS spectra of as-synthesized ZSM-5 are due to aluminium atoms occupying crystallographically inequivalent T sites.[244]

6.2.4 Rotational echo adiabatic passage double resonance

The REAPDOR sequence is a more robust experiment than TRAPDOR, which combines the REDOR concept with the idea of adiabatic passage.[237,245–247] The sequence uses an almost identical disposition of the π pulses in the I-spin-1/2 channel with respect to REDOR (cf. Figs. 4.38 and 4.42). The major difference lies on the presence of a middle adiabatic pulse length of $1/3\tau_R$ at the quadrupolar S-spin. The reason for this particular pulse length is because it corresponds to the optimum number of $\omega_D(t)$ zero-crossings, which enables the maximum fraction of the spins, $\sim$70%, able to change their spin states and thus to effectively contribute to the dipolar dephasing. It was shown by extensive numerical simulations that if sufficient care is taken in the choice of parameters for the REAPDOR experiment, a universal curve can be devised, that is independent on the quadrupolar interaction and its orientation with respect to the internuclear vector. It was shown that a single fit parameter is required to fit the experimental data.[245,246] Universal REAPDOR dephasing curves were derived for S = 1, 3/2, and 5/2 through numerical simulations and experiments.[228,245] A work presented by Kalwei and Koller provides a detailed quantitative comparison of REAPDOR and TRAPDOR experiments using numerical simulations to measure H–Al distances in acid sites of two Zeolites with MFI and IFR framework topologies containing Al sites with C_Q up to 16 MHz. The authors have shown that REAPDOR outperforms TRAPDOR comparing experimental and theoretical dephasing curves.

An overview of applications using the above-mentioned recoupling NMR methods are available in Table 4.8. Full details about REDOR, TRADOR, and REAPDOR may be found in several reviews.[224,228,248]

6.2.5 Other sophisticated NMR methods

2D DQ-homonuclear NMR correlation techniques belong to the family of homonuclear recoupling NMR methods and are among the most useful method to obtain internuclear proximities in solids.[249] The method is based on the excitation of DQ coherences (DQC) during a time τ ($0 \rightarrow \pm 2$), which will evolve during the indirect dimension; subsequently, the DQ coherences are reconverted during a time τ ($\pm 2 \rightarrow 0$), to 0Q coherences

followed by a last 90° read pulse, which converts the signal into observable SQ coherences ($0 \rightarrow -1$). Figure 4.43 shows the coherence transfer pathway of DQ recoupling NMR experiments. The sum of the excitation and reconversion times is called the recoupling time. The intensity of a DQ signal depends on dipolar coupling between the respective interacting pair of nuclei i and j, and for short excitation/reconversion times the signal intensity is

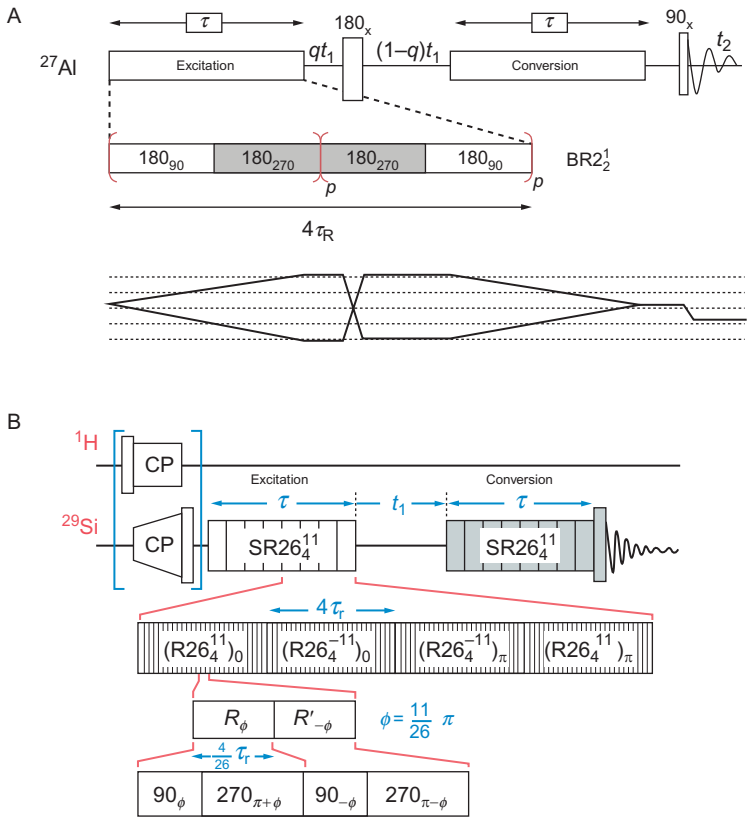

Figure 4.43 Pulse sequences for 2D homonuclear DQMAS NMR experiments. (A) ^{27}Al DQMAS sequence using a symmetry-based $BR2_1^2$ recoupling block for the excitation and reconversion of DQC. All rf pulses depicted in the figure are CT-selective. Adapted from Ref. 182, Copyright (2009), with permission from Elsevier. The selected coherence transfer pathway is shown. The *q* parameter is used to scale all interactions in order to avoid folding of the resonances along the F1 dimension. (B) ^{29}Si DQMAS sequence using a symmetry-based $SR26_4$ recoupling block for the excitation and reconversion of DQC. The DQ recoupling time is denoted by τ. *Reprinted with permission from Ref. 49. Copyright (2005) American Chemical Society.*

proportional to the internuclear proximities between i and j. In practice, the experiment yields a 2D spectrum having an DQ F1 dimension and a SQ F2 dimension. The DQ dimension shows cross peaks of the signals corresponding to the sum of the chemical shifts of the two nuclei involved in the DQC: $\delta_{AB} = \delta_A + \delta_B$ for nuclei of types A and B. In the SQ dimension, the signal splits up into the two single-spin resonances, δ_A and δ_B, so that for $\delta_A \neq \delta_B$, pairs of signals located at $(\delta_A + \delta_B, \delta_A)$ and $(\delta_A + \delta_B, \delta_B)$ are observed in the DQ spectrum as off-diagonal cross peaks, while for AA correlations, a single cross peak is found at $(2\delta_A, \delta_A)$ along the DQ diagonal. That is, nuclear pairs close in space that are chemically inequivalent will appear as a pair of horizontal cross peaks, out of the diagonal while pairs of nuclei, which are chemically equivalent will appear as a single cross peak along the diagonal. If a given nucleus with chemical shift C is not close to a second nucleus D, no cross peak will be observed for CD. Only interacting spin pairs are able to generate DQC.

Figure 4.43A shows a DQ-homonuclear recoupling sequence to probe Al···Al proximities and was designed to recouple homonuclear quadrupolar spin pairs. A supercycled $R2_2^1$ symmetry-based dipolar recoupling block, designated as $BR2_2^1$, is used for excitation and reconversion of DQC. The experiment uses a CT-selective $\pi/2$ and π pulses for ^{27}Al employing a nutation frequency of 4–7 kHz. The rf power level employed during the recoupling blocks are $\nu_{rec} = \nu_R/(2S+1)$. Therefore, for a S spin = 5/2 (27Al) using a $\nu_R = 13.5$ kHz implies that $\nu_{rec} = 2.25$ kHz. This DQ recoupling method have been used to record 2D ^{27}Al DQMAS spectra to reveal detailed spatial proximities among various Al species in dealuminated H–Y zeolites.[126] Recently, the use of the same experiment revealed that Lewis acid sites are in close proximity to Brønsted acid sites, suggesting the existence of Brønsted/Lewis acid synergy in dealuminated H–ZSM-5 and H-MOR zeolites. In addition, the technique demonstrated that six-coordinate $Al(OH)_3$ and five-coordinate $Al(OH)_2^+$ are the preferred extraframework Al species and are in close proximity to four-coordinate framework Al species in the dealuminated zeolites.[127] A more detailed description of the experimental results is included in Section 3.4.

Figure 4.43B shows a ^{29}Si–^{29}Si DQ recoupling pulse sequence, also based on rotor-synchronized RN symmetry that has also been used to solve the crystal structure of a blind test sample of a siliceous zeolite ITQ-4 taking as starting point powder XRD unit cell parameters. The distances for each crystal structure generated during each refinement step were tested against the experimental ^{29}Si···^{29}Si DQ buildup curves data and the solution was the

structure which gave the best fit.[49] Other methods such as ^{29}Si–^{29}Si CSA recoupling have also been used in the context of NMR crystallography to solve the crystal structures of the zeolites. Sigma-2 and ZSM-12. It is shown that the principal values of the ^{29}Si CSA tensors are extremely sensitive to the local structure around each Si atom.[51] These experiments have been incorporated to the NMR crystallography methodology, depicted in more detail in Section 2.2. A ^{27}Al–^{29}Si CP-HETCOR experiment combining CPMG and RAPT strategies for sensitivity enhancement was used to obtain a 2D spectrum of zeolite ZSM-4. This particular pulse sequence increases spectral sensitivity by a factor of ca. 4 and seems the best strategy for the observation of ^{27}Al–^{29}Si spin pairs in aluminosilicates.[163]

7. CONCLUSIONS

Solid state NMR technique gives information on the local structure of the various atoms occurring in zeolites and is very helpful in the structural elucidation, providing complementary information to XRD. In this review, we have shown that NMR spectroscopy is essential for the investigation of the nature of chemical species present in zeolites, which are potential active sites in catalysis. The results summarized in this review highlight the use of advanced solid state NMR techniques newly developed in the characterization of local structures in zeolites over the last years.

ACKNOWLEDGEMENTS

J. A. V.-M. and T. B. acknowledge Spanish MICINN (Projects MAT-2009-14528-C02-01; CTQ-2009-14495), Consolider-Ingenio 2010-Multicat and Generalitat Valenciana (GV PROMETEO/2008/130) for financial support during the elaboration of this chapter. L. M. thanks FCT, QREN, COMPETE, and EU for financial support. The Portuguese NMR Network (RNRMN) is acknowledged. F. C. T. is also acknowledged for other funding, R&D Project PTDC/QUI-QUI/100998/2008. L. M. also greatly acknowledges the Campus de Excelencia Internacional Ad Futurum de la Universidad de Oviedo (FUTTALENT Program).

REFERENCES

1. Armor JN. A history of industrial catalysis. *Catal Today* 2011;**163**:3.
2. Perego C, Caratí A. Zeolites and zeolite-like materials in industrial catalysis. In: Cejka J, Perez-Pariente J, Roth WJ, editors. *Zeolites: from model materials to industrial catalysts*. Trivandrum, India: Transworld Research Network; 2008 p. 357.
3. Anastas PT, Kirchhoff MM, Williamson TC. Catalysis as a foundational pillar of green chemistry. *Appl Catal A Gen* 2001;**221**:3.

4. Centi G, Perathoner S. Environmental catalysis over zeolites. In: Cejka J, Corma A, Zones S, editors. *Zeolites and catalysis: synthesis, reactions and applications*, vol. 2. Weinheim, Germany: WILEY-VCH Verlag GmbH & Co. KGaA; 2010. p. 745.
5. Corma A. From microporous to mesoporous molecular sieve materials and their use in catalysis. *Chem Rev* 1997;**97**:2373.
6. Di Renzo F, Fajula F. Introduction to molecular sieves: trends of evolution of the zeolite community. *Stud Surf Sci Catal* 2005;**157**:1.
7. Derouane EG. *Catalysis for fine chemicals: microporous and mesoporous solid catalysts*. Chichester, UK: John Wiley & Sons Ltd; 2006.
8. Climent MJ, Corma A, Iborra S. Zeolites as catalysts for the synthesis of fine chemicals. In: Cejka J, Corma A, Zones S, editors. *Zeolites and catalysis: synthesis, reactions and applications*, vol. 2. Weinheim, Germany: WILEY-VCH Verlag GmbH & Co. KGaA; 2010. p. 775.
9. Corma A, Diaz-Cabanas MJ, Jorda JL, Martinez C, Moliner M. High-throughput synthesis and catalytic properties of a molecular sieve with 18- and 10-member rings. *Nature* 2006;**443**:842.
10. Sun J, Bonneau C, Cantin A, Corma A, Diaz-Cabanas MJ, Moliner M, Zhang D, Li M, Zou X. The ITQ-37 mesoporous chiral zeolite. *Nature* 2009;**458**:1154.
11. Corma A, Díaz-Cabañas MJ, Jiang J, Afeworki M, Dorset DL, Soled SL, Strohmaier KG. Extra-large pore zeolite (ITQ-40) with the lowest framework density containing double four- and double three-rings. *Proc Natl Acad Sci USA* 2010;**107**:13997.
12. Simancas R, Dari D, Velamazán N, Navarro MT, Cantín A, Jordá JL, Sastre G, Corma A, Rey F. Modular organic structure-directing agents for the synthesis of zeolites. *Science* 2010;**330**:1219.
13. Strohmaier KG, Vaughan DEW. Structure of the first silicate molecular sieve with 18-ring pore openings, ECR-34. *J Am Chem Soc* 2003;**125**:16035.
14. Martinez C, Corma A. Inorganic molecular sieves: Preparation, modification and industrial application in catalytic processes. *Coordin Chem Rev* 2011;**255**:1558.
15. Loewenstein W. The distribution of aluminum in the tetrahedra of silicates and aluminosilicates. *Am Mineral* 1954;**39**:92.
16. Sánchez-Sánchez M, Blasco T, Corma A. On the Use of CHClF2 as a probe of basic sites in zeolites: the host−guest interactions investigated by multinuclear NMR. *J Phys Chem C* 2008;**112**:16961.
17. Sanchez-Sanchez M, Blasco T. Pyrrole as an NMR probe molecule to characterise zeolite basicity. *Chem Commun* 2000;491.
18. http://www.iza-structure.org/databases/.
19. Wilson ST, Lok BM, Messina CA, Cannan TR, Flanigen EM. Aluminophosphate molecular sieves: a new class of microporous crystalline inorganic solids. *J Am Chem Soc* 1982;**104**:1146.
20. Engelhardt G, Michael D. *High-resolution solid-state NMR of silicates and zeolites*. Chichester: Wiley; 1987.
21. Klinowski J. Solid-state NMR studies of molecular sieve catalysts. *Chem Rev* 1991;**91**:1459.
22. Fyfe CA, Feng Y, Grondey H, Kokotailo GT, Gies H. One- and two-dimensional high-resolution solid-state NMR studies of zeolite lattice structures. *Chem Rev* 1991;**91**:1525.
23. Hunger M. Multinuclear solid-state NMR studies of acidic and non-acidic hydroxyl protons in zeolites. *Solid State Nucl Mag* 1996;**6**:1.
24. Jiang Y, Huang J, Dai W, Hunger M. Solid-state nuclear magnetic resonance investigations of the nature, property, and activity of acid sites on solid catalysts. *Solid State Nucl Mag* 2011;**39**:116.

25. Epping JD, Chmelka BF. Nucleation and growth of zeolites and inorganic mesoporous solids: molecular insights from magnetic resonance spectroscopy. *Curr Opin Colloid In* 2006;**11**:81.
26. Zheng A, Huang S-J, Liu S-B, Deng F. Acid properties of solid acid catalysts characterized by solid-state ^{31}P NMR of adsorbed phosphorous probe molecules. *Phys Chem Chem Phys* 2011;**13**:14889.
27. Stepanov A. Results of NMR spectroscopic studies of hydrocarbon conversions on solid acid catalysts in the last 25 years. *Kinet Catal* 2010;**51**:854.
28. Hunger M. In situ flow MAS NMR spectroscopy: state of the art and applications in heterogeneous catalysis. *Prog Nucl Mag Res Sp* 2008;**53**:105.
29. Hunger M, Wang W. Characterization of solid catalysts in the functioning state by nuclear magnetic resonance spectroscopy. In: Bruce CG, Helmut K, editors. *Advances in catalysis* 2006;**50**:149.
30. Hunger M. Applications of in situ spectroscopy in zeolite catalysis. *Micropor Mesopor Mat* 2005;**82**:241.
31. Blasco T. Insights into reaction mechanisms in heterogeneous catalysis revealed by in situ NMR spectroscopy. *Chem Soc Rev* 2010;**39**:4685.
32. Ivanova II, Kolyagin YG. Impact of in situ MAS NMR techniques to the understanding of the mechanisms of zeolite catalyzed reactions. *Chem Soc Rev* 2010;**39**:5018.
33. Haw JF. Zeolite acid strength and reaction mechanisms in catalysis. *Phys Chem Chem Phys* 2002;**4**:5431.
34. Fyfe CA, Brouwer DH. Optimization, standardization, and testing of a New NMR method for the determination of zeolite host−organic guest crystal structures. *J Am Chem Soc* 2006;**128**:11860.
35. Sánchez-Sánchez M, Blasco T. Investigation on the nature of the adsorption sites of pyrrole in alkali-exchanged zeolite Y by nuclear magnetic resonance in combination with infrared spectroscopy. *J Am Chem Soc* 2002;**124**:3443.
36. Lim KH, Grey CP. Characterization of extra-framework cation positions in zeolites NaX and NaY with very fast ^{23}Na MAS and multiple quantum MAS NMR spectroscopy. *J Am Chem Soc* 2000;**122**:9768.
37. Fyfe CA, Feng Y, Grondey H. Evaluation of chemical shift—structure correlations from a combination of X-ray diffraction and 2D MAS NMR data for highly siliceous zeolite frameworks. *Microporous Mater* 1993;**1**:401.
38. Fyfe CA, Gies H, Feng Y. Three-dimensional lattice connectivities from two-dimensional high-resolution solid-state NMR. Silicon-29 magic angle spinning NMR investigation of the silicate lattice of zeolite ZSM-39 (Dodecasil 3C). *J Am Chem Soc* 1989;**111**:7702.
39. Fyfe CA, Strobl H, Kokotailo GT, Pasztor CT, Barlow GE, Bradley S. Correlations between lattice structures of zeolites and their ^{29}Si MAS NMR Spectra: zeolites KZ-2, ZSM-12, and Beta. *Zeolites* 1988;**8**:132.
40. Fyfe CA, Grondey H, Feng Y, Kokotailo GT. Natural-abundance two-dimensional ^{29}Si MAS NMR investigation of the three-dimensional bonding connectivities in the zeolite catalyst ZSM-5. *J Am Chem Soc* 1990;**112**:8812.
41. Fyfe CA, Grondey H, Feng Y, Kokotailo GT. Investigation of the three-dimensional SiOSi connectivities in the monoclinic form of zeolite ZSM-5 by two-dimensional ^{29}Si INADEQUATE experiments. *Chem Phys Lett* 1990;**173**:211.
42. Fyfe CA, Gies H, Feng Y, Grondey H. Two-dimensional ^{29}Si MAS n.m.r. Investigation of the three-dimensional structure of zeolite DD3R. *Zeolites* 1990;**10**:278.
43. Kolodziejski W, Barrie PJ, He H, Klinowski J. Two-dimensional J-scaled ^{29}Si NMR COSY of highly siliceous mordenite. *J Chem Soc Chem Commun* 1991;961.

44. Fyfe CA, Feng Y, Grondey H, Kokotailo GT, Mar A. Natural abundance, two-dimensional silicon-29 MAS NMR investigation of the three-dimensional bonding connectivities in the high- and low-temperature forms of zeolite ZSM-11. *J Phys Chem* 1991;**95**:3747.
45. Fyfe CA, Grondey H, Feng Y, Kokotailo GT, Ernst S, Weitkamp J. Two-dimensional solid-state 29Si nmr Investigation of the three-dimensional bonding connectivities and structure of zeolite ZSM-23. *Zeolites* 1992;**12**:50.
46. Morris RE, Weigel SJ, Henson NJ, Bull LM, Janicke MT, Chmelka BF, Cheetham AK. A synchrotron X-ray diffraction, neutron diffraction, ^{29}Si MAS-NMR, and computational study of the siliceous form of zeolite ferrierite. *J Am Chem Soc* 1994;**116**:11849.
47. Brouwer DH, Kristiansen PE, Fyfe CA, Levitt MH. Symmetry-based ^{29}Si dipolar recoupling magic angle spinning NMR spectroscopy: a new method for investigating three-dimensional structures of zeolite frameworks. *J Am Chem Soc* 2005;**127**:542.
48. Shayib RM, George NC, Seshadri R, Burton AW, Zones SI, Chmelka BF. Structure-directing roles and interactions of fluoride and organocations with siliceous zeolite frameworks. *J Am Chem Soc* 2011;**133**:18728.
49. Brouwer DH, Darton RJ, Morris RE, Levitt MH. A solid-state NMR method for solution of zeolite crystal structures. *J Am Chem Soc* 2005;**127**:10365.
50. Brouwer DH. NMR crystallography of zeolites: refinement of an NMR-solved crystal structure using ab initio calculations of ^{29}Si chemical shift tensors. *J Am Chem Soc* 2008;**130**:6306.
51. Brouwer DH, Enright GD. Probing local structure in zeolite frameworks: ultrahigh-field NMR measurements and accurate first-principles calculations of zeolite 29Si magnetic shielding tensors. *J Am Chem Soc* 2008;**130**:3095.
52. Brouwer DH, Moudrakovski IL, Darton RJ, Morris RE. Comparing quantum-chemical calculation methods for structural investigation of zeolite crystal structures by solid-state NMR spectroscopy. *Mag Reson Chem* 2010;**48**:S113.
53. Cadars S, Brouwer DH, Chmelka BF. Probing local structures of siliceous zeolite frameworks by solid-state NMR and first-principles calculations of ^{29}Si-O-^{29}Si scalar couplings. *Phys Chem Chem Phys* 2009;**11**:1825.
54. Rojas A, Gómez-Hortigüela L, Camblor MA. Zeolite structure direction by simple Bis (methylimidazolium) cations: the effect of the spacer length on structure direction and of the imidazolium ring orientation on the ^{19}F NMR resonances. *J Am Chem Soc* 2012;**134**:3845.
55. Moliner M, Gonzalez J, Portilla MT, Willhammar T, Rey F, Llopis FJ, Zou X, Corma A. A new aluminosilicate molecular sieve with a system of pores between those of ZSM-5 and beta zeolite. *J Am Chem Soc* 2011;**133**:9497.
56. Jiang J, Jorda JL, Yu J, Baumes LA, Mugnaioli E, Diaz-Cabanas MJ, Kolbe U, Corma A. Synthesis and structure determination of the hierarchical meso-microporous zeolite ITQ-43. *Science* 2011;**333**:1131.
57. Jiang J, Jorda JL, Diaz-Cabanas MJ, Yu J, Corma A. The synthesis of an extra-large-pore zeolite with double three-ring building units and a Low framework density. *Angew Chem Int Ed* 2010;**49**:4986.
58. Blasco T, Corma A, Díaz-Cabañas MJ, Rey F, Vidal-Moya JA, Zicovich-Wilson CM. Preferential location of Ge in the double four-membered ring units of ITQ-7 zeolite. *J Phys Chem B* 2002;**106**:2634.
59. Sastre G, Vidal-Moya JA, Blasco T, Rius J, Jordá JL, Navarro MT, Rey F, Corma A. Preferential location of Ge atoms in polymorph C of beta zeolite (ITQ-17) and their structure-directing effect: a computational, XRD, and NMR spectroscopic study. *Angew Chem Int Ed* 2002;**114**:4916.

60. Blasco T, Corma A, Díaz-Cabañas MJ, Rey F, Rius J, Sastre G, Vidal-Moya JA. Synthesis, characterization, and framework heteroatom localization in ITQ-21. *J Am Chem Soc* 2004;**126**:13414.
61. Vidal-Moya JA, Blasco T, Rey F, Corma A, Puche M. Distribution of fluorine and germanium in a new zeolite structure ITQ-13 studied by ^{19}F nuclear magnetic resonance. *Chem Mater* 2003;**15**:3961.
62. Caullet P, Guth JL, Hazm J, Lamblin JM, Gies H. Synthesis, characterization and crystal structure of the new clathrasil phase octadecasil. *Eur J Solid State Inorg Chem* 1991;**28**:345.
63. Koller H, Wölker A, Villaescusa LA, Díaz-Cabañas MJ, Valencia S, Camblor MA. Five-coordinate silicon in high-silica zeolites. *J Am Chem Soc* 1999;**121**:3368.
64. Vidal-Moya JA, Blasco T, Corma A, Navarro MT, Rey F. The investigation of beta polymorphs by ^{19}F nuclear magnetic resonance. *Stud Surf Sci Catal* 2004;**154**:1289.
65. Barrett PA, Boix T, Puche M, Olson DH, Jordan E, Koller H, Camblor MA. ITQ-12: a new microporous silica polymorph potentially useful for light hydrocarbon separations. *Chem Commun* 2003;**2114**.
66. Corma A, Rey F, Rius J, Sabater MJ, Valencia S. Supramolecular self-assembled molecules as organic directing agent for synthesis of zeolites. *Nature* 2004;**431**:287.
67. Corma A, Diaz-Cabanas MJ, Jorda JL, Rey F, Sastre G, Strohmaier KG. A zeolitic structure (ITQ-34) with connected 9- and 10-ring channels obtained with phosphonium cations as structure directing agents. *J Am Chem Soc* 2008;**130**:16482.
68. Cantín A, Corma A, Diaz-Cabanas MJ, Jordá JL, Moliner M. Rational design and HT techniques allow the synthesis of new IWR zeolite polymorphs. *J Am Chem Soc* 2006;**128**:4216.
69. Dorset DL, Kennedy GJ, Strohmaier KG, Diaz-Cabañas MJ, Rey F, Corma A. P-derived organic cations as structure-directing agents: synthesis of a high-silica zeolite (ITQ-27) with a Two-dimensional 12-ring channel system. *J Am Chem Soc* 2006;**128**:8862.
70. Camblor MA, Barrett PA, Díaz-Cabañas Ma-J, Villaescusa LA, Puche M, Boix T, et al. High silica zeolites with three-dimensional systems of large pore channels. *Micropor Mesopor Mat* 2001;**48**:11.
71. Fyfe CA, Brouwer DH, Lewis AR, Villaescusa LA, Morris RE. Combined solid state NMR and X-ray diffraction investigation of the local structure of the five-coordinate silicon in fluoride-containing as-synthesized STF zeolite. *J Am Chem Soc* 2002;**124**:7770.
72. Paillaud J-L, Harbuzaru B, Patarin J. Synthesis and characterisation of as-synthesised Mu-26, a zeolitic material with the STF framework topology. *Micropor Mesopor Mat* 2007;**105**:89.
73. Rojas A, Gomez-Hortiguela L, Camblor MA. Zeolite structure direction by simple bis (methylimidazolium) cations: the effect of the spacer length on structure direction and of the imidazolium ring orientation on the F-19 NMR resonances. *J Am Chem Soc* 2012;**134**:3845.
74. Koller H, Wölker A, Eckert H, Panz C, Behrens P. Five-coordinate silicon in zeolites: probing $SiO_{4/2}F$-sites in nonasil and ZSM-5 with ^{29}Si solid-state NMR spectroscopy. *Angew Chem Int Ed*. 1997;**36**:2823.
75. Cantín A, Corma A, Leiva S, Rey F, Rius J, Valencia S. Synthesis and structure of the bidimensional zeolite ITQ-32 with small and large pores. *J Am Chem Soc* 2005;**127**:11560.
76. Villaescusa LA, Bull I, Wheatley PS, Lightfoot P, Morris RE. The location of fluoride and organic guests in 'as-made' pure silica zeolites FER and CHA. *J Mater Chem* 2003;**13**:1978.

77. Wang Y, Song J, Gies H. The substitution of germanium for silicon in AST-type zeolite. *Solid State Sci* 2003;**5**:1421.
78. Attfield MP, Catlow CRA, Sokol AA. True structure of trigonal bipyramidal SiO_4F-species in siliceous zeolites. *Chem Mater* 2001;**13**:4708.
79. Darton RJ, Brouwer DH, Fyfe CA, Villaescusa LA, Morris RE. Solid-state NMR studies of the fluoride-containing zeolite SSZ-44. *Chem Mater* 2004;**16**:600.
80. Fyfe CA, Lewis AR, Chézeau JM, Grondey H. $^{19}F/^{29}Si$ Distance determinations in fluoride-containing octadecasil from solid-state NMR measurements. *J Am Chem Soc* 1997;**119**:12210.
81. Bertani P, Raya J, Hirschinger J. 19F/29Si Rotational-echo double-resonance and heteronuclear spin counting under fast magic-angle spinning in fluoride-containing octadecasil. *Solid State Nucl Mag* 2002;**22**:188.
82. Fyfe CA, Brouwer DH, Lewis AR, Chézeau J-M. Location of the fluoride Ion in tetrapropylammonium fluoride silicalite-1 determined by $^{1}H/^{19}F/^{29}Si$ triple resonance CP, REDOR, and TEDOR NMR experiments. *J Am Chem Soc* 2001;**123**:6882.
83. Deng F, Yue Y, Ye C. Observation of nonframework Al species in zeolite β by solid-state NMR spectroscopy. *J Phys Chem B* 1998;**102**:5252–6.
84. Kentgens APM, Iuga D, Kalwei M, Koller H. Direct observation of Brønsted acidic sites in dehydrated zeolite H-ZSM5 using DFS-enhanced ^{27}Al MQMAS NMR spectroscopy. *J Am Chem Soc* 2001;**123**:2925.
85. Fyfe CA, Bretherton JL, Lam LY. Detection of the 'invisible aluminium' and characterisation of the multiple aluminium environments in zeolite USY by high-field solid-state NMR. *Chem Commun* 2000;1575.
86. Fyfe CA, Bretherton JL, Lam LY. Solid-state NMR detection, characterization, and quantification of the multiple aluminum environments in US-Y catalysts by ^{27}Al MAS and MQMAS experiments at very high field. *J Am Chem Soc* 2001;**123**:5285.
87. Jiao J, Kanellopoulos J, Wang W, Ray SS, Foerster H, Freude D, et al. Characterization of framework and extra-framework aluminum species in non-hydrated zeolites Y by ^{27}Al spin-echo, high-speed MAS, and MQMAS NMR spectroscopy at B0 = 9.4 To 17.6 T. *Phys Chem Chem Phys* 2005;**7**:3221.
88. Li S, Zheng A, Su Y, Fang H, Shen W, Yu Z, et al. Extra-framework aluminium species in hydrated faujasite zeolite as investigated by two-dimensional solid-state NMR spectroscopy and theoretical calculations. *Phys Chem Chem Phys* 2010;**12**:3895.
89. Pinar AB, Márquez-Álvarez C, Grande-Casas M, Pérez-Pariente J. Template-controlled acidity and catalytic activity of ferrierite crystals. *J Catal* 2009;**263**:258.
90. Dwyer J, Karim K, Smith WJ, Thompson NE, Harris RK, Apperley DC. A comparison of siliceous faujasitic zeolites produced by direct synthesis or by secondary synthesis. *J Phys Chem* 1991;**95**:8826.
91. García-Pérez E, Dubbeldam D, Liu B, Smit B, Calero S. A computational method to characterize framework aluminum in aluminosilicates. *Angew Chem Int Ed* 2007;**46**:276.
92. Bodart P, Nagy JB, Debras G, Gabelica Z, Jacobs PA. Aluminum siting in mordenite and dealumination mechanism. *J Phys Chem* 1986;**90**:5183.
93. Korányi TI, Nagy JB. Distribution of aluminum in different periodical building units of MOR and BEA zeolites. *J Phys Chem B* 2005;**109**:15791.
94. Korányi TI. Distribution of aluminum in the periodical building units of faujasites. *J Phys Chem C* 2007;**111**:2520.
95. Chao K-j, Shy D-s, Sheu S-p, Lin C-f. Study of Si and Al ordering in the framework of siliceous cubic and hexagonal faujasite zeolites. *Microporous Mater* 1994;**2**:91.
96. Feijen EJP, Lievens JL, Martens JA, Grobet PJ, Jacobs PA. Silicon and aluminum ordering in frameworks of FAU and EMT aluminosilicate zeolites crystallized in the presence of crown ethers. *J Phys Chem* 1996;**100**:4970.

97. Lippmaa E, Samoson A, Magi M. High-resolution aluminum-27 NMR of aluminosilicates. *J Am Chem Soc* 1986;**108**:1730.
98. Sklenak S, Dědeček J, Li C, Wichterlová B, Gábová V, Sierka M, et al. Aluminum siting in silicon-rich zeolite frameworks: a combined high-resolution 27Al NMR spectroscopy and quantum mechanics/molecular mechanics study of ZSM-5. *Angew Chem Int Ed* 2007;**46**:7286.
99. Sklenak S, Dědeček J, Li C, Wichterlova B, Gabova V, Sierka M, et al. Aluminium siting in the ZSM-5 framework by combination of high resolution ^{27}Al NMR and DFT/MM calculations. *Phys Chem Chem Phys* 2009;**11**:1237.
100. Dědeček J, Sklenak S, Li C, Gao F, Brus Ji, Zhu Q, et al. Effect of Al/Si substitutions and silanol nests on the local geometry of Si and Al framework sites in silicone-rich zeolites: a combined high resolution ^{27}Al and ^{29}Si NMR and density functional theory/molecular mechanics study. *J Phys Chem C* 2009;**113**:14454.
101. Dědeček J, Lucero MJ, Li C, Gao F, Klein P, Urbanova M, et al. Complex analysis of the aluminum siting in the framework of silicon-rich zeolites. A case study on ferrierites. *J Phys Chem C* 2011;**115**:11056.
102. Abraham A, Lee S-H, Shin C-H, Bong Hong S, Prins R, van Bokhoven JA. Influence of framework silicon to aluminium ratio on aluminium coordination and distribution in zeolite beta investigated by ^{27}Al MAS and ^{27}Al MQ MAS NMR. *Phys Chem Chem Phys* 2004;**6**:3031–6.
103. van Bokhoven JA, Koningsberger DC, Kunkeler P, van Bekkum H, Kentgens APM. Stepwise dealumination of zeolite βeta at specific T-sites observed with ^{27}Al MAS and ^{27}Al MQ MAS NMR. *J Am Chem Soc* 2000;**122**:12842.
104. Sarv P, Wichterlová B, Čejka J. Multinuclear MQMAS NMR study of NH_4/Na-ferrierites. *J Phys Chem B* 1998;**102**:1372.
105. Sarv P, Fernandez C, Amoureux J-P, Keskinen K. Distribution of tetrahedral aluminium sites in ZSM-5 type zeolites: an 27Al (multiquantum) magic angle spinning NMR study. *J Phys Chem* 1996;**100**:19223.
106. Dědeček J, Sklenak S, Li C, Wichterlová B, Gábová V, Brus Ji, et al. Effect of Al−Si−Al and Al−Si−Si−Al pairs in the ZSM-5 zeolite framework on the ^{27}Al NMR spectra. A combined high-resolution 27Al NMR and DFT/MM study. *J Phys Chem C* 2009;**113**:1447.
107. Bourgeat-Lami E, Massiani P, Di Renzo F, Espiau P, Fajula F, Des Courières T. Study of the state of aluminium in zeolite-β. *Appl Catal* 1991;**72**:139.
108. Beck LW, Haw JF. Multinuclear NMR studies reveal a complex acid function for zeolite beta. *J Phys Chem* 1995;**99**:1076.
109. de Ménorval LC, Buckermann W, Figueras F, Fajula F. Influence of adsorbed molecules on the configuration of framework aluminum atoms in acidic zeolite-β. A *2*7Al MAS NMR study. *J Phys Chem* 1996;**100**:465.
110. Jia C, Massiani P, Barthomeuf D. Characterization by infrared and nuclear magnetic resonance spectroscopies of calcined beta zeolite. *J Chem Soc Faraday Trans* 1993;**89**:3659.
111. Woolery GL, Kuehl GH, Timken HC, Chester AW, Vartuli JC. On the nature of framework Brønsted and Lewis acid sites in ZSM-5. *Zeolites* 1997;**19**:288.
112. Wouters BH, Chen TH, Grobet PJ. Reversible tetrahedral−octahedral framework aluminum transformation in zeolite Y. *J Am Chem Soc* 1998;**120**:11419.
113. Wouters BH, Chen T, Grobet PJ. Steaming of zeolite Y: formation of transient Al species. *J Phys Chem B* 2001;**105**:1135.
114. Omegna A, van Bokhoven JA, Prins R. Flexible aluminum coordination in alumino−silicates. Structure of zeolite H−USY and amorphous silica−alumina. *J Phys Chem B* 2003;**107**:8854.
115. Kletnieks PW, Ehresmann JO, Nicholas JB, Haw JF. Adsorbate clustering and proton transfer in zeolites: NMR spectroscopy and theory. *Chem Phys Chem* 2006;**7**:114.

116. Jiao J, Kanellopoulos J, Behera B, Jiang Y, Huang J, Reddy Marthala VR, et al. Effects of adsorbate molecules on the quadrupolar interaction of framework aluminum atoms in dehydrated zeolite H, Na-Y. *J Phys Chem B* 2006;**110**:13812.
117. Huang J, Jiang Y, Marthala VRR, Thomas B, Romanova E, Hunger M. Characterization and acidic properties of aluminum-exchanged zeolites X and Y. *J Phys Chem C* 2008;**112**:3811.
118. Kunkeler PJ, Zuurdeeg BJ, van der Waal JC, van Bokhoven JA, Koningsberger DC, van Bekkum H. Zeolite beta: the relationship between calcination procedure, aluminum configuration, and Lewis acidity. *J Catal* 1998;**180**:234.
119. van Bokhoven JA, van der Eerden AMJ, Koningsberger DC. Three-coordinate aluminum in zeolites observed with in situ X-ray absorption near-edge spectroscopy at the Al K-edge: flexibility of aluminum coordinations in zeolites. *J Am Chem Soc* 2003;**125**:7435.
120. Carvajal R, Chu P-J, Lunsford JH. The role of polyvalent cations in developing strong acidity: a study of lanthanum-exchanged zeolites. *J Catal* 1990;**125**:123.
121. Corma A, Fornés V, Rey F. Extraction of extra-framework aluminium in ultrastable Y zeolites by $(NH_4)_2SiF_6$ treatments: I. physicochemical characterization. *Appl Catal* 1990;**59**:267.
122. Corma A. Inorganic solid acids and their Use in acid-catalyzed hydrocarbon reactions. *Chem Rev* 1995;**95**:559–614.
123. Shannon RD, Gardner KH, Staley RH, Bergeret G, Gallezot P, Auroux A. The nature of the nonframework aluminum species formed during the dehydroxylation of H-Y. *J Phys Chem* 1985;**89**:4778.
124. Li S, Zheng A, Su Y, Zhang H, Chen L, Yang J, Ye C, Deng F. Brønsted/lewis acid synergy in dealuminated HY zeolite: a combined solid-state NMR and theoretical calculation study. *J Am Chem Soc* 2007;**129**:11161.
125. Li S, Huang S-J, Shen W, Zhang H, Fang H, Zheng A, Liu S, Deng F. Probing the spatial proximities among acid sites in dealuminated H-Y zeolite by solid-state NMR spectroscopy. *J Phys Chem C* 2008;**112**:14486.
126. Yu Z, Zheng A, Wang Q, Chen L, Xu J, Amoureux J-P, Deng F. Insights into the dealumination of zeolite HY revealed by sensitivity-enhanced ^{27}Al DQ-MAS NMR spectroscopy at high field. *Angew Chem Int Ed* 2010;**49**:8657.
127. Yu Z, Li S, Wang Q, Zheng A, Jun X, Chen L, et al. Brønsted/lewis acid synergy in H–ZSM-5 and H–MOR zeolites studied by ^{1}H and ^{27}Al DQ-MAS solid-state NMR spectroscopy. *J Phys Chem C* 2011;**115**:22320.
128. Fild C, Shantz DF, Lobo RF, Koller H. Cation-induced transformation of boron-coordination in zeolites. *Phys Chem Chem Phys* 2000;**2**:3091.
129. Koller H, Fild C, Lobo RF. Variable anchoring of boron in zeolite beta. *Micropor Mesopor Mat* 2005;**79**:215–24.
130. Hwang S-J, Chen C-Y, Zones SI. Boron sites in borosilicate zeolites at various stages of hydration studied by solid state NMR spectroscopy. *J Phys Chem B* 2004;**108**:18535.
131. Tong HTT, Koller H. Control of Al for B framework substitution in zeolite beta by counterions. *Micropor Mesopor Mat* 2012;**148**:80.
132. Reddy Marthala VR, Wang W, Jiao J, Jiang Y, Huang J, Hunger M. Effect of probe molecules with different proton affinities on the coordination of boron atoms in dehydrated zeolite H-[B]ZSM-5. *Micropor Mesopor Mat* 2007;**99**:91.
133. Lezcano-Gonzalez I, Vidal-Moya A, Boronat M, Blasco T, Corma A. Modelling active sites for the Beckmann rearrangement reaction in boron-containing zeolites and their interaction with probe molecules. *Phys Chem Chem Phys* 2010;**12**:6396.
134. Hunger M. Catalytically active sites: generation and characterization. In: Cejka J, Corma A, Zones S, editors. *Zeolites and catalysis: synthesis, reactions and applications*, vol. 2. Weinheim, Germany: WILEY-VCH Verlag GmbH & Co. KGaA; 2010. p. 493.

135. Koller H, Lobo RF, Burkett SL, Davis ME. SiO-. . .HOSi hydrogen bonds in as-synthesized high-silica zeolites. *J Phys Chem* 1995;**99**:12588.
136. Mafra L, Klinowski J. Molecular sieves: crystalline systems and advanced solid-state NMR techniques for the study of molecular sieves. In: Harris RK, Wasylishen, RE, editor-in-chief. *Encyclopedia of magnetic resonance*. Chichester: John Wiley, 2012 [in press].
137. Chae SA, Han OH, Lee SY. Simulation of ^{27}Al MQMAS NMR spectra of mordenites using point charge model with first layer only and multiple layers of atoms. *Bull Kor Chem Soc* 2007;**28**:2069.
138. Abraham A, Hong SB, Prins R, van Bokhoven JA. Stability of zeolite MCM-22 with varying SiAl ratios: a solid-state NMR investigation. *Stud Surf Sci Catal* 2005;679.
139. Chen JX, Chen TH, Guan NJ, Wang JZ. Dealumination process of zeolite omega monitored by ^{27}Al 3QMAS NMR spectroscopy. *Catal Today* 2004;627.
140. Zhuang J, Ma D, Yang G, Yan Z, Liu X, Liu X, et al. Solid-state MAS NMR studies on the hydrothermal stability of the zeolite catalysts for residual oil selective catalytic cracking. *J Catal* 2004;**228**:234.
141. Altwasser S, Jiao J, Steuernagel S, Weitkamp J, Hunger M. Elucidating the dealumination mechanism of zeolite H-Y by solid-state NMR spectroscopy. *Stud Surf Sci Catal* 2004;1212.
142. Gore KU, Abraham A, Hegde SG, Kumar R, Amoureux J-P, Ganapathy S. ^{29}Si and ^{27}Al MAS/3Q-MAS NMR studies of high silica USY zeolites. *J Phys Chem B* 2002;**106**:6115.
143. Quoineaud AA, Montouillout V, Gautier S, Lacombe S, Fernandez C. Characterization and quantification of aluminum species in zeolites using high resolution ^{27}Al solid state NMR. *Stud Surf Sci Catal* 2002;391.
144. Yan Z, Ma D, Zhuang J, Liu X, Liu X, Han X, et al. On the acid-dealumination of USY zeolite: a solid state NMR investigation. *J Mol Catal A Chem* 2003;**194**:153.
145. Ehresmann JO, Wang W, Herreros B, Luigi D-P, Venkatraman TN, Song W, et al. Theoretical and experimental investigation of the effect of proton transfer on the 27Al MAS NMR line shapes of zeolite−adsorbate complexes: an independent measure of solid acid strength. *J Am Chem Soc* 2002;**124**:10868.
146. Chen T-H, Wouters BH, Grobet PJ. Aluminium coordinations in zeolite mordenite by ^{27}Al multiple quantum MAS NMR spectroscopy. *Eur J Inorg Chem* 2000;**2000**:281.
147. Lentz P, Carvalho AP, Delevoye L, Fernandez C, Amoureux JP, Nagy JB. Characterization of offretite during hydrothermal treatment by high-resolution solid-state ^{29}Si magic angle spinning NMR and ^{27}Al triple-quantum magic angle spinning NMR spectroscopy. *Magn Reson Chem* 1999;**37**:S55.
148. Gueudré L, Quoineaud AA, Pirngruber G, Leflaive P. Evidence of multiple cation site occupation in zeolite NaY with high Si/Al ratio. *J Phys Chem C* 2008;**112**:10899.
149. Hunger M, Sarv P, Samoson A. Two-dimensional triple-quantum ^{23}Na MAS NMR spectroscopy of sodium cations in dehydrated zeolites. *Solid State Nucl Mag* 1997;**9**:115.
150. Ernst H, Freude D, Kanellopoulos J, Loeser T, Prochnow D, Schneider D. Has ^{17}O NMR been established as a spectroscopic tool for zeolite characterization? *Stud Surf Sci Catal* 2004;**154**:1173.
151. Freude D, Loeser T, Michel D, Pingel U, Prochnow D. 17O NMR studies of low silicate zeolites. *Solid State Nucl Mag* 2001;**20**:46.
152. Amoureux JP, Bauer F, Ernst H, Fernandez C, Freude D, Michel D, et al. ^{17}O Multiple-quantum and ^{1}H MAS NMR studies of zeolite ZSM-5. *Chem Phys Lett* 1998;**285**:10.
153. Readman JE, Kim N, Ziliox M, Grey CP. ^{17}O MQMAS NMR studies of Na-A and Ca-A. *Chem Commun* 2002;2808.

154. Amoureux JP, Fernandez C. Triple, quintuple and higher order multiple quantum MAS NMR of quadrupolar nuclei. *Solid State Nucl Mag* 1998;**10**:211.
155. Brown SP, Ashbrook SE, Wimperis S. 27Al Multiple-quantum magic angle spinning NMR study of the thermal transformation between the microporous aluminum methylphosphonates AlMePO-beta and AlMePO-alpha. *J Phys Chem B* 1999;**103**:812.
156. Schneider D, Toufar H, Samoson A, Freude D. ^{17}O DOR and other solid-state NMR studies concerning the basic properties of zeolites LSX. *Solid State Nucl Mag* 2009;**35**:87–92.
157. Feuerstein M, Hunger M, Engelhardt G, Amoureux JP. Characterisation of sodium cations in dehydrated zeolite NaX by ^{23}Na NMR spectroscopy. *Solid State Nucl Mag* 1996;**7**:95.
158. Hunger M, Engelhardt G, Weitkamp J. Solid-state ^{23}Na, ^{139}La, ^{27}Al and ^{29}Si nuclear magnetic resonance spectroscopic investigations of cation location and migration in zeolites LaNaY. *Microporous Mater* 1995;**3**:497.
159. Koller H, Overweg AR, van Santen RA, de Haan JW. ^{13}C and ^{23}Na solid-state NMR study on zeolite Y loaded with $Mo(CO)_6$. *J Phys Chem B* 1997;**101**:1754.
160. Kovalakova M, Grobet PJ. Double rotation ^{27}Al NMR in molecular sieves. *Appl Magn Reson* 1996;**10**:447.
161. Rawal A, Smith BJ, Athens GL, Edwards CL, Roberts L, Gupta V, et al. Molecular silicate and aluminate species in anhydrous and hydrated cements. *J Am Chem Soc* 2010;**132**:7321.
162. Wiench JW, Lin VSY, Pruski M. ^{29}Si NMR in solid state with CPMG acquisition under MAS. *J Magn Reson* 2008;**193**:233.
163. Kennedy GJ, Wiench JW, Pruski M. Determination of ^{27}Al–^{29}Si connectivities in zeolites with 2D ^{27}Al→^{29}Si RAPT–CPMG–HETCOR NMR. *Solid State Nucl Mag* 2008;**33**:76.
164. Xu J, Chen L, Zeng D, Yang J, Zhang M, Ye C, et al. Crystallization of AlPO4–5 aluminophosphate molecular sieve prepared in fluoride medium: a multinuclear solid-state NMR study. *J Phys Chem B* 2007;**111**:7105.
165. Peng L, Huo H, Liu Y, Grey CP. ^{17}O Magic angle spinning NMR studies of brønsted acid sites in zeolites HY and HZSM-5. *J Am Chem Soc* 2007;**129**:335.
166. Afeworki M, Cao G, Dorset DL, Strohmaier KG, Kennedy GJ. Multinuclear and multidimensional solid-state NMR characterization of EMM-8. *Micropor Mesopor Mat* 2007;**103**:216.
167. Fyfe CA, Brouwer DH. Determination of the location of naphthalene in the zeolite ZSM-5 host framework by solid-state ^{1}H/^{29}Si CP MAS NMR spectroscopy. *Can J Chem* 2006;**84**:345.
168. Trebosc J, Hu B, Amoureux JP, Gan Z. Through-space R3-HETCOR experiments between spin-1/2 and half-integer quadrupolar nuclei in Solid-State NMR. *J Magn Reson* 2007;**186**:220.
169. Azais GHT, Quignard S, Laurent G, Tourne-Peteilh C, Devoisselle J, Babonneau F. Solid-state NMR characterization of drug-model molecules encapsulated in MCM-41 silica. *Pure Appl Chem* 2009;**81**:1345.
170. Zhu J, Trefiak N, Woo T, Huang Y. An investigation of the adsorption of aromatic hydrocarbons in zeolite Na–Y by solid-state NMR spectroscopy. *Micropor Mesopor Mat* 2008;**114**:474.
171. Zhu J, Mosey N, Woo T, Huang Y. Study of the adsorption of toluene in zeolite LiNa-Y by solid-state NMR spectroscopy. *J Phys Chem C* 2007;**111**:13427.
172. Kao HM, Chang PC, Liao Y-W, Lee LP, Chien CH. Solid-state NMR characterization of the acid sites in cubic mesoporous Al-MCM-48 materials using trimethylphosphine oxide as a ^{31}P NMR probe. *Micropor Mesopor Mat* 2008;**114**:352.

173. Fyfe CA, Wong-Moon KC, Huang Y, Grondey H, Mueller KT. Dipolar-based 27Al. Fwdarw. ^{29}Si solid-state NMR connectivity experiments in zeolite molecular sieve frameworks. *J Phys Chem* 1995;**99**:8707.
174. Fild C, Eckert H, Koller H. Charge-induced partial ordering of boron around structure directing agents in zeolites observed by ^{13}C{^{11}B} rotational echo double resonance NMR. *J Am Chem Soc* 2000;**122**:12590.
175. Fyfe CA, Darton RJ, Schneider C, Scheffler F. Solid-state NMR investigation of the possible existence of "nanoblocks" in the clear solution synthesis of MFI materials. *J Phys Chem C* 2007;**112**:80.
176. Holland GP, Cherry BR, Alam TM. ^{15}N Solid-state NMR characterization of ammonia adsorption environments in 3A zeolite molecular sieves. *J Phys Chem B* 2004;**108**:16420.
177. Guillon E, Quoineaud AA, Armaroli T, Lacombe S, Gautier S. Characterization of the superacidit Y in zeolite Y by ^{27}Al MAS and ^{1}H/^{27}Al trapdor NMR and FTIR: corrrelation with catalytic activity. *Stud Surf Sci Catal* 2004;**154**:1539.
178. Luo Q, Deng F, Yuan Z, Yang J, Zhang M, Yue Y, Ye C. Using trimethylphosphine as a probe molecule to study the acid sites in Al−MCM-41 materials by solid-state NMR spectroscopy. *J Phys Chem B* 2002;**107**:2435.
179. Kao H-M, Yu C-Y, Yeh M-C. Detection of the inhomogeneity of Brønsted acidity in H-mordenite and H-β zeolites: a comparative NMR study using trimethylphosphine and trimethylphosphine oxide as ^{31}P NMR probes. *Micropor Mesopor Mat* 2002;**53**:1.
180. Liu H, Kao H-M, Grey CP. ^{1}H MAS and ^{1}H/^{27}Al TRAPDOR NMR studies of oxygen-zeolite interactions at Low temperatures: probing bronsted acid site accessibility. *J Phys Chem B* 1999;**103**:4786.
181. Holland GP, Alam TM. Location and orientation of adsorbed molecules in zeolites from solid-state REAPDOR NMR. *Phys Chem Chem Phys* 2005;**7**:1739.
182. Wang Q, Hu B, Lafon O, Trébosc J, Deng F, Amoureux JP. Double-quantum homonuclear NMR correlation spectroscopy of quadrupolar nuclei subjected to magic-angle spinning and high magnetic field. *J Magn Reson* 2009;**200**:251.
183. Liu Y, Zhang W, Liu Z, Xu S, Wang Y, Xie Z, et al. Direct observation of the mesopores in ZSM-5 zeolites with hierarchical porous structures by laser-hyperpolarized ^{129}Xe NMR. *J Phys Chem C* 2008;**112**:15375.
184. Thursfield A, Anderson MW. ^{1}H, ^{2}H, And ^{13}C solid-state NMR studies of methanol adsorbed on a series of acidic microporous zeotype materials. *J Phys Chem* 1996;**100**:6698.
185. Laha SC, Venkatesan C, Sakthivel A, Komura K, Kim TH, Cho SJ, Huang S, Wu P-H, Liu S-B, Sasaki Y, Kobayashi M, Sugi Y. Highly stable aluminosilicates with a dual pore system: simultaneous formation of meso- and microporosities with zeolitic BEA building units. *Micropor Mesopor Mat* 2010;**133**:82.
186. Jin C, Li G, Wang X, Zhao L, Liu L, Liu H, Liu Y, Zhang W, Han X, Bao X. Synthesis, characterization and catalytic performance of Ti-containing mesoporous molecular sieves assembled from titanosilicate precursors. *Chem Mater* 2007;**19**:1664.
187. Xu M, Harris KDM, Thomas JM. In situ solid-state ^{1}H NMR studies of hydration of the solid acid catalyst ZSM-5 in its ammonium form. *Solid State Nucl Mag* 2009;**35**:93.
188. Xu M, Harris K, Thomas J. Preferential clustering of water molecules during hydration of the ammonium form of the solid acid catalyst ZSM-5. *Catal Lett* 2009;**131**:16.
189. Lezcano-González I, Boronat M, Blasco T. Investigation on the Beckmann rearrangement reaction catalyzed by porous solids: MAS NMR and theoretical calculations. *Solid State Nucl Mag* 2009;**35**:120.
190. Arzumanov SS, Gabrienko AA, Freude D, Stepanov AG. In situ high temperature MAS NMR study of the mechanisms of catalysis. Ethane aromatization on Zn-modified zeolite BEA. *Solid State Nucl Mag* 2009;**35**:113.

191. Reddy Marthala VR, Rabl S, Huang J, Rezai SAS, Thomas B, Hunger M. In situ solid-state NMR investigations of the vapor-phase Beckmann rearrangement of ^{15}N-cyclohexanone oxime on MFI-type zeolites and mesoporous SBA-15 materials in the absence and presence of the additive ^{13}C-methanol. *J Catal* 2008; **257**:134–41.
192. Wang W, Jiang Y, Hunger M. Mechanistic investigations of the methanol-to-olefin (MTO) process on acidic zeolite catalysts by in situ solid-state NMR spectroscopy. *Catal Today* 2006;**113**:102–14.
193. Ivanova II, Nesterenko NS, Fernandez C. In situ MAS NMR studies of alkylaromatics transformations over acidic zeolites. *Catal Today* 2006;**113**:115.
194. Seiler M, Wang W, Hunger M. Local structure of framework aluminum in zeolite H−ZSM-5 during conversion of methanol investigated by in situ NMR spectroscopy. *J Phys Chem B* 2001;**105**:8143.
195. Stepanov AG, Luzgin MV. Interaction of acetonitrile with olefins and alcohols in zeolite H-ZSM-5: in situ solid-state NMR characterization of the reaction products. *Chem Eur J* 1997;**3**:47.
196. Man PP. Quadrupolar interactions. In: Harris, RK, Wasylishen, RE, eds-in-chief. *Encyclopedia of magnetic resonance*. Chichester: John Wiley. http://dx.doi.org/10.1002/9780470034590.emrstm0429, Published Online: 15 DEC 2011.
197. Samoson A, Lippmaa E, Pines A. High-resolution solid-state NMR averaging of 2nd-order effects by means of a double-rotor. *Mol Phys* 1988;**65**:1013.
198. Llor A, Virlet J. Towards high-resolution NMR of more nuclei in solids - sample spinning with time-dependent spinner axis angle. *Chem Phys Lett* 1988;**152**:248.
199. Dupree, R. Double rotation NMR. In: Harris, RK, Wasylishen, RE, eds-in-chief. *Encyclopedia of magnetic resonance*. Chichester: John Wiley. http://dx.doi.org/10.1002/9780470034590.emrstm1203, Published Online: 15 SEP 2011.
200. Goldbourt A, Madhu PK. Multiple-quantum magic-angle spinning: high-resolution solid-state NMR of half-integer spin quadrupolar nuclei. *Annu Rep NMR Spectroc* 2005;**54**:81.
201. Haeberlen U. High resolution NMR in solids: selective averaging. *Adv Magn Reson* 1976;(Suppl. 1) New York: Academic; 1976.
202. Waugh, JS. Average Hamiltonian theory. In: Harris, RK, Wasylishen, RE, eds-in-chief. *Encyclopedia of magnetic resonance*. Chichester: John Wiley. http://dx.doi.org/10.1002/9780470034590.emrstm0020, Published Online: 15 MAR 2007.
203. Duer MJ. *Solid state NMR spectroscopy: principles and applications*. Oxford, UK: Blackwell Science Ltd; 2002. 567pp.
204. FreudeD.Quadrupolar nuclei in solid-state nuclearmagnetic resonance. Encyclopedia of Analytical Chemistry. 2006, Published Online: 15 SEP 2006 http://dx.doi.org/10.1002/9780470027318.a6112.
205. Jung JK, Han OH, Choh SH. Sodium-23 MAS NMR study on nuclear quadrupole interaction in $Na_{1-x}Ag_xNO_2$. *Solid State Nucl Mag* 1999;**13**:255.
206. Vega AJ. Quadrupolar nuclei in solids. In: Harris, RK, Wasylishen, RE, eds-in-chief. *Encyclopedia of magnetic resonance*. Chichester: John Wiley. http://dx.doi.org/ 10.1002/9780470034590.emrstm0431.pub2, Published Online: 15 MAR 2010.
207. Vega S, Pines A. Operator formalism for double quantum NMR. *J Chem Phys* 1977;**66**:5624.
208. Rocha J, Morais CM, Fernandez C. Novel nuclear magnetic resonance techniques for the study of quadrupolar nuclei in clays and other layered materials. *Clay Miner* 2003;**38**:259.
209. DePaul SM, ERnst M, Shore JS, Stebbins JF, Pines A. Cross-polarization from quadrupolar nuclei to silicon using low-radio-frequency amplitudes during magic-angle spinning. *J Phys Chem B* 1997;**101**:3240.
210. Vega AJ. CP/MAS of quadrupolar S = 3/2 nuclei. *Solid State Nucl Mag* 1992;**1**:17.

211. Vega AJ. MAS NMR spin locking of half-integer quadrupolar nuclei. *J Magn Reson* 1992;**96**:50.
212. Vega S. Multiple-quantum cross-polarization NMR on spin systems with I=1/2 and S=3/2 in solids. *Phys Rev A* 1981;**23**:3152.
213. Sun W, Stephen JT, Potter LD, Wu Y. Rotation-induced resonance and second-order quadrupolar effects on spin locking of half-integer quadrupolar nuclei. *J Magn Reson Ser A* 1995;**116**:181.
214. Ashbrook SE, Wimperis S. Spin-locking of half-integer quadrupolar nuclei in nuclear magnetic resonance of solids: creation and evolution of coherences. *J Chem Phys* 2004;**120**:2719.
215. Amoureux JP, Pruski M. Theoretical and experimental assessment of single- and multiple-quantum cross-polarization in solid state NMR. *Mol Phys* 2002;**100**:1595.
216. Ashbrook SE, Brown SP, Wimperis S. Multiple-quantum cross-polarization in MAS NMR of quadrupolar nuclei. *Chem Phys Lett* 1998;**288**:509.
217. Hayashi S. Magic-angle-spinning nuclear-magnetic-resonance of half-integer quadrupole nuclei - effect of spin-locking efficiency on powder lineshapes. *Solid State Nucl Mag* 1994;**3**:93.
218. Ding SW, Mcdowell CA. Spin-locking spectral lineshapes of the central transition of half-integer quadrupole systems under magic-angle-spinning. *J Mol Struct* 1995;**355**:135.
219. Frydman L, Harwood JS. Isotropic spectra of half-integer quadrupolar spins from bidimensional magic-angle-spinning NMR. *J Am Chem Soc* 1995;**117**:5367.
220. Frydman, L. Multiple-quantum magic-angle spinning NMR of half-integer quadrupolar nuclei: fundamentals. In: Harris, RK, Wasylishen, RE, eds-in-chief. *Encyclopedia of magnetic resonance*. Chichester: John Wiley. http://dx.doi.org/10.1002/9780470034590.emrstm0333, Published Online: 15 MAR 2007.
221. Gan ZH. Isotropic NMR spectra of half-integer quadrupolar nuclei using satellite transitions and magic-angle spinning. *J Am Chem Soc* 2000;**122**:3242.
222. Gan, Z. Satellite transition NMR spectroscopy of half-integer quadrupolar nuclei under magic-angle spinning. In: Harris, RK, Wasylishen, RE, eds-in-chief. *Encyclopedia of magnetic resonance*. Chichester: John Wiley. http://dx.doi.org/10.1002/9780470034590.emrstm0481, Published Online: 15 MAR 2007.
223. Ashbrook SE, Wimperis S. High-resolution NMR of quadrupolar nuclei in solids: the satellite-transition magic angle spinning (STMAS) experiment. *Prog Nucl Mag Res Sp* 2004;**45**:53.
224. Smith ME, van Eck ERH. Recent advances in experimental solid state NMR methodology for half-integer spin quadrupolar nuclei. *Prog Nucl Mag Res Sp* 1999;**34**:159.
225. Amoureux, JP, Pruski, M. MQMAS NMR: experimental strategies and applications. In: Harris, RK, Wasylishen, RE, eds-in-chief. *Encyclopedia of magnetic resonance*. Chichester: John Wiley. http://dx.doi.org/:10.1002/9780470034590.emrstm0319.pub2, Published Online: 15 DEC 2008.
226. Amoureux JP, Fernandez C, Steuernagel S. z filtering in MQMAS NMR. *J Magn Reson Ser A* 1996;**123**:116.
227. Brown SP, Wimperis S. Two-dimensional multiple-quantum MAS NMR of quadrupolar nuclei. Acquisition of the whole echo. *J Magn Reson* 1997;**124**:279.
228. Gullion T, Vega AJ. Measuring heteronuclear dipolar couplings for I=1/2, S > 1/2 spin pairs by REDOR and REAPDOR NMR. *Prog Nucl Mag Res Sp* 2005;**47**:123.
229. Gullion T. Introduction to rotational-echo, double-resonance NMR. *Concept Magn Res*. 1998;**10**:277.
230. Huo H, Peng L, Grey CP. Measuring bronsted acid site O-H distances in zeolites HY and HZSM-5 with Low-temperature O-17-H-1 double resonance MAS NMR spectroscopy. *J Phys Chem C* 2011;**115**:2030.

231. Vaneck ERH, Veeman WS. Spin-density description of rotational-echo double-resonance, transferred-echo double-resonance and 2-dimensional transferred-echo double-resonance solid-state nuclear-magnetic-resonance. *Solid State Nucl Mag* 1993;**2**:307.
232. Hing AW, Vega S, Schaefer J. Transferred-echo double-resonance NMR. *J Magn Reson* 1992;**96**:205.
233. Hing AW, Vega S, Schaefer J. Measurement of heteronuclear dipolar coupling by transferred-echo double-resonance NMR. *J Magn Reson Ser A* 1993;**103**:151.
234. Gullion T. Measuring ^{13}C-^{2}D dipolar couplings with a universal REDOR dephasing curve. *J Magn Reson* 2000;**146**:220.
235. Nimerovsky E, Goldbourt A. Efficient rotational echo double resonance recoupling of a spin-1/2 and a quadrupolar spin at high spinning rates and weak irradiation fields. *J Magn Reson* 2010;**206**:52.
236. Grey CP, Vega AJ. Determination of the quadrupole coupling-constant of the invisible aluminum spins in zeolite HY with ^{1}H/^{27}Al TRAPDOR NMR. *J Am Chem Soc* 1995;**117**:8232.
237. Gullion T. Measurement of dipolar interactions between spin-1/2 and quadrupolar nuclei by rotational-echo, adiabatic-passage, double-resonance NMR. *Chem Phys Lett* 1995;**246**:325.
238. Vaneck ERH, Janssen R, Maas WEJR, Veeman WS. A novel application of nuclear spin-echo double-resonance to aluminophosphates and aluminosilicates. *Chem Phys Lett* 1990;**174**:428.
239. Li XJ, Zhang WP, Liu SL, Han XW, Xu LY, Bao XH. A high-resolution MAS NMR study on the potential catalysts Mo/HBeta for olefin metathesis: the interaction of Mo species with HBeta zeolite. *J Mol Catal A-Chem* 2006;**250**:94.
240. Simon A, Gougeon RD, Paillaud J-L, Valtchev V, Kessler H. Characterization of the acidity of Mu-14 by solid-state NMR and NH3-STD. *Phys Chem Chem Phys* 2001;**3**:867.
241. Ma D, Deng F, Fu R, Han X, Bao X. MAS NMR studies on the dealumination of zeolite MCM-22. *J Phys Chem B* 2001;**105**:1770.
242. Isobe T, Watanabe T, de la Caillerie JBD, Legrand AP, Massiot D. Solid-state ^{1}H and ^{27}Al NMR studies of amorphous aluminum hydroxides. *J Colloid Interf Sci* 2003;**261**:320.
243. Kao HM, Grey CP. Determination of the ^{31}P-^{27}Al- J-coupling constant for trimethylphosphine bound to the Lewis acid site of zeolite HY. *J Am Chem Soc* 1997;**119**:627.
244. Abraham A, Prins R, van Bokhoven JA, van Eck ERH, Kentgens APM. TRAPDOR double-resonance and high-resolution MAS NMR for structural and template studies in zeolite ZSM-5. *Solid State Nucl Mag* 2009;**35**:61.
245. Goldbourt A, Vega S, Gullion T, Vega AJ. Interatomic distance measurement in solid-state NMR between a spin-1/2 and a spin-5/2 using a universal REAPDOR curve. *J Am Chem Soc* 2003;**125**:11194.
246. Hughes E, Gullion T, Goldbourt A, Vega S, Vega AJ. Internuclear distance determination of S=1, I=1/2 spin pairs using REAPDOR NMR. *J Magn Reson* 2002;**156**:230.
247. Chopin L, Vega S, Gullion T. A MAS NMR method for measuring ^{13}C-^{17}O distances. *J Am Chem Soc* 1998;**120**:4406.
248. Naito A, Saitô H. Accuracy limitations on internuclear distances measured by REDOR. In: Harris RK, Wasylishen, RE, editors-in-chief. *Encyclopedia of magnetic resonance*. Chichester: John Wiley. http://dx.doi.org/:10.1002/9780470034590.emrstm0002, Published Online: 15 MAR 2007.
249. Schnell I. Dipolar recoupling in fast-MAS solid-state NMR spectroscopy. *Prog Nucl Mag Res Sp* 2004;**45**:145.

INDEX

Note: Page numbers followed by "*f*" indicate figures, and "*t*" indicate tables.

D

E

F

G

H

I

L

M

N

O

P

Q

R

S

T

X

Z